

*See
Ved for Kadish*

Environmental Assessment of the Alaskan Continental Shelf

LIBRARY
ARCTIC REGION
NOAA
ANCHORAGE, ALASKA 99507

Final Reports of Principal Investigators Volume 3. Physical Science Studies



U.S. DEPARTMENT OF COMMERCE
National Oceanic & Atmospheric Administration
Office of Marine Pollution Assessment



U.S. DEPARTMENT OF INTERIOR
Bureau of Land Management

October 1981

Environmental Assessment of the Alaskan Continental Shelf

Final Reports of Principal Investigators
Volume 3. Physical Science Studies

ARCTIC

ANCHORAGE, ALASKA



U.S. DEPARTMENT OF COMMERCE
National Oceanic & Atmospheric Administration
Office of Marine Pollution Assessment



U.S. DEPARTMENT OF INTERIOR
Bureau of Land Management

October 1981

The facts, conclusions and issues appearing in these reports are based on interim results of an Alaskan environmental studies program managed by the Outer Continental Shelf Environmental Assessment Program (OCSEAP) of the National Oceanic and Atmospheric Administration (NOAA), U.S. Department of Commerce, and primarily funded by the Bureau of Land Management (BLM), U.S. Department of Interior, through interagency agreement.

DISCLAIMER

Mention of a commercial company or product does not constitute an endorsement by National Oceanic and Atmospheric Administration. Use for publicity or advertising purposes of information from this publication concerning proprietary products or the tests of such products is not authorized.

TABLE OF CONTENTS
Volume 3 - Physical Science Studies

<u>RU</u>	<u>PI/Agency</u>	<u>Title</u>	<u>Page</u>
016	Aagaard, K. -University of Washington Seattle, WA	Current Measurements in Possible Dispersal Regions of the Beaufort Sea	001
138	Muench, R.D. <u>et al.</u> -Pacific Marine Env. Lab Seattle, WA	Physical Oceanographic and Meteorological Conditions in the Northwest Gulf of Alaska	075
436	Schleuter, R.S. and C.I. Rauw	Oil Spill Trajectory Simulation Lower Cook Inlet - Shelikof Strait, Alaska	231
436	Schleuter, R.S. and M.W. Miller -Dames and Moore Los Angeles, CA	Wind Field Transition Matrix Analysis Lower Cook Inlet--Shelikof Strait, Alaska	347
436	Schleuter, R.S. and C.I. Rauw -Dames and Moore Los Angeles, CA	Evaluation of CODAR Data Lower Cook Inlet, Alaska	381
568	Cox, J.C. <u>et al.</u> -ARTEC, Incorporated Columbia, MD	The Transport and Behavior of Oil Spilled In and Under Sea Ice	427

*Note: title page
has RU 91*

FINAL NARRATIVE REPORT

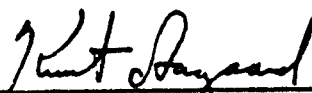
Contract No.: 03-5-022-67, T.O. 3
Research Unit No.: 91
Reporting Period: 1 October 1979-31 December 1980
Number of Pages: 74

Current Measurements in Possible Dispersal Regions
of the Beaufort Sea

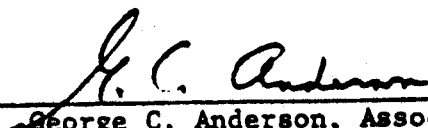
Knut Aagaard

Department of Oceanography
University of Washington
Seattle, Washington 98195

21 January 1981



Knut Aagaard, Research Professor
Principal Investigator



George C. Anderson, Associate Chairman
for Research, Dept. of Oceanography

Introduction

The Alaskan Beaufort Sea shelf extends some 600 km along the entire north coast of Alaska, from 156°30' - 141°W. The shelf is relatively narrow, with the shelf break typically 80-90 km offshore. Much of the coast is marked by numerous shallow embayments and by lagoons and barrier islands.

An important oceanographic factor is the sea ice, which essentially covers the entire area for all but 2-3 months of the year. Its physical effects include the following. (1) It provides thermostatic control, buffering the nearby temperature field in such a way as to keep it at the freezing point. (2) During its formation the ice serves as surface salt source (and hence a density source) by virtue of brine rejection. This drives gravitational convection. (3) During melting, the ice serves as a fresh water source (and hence a buoyancy source), stabilizing the surface layers. This has consequences for solar heat retention, for example. (4) The wind stress acts through the medium of the ice. This is most important nearshore, where the ice is landfast, so that the water is to some extent insulated from the local wind stress.

As to fresh water runoff from land, good estimates are lacking, since only three of the rivers have been gauged. However, on an annual basis, the fresh water discharge is not large. For example, Walker (1973) has estimated the annual discharge of the Colville, which is the largest of the rivers, as about 10^{10} m^3 , or only one-twentieth that of the Yukon. The runoff is highly seasonal, with the majority occurring during a short period in early summer.

The wind field is known primarily from surface wind observations at coastal stations, which show predominantly ENE winds in the western portion, but a bimodal ENE-WSW distribution in the eastern portion (compare Searby and Hunter,

1971, and Hufford, Lissauer and Welsh, 1976). Winds are moderately strong, with monthly mean speeds in excess of 6 m sec^{-1} .

Sea level variations are caused by both meteorological and astronomical tides. The largest sea level variations in the Beaufort Sea are due to storm surges, with measured sea level departures ranging from +3.0 m to -0.9 m (Schaeffer, 1966; Matthews, unpublished data). The largest setup appears to occur in the fall, when relatively long stretches of open water provide maximum fetch. Negative surges apparently are most common in winter (Henry, 1975).

The astronomic tides in the Beaufort Sea, which are mixed semidiurnal, are small, with mean ranges from 10-30 cm, i.e., only one-tenth the largest meteorological tides. For example, Matthews (1971) has estimated the amplitude of the principal lunar tide (M_2) at Pt. Barrow as 4.7 cm. The tide wave appears to approach the shelf from the north, showing little phase change from Barrow to Demarcation Point.

It is against this background that we shall discuss our work in the Beaufort Sea, the primary goal of which was a description and understanding of the shelf circulation, including its relationship to adjacent regions. The work involved both hydrographic sections (R.U. 151) and moored current measurements (R.U. 91).

The measurements

The hydrography consisted of about 110 CTD stations. The first year of field work, three CTD sections were run across the shelf by helicopter during each of the periods October-November 1975, February 1976 and May 1976, which were taken to respectively represent the fall, winter and spring. The following field season, four sections were run, again by helicopter, in each of the periods

October-November 1976 and March 1977. The approximate location of all of these sections is shown schematically in Figure 1, where PP (Pitt Point), NI (Narwhal Island), and HB (Humphrey Bay) denote the 1975-76 sections, and LW and LE (Lonely West and East) and OW and OE (Oliktok West and East) denote the 1976-77 sections. The temporal coverage is indicated in Figure 2. These data have been discussed earlier in RU 151 reports, including the Final Report of 21 June 1978, but we shall have frequent occasion to further use the results in the present discussion of the shelf circulation.

The current measurements were made with bottom-moored instruments, using the techniques for ice-covered waters described by Aagaard, Darnall and Karig (1978). Exceptions are the two records offshore from Narwhal Island (NAR-1 and -2), which are from instruments suspended from fast ice. All measurements are therefore in a true Eulerian reference frame, except for the last few days of the NAR-2 record, when the ice from which the instrument was suspended began to move. However, radar tracking of the site allowed this motion to be subtracted from the current record. The current meters also recorded time series of temperature. The sampling interval for the various instruments ranged from 15-60 minutes, depending upon the intended deployment time. A total of about 2335 days of usable records were obtained. The temporal distribution of the measurements is again shown in Figure 2, while Figure 3 shows the spatial coverage. A listing of mooring particulars is given in Table 1.

Implications of the hydrography

The principal features of the temperature and salinity distributions form a useful starting point for a discussion of the shelf circulation.

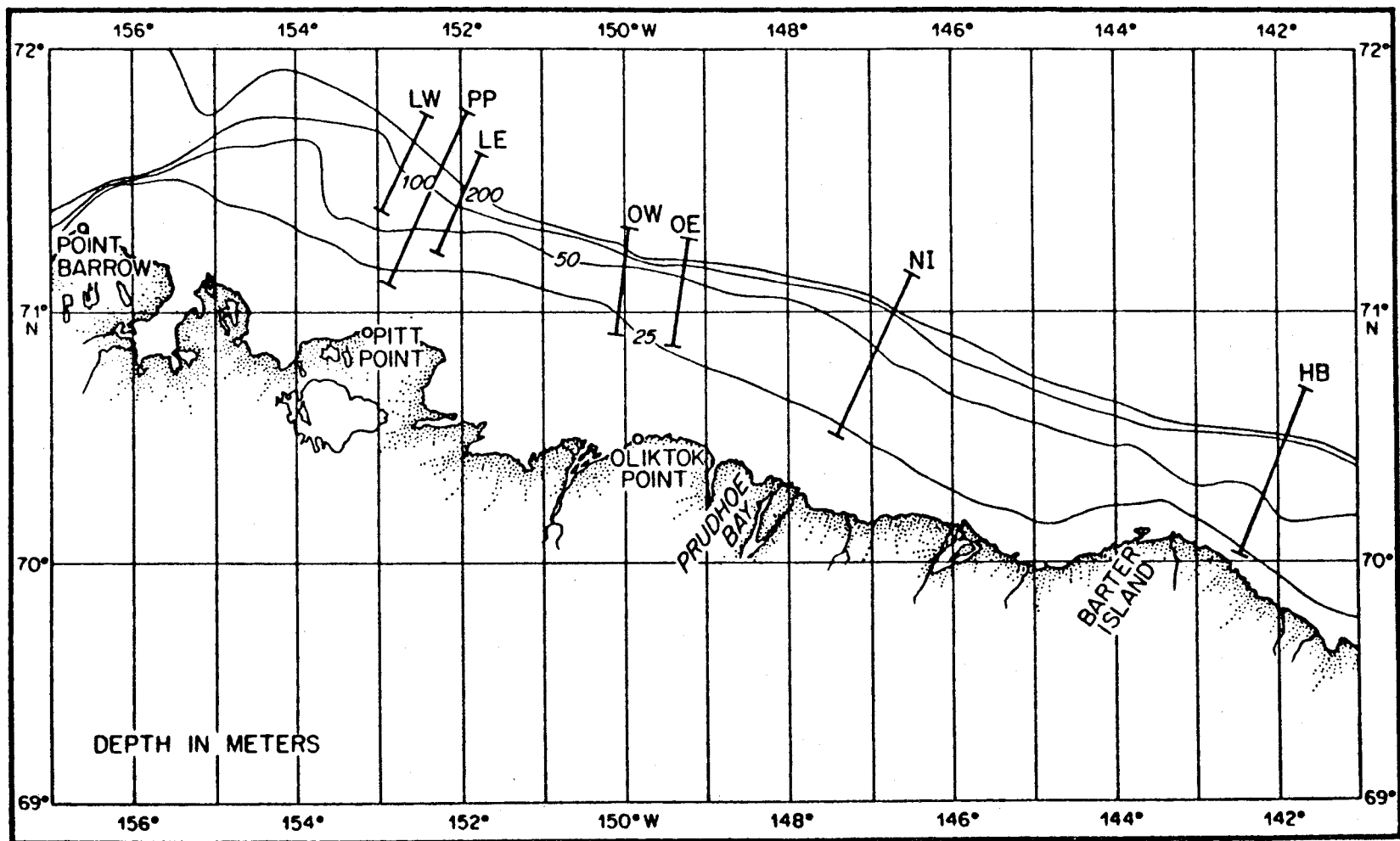


Figure 1. Location of CTD sections, 1975-1977.

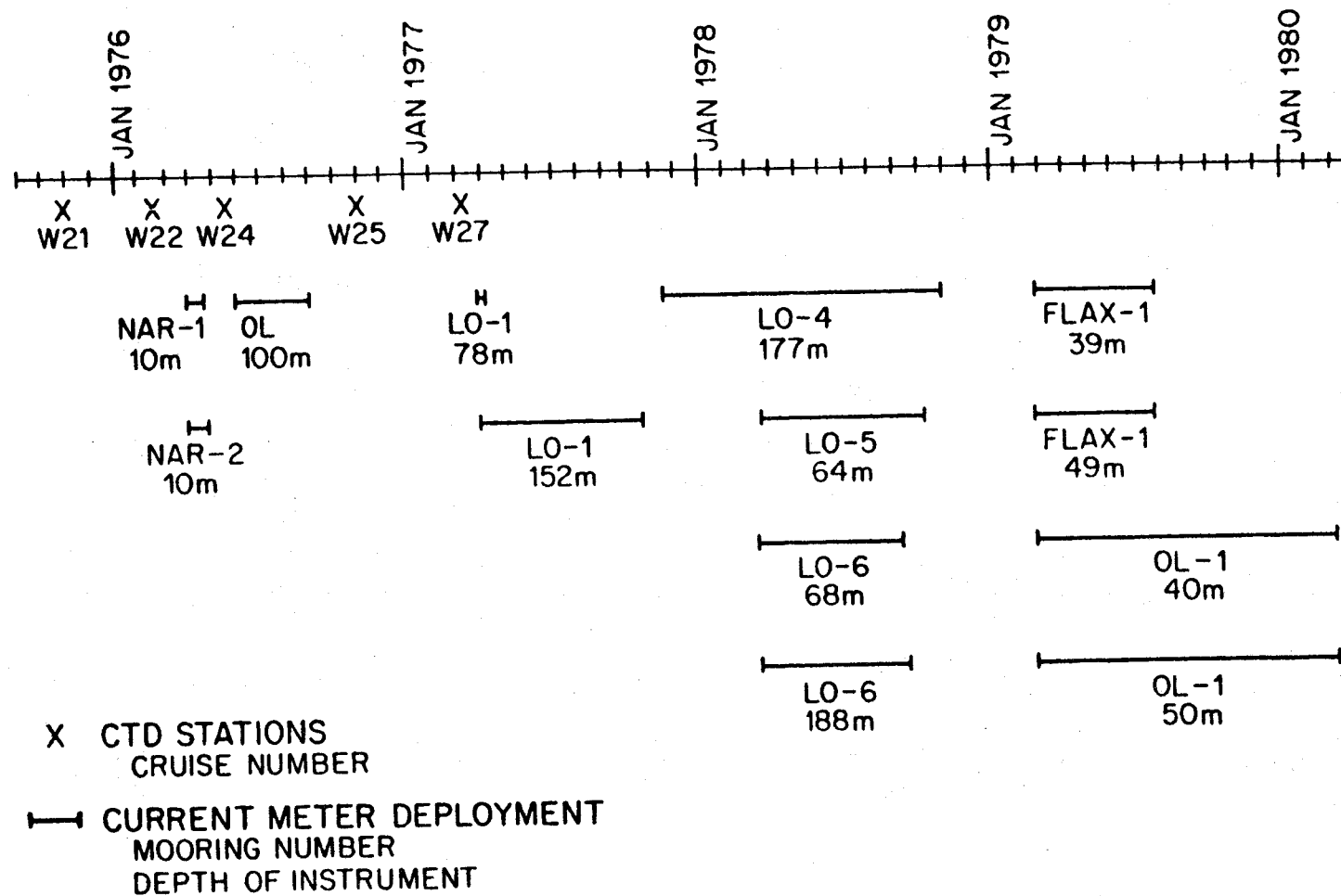


Figure 2. Distribution in time of CTD and current measurements.

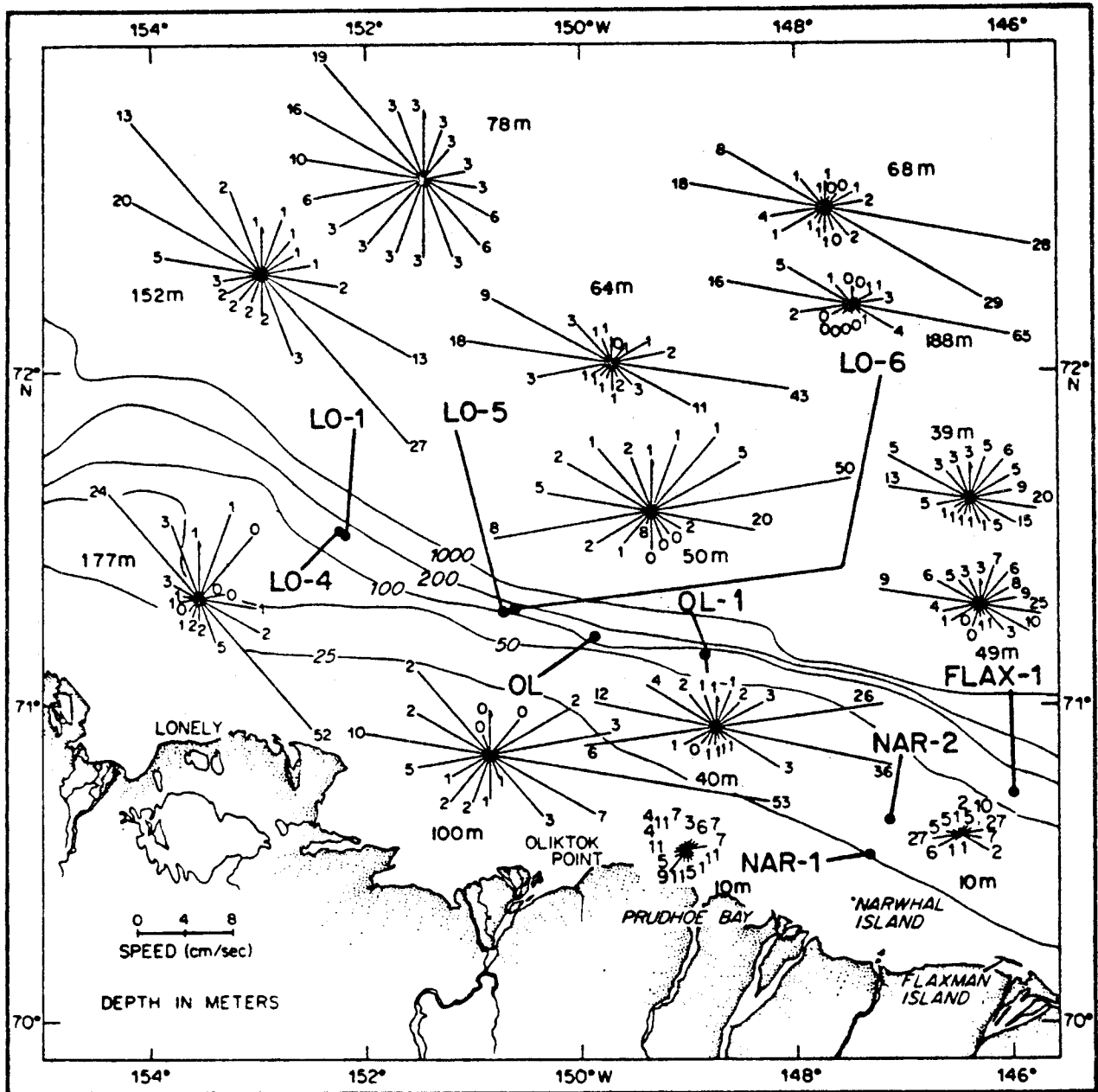


Figure 3. Current roses at all mooring sites. Each vector represents the mean current in a sector of 20°. The number at the end of each vector is the frequency of occurrence of a current within that sector. Depth of measurement shown adjacent to each rose. Heavy dots show mooring locations.

TABLE 1
RU 91 Current Records

Mooring	Latitude	Longitude	Sounding	Instrument Depth	Valid Record	
					Begins (GMT)	Ends
NAR-1	70°38.7'N	147°09.0'W	27 m	10 m	28 March 1976	19 April 1976
NAR-2	70°32.2'N	147°20.0'W	38 m	10 m	"	22 April 1976
OL	71°12.6'N	149°53.0'W	225 m	100 m	27 May 1976	1 Sept. 1976
LO-1	71°31.1'N	152°11.3'W	192 m	78 m	29 March 1977	6 April 1977
LO-1	"	"	192 m	152 m	"	20 October 1977
LO-4	71°31.8'N	152°15.3'W	192 m	177 m	13 Nov. 1977	30 October 1978
LO-5	71°17.0'N	150°44.1'W	99 m	64 m	13 March 1978	7 October 1978
LO-6	71°17.7'N	150°37.9'W	203 m	68 m	11 March 1978	4 September 1978
LO-6	"	"	203 m	188 m	"	14 September 1978
FLAX-1	70°43.6'N	146°00'W	59 m	39 m	22 Feb. 1979	22 July 1979
FLAX-1	"	"	59 m	49 m	"	"
OL-1	71°10.0'N	148°52.7'W	60 m	40 m	21 Feb. 1979	6 March 1980
OL-1	"	"	60 m	50 m	"	"

Influx from the Bering Sea. In summer the most prominent hydrographic signal on the shelf is a subsurface temperature maximum, generally found seaward of about 40-50 m. An example is given in Figure 4, showing a temperature section across the shelf at 150°W during August 1972 (from Mountain, 1974). This temperature maximum is associated with the eastward flow of water originating in the Bering Sea. The influx was first described by Johnson (1956), and it has since been discussed by Hufford (1973), Mountain (1974), Paquette and Bourke (1974) and others.

The warm water that enters the Beaufort Sea has come through eastern Bering Strait and followed the Alaskan coast around Barrow. This intrusion is in fact composed of two water masses, called Alaskan coastal water and Bering Sea water by Mountain (1974). The former can have summer temperatures west of Barrow as high as 5-10°C, but the salinities are low, being less than 31.5‰. The Bering Sea water is more saline and is contained in the density range 25.5 to slightly over 26.0 (in sigma-t), as has been demonstrated in the detailed analyses of Mountain (1974) and Coachman, Aagaard and Tripp (1975). Figures 5 and 6 are adapted from Mountain (1974) and show the temperature on density surfaces associated with the two intruding water masses. The restriction of the eastward flow to the outer continental shelf and slope is clear, as is the difference in extent of influence of the two water masses. The Alaskan coastal water mixes rapidly with the ambient surface water as it moves eastward and is not clearly identifiable east of about 147-148°W. On the other hand, the Bering Sea water, with its deeper temperature maximum (in the sigma-t range 25.5-26.0), can be traced at least as far as Barter Island at 143°W.

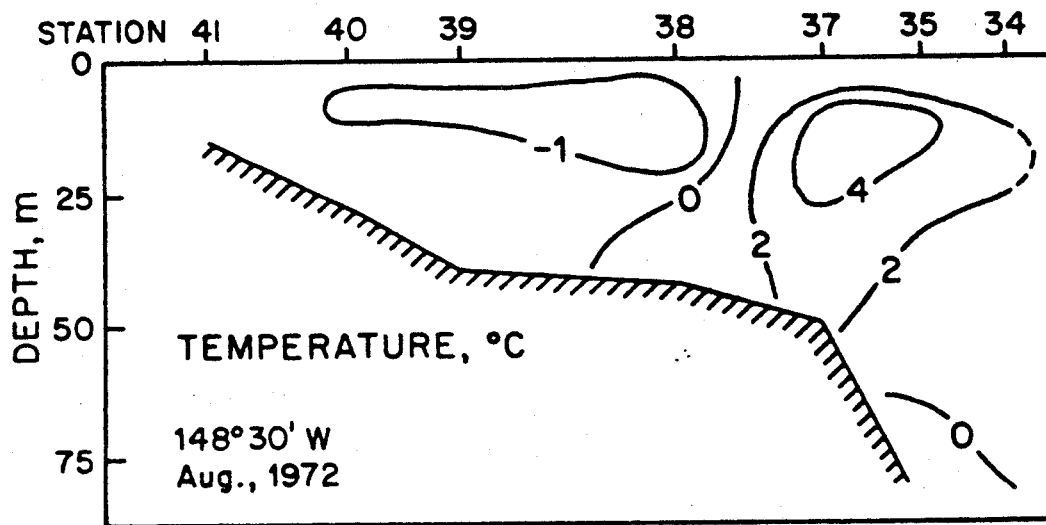


Figure 4. Summer temperature section across the shelf.
From Mountain (1974).

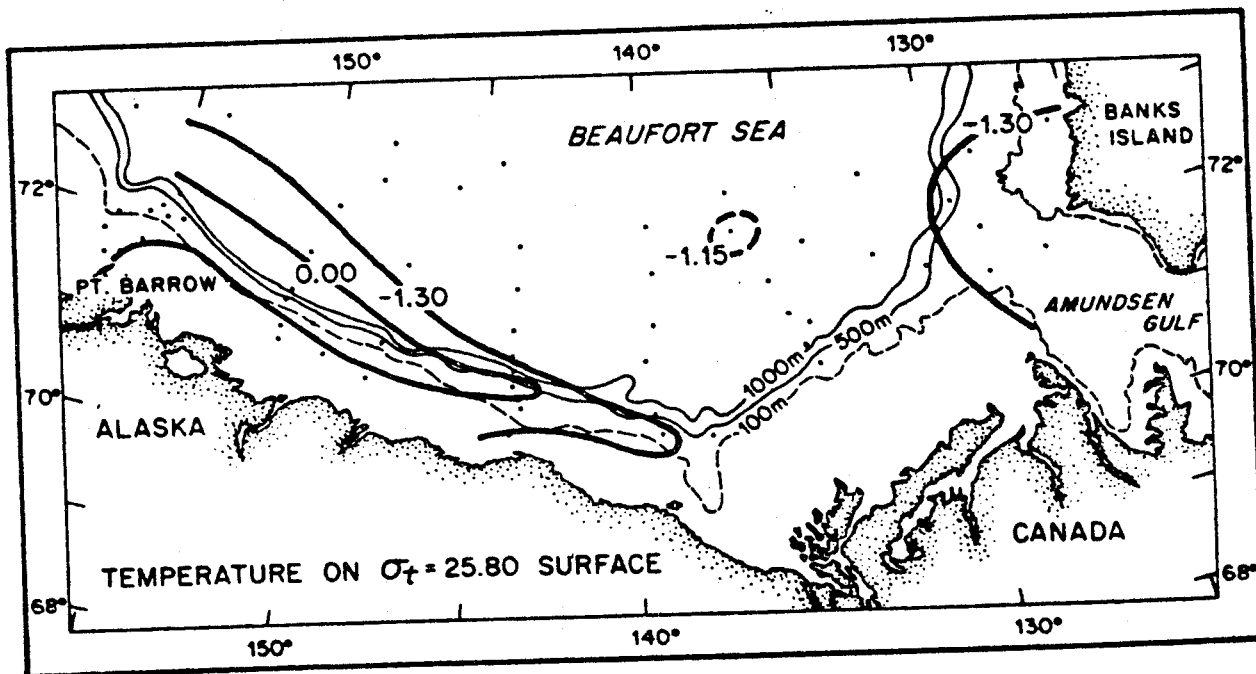
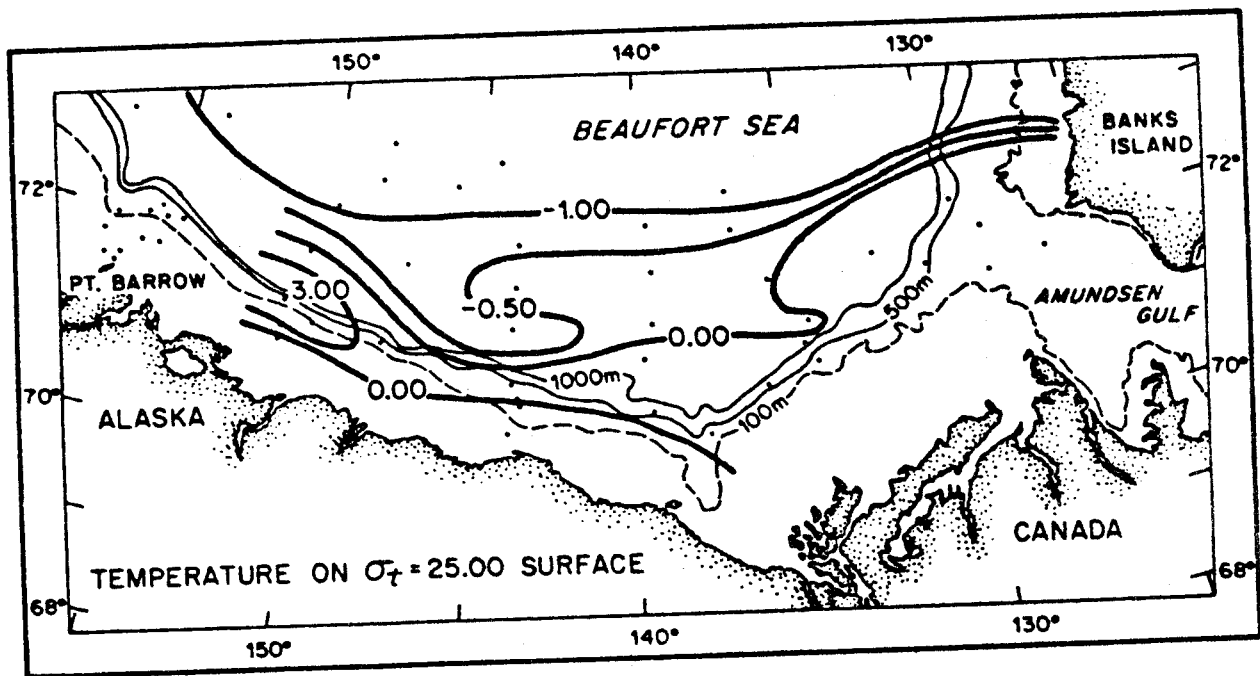


Figure 5. Temperature on density surfaces corresponding to Alaskan coastal water ($\sigma_t = 25.00$) and Bering Sea water ($\sigma_t = 25.80$), August-September 1951. Adapted from Mountain (1974).

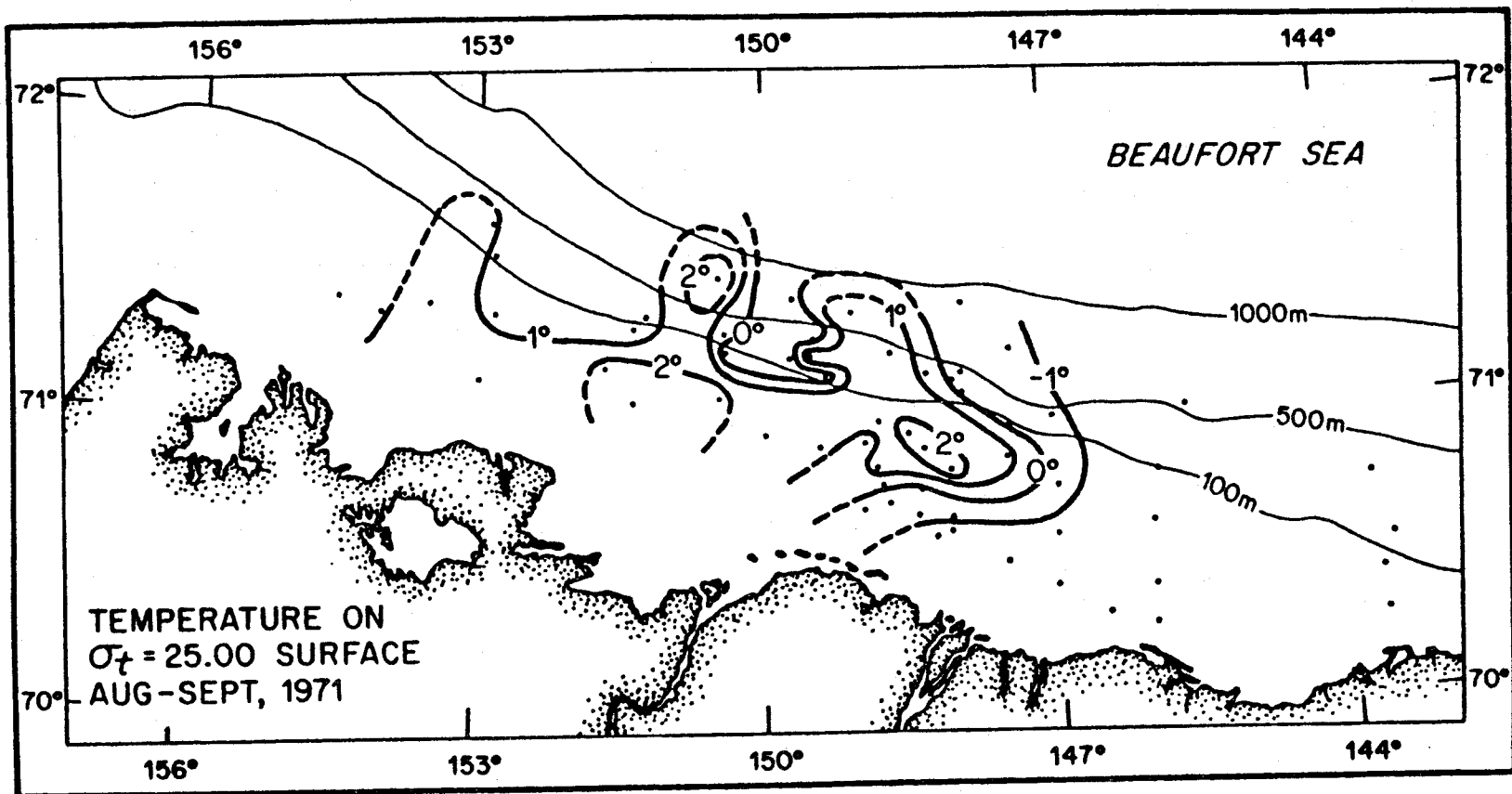


Figure 6. Summer temperature on density surface $\sigma_t = 25.00$. Adapted from Mountain (1974).

The patchiness of the temperature distribution in Figure 6 is of particular interest. Mountain (1974) has attributed such features to variations in the influx of warm water onto the Beaufort shelf, and in fact the appropriate variability has been observed upstream along the Chukchi Sea coast. In Mountain's view the eastward flow over the Beaufort shelf is driven externally by the momentum flux of the upstream flow, with its attendant pulsations. While both scale analysis and observations available at that time suggested that the interpretation may be reasonable, it is not clear why such a flow should follow the isobaths eastward, as it appears to do (e.g., cf. Figure 5), for the geometry is such as to destabilize an eastward flow attempting to conserve potential vorticity.

The temperature maximum on the shelf is primarily a summer phenomenon. Figure 7 shows the T-S correlation at two stations in the LW section. Station W 25-19 was taken in early November 1976 and W 27-1 at the same location the following March. The temperature maximum of about -0.9°C at 43 m at station 19 occurred at $\sigma_t = 25.8$ and represents Bering Sea water having rounded Point Barrow earlier in the year at a higher temperature. Sometime later in the winter, the Bering Sea temperature signal is effectively erased on the shelf, as shown by the T-S correlation in the upper 50 m at station W 27-1: down to about 40 m, where the density is 26.5 m in sigma-t, the water is at the freezing point. Such low temperatures extending into or past the density range of the core of Bering Sea water are typical on the shelf in winter, and in fact these conditions can readily be found already in November. One can therefore in general probably not trace the Bering Sea water on the Beaufort shelf much past freeze-up in the fall. We should also note that after that time the new water entering the Beaufort Sea from the Chukchi is itself near the freezing point after being cooled in its fall and winter transit northward.

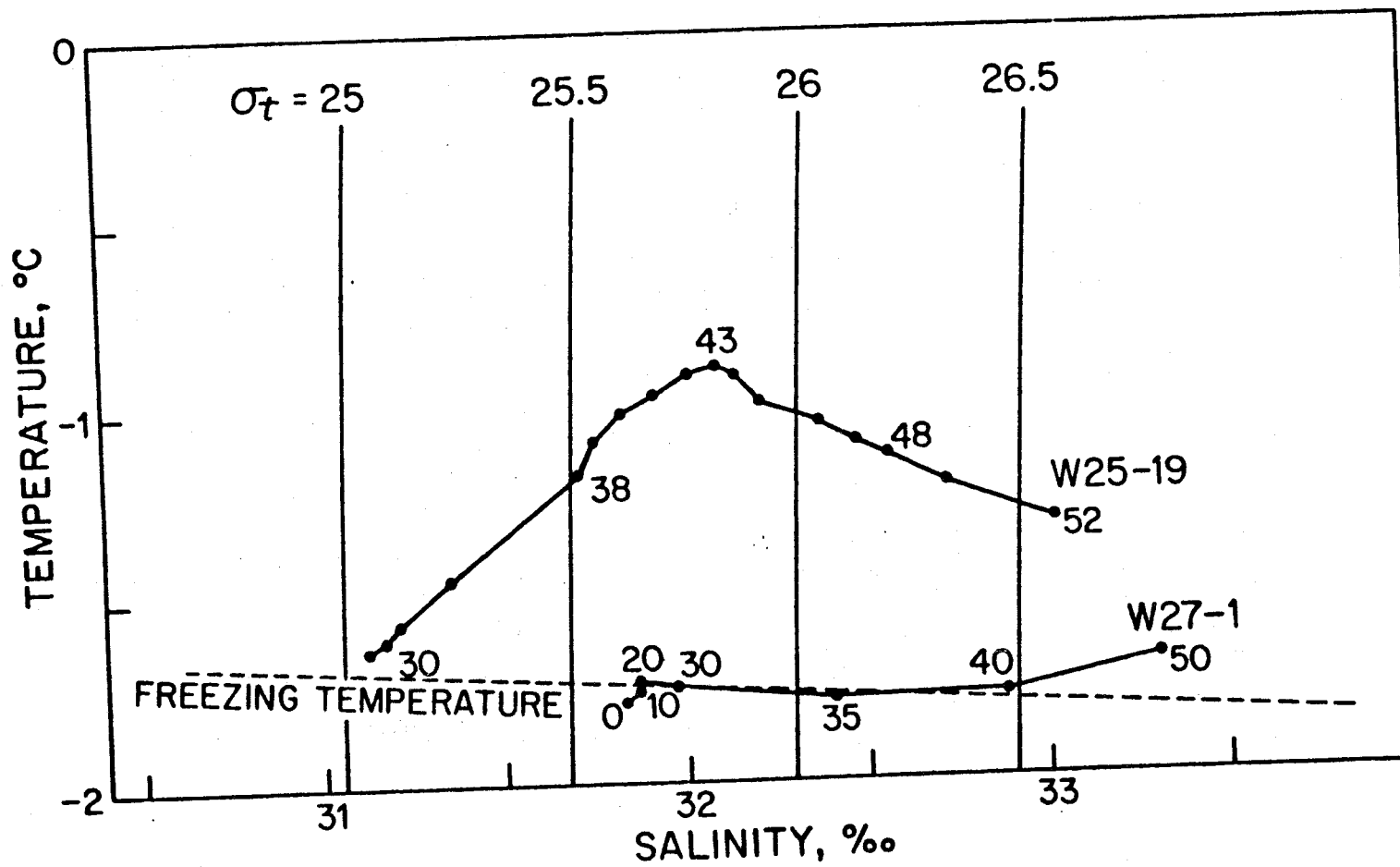


Figure 7. Temperature-salinity correlations at a fall and winter station in Section LW.

Upwelling. There are also other hydrographic signals which provide significant information on the shelf circulation. Among these are the various indicators of upwelling. That is, water has been found on the shelf with characteristics appropriate to a location relatively deep offshore. Such hydrographic anomalies may occur in temperature, salinity, oxygen, nutrients, and other fields. An example from the eastern Alaskan Beaufort shelf during summer was described by Hufford (1974), who found evidence for upwelling from about the 125 m level offshore (cf. Figure 8). He ascribed the upwelling to easterly winds driving a coastal Ekman divergence during periods of open water.

We have observed what appears to be a very different kind of upwelling, with the upwelled water derived from offshore depths of 200 m or more. Figure 9, showing sections LW and OE during October-November 1976, provides an example. Note that in the OE section, water warmer than 0°C and more saline than 34.5‰ was observed as shallow as 91 m. Comparison with conditions the following winter at the same location (Figure 10) shows that such water is found offshore at about the 200 m level during undisturbed conditions (no upwelling). Note further that at section LW, some 120 km to the west, upwelling was also observed, with relatively warm and saline water apparent even at the innermost station, where the bottom 10 m were warmer than -1°C and more saline than 34‰ . The upwelling is therefore not a strictly local phenomenon, but can occur over long stretches of the shelf. However, it is important to note that neither during nor within at least 10 days prior to the section occupations in the fall of 1976 were there strong or prolonged easterly winds, so that the elevated isopleths are not readily explainable as representing a wind-driven coastal upwelling event.

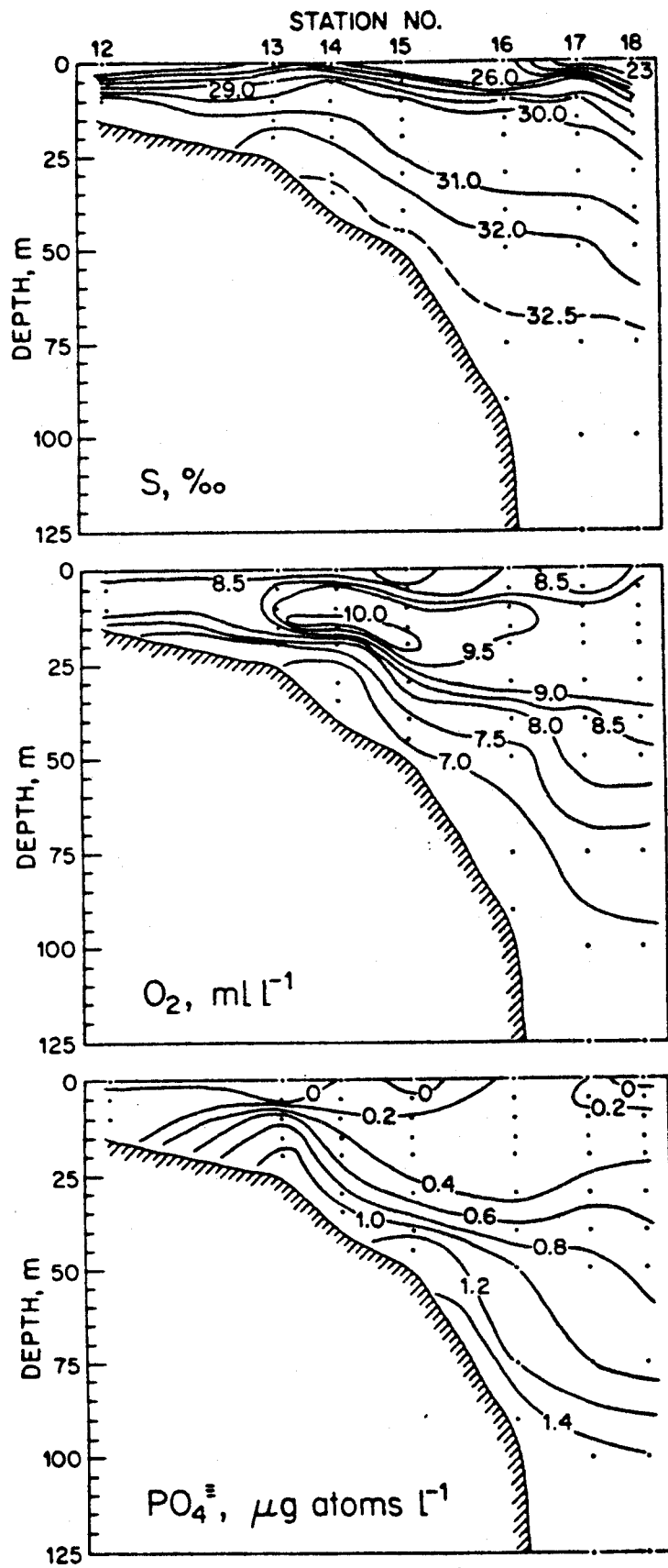


Figure 8. Salinity, oxygen and phosphate distributions in an August 1972 section along 145°W. Adapted from Hufford (1974).

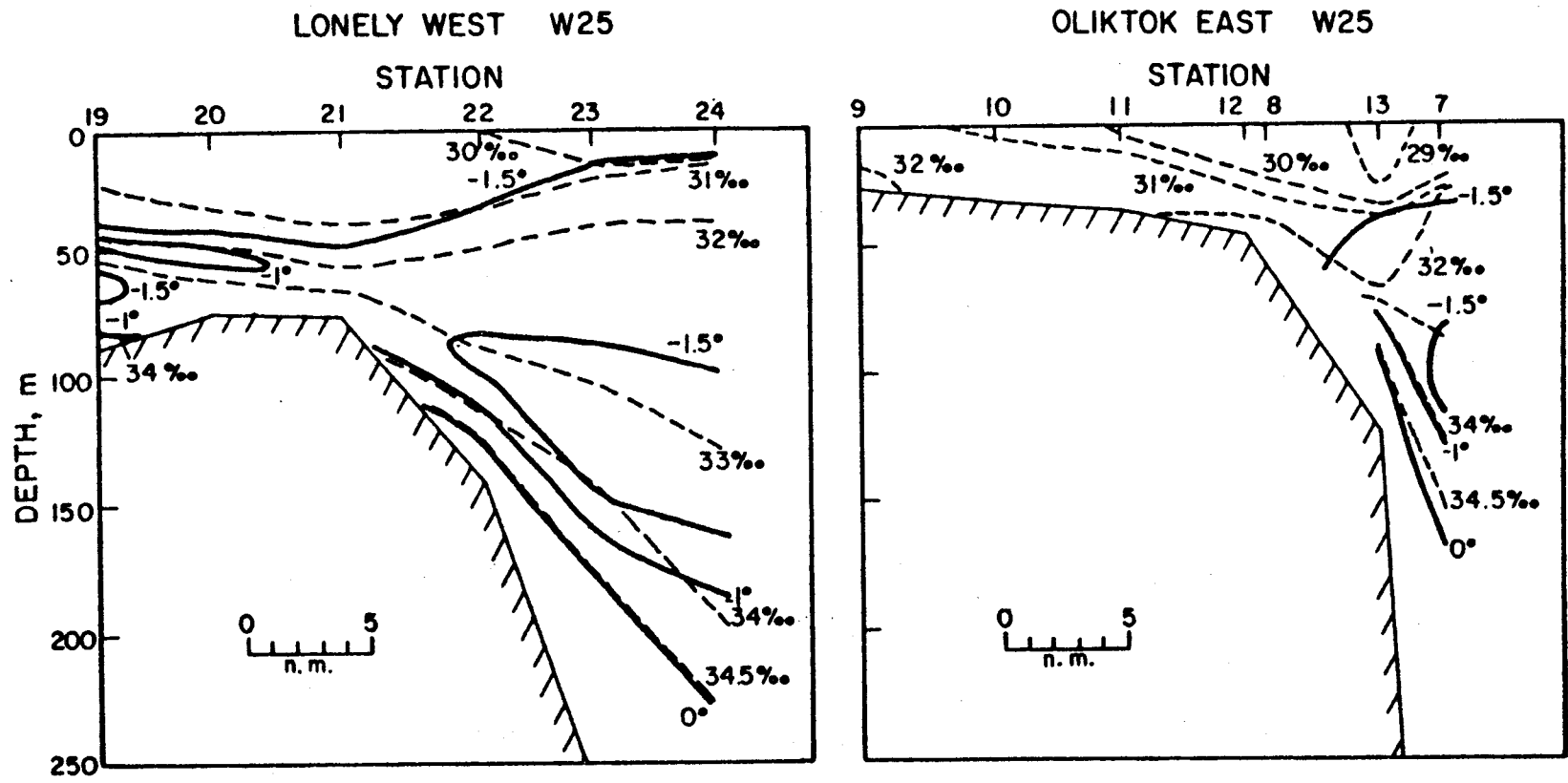


Figure 9. Temperature and salinity distribution along Sections LW and OE, October-November 1976.

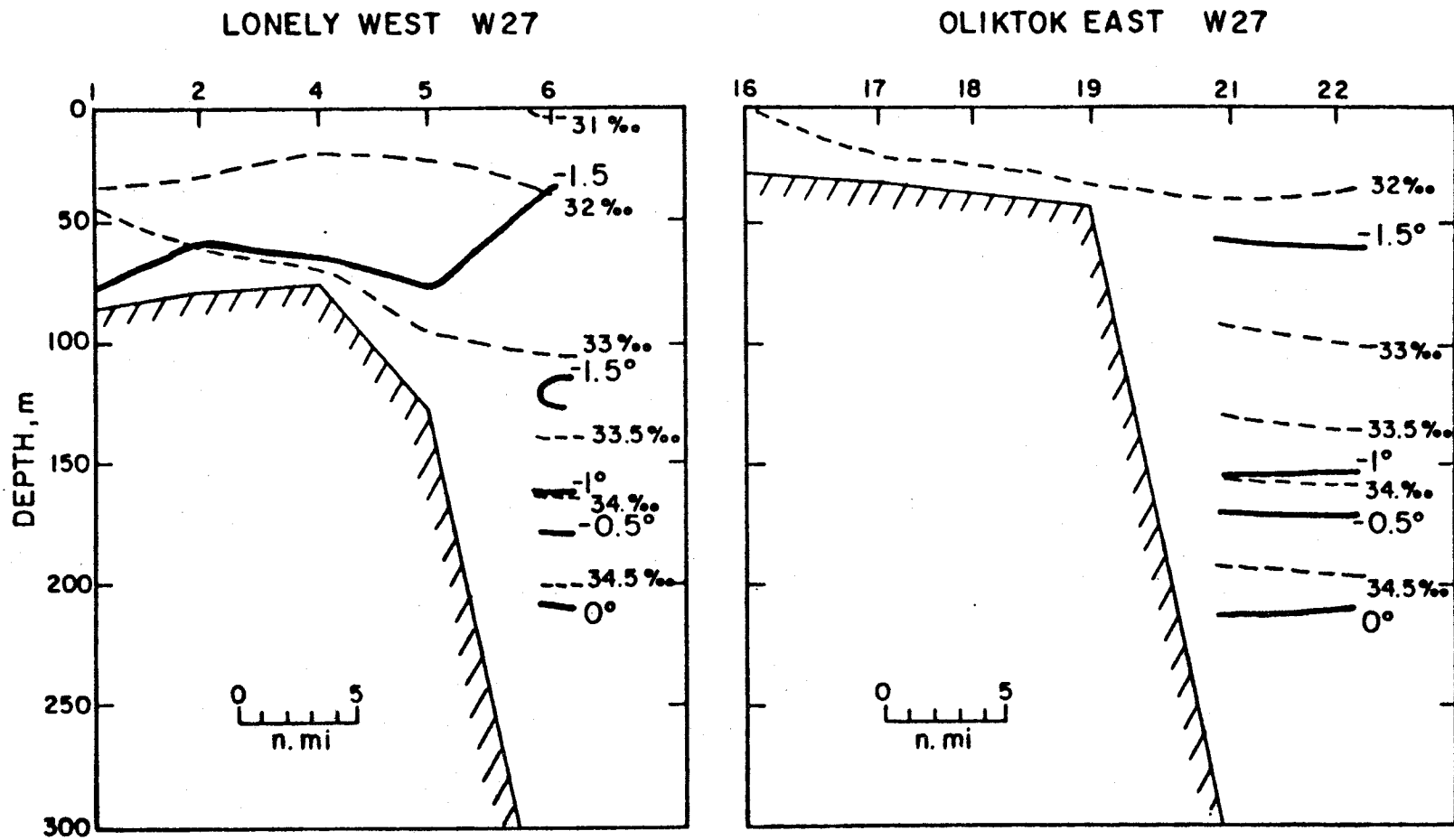


Figure 10. Temperature and salinity distribution along Sections LW and OW, March 1977.

We have seen the deep isopycnals sloping upward toward the shelf in a sufficiently large number of the sections to suggest that the phenomenon is relatively common. Furthermore, there is often a change in the sign of the vertical geostrophic shear at the outermost stations in these sections. Typically, this occurs at a depth of 50-80 m, and while the geostrophic flow field cannot be uniquely determined from these measurements alone, a reasonable reconstruction is that a core of relatively dense water at mid-depth (50-100 m) was moving westward with a component up-slope. The core speed at such times may be quite high, as suggested by a geostrophic velocity difference between 70 and 200 db of 55 cm sec^{-1} at the time of the stations in Figure 9.

Cross-shelf circulation. A third feature of the hydrography also has implications for the shelf circulation, viz. the seasonal change in the cross-shelf salinity gradient in the upper layer. During summer the salinity in the upper layer increases seaward across the shelf. This situation persists into the fall as a relic feature, but by mid-winter the gradient has reversed, with salinity decreasing seaward. An example is seen in Figures 11 and 12, respectively showing the HB section in November 1975 and February 1976. In Figure 11 the remnants of the summer situation are still dominant, with the near-surface salinity increasing outward across the shelf by $2^\circ/\text{‰}$. However, in Figure 12 the situation is reversed, the salinity decreasing from $30.7^\circ/\text{‰}$ at station 18 to $29.9^\circ/\text{‰}$ at station 24.

While the summer salinity distribution almost certainly represents the effect of fresh water runoff, the winter distribution likely results from a cross-shelf circulation component. Two possibilities suggest themselves.

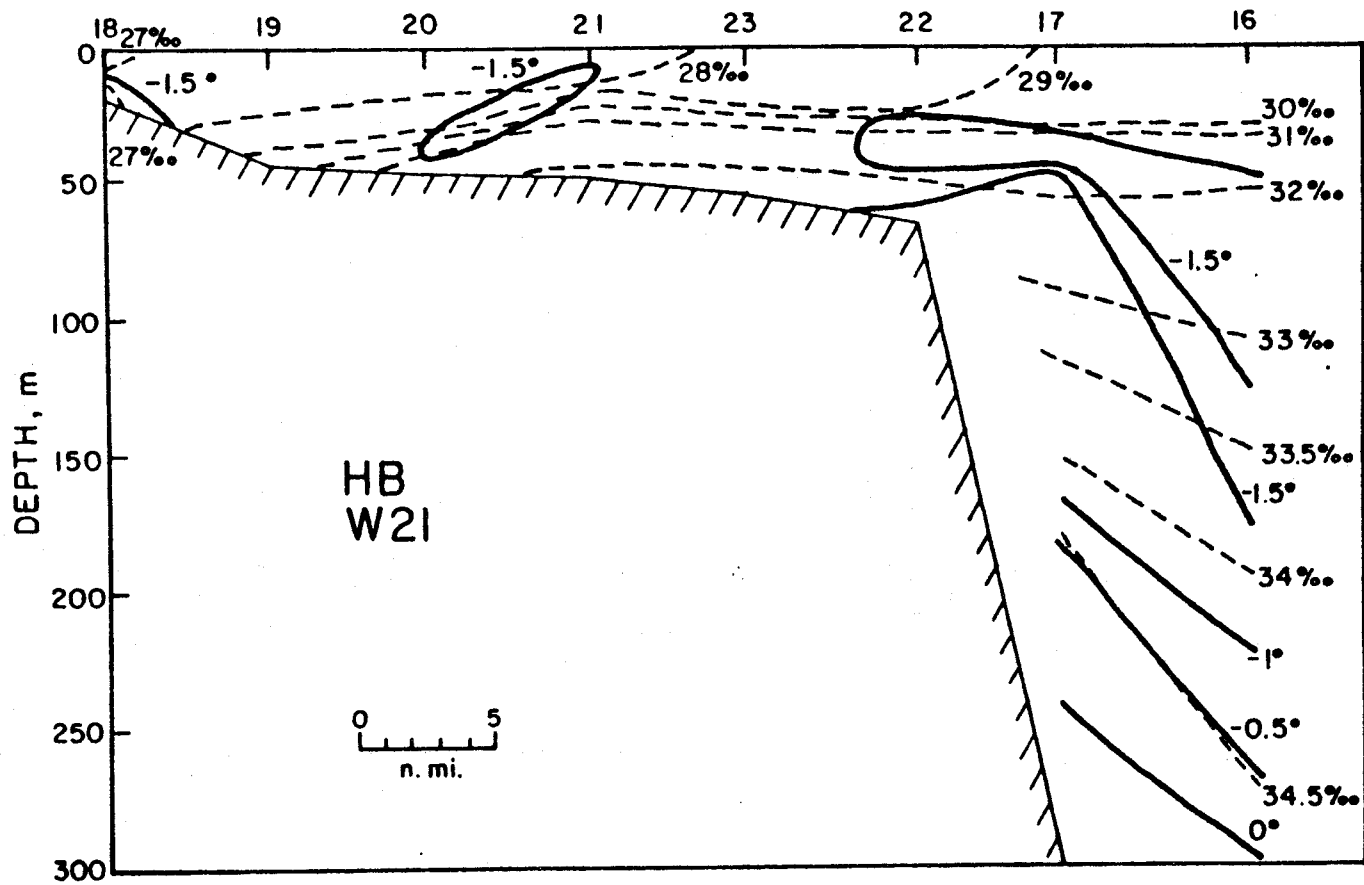


Figure 11. Temperature and salinity distribution along Section HB, November 1975.

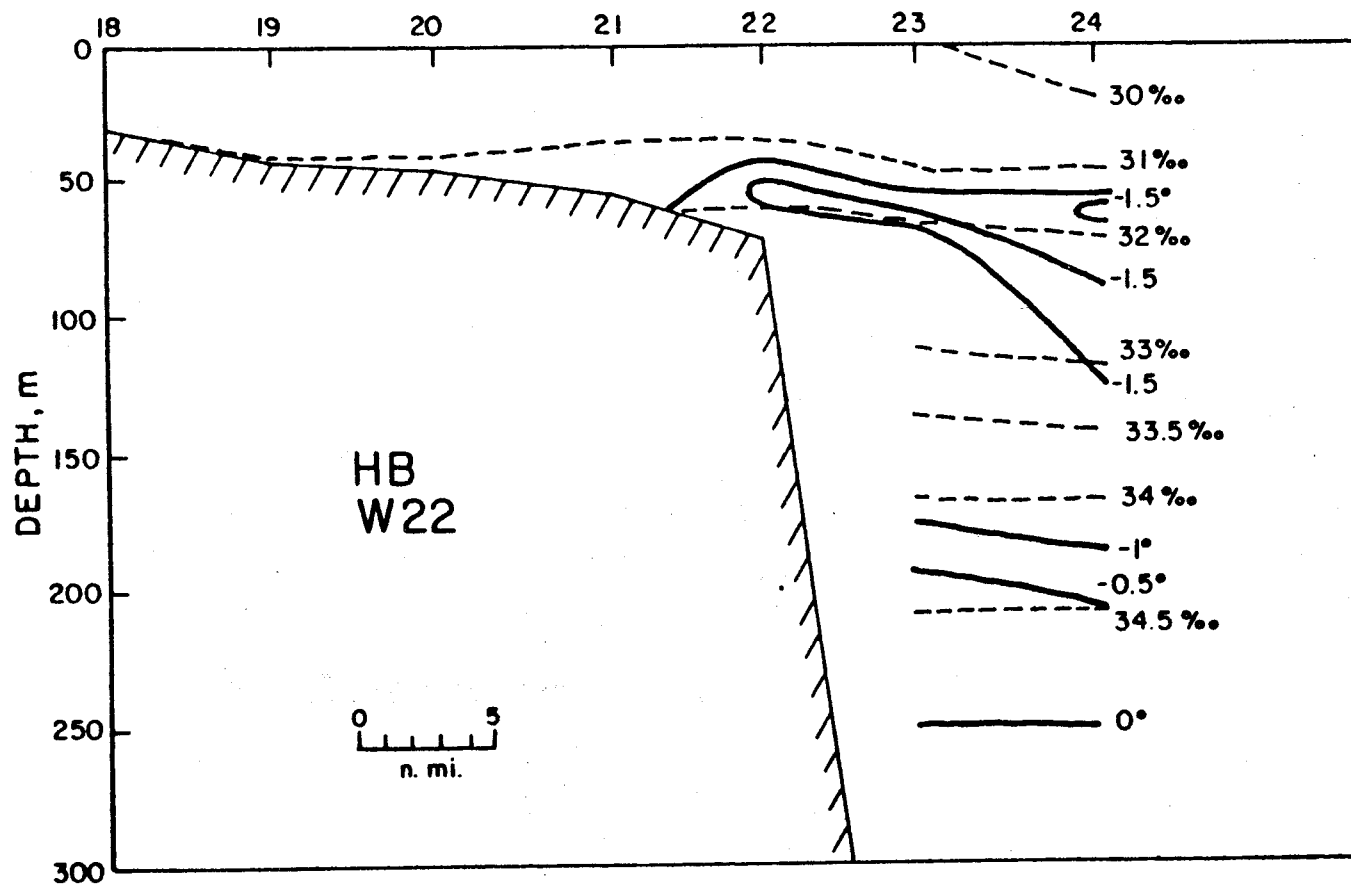


Figure 12. Temperature and salinity distribution along Section HB, February 1976.

One is that relatively dense water sinking from the upper layer above the shelf moves into the Arctic Ocean at mid-depth and is replaced by less saline water moving inshore in the upper layer. Such a transverse circulation is in the counter-clockwise sense (looking westward along the shelf) and would be driven by a shallow salt source on the shelf. Freezing is of course an obvious example of such a salt source, its relatively greater intensity inshore conceivably being due either to the volume of water underlying a given surface area being less there, or to the amount of ice actually formed on the shelf being greater than offshore, for example due to a wind-driven divergence along the coast such as has been shown to be of major import in the Bering and Chukchi seas (Aagaard, Coachman and Carmack, in press). Speaking against the latter possibility is the fact that the Beaufort coast does not typically show persistent ice-free areas in winter. Alternatively, relatively saline water being advected onto the shelf from the Chukchi Sea and later sinking from the shelf could also drive such a transverse circulation. Regardless of the details, a counter-clockwise circulation involves some form of free gravitational convection and is driven by a source of dense water on the shelf. The importance to the climatology of the Arctic Ocean of such mechanisms operating in the shelf seas has recently been discussed by Aagaard, Coachman and Carmack (in press).

The second possible mechanism responsible for the observed salinity distribution is upward movement of saline water onto the shelf from deeper levels in the Arctic Ocean. This water would have to flow in near the bottom and then be subjected to a relatively effective vertical mixing on the inner or middle shelf. Such a transverse circulation is in the clockwise sense (looking westward) and would in effect be driven by a deep salt source

seaward of the shelf. It thus represents a forced convection. We have already discussed the evidence that such upwelling actually occurs, and in a later consideration of the temperature records from the moored instruments we shall see that it is a frequent occurrence throughout the year.

As a word of caution, we should not assume that the cross-shelf circulation is merely in a transverse mode, for there are rotational constraints on the dynamics. For example, for the case of a salt source on the shelf, the dense, saline waters attempting to flow off the shelf will be deflected by the effect of the Earth's rotation until geostrophic equilibrium is reached. Therefore the actual feeding of the dense shelf water into the Arctic Ocean likely would either depend on transport in the bottom Ekman layer or on channeling by submarine bathymetry. Once the dense water crosses the shelf break, it must eventually sink to the depth where its density matches that of the ambient oceanic waters, at which point it will detach from the bottom and spread into the interior ocean.

Mixed-layer depth. A final winter hydrographic feature with implications for the ^{circulation} ~~hydrography~~ is that the depth to which a layer is mixed (in the sense that above this depth the density is nearly uniform) is considerably shallower than the depth to which the water is at the freezing point. Two examples are shown in Figure 13, one a fall and the other a winter station. At both stations a notable pycnocline (caused by a salinity gradient) of about 0.05 in σ_t per meter begins at about 20 m, while the water is at the freezing point to more than twice this depth. Thus, water that has clearly been conditioned by the freezing process can subsequently be found within or below the pycnocline. In effect, the water must have moved obliquely down to the depth locally

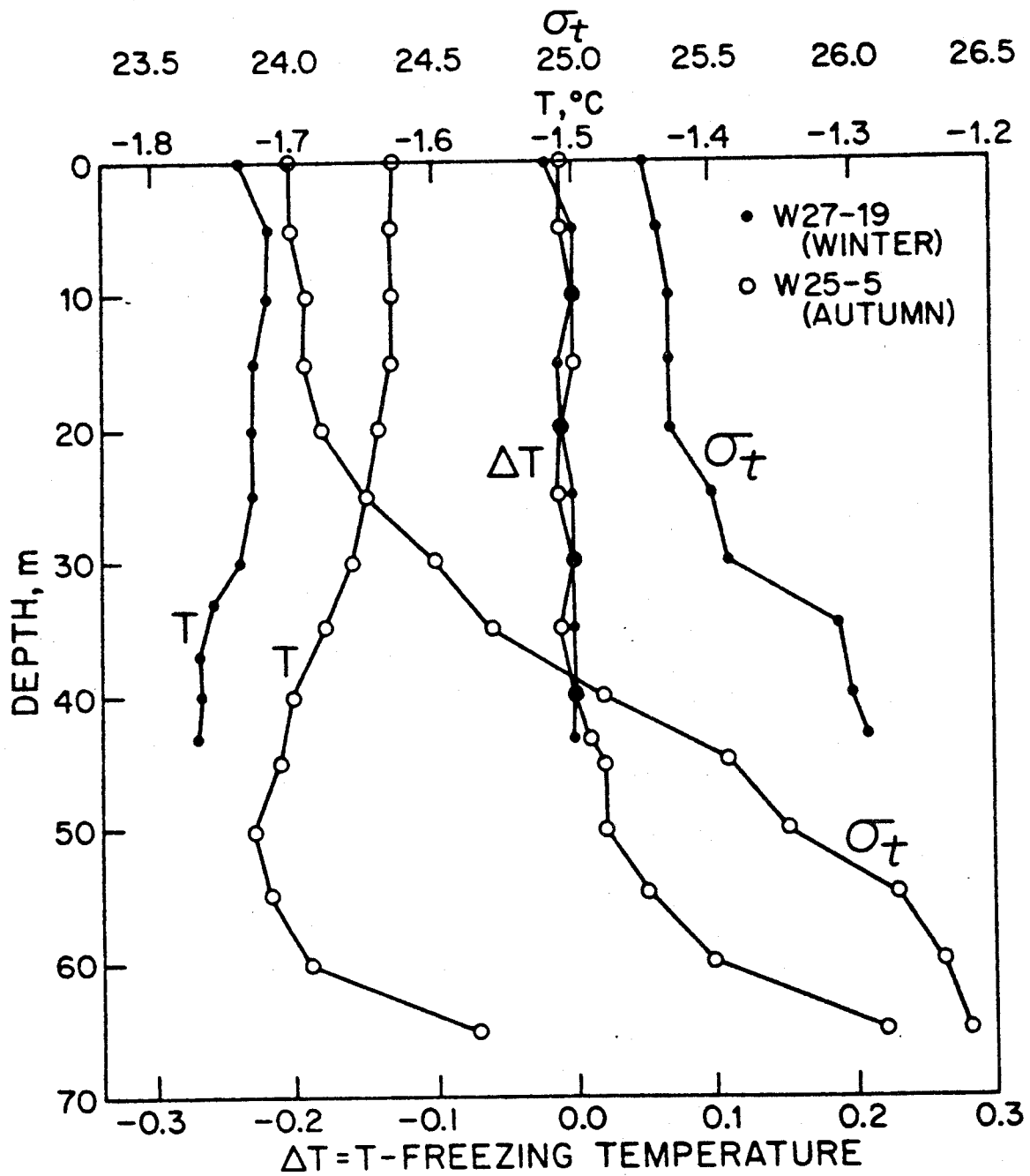


Figure 13. Vertical distributions of temperature, density (σ_t), and departure from freezing point at a fall and winter station on the shelf.

appropriate to its density. An observed winter water column on the shelf is thus not simply representative of a local and vertically extensive mixing process driven by freezing, but rather it represents a layering of waters that may have been influenced by freezing at a variety of locations and times. After being cooled, and probably also having their salinity altered, the various parcels of water then arrange themselves in a stably stratified layer through differential motion. In other words, the hydrography shows that the time history of a column of water involves considerable vertical shearing even in winter.

The inner shelf

We noted earlier that the water moving eastward from the Chukchi Sea is normally found seaward of the 40-50 m isobaths. This depth range proves to be a convenient demarcation zone, separating two different circulation regimes, *viz.* the inner and outer shelf. We shall treat the inner shelf first.

Current measurements on the inner shelf are extremely sparse, largely because of the difficulty of maintaining moorings in ice-covered shallow waters; the moorings are simply ripped away by the drifting ice. However, in March-April of 1976 we obtained two three-week records on the inner shelf, NAR-1 and -2 in, respectively, just under 30 and 40 m of water (cf. Figure 3 and Table 1). In each case an instrument was suspended at 10 m depth from fast ice.

Figure 3 shows the current roses for these two instruments, as well as for the other current records obtained on the shelf under our OCSEAP work. Note that at each indicated mooring site, the current rose for a particular

instrument (instrument depth given adjacent to the rose) represents both the mean speed and the direction, the latter in terms of the frequency of occurrence of the current in each sector of angular measure 20 degrees of arc. For example, at mooring LO-5 on the outer shelf, which recorded from 13 March to 7 October 1978 (cf. Table 1), the current was predominantly toward $100 \pm 10^\circ T$. It registered in this sector 43% of the time, and the mean speed over the nearly 7 months was about 15 cm sec^{-1} . At the same location the next most commonly observed current was in the reciprocal direction, and in the mean it was about 2 cm sec^{-1} slower (i.e., 13 cm sec^{-1}). Note that Figure 3 by itself provides no information on observational time spans, and must therefore be examined together with Table 1. For example, at site LO-1 the rather round current rose at 78 m represents just over a week of measurements, whereas the elongated elliptical rose at 152 m represents nearly seven months and is therefore in a probabilistic sense far more representative of the current conditions.

Consider now the NAR-1 and -2 records in Figure 3. It is apparent both that the flow was quite slow and that there was little net motion. Examination of the individual records shows that the currents never exceeded 10 cm sec^{-1} and were generally less than 5 cm sec^{-1} . The mean flow during the three weeks was essentially negligible, being only 0.1 cm sec^{-1} at NAR-2 and 0.3 cm sec^{-1} at NAR-1; both were directed WSW.

The two instruments were separated by only 14 km, and the progressive vector diagrams (Figure 14) show that the low-frequency variability was quite similar at the two sites. For example, after some initial motion NE, both instruments showed SW motion from about 1-6 April, followed by some irresolute wandering (but with a small net northward displacement) until 14 April, when two days of stronger motion toward the east occurred. Finally, from 16 April

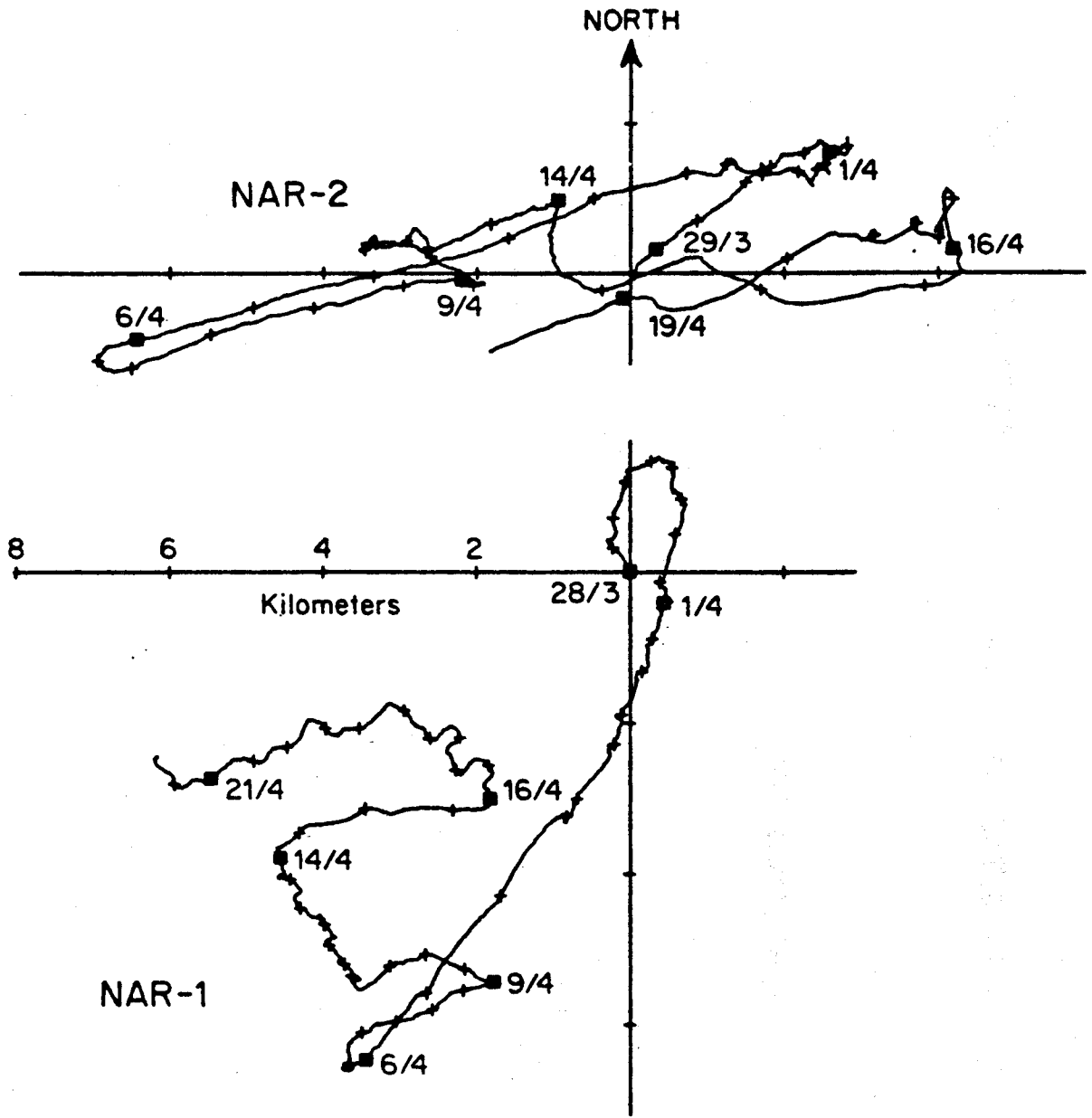


Figure 14. Progressive vector diagrams at NAR-1 and NAR-2.

until the end of the record the motion was westerly. A comparison with the simultaneous wind record from Narwhal Island suggests that the flows were in fact wind-driven. That is, the winds the last few days of March were from the WSW up to 14 knots. Then followed a long period of NE winds with speeds to 13 knots. From 6-13 April the wind was variable, but from 13-15 April strong winds (to 18 knots) blew from between NW and SW. Finally, from late on 15 April until the end of the record, generally E or NE winds prevailed. Comparison with the wind statistics of Searby and Hunter (1971) and Hufford, Lissauer and Welsh (1976) shows these observed wind conditions to be climatically representative in the distributions both of speed and direction. While it might appear puzzling at first why the currents under fast ice should reflect the wind conditions so well, the key probably lies in the instruments being quite close to the edge of the fast ice. (In fact, during the last few days of the NAR-2 record, the ice from which the current meter was suspended broke loose and was in motion.) Close to the edge, the water may, for example, be moved by lateral entrainment. We should expect a decreasing wind response landward of the fast ice edge, as the shore is approached, and in fact Figure 14 suggests that this is indeed the case. That is, the indicated water displacements at the inshore site (NAR-1) under strengthened wind conditions are appreciably less than at the offshore site (NAR-2). For example, contrast the displacements at the two sites from 14-16 April under relatively strong W winds and from 16 April onward under E winds.

The suggestion of a relatively direct wind-driven regime in winter near- and offshore from the fast ice edge is in accord with the observed summer situation on the inner shelf. For example, Barnes and Reimnitz (1974); Barnes, Reimnitz and McDowell (1977); Drake (1977); Hufford and Bowman (1974);

Hufford, Fortier, Wolfe, Doster and Noble (1974); Hufford, Thompson and Farmer (1977); and Wiseman, Sukeyda, Hsu, and Walters (1974) have all shown evidence of such wind-driven effects. In general there is a westward water motion corresponding to the prevailing easterly winds, but the circulation responds rapidly to changing wind conditions, such that under westerly winds (which is the secondary wind mode) the motion is eastward. An interesting summer feature that has been pointed out by Barnes and Toimil (1979) is that east of about 146°W the nearshore flow appears to be predominantly easterly. They suggested that it is associated with the more frequent occurrence of westerly winds in the eastern Beaufort Sea than in the western portion. If this is in fact so, then the tendency should be greatest in winter, when the westerly winds achieve their greatest prominence as a result of mountain barrier baroclinicity (Schwerdtfeger, 1974).

In any case the clear suggestion of our very sparse winter flow measurements on the inner shelf is that even though the kinetic energy levels are suppressed in winter (at least under the fast ice), the circulation is predominantly wind-driven throughout the year. How far inshore under the fast ice the wind effects persist, is not known.

Neither can we at this point say anything conclusive about the transverse circulation on the inner shelf. In addition to the direct driving by the wind, at least three possible mechanisms are available for forcing such a circulation. The first is an estuarine effect, in which in the pure case the upper-layer flow is driven seaward by the accumulated effect of runoff; there would normally be a compensating deeper landward flow in all but the shallowest water. Because of the extremely seasonal character of the runoff, this mechanism could only be of significance during peak runoff in early summer. [For example, note the

absence of an effluent plume off the Colville River in August in the work of Hufford and Bowman (1974).] Furthermore, the lack of lateral constraints on the flow means that rotational effects would give rise to primarily a longshore current rather than one normal to the coast. Under these circumstances the cross-shelf transport would have to be accomplished in an Ekman layer, or by turbulent diffusion, or by some other non-estuarine means.

A second possible mechanism for cross-shelf circulation is wind-driven upwelling (or downwelling) at the edge of the fast ice. For example, under easterly winds, a surface Ekman layer divergence at the ice edge would drive upwelling, the water for which in the net would have to be supplied by an onshore flow at lower levels. Experimental evidence for the existence of such upwelling along a free ice edge has been found by Buckley, Gammelsrød, Johannessen, Johannessen and Røed (1979). Under westerly winds the effect would be reversed, with a deep offshore flow.

The third mechanism for a transverse circulation is the production during ice formation of very dense water inshore, which in some manner has to flow seaward. We have already discussed this process in an earlier section, and while there is reason to doubt the existence of a large circulation mode of this kind on the Beaufort shelf (primarily because of the absence of large areas of thin ice or open water in winter), certainly the existence of very dense water in restricted shallow areas during winter could make the mechanism locally important. For example, salinity values of 80-100‰ are common in May in Simpson Lagoon.

The outer shelf

Mean flow. We turn now to the area seaward of the 40-50 m isobaths,

viz. the outer shelf. Again Figure 3 provides a useful starting point. The principal feature of the indicated velocity field is the predominance of relatively strong flow locally aligned with the isobaths. Note, for example, the nearly E-W orientation of the prevailing currents at OL-1, corresponding to the orientation of the depth contours at that point, whereas at LO-1 and LO-4 the isobaths and major current axes are both aligned SE-NW. (While Figure 3 suggests the local isobath trend at LO-4 to be about 120° T, other more detailed bathymetric constructions for the area indicate a southwestward indentation in the topography in this area. The local isobath orientation may therefore well be more SE-NW, as the current measurements at both LO-1 and LO-4 suggest.) Because of the regional variation in isobath trend, the actual orientation of the prevailing current varies by about 45° over the area, but for simplicity we shall consider the entire octant E-SE as easterly and W-NW as westerly. Note further in Figure 3 both that the statistically prevailing current direction at each site is easterly and also that this sector contains the strongest currents (except at FLAX-1). The net motion is therefore everywhere toward the east (cf. Table 2). This is particularly notable since descriptions of flow in the area have generally considered the mean motion of both water and ice to be westward, representing the southern edge of the anti-cyclonic Beaufort Sea gyre (e.g., compare Figure 17 in Coachman and Aagaard, 1974 with Figure 11 in Hibler, 1979).

The reason for the mean eastward flow over the outer shelf is not entirely clear, although it is obviously of fundamental importance to understanding and modeling the shelf circulation. Certainly the mean winds over the southern Beaufort Sea are easterly, so that local wind driving is not a viable mechanism for the eastward flow. Neither do the regional circulation schemes, whether

based on the large-scale dynamic topography or on Sverdrup-type calculations using the curl of the wind stress, indicate anything but westerly flow in the area (cf. Newton, 1973, pp. 19-25 and 39-50). Mountain (1974) has argued that a mean eastward motion might be driven by the momentum flux of the upstream flow, i.e., the flow through Bering Strait, which continues northward along the Chukchi coast of Alaska, and a similar opinion was advanced by Hufford (1975). In this view the outer shelf flow in the Beaufort Sea would be strongly inertial, with the local momentum balance being maintained by the advective influx of momentum (inertia), the retarding effect of bottom friction, and the augmenting or retarding effect of winds, depending on whether they are westerly or easterly. Mountain (1974) showed through a scale analysis that in the absence of favorable (i.e., westerly) winds, such an inertial current likely would be restricted by the bottom friction to lie west of about 143°-145°W. Since the prevailing winds in fact are easterly and the wind effects are very important to the momentum balance, we should not expect an inertially driven flow to continue eastward into the Canadian Beaufort Sea (east of 141°W), even if Mountain's scaling had overestimated the effects of bottom friction.

There are, however, a number of indications that a mean eastward flow over the outer shelf extends not only across the entire Canadian Beaufort Sea, but continues northward along the west coast of Banks Island and then turns eastward into M'Clure Strait, probably extending eastward through Lancaster Sound and into Baffin Bay. For example, such a circulation is compatible with the current schemes of Bailey (1957), Collin (1963), and Herlinveaux (1974, adapted in Walker, 1977). More convincingly, the moored current

measurements made at a number of sites on the outer shelf of the Canadian Beaufort Sea between 137°-129°W by Huggett, Woodward, Stephenson, Hermiston, and Douglas (1975) showed mean flow toward the northeast of up to 8 cm sec⁻¹ over 3½ months during 1975. They speculated (p. 11) that this flow "is part of a large-scale circulation which is as yet unknown." If in fact the generally eastward mean flow is continuous from the Chukchi Sea through the Canadian Archipelago, then an inertial-frictional momentum balance cannot satisfactorily account for the dynamics. Rather, there must be an important local driving force, almost certainly in the form of an alongshore pressure gradient. (The gradient is probably too small for leveling along the north Alaskan coast to demonstrate its existence, and as Mountain (1974) has pointed out, steric anomaly values calculated from hydrographic data on the shelf have given no indication of it.)

Taken to its ultimate conclusion, the present argument leads to the hypothesis that the mean eastward flow over the outer Beaufort Sea shelf is ascribable to the difference in sea level between the Atlantic and Pacific oceans. In effect, the higher stand of the Pacific drives a flow through Bering Strait, a portion of which is constrained in its course toward the Atlantic to skirt the edge of the large-scale wind-driven Beaufort gyre, running eastward in a thin ribbon along the shelf edge. While this construction is obviously only speculative, there seems little doubt that the surface of the Bering Sea stands higher than that of the Arctic Ocean, probably by something like 1 m (cf. pp. 146-152 in Coachman, Aagaard and Tripp, 1975). Likewise Muench (1970, p. 108) has suggested that the surface of the Canadian Basin of the Arctic Ocean stands higher than that of Baffin Bay by at least one-third of this.

In one sense these speculations are peripheral to the Beaufort Sea shelf circulation. However, because the mean eastward flow is such a prominent feature on the shelf, and because no model of the Arctic Ocean to date has recognized this feature, it is of very great importance to ascertain its origin. Indeed, if the above argument is approximately correct, then this rather intense narrow current is conditioned by nothing less than the global climatology which maintains the Atlantic and Pacific oceans at their present different levels.

The discussion so far has been restricted to the subsurface flow. We do not, of course, have current measurements on the outer shelf above about 40 m depth, so that we cannot be sure of the motion near the surface. It is in fact quite possible that the mean surface motion is westward. Not only are the prevailing easterly winds appropriate to such driving, but the baroclinic structure on the outer shelf is also appropriate. For example, in the 17 CTD sections we took across the shelf, the dynamic topography over the outer shelf was, in about 80% of the cases, such as to sustain a geostrophic shear in which the motion at the surface was westward relative to that at 40 db. A mean geostrophic velocity difference between these levels (excluding cases of reversed shear) was about 7 cm sec^{-1} . Examination of Table 2 shows that this roughly corresponds to the mean easterly flows calculated from the current records, suggesting little or no mean geostrophic motion at the surface. Note also in Table 2 that at the shallowest of the paired measurements made in the strong eastward flow, viz. OL-1, the observed long-term mean shear (2 cm sec^{-1} over 10 m) is just about what we calculated above as the mean baroclinic effect (7 cm sec^{-1} over 40 m). The geostrophically balanced baro-

Table 2
Outer Shelf Mean and Maximum Currents

Mooring	Instrument depth (m)	Record length (days)	Mean velocity		Maximum speed (cm sec ⁻¹)
			Speed (cm sec ⁻¹)	Direction (°T)	
OL	100	95	12.8	099	56
LO-1	78	9	record too short for meaningful statistics		
LO-1	152	205	2.3	154	61
LO-4	177	352	4.8	142	66
LO-5	64	208	3.8	100	66
LO-6	68	172	6.4	112	60
LO-6	188	188	6.9	102	57
FLAX-1	39	149	1.0	067	34
FLAX-1	49	149	1.3	073	33
OL-1	40	380	7.0	089	73
OL-1	50	380	9.2	082	70

clonicity in the upper layer may therefore by itself be sufficient to offset the deeper mean eastward flow. Note further that this baroclinic structure results from an upper-layer salinity that decreases seaward, such as we discussed earlier in the section on hydrography. The interesting possibility thus arises that a mean westward motion in the upper layer, if it exists, may be due as much to the presence of dense water on the shelf (whether by brine formation or upwelling) as to direct wind effects. Appropriate models would in that case have to be both thermohaline and wind-driven.

Low-frequency variations. While both the mean and the strongest motion are seen to be eastward on the outer shelf, at least below the surface layer, Figure 3 shows the secondary mode to be westerly and to contain the next-fastest flow. Figure 15, showing the daily mean current over a year at LO-4, illustrates the characteristics of these flows. The figure can be taken as representative of the low-frequency longshore flow on the outer shelf. The motion is seen to alternate sharply between about 140°T (the primary mode) and 320°T (the secondary mode). The consistently parallel orientation of the velocity vectors is remarkable and in this respect resembles the flow found on narrow shelves elsewhere (e.g., cf. Hickey, 1979). The nominally easterly flow (actually SE) is, as noted earlier, both the fastest and the most persistent of the two principal flow directions, so that we are seeing a mean easterly motion upon which is superimposed a strong reciprocating low-frequency signal, the typical period of which is in the neighborhood of 3-10 days (Figure 15).

Figure 16 shows the (energy-conserving) spectral characteristics for the first six months of the LO-4 record. The reference coordinates for the current

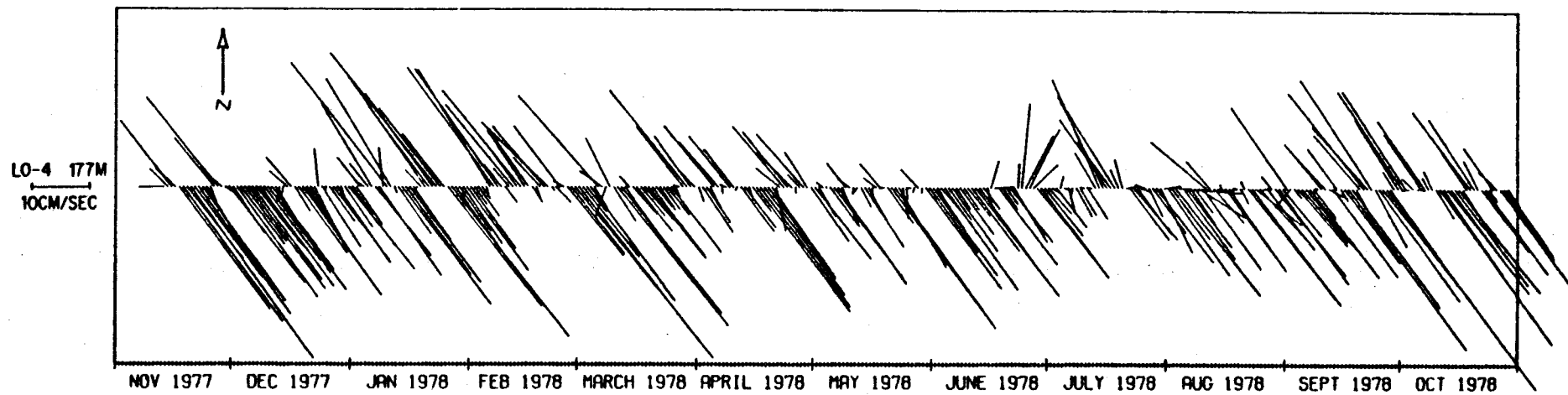
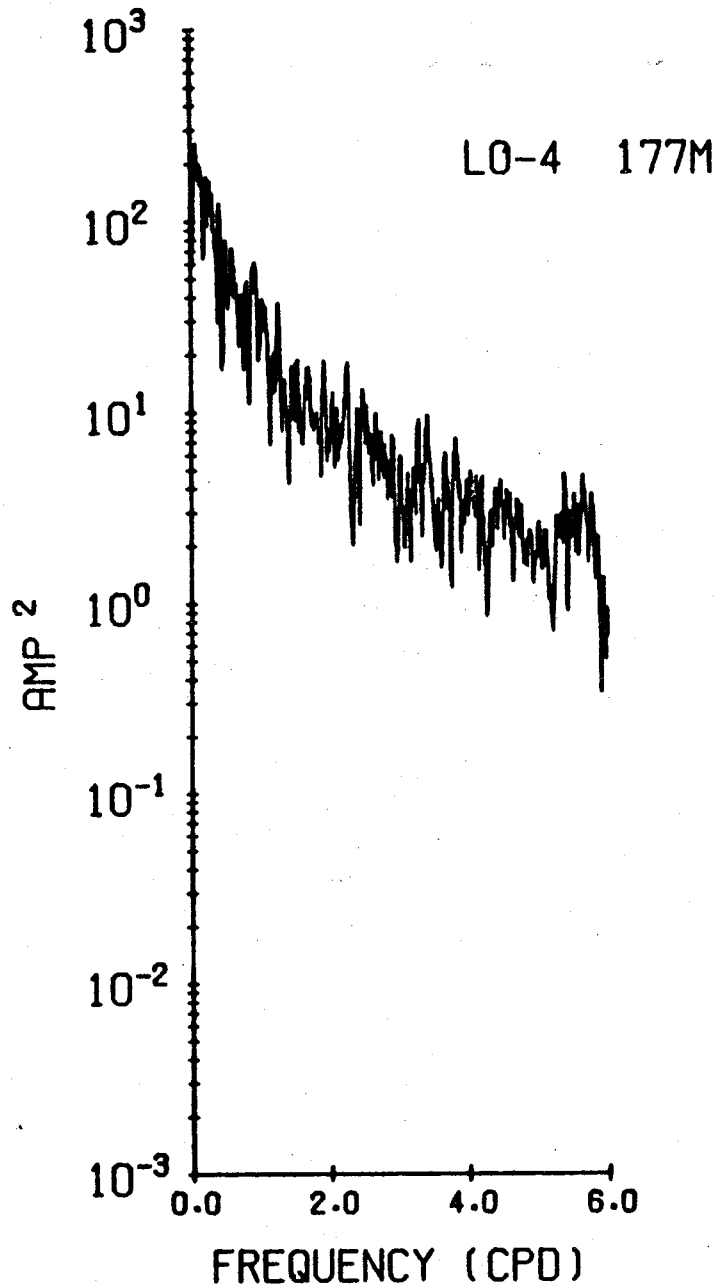


Figure 15. Daily mean current at LO-4.

U-COMP FIRST HALF OF SERIES ENERGY CONSERVING



V-COMP FIRST HALF OF SERIES ENERGY CONSERVING

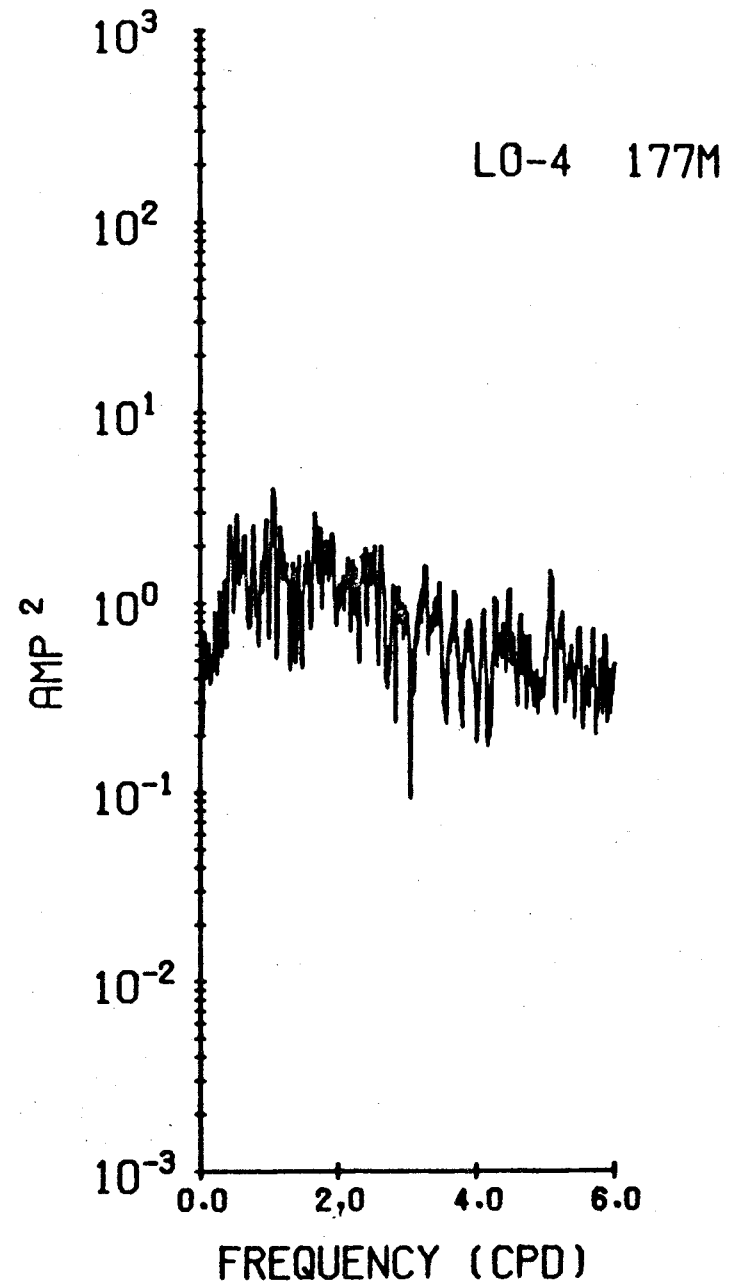


Figure 16. Energy-conserving spectra for first one-half of LO-4 current record. U-component is longshore (140°T) and V-component offshore (050°T).

have been rotated 50° clockwise, such that the u-component is oriented in the direction $140^\circ T$, i.e., parallel with the principal current axis (and presumably also parallel with the isobaths). The energy is seen to be almost entirely contained in the longshore mode (u-component), and then principally at the lowest frequencies. By contrast, the already low energy level in the cross-shelf (v) component drops off even further at frequencies less than about 0.5 cpd. A more detailed representation of the frequency band between about 0.1-0.4 cpd (Figure 17a) reveals considerable spectral structure, and comparison with the similar representation for the second six months of the LO-4 record (Figure 17b) shows notable differences between the two portions of the record. The low-frequency statistics are thus non-stationary. In effect, the dynamics of this current regime appear to have a rather broad low-frequency forcing and admittance, such as, for example, would be expected for a wind-driven regime.

Coherence calculations reveal some further characteristics of the reciprocating motion. Figure 18 shows the coherence and phase for the u-component at the two LO-6 instruments. Again, the coordinates have been rotated such that the u-axis coincides with the principal current axis for that mooring (as was done in Figures 16-18 for LO-4); we shall utilize this procedure in the remainder of this report unless otherwise noted. The low-frequency band is seen in Figure 18 to be both coherent and nearly in phase vertically over a depth of 120 m. Furthermore, examination of both the daily means and the energy spectra for the two instruments shows that while there are minor differences, the low-frequency energy levels are overall not sub-

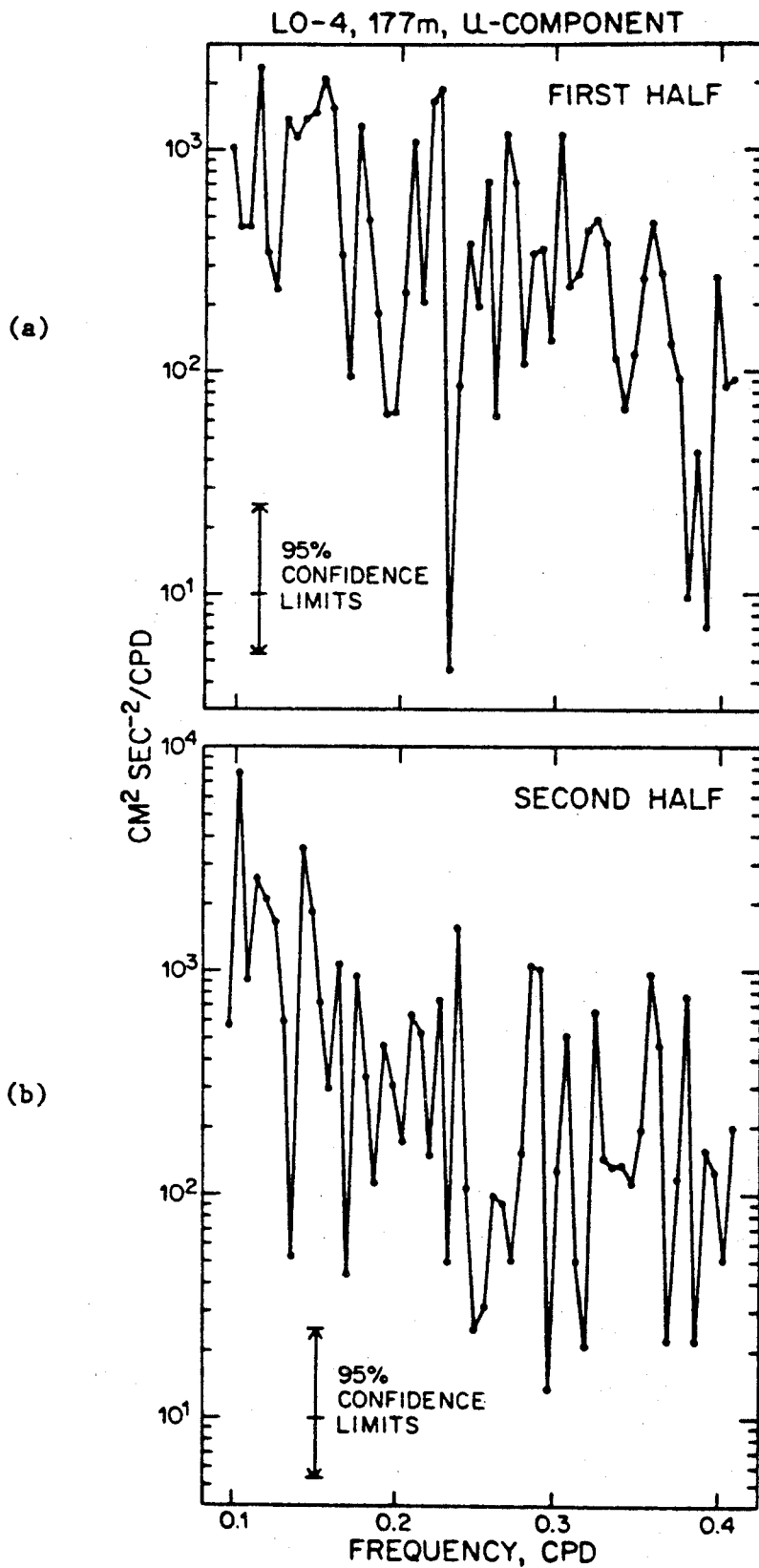


Figure 17. (a) Power spectrum for first one-half of LO-4 current record, U-component, over frequency range 0.1-0.4 cpd.
 (b) Power spectrum for second one-half of LO-4 current record, U-component, over frequency range 0.1-0.4 cpd.

L0-6, 68m, 3/13-8/16
L0-6, 188m, 3/13-8/16

U-COMP
U-COMP

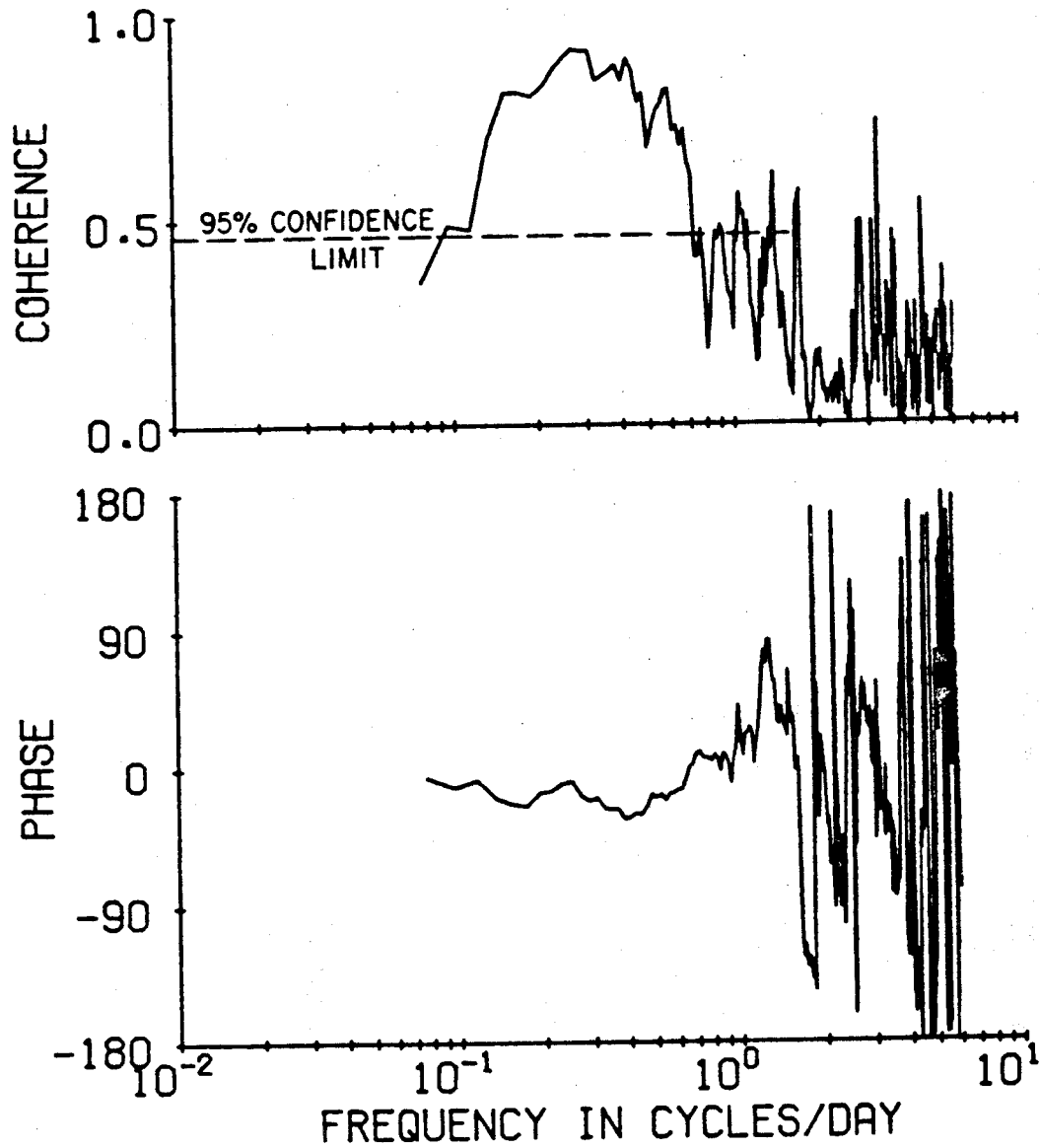


Figure 18. Coherence and phase relations for the upper and lower current records at L0-6, U-component (longshore, directed $105^\circ T$).

stantially different (cf. also Table 2). The suggestion is therefore that the entire water column between these levels responds as a single unit. Since the largest density stratification occurs above the level of the upper instrument, this is dynamically reasonable. That is, in the observed depth range we may, for example, be seeing a barotropic signal, or an internal wave in a two-layer stratified system.

Figure 19 shows the extremely high low-frequency coherence between the u-components at the LO-5 and upper LO-6 instruments. These current meters were separated by only 4 km, although they represent somewhat different total water depths, LO-5 being in 99 m of water and LO-6 in 203 m. Note that each instrument was at the same depth below the surface, however. The phase spectrum suggests that the current at LO-5 leads by an amount that increases with the frequency; the phase difference converts to a relatively constant lead time over the low-frequency band of 15-20 hrs. The LO-5 mooring was actually located about 3.5 km upstream of LO-6 (in the sense of the projection of their separation distance on the isobath trend), so that if the phase difference is due to an eastward longshore signal propagation, it implies a very slow phase velocity of only 5-6 cm sec⁻¹. This is less by an order of magnitude than would be expected for even the slowest long waves propagating along the coast, and even if the distance between LO-5 and LO-6 were in error by 3-4 km, it could at most increase the calculated phase speed to about 10 cm sec⁻¹. This can be contrasted with, for example, an internal Kelvin wave propagating along the slope. For a two-layer model with density structure corresponding approximately to a winter station near the mooring site (e.g., station W 27-25), the phase velocity of such a wave would be close to 65 cm

L0-5, 64m, 3/13-8/16
L0-6, 68m, 3/13-8/16

U-COMP
U-COMP

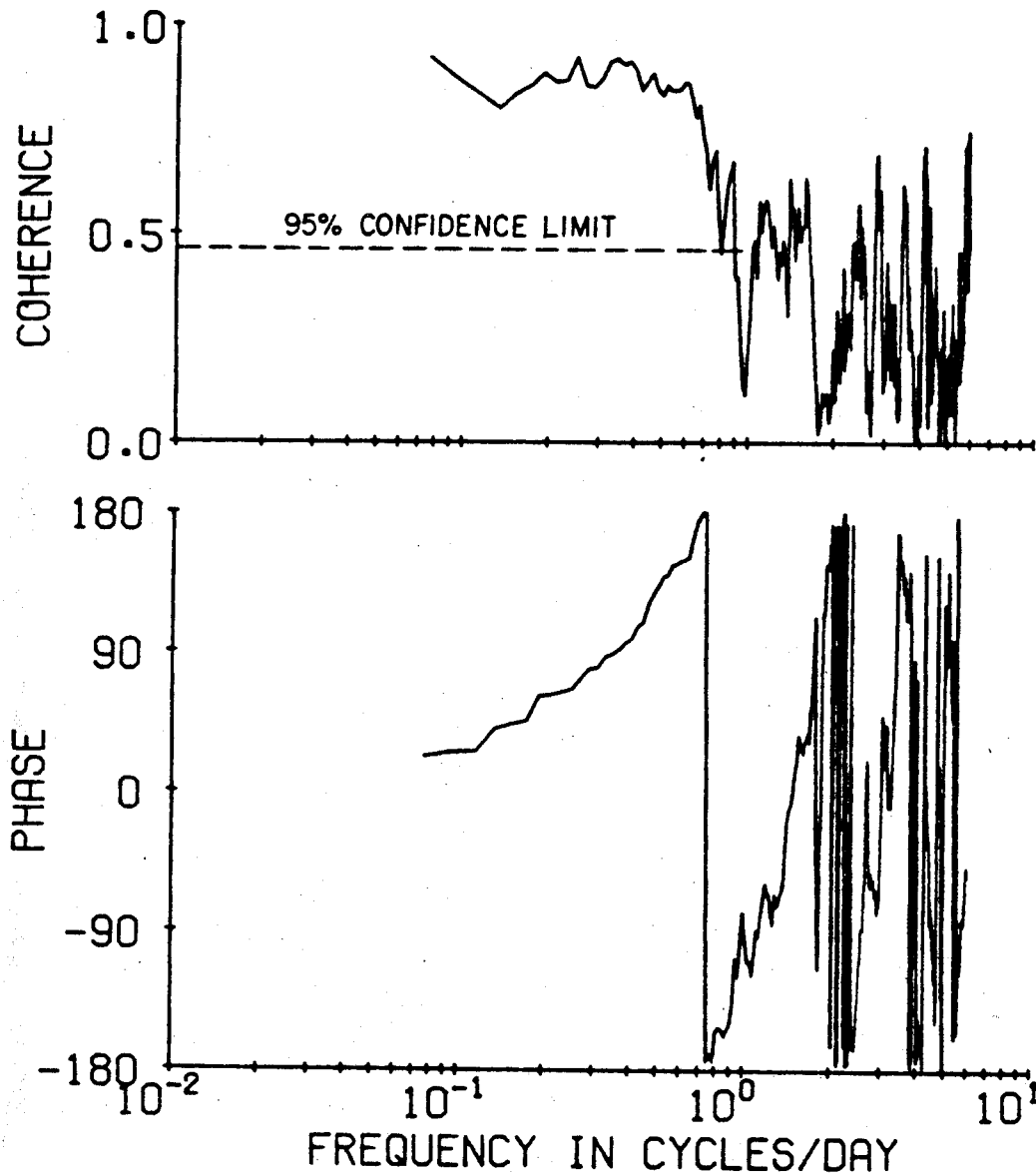


Figure 19. Coherence and phase relations for the L0-5 and upper L0-6 current records, U-component (longshore, directed $105^\circ T$ at L0-5).

sec^{-1} . While we cannot preclude a wave explanation for the low-frequency variability, based on this rather meager observational basis, certainly such an explanation faces a substantial initial difficulty in the large observed phase difference. Note, however, that a signal propagation of about 5 cm sec^{-1} is close to the mean velocity (cf. Table 2), suggesting that flow events may be carried with the mean current. In that case, the inertial terms in the momentum equation would be important in locally accelerating the flow, as was initially suggested by Mountain (1974) and was discussed earlier in connection with the mean easterly flow.

At large horizontal separations the longshore coherence tends to break down more rapidly than would be expected. Figure 20 shows the coherence between the LO-4 and deep LO-6 records; the moorings were separated by 65 km. The lack of coherence is surprising, since both long waves and wind driving as explanations for the low-frequency variability would require coherence at this spatial scale. For example, the wave length of an internal Kelvin wave of phase speed 65 cm sec^{-1} (see above) and period 0.2 cpd would be 270 km, i.e., over four times the mooring separation. Similarly, major wind events capable of forcing a circulation along the shelf, would have a spatial scale of several hundred kilometers. In either case, the velocity field in the ocean should be coherent at lesser distances.

Therefore, if the lack of coherence is real, it presents major conceptual problems, probably resolvable only by resorting to such mechanisms as flow instability. However, examination of the individual time series at LO-4 and LO-6 suggests an alternate explanation. Figure 21 shows the daily mean u-components at the two instruments. It is clear that much of the variability is in fact quite coherent, as for example is the case for the events from

L0-4, 177m, 3/13-8/16
L0-6, 188m, 3/13-8/16

U-COMP
U-COMP

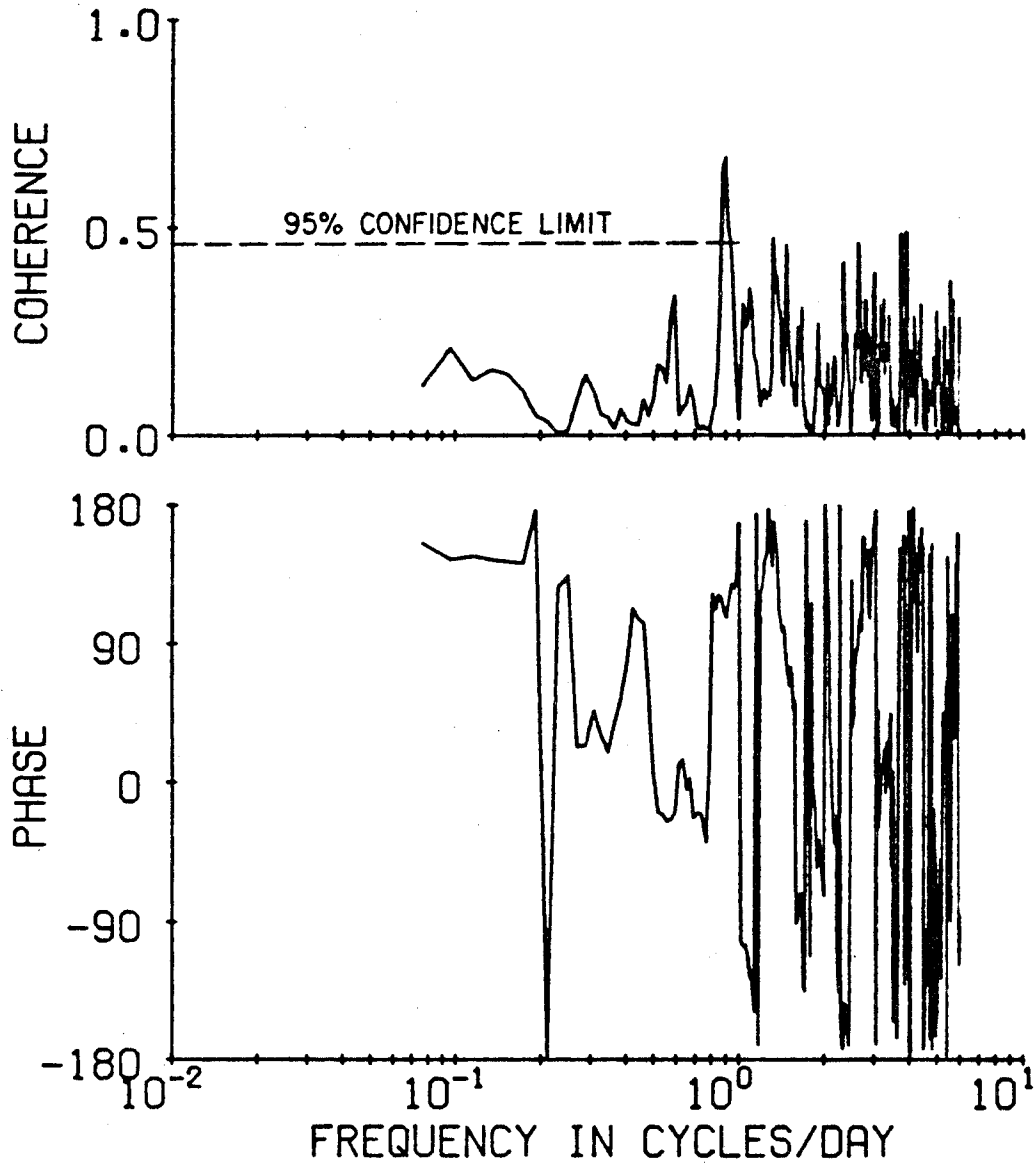


Figure 20. Coherence and phase relations for the L0-4 and lower L0-6 current records, U-component.

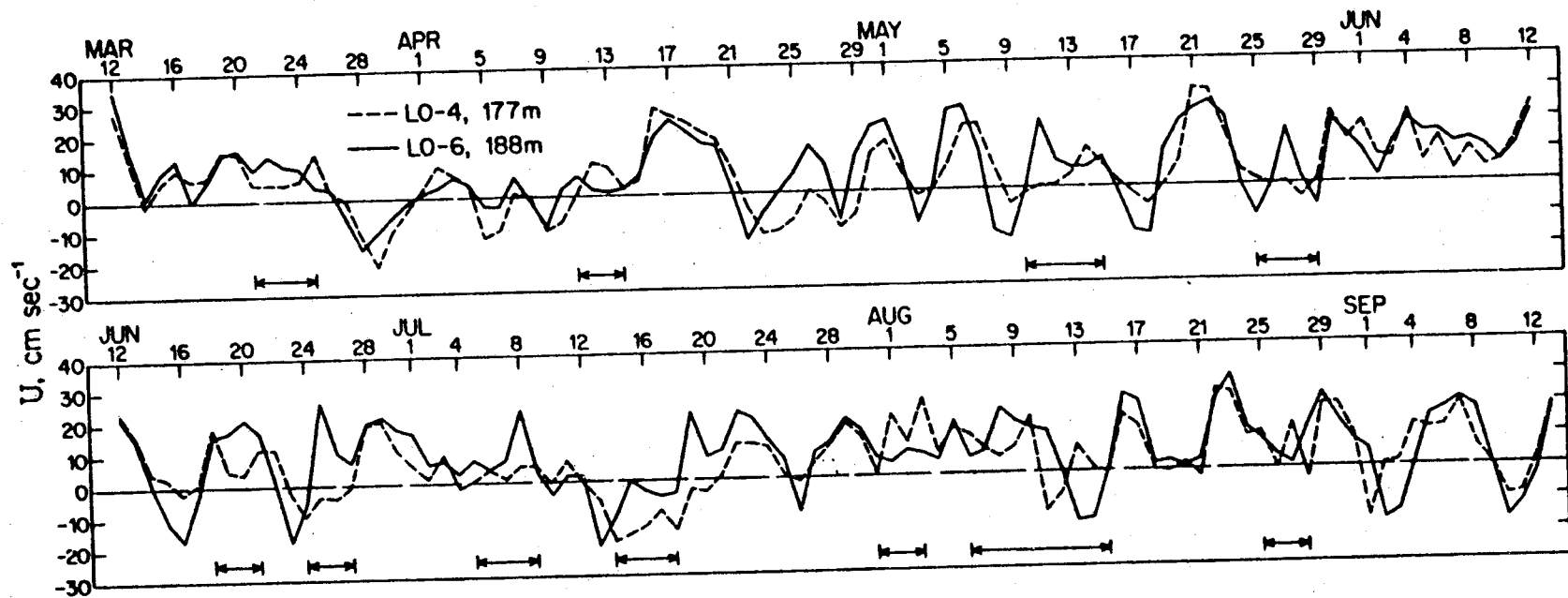


Figure 21. Daily mean U-component at the LO-4 and lower LO-6 instruments. The bracketed arrows indicate times when the signals were visibly uncorrelated.

14 April-9 May. However, about 25% of the time, events were obviously dissimilar, as was true during 6-15 August. Therefore, while the majority of the low-frequency events are coherent over these spatial scales, as one would expect to be the case, there are a sufficient number of uncorrelated events to degrade the coherence statistics. Figure 21 also suggests that the majority of the coherent events are in phase to within about one day. For the given station separation, this means a phase propagation of at least 70 cm sec^{-1} , which in turn means that the signals are not inertially transmitted. We thus have an indication that is quite different from that of the LO-5/LO-6 phase relationship.

As we shall presently see, there is evidence that at least a portion of the low-frequency variability on the outer shelf is related to the wind field. However, before examining that relationship, we'll consider another indication of the possible role of advective momentum transport. During 25 August 1976-10 August 1977, we had a current meter moored west of Cape Lisburne in the Chukchi Sea. Designated NC-7 (cf. Coachman and Aagaard, in press), it was located in the core of the northerly flow along the Chukchi coast. Note that it overlaps in time the LO-1 record during the period 29 March-10 August 1977. Comparison of these two records initially suggested no relationship. However, if the time scale is shifted about 106 days, so that 14 December 1976 in the NC-7 record coincides with 29 March 1977 in the record from LO-1 (cf. Figure 22), then there is a remarkable similarity. Specifically, at the beginning of the LO-1 record, there were two long periods of nearly uninterrupted westward flow, 24 and 28 days in duration and separated by six days of eastward flow. Each major period of reversed flow had 4-5

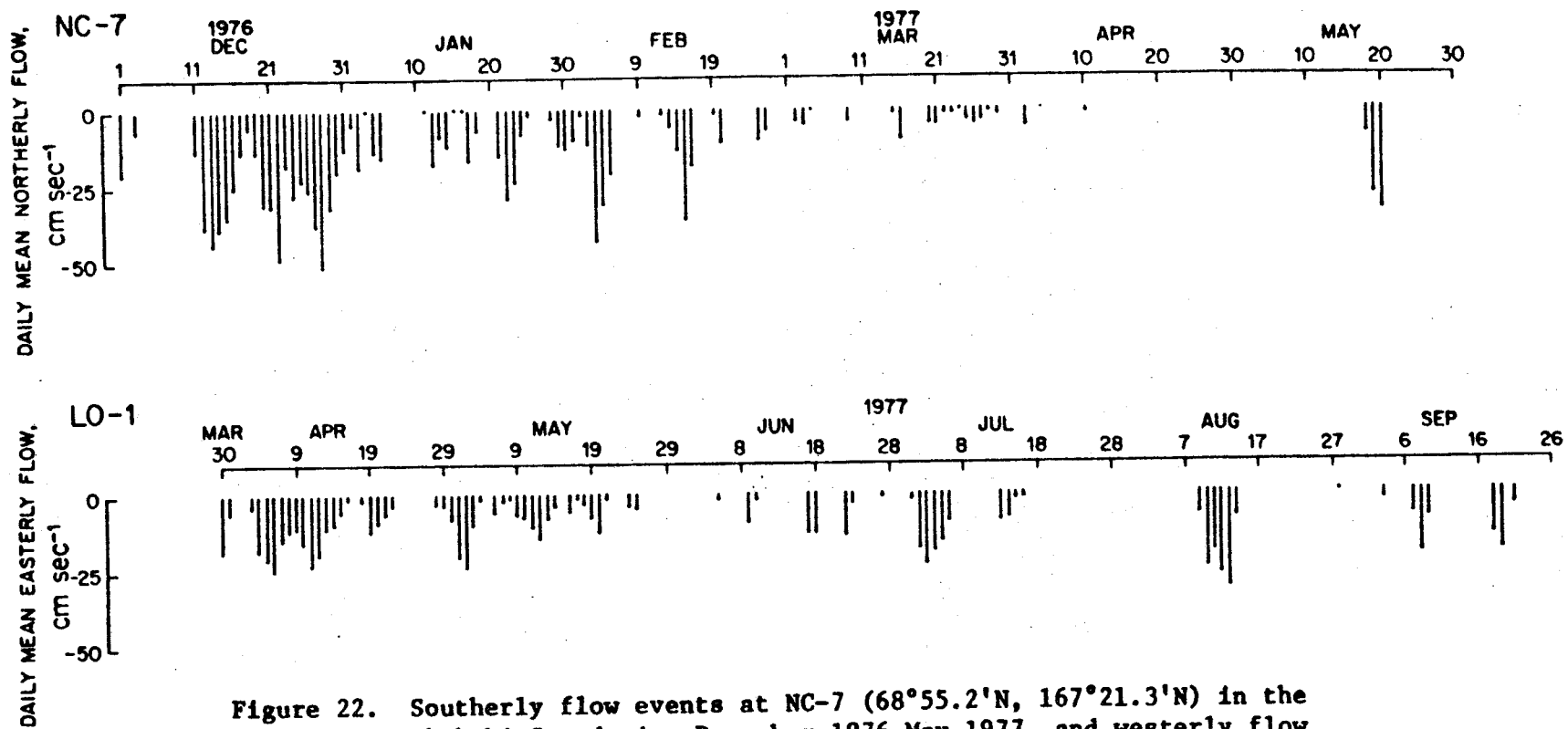


Figure 22. Southerly flow events at NC-7 ($68^{\circ}55.2'N$, $167^{\circ}21.3'N$) in the Chukchi Sea during December 1976-May 1977, and westerly flow events at LO-1 during March-September 1977. Note that the time scales are offset.

subordinate oscillations within it. These major reversals are unique in our Beaufort Sea records, as there are no other reversals of comparable duration. Similarly, beginning 11 December 1976 there were two 26-day long periods of southward flow at NC-7, again interrupted by six days of normal flow. Each major reversal had 4-5 embedded subordinate oscillations. There were no other reversals of comparable duration at any time during the year-long record, nor anywhere else at a large number of mooring sites farther west in the Chukchi Sea, in Bering Strait, and in the northern Bering Sea, other than at the mooring immediately west of NC-7 (NC-6), which was also in the core of the mean northward flow along the Chukchi coast. Finally, there is nothing in the wind records (from Barrow) to suggest local wind forcing as the cause of the prolonged LO-1 current reversals. Winds during the period 30 March-25 May 1977 were from the easterly sector about 75% of the time, but were very light, reaching 5 m sec^{-1} on only one day and were usually in the range 1-3 m sec^{-1} . The similarity between the two current records with respect to these unusual events is therefore such that one cannot discount the possible dynamic importance of momentum advection by the mean flow in at least these instances. That is, the long periods of reversed flow at LO-1 may in large degree reflect the absence of momentum input during a period that was determined by upstream events. Note further that NC-7 and LO-1 were separated by about 650 km, suggesting a signal propagation ratio of 7 cm sec^{-1} , i.e., roughly comparable to the long-term mean flow in the area.

Wind influence. We turn now to the role of the wind in promoting the low-frequency variability. Wind records suitable for comparison with the current measurements are available in the form of calculated geostrophic

winds at 72°N, 150°W during 18 February-31 July 1979, i.e., at a nominal point about 100 km from OL-1 and 200 km from FLAX-1; the calculations were made by T. Kozo. Surface winds (and pressures) are also available from Barter Island, over 100 km to the east of FLAX-1, during 23 February-4 May 1979 and 30 May-22 July 1979. We shall refer to these latter two periods as parts 1 and 2 of the surface wind records.

Statistically, the wind and current records are moderately correlated at low frequencies. For example, Figure 23 shows the coherence and phase spectra between the u-components of current at the upper FLAX-1 instrument and of the surface wind at Barter Island during part 1. Likewise, Figure 24 shows the coherence between the u-component at the upper OL-1 instrument and the geostrophic wind. (The records from the lower instruments at each mooring are very similar to those from the upper.) While the correlation with the geostrophic wind is somewhat poorer than with the surface wind, the overall suggestion of the two figures is of a current moderately coherent with the wind at time scales longer than about 2-3 days. Figure 23 shows no statistically significant phase difference, while Figure 24 suggests a changing phase relation, with the current lagging the wind at the lowest frequencies, but leading at frequencies greater than about 0.2 cpd. Note, however, that except close to the coherence and phase peaks near 0.3 cpd, the positive phase difference is not statistically significant. (The 95% confidence phase limits for a coherence of 0.46, which is the 95% confidence limit on coherence, is about $\pm 39^\circ$.) In this connection it should also be noted that there was no significant positive phase difference between the current and the surface wind during part 2 of the Barter Island wind record.

FLAX-UPPER PART 1
SURF. WINDS PART 1

U-COMP
U-COMP

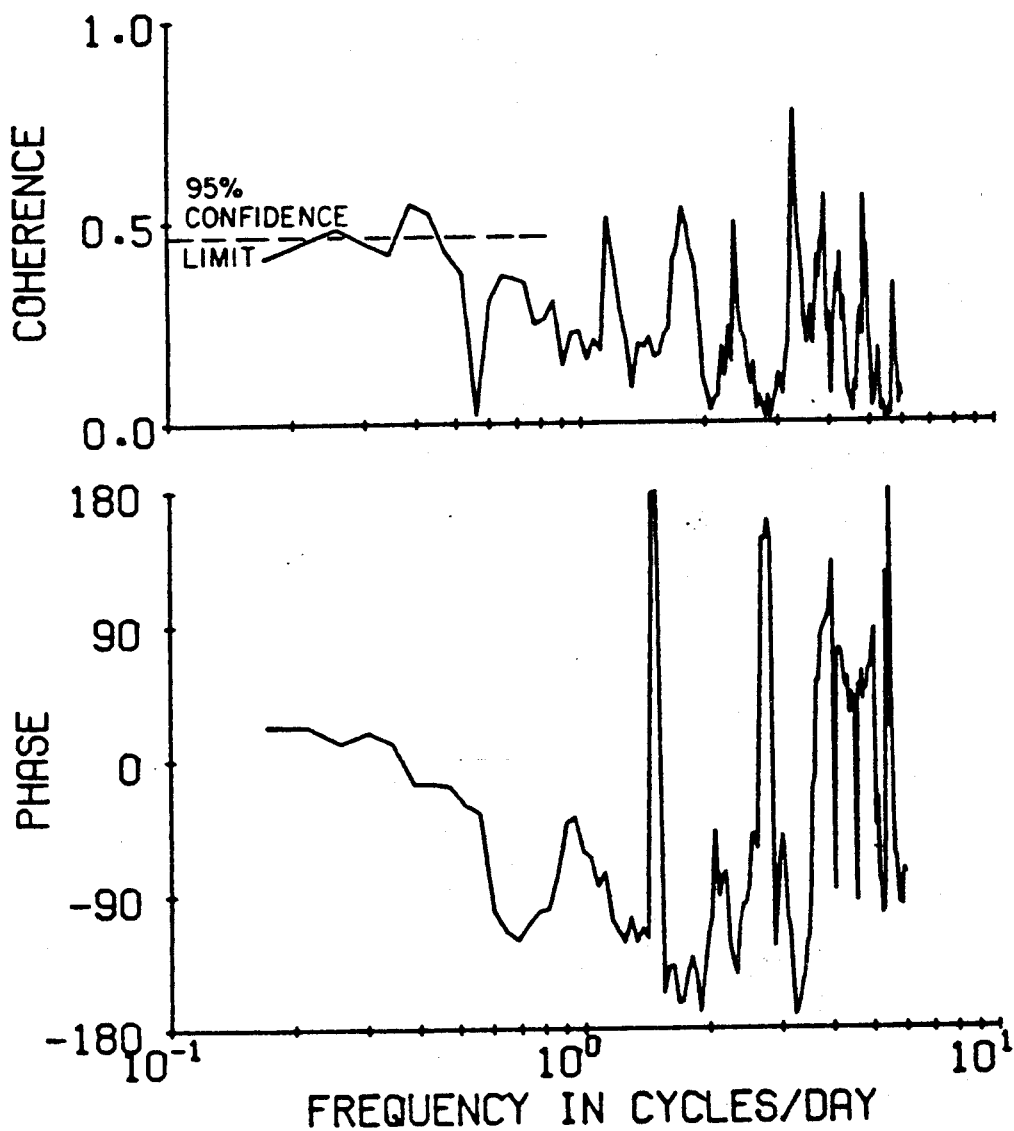


Figure 23. Coherence and phase relations for the upper FLAX-1 current record and the Barter Island surface winds, 23 February-4 May 1979, U-component (longshore, directed $105^\circ T$).

OLIK-UPPER UNROTATED
GEOWIND UNROTATED

U-COMP
U-COMP

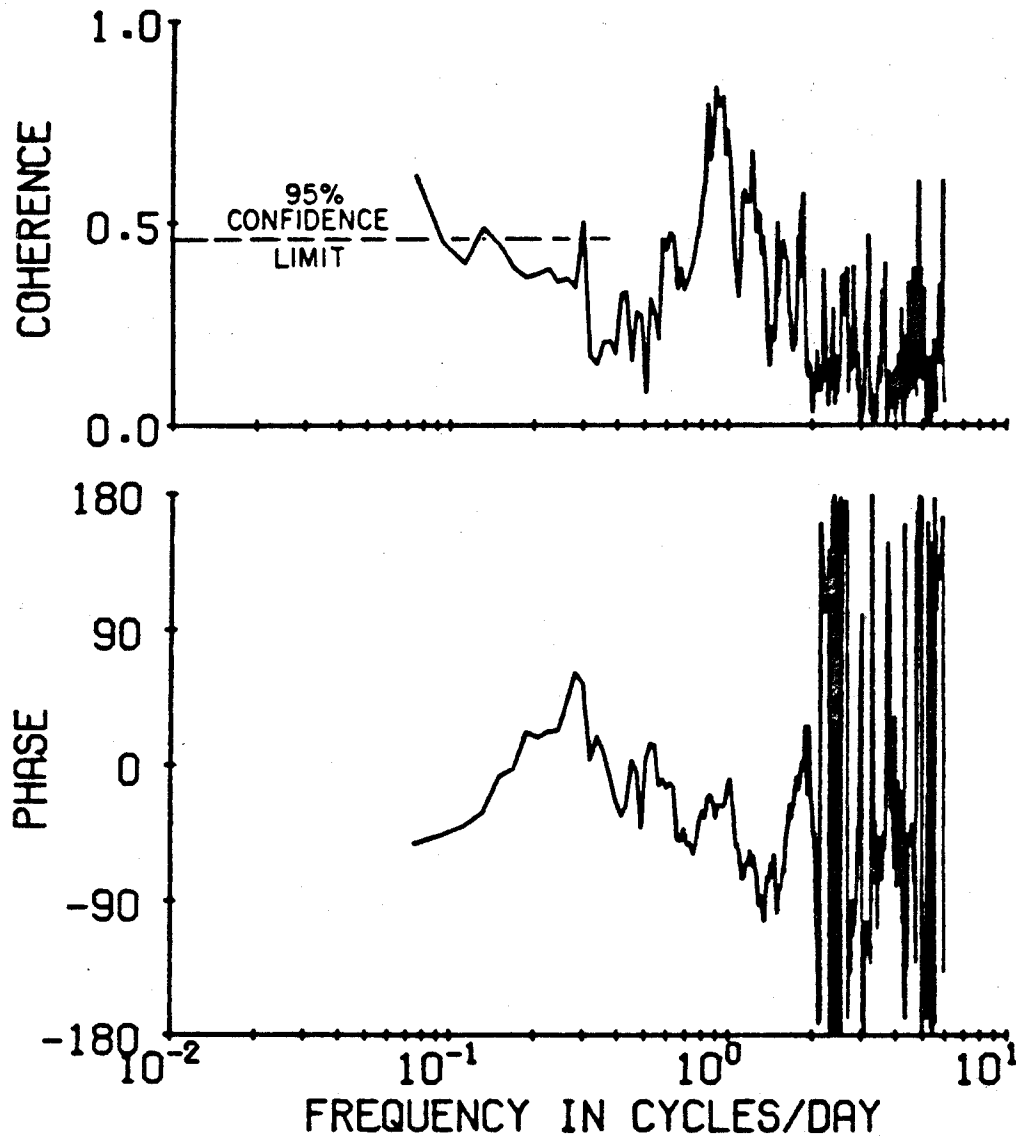


Figure 24. Coherence and phase relations for the upper OL-1 current record and the geostrophic wind at 72°N, 150°W, 18 February-31 July 1979, U-component (longshore, directed 090°T).

Except for a significant (but slightly smaller) correlation between the east component of current and the north component of wind (zero phase difference), no other wind and current combinations prove coherent. The implication of these calculations is therefore that a portion of the low-frequency variability in the longshore current is wind-driven, primarily by the longshore wind component, with which it is nearly in phase. Whether the governing mechanism is one of direct wind stress application to a two-dimensional flow, or whether it involves a coastal (or fast-ice edge) Ekman layer divergence and geostrophically induced longshore flow, or whether it is governed by still some other set of dynamics, is not clear. However, the presence of large, presumably at least in part wind-driven, variability over the outermost shelf, a considerable distance seaward of the coast or the fast ice edge, suggests that the second mechanism is unlikely. This is also the implication of the near-zero phase lag, since the spinup time for a geostrophic longshore current is typically the order of a few days (Allen, 1973), which would correspond to a substantial phase difference.

Examination of individual events in the current records also suggests wind forcing as contributing to the low-frequency variability. For example, comparison of the Barter Island winds with the OL-1 and FLAX-1 current records shows that under strong easterly winds the current normally reverses. This appears to hold in about 75-80% of the instances when the easterly winds exceed $8-10 \text{ m sec}^{-1}$. On the other hand, current reversals also occur that are not obviously related to the wind. Figure 25 shows an example of both kinds of events, depicting surface winds and OL-1 and FLAX-1 currents during 22 February-8 March 1979. Initially, winds and currents were in the same

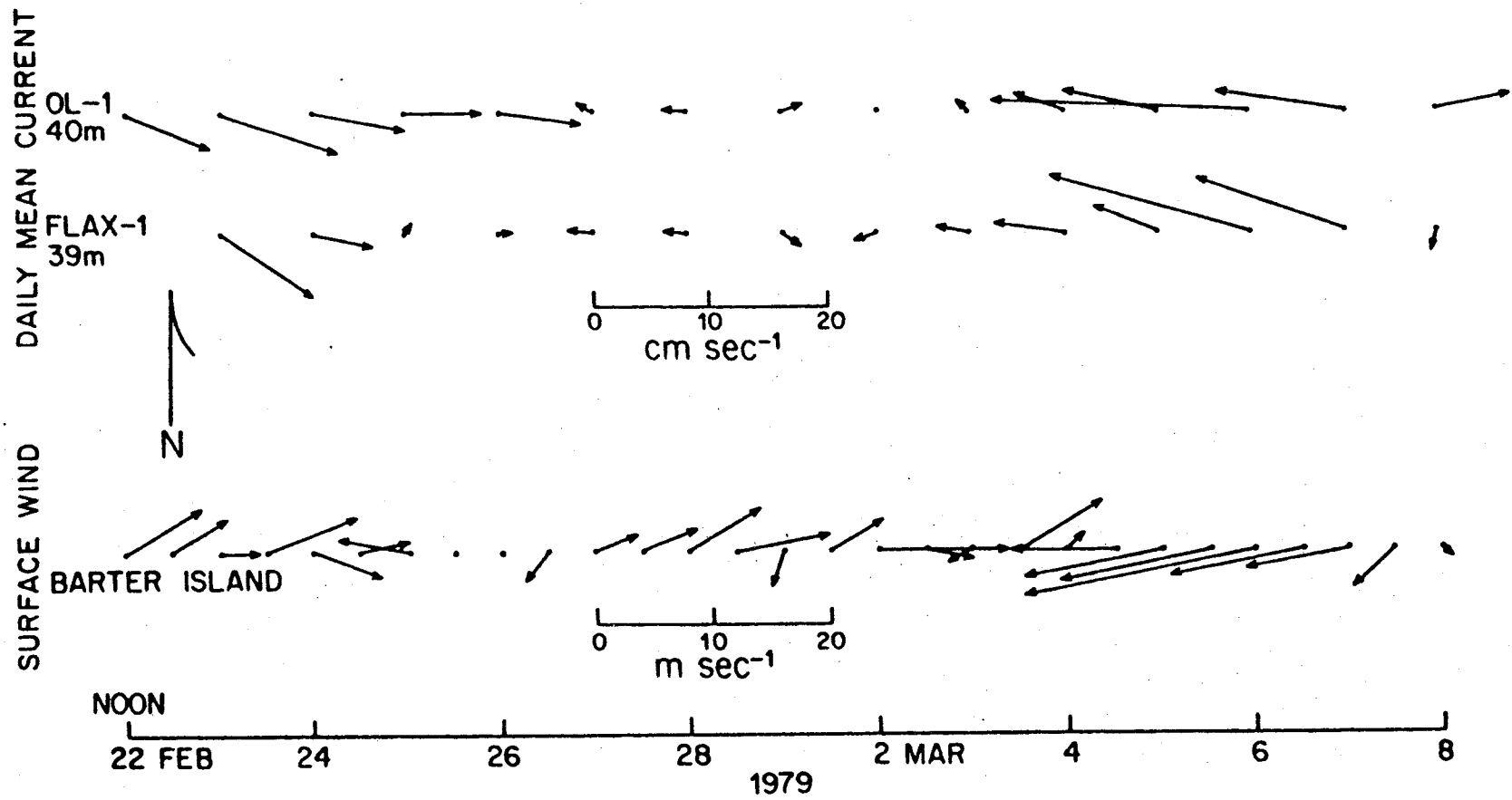


Figure 25. Daily mean current at the upper OL-1 and FLAX-1 instruments and surface wind at Barter Island, 22 February-8 March 1979.

direction (eastward), but during the period centered around 28 February, the currents were weak and variable (and included some westward motion), while the winds continued moderately strong toward the east. About 4 March the currents entered an increasingly pronounced reversed mode which peaked on 6 March. The winds at Barter Island, meanwhile, began blowing toward the west at midnight on 4 March; they reached their maximum strength on 6 March, coincident with the current peak.

The conclusion from these considerations is that the longshore wind plays an important, but certainly not all-prevailing, role in the low-frequency variability of the subsurface longshore flow. The wind appears to be particularly important in flow reversals. Specifically, when the winds are easterly at $8-10 \text{ m sec}^{-1}$ or more, the currents over this part of the shelf will normally reverse and set westerly. Ascertaining the dynamics of the wind-driven flow with some certainty and detail will require special experiments, the most difficult part of which undoubtedly will be to obtain good measurements of the offshore wind field. Quite possibly the high noise level in the present wind/current coherence calculations is in fact due to an inadequate definition of the wind stress.

Seasonal variability. Our present current records should be long enough to get an indication of variability on the seasonal time scale. Figure 26 shows the three-week mean longshore currents over two different years at two different locations. There is no apparent seasonal signal, and in fact both the strongest eastward and westward mean currents occurred in late January-early February. A distribution-free "runs-test" indicates that the three-week means in fact constitute a random sequence. There is, however, some

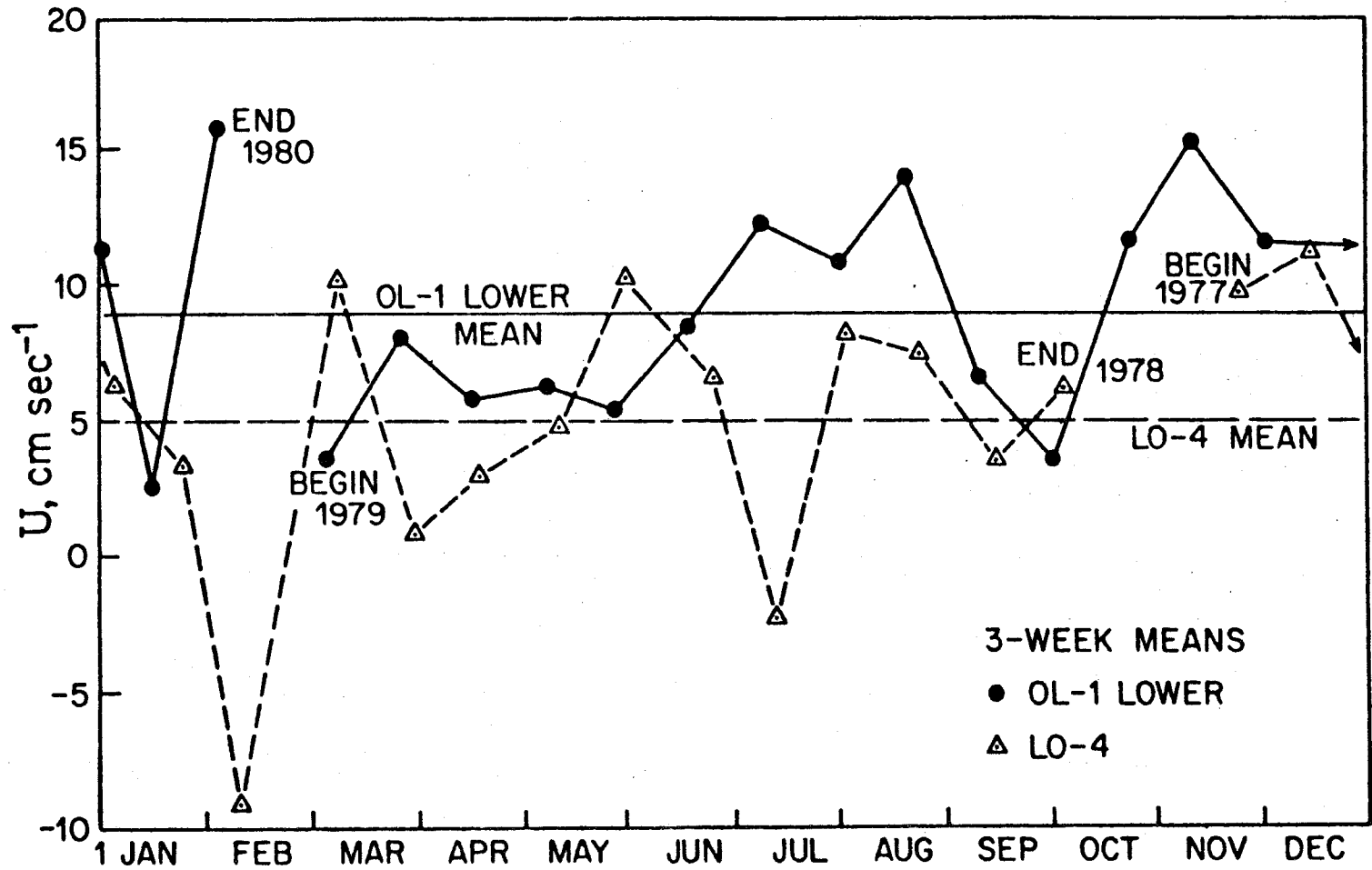


Figure 26. Three-week mean current, U-component, at the LO-4 and lower OL-1 instruments. The horizontal lines represent the annual mean at each location.

tendency toward the lower significance limit on the number of runs, i.e., there is some indication of a persistence of currents weaker or stronger than the mean, on time scales several multiples of the three-week time base.

Overall, the impression is of a long-term mean easterly flow which, although variable on extremely long time scales, does not exhibit any regular seasonal variations. Rather, there are random fluctuations on a time scale of 1-2 months or more.

Upwelling. We discussed earlier the hydrographic evidence for deep upwelling, i.e., from offshore depths of 200 m or more. Such upwelling events are characterized by the elevation of abnormally warm and saline water onto the shelf. Since the current meters are equipped with recording temperature sensors, they provide long time series of thermal evidence for possible upwelling. As an example, Figure 27 depicts the temperature at 177 m at LO-4. Over the year the temperature fluctuated between near-freezing and about 0.3°C; the record is marked by a large variability with a typical time scale of a few weeks. Vertical temperature gradients at this depth are characteristically in the range 0.01-0.03°C m⁻¹, but may reach 0.05°C m⁻¹ in extreme upwelling situations (compare Figures 9-12). Since the major thermal events of Figure 27 have an amplitude of order 1°C, this represents a vertical excursion of 30-100 m. Alternatively, since in the absence of upwelling the 0°C isotherm is located below about 200-250 m on the slope (cf. Figures 10 and 12), the elevation of this isotherm in Figure 9 to 90-120 m over the outer shelf, represents a deep upwelling of about 100 m. Figure 27 suggests that upwelling events are common and that their thermal effects typically persist at a location for a week or more.

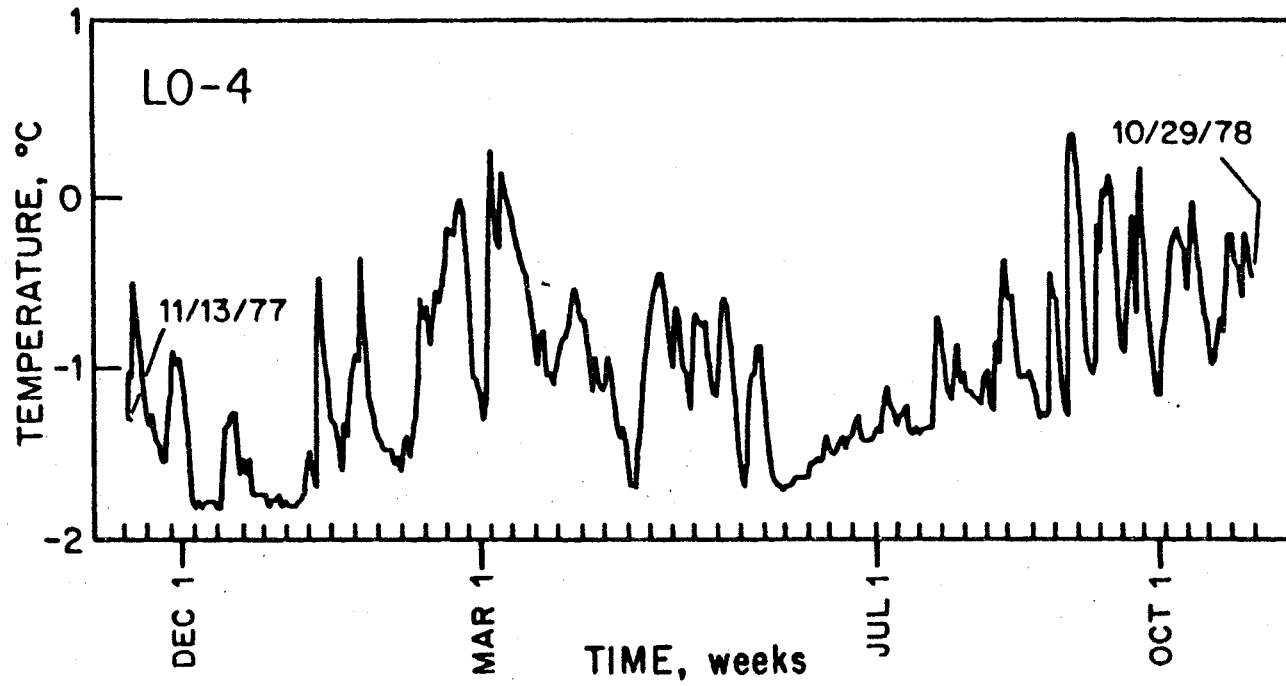


Figure 27. Temperature at LO-4 (177 m).

Inspection of the temperature records from other instruments shows that the thermal influence of upwelling is restricted to the area seaward of about the 60 m isobath. For example, no identifiable upwelling events occurred at the FLAX-1 site (59 m sounding) and only two probable upwelling events were seen at the OL-1 site (60 m sounding). While no upwelling was seen at LO-5 (99 m sounding) the temperature sensor was located 35 m off the bottom and may therefore have been too high in the water column to detect a temperature signal. Certainly Figure 9 shows upwelled water inshore of the 90 m isobath in Section LW.

Upwelling events are widespread in the longshore direction, as was apparent in our earlier examination of the hydrography (recall that Sections LW and OE in Figure 9 were separated by about 120 km). Similarly, inspection of the temperature records from 177 m at LO-4 and 188 m at LO-6 (separated by 65 km) shows them to be remarkably coherent over most of the record; they are also in phase. The chief difference between the two records is a stronger upwelling signal at LO-6. The reason for this difference is not clear, since the moorings were in comparable depths of water (192 and 203 m) and the instruments were located 15 m off the bottom in both instances; conceivably, differences in the local bathymetry are involved.

Comparison of the various temperature records also shows that while the vertical extent of the upwelling is limited (e.g., it did not show at the LO-6 instrument at 68 m depth, some 135 m off the bottom), the upwelled water is probably not restricted to a bottom boundary layer, as would be the case if its influx were due to onshore movement within an Ekman layer driven by a westward longshore geostrophic flow. For example, at LO-1 the temperature sensor was located 40 m off the bottom, but upwelling events are still clearly

evident, although not as pronounced as at LO-4, 15 m off the bottom. Taken together with the evidence from the CTD sections (cf. Figure 9), the temperature records suggest a vertical extent above the bottom of the upwelled water of perhaps 50 m. This is most likely outside the bottom Ekman layer (which is probably of order 10 m). Support for this conclusion comes from examination of the current roses for LO-6 (Figure 3), which do not show any onshore turning of the deep current vector, relative to the shallow vector, during periods of westerly flow, even though the deep current meter was only 15 m off the bottom. We therefore conclude that onshore transport within the bottom boundary layer is not a likely primary cause of upwelling, although it may be a contributing factor.

Coherence calculations between the velocity and temperature fields show that at the instruments where frequent upwelling was indicated, the longshore current and the temperature are coherent at time scales of 1-2 weeks; the current lags by about 90° (but close to 135° at 188 m at LO-6), or equivalently, westerly currents are followed by increasing temperatures one-quarter (three-eighths at LO-6) cycle later. As an example, Figure 28 shows the coherence and phase spectra for the first one-half of the longshore velocity component and temperature records at LO-4. We saw earlier that strong easterly winds, such as might be expected to produce coastal upwelling, normally could reverse the prevailing eastward current. However, the wind and current were essentially in phase during such events, and since the longshore current and temperature are approximately in quadrature (90° out of phase), we are almost certainly not seeing wind-driven coastal upwelling. Note that we had tentatively arrived at the same conclusion in our earlier discussion of

LO-4 PT1 HRLY ROT
LO-4 PT1 HRLY ROT

U-COMP
TEMP

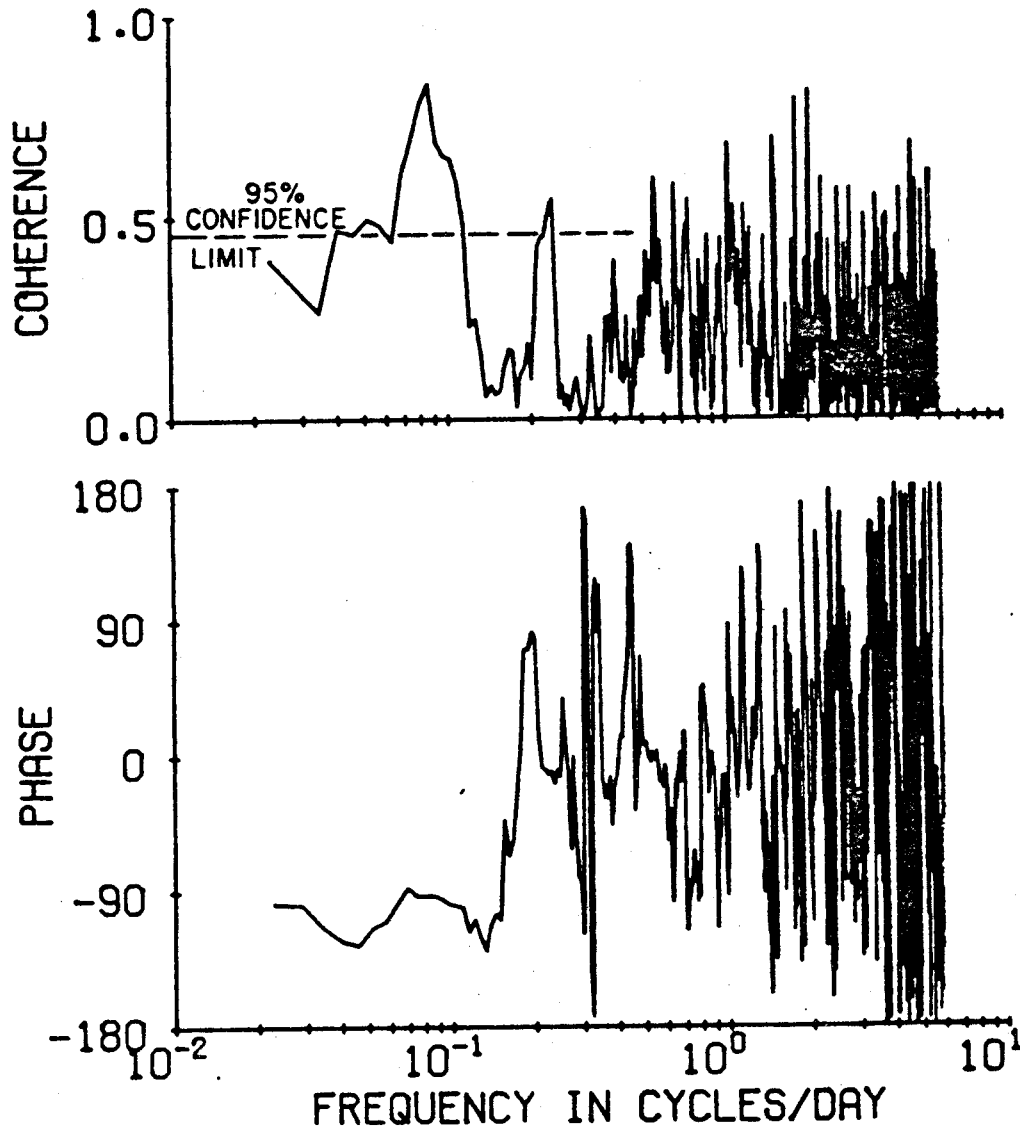


Figure 28. Coherence and phase relations for the first one-half of the records of U-component of velocity and of temperature at LO-4.

the hydrographic evidence for upwelling.

The simultaneous invasion of upwelled water over very long stretches of the shelf (certainly over more than 100 km) also precludes purely local causes, such as quasi-geostrophic eddies. Within these constraints (i.e., that the upwelling is regional in extent, not directly wind-driven, and probably not restricted to a bottom boundary layer), there are still several different conceptual models possible. Consider, for example, the following sequence of events. In the mean state, geostrophic equilibrium requires a pressure gradient directed southward on the southern flank of the Beaufort gyre, and directed northward over the outer shelf, where the mean flow is eastward (possibly reduced near the surface due to the baroclinicity discussed earlier in the section on mean flow). A nominally east-west topographic trough would therefore exist somewhat seaward of the shelf break, and the eastward flow in effect forms a barrier between the Beaufort gyre and the shelf. Suppose now that the flow begins to reverse toward the west. The previously geostrophically adjusted pressure gradient must also change, so that at some point it is directed southward. An ageostrophic onshore flow component could then exist over a limited time, during which the deeper onshore flow would encounter the upward-sloping bottom and be forced to upwell. The presence of the coast would limit the shoreward penetration of this motion, effectively through continuity requirements leading to a pressure gradient directed offshore. At some later time the westward long-shore flow will be fully developed and geostrophically balanced so that the southward-directed pressure gradient which forms the dynamic south wall of the Beaufort gyre will extend in over the outer shelf. The effect of the upwelled water on the shelf is to reduce the horizontal pressure gradient with depth,

so that the westward geostrophic flow would also be reduced.

While this construction is somewhat intuitive, there are in fact data that are consistent with it. Consider, for example, Figure 29, showing the daily mean velocity at the two LO-6 instruments, along with the temperature record from the deeper one. (The temperature in Figure 29 is probably uniformly too high by 0.1-0.2°C.) The upwelling events are generally preceded by westward flow, and this westward flow is normally both stronger and more frequent at the upper instrument, as would be expected in a baroclinic flow. As further evidence, Figure 30 shows the dynamic topography of the 70 db surface relative to 200 db during the upwelling event observed at the W 25 sections. We do not, of course, know the stage of the upwelling at the time of the sections, but the dynamic topography corresponds to a strong westward baroclinic current, such as might be expected to occur after the main onshore upwelling movement. The geostrophic shear above 70 db reverses, so that Figure 30 portrays the probable current core. (The apparent lack of dynamic relief inshore of Stations 6 and 7 is an artifact due to the lack of inshore stations deeper than 200 m; examination of the gradients across the shelf break at shallower levels in Sections OW and OE suggests very strong currents.) As a final line of evidence, the two probable upwelling events at OL-1, in early October and late January, were both associated with abnormally strong westerly flow. The October event followed 7 days of westerly current up to 57 cm sec^{-1} , and the January event began about a day after the start of a five-day period of westerly flow of up to 62 cm sec^{-1} .

Other conceptual models of the upwelling are also possible, involving, for example, geostrophically balanced onshore flow associated with a longshore

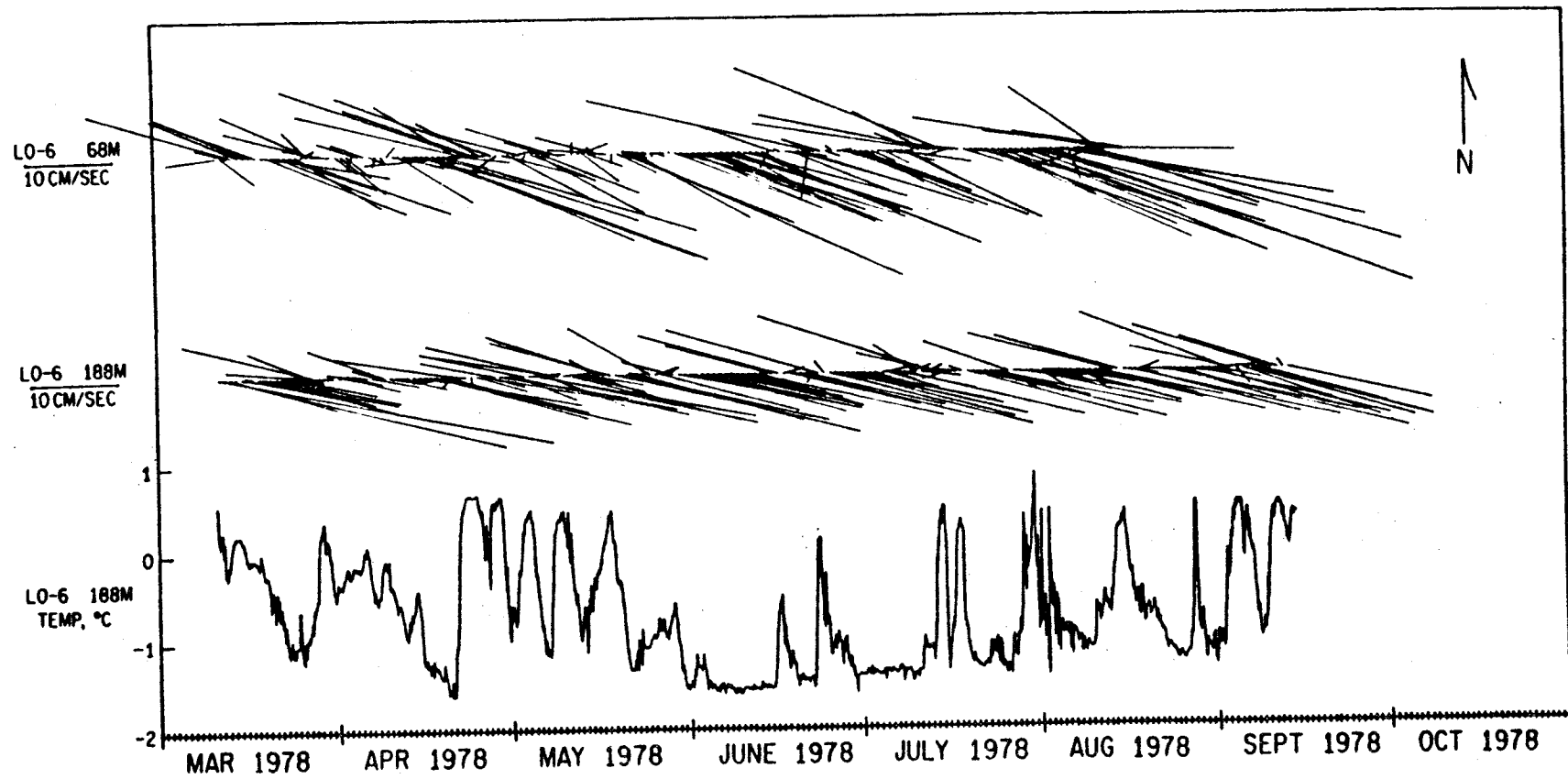


Figure 29. Daily mean current at LO-6 and temperature at 188 m at LO-6.

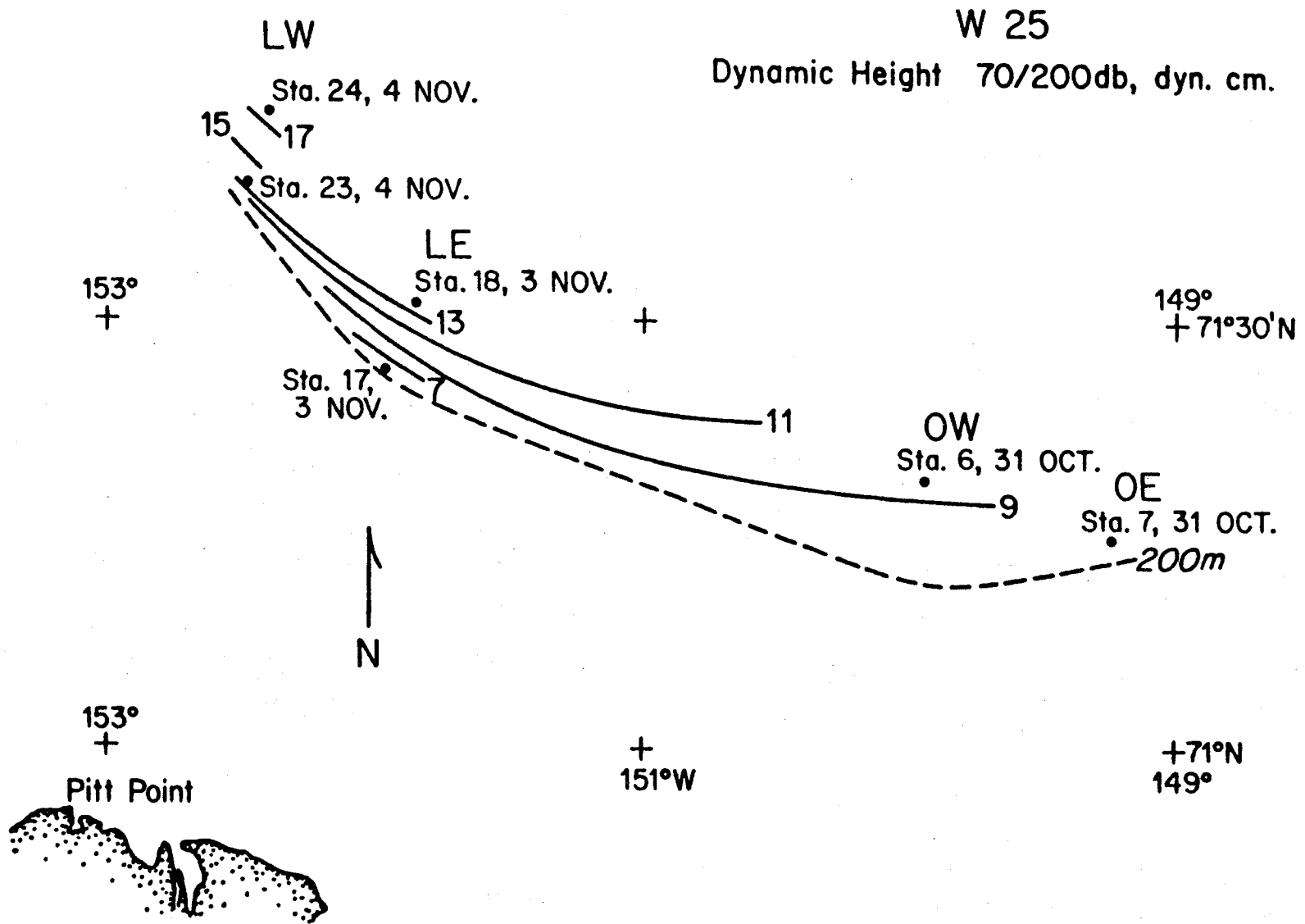


Figure 30. Dynamic topography, 70/200 db, seaward of the shelf break during W-25.

pressure gradient. Note that in Figure 30 the dynamic topography does in fact stand higher toward the west, suggesting an onshore geostrophic flow, so that a variety of combinations of dynamics are possible. Certainly, the further clarification of the dynamics of deep upwelling on the Beaufort shelf will require both designated experiments and modeling efforts.

A final implication of the moored temperature records relates to the depth of influence of the Bering Sea water. Mountain's (1974) data suggest that this influence probably does not extend below about 100-125 m. However, comparison of the records from LO-6 show the likelihood that even at the lower instrument, at 188 m, the arrival of the Bering Sea water in late July can be seen in the temperature signal: the initial very large temperature pulse signaling the influx of the Bering Sea water at 68 m is duplicated with somewhat reduced amplitude at 188 m. An occasional direct Bering Sea influence should therefore be expected to extend to the bottom even on the outer shelf.

The transition zone

At some offshore distance over the shelf there must be a transition from the outer to the inner shelf regime, e.g., to a regime that is more nearly isotropic in its current distribution, or in which the invasion of Bering Sea water is relatively rare. In one sense, of course, we should not dwell unduly on the concept of a transition zone, for it is not necessarily a dynamically unique region. More likely it is simply an area of the shelf where at one time, the motion resembles that of the outer shelf, and at another time it is more like that of the relatively shallow and flat inner shelf. Nonetheless, Figure 3 suggests that the FLAX-1 mooring is close to such a transition area, since the current roses have a markedly less bimodal

directional character than at other installations further seaward. (This may also be true at OL-1, but to a lesser extent). Since FLAX-1 was located in 59 m depth, our earlier estimated demarcation between the outer and inner shelf regimes near the 40-50 m isobaths is probably not far removed from a useful rule-of-thumb.

Figure 31 shows the daily mean current at FLAX-1. It is obvious that off-shore flow events were more common than onshore ones (compare also the current roses in Figure 3), were fairly strong (daily means frequently exceeded 5 cm sec^{-1}), and typically had a duration of three days or more. Identifying a likely cause of the offshore events has thus far been futile. Offshore flow occurred most frequently during the first three months, although there is no obvious reason why this should be so. Most surprisingly, there appears to be no significant correlation between the cross-shelf flow and either wind component. Conceivably this may be due to an inadequate representation of the local wind field, but while a wind-driven origin of such cross-shelf flow events cannot be entirely discounted on the basis of the present data, it seems unlikely. Speculation as to other causes remains just that.

Concluding remarks

An important facet of the outer shelf circulation (say, seaward of the 50 m isobath) is that it is energetic throughout the year. Not only is there large variability at time scales of days to weeks, but because of the relatively large long-term mean flow, there is an intimate connection between the shelf and areas far removed from it. Specifically, the strong longshore current on the outer shelf is a very efficient transport mechanism. This

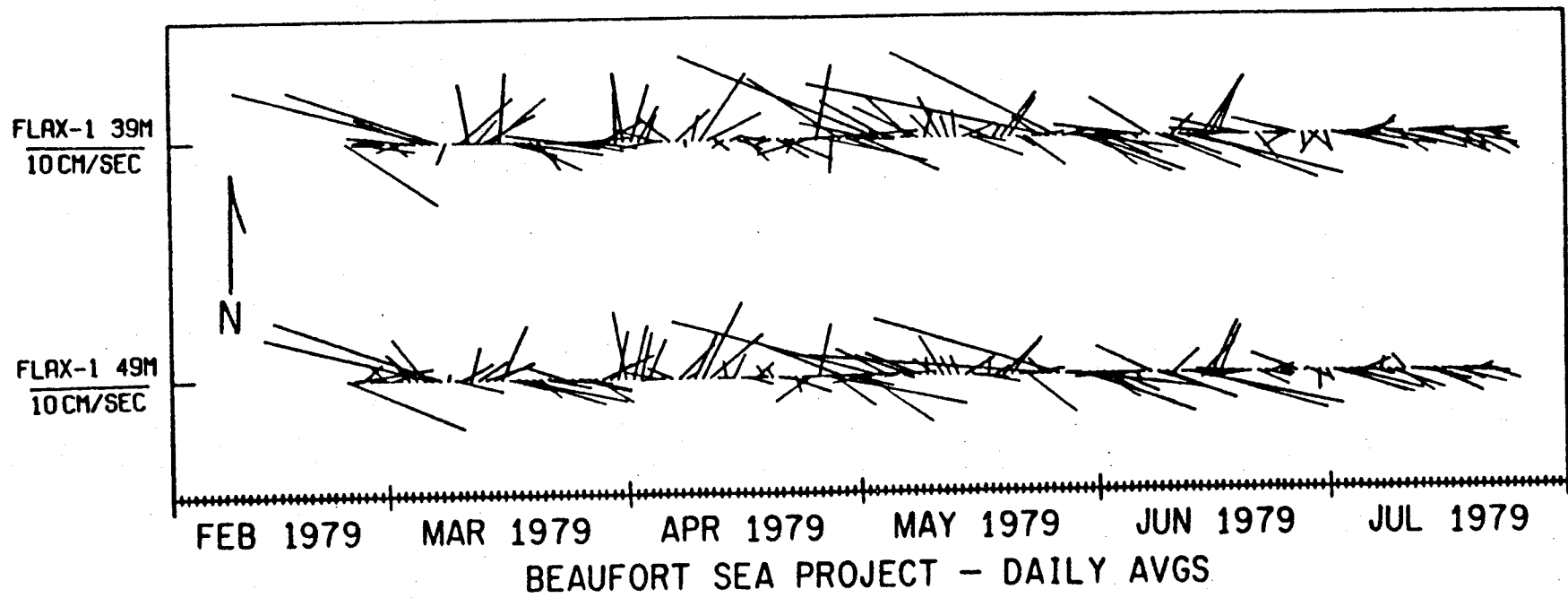


Figure 31. Daily mean current at FLAX-1.

means not only that events on the Alaskan shelf can propagate long distances, e.g., into the Canadian Beaufort, and probably through the Canadian Archipelago as well, but it also means that events in other places affect the north Alaskan shelf. For example, water from the Bering Sea has a major impact on the Beaufort shelf hydrography and undoubtedly also on the biota.

There is also clear communication with the Arctic Ocean, most dramatically through the relatively frequent upwelling events. To illustrate how far-reaching such connections can be, I venture to predict that within the next 2-3 decades, tracer sampling of upwelling events on the outer shelf will yield $^{137}\text{Cs}/^{90}\text{Sr}$ ratios of 2 or more. These would be unequivocal evidence of influx from the British Windscale nuclear fuel processing plant in the Irish Sea, entering the Arctic Ocean with the Atlantic water that flows northward through the Norwegian and Greenland seas. The point of these remarks is that only on relatively short time scales (say, a month or less) could the north Alaskan shelf be considered self-contained.

A second important facet of the shelf circulation is that there are frequent cross-shelf motions (in addition to the upwelling events). These are probably of several different types and origins, each with its own characteristics. There is therefore ample opportunity for inshore events to propagate offshore and *vice versa*. In the long-term mean, there must of course be a small offshore net flow due to runoff. However, the inshore sinks and sources of buoyancy and water (e.g., winter brine production and summer river discharge) are certainly not uniform line sources. Coupled with long-shore differences in bathymetry, these non-uniformities will almost certainly lead to preferred local avenues of cross-shelf exchange. Such preferred regions might be of quite small lateral extent.

A third matter is that while tidal currents have been outside the thrust of this discussion of the shelf circulation, it's important to note that they may be sufficiently large on the shelf to figure in certain mixing and dispersion problems. For example, the FLAX-1 records show a semi-diurnal component in the range 5-10 cm sec⁻¹. This contrasts with Mountain's (1974) estimate for Barrow Canyon of less than 1 cm sec⁻¹ and with 1-2 cm sec⁻¹ at the NAR-1 and -2 sites in winter, but is similar to values at our outer shelf moorings.

Finally, it is important to point out that there are a great many voids in our knowledge. These range from the most basic descriptive deficiencies (this is probably most pronounced on the inner shelf, where there is a remarkable lack of the long time series necessary to establish useful statistics) to an understanding of the dynamics that at present is largely conjectural. While filling the most glaring of these voids is certainly a major exercise, there is no doubt that the skills and experience exist to do so. What in fact has been achieved these past five years is 1) a first-level understanding that is both sufficiently broad and quantitative to let us ask intelligent and meaningful questions, and 2) the demonstrated experimental ability to answer such questions.

References

- Aagaard, K., L.K. Coachman and E.C. Carmack. In press. On the halocline of the Arctic Ocean. *Deep-Sea Res.*
- Aagaard, K., C. Darnall and F. Karig. 1978. Measurements with moored instruments in ice-covered waters. *Deep-Sea Res.*, 25, 127-128.
- Allen, J.S. 1973. Upwelling and coastal jets in a continuously stratified ocean. *J. Phys. Oceanogr.*, 3, 245-257.
- Bailey, W.B. 1957. Oceanographic features of the Canadian Archipelago. *J. Fish. Res. Board, Canada*, 14(5), 731-769.
- Barnes, P., E. Reimnitz, and D. McDowell. 1977. Current meter and water level observations in Stefansson Sound, Summer 1976. *U.S.G.S. Open-file Report 77-477*, 7 pp.
- Barnes, P.W. and L.J. Toimil. 1979. Inner shelf circulation patterns, Beaufort Sea, Alaska. *U.S.G.S. Miscellaneous Field Studies Map MF-1125*.
- Barnes, P. and E. Reimnitz. 1974. Sedimentary processes on arctic shelves off the northern coast of Alaska. Pp. 439-476 in *The Coast and Shelf of the Beaufort Sea*, J.C. Reed and J.E. Sater, eds., Arctic Institute of North America, Arlington, VA 750 pp.
- Buckley, J.R., T. Gammelsrød, J.A. Johannessen, O.M. Johannessen and L.P. Røed. 1979. Upwelling: oceanic structure at the edge of the arctic ice pack in winter. *Science*, 203(4376), 165-167.
- Coachman, L.K. and K. Aagaard. 1974. Physical oceanography of arctic and subarctic seas. Pp. 1-72 in *Marine Geology and Oceanography of the Arctic Seas*, Y. Herman, ed., Springer-Verlag, New York, 397 pp.

- Coachman, L.K. and K. Aagaard. In press. Re-evaluation of water transports in the vicinity of Bering Strait. In *Oceanography of the Bering Sea Shelf*, D. Hood, ed.
- Coachman, L.K., K. Aagaard and R.B. Tripp. 1975. *Bering Strait: The Regional Physical Oceanography*. University of Washington Press, Seattle, 172 pp.
- Collin, A.E. 1963. Waters of the Canadian Arctic Archipelago. Pp. 128-139 in *Proceedings of the Arctic Basin Symposium*, Arctic Institute of North America, Washington, D.C., 313 pp.
- Drake, D. 1977. Suspended matter in nearshore waters of the Beaufort Sea. *U.S.G.S. Open-file Report 77-477*, 13 pp.
- Henry, R.F. 1975. Storm surges. *Tech. Rept. No. 19, Beaufort Sea Project*. Dept. Environment, Victoria, B.C. 41 pp.
- Herlinveaux, R.M. 1974. Surface movements in Canadian arctic waters with some accompanying temperature and salinity observations. Unpublished manuscript, *Pacific Marine Science Report*, Marine Sciences Directorate, Pacific Region, Environment Canada, Victoria, B.C., 36 pp.
- Hibler, W.D., III. 1979. A dynamic thermodynamic sea ice model. *J. Phys. Oceanogr.*, 9(4), 815-846.
- Hickey, B.M. 1979. The California Current system. *Prog. Oceanogr.*, 8, 191-279.
- Hufford, G.L. 1973. Warm water advection in the southern Beaufort Sea August-September 1971. *J. Geophys. Res.*, 78(15), 2702-2707.
- Hufford, G.L. 1974. On apparent upwelling in the southern Beaufort Sea. *J. Geophys. Res.*, 79, 1305-1306.

- Hufford, G.L. 1975. Some characteristics of the Beaufort Sea shelf current. *J. Geophys. Res.*, 80(24), 3465-3468.
- Hufford, G.L. and R.D. Bowman. 1974. Airborne temperature survey of Harrison Bay. *Arctic* 27(1), 69-70.
- Hufford, G.L., S.H. Fortier, D.E. Wolfe, J.F. Doster and D.L. Noble. 1974. Physical oceanography of the western Beaufort Sea. In *Marine Ecological Survey of the Western Beaufort Sea*. U.S.C.G. Oceanogr. Rept. CG-373.
- Hufford, G.L., I.M. Lissauer and S.P. Welsh. 1976. Movement of spilled oil over the Beaufort Sea, a forecast, *U.S.C.G. Oceanogr. Rept. CG-D-101-76*, 87 pp.
- Hufford, G.L., B.D. Thompson and L.D. Farmer. 1977. Surface Currents of the northeast Chukchi Sea. *Annual Report RU 81 OCSEAP Arctic Project*, unpublished manuscript.
- Huggett, W.S., M.J. Woodward, F. Stephenson, W. Hermiston and A. Douglas. 1975. Near bottom currents and offshore tides. *Tech. Rept. No. 16, Beaufort Sea Project*. Dept. of Environment, Victoria, Canada. 38 pp.
- Johnson, M.W. 1956. The plankton of the Beaufort and Chukchi Sea areas of the Arctic and its relation to the hydrography. *Arctic Institute of North America, Tech. Pap. No. 1*, 32 pp.
- Matthews, J.B. 1971. Long period gravity waves and storm surges on the Arctic Ocean continental shelf. *Proc. Joint Oceanogr. Assembly, Tokyo 1970*. D1-I-7, 332.
- Mountain, D.G. 1974. Bering Sea water on the north Alaskan shelf. Unpublished thesis, University of Washington, 153 pp.

- Newton, J.L. 1973. The Canada Basin; mean circulation and intermediate scale flow features. Unpublished thesis, University of Washington, 157 pp.
- Paquette, R.G. and R.H. Bourke. 1974. Observations on the coastal current of arctic Alaska. *J. Mar. Res.*, 32(2), 195-207.
- Schaeffer, P.J. 1966. Computation of a storm surge at Barrow, Alaska. *Archiv für Meteorologie, Geophysik und Bioklimatologie, Ser. A Meteorologie und Geophysik*, 15(3-4), 372-393.
- Schwerdtfeger, P.J. 1974. Mountain barrier effect on the flow of stable air north of the Brooks Range. Pp. 204-208 in *Climate of the Arctic*, Geophysical Institute, University of Alaska, Fairbanks.
- Searby, H.W. and M. Hunter. 1971. Climate of the North Slope of Alaska. *NOAA Tech. Memo. NWS AR-4*, Anchorage, 53 pp.
- Walker, E.R. 1977. Aspects of oceanography in the Archipelago. IOS Note 3, Institute of Ocean Sciences, Patricia Bay, Sidney, B.C., 186 pp.
- Walker, H.J. 1973. Spring discharge of an arctic river determined from salinity measurements beneath sea ice. *Water Resources Res.*, 9(2), 474-480.
- Wiseman, W.J., J.N. Suhayda, S.A. Hsu and C.D. Walters. 1974. Characteristics of nearshore oceanographic environment of Arctic Alaska. Pp. 49-64 in *The Coast and Shelf of the Beaufort Sea*, J.C. Reed and J.E. Sater, eds., Arctic Institute of North America, Arlington, VA 750 pp.

NOAA Technical Memorandum ERL PMEL-22

PHYSICAL OCEANOGRAPHIC AND METEOROLOGICAL CONDITIONS
IN THE NORTHWEST GULF OF ALASKA

Robin D. Muench
James D. Schumacher

Contributors:
C. A. Pearson
R. M. Reynolds
R. Overstreet

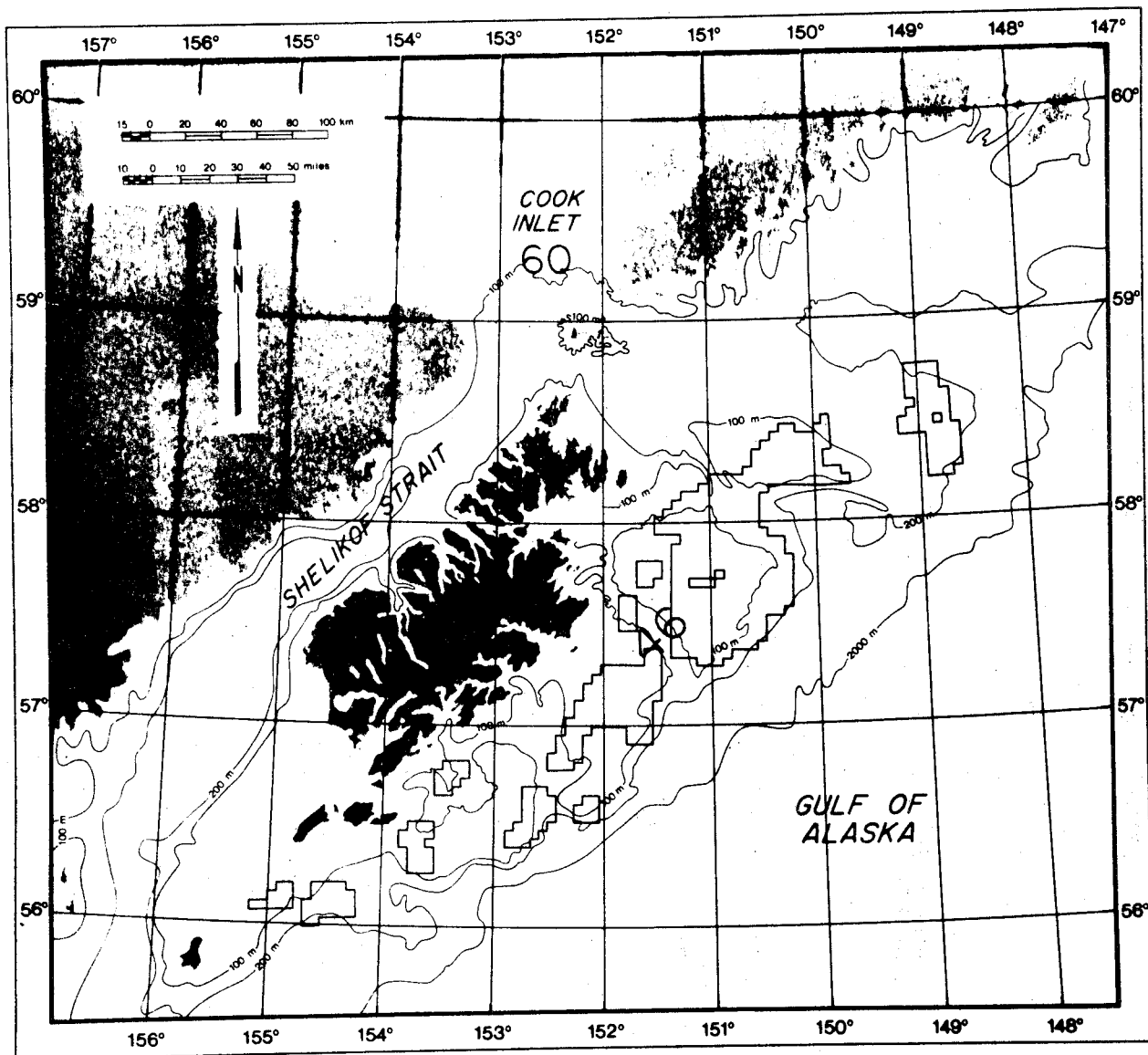
Pacific Marine Environmental Laboratory
Seattle, Washington
October 1980



**UNITED STATES
DEPARTMENT OF COMMERCE**
Philip M. Klutznick, Secretary

NATIONAL OCEANIC AND
ATMOSPHERIC ADMINISTRATION
Richard A. Frank, Administrator

Environmental Research
Laboratories
Joseph O. Fletcher, Acting Director



Frontispiece. Geographical locations in the northwest Gulf of Alaska, showing specific locations of present Outer Continental Shelf lease areas south of Kodiak Island (Sale 46) and general location of present lease area in lower Cook Inlet (Sale 60).

TABLE OF CONTENTS

EXECUTIVE SUMMARY	79
1. INTRODUCTION	84
1.1 Statement of Purpose	84
1.2 Geographical Setting	89
1.3 History of Past Research	94
1.4 Oceanographic and Meteorological Setting	97
2. OBSERVATIONAL PROGRAM	103
2.1 Program Rationale	103
2.2 Current Observation Program	104
2.2.1 Taut-Wire Moorings	104
2.2.2 Drift Card Studies	112
2.2.3 Satellite-Tracked Buoys	113
2.2.4 Wave Radar (CODAR) Observations	114
2.3 Temperature and Salinity Observations	116
2.4 Meteorological Observations	117
3. RESULTS AND DISCUSSION	121
3.1 Mean Currents, Seasonal Variability and the Temperature, Salinity and Density Fields	121
3.1.1 Introduction	121
3.1.2 The General Northwestern Gulf Region	121
3.1.3 The Kenai Current	124
3.1.4 Shelikof Strait and Lower Cook Inlet	135
3.1.5 The Bank and Trough Region	142
3.2 Behavior of Low-Frequency Current Fluctuations	150
3.2.1 Introduction	150

3.2.2	The Bank-Trough Region	150
3.2.3	Shelikof Strait	154
3.2.4	Lower Cook Inlet	162
3.3	Tidal Currents	172
3.4	Partitioning of Current Energy with Frequency	183
3.5	Wind Observations	190
3.5.1	Orographic Control	190
3.5.2	Lower Cook Inlet Meteorology	191
4.	ACKNOWLEDGEMENTS	214
5.	REFERENCES	215
6.	APPENDIX A: Current Meter Statistics for Northwest Gulf of Alaska Moorings	219
	APPENDIX B: Release and Recovery Information for Draft Cards Released in the Kodiak Island Region During 1978	222
	APPENDIX C: Release and Recovery Information for Seabed Drifters, Including Returns Through February 1980	228
	APPENDIX D: CTD Stations used in NWGOA Program, Listed by Cruises	230

EXECUTIVE SUMMARY

This report presents a summary of the major findings of Outer Continental Shelf Environmental Assessment Program research into physical oceanographic conditions in the northwest Gulf of Alaska. The stress is on circulation features, since water circulation plays a major role in the path and dispersal of surface contaminants, a problem of major impetus for the OCSEAP program. Reference is made throughout this summary section to Figure i, which summarizes the net circulation regime as deduced from this study. On the figure, arrows depict sense of net flow while the numbers represent a typical range of current speeds, in centimeters per second, which might be encountered in that region. In general, the smaller numbers represent spring-summer conditions while the larger numbers represent autumn-winter conditions. It is stressed here that instantaneous flow observed at a given time need not agree with our simplified graphical depiction. The patterns shown are, rather, indicative of mean conditions and of a normal response to the dynamics which we feel exert dominant control over the system.

The results can be summarized as follows:

1. The Alaskan Stream is a major regional oceanic circulation feature. It flows southwesterly, roughly coincident with the shelf break and slope, with mean speeds of 50-100 cm sec⁻¹. Its width is about 50 km, and its computed annual mean baroclinic volume transport is about $12 \times 10^6 \text{ m}^3 \text{ sec}^{-1}$. There was no significant annual variability detected either in baroclinic current speed or volume transport. There were eddy-like perturbations observed in the current, at times, which appeared to be related to bottom

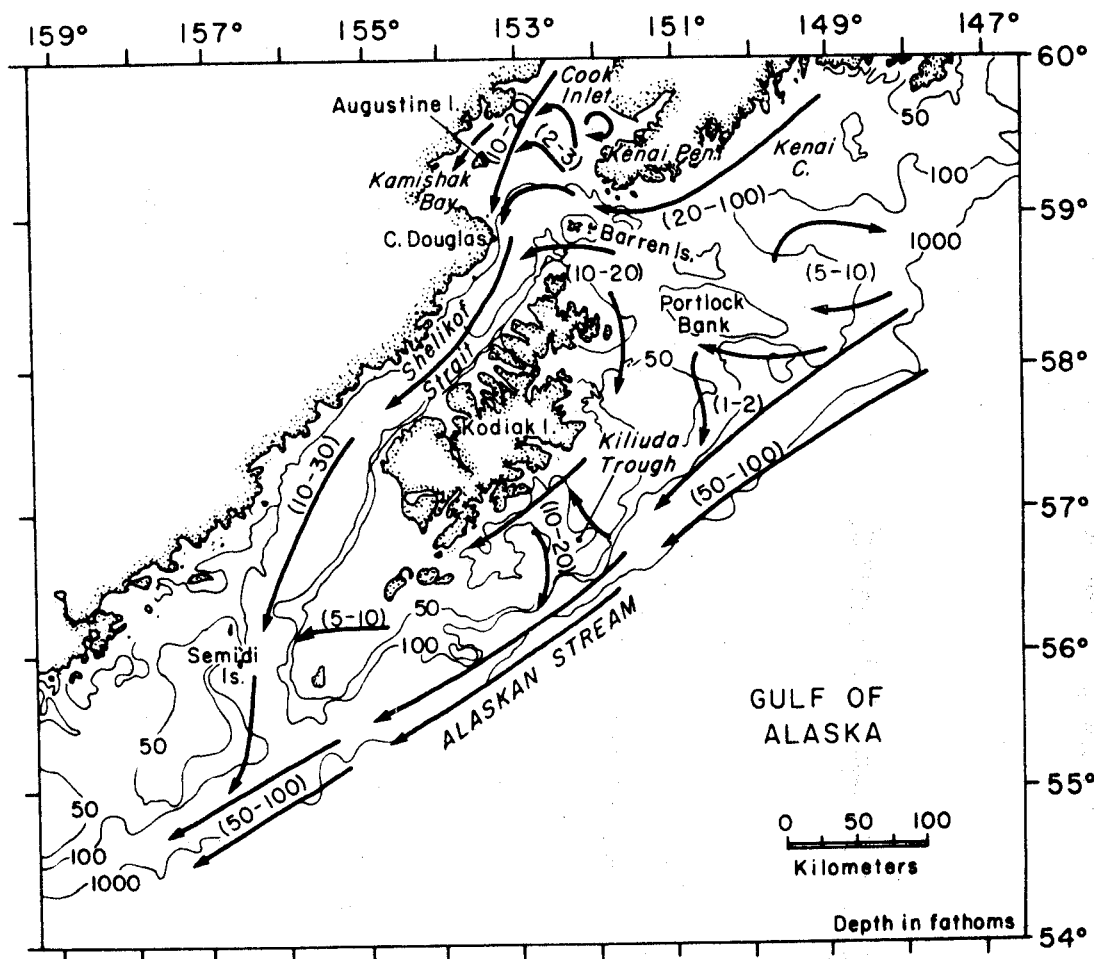


Figure i. Schematic diagram of net circulation in the northwest Gulf of Alaska. Arrows indicate direction of mean surface flow, and numbers in parentheses indicate approximate range of speeds in cm sec^{-1} .

topography. A principal driving force for the Alaskan Stream is the wind stress curl over the Gulf of Alaska, which forces the North Pacific subarctic gyre. The Alaskan Stream is the intensified, northwestern leg of this gyre.

2. Dominant circulation on the banks south and southeast of Kodiak Island is predominantly driven by the Alaskan Stream. This includes a poorly defined, weak ($5-10 \text{ cm sec}^{-1}$) anticyclonic circulation over Portlock Bank, and a complex flow regime connected with the bank-trough region to the southwest. This bank-trough flow, which apparently represents a bathymetric effect upon the inshore edge of the Alaskan Stream, consists of shoreward flow along the upstream (northeastern) sides of the troughs and a compensatory seaward flow along the downstream (southwestern) sides. The coastal southwesterly flow at the head of Kiliuda Trough reflects this residual circulation, but is probably also due in part to a baroclinic coastal wedge consequent to freshwater input along the south coast of Kodiak Island.

3. A nearshore southwesterly flow along the Kenai Peninsula, the Kenai Current, is a baroclinic coastal current driven by the density field created by freshwater input along the Alaskan coast. This flow is 20-30 km in width and attains maximum current speeds in autumn following the annual period of maximum coastal precipitation and freshwater input. This flow is at its annual minimum during spring and early summer.

4. Flow through Shelikof Strait is southwesterly, with observed speeds during winter ($\sim 20 \text{ cm sec}^{-1}$) twice those in summer ($\sim 10 \text{ cm sec}^{-1}$). No flow reversals were observed during winter; during summer, the weaker mean flow was accompanied by occasional reversals. This flow is driven in part by the Kenai current upstream and in part by a large-scale alongshore pressure gradient established by the Alaskan Stream. The flow through Shelikof Strait continues to the southwest in a well-defined channel bounded by

relatively shallow banks, merging with the Alaskan Stream some 200 km southwest of Kodiak Island.

5. Circulation in lower Cook Inlet is dominated by the southwesterly flow into Shelikof Strait, which is constrained by bottom topography to traverse an arcuate east-west path across the lower Inlet. Off Cape Douglas, this flow merges with a weaker southward current generated by the freshwater input to upper Cook Inlet, creating a particularly intense southward flow in the region off Cape Douglas. Flow in the central lower inlet out of these two well-defined currents is weak and highly variable.

6. Currents throughout the study region are characterized by speed and direction fluctuations having time scales between about 2 days and a week. These fluctuations are probably related either to meteorological factors or to propagation of ocean eddies across the shelf, though the exact mechanisms are uncertain. In regions such as Shelikof Strait, with a strong mean flow, these fluctuations are of lesser significance relative to the mean flow, leading to speed fluctuations but only minor perturbations to direction. In regions of weak mean flow, such as in central lower Cook Inlet and on Portlock Bank, the fluctuations both in speed and direction are the dominant flow characteristics.

7. Tidal currents vary widely in magnitude throughout the study region. Tidal current effects in Shelikof Strait are minimal because of the standing wave nature of the tidal wave there, and tidal currents become small as the coast is approached south of Kodiak Island. Lower Cook Inlet is characterized, conversely, by large tidal currents particularly in the passages north and south of the Barren Islands due to the near-resonant conditions which lead to extremely large tides in upper Cook Inlet. Tidal currents are also significant in comparison with mean flow on the banks south of Kodiak Island.

8. Winds are controlled by the interaction between large-scale north-eastward migrating cyclonic low pressure systems and regional topography. Over the banks south of Kodiak Island, observed winds appear to agree reasonably well with geostrophic winds computed from the atmospheric surface pressure distributions. In lower Cook Inlet, winds are orographically channelled into two orthogonal paths whose axes are aligned with upper Cook Inlet-Shelikof Strait and Barren Islands-Kamishak Bay. This leads to a complex wind pattern there which results from the interaction between these orthogonal flows. Katabatic (drainage) winds may be important locally, particularly in lower Cook Inlet and Shelikof Strait, and wake effects perturb the wind field downstream from such features as Augustine Island.

The picture presented here of major circulation features in the northwest Gulf of Alaska is one of extreme complexity. The various possible combinations of mean, low frequency fluctuating and tidally fluctuating flow lead to a regime wherein prediction of instantaneous flow is impossible. We believe, however, that the flow field has been sufficiently well defined to allow a good prediction of seasonal mean flow. Combined with knowledge of the local and regional wind field, this allows at least an approximate predictability of contaminant dispersion and trajectory.

PHYSICAL OCEANOGRAPHIC AND METEOROLOGICAL CONDITIONS
IN THE NORTHWEST GULF OF ALASKA¹

Robin D. Muench² and James D. Schumacher

1. INTRODUCTION

1.1 Statement of Purpose

1.1.1. Objectives

The primary objective of the Alaska OCS Environmental Studies Program is to provide background information for management decisions that may be necessary to protect the OCS marine environment from damage during oil and gas exploration and development. Meaningful data must be readily available in useable form so that informed management decisions can be made before serious or irreversible damage occurs. Protection of the marine and coastal environment is a direct outgrowth of the National Environmental Policy Act of 1969.

In an assessment of the potential impact of OCS development on the marine environment, transport and transformation of petroleum-related contaminants is of key significance. Petroleum or other contaminants introduced into the environment can be transported in the atmosphere, water column and sea ice. During transport, oil and other contaminants undergo continual physical and chemical change brought about by such processes as evaporation, flocculation, emulsification, weathering, biodegradation, and chemical decomposition.

Transport studies are specifically designed to provide data that will enable the Department of the Interior and other agencies to:

- . Plan stages and siting of offshore petroleum development so as to minimize potential risk to environmentally sensitive areas.

¹Contribution No. 482 from the NOAA Pacific Marine Environmental Laboratory
²Now at SAI/Northwest, 13400B Northrup Way #36, Bellevue, WA 98005

- . Provide trajectory, coastal landfall, and impact predictions required for cleanup operations in the event of an oil spill or the introduction of other contaminants.
- . Assist in planning the locations of long-term environmental monitoring stations in the study area.

The programmatic objectives described above have resulted in several disciplinary studies of which one element, coastal oceanography and meteorology, directly addresses the problem of movement of contaminants in continental shelf waters.

The primary objective of the OCSEAP oceanography/meteorology studies in the western Gulf of Alaska is to provide, through experimental and theoretical studies, a capability to predict movement and distribution of contaminants introduced into the marine environment through OCS oil and gas development activities. Specific program elements have required the development of methodologies and implementation of studies designed to supply information on:

- . Energetics and temporal and spatial variability of coastal ocean circulation in the northwestern Gulf of Alaska;
- . Energetics and spatial variability of tidal currents;
- . Local wind fields and their influence on coastal circulation;
- . Influence of the seasonal heat budget, runoff and precipitation on coastal and estuarine circulation and water mass structure;
- . Bathymetric influence on tidal and nontidal circulation and turbulent mixing; and
- . Ways to apply data to the prediction of pathways and impact areas of potential pollutants (especially oil) that will aid the assessment of vulnerability of biotic resources and the design of more effective cleanup strategies.

This presents an integrated description of the oceanography and meteorology of the western Gulf of Alaska continental shelf. This description

includes the rationale for the various elements of the study program and a presentation of results, analysis techniques and interpretive procedures by which these program elements have been combined to provide an improved understanding of coastal circulation and winds and their likely influence on pollutant transport.

1.1.2 Rationale

Development of an information base that permits prediction, in a probabilistic sense, of the spatial and temporal distribution of petroleum-related contaminants following hypothetical release in coastal waters is a primary function of the OCSEAP transport studies. Such information, in conjunction with seasonal and spatial description of potentially vulnerable marine resources, provides a critical input to the Bureau of Land Management's (BLM's) environmental assessment process. Insofar as this assessment concerns the potential impacts of OCS-related pollutants, BLM's major effort is focused on spilled oil and its subsequent movement on the water surface.

In the Draft Environmental Impact Statement (DEIS), which is to be prepared by the Bureau of Land Management, the most readily apparent use of the oceanographic and meteorological study results is the oil spill risk analysis performed by the U.S. Geological Survey. However, problems of oil incorporation into the water column and sediments and potential impacts of drilling muds, toxic metals, formation waters and other potential pollutants are also of concern. Hence the oceanographic and meteorological studies provide information on both surface and subsurface phenomena that have bearing on the overall problem of contaminant distributions on the continental shelf. Similarly the modeling activities, aside from producing information for the calculation of spilled oil trajectories, also perform important roles in data synthesis, hypothesis formulation and field study design.

Prior to OCSEAP, no systematic studies had addressed mesoscale oceanographic features on the Gulf of Alaska continental shelf. Oceanographic knowledge was limited to a description of large-scale circulation obtained almost exclusively from water mass analyses based on irregular, widely spaced hydrographic data. While knowledge of large-scale flow features such as the Alaska Current and Alaskan Stream was useful in providing a gross picture of Gulf of Alaska circulation, it furnished little insight into smaller scale features present on the continental shelf and responsible for near-coastal transport of contaminants. A need for such information has required the development, through OCSEAP, of a systematic program of mesoscale physical oceanographic and meteorological studies on the continental shelf.

Oceanographic studies in the western Gulf of Alaska cover the geographic region comprising the present Kodiak (Sale 46) and lower Cook Inlet-Shelikof Strait (Sale 60) OCS lease areas shown on the frontispiece. The region consists of the Alaska continental shelf area between Seward and Mitrofanina Island on the Alaska Peninsula, including Shelikof Strait and that portion of Cook Inlet south of Kalgin Island.

Oceanographic field studies have employed a variety of techniques including seasonal hydrographic surveys, time series observations of currents, pressure and water properties, Lagrangian current observations, HF Doppler radar current observations, and drift cards. The primary purpose of these studies is to provide the information necessary to develop a picture of continental shelf circulation and mixing processes, including significant temporal and spatial variability scales, relevant to the transport of pollutants.

The importance of local wind forcing to the dynamics of continental shelf waters and to the subsequent movements of potential contaminants was recognized from the program's beginning. It was also recognized that local winds along the Gulf of Alaska coast can differ significantly, because of the effects of coastal orography and land-sea boundaries, from those determined from synoptic weather charts or land-based stations. These differences can lead to substantial errors in pollutant transport predictions based on traditional synoptic geostrophic wind calculations or inappropriately located (for OCSEAP's requirements) weather stations. Consequently, the oceanographic program has been accompanied by concurrent coastal meteorological investigations that include an expanded network of shore stations, over-the-water wind and pressure measurements from meteorological data buoys and ships of opportunity, and computer simulations of coastal winds. These studies have resulted in the development of a technique for determination of mesoscale wind fields that consists of (1) derivation of a synoptic weather pattern climatology in the form of a limited number of surface pressure distributions, based on historical data and judged adequate in number to characterize the region; (2) development of appropriate synoptic climatology statistics, including pattern durations and transition probabilities; (3) calculation, via a combination of direct observations and modeling, of the mesoscale wind field most likely to be associated with and driven in part by each synoptic pattern; and (4) use of (1) - (3) above to derive a statistical description of the local wind climatology. This technique attempts to correlate local wind patterns with regional synoptic distributions which have a statistically meaningful data base and are routinely observable.

Oceanographic and meteorological field studies in the western Gulf of Alaska have been accompanied by computer simulation models of coastal

circulation patterns and likely pollutant trajectories. Models employed to date have been of three general types: (1) a diagnostic circulation model utilizing observed winds and hydrography as input and observed currents as calibration data; (2) a tidal model; and (3) an empirical model based on observed currents and winds. Specific model application has depended on the study area in question and the driving forces and physical mechanisms believed to be dominant in that region. These models have been used both in a predictive sense and as vehicles for the synthesis and interpretation of observed data.

Collectively, the modeling activities and oceanographic field studies have been employed in an interactive fashion to provide an improved understanding of coastal circulation patterns and dynamical processes.

1.2 Geographical Setting

In discussing physical oceanographic processes in the northwestern Gulf of Alaska, we focus primarily upon coastal and continental shelf regimes. Physical factors which are known to exert primary controls over circulation in such regions include bottom depth and slope, continental shelf width, and orientation of the coastline relative to north. On a smaller scale, coastline and bottom topographic irregularities can exert significant influence over local circulation features. Since we address a broad range of both temporal and spatial scales of oceanographic processes, it is necessary to discuss in some detail those geographical and bottom features which we expect a priori to significantly affect oceanographic conditions.

The northern Gulf of Alaska is an arcuate, east-west trending bight which forms the northern boundary of the northeastern Pacific Ocean (Fig. 1). We are concerned here with the portion of the Gulf extending from the shoreline seaward to the continental shelf break, as defined approximately

by the 200-m isobath, and westward from 148°W to about 160°W. This area encompasses a segment of continental shelf characterized by complex shoreline and bottom topography which includes numerous embayments and channels, banks and troughs. The shelf is about 175 km wide throughout our study region. Kodiak Island, along with its smaller adjacent islands, may be viewed as a barrier to flow which is centrally located on the shelf and surrounded by a system of relatively shallow banks. Alternately, the shelf may be considered to occupy the region southeast and east of Kodiak Island, with Shelikof Strait being a major channel separate from the shelf proper. (Both viewpoints will be used, depending upon the context.) Cook Inlet extends northeasterly from the shelf directly north of Kodiak Island; the lower Cook Inlet-Shelikof Strait system comprises a complex system of deep channels. Overall alongshore orientation of this continental shelf system is northeast-southwest. Seaward of the 200-m deep shelf break, the bottom drops abruptly to attain maximum depths of 5000-6000 m in the Aleutian Trench.

The continental shelf area southeast of Kodiak Island is about 60 km wide. Bottom topography there and to the northeast is dominated by four relatively shoal (~90 m) areas separated from one another by deeper channels which transect the shelf in a direction roughly normal to the coastline (Fig. 1). The shoals are, from northeast to southwest, Portlock and North, Middle and South Albatross Banks. At the northeastern extremity of this system of banks, Amatuli Trough trends east-west with depths exceeding 200 m. At its western end, this trough bifurcates to form the deeper portions of the channels entering Cook Inlet via Kennedy and Stevenson Entrances and, in so doing, provides a relatively deep access (~100 m) from the shelf break to the waters of lower Cook Inlet. To the south of Amatuli Trough lies Portlock Bank, which has depths of less than 50 m and is separated from

North Albatross Bank to the southwest by Stevenson Trough. At its shallowest point, in the narrow channel west of Portlock Bank, Stevenson Trough is about 110 m deep. Depths on North Albatross Bank are 70-90 m. North and Middle Albatross Banks are separated by Chiniak Trough, which has maximum depths of about 145 m. Minimum depths on both Middle and South Albatross banks are about 30 m and are found at the seaward boundary of the banks. Kiliuda Trough separates Middle and South Albatross Banks, has maximum depths of about 150 m, and near the coastline turns and trends southwest to form an inverted L-shaped depression with generally complex topography. Maximum vertical relief in this system of banks and troughs is found surrounding Kiliuda Trough.

Shelikof Strait lies between Kodiak and Afognak Islands and the Alaska Peninsula and is uniformly about 45 km wide, forming a major channel for alongshore flow. At its northern end it is connected to the open shelf via Kennedy Entrance north of the Barren Islands, and via Stevenson Entrance between the Barren Islands and Afognak Island. Kennedy Entrance is the narrower of the two but has greater depths (~200 m). Maximum depths in Stevenson Entrance are about 120 m. The northeastern half of Shelikof Strait is somewhat shallower than the southwestern half, or about 180 m as compared to 200 m. The extension of the Strait across the shelf southwest of Kodiak Island is bounded on both sides by banks and has maximum depths of about 200 m. The adjacent banks are 30-40 m deep to the southeast and 100 m deep to the northwest where they shoal to form Sutwik and the Semidi Islands.

Cook Inlet is a broad (70-90 km), shallow (mean depth about 60 m), elongate embayment extending northeastward from the confluence between Shelikof Strait and Kennedy and Stevenson Entrances (Fig. 2). This study deals only with the lower portion of the Inlet defined as that region

bounded on the north by the Forelands and on the south by Kennedy and Stevenson Entrances and Shelikof Strait. At the northern end of lower Cook Inlet, Kalgin Island and its associated shoals reduce water flow in the western half of the Inlet. In the central portion of the lower Inlet, bottom depths are 60-80 m. Depth increases to the south in regular fashion except for a prominent ramp-like feature which traverses the inlet from east to west in arcuate fashion along the 100-m isobath. Maximum depths in the inlet occur in a depression just west of Stevenson Entrance. Several embayments extend laterally from the Inlet.

Land areas surrounding the northwestern Gulf of Alaska are extremely mountainous. On Kodiak Island, these mountains rise to elevations of 1000-2000 m, while along the northern shores of Cook Inlet and Shelikof Strait elevations are 2000-3000 m. The mountains are transected by valleys, many containing glaciers or snowfields at their heads. This rugged topography surrounding the study region is of interest because it exerts a marked effect upon local winds, which in turn can affect water circulation.

1.3 History of Past Research

Prior to commencement of the OCSEAP studies, little information was available concerning physical oceanographic conditions on the northern Gulf of Alaska shelf. Few field data were available from the shelf region, since early investigations were confined primarily to the Alaskan Stream or the Gulf of Alaska subarctic gyre. The Alaskan Stream is an offshore boundary current which flows southwestward along the shelf break, forming the northwestern branch of the subarctic gyre. The single exception to this was the early work of McEwen, et al. (1930), who used temperature and salinity data obtained along sections normal to the coastline in the northeast Gulf of Alaska to describe and analyze temperature, salinity and current structures over the shelf and shelf break.

Some three decades following the work of McEwen, et al. (1930), acquisition of substantial sets of new field data allowed investigators to concentrate on the northwestern Gulf. Resulting manuscripts used temperature and salinity data to address circulation processes in the Alaskan Stream southwest of Kodiak Island and westward along the Aleutian Islands (Dodimead et al., 1963; Favorite, 1967; Roden, 1969; Favorite et al., 1976). These analyses led to definition of the Alaskan Stream as a western boundary current which acts as a return flow for the wind-driven circulation in the northern Gulf of Alaska (Favorite et al., 1976), an observation which was subsequently supported by the theoretical work of Thomson (1972). Reed and Taylor (1965) computed peak baroclinic surface speeds in the Alaskan Stream of order 100 cm sec^{-1} , and presented evidence that the flow was predominantly baroclinic and in geostrophic balance. Ingraham et al. (1976) computed Sverdrup transports in the Gulf of Alaska using calculated geostrophic winds, and concluded that transports in the Alaskan Stream can vary from about $20 \times 10^6 \text{ m}^3 \text{ sec}^{-1}$ in winter to less than $5 \times 10^6 \text{ m}^3 \text{ sec}^{-1}$ during summer. Reed et al. (1980) have used OCSEAP temperature and salinity data to show, however, that a mean baroclinic transport of about $12 \times 10^6 \text{ m}^3 \text{ sec}^{-1}$ in the Alaskan Stream does not reflect the large annual variation of wind stress curl over the Gulf of Alaska.

Direct observations of circulation in the Gulf of Alaska are sparse, consisting primarily of the drift-card studies carried out by Favorite (1964) and Favorite and Fisk (1971) which provided qualitative support for cyclonic circulation in the Gulf of Alaska and a westerly flow south of the Aleutians. An excellent summary of subarctic Pacific oceanography was prepared by Favorite et al. (1976). Most recently Reed (1980) used satellite-tracked drogued buoys to document the closed gyre circulation in the Gulf of Alaska.

Prior to inception of the OCSEAP research program, acquisition of new temperature and salinity data from the Gulf of Alaska continental shelves allowed characterization of seasonal variations in the water column (Royer, 1975). Royer and Muench (1977) discussed some large-scale features in the surface temperature distribution and related these to the regional circulation and to vertical mixing regimes on the shelf. Hayes and Schumacher (1976) and Hayes (1979) described and discussed the interrelations between winds, currents and bottom pressures on the continental shelf in the north-eastern Gulf. Their work suggests that oceanic forcing is dominant at the shelf break, but that inner shelf or coastal circulation is primarily dependent upon other factors. This was substantiated by Royer et al. (1979), who provided evidence for a coastal flow extending some 500 km east from Prince William Sound in a 15- to 20-km wide coastal band. Royer (1979) discussed the impact that extensive precipitation and runoff can have on the near-coastal circulation. In related work Schumacher et al. (1978; 1979) indicated that for the northwest Gulf of Alaska shelf the Alaskan Stream acts as an offshore feature whose typically high speeds (50-100 cm sec⁻¹) do not extend appreciably onto the shelf. However, they indicate that the hydrographic data show a shoreward flux of heat and salt over the shelf.

Previous work in Cook Inlet, which forms a major embayment on the northwest Gulf of Alaska shelf and is especially subject to pollution problems because of active petroleum activities and other industrial development, has been limited primarily to unpublished manuscripts from various sources (e.g. Kinney et al. 1970a, 1970b; Knull and Williamson, 1969; Wright et al., 1973; Gatto, 1976; Burbank, 1977). Previous field activities focused primarily upon the upper portion of the Inlet (e.g. Kinney et al., 1970a, 1970b). Studies using surface drifters have attempted to define the circula-

tion in Kachemak Bay (Knull and Williamson, 1969) and in the lower Inlet (Burbank, 1977). Landsat data, which qualitatively indicate suspended sediment distributions in near-surface waters, have led to several qualitative expositions on Cook Inlet surface circulation (Wright et al., 1973; Gatto, 1976). In the most recent work on lower Cook Inlet, Muench et al. (1978) used summer 1973 oceanographic data obtained by the National Ocean Survey of NOAA to qualitatively discuss circulation and hydrography in the lower Inlet.

At the time of preparation of this report, then, much is known of the general, large-scale circulation on the northwest Gulf of Alaska continental shelf and in lower Cook Inlet, a major appended embayment. Our goal has been to synthesize this general information while at the same time incorporating the data from our experimental and theoretical studies.

1.4 Oceanographic and Meteorological Setting

In order to clarify the rationale used for field sampling, it is necessary to discuss in general fashion the main physical features which control regional oceanographic processes. The major oceanographic feature in the northwest Gulf of Alaska is the Alaskan Stream, an intense, southwestward-flowing current lying along the continental shelf break and slope to the southeast of Kodiak Island (Fig. 3). This current is the northwestern branch of the closed subarctic Pacific gyre which occupies the Gulf of Alaska and is driven primarily by the wind-stress curl over the North Pacific (Reed et al., 1980). The current is generally most intense near the shelf break, where it can attain daily mean surface speeds of order 100 cm sec^{-1} or more. Speeds taper off to seaward, and the current width from the shelf break to the point where speeds approach zero is of order 50 km. Baroclinic

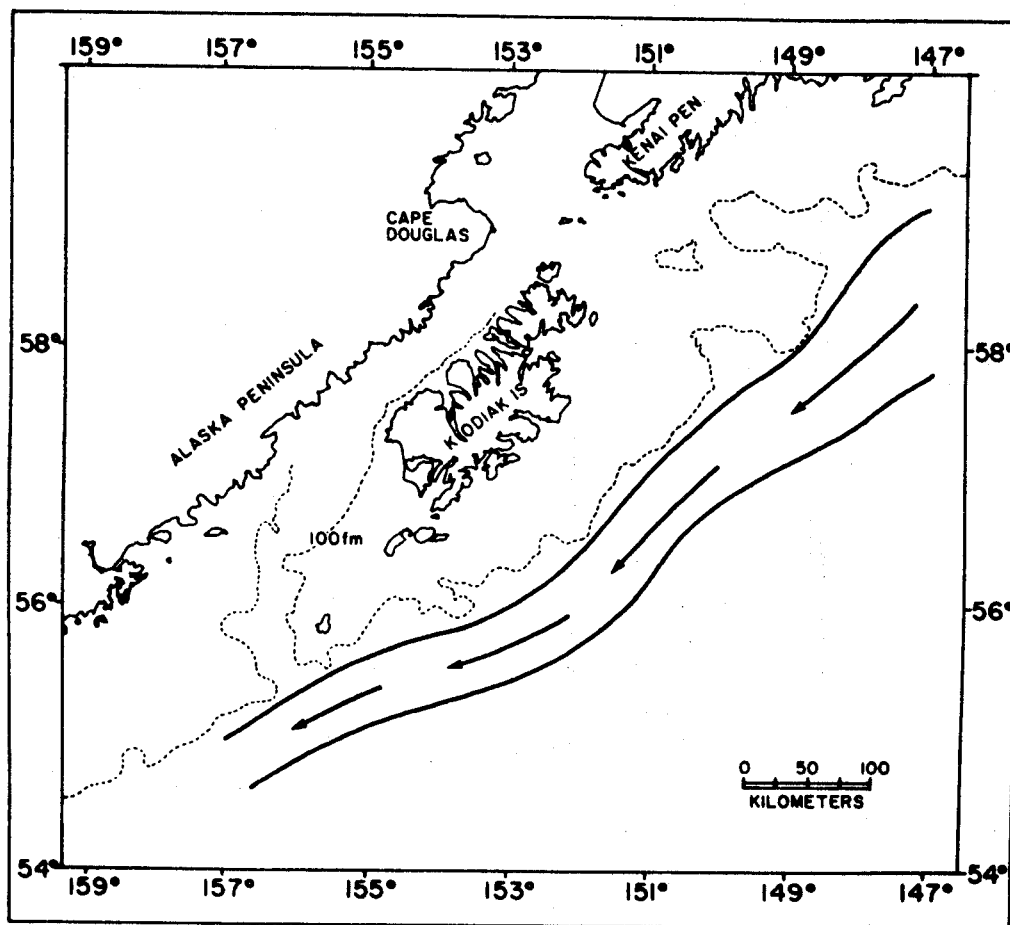


Figure 3. Approximate location of the Alaskan Stream along the shelf edge in the northwest Gulf of Alaska.

volume transport in the Alaskan Stream averages about $12 \times 10^6 \text{ m}^3 \text{ sec}^{-1}$, as computed using available temperature and salinity data; there does not appear to be a significant seasonal signal in this transport, contrary to what we would expect considering the large annual variation in wind-stress curl over the Gulf of Alaska (Reed et al., 1980). Since there are few direct observations of current in the Alaskan Stream, magnitude of the total volume transport remains uncertain.

Flow on the continental shelf and in Shelikof Strait is toward the southwest throughout the year. This flow is driven primarily by a combination of alongshore sea-level slope, consequent to the presence along the shelf break of the westward-flowing Alaskan Stream, and the baroclinic field established by freshwater input along the Alaskan coast (Muench et al., 1978; Schumacher and Reed, 1980).

Annual variability of shelf water properties in the northern Gulf of Alaska has been characterized by Royer (1975) (Figure 4). During winter, intensification of cyclonic atmospheric circulation over the Gulf of Alaska leads to easterly coastal winds and a downwelling tendency. At the same time, wind and thermohaline processes contribute to vertical mixing. Consequently, the water is characterized during winter by vertical near-homogeneity, elevated salinities and low temperatures. During summer, coastal winds diminish to allow relaxation of downwelling and create a weak upwelling tendency, and freshwater input and solar insolation act to increase stratification. As a result, the coastal waters are stratified in temperature, salinity and density during summer and fall, during which time temperature and salinity attain their maximum and minimum values, respectively, with respect to the annual cycle.

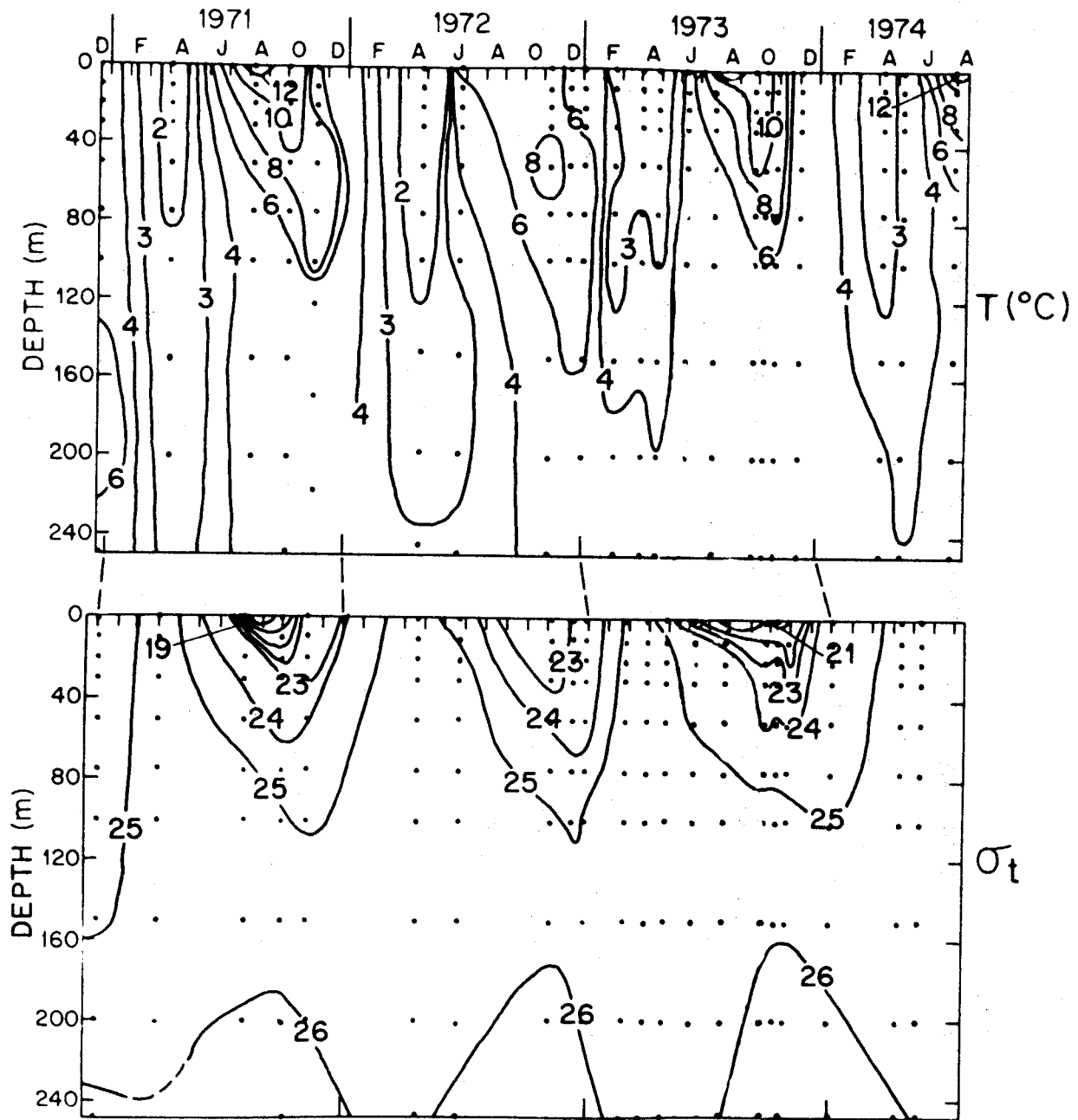


Figure 4. Variation of temperature and density (as sigma-t) at a location on the northern central Gulf of Alaska shelf (after Royer, 1975).

Regional meteorology is dominated by the Aleutian atmospheric low pressure system. During winter this system intensifies and intense, cyclonic low pressure systems migrate northeasterly off Kodiak Island. During summer, the North Pacific atmospheric high pressure region dominates, and the intensity and frequency of cyclonic storms decreases, leading to weak and variable winds. Air temperatures are occasionally below 0°C. during winter, but rise to well above freezing during summer. A useful summary of such regional climatological data has been prepared by Brower et al. (1977).

A final factor which can be significantly effective upon continental shelf circulation is freshwater input from continental sources. This input is not generally well known along the northwestern Gulf of Alaska coast, due to the scarcity of gaging stations. It is known, however, that there are generally two annual peaks in runoff. The first, or spring peak, results from melting of the previous winter's snow cover. The second, or autumn, peak occurs with the onset of severe storms which bring large quantities of rain to coastal regions. This second peak drops off once air temperatures have become low enough so that the precipitation occurs as snow rather than rain. In some areas, one of the peaks may be negligible, or the low-flow period between peaks may disappear. The latter is true of major river input into upper Cook Inlet because of the long duration of the spring snow-melt peak, which actually continues well into summer, coupled with low summer rainfall (cf. Muench et al., 1978).

Sea ice is not generally encountered in the northern Gulf of Alaska. The exception is in Cook Inlet, where low air temperatures and a high freshwater content due to river input lead to local ice formation in the upper Inlet. Some landfast and floe ice also occurs in Kachemak Bay during extreme winters. In Kamishak Bay, a combination of landfast ice in the embayments

and floes from the upper Inlet can result in heavy winter ice accumulation. Much of this ice is advected southward along the western shore of the Inlet by wind and water circulation, and is occasionally found as far south as Cape Douglas.

The factors summarized in this section, in conjunction with bathymetric features discussed in Section 1.2, ultimately determine the physical oceanographic characteristics of the northwestern Gulf of Alaska shelf.

2. OBSERVATIONAL PROGRAM

2.1 Program Rationale

The OCSEAP field observation program in the Gulf of Alaska was designed to define and explain the fields of wind and water motion as they affect contaminant trajectories and dispersion. At the outset of the study, little was known either of local winds or of water motion on the Gulf of Alaska continental shelf. Therefore, the initial phases of the program attempted a large-scale definition of motion and the associated temperature-salinity-density (for water) and pressure (for winds) fields needed to address the regional oceanographic and meteorological dynamics. Early phases of the program involved field work extending from east of Kodiak Island westward to Unimak Pass in the Aleutians, but were of too coarse a resolution to define specific local features. Once large-scale winds and water flow on the shelf had been defined, specific process-oriented experiments such as the meteorological-oceanographic study of lower Cook Inlet and the intensive oceanographic study of the bank and trough region off Kodiak Island were undertaken. In this way the field program evolved continually, with new phases of the field work being determined by the outcome of previous phases. The emphases were always on more localized, process-oriented studies as time progressed. Thus, the general survey of oceanic circulation on the shelf between Kodiak Island and Unimak Pass evolved into separate process studies in Cook Inlet, in Shelikof Strait and in the Kiliuda Trough area south of Kodiak Island. Results from the general scientific literature, obtained from experiments in other parts of the world ocean, were also used in planning the process studies and in attempting to foresee results. Results of the studies were integrated with related results from other regions to comprise contributions to basic science, as well as further knowledge of

the northern Gulf of Alaska. Aspects of this development will be further clarified in the following discussion.

2.2 The Current Observation Program

Currents were observed in the northwest Gulf of Alaska using moored current meters deployed on subsurface arrays, surface drift cards, satellite-tracked, drogued drifters and HF radar. The first method yielded time series of currents at fixed locations, or Eulerian measurements. The second method provided us with points of release and recovery which, in turn, allowed crude estimation of Lagrangian drift trajectories. The third method provided us with Lagrangian drift trajectories which approximate those followed by a water parcel. The final method yielded actual observations of surface water motions.

2.2.1 Taut-Wire Moorings

Moored current meters were deployed using taut-wire moorings and acoustic releases (Fig. 5). Aanderaa RCM-4 recording current meters were used for all moorings. These use Savonius rotors to measure current speed and vane/compass assemblies for determining current direction relative to magnetic north.

The pattern for deployment of the moorings can be divided into subsets. The first set of moorings was designed to investigate large-scale (~500 km) alongshelf flow seaward of Kodiak Island and as far southwest as Unimak Pass (Fig. 6). Durations of these observations, broken down according to individual instruments on each mooring, are indicated in Appendix A. These moorings carried the prefix designation "WGC".

The second set of moorings was designed to investigate circulation around Kodiak Island, and included deployments in Shelikof Strait and on the banks southeast of the island (Fig. 7).

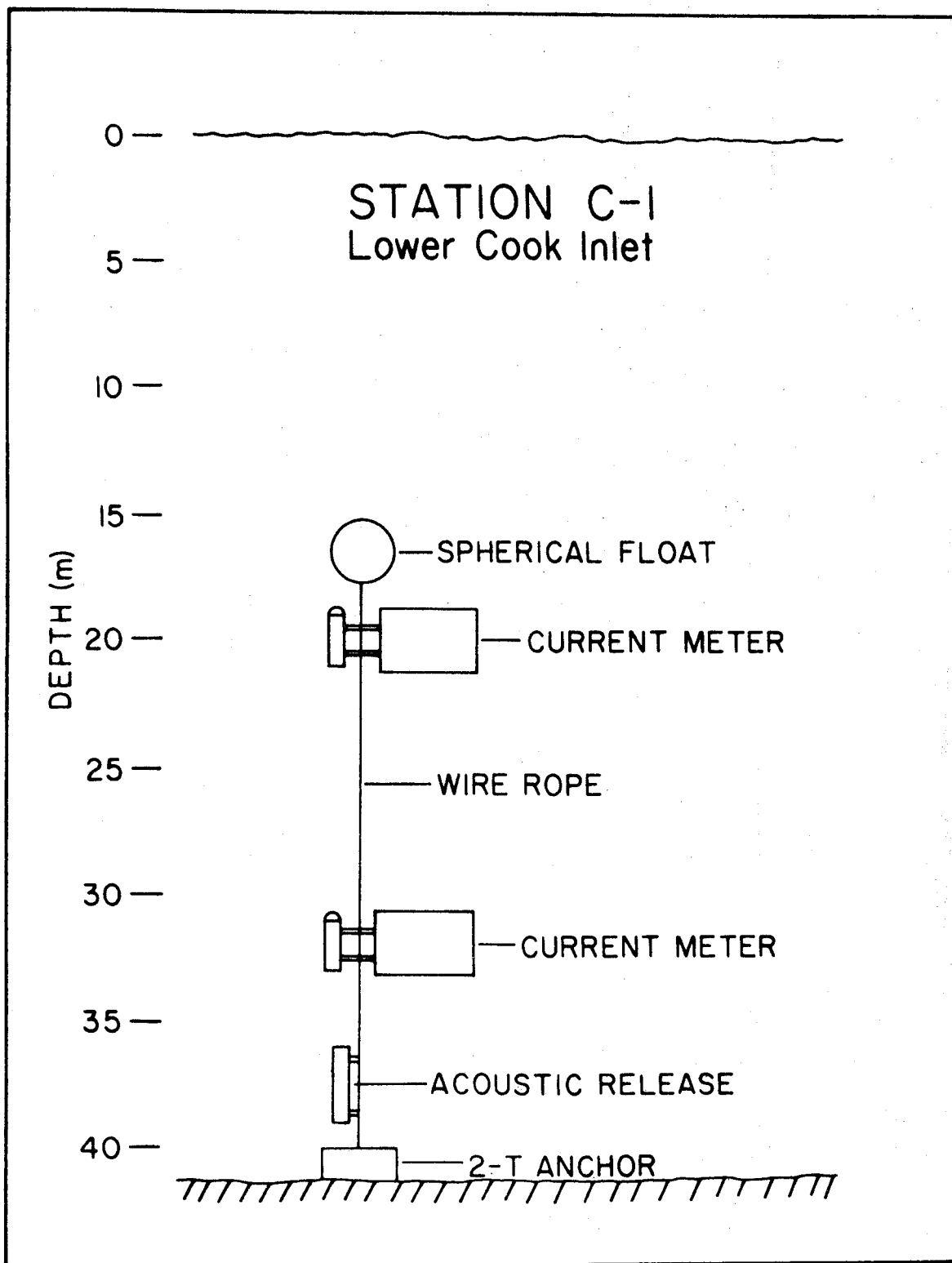


Figure 5. Example of configuration of taut-wire current meter mooring used in the northwest Gulf of Alaska. Number of meters and their vertical spacing varied with different stations and depended upon such factors as water depth and stratification.

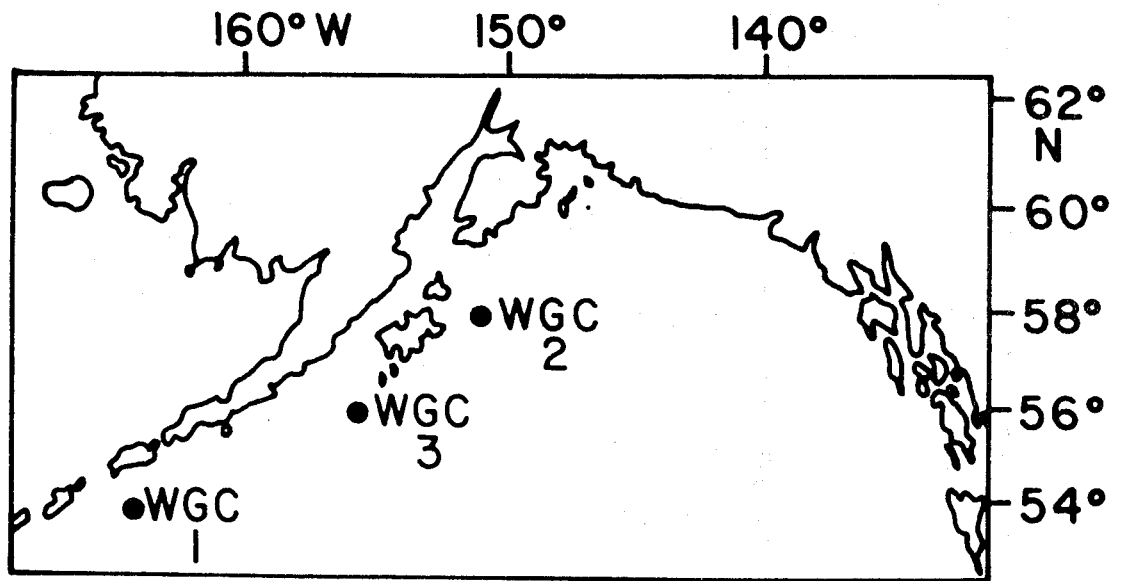


Figure 6. Current meter mooring locations for preliminary, large-scale investigations of shelf flow in the northwest Gulf of Alaska. Mooring statistics are given in Appendix A.

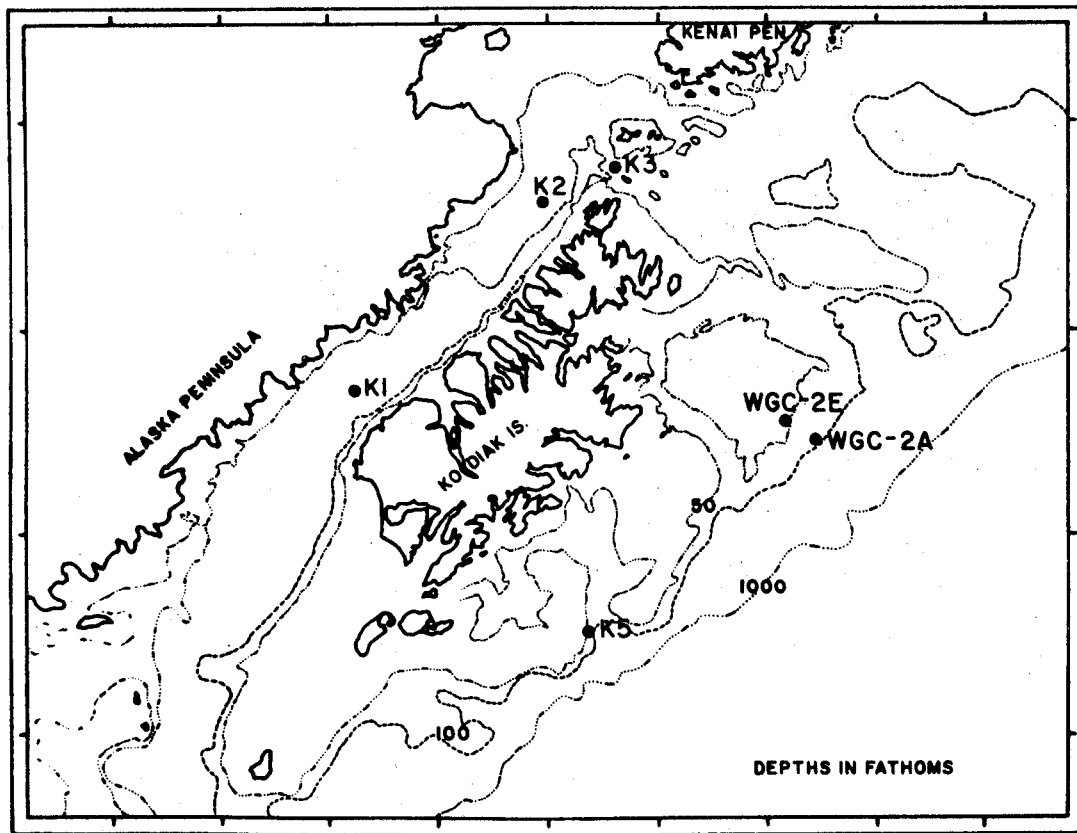


Figure 7. Locations of current meter moorings deployed during winter 1976-77 in the region surrounding Kodiak Island. Mooring statistics are given in Appendix A.

A third set of moorings was deployed on two separate occasions, approximately 5-mo periods in winter 1977-78 and again in summer 1978. These moorings encompassed three separate process-oriented studies. Moorings C1-C13 were deployed in lower Cook Inlet in an attempt to better understand circulation connected with the bathymetry and in the region of convergence defined by Muench *et al.* (1978) (cf. Section 3.2)(Fig. 8). Moorings K6-K13 were deployed in the region surrounding Kodiak Island as an extension of the experiment initiated with K1-K5 to investigate circulation around the island (Fig. 9). A particularly important aim of this experiment was investigation of circulation in the region south of Kodiak Island where the shelf is transected by banks and troughs. Finally, moorings M1-M4 were deployed, during winter 1977-78 only, in the coastal region off Mitrofanina Island southwest of Kodiak Island to attempt a comparison between the coastal dynamics there and in the northeast Gulf of Alaska where a similar experiment had been carried out (cf. Hayes, 1979) (Fig. 10). Failure to recover the shelf break mooring M3 severely limited the usefulness of this data set, however.

The current meters sampled at 15- or 20-min intervals. Raw data were low-pass filtered to remove high-frequency noise; this filter passed more than 99% of the amplitude at periods greater than 5 h, 50% at 2.86 h and less than 0.5% at 2 h. This series was then further filtered to remove most of the tidal energy; the second filter passed more than 99% of the amplitude at periods of more than 55 h, 50% at 35 h and less than 0.5% at 25 h. This second, low-pass filtered series was then resampled at 6-hr intervals and was used for examining nontidal circulation. Details of this processing are discussed in Charnell and Krancus (1976).

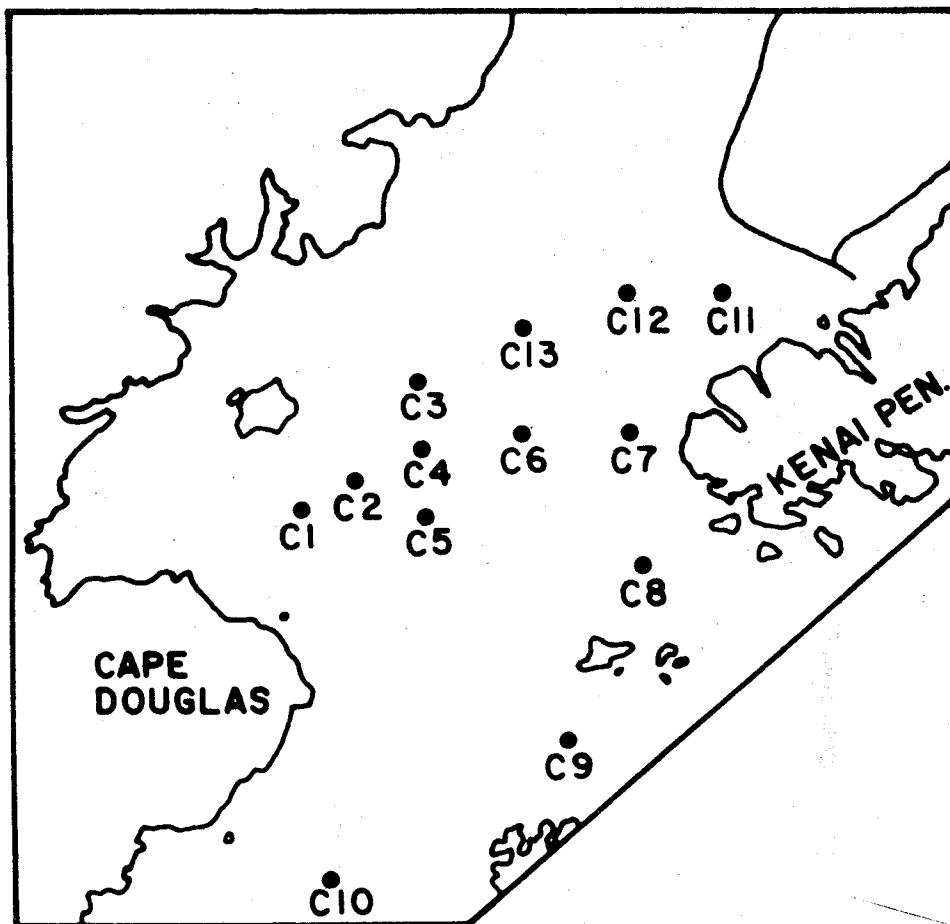


Figure 8. Locations of current meter moorings in lower Cook Inlet in 1977-78. Mooring statistics are given in Appendix A.

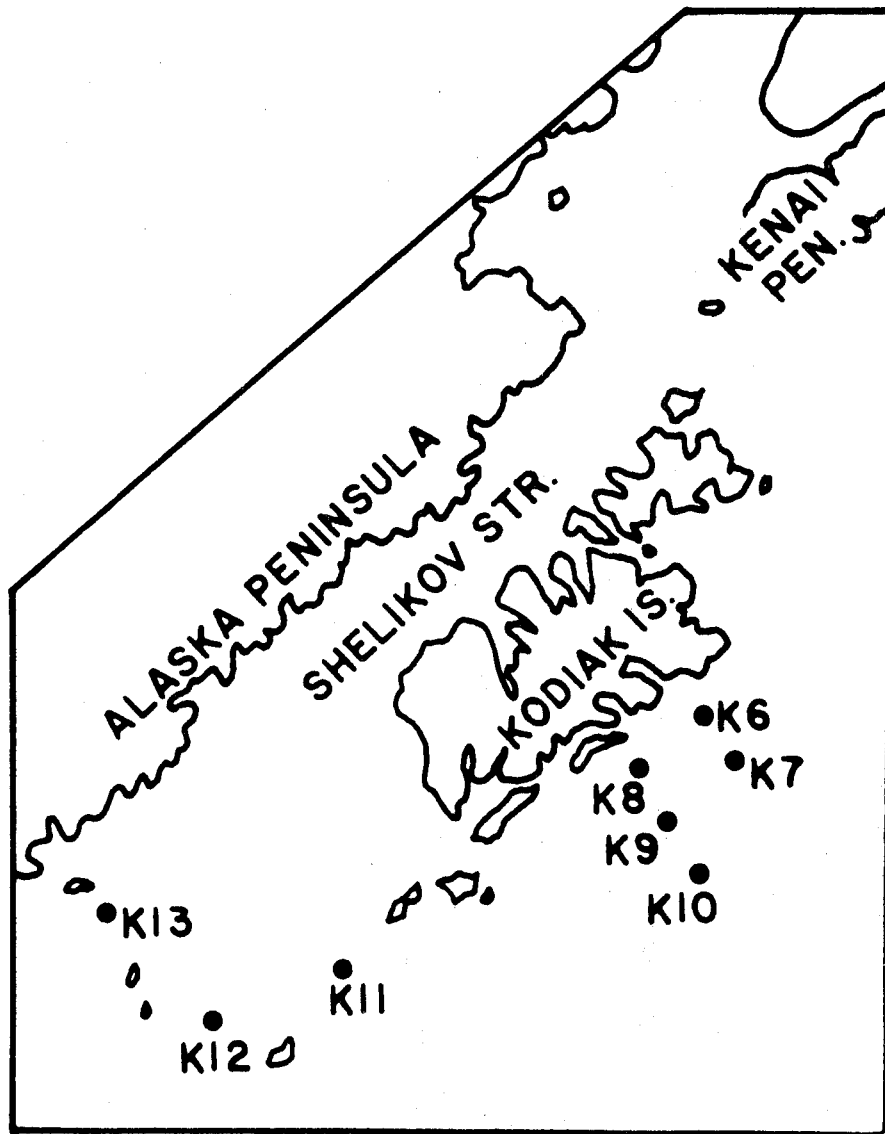


Figure 9. Current meter mooring locations south and west of Kodiak Island in 1977-78. Mooring statistics are given in Appendix A.

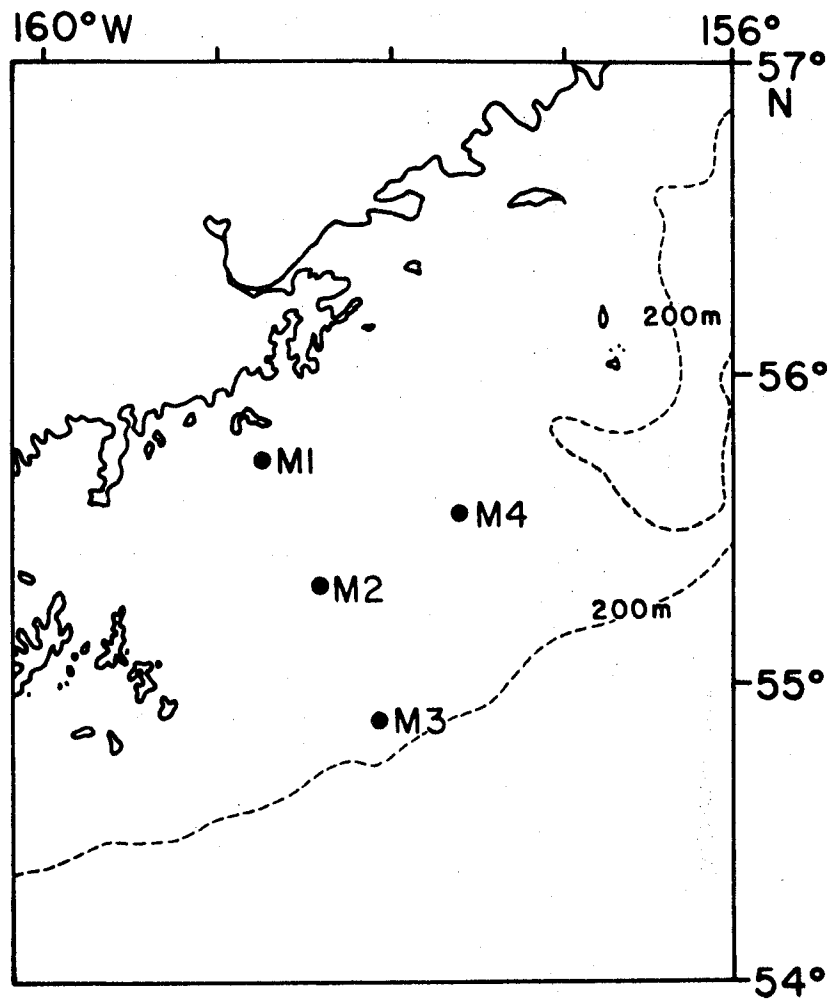


Figure 10. Locations of current meter moorings used for the winter 1977-78 Mitrofanina Island experiment.

2.2.2 Drift-Card and Seabed Drifter Studies

Since a major objective of the program in the northwest Gulf of Alaska was to provide information that would aid in prediction of the ultimate fate of an oil spill, it was decided to deploy drift cards which float at the surface and which should behave similarly to an oil spill and indicate where beaching might occur. Cards used for this purpose were made of plastic, were 3" x 5" in size and had a specific gravity of about 0.9 which caused them to float nearly submerged at the water surface. The resultant low above-water profile minimizes wind effect upon the cards, consequently movements should be representative of surface water motions. It should be stressed that the cards were not intended to yield actual trajectories, rather to provide, by distribution of their recoveries, a description of possible areas for grounding of an oil spill occurring at a given location. No attempts were made to compute transit times, since there was no way of knowing how long the cards had lain upon the beaches from which they were recovered. This was particularly true in our study region, where the beaches are relatively uninhabited.

Three sets of cards were released: 1400 cards in early March 1978, 1000 cards in late May 1978 and 2000 cards in early October 1978. The release locations were situated to sample flow in three localities: (1) along the Kenai Peninsula; (2) through the entrances to lower Cook Inlet; and (3) along the Kodiak Island shelf. By the end of 1978 the number of responses to the request for recovery information had reached 137 or 3% of the total number of cards released. This was a surprisingly high recovery rate in view of the remote nature of the sampled area. Overall drift-card returns as of the end of 1978 are listed in Appendix B.

In an attempt to define near-bottom water motion on the bank and trough region south of Kodiak Island, sea-bed drifters were deployed by NMFS/NOAA during winter 1977-78 (Dr. Gene Dunn, NMFS/NOAA, personal communication).^{*} These drifters follow water motions within about 1 m of the seabed. Release and recovery data are tabulated in Appendix C.

2.2.3 Satellite-Tracked Drift Buoys

Surface buoys having subsurface window-shade drogues were deployed at various locations in the eastern (i.e. upstream) part of the study region. The buoys, designed and constructed at Nova University on contract to the NOAA Data Buoy Office, were fiberglass spars about 5 m long attached to a 2-m x 10-m window-shade drogue by a 30-m long nylon tether. The designed center of drogue resistance was therefore near a depth of 35 m. Location of the buoys was determined by means of the Random Access Measurements System (RAMS) of the NIMBUS-6 satellite (Levanon, 1975). At the latitude of the northern Gulf of Alaska, the system provided up to five locations per day for each buoy, but at irregular times.

The rms location error was about 4 km. Each satellite overpass provided data for an ambiguous pair of locations. Between sequential orbits it was usually, but not always, possible to identify the proper location. Hence in addition to the location error arising from uncertainties in the satellite orbit, Doppler measurement, etc., individual errors of tens or even hundreds of kilometers were present in the data. These erroneous locations were removed by an objective routine that checked each location for displacement from preceding and succeeding locations, then rejected all locations that implied velocities in excess of an assignable criterion. For this Gulf of Alaska data set we used 150 cm sec^{-1} as the criterion, which retained 70 to 80% of the original data. To facilitate automated computation of

^{*}NMFS/NOAA, Seattle, WA 98105.

velocity time series and plotting of results, the position component data were smoothed and interpolated to 6-hr intervals by piecewise least-square fit to a low-order (usually cubic) polynomial. Velocity series were additionally smoothed by a simple three-point triangular filter. The result of this procedure was a set of trajectories and associated velocity time series comparable to what would be done by a skilled subjective analyst, and in which features having a time scale of about 2 days were retained. Tidal flows and inertial currents, where important, were suppressed along with other rapid accelerations.

2.2.4 Wave Radar (CODAR) Observations

Investigations of surface currents were carried out in lower Cook Inlet using a Doppler-shift radar method which is fully described by Barrick et al. (1977). This method utilizes the Doppler shift of surface waves under the effect of a current to measure the current field, and has the advantage of providing an instantaneous picture of actual surface currents, an observation virtually impossible by other means. These observations covered the region just off Kachemak Bay and the area between Cape Douglas and Augustine Island (Fig. 11). The observation periods were short in duration compared to the moored current meter measurements, of order 1 week or less, and provided both instantaneous and daily mean values of surface currents in the indicated regions.

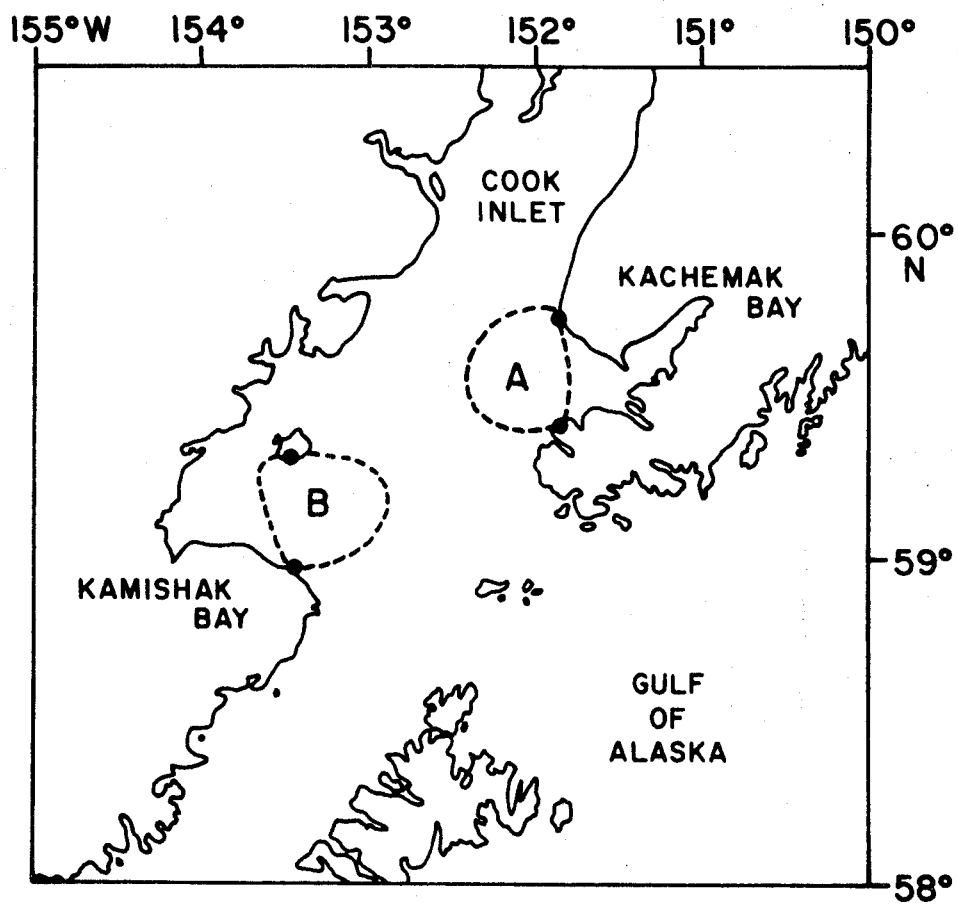


Figure 11. Areas, designated A and B, where surface current observations were carried out using the Doppler-shift wave radar (CODAR) unit. Solid circles indicate locations at which radar units were deployed.

2.3 Temperature and Salinity Observations

Temperature and salinity data were obtained from shipboard using Plessey Model 9040 conductivity/temperature/depth (CTD) profiling systems. These data were recorded during the downcast, and descent rate was held to about 1 m sec⁻¹ or less to minimize error in the recorded data due to thermal lag in the sensors in regions where large vertical temperature gradients were present. In some areas, the descent rate during the upper 200 m of the cast was limited to 0.5 m sec⁻¹ due to extreme vertical gradients.

Since the Plessey systems are subject to drift and other possible problems, it was necessary to provide data calibration at frequent intervals. To this end, water samples were obtained and analyzed for conductivity and temperature at roughly half of the CTD stations. These samples were obtained using a rosette sampler equipped with calibrated reversing thermometers. Conductivity was measured aboard ship using a portable salinometer calibrated with standard seawater. These calibration data confirmed an overall accuracy for the CTD temperature and salinity values of $\pm 0.02^{\circ}\text{C}$ and $\pm 0.02^{\circ}/\text{oo}$, respectively.

Temperature and salinity data were used for water mass analyses and for computing geostrophic current speeds and transports, therefore, it is of interest to consider the accuracy of the derived parameters used in these analyses. Given temperature and salinity accuracies of $\pm 0.02^{\circ}\text{C}$ and $\pm 0.02^{\circ}/\text{oo}$, density may be computed to an accuracy of $\pm 0.02 \text{ kg m}^{-3}$. Use of these density values in calculating dynamic heights led to an accuracy of within 1.0 dyn cm referred to the 1500 db level. Using these values to compute surface current speed between two stations spaced 40 km apart, the results were accurate to $\pm 4 \text{ cm sec}^{-1}$.

Temperature and salinity data obtained during the OCSEAP program in the northwest Gulf of Alaska bracket all seasons for the 1976-78 period. Appendix D lists stations occupied according to cruise number and date. All data are archived at, and available on request from, the National Oceanographic Data Center.

2.4 Meteorological Observation Program

This program was designed to define the dominant meteorological features in three specific coastal subregions in the northwest Gulf of Alaska: lower Cook Inlet, Kiliuda Bay and Albatross Bank (Fig. 12). Data sources for this study include land based weather stations, moored data buoys, oil drilling platforms, NOAA research vessels, ships of opportunity, ferries, AMOS stations and remote weather recording installations which were deployed as part of this study (Table 1). The data base also includes information in the form of synoptic data from the U. S. Navy's Fleet Numerical Weather Central (FNWC) analyses. The data collection effort occurred primarily during early 1978 (Table 2), a period which coincided with intensive current observation programs in the lower Cook Inlet and Kodiak Island areas.

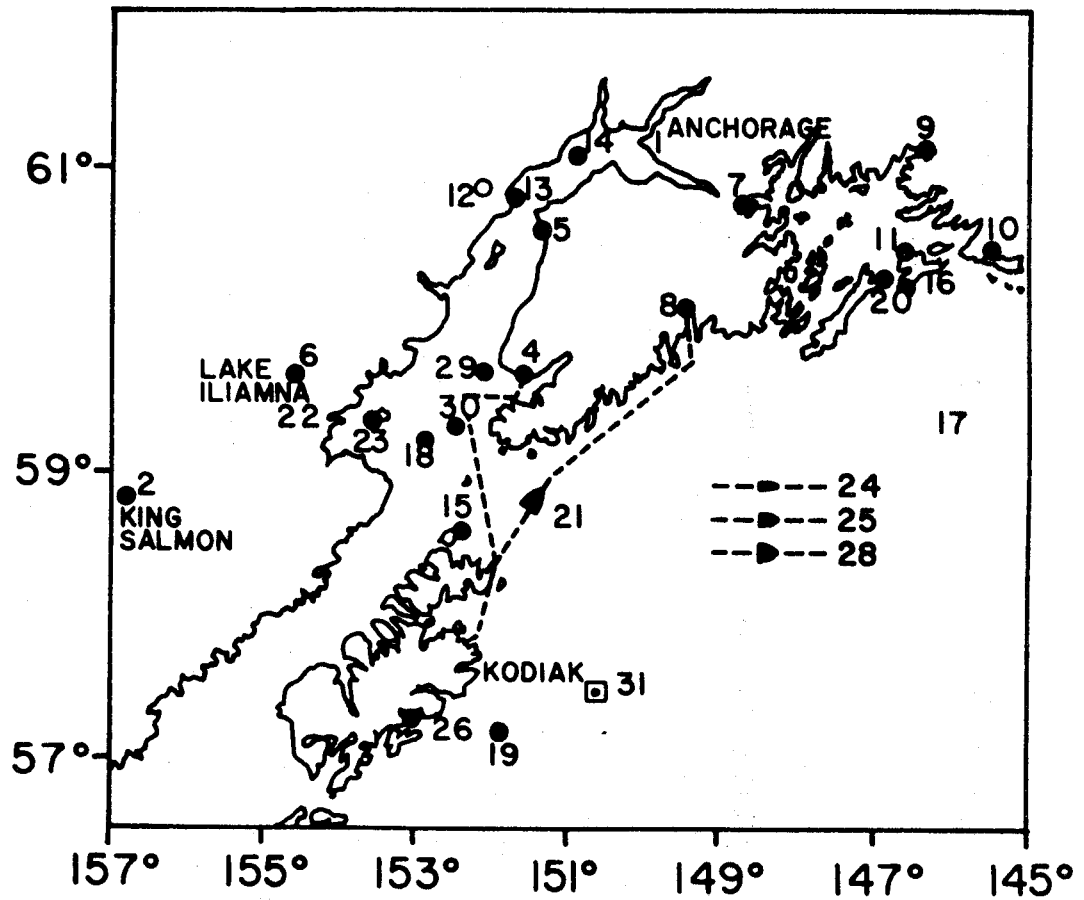


Figure 12. Map of the study area showing sources of data which are included in this study. Names of numbered stations, sources of data and time periods of data collection are given in Tables 1 and 2.

TABLE 1

Listing of meteorological data collection stations shown on Figure 12.

1.	Anchorage	NWS ¹
2.	King Salmon	NWS
3.	Kodiak	NWS
4.	Homer	NWS
5.	Kenai	NWS
6.	Iliamna	NWS (part-time AMOS ²)
7.	Whittier	NWS
8.	Seward	NWS
9.	Valdez	NWS
10.	Cordova	NWS
11.	Johnston Point	NWS (Air Force)
12.	Big River Lake	NWS (contract)
13.	"Dolly Varden"	Oil Platform
14.	"Phillips"	Oil Platform
15.	Shuyak	NWS (remote wind)
16.	Cape Hinchinbrook	NWS (AMOS)
17.	Middleton Island	NWS (AMOS)
18.	EB-346007	NDBO ³
19.	EB-46008	NDBO
20.	EB-46009	NDBO
21.	<i>TUSTUMENA</i>	Alaska State Ferry
22.	Contact Point	NOAA/PMEL remote ⁴
23.	Augustine Island	NOAA/PMEL remote
24.	<i>SURVEYOR</i>	NOAA vessel
25.	<i>DISCOVERER</i>	NOAA vessel
26.	Kiliuda Bay	NOAA/PMEL remote
27.	Copper River	NOAA/PMEL remote
28.	Ships of opportunity	Miscellaneous
29.	"Diamond M. Dragon"	Oil Platform
30.	"Ocean Bounty"	Oil Platform
31.	FNWC ⁵	Computer

¹National Weather Service, NOAA.

²Automatic weather station.

³National Data Buoy Office, NOAA.

⁴Remote recording weather station.

⁵Fleet Numerical Weather Central.

3. RESULTS AND DISCUSSION

3.1 Mean Currents, Seasonal Variations and the Temperature, Salinity and Density Fields

3.1.1 Introduction

The internal density structure of an oceanic system reflects the baroclinic portion of the total time-averaged mean flow. Because of the time interval required for readjustment of this density field following any change in current patterns, the density field reflects time-averaged circulation and can be used to detect seasonal variability. It does not generally reflect, however, the 2- to 10-day period events or tidal fluctuations which are prominent in the northwest Gulf (cf. Section 3.2).

Mean flow can be obtained only by computing a time average of measured current, where the observation and averaging time must extend over a long enough period to allow averaging out of prominent low-frequency fluctuations such as those to be discussed in Section 3.2. In the present study this generally required a record at least 1 mo in length. Since the time scale for seasonal events is of order 3 mo, records longer than 3 mo but shorter than several years record conditions spanning more than one season but still not representing a true annual mean. As our current moorings generally were deployed for periods of 4-5 mo, this limitation must be borne in mind. Lengths of the individual current records are listed in Appendix A.

3.1.2 The General Northwestern Gulf Region

Winter net flow is well represented by the observed mean current vectors depicted on Figure 13. The southwesterly flow at the shelf break at 20 m was about 35 cm sec^{-1} (Station WGC2A). This agreed with a later drogue trajectory (cf. drogue 1220, Fig. 14), which indicated net summer speeds

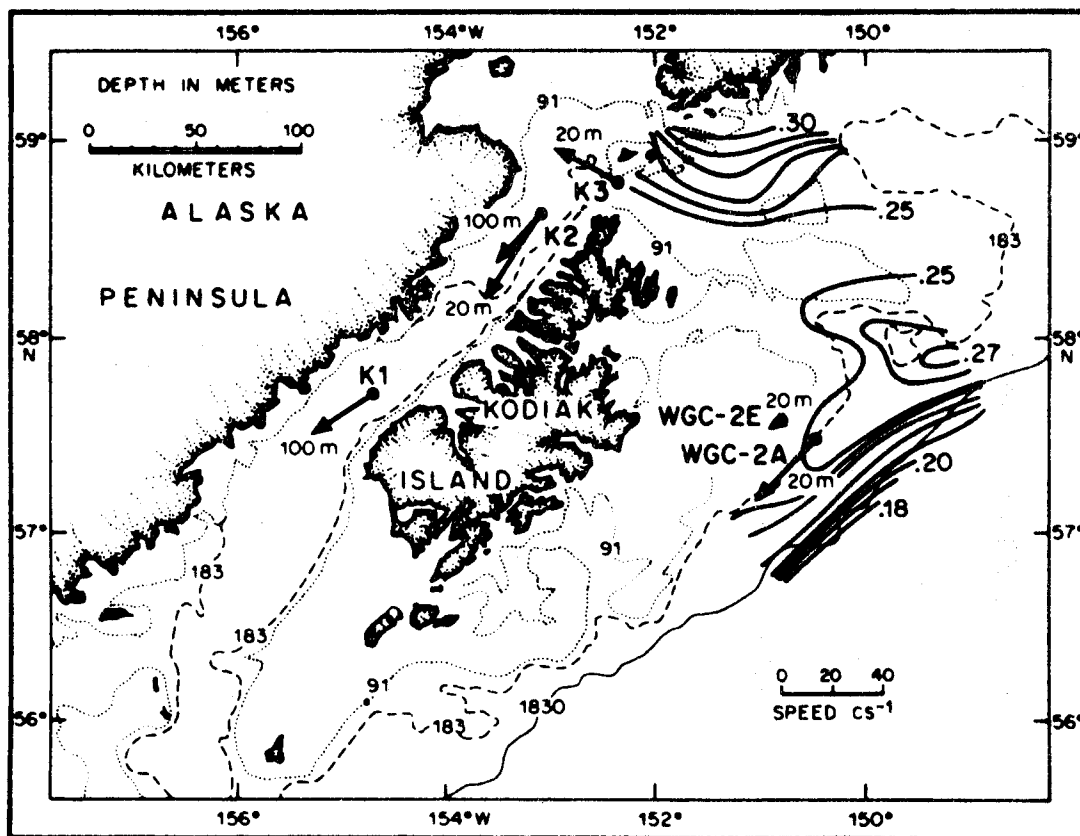


Figure 13. Mean winter 1976-77 current speed vectors at five locations on the northwest Gulf of Alaska shelf. Actual mooring periods are given in Appendix A. The dynamic topography has a contour interval of 0.01 dyn m and was constructed using March 1977 data.

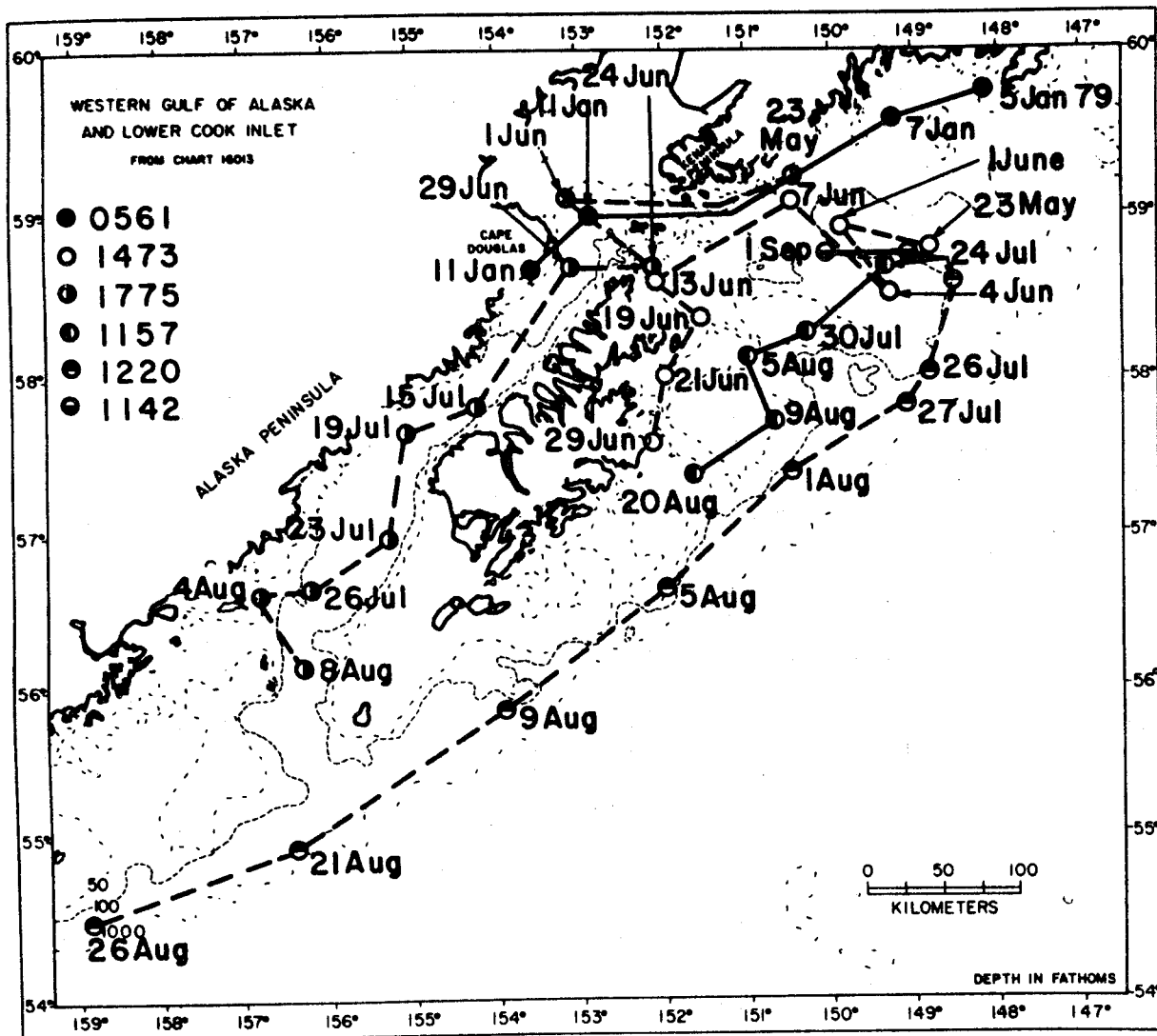


Figure 14. Satellite-tracked drogued trajectories in the northwest Gulf of Alaska. Drogued buoys were deployed in 1978, and were drogued to track at a water depth of about 25 m.

in the Alaskan Stream of about 40 cm sec^{-1} off Kodiak Island. At a later period the mooring had been moved about 20 km farther inshore (to WGC2E), due to repeated damage from fishing activity at the original location. At the new location, mean speed had dropped to about 5 cm sec^{-1} , still in a southwesterly direction. These two moorings bracketed the zone of large horizontal shear at the inshore edge of the Alaskan Stream.

Moorings K1-K3 were deployed in Shelikof Strait as shown (Fig. 7) during the same period as WGC2E. These indicated a mean 100-m deep flow through Shelikof Strait of about 25 cm sec^{-1} to the southwest. At 20-m depth mean flow was somewhat higher, about 35 cm sec^{-1} , and also southwesterly. These observations were the first current measurements obtained in the region and indicated a general southwesterly flow with its most intense region manifested as the Alaskan Stream along the shelf break. This southwesterly flow, both through Shelikof Strait and south of Kodiak Island, was qualitatively demonstrated by the results of the satellite-tracked buoy and drift card programs (Figs. 14-18).

3.1.3 The Kenai Current

During March, September and October-November 1977 (Fig. 19, 20 and 21), two baroclinic flow regimes were evident on these dynamic topographies: (1) the southwestward-flowing Alaskan Stream over the continental slope south and east of Kodiak Island, accompanied by apparent inshore counterflows east of Portlock Bank; and (2) a well-defined westerly coastal flow along the Kenai Peninsula, designated by Schumacher and Reed (1980) as the Kenai Current. Generally weak and variable circulation occurred between these two relatively well-organized flows. This was supported by summer drogue data, which

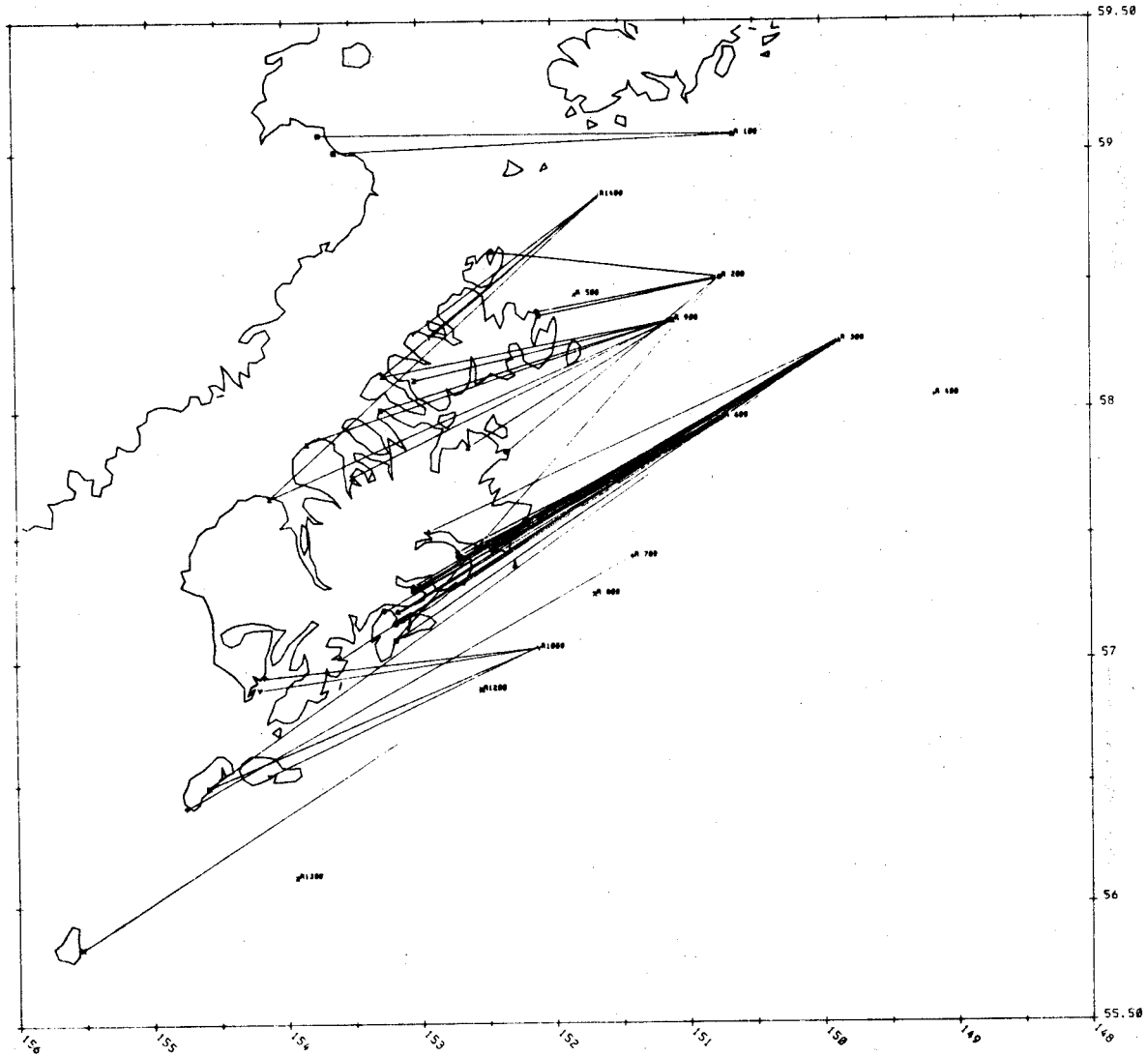


Figure 15. Summary of recovery and release points for drift cards released in March 1978.

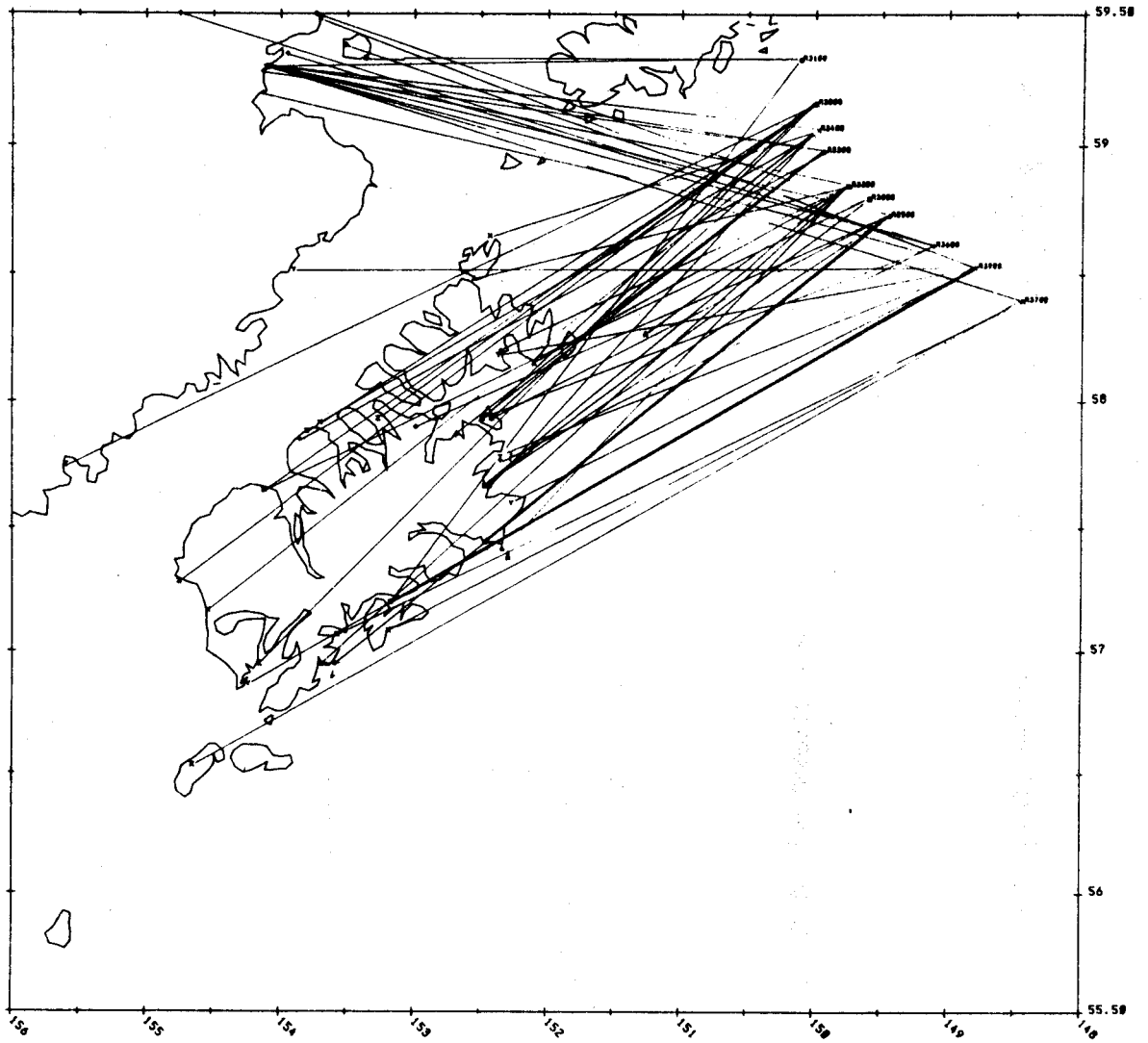


Figure 16. Summary of recovery and release points for drift cards released in May 1978.

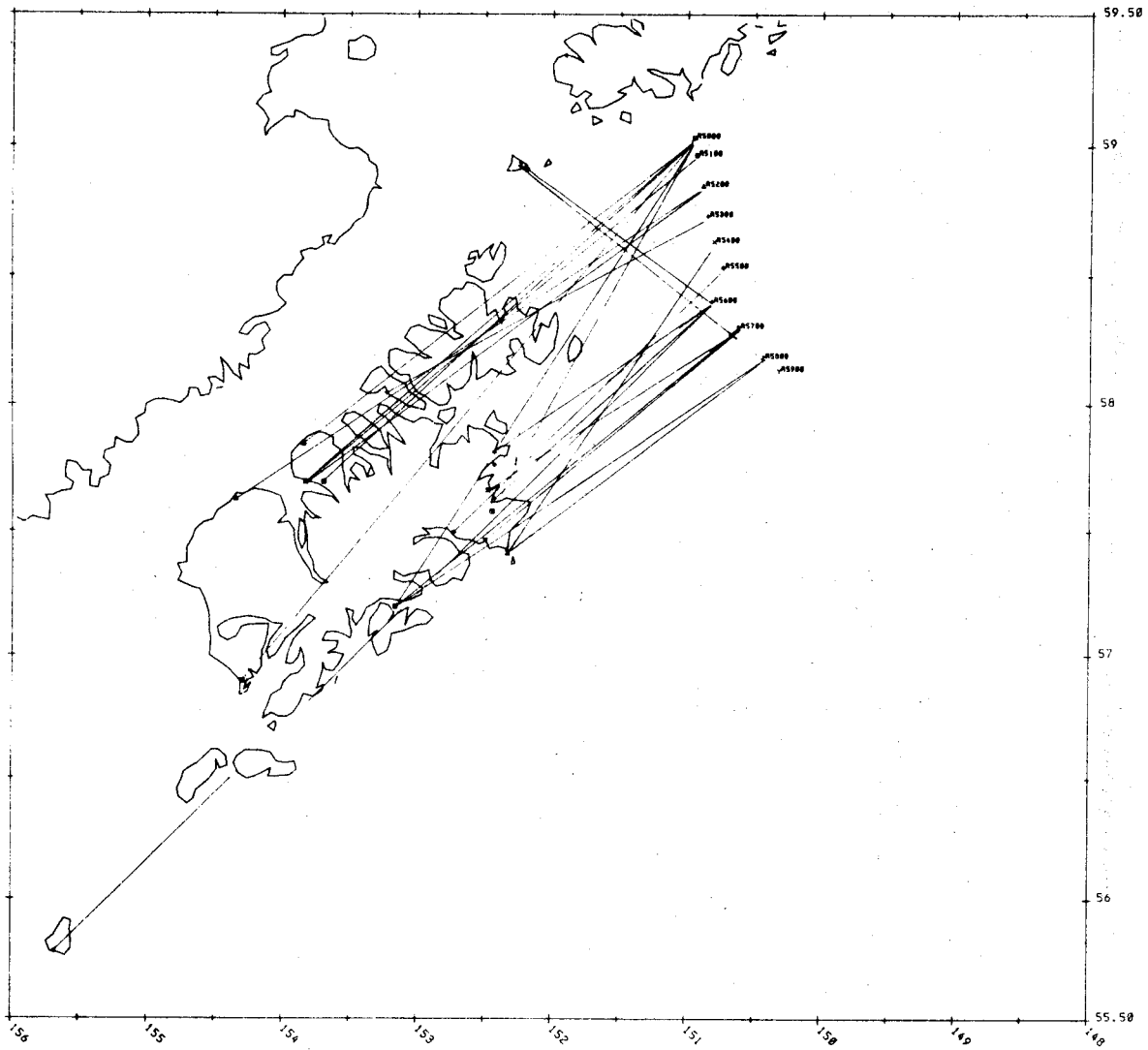


Figure 17. Summary of recovery and release points for drift cards released in October 1978.

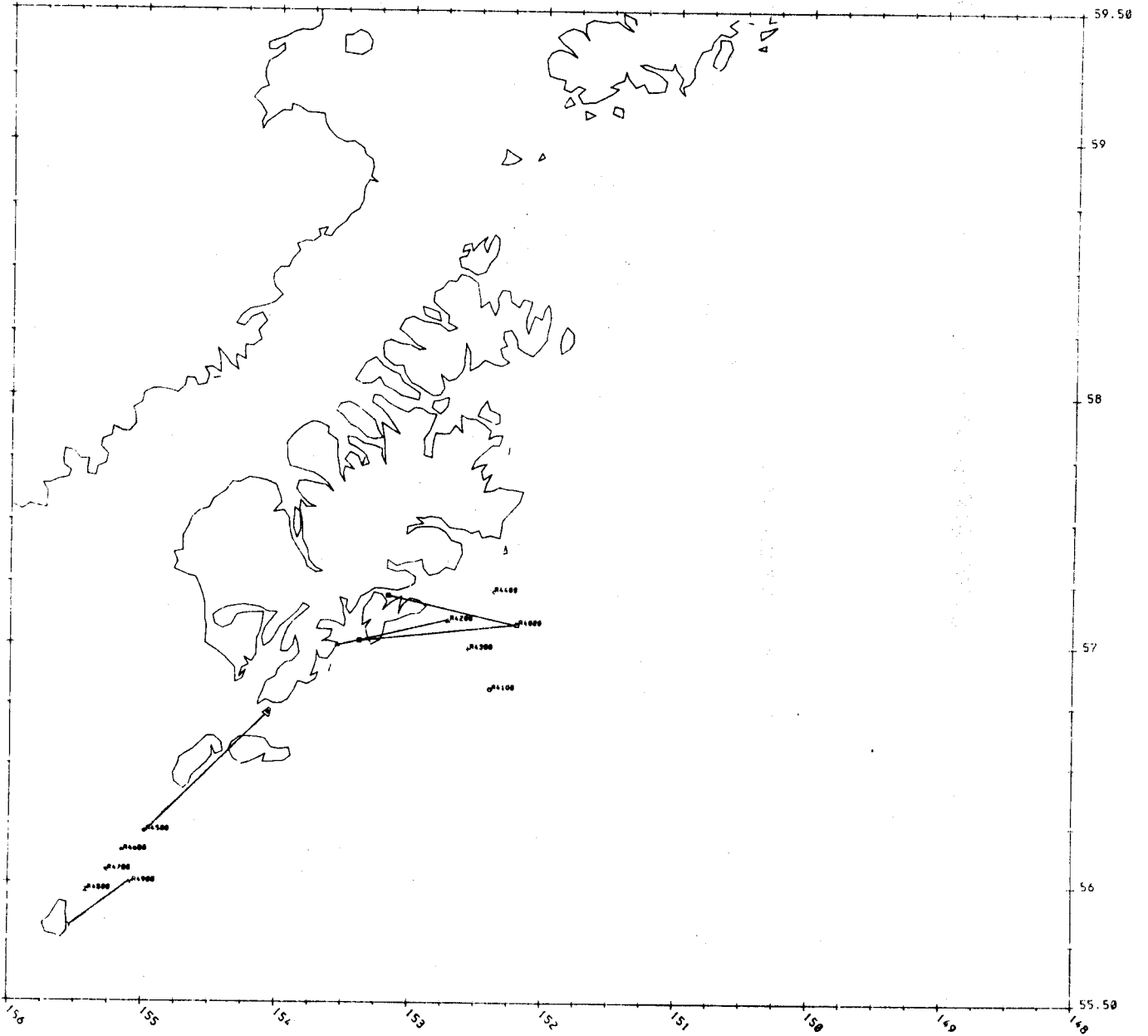


Figure 18. Summary of recovery and release points for drift cards released in October 1978.

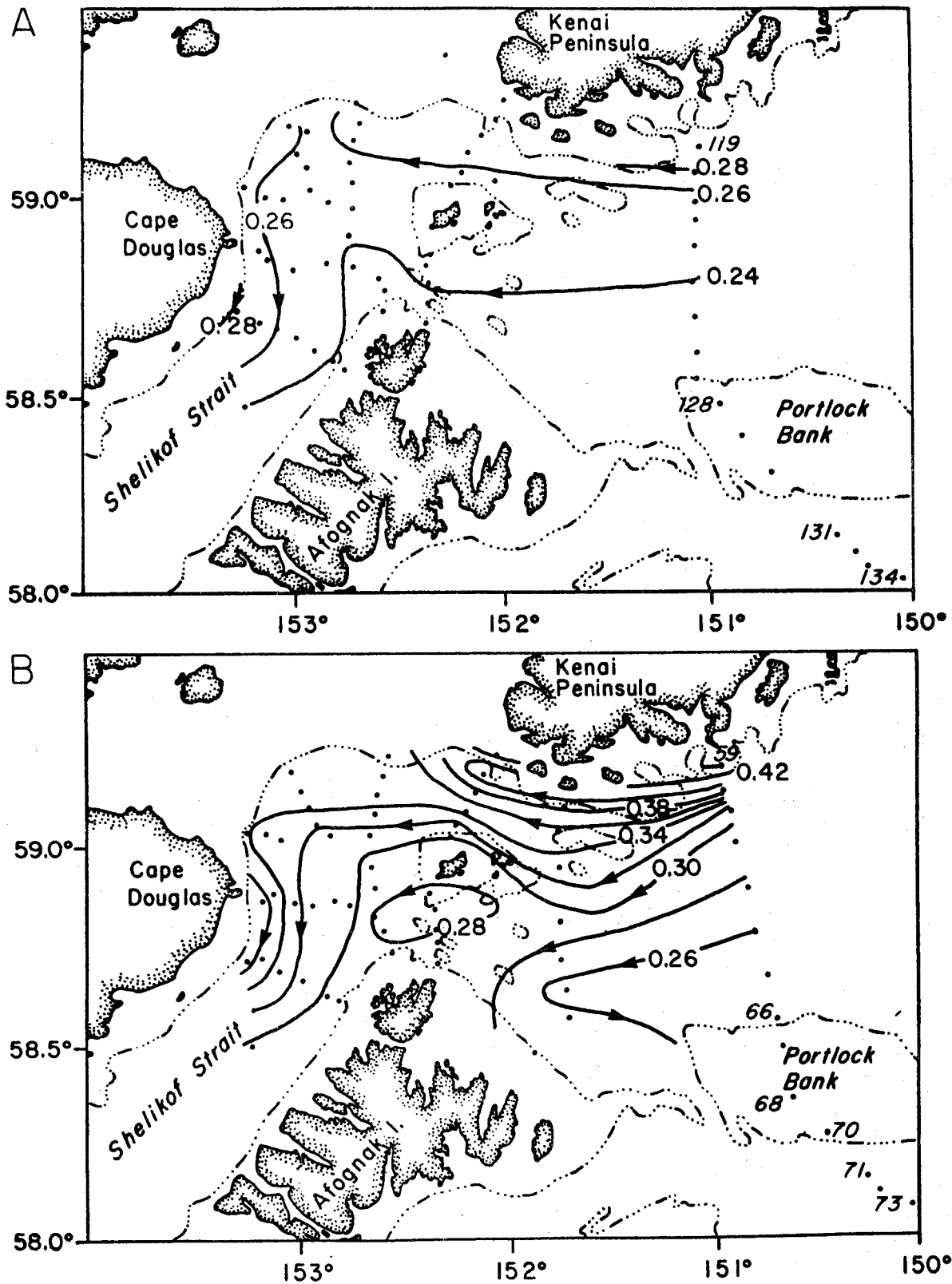


Figure 19. Dynamic topographies depicting flow in the Kenai Current and into lower Cook Inlet during March (upper) and October (lower) 1978.

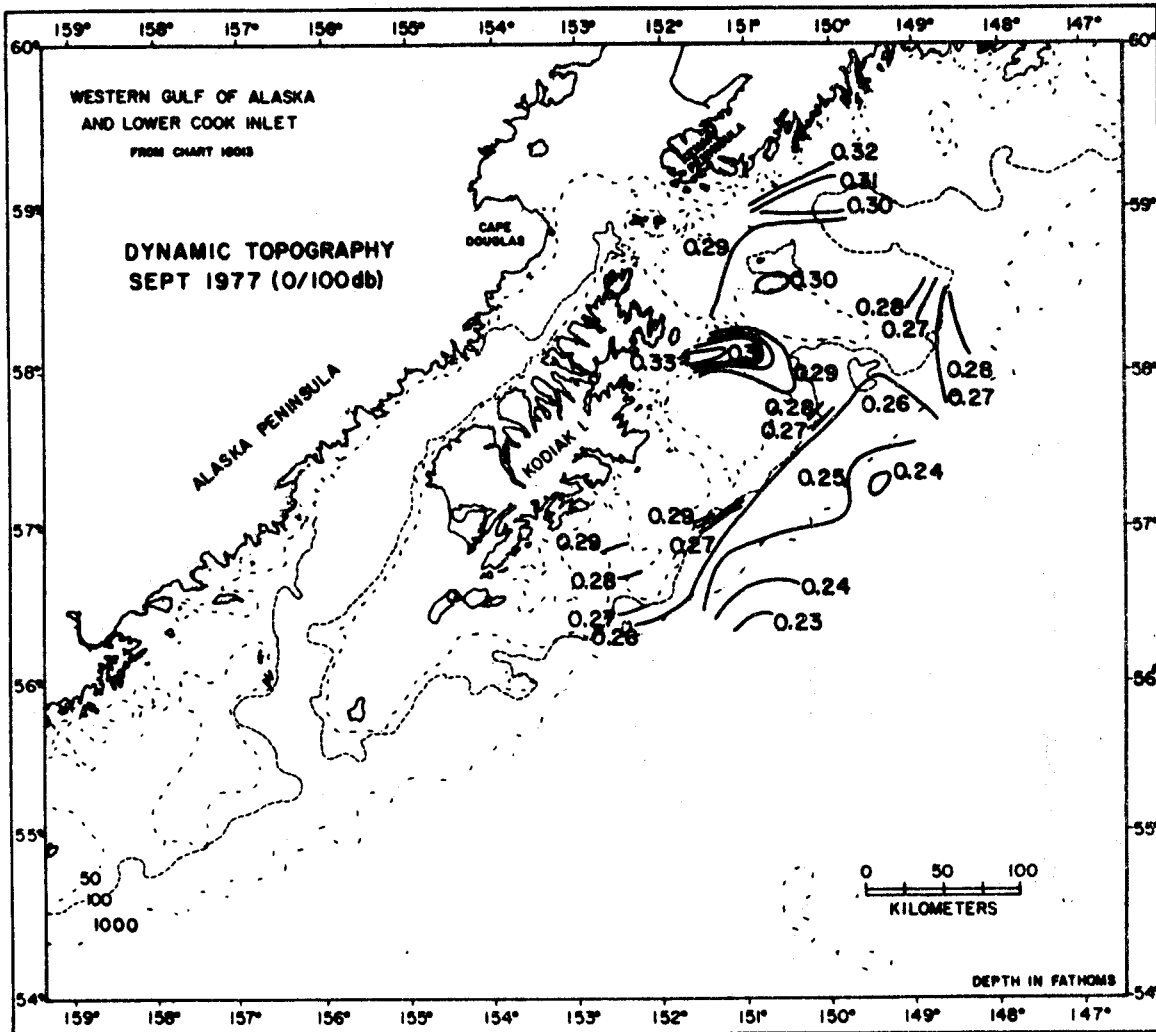


Figure 20. Dynamic topography of the 0/100-db surface in the northwest Gulf of Alaska in September 1977. Contour interval is 0.01 dyn m.

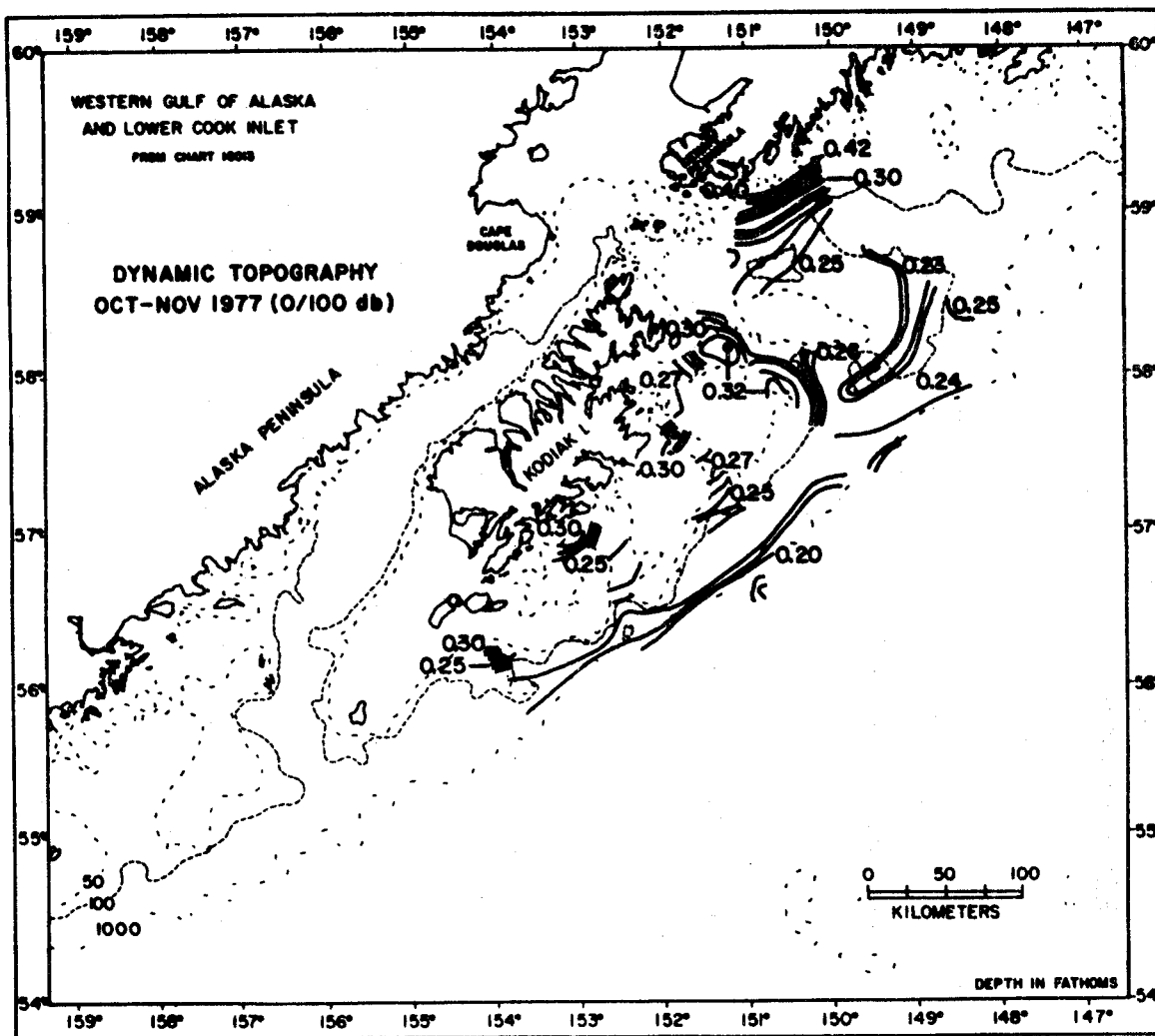


Figure 21. Dynamic topography of the 0/100-dB surface in the northwest Gulf of Alaska in October-November 1977. Contour interval is 0.01 dyn m.

revealed erratic flow directions and weak net speeds ($\sim 5 \text{ cm sec}^{-1}$) (cf. drogues 1473 and 1157, Fig. 14). During September and October a southward extension of this coastal flow appeared east of Kodiak and Afognak Islands and may have contributed to formation of a well-developed (relief of about 0.04 dyn m) gyre-like feature between Portlock and North Albatross Banks. Relief across the coastal flow itself was about 0.05 dyn m in March and September, but had increased threefold by October. The salinity distribution (not shown) suggested that this increase in dynamic relief was due to coastal freshwater addition which resulted in depressed salinities along the coast. This was in agreement with Favorite and Ingraham (1977), who suggested westward baroclinic flow near the entrances to lower Cook Inlet and Shelikof Strait during April-May 1972.

Vertical sections of temperature, salinity, and sigma-t along the CTD sections off the Kenai Peninsula (stations 59-68, 70-73 in October 1978; stations 119-134 in March 1978) are presented in Figures 22 and 23. The October sections display a narrow band ($\sim 20 \text{ km}$) of warm, dilute, low-density water adjacent to the Kenai Peninsula; this strong baroclinicity coincided with the westward coastal flow entering Shelikof Strait. Indications of relatively weak westward flow extend, however, south of this band to about the northern flank of Portlock Bank. The three stations (67, 68, and 70) over Portlock Bank show weak vertical stratification, and the water at station 68 (63-m depth) was completely mixed. South of Portlock Bank, varying isopycnal slopes suggest that peak speeds in the Alaskan Stream occurred seaward of station 73. In March (Fig. 23), gradients across the coastal flow were much weaker than in fall. There were no indications of significant baroclinicity elsewhere. Minimum temperatures were near the surface, rather than near-bottom as in October, and there was significantly

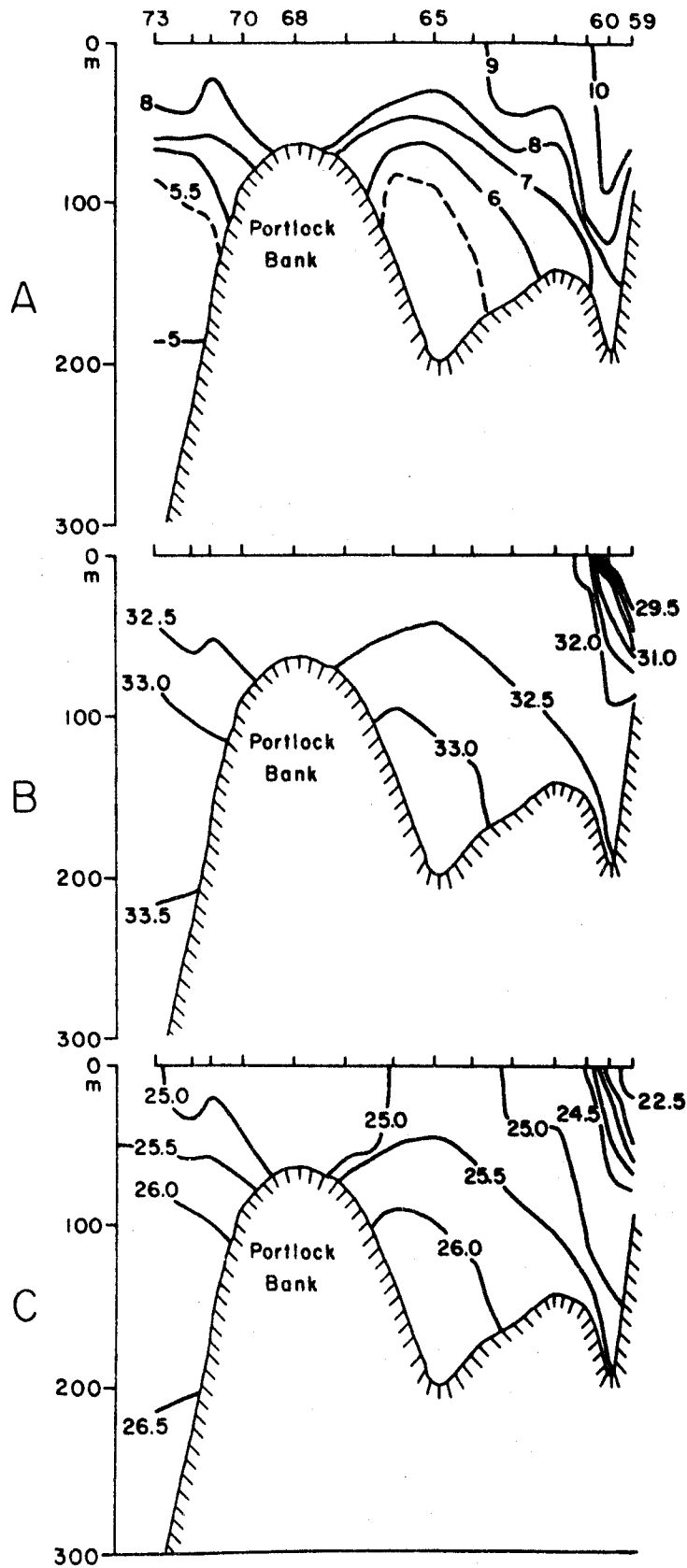


Figure 22. Cross sections of temperature (A), salinity (B) and density as σ_t (C) across the Kenai Current and Portlock Bank in October 1978. Right-hand side of the section is north.

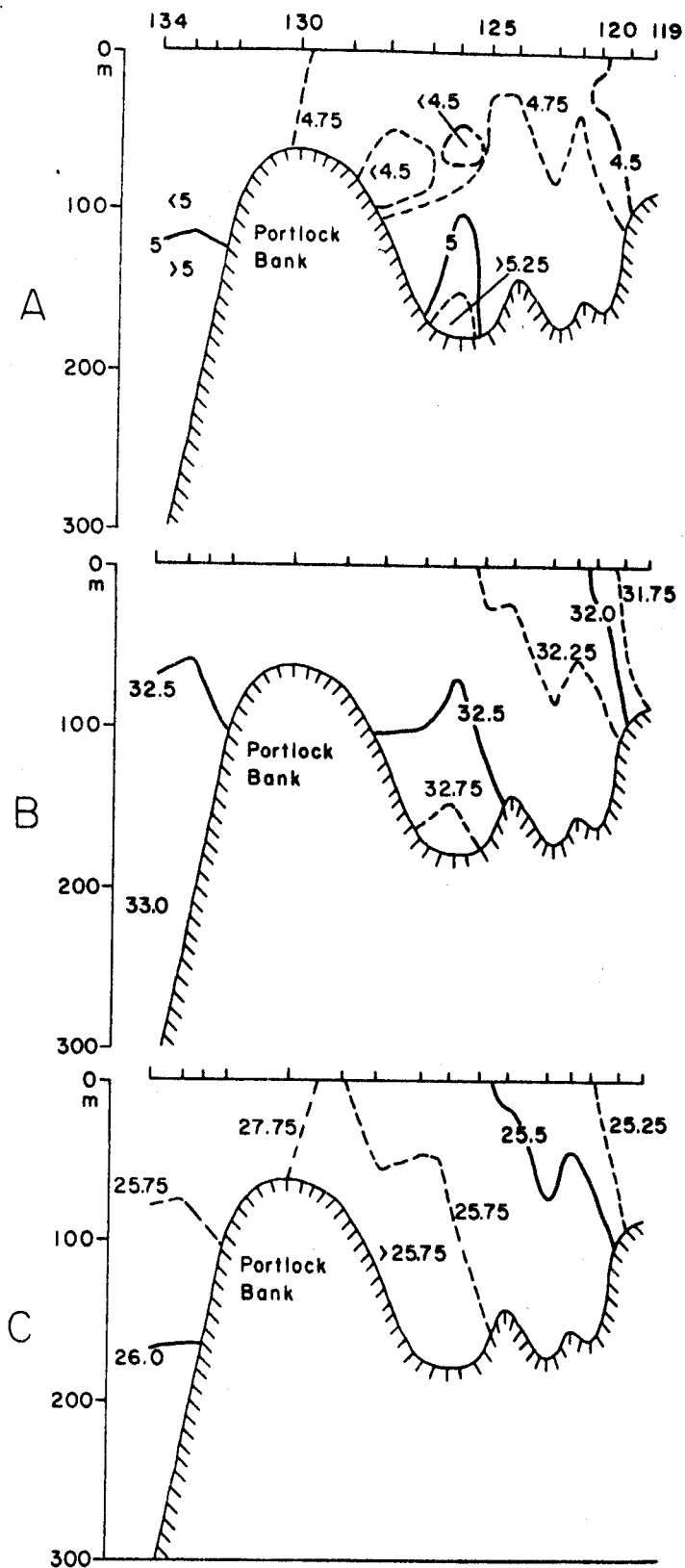


Figure 23. Cross sections of temperature (A), salinity (B) and density as σ_t (C) across the Kenai Current and Portlock Bank in March 1978. Right-hand side of the section is north.

lower stratification than that observed in fall. The homogeneous water atop Portlock Bank extended about 15 m deeper than in October, which suggests that total mixing (presumably a combination of wind mixing near the surface and tidal mixing near the bottom) was more pronounced in winter than in summer-fall, a result consistent with physical reasoning. The intermediate and deep parts of the water column were more saline in October than in March, while coastal flow near the Kenai Peninsula was more dilute during October. This pattern of decreased surface salinity and increased intermediate and deep salinity during fall is consistent in our data and suggests that the saline water is "drawn up" during periods of peak transport in the Kenai Current, perhaps as an interior upwelling in conjunction with buoyancy flux (Pietrafesa and Janowitz, 1979) similar to estuarine circulation.

3.1.4 Shelikof Strait and Lower Cook Inlet

The flow through Shelikof Strait was measured for 5-mo periods during winter 1977-78 and summer 1978. These observations reaffirmed the southwesterly flow and revealed that mean speeds during summer were about half those during winter; winter 1977-78 speeds were in agreement with those measured in 1976-77. We therefore conclude that mean winter currents in Shelikof Strait flow southwest at about $20\text{-}30\text{ cm sec}^{-1}$ with slightly higher speeds at the surface than at depth. Limited evidence has also been presented by Schumacher *et al.* (1978; 1979) that these observed mean flows agreed with baroclinic flow inferred from the 0/100-db dynamic topography (Figs. 19-21).

Baroclinic coastal flow in the Kenai Current has a significant effect on flow through lower Cook Inlet and Shelikof Strait. This is illustrated by 0/100-db geopotential topographies which encompassed both regions during March and October 1978 (Fig. 21). In March, the baroclinic coastal flow

had a dynamic relief of about 0.06 dyn m. It entered Shelikof Strait through passages north and south of the Barren Islands and veered south off Cape Douglas. In October the flow was considerably stronger, with a dynamic relief of about 0.20 dyn m, and a portion of the flow appeared to turn south near Afognak Island without entering Shelikof Strait.

Inflow into northern Shelikof Strait due to the influence of the Kenai Current was supported by the moored current meter observations. Additional evidence was available in the form of satellite-tracked, drogued drift buoy results (Fig. 14), which showed direct evidence of the westward flow through the year. Buoy 0561 indicated a mean speed of about 55 cm sec^{-1} in January. Buoys 1775 and 1473 indicated much lower mean speeds, about 20 cm sec^{-1} , in May-June. The early spring lowering in speed is in agreement with our hypothesis that this flow is largely baroclinic and driven by coastal freshwater input; in early spring, freshwater content in the coastal waters is near its annual minimum.

The persistent westward flow of the Kenai Current into Shelikof Strait exerts a primary control on circulation in lower Cook Inlet. This was first recognized by Muench *et al.* (1978), who derived a qualitative circulation scheme for lower Cook Inlet using summer 1973 current and temperature-salinity observations (Fig. 24). The prominent westward flow in the southern Inlet is topographically controlled; it follows the path depicted and turns to the south off Cape Douglas. The southward flow from the upper Inlet is due to freshwater input; this flow merges with the westerly flow off Cape Douglas to produce a strong southerly current there. Flow elsewhere throughout the inlet is weak and variable. More recent current data have corroborated this circulation pattern and quantified the mean winter current speeds. Vectors showing the observed mean winter 1977-78 currents in lower Cook Inlet are

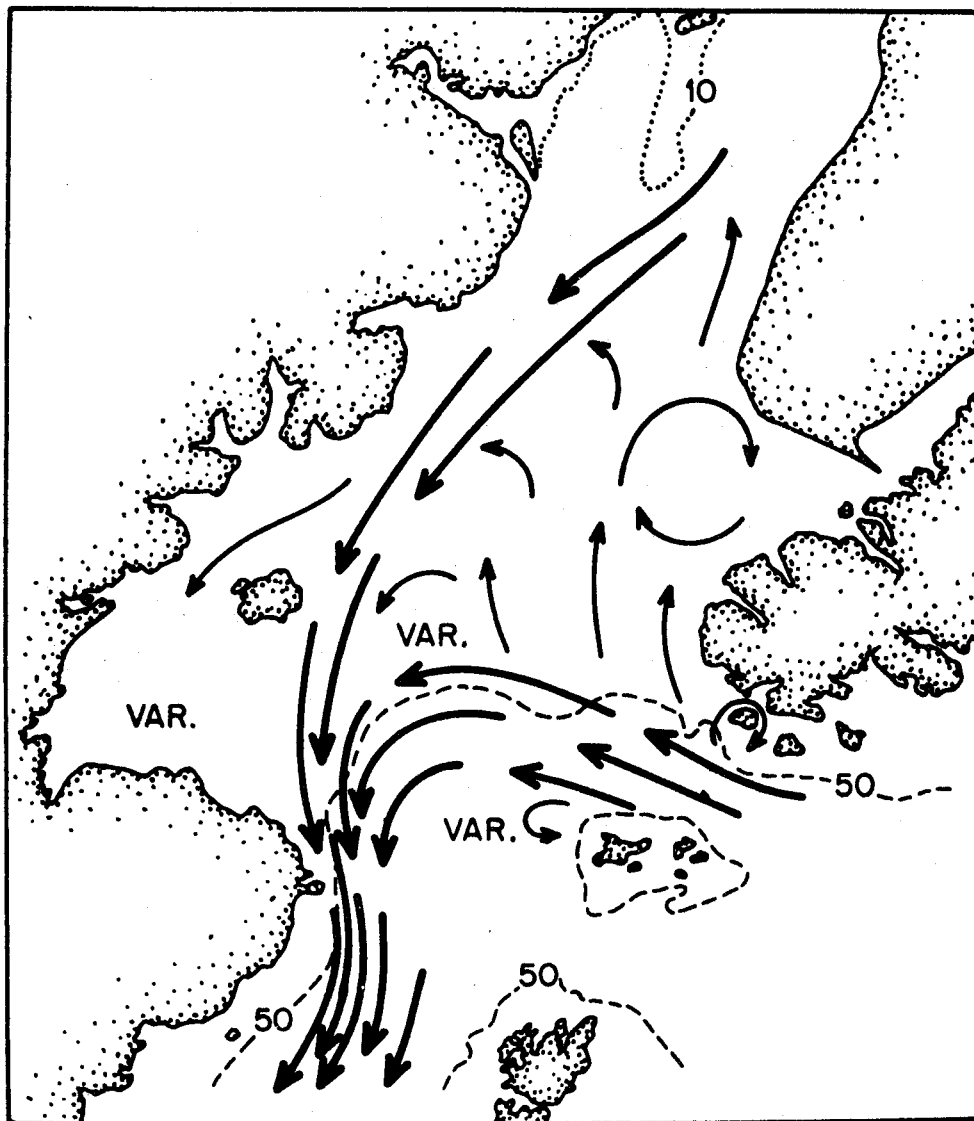


Figure 24. Depiction of qualitative mean flow pattern in lower Cook Inlet derived by Muench *et al.* (1977) from summer 1973 temperature, salinity and current data. Depths are in fathoms.

depicted on Figure 25. Westerly mean flow across the lower Inlet was about 20 cm sec^{-1} , while southward flow in the western Inlet was $5-10 \text{ cm sec}^{-1}$. Away from these two major flows, mean speeds were only $1-2 \text{ cm sec}^{-1}$.

A similar current observation program was carried out during summer 1978. Preliminary examination of these data has indicated that the flow pattern is the same as during winter. The westerly flow was smaller during summer, and the southerly flow in the western Inlet somewhat larger. Surface current observation carried out in summer 1978 using the CODAR (cf. Section 2.2.4) further substantiated this current pattern; an example of their results is shown in Figure 26.

The circulation depicted on Figure 24 for lower Cook Inlet was also corroborated by drogue results. Westerly drift across the lower Inlet was shown in January, with a mean speed of about 65 cm sec^{-1} (Fig. 14). This relatively high speed, compared with computed mean speeds obtained from moored current meters (Fig. 25), may indicate a current pulse during the observation period. A June drogue track plotted on the same scale did not show sufficient detail for speed computation. The same drogue track was plotted on an expanded scale, however, and compared to a second track on Figure 27. Drogue 1775 followed the bathymetry until 1 June, at which time the data became incomplete. Failure of drogue 1473 to enter Stevenson Entrance from the east suggests that a counterflow may have occurred during June. Drogue 1421 also indicated a westerly flow, though somewhat north of the earlier track and with apparent cross-isobath flow from 1-9 June. We would expect to see this sort of departure of drogue tracks from our conceptual mean flow; the drogues follow instantaneous flow. Both drogues yielded mean westward speeds of order 15 cm sec^{-1} , in agreement with summer mean flows observed using moored current meters.

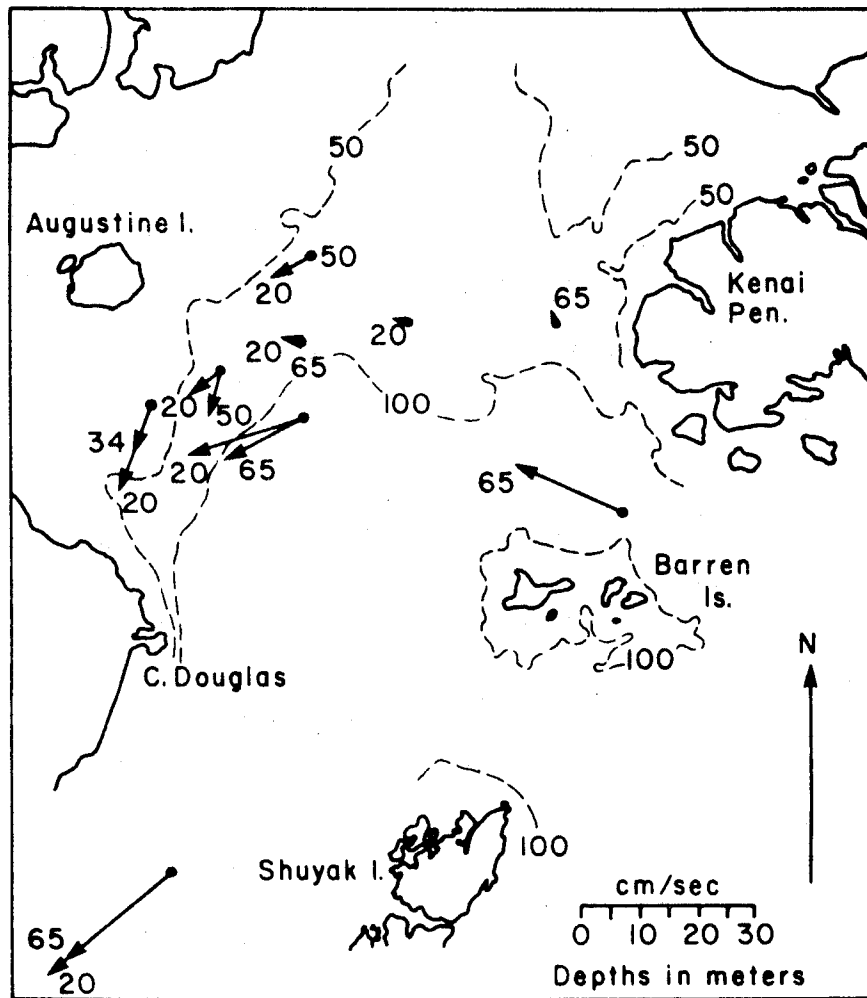


Figure 25. Observed mean current vectors in the lower Cook Inlet region during winter 1977-78. Statistics for individual moorings are given in Appendix A. Numbers indicate current meter depths in meters.

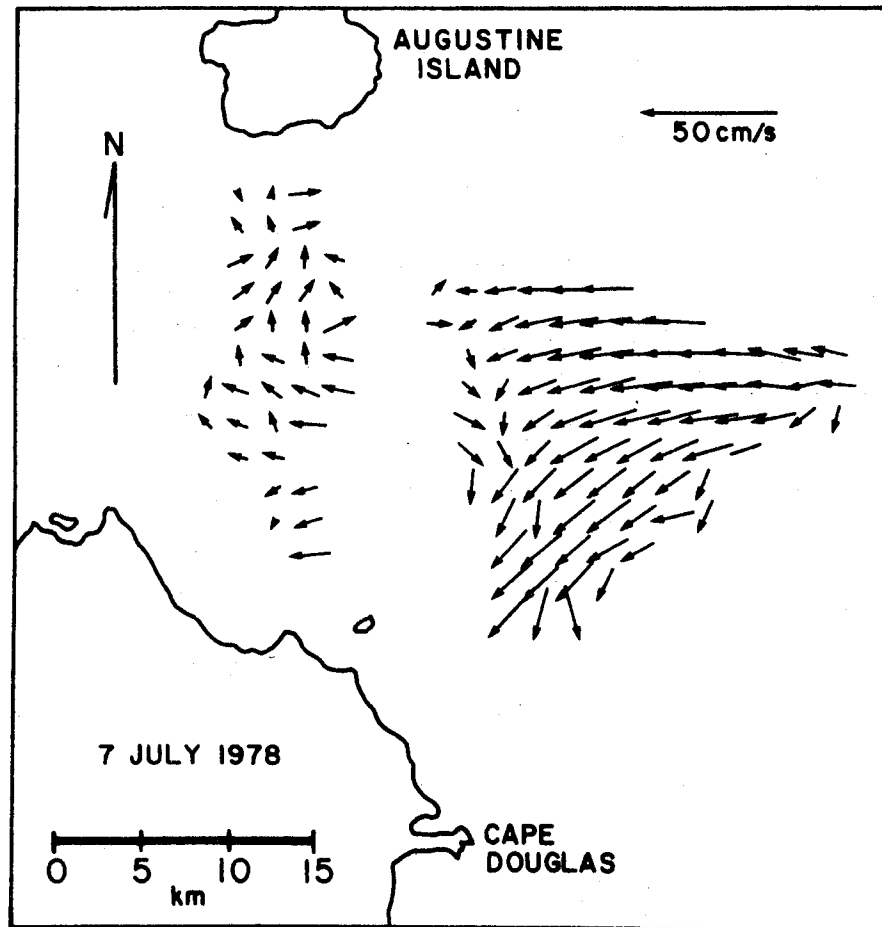


Figure 26. Twenty-four-hour mean surface currents observed on 7 July 1978 in lower Cook Inlet using the surface wave radar unit. Data are from Dr. A. S. Frisch, NOAA/WPL.

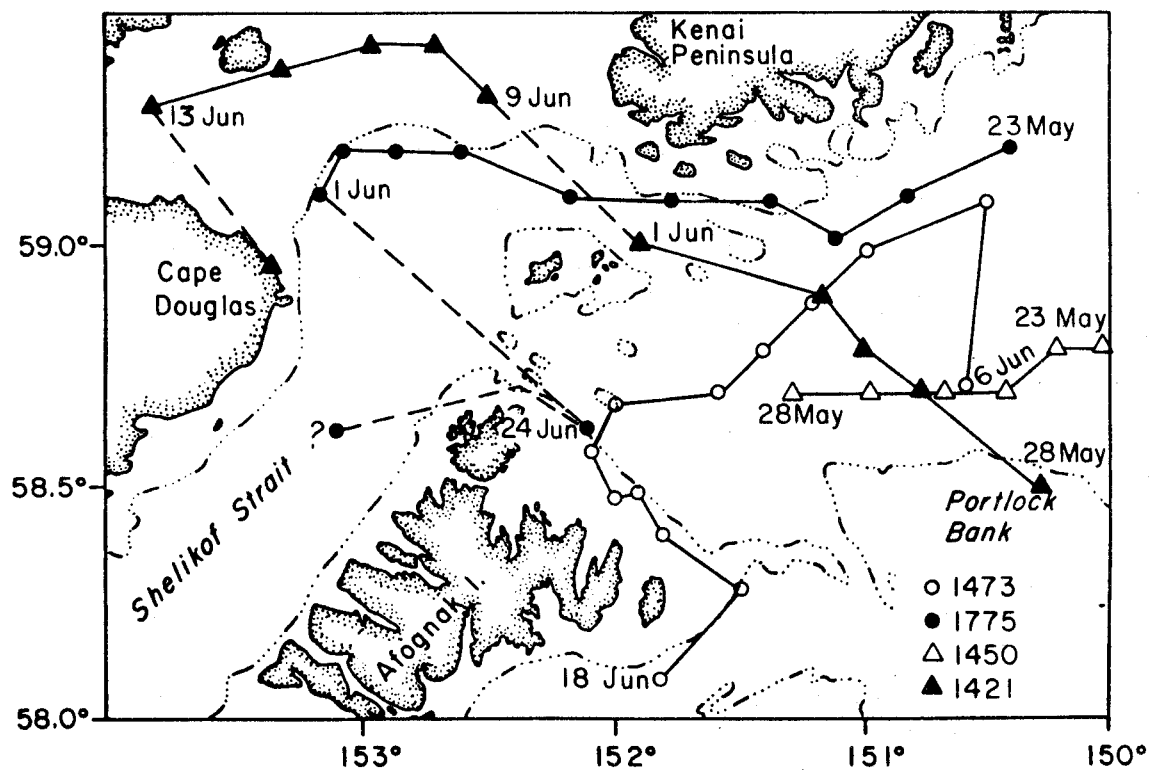


Figure 27. Details of drogued buoy trajectories in the lower Cook Inlet region in 1978. Buoy locations are plotted at 1-day intervals.

3.1.5 The Bank and Trough Region

The area of complex bank and trough bathymetry south of Kodiak Island is of interest because we expect a priori that the topography exerts a control both on currents and on vertical mixing processes. To supplement the current data obtained from mooring WGC2 (cf. Fig. 13), moorings were deployed in the Kiliuda Trough region during winter 1977-78 and summer 1978 (cf. Section 2.2).

Whereas results from WGC2 located approximately the inshore edge of the Alaskan Stream, moorings in Kiliuda Trough defined the effect of the bank-trough-bank configuration on currents. Winter mean currents observed are shown on Figure 28. There was a clearly defined shoreward flow on the upstream (northeastern) side of Kiliuda Trough, just inside the 91-m (50 fm) isobath. Current speeds here were of order 10 cm sec^{-1} . Along the axis of the trough, there was a weak ($\sim 5 \text{ cm sec}^{-1}$) shoreward mean flow which showed a tendency to curve left toward the head of the trough. Inward flow into the trough was supported qualitatively by release and recovery data from seabed drifters which indicated a shoreward flow of bottom water into the trough (Fig. 29). Flow at the head of the trough was dominated by a relatively strong ($\sim 20 \text{ cm sec}^{-1}$) southwesterly alongshore flow. The overall tendency was for a cyclonic circulation pattern over the trough. This is reasonable dynamically because of the high-latitude tendency for streamlines to parallel isobaths and hence conserve potential vorticity. The inshore portion of the Alaskan Stream would, in tending to follow isobaths, flow shoreward along the northeastern side of the trough as observed. The southwesterly coastal flow near the head of the trough may be, in part, a baroclinic effect due to coastal freshwater addition, either locally or more likely as part of the Kenai Current. This tends to augment the topographically controlled flow.

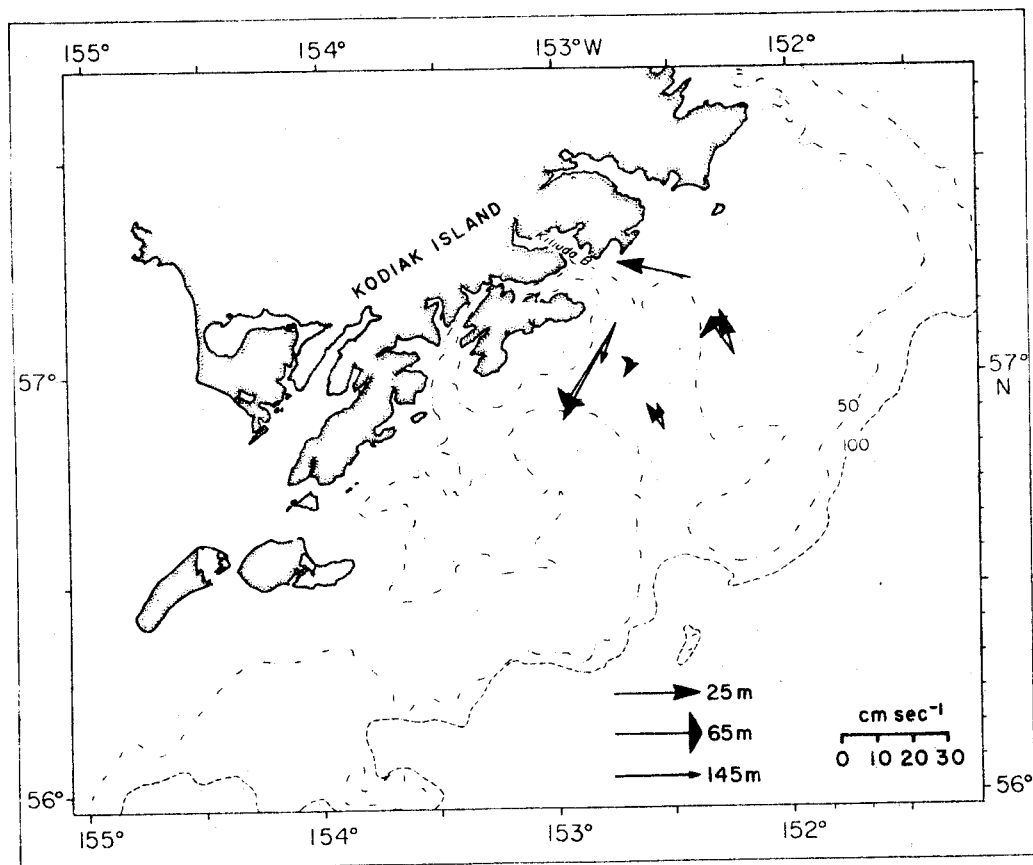


Figure 28. Mean currents observed in the bank-trough region south of Kodiak Island during winter 1977-78. Mooring statistics (moorings K6-K10 A-series) are given in Appendix A.

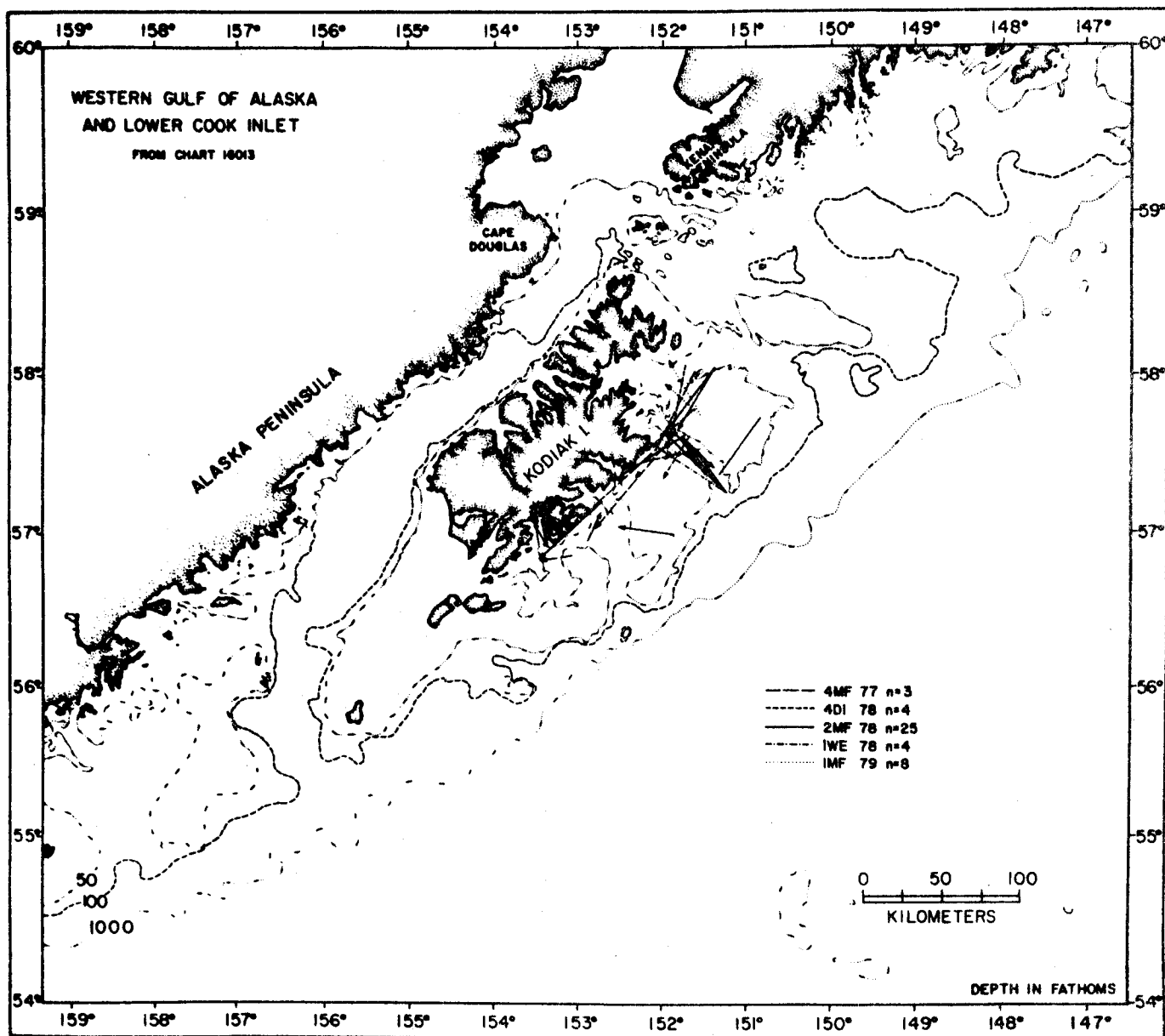


Figure 29. Deployment and recovery locations of seabed drifters, showing inferred directions of movement. Specific positions and dates of deployment and recovery are listed in Appendix C. The figure includes drifters recovered through September 1979, while Appendix C contains recoveries as recent as February 1980.

Sufficient temperature and salinity data were obtained on the banks east of Kodiak Island to allow speculation on processes which influence temperature and salinity distribution. As these banks are bounded on the north by the Kenai Current and on the south by the Alaskan Stream, we might expect considerable complexity there. Of major interest is the vertical density stratification, which reflects vertical mixing processes and mechanisms (such as freshwater input) that act to maintain stratification. With precipitation ($>130 \text{ cm yr}^{-1}$) exceeding evaporation ($<50 \text{ cm yr}^{-1}$), a net dilution of surface waters occurs (Jacobs, 1951), so that surface changes in salt content usually provide a positive buoyancy flux. During times of minimum precipitation, surface exchange of heat may result in a negative buoyancy flux. Under conditions of negative buoyancy flux, wind and wave mixing at the surface and tidal mixing from the bottom act to stir the entire water column; conversely, with a sufficient positive buoyancy flux, stratification occurs.

We present the distribution of the σ_t difference between 50 m and the surface (Figs. 30 and 31) compiled from the two cruises having the most complete spatial coverage. The σ_t differences for September 1977 are representative of summer conditions, whereas those for October-November 1977 represent fall.

The greatest stratification was associated with the Kenai Current. This was caused primarily by dilute (low density) near-surface water, and values were reduced somewhat by enhanced tidal mixing near the Kenai Peninsula and over the banks. During September 1977, the σ_t distribution suggests that some portion of the Kenai Current did not enter Shelikof Strait but instead turned south near Afognak Island. The effect of more dilute Kenai Current water, in concert with locally added fresh water, was manifested by increased $\Delta\sigma_t$ along Kodiak Island and southwest extension over Middle

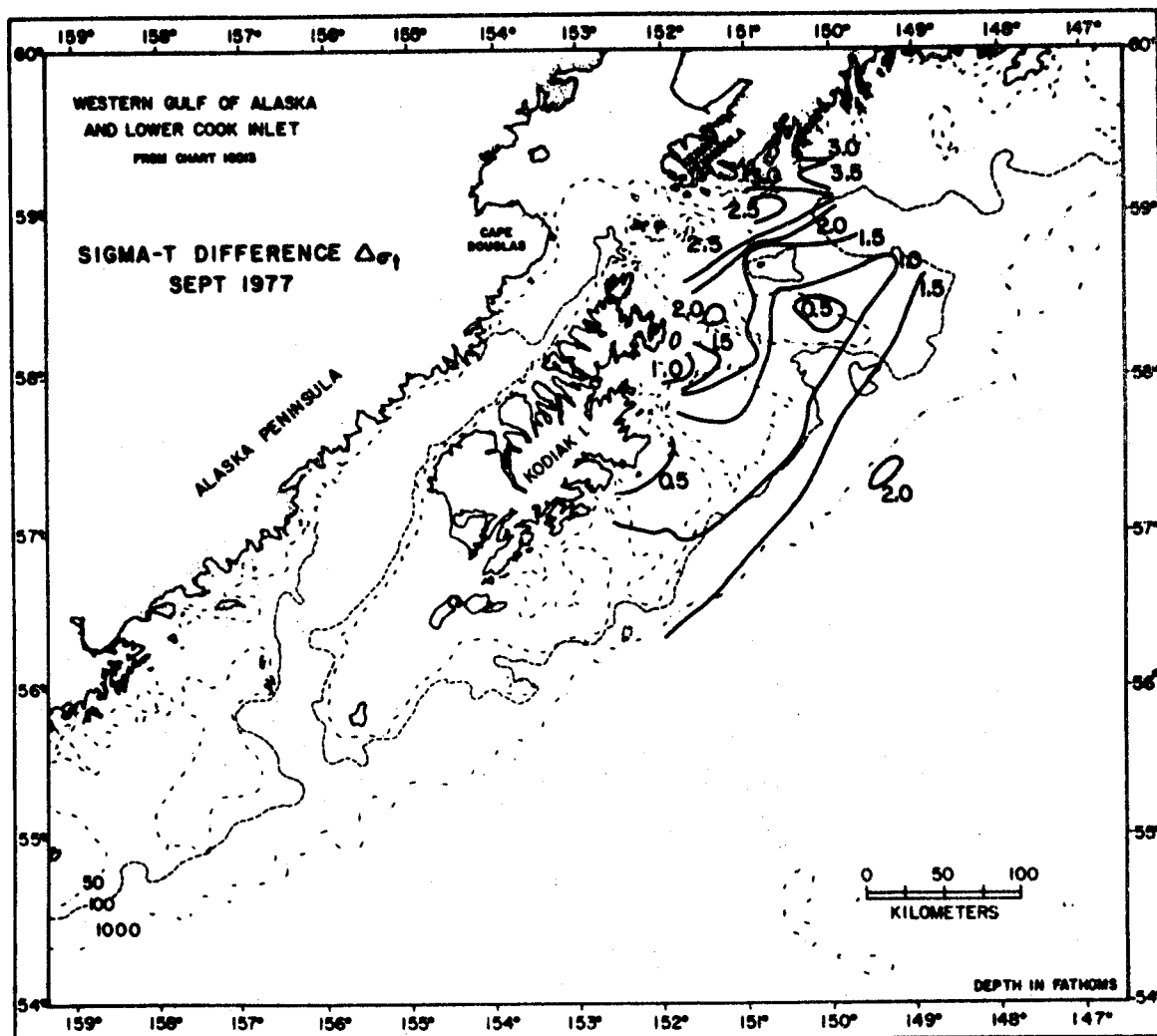


Figure 30. Difference in density (as sigma-t) between the surface and 50-m depths on the banks south and east of Kodiak Island in September 1977.

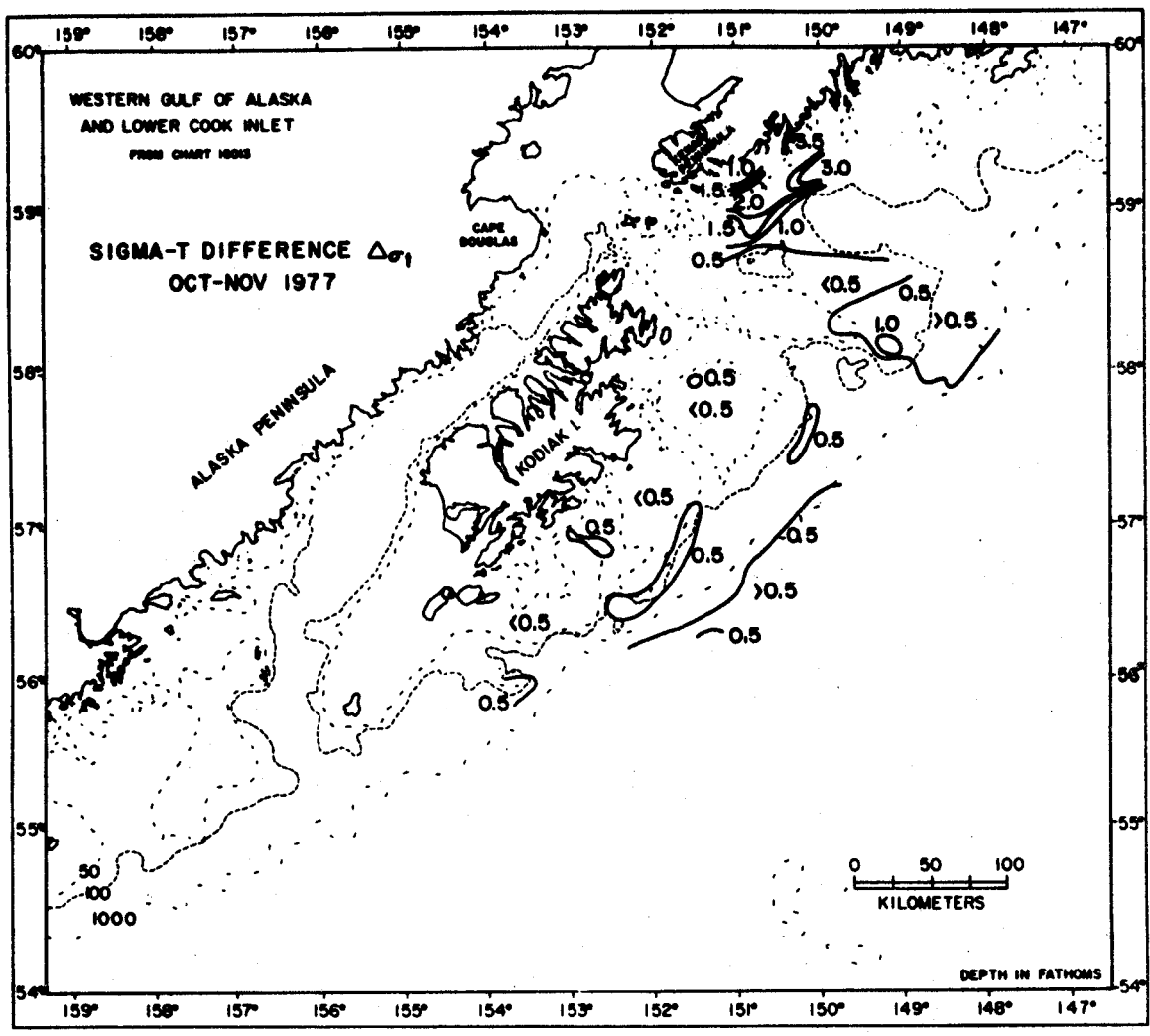


Figure 31. Difference in density (as sigma-t) between the surface and 50-m depths on the banks south and east of Kodiak Island in October-November 1977.

Albatross Bank. During October-November 1977 the wind stress changed from weak northeast to strong southwest, surface cooling became an important factor, and stratification was reduced.

Mechanisms other than thermohaline convection can influence stratification. For example, on 17 October, after occupation of stations 203 and 202.1 over Portlock Bank (Fig. 32), work was discontinued because of high winds from the north (wind speeds $> 25 \text{ m sec}^{-1}$). These two stations were reoccupied 41-42 hours later. The storm had produced marked cooling and an increase in salinity of the upper ocean. Although the cooling rates are plausible as a result of surface heat exchange (about $0.6 \text{ cal cm}^{-2} \text{ min}^{-1}$ was estimated from bulk formulas), the large changes in salinity and almost complete homogeneity of the water suggest that a combination of processes including localized upwelling and vertical turbulent mixing occurred in response to the storm. These data point out that the upper ocean may vary widely over short time spans.

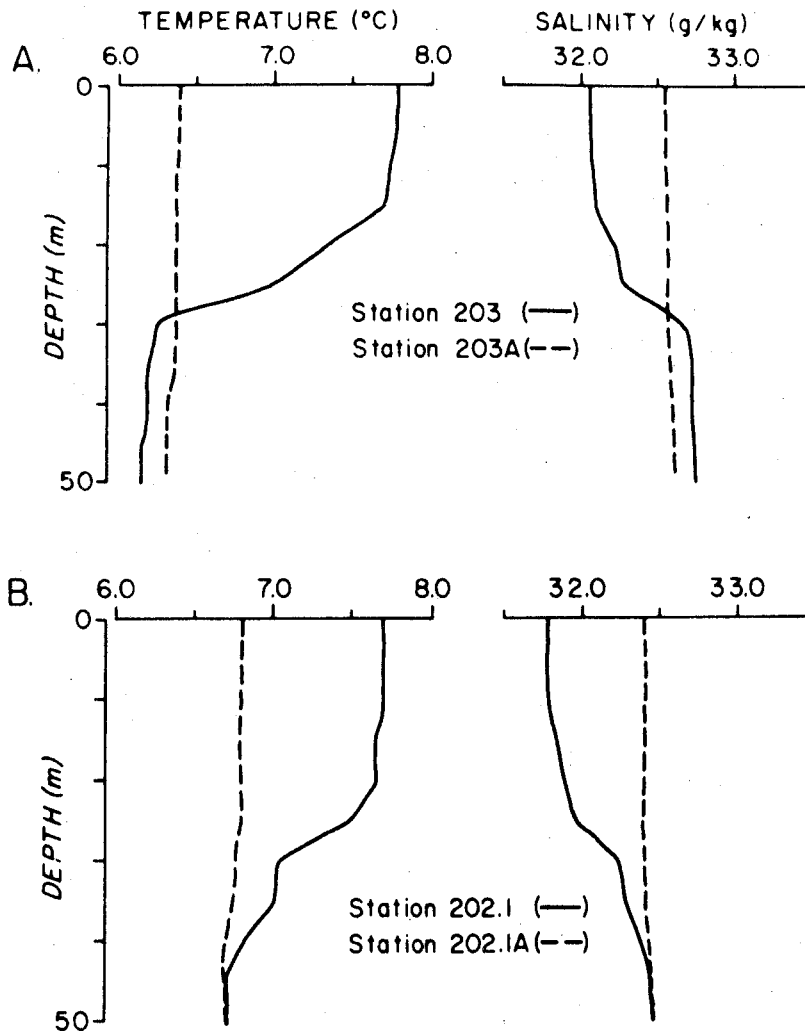


Figure 32. Vertical profiles of temperature and salinity before (solid line) and following (dashed line) a severe storm over Portlock Bank.

3.2 Behavior of Low-Frequency Current Fluctuations

3.2.1 Introduction

In this section, we discuss prominent current fluctuations having periods longer than diurnal tidal, or about 24 hours, but less than seasonal. Currents throughout the northwest Gulf of Alaska and into lower Cook Inlet are characterized by these fluctuations, which attain dominant control over the flow in regions having weak mean currents. For example, in some locations in lower Cook Inlet and on Albatross Bank where the mean flow was small ($< 5 \text{ cm sec}^{-1}$) these fluctuations accounted for more than 90% of the kinetic energy in the nontidal water motion, so they must be of paramount importance in material transport. In regions of strong mean flow ($> 20 \text{ cm sec}^{-1}$), such as Shelikof Strait, the fluctuations are relatively less important when compared with the mean flow. Figure 33 illustrates the nature of these fluctuations and exemplifies the pattern found throughout the northwestern Gulf. Time scales for the fluctuations are on the order of a week, though they have no clearly defined periodicity. The records used here as illustration are from near-bottom, minimizing biasing of the current records by surface wave noise or mooring motion.

The way in which these low-frequency fluctuations propagate through the northwestern Gulf of Alaska shelf region is of particular interest. We approach this by discussing selected aspects of the fluctuations in specific subregions, commencing with the outer and mid-shelf regions southeast and south of Kodiak Island (Fig. 1).

3.2.2 The Bank-Trough Region

Winter and summer subtidal current variance spectra from outer Albatross Bank (Station WGC2 on Fig. 6) are shown on Figure 34. These spectra are representative of conditions on the banks seaward of Kodiak Island. Most of

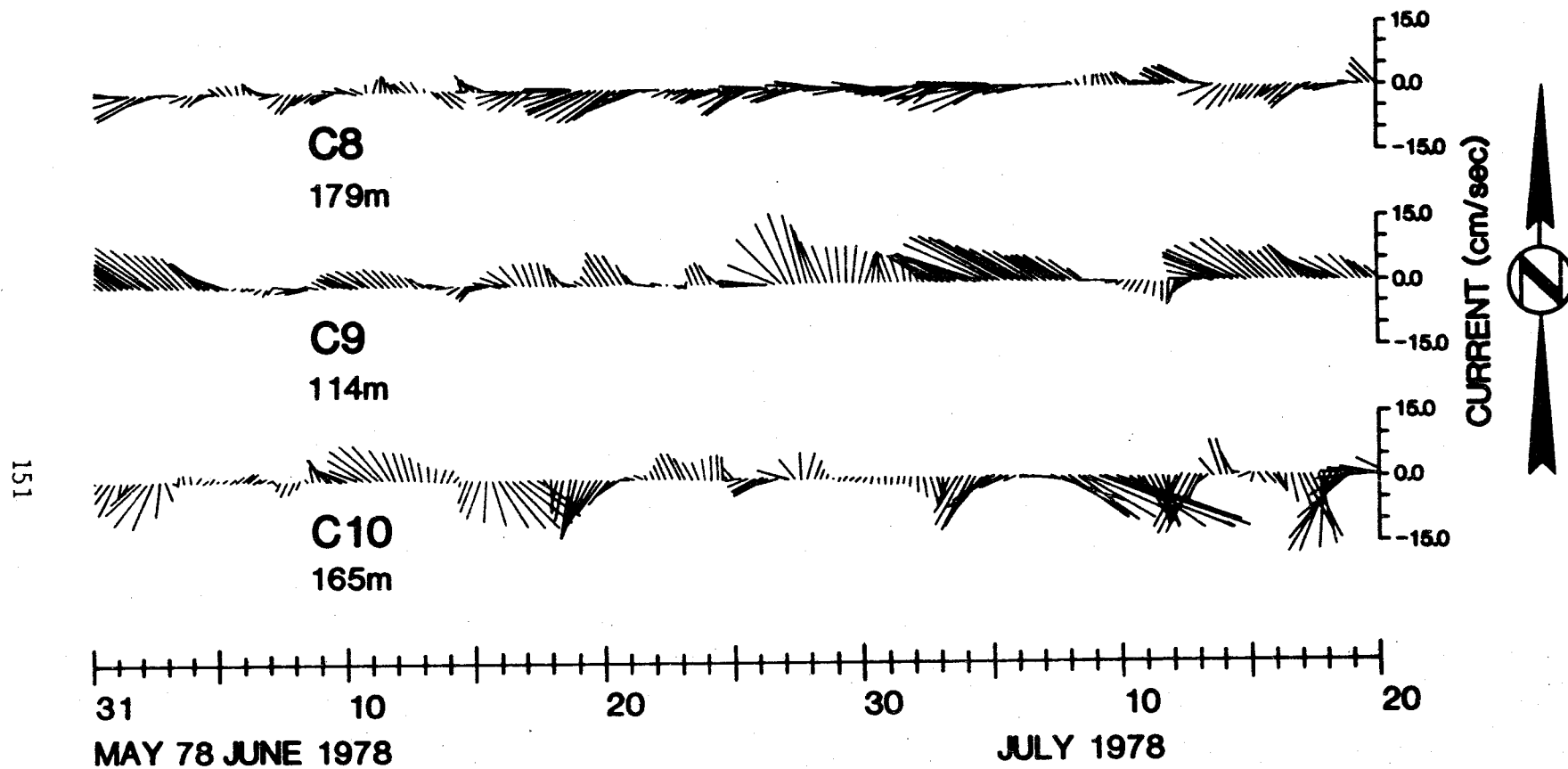


Figure 33. Representative time-series segments of near-bottom currents in Kennedy Entrance (C8), Stevenson Entrance (C9) and northern Shelikof Strait (C10). These records have been low-pass filtered through a 35-h filter to remove the tidal signals.

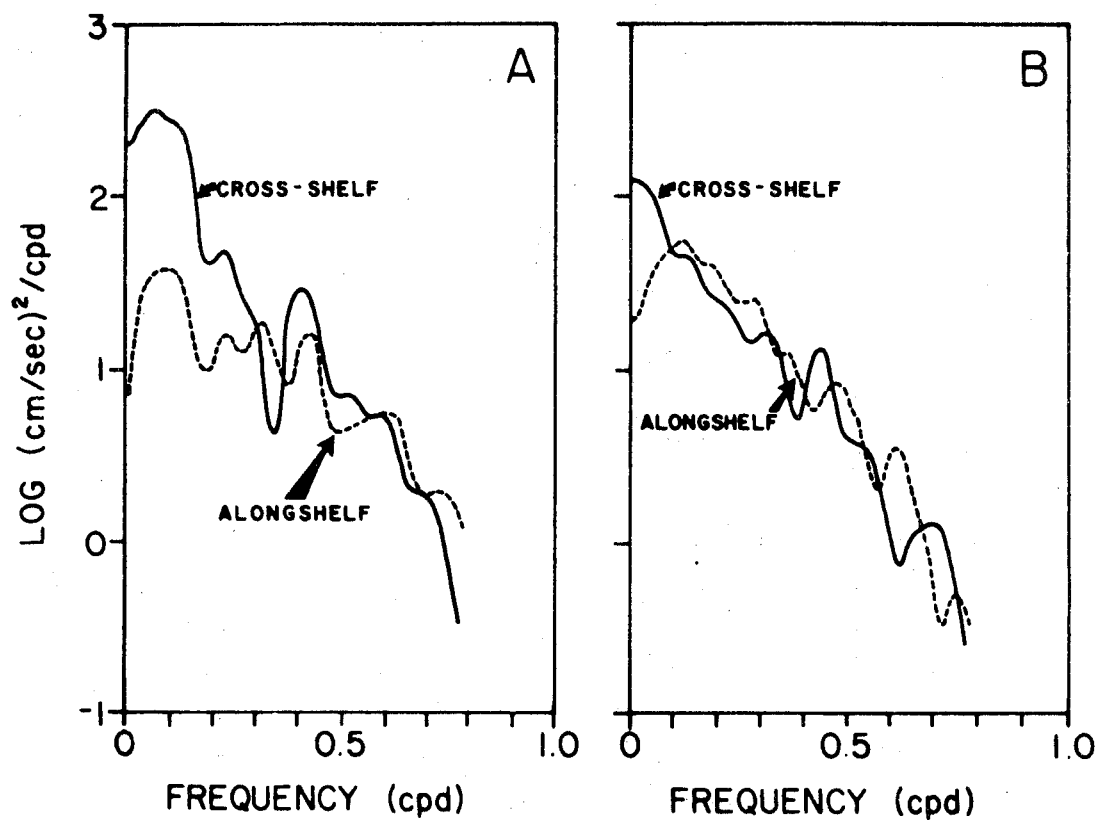


Figure 34. Winter variance spectra at station WGC2 on the banks southeast of Kodiak Island (left) and at station WGC3 off the entrance to Shelikof Strait southwest of Kodiak Island. Both current records were from about 24-m depths. Station locations are indicated on Figure 6.

the low-frequency variance energy is contained in bands below 0.5 cpd, and very low relative amounts of energy occur at 0.75 cpd, the high frequency cutoff. There was a marked change in slope of the spectra at about 0.5 cpd, with variance energy dropping off more sharply at higher frequencies. Shallower observations at the same location indicated higher overall energy levels, while deeper observations showed lower energy levels; the characteristic shapes of the spectra were the same. For comparison purposes, we also show subtidal variance spectra obtained from observations at Station WGC3 just seaward of the southern extremus of Shelikof Strait. The shapes of the spectra at the two locations are similar, though energy levels differ somewhat.

Spectral analyses of the current data from mooring WGC2 on the shelf south of Kodiak Island (Fig. 6) indicated only one significant energy peak; this occurred at about 0.4 cpd or at a period of about 2.5 days and is shown most clearly on the cross-shelf spectra (Fig. 34). Analysis of the current records from moorings WGC1, 2, and 3 have indicated that this peak was coherent in the alongshelf direction, and that motions of this period propagate to the northeast with speeds of about 5 m sec^{-1} . The peak was most pronounced in the cross-shelf component, being in many cases absent entirely from the alongshore component. It decreased in magnitude with increasing depth of observation. It is impossible to discern whether this peak was more energetic on Albatross Bank than elsewhere; overall energy levels were lower on Albatross Bank, and it is possible that a 2.5-day peak of similar magnitude existed at other locations (such as at WGC3 off Shelikof Strait) but was masked by the higher overall spectral energy.

While the WGC series of current moorings were designed to obtain long-term, large-scale information on alongshelf coherency south of Kodiak Island, a more recent series of moorings was deployed in the complex topographic

bank and trough region southeast of central Kodiak Island (cf. Fig. 9), providing further definition of the low frequency flow. The low-pass (35-h) filtered current time series from the 1977-78 winter experiment is shown in Figures 35 and 36. The characteristic low-frequency pulses were clearly present but were manifested in different fashions at different locations relative to the banks and troughs. At stations 6 and 7 on the bank and particularly at station 8 in the shoreward portion of the trough, the pulses were primarily in speed with little directional variation. In the central portion of the trough at stations 9 and 10, however, the pulses were manifested as large variations in both speed and direction leading to frequent reversals. While the records from stations 6 and 7 over the bank suggested that events there were correlated, pulses in the trough were not. It is possible that the instruments deployed in the trough were sampling different flow regimes, as these instruments were in the vicinity of an apparent transition from alongshelf flow on the open shelf to cross-shelf flow connected with the trough.

Analysis of variance contained in different frequency bands in the bank-trough region indicated a flatter distribution than observed farther offshore at WGC2. Subtidal variance was distributed approximately evenly across the band, with a more gradual tapering off of energy levels at higher frequencies than was observed at WGC2, and there were no spectral peaks significant at the 95% confidence level.

3.2.3 Shelikof Strait

Shelikof Strait may be defined as an alongshore channel, and we suspect that, due to its confining lateral boundaries, its fluctuating flow might have somewhat different characteristics than to the southeast upon the open shelf. A winter 1976-77 current observation program in Shelikof Strait obtained

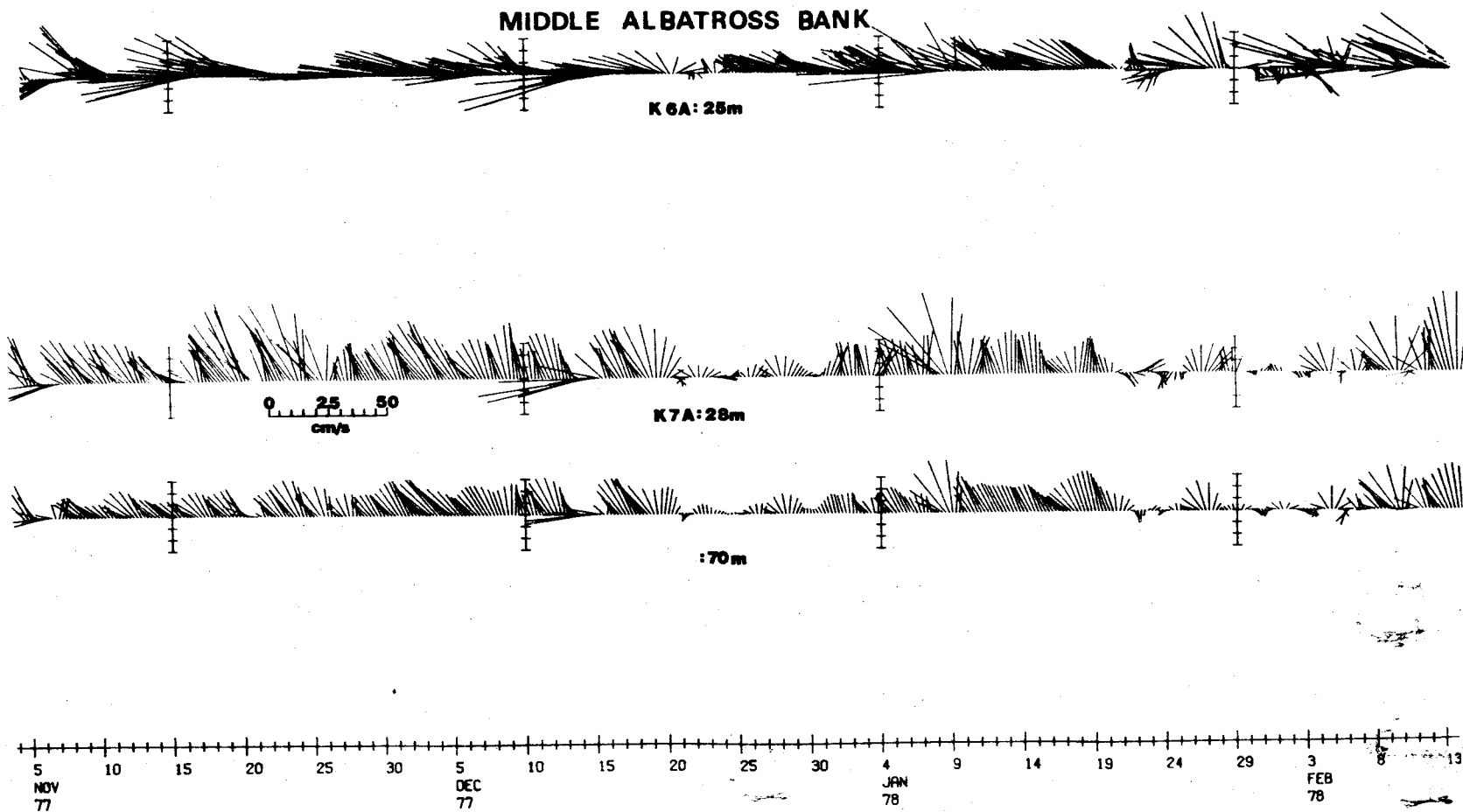


Figure 35. Low-pass (35-h) filtered currents during winter 1977-78 over the bank area south of Kodiak Island. Station locations are indicated on Figure 9.

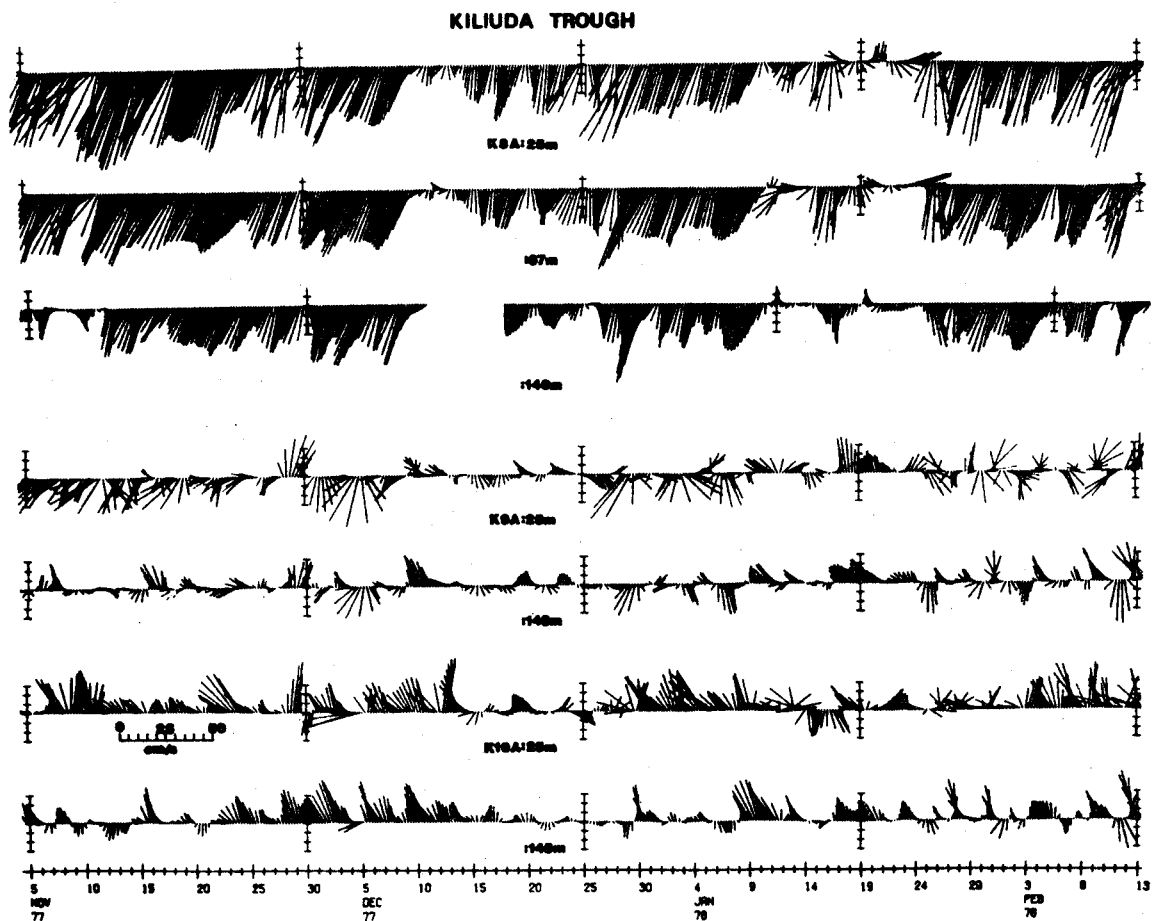


Figure 36. Low-pass (35-h) filtered currents during winter 1977-78 in Kiliuda Trough south of Kodiak Island. Station locations are indicated on Figure 9.

time-series records from the northeast and southwest ends of the Strait, providing data for a comparison of motions through the Strait (cf. Fig. 7).

Representative segments of the low-pass (35-h) filtered time series from the two ends of the Strait are shown in Figure 37. Due to the strong winter mean flow through the Strait, the fluctuations were evidenced as pulses in speed rather than as changes in direction. A generally good visual correlation is evident between the records at both ends of the Strait, as we would expect due to the confining lateral boundaries; volume continuity requires that an inflowing pulse at the upstream end of the Strait result in a corresponding outflow at the downstream or southwestern end.

Spectral analyses have been applied to the records from K1 and K2 and indicate a significant shift in cross-channel variance energy from higher and lower frequencies toward a spectral band between 0.1 and 0.3 cpd (Fig. 38). In general, subtidal variance was greater at the downstream than at the upstream end of the Strait. This downstream amplification of cross-channel fluctuations in flow was indicated also on infrared satellite photographs. A representative image is shown in Figure 39, and reveals a wave-like feature defined by the boundary between the low-temperature water from Cook Inlet and the warmer water from the Gulf of Alaska. This boundary appears to oscillate with larger amplitudes towards the southwest end of the Strait before it loses its identity. The same feature has been commonly observed on satellite imagery by G. Hufford (NOAA/NESS, Anchorage, AK 99510). We point out that although the temperature boundary which we use as a tracer loses its identity, it does not necessarily follow that the wave-like feature has ceased to exist.

Application of coherency analyses to the 100-m deep records from K1 and K2 at opposite ends of the strait reveals a confusing picture (Fig. 40).

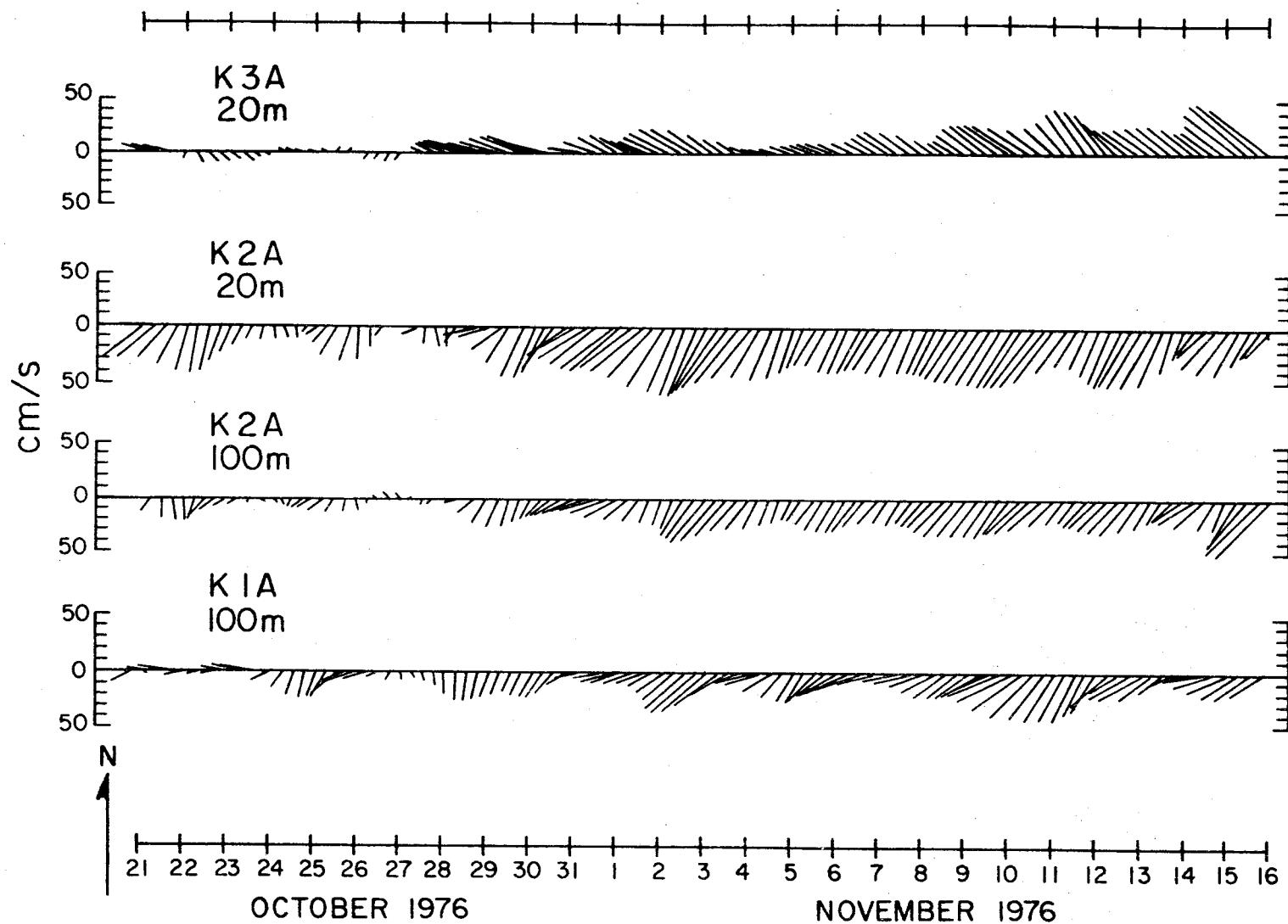


Figure 37. Representative winter segments of low-pass (35-h) filtered current data from northeastern Shelikof Strait (K2A and K3A) and from the southwestern end of the strait (K1A), illustrating continuity of low-frequency flow events through the Strait. Station locations are indicated on Figure 7.

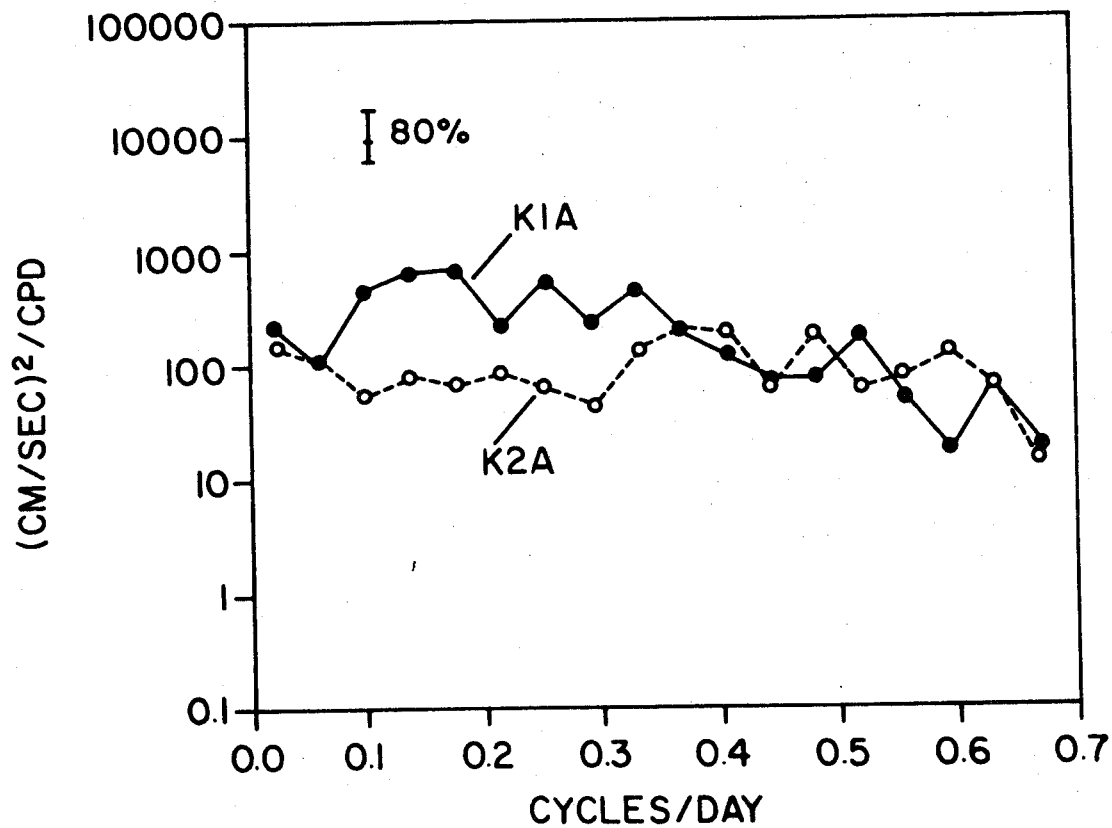


Figure 38. Variance spectra from the northeastern end (K2A) and the southwestern end (K1A) of Shelikof Strait for the cross-channel component of the 100 m deep records, showing the shift of energy into the 0.1-0.35 cpd band from K2A to K1A. Data were obtained during winter 1976-77, and station locations are indicated on Figure 7.



Figure 39. Infrared satellite image of the northwest Gulf of Alaska on 25 February 1977, showing undulating feature defined in northeastern Shelikof Strait by the boundary between cold water (light colored) from Cook Inlet and warmer (darker) water from the Gulf of Alaska.

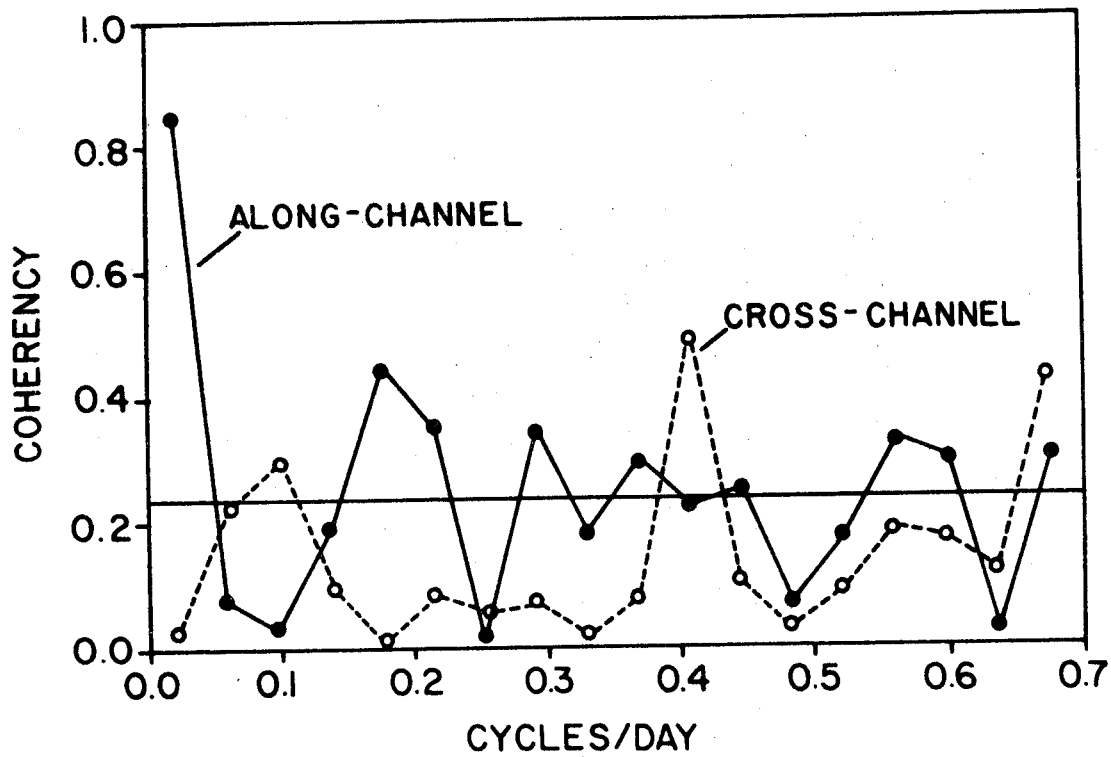


Figure 40. Coherency between cross-channel flow components at northeastern end (K2A) and southwestern end (K1A) of Shelikof Strait using winter 1976-77 data. Station locations are indicated on Figure 7.

The along-channel flow was coherent, as expected, at very low frequencies. The only other significant peaks were at about 0.2 cpd, and at about 0.4 cpd where a cross-channel peak corresponded to our ubiquitous 2.5-day peak. The correlations which are apparent from the time series shown in Figure 37 apparently relate to nonperiodic phenomena, and do not lend themselves to stationary statistical analysis. Based on the above, we conclude that there is generally a good correlation between the along-channel current fluctuations through Shelikof Strait, and that there is a significant coherency between the cross-channel fluctuations at 2.5-day periods. The 2.5-day period pulses are periodic in nature, and manifest themselves in the surface temperature field as wave-like features observable on satellite imagery.

Data obtained from northeastern Shelikof Strait during winter 1977-78 were adequate to test for vertical coherency in the fluctuating flow. Coherency analysis of the entire 5-months record indicated that the flow was vertically coherent throughout the subtidal frequencies. We conclude from this that these pulses are primarily barotropic in nature.

3.2.4 Lower Cook Inlet

A somewhat more detailed analysis of low-frequency fluctuations was possible for lower Cook Inlet than for other regions because of the relatively dense array of current meters used there (Fig. 8). Representative segments of the low-pass filtered currents from six stations in the lower Inlet are shown on Figure 41. It is clear from these plots that the time scales of variability are the same as for other regions considered, on the order of a week, and that the fluctuations are the controlling features of nontidal currents in lower Cook Inlet. At station C4, for instance, it is impossible

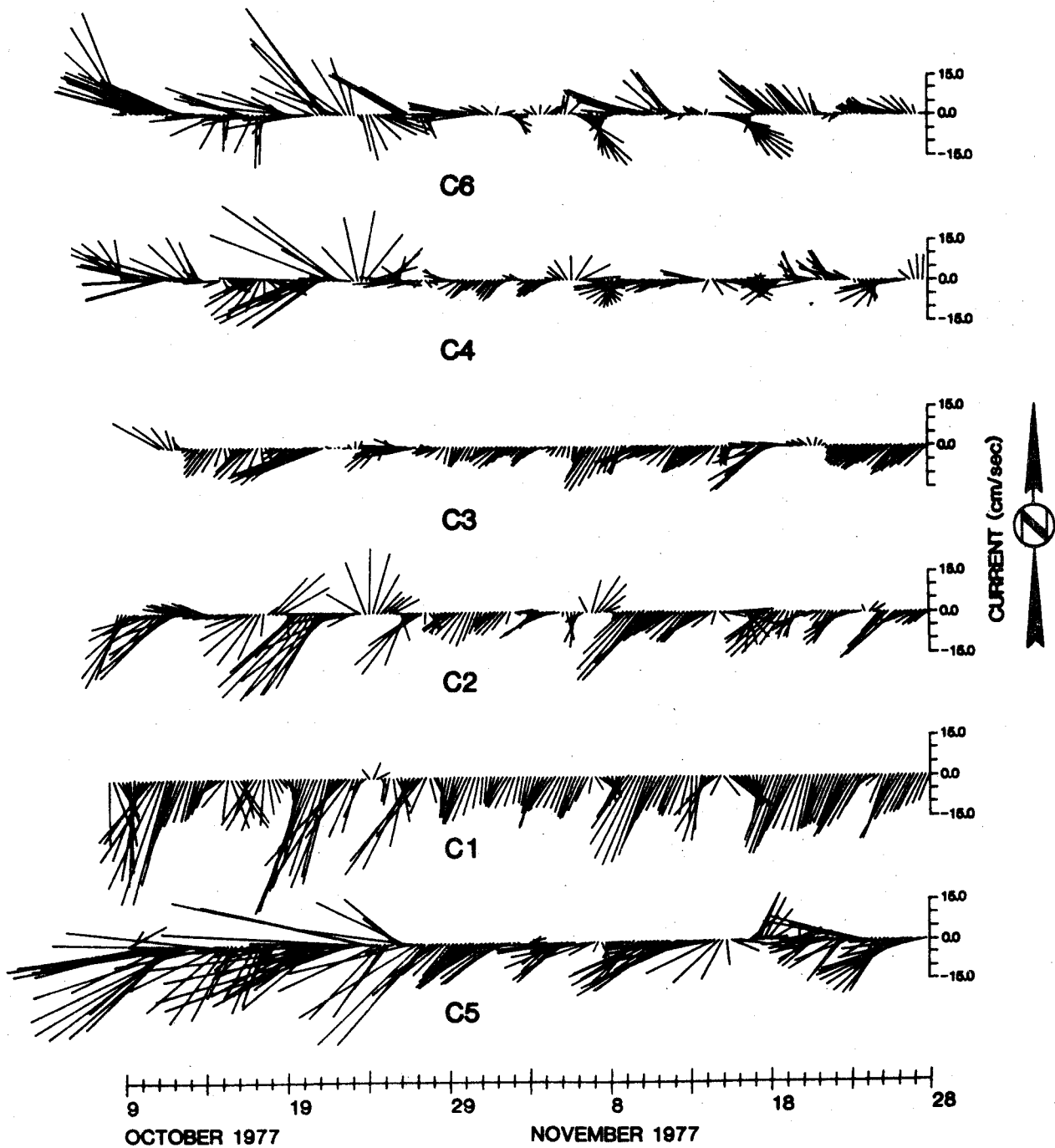


Figure 41. Representative segments of low-pass (35-h) filtered current records obtained from 20 m in lower Cook Inlet. Station locations are indicated on Figure 8.

to detect mean flow direction from a visual inspection of the time-series plot, as the flow was dominated by events. Comparison between the time series shown on Figure 41 reveals a confused pattern of correlation between fluctuations at different locations. For example, a northerly flow event occurred on about 25 October at stations C1, C2 and C4 but not elsewhere. Station C3 showed, in particular, little correlation with events elsewhere in the lower Inlet. Computation of horizontal coherencies between the 20-m records produced no consistent results.

Vertical correlations between the low-frequency pulses varied over the Inlet. At stations C3 and C4 vertical correlations were poor (Fig. 42), even though the records were vertically separated by only 30 and 45 m, respectively. Station C1 showed, conversely, excellent visual correlations in the vertical (Fig. 43) during winter, with correlations somewhat less evident during summer. Station C10, in northern Shelikof Strait, showed high visual correlation in the vertical during both winter and summer. Further analyses are in progress.

Seasonal changes in the low-frequency fluctuations are illustrated by the records from stations C1 and C10 (Fig. 43 and 44). The fluctuations were larger in winter than summer, as evidenced particularly well at station C1. There was no significant seasonal change, however, in time scales or in the lack of horizontal correlation.

In an attempt to further "filter" the current data, 7-day running means of speed were computed. These values, plotted in Figures 45 and 46, allow a better visual definition of correlation between the flow events having time scales longer than 1 week, and also reveal the longer term trends. During the winter observations (Fig. 45) the autumn decrease in flow was evident at all stations except C3. A slight increase later in the winter, particularly

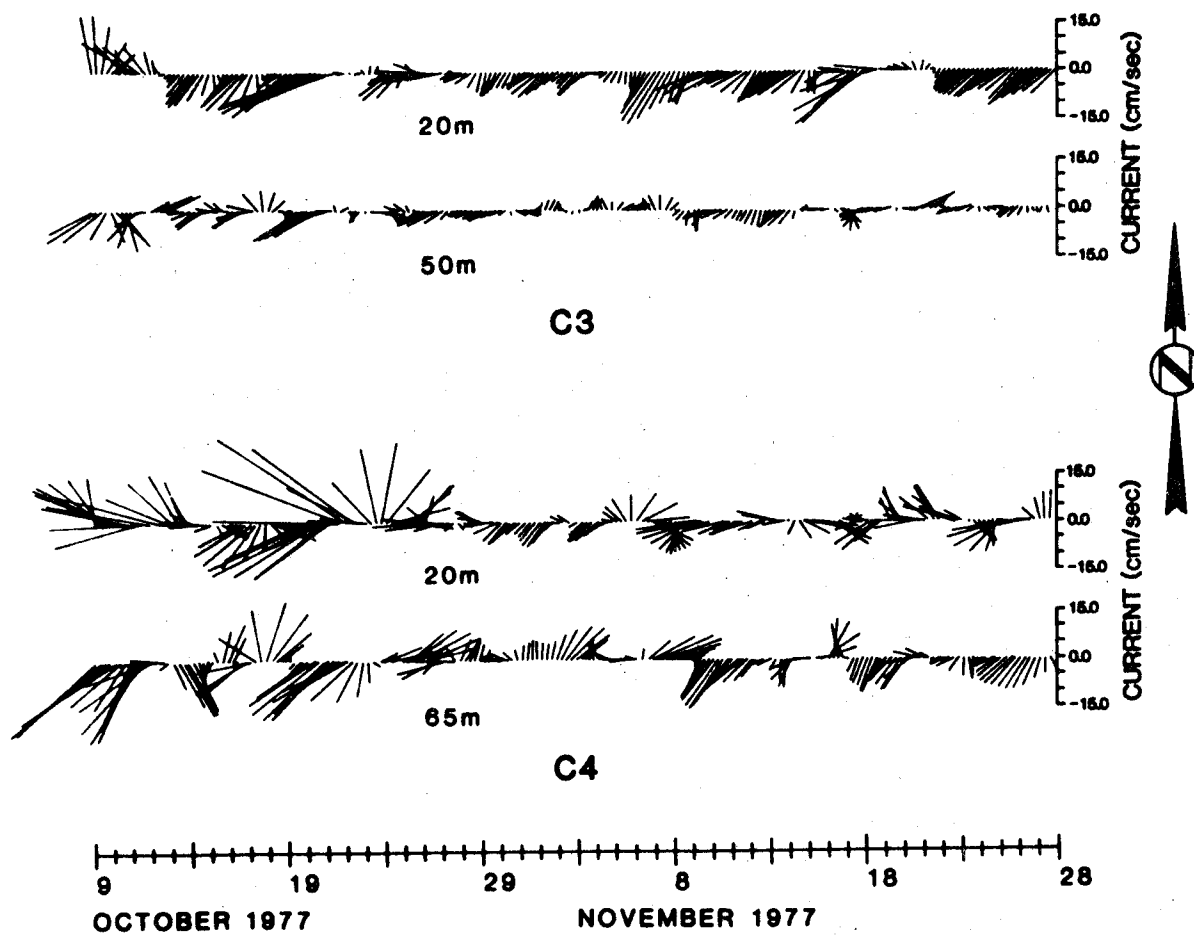


Figure 42. Vertical comparison of low-pass (35-h) filtered current records during winter from two locations in lower Cook Inlet. Mooring locations are indicated on Figure 8.

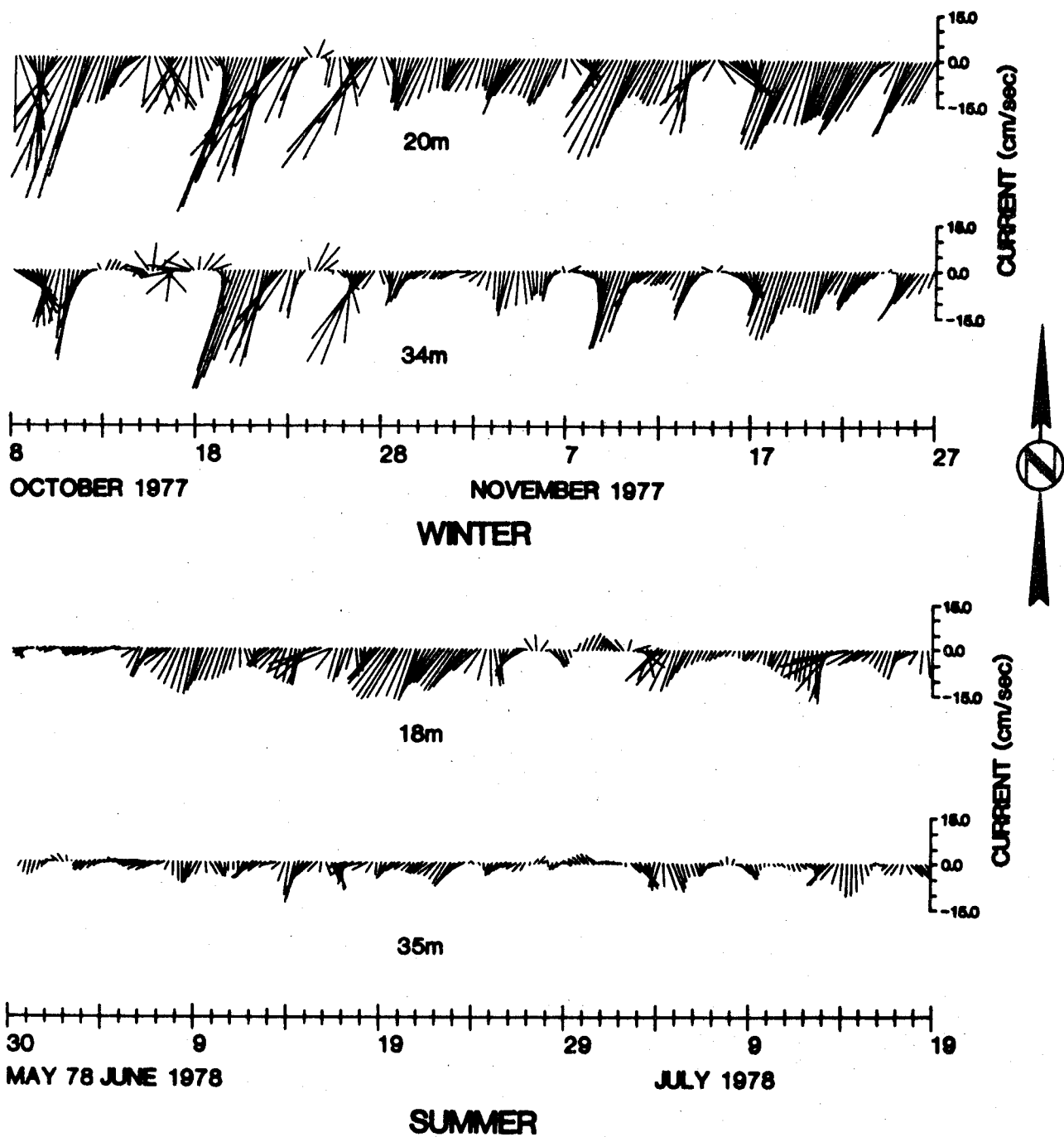


Figure 43. Seasonal comparison of low-pass (35-h) filtered current records from station C1 in lower Cook Inlet at two different depths. Mooring location is indicated on Figure 8.

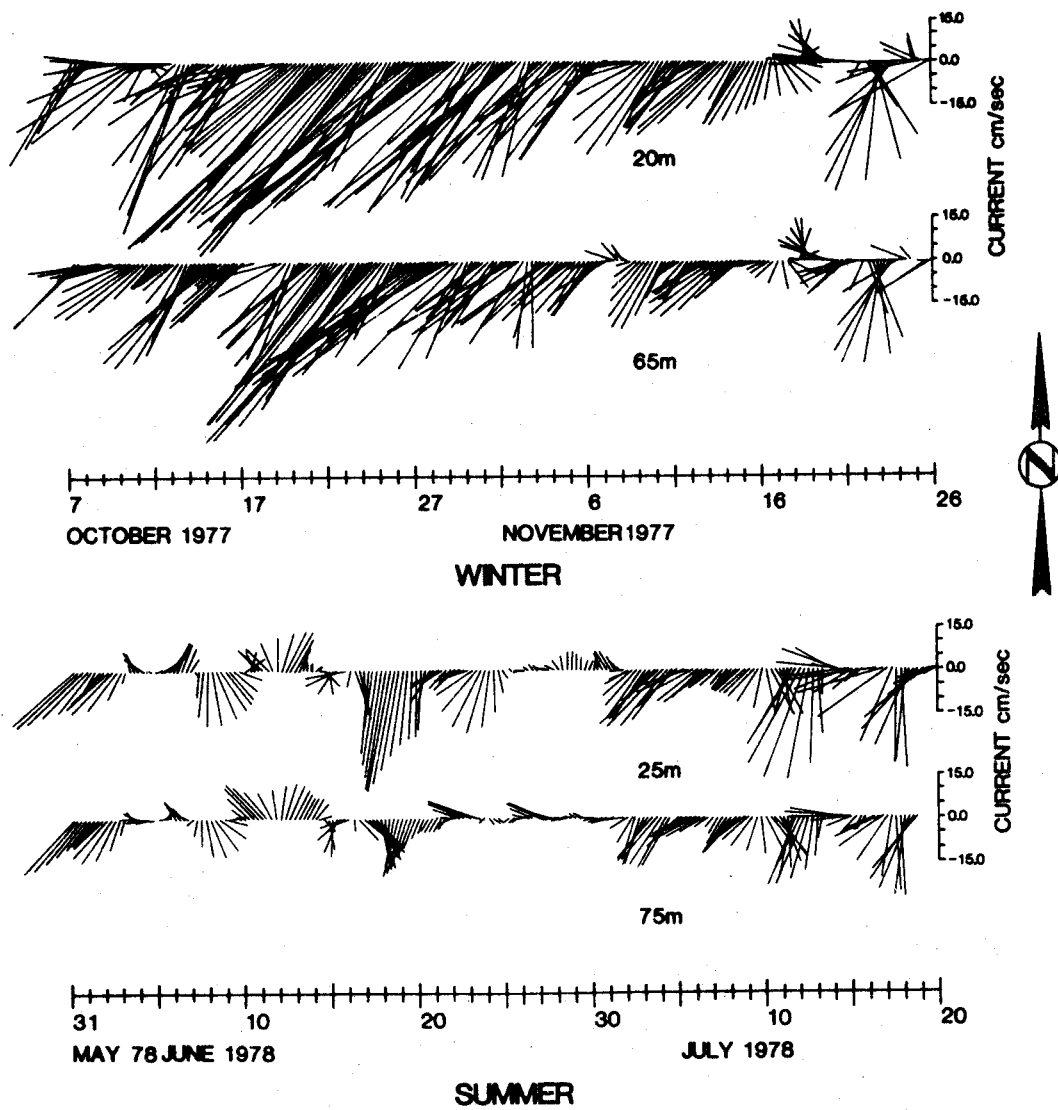


Figure 44. Seasonal comparison of low-pass (35-h) filtered current records from station C10 in northern Shelikof Strait. Mooring location is indicated on Figure 8.

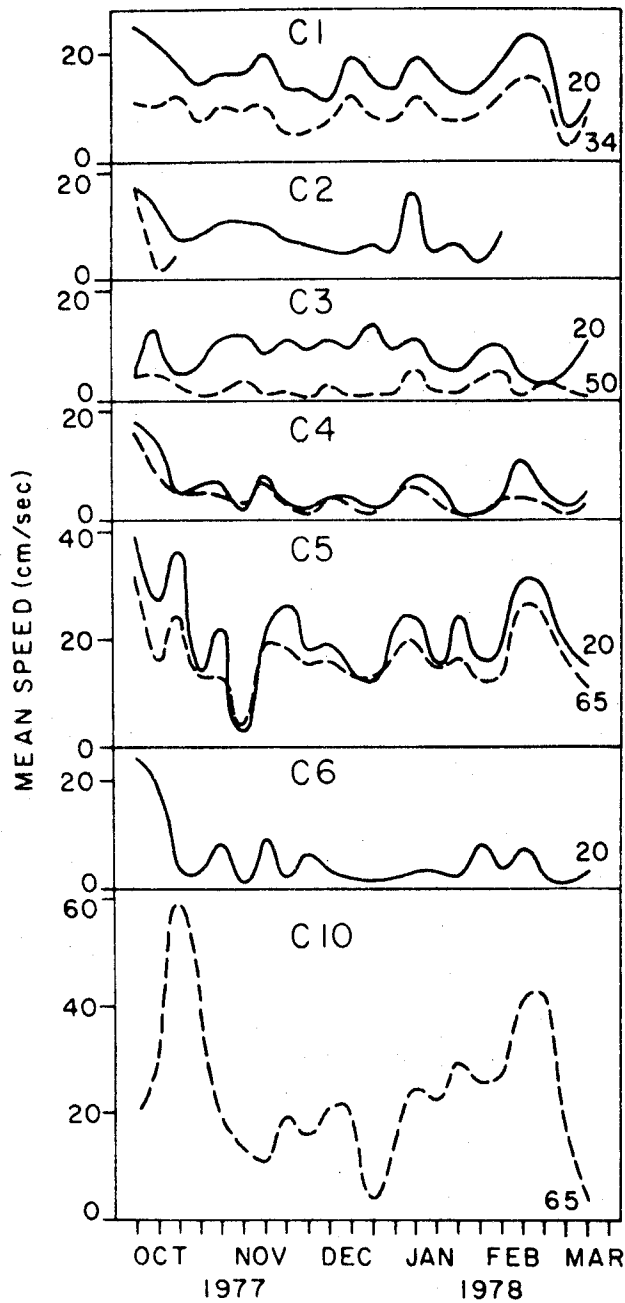


Figure 45. Seven-day running mean speeds at seven stations in lower Cook Inlet. Numbers at right-hand ends of curves indicate observation depths in meters. Station locations are indicated on Figure 8.

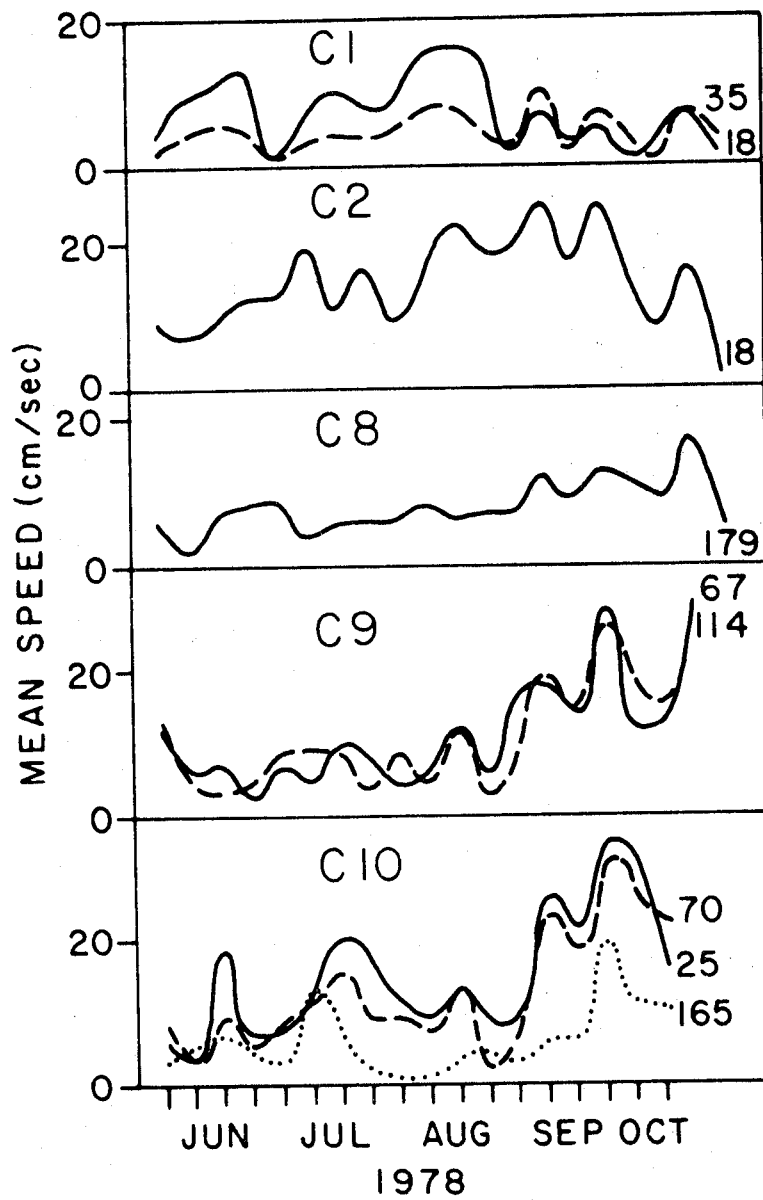


Figure 46. Selected 7-day mean speeds at five stations in lower Cook Inlet during summer 1978. Numbers at right-hand ends of curves indicate observation depths in meters. Station locations are indicated on Figure 8.

apparent at stations C5 and C10, may have been a reflection of winter spin-up of the coastal currents. In addition to the seasonal changes, there were several shorter period (order of weeks) fluctuations that were always correlated at more than one location but rarely at all of them. Stations C5 and C10 were the best correlated, while C3 showed the least correlation with the other records. Generally, vertical correlations were good except for station C3.

Summer current records were relatively incomplete, but indicate the same general patterns that were observed during winter (Fig. 46). The later portion of the records clearly indicates the autumn flow increase consequent to freshwater addition along the Alaskan coast to the east of lower Cook Inlet (Schumacher and Reed, 1980).

The behavior of low-frequency fluctuations in lower Cook Inlet suggests that the pulses tend to follow the same path as the mean flow, that is, an accurate east-west path paralleling the bathymetry. This was manifested as a generally good visual correlation between events at stations C8, C9, C10 and C5. However, these pulses penetrated northward into Cook Inlet only part of the time, so that the frequency of events which can be correlated with those at C5 becomes lower as we progress northward into the Inlet and reaches its lowest value at the northernmost station C3. Conversely, it seems likely that some flow events might be generated in, and confined primarily to, the upper Inlet; these might be evident at the northern stations but not in Shelikof Strait.

The cause of the predominantly aperiodic, low-frequency fluctuations discussed here is uncertain, but is probably related in part to atmospheric forcing. To test for causal factors, selected large events were compared with the local and regional meteorological parameters. Results of these

comparisons were inconclusive, and it is felt that this was probably due at least in part to inadequate meteorological data. As discussed in Section 3.5, the atmospheric pressure field is not necessarily representative of actual winds either inside or outside the Inlet. The existing shore stations have also been shown to bear little relation to over-water winds.

Research into the nature of similar flow fluctuations in other large estuarine systems has revealed that such systems are strongly responsive to atmospheric forcing on the continental shelf outside the mouth of the estuary (Wang and Elliot, 1978; Wang, 1978; Winant and Beardsley, 1979; Holbrook *et al.*, 1979). The meteorology of the lower Cook Inlet region is dominated, particularly in winter, by the northeastward migration of intense atmospheric low-pressure systems. We would expect the coastal sea-level variations attendant upon these cyclonic storms to drive significant flow through lower Cook Inlet and Shelikof Strait. Propagation of these pulses northward into the Inlet would then be subject to modification by bathymetry, stratification and local winds. While we have sufficient information on both the bathymetry and stratification to address this problem, the local wind field during our current observations was not defined due to malfunction of environmental buoy EB-46007, which was located centrally in the lower Inlet so as to define the general wind field there. We retain the hypothesis that the fluctuations are driven primarily by atmospheric events over the continental shelf, with local modification to the flow due to stratification, bathymetry and local winds within the lower Inlet itself. Based on work elsewhere, eddies propagating across the shelf could also contribute to these fluctuations. Quantification of these mechanisms awaits further analysis of current data from within the lower Inlet in combination with regional and local wind data.

3.3 Tides and Tidal Currents

The pressure gage data were analysed for tidal components using the Munk-Cartwright Response method (Munk and Cartwright, 1966) with the tide potential as reference series. Results of these analyses are given in Table 3. These analyses were used, along with historical harmonic constants found in Pearson (1973), Rapatz and Huggett (1977), the International Hydrographic Bureau tables (1966), unpublished National Ocean Survey data, and information obtained from the Tide Tables, to describe tidal characteristics and tidal wave propagation in the study area.

Empirical cotidal charts have been constructed for the M_2 (principal lunar semidiurnal) and K_1 (luni-solar diurnal) constituents (Fig. 47 and 48, respectively). These charts show lines of equal phase, or times of high water, and equal amplitude for each constituent. They have been constructed by interpolation between observed values where stations were close-spaced relative to the tidal wavelength, and by estimation in areas where data were sparse. The M_2 and K_1 are the largest of, and generally representative of, semidiurnal and diurnal constituents, respectively.

Both the diurnal and semidiurnal tides propagate from east to west in the Gulf of Alaska in Kelvin wave fashion as part of a north Pacific amphidromic system. According to the cotidal charts of Luther and Wunch (1975) for the central Pacific, the M_2 amphidrome is located at approximately 25°N and 135°W , and the K_1 amphidrome is at 21°N and 177°E . On the outer shelf, M_2 amplitudes decrease from about 110 cm in the vicinity of Middleton Island to 80 cm near Mitrofanina Island. Amplitudes increase to about 160 cm up Shelikof Strait toward Cook Inlet. Large amplitudes are found in Cook Inlet, where the semidiurnal tides are near resonance. Amplitudes are largest on the east side in concurrence with Kelvin wave dynamics (Matthews and Mungall,

TABLE 3

Tidal components derived from pressure gage data using the Munk-Cartwright response method (Munk and Cartwright, 1966) with the tide potential as reference series.

Station	LAT	LONG	O1	P1	K1	N2	M2	S2	FROM	TO	DAYS
K8A	57 07	152 45	24.3 261	12.1 273	36.6 274	19.1 276	92.8 299	29.7 329	77 292	78 001	74
K9A	57 01	152 37	25.4 260	12.9 272	39.2 273	19.0 275	92.7 298	30.5 327	77 292	78 068	141
K10A	56 51	152 26	27.0 260	13.9 273	42.2 274	18.9 275	92.6 298	30.5 328	77 292	78 059	133
C1B	59 11	153 19	32.1 271	16.6 286	50.6 287	36.7 303	172.9 326	64.6 002	78 148	78 291	144
C4A	59 17	152 54	34.0 269	17.6 284	53.6 286	37.7 303	177.0 327	65.5 002	77 280	78 074	160
C9B	58 47	152 16	31.8 262	16.0 276	48.8 277	32.4 282	153.6 305	56.1 341	78 149	78 207	58
M1B	55 25	157 59	28.3 267	14.6 280	44.5 281	17.1 291	81.3 314	27.2 343	77 301	78 065	129
WGC2C	57 27	150 30	29.8 256	15.5 271	47.1 273	20.3 271	98.4 295	32.2 325	76 070	76 160	90

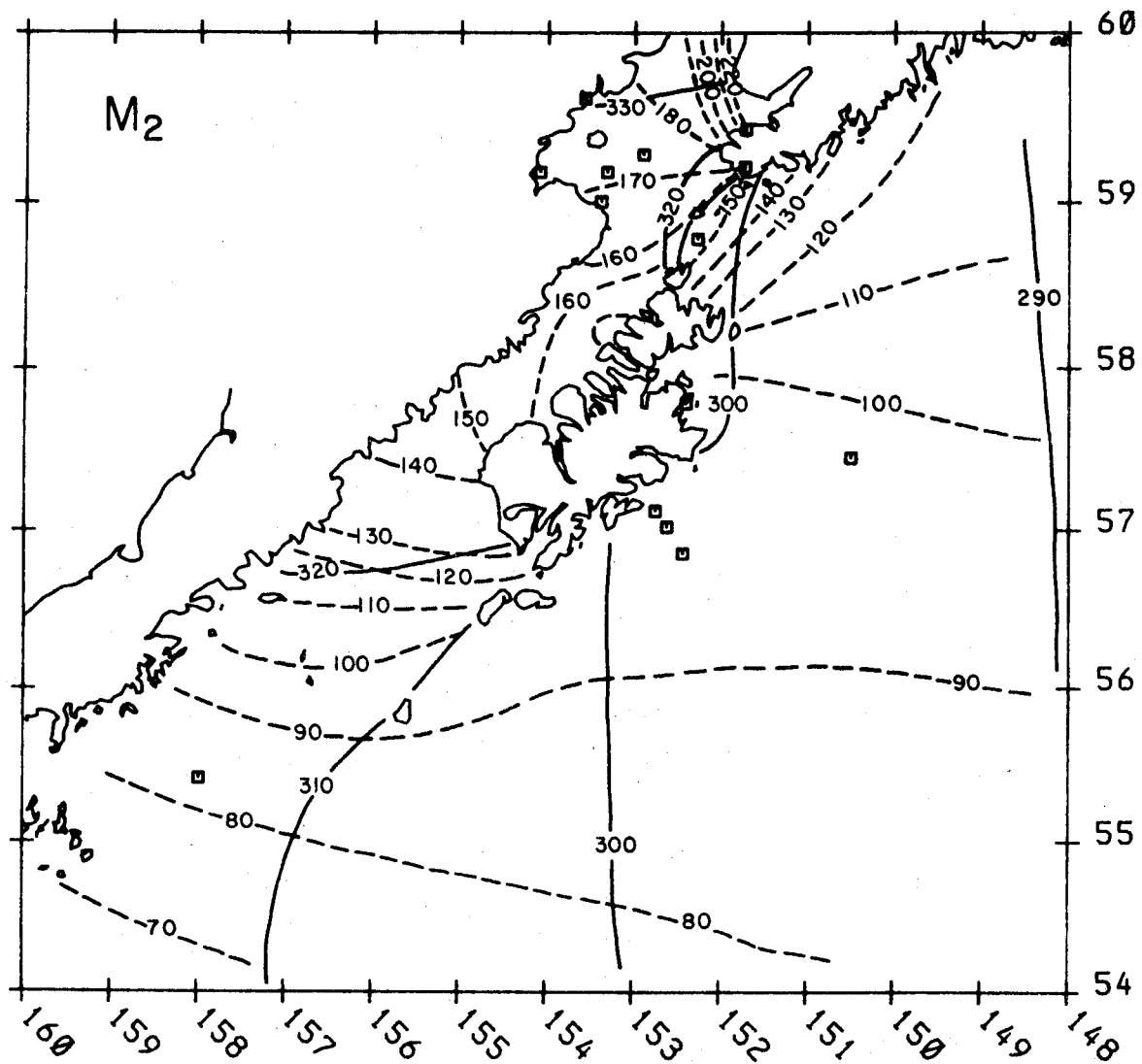


Figure 47. Cotidal chart for the M_2 tides. Solid lines are cophase lines referred to Greenwich. Dashes are coamplitude in cm.

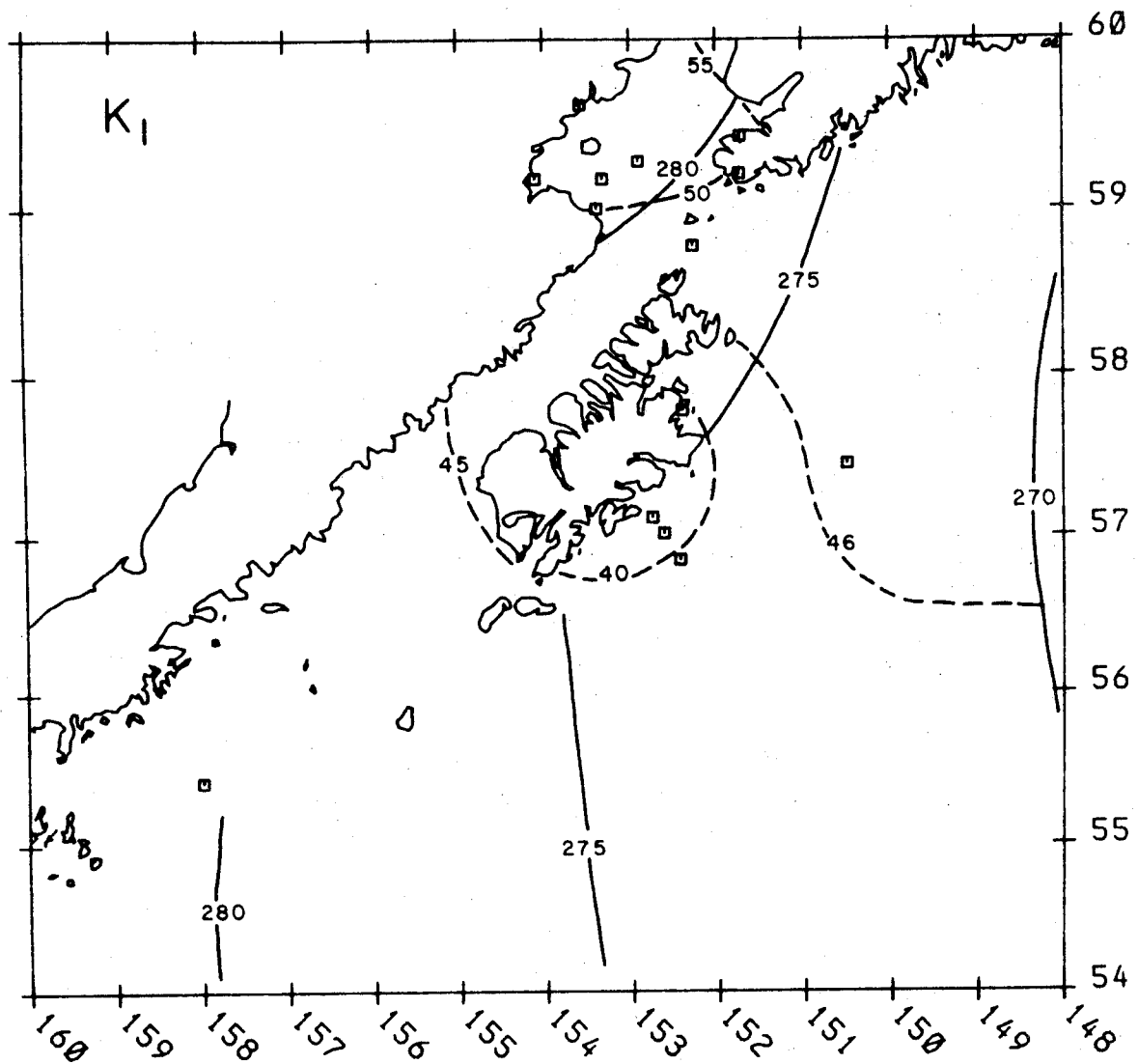


Figure 48. Cotidal chart for the K_1 tides. Solid lines are cophase lines referred to Greenwich. Dashes are coamplitude in cm.

1972). M_2 amplitudes increase from 154 cm at C9 in Stevenson Entrance to 179 cm at C4 in lower Cook Inlet to near 400 cm in the upper Inlet. The K_1 amplitudes are much more uniform in the western Gulf area, ranging from 40 to 50 cm, with somewhat higher values in Cook Inlet.

Tide type may be defined by the ratio of the sums of the amplitudes of K_1 and O_1 to M_2 and S_2 :

$$F = \frac{K_1 + O_1}{M_2 + S_2}$$

F values of 0.25 to 1.5 denote mixed, predominantly semidiurnal tides which are found throughout the Gulf of Alaska region. This type of tide has two high and two low waters per day, but with pronounced inequalities in the high and/or low waters. In the western Gulf, F varies typically from 0.5 to 0.7, with lower values in Cook Inlet where the semidiurnal tide is predominant.

The average spring tide range, defined as $2.1(M_2 + S_2)$, decreases from about 3 m near Middleton Island to 2.5 m near Mitrofanina Island, but increases to 5 m and higher in Cook Inlet.

Figure 49 is a plot of the observed bottom pressure for the month of November 1977 at station K9, which is typical of the outer shelf region. The mixed, predominantly semidiurnal tide is evident. Note the large range (3.8 m) observed on the 12th and 13th. This occurred when the new moon, lunar perigee, and extreme lunar declination approximately coincided.

The east and north components of current were analysed for tidal constituents using the response method. Predicted tidal heights from station K9 formed the reference series. The component constituents were then combined in an ellipse representation.

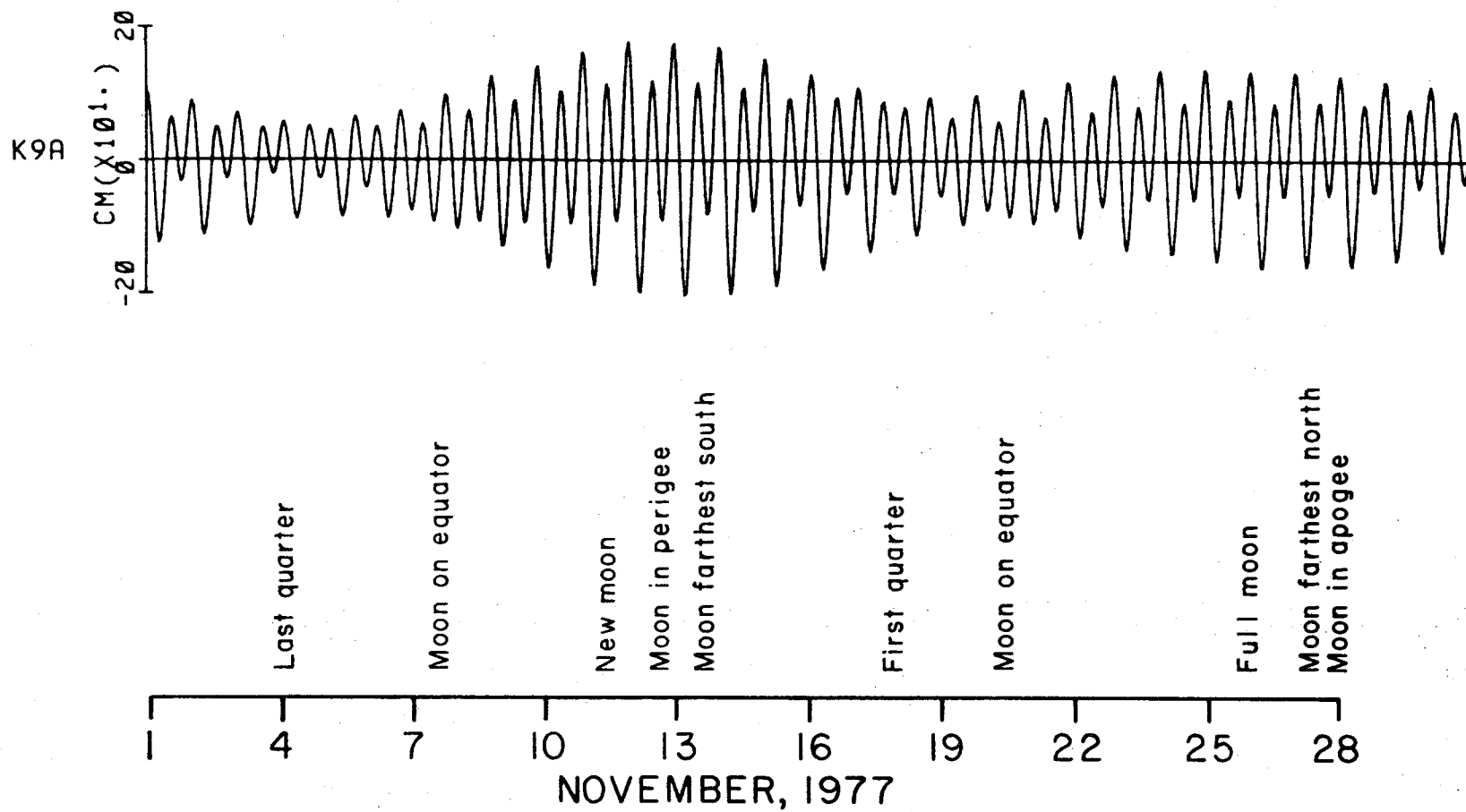


Figure 49. Observed bottom pressure at station K9 for November 1977. Station location is indicated on Figure 9.

In order to minimize possible effects of wave-induced mooring noise, records from summer are presented where possible. However, rotor pumping is not thought to be significant, as discussed in Section 3.1. The results are presented in Table 4. Tidal current ellipses for the M_2 and K_1 constituents are presented in Figures 50 and 51.

The M_2 ellipses show a great deal of spatial variability. Large M_2 tidal currents are found over North Albatross Bank, in Kennedy and Stevenson Entrances and southwest of Kodiak Island. M_2 tidal currents are particularly large in eastern lower Cook Inlet and in upper Cook Inlet. Currents are smaller in central and western lower Cook Inlet, although no further evidence was found of the extremely low tidal currents found at one station in central lower Cook Inlet by Muench *et al.* (1978). Unusually small M_2 currents are found over Middle Albatross Bank and in northern Shelikof Strait. The small currents over Middle Albatross Bank are evidently the result of Kodiak Island acting as a barrier to the incident tide wave, as the cophase lines roughly parallel the bathymetry there. In northern Shelikof Strait an antinode exists, where the tide wave entering Cook Inlet around the north end of Afognak Island meets the tide wave which has arrived from around the south end of Kodiak Island. The point of meeting, where no M_2 current should exist, is somewhere near station C10. The tidal current there is extremely weak and variable. The semidiurnal tide has standing wave characteristics in Shelikof Strait and over Albatross Bank, while it is more progressive across Portlock Bank and in the entrances to Cook Inlet.

The diurnal K_1 tide exhibits a more uniform speed distribution than M_2 . Speeds are very low in Shelikof Strait because, as in the case of the M_2 tide, the waves coming around Kodiak and Afognak islands meet in Shelikof Strait and form an antinode. There is little decrease in the diurnal tidal current

TABLE 4

Tidal current components for four major species derived from current data using the Munk-Cartwright Response method (Munk and Cartwright, 1966) and predicted tidal heights from station K9 as the reference series.

Station	Bottom Depth (m)	Meter Depth (m)	Latitude	Longitude	Start Date (YR/ID)	O ₁			K ₁			S ₂			M ₂			Record Length (Days)								
						H	Major G	D	H	Major G	D	H	Major G	D	H	Major G	D		H	Major G	D					
K1A	228	100	57 45	154 44	76 290	1.2	239	44	0.3	C	3.0	221	51	0	A	5.7	277	49	.1	A	14.9	239	51	.3	C	163
K2A	164	20	58 37	153 05	76 290	2.0	222	30	0.1	A	3.7	272	3	.3	C	3.8	199	201	2.6	C	11.8	195	218	5.3	C	163
K5A	95	20	56 33	152 39	76 292	11.6	92	217	5.0	C	18.4	121	223	9.5	C	4.7	246	327	2.5	C	14.1	210	333	7.8	C	158
K6B	82	32	57 14	152 23	78 141	10.2	57	234	4.3	C	17.9	87	239	7.9	C	3.3	350	40	1.9	C	7.9	329	47	6.3	C	138
K7B	84	29	57 06	152 13	78 141	10.5	43	219	4.6	C	16.9	81	227	7.8	C	2.9	14	50	2.6	C	8.0	284	344	6.6	C	116
KRB	155	30	57 07	152 43	78 141	5.2	71	210	0.4	A	7.7	91	223	1.3	A	1.4	311	340	1.3	C	3.5	256	330	2.5	C	136
K9A	157	25	57 01	152 37	77 292	6.7	69	218	0.8	A	13.3	93	224	1.3	A	1.9	284	323	1.3	C	4.5	236	327	2.2	C	141
K10B	153	24	56 50	152 24	78 141	6.4	68	224	1.5	C	11.6	98	226	4.2	C	1.6	335	320	1.1	C	3.7	264	320	1.5	C	136
K11B	83	25	56 02	155 06	78 142	6.8	177	308	.1	A	9.2	206	303	.9	A	20.6	238	329	12.5	C	59.9	208	327	35.6	C	68
K13B	115	28	56 24	156 49	78 142	2.7	155	62	.1	C	4.8	175	62	.2	C	10.4	287	38	2.9	C	24.3	247	41	5.6	C	138
WGC2C	185	24	57 27	150 30	76 070	4.6	150	322	3.8	C	7.7	189	340	6.5	C	5.9	309	304	2.2	C	16.2	289	311	5.6	C	90
WGC2D	93	20	57 34	150 49	76 160	10.4	226	44	7.2	C	16.2	236	34	12.3	C	11.9	298	328	7.3	C	32.4	265	324	22.3	C	132
WGC3D	112	20	55 12	156 57	77 119	3.5	139	24	1.5	C	5.8	178	15	4.2	C	13.8	280	337	8.1	C	36.8	243	341	25.3	C	132
C1B	40	18	59 11	153 19	78 148	3.6	237	34	3.4	C	6.5	229	323	4.8	C	13.6	294	313	5.9	C	33.2	261	306	19.1	C	87
C4A	84	19	59 17	152 55	77 280	6.3	222	14	2.3	C	9.7	242	4	3.7	C	16.8	330	355	6.2	C	46.3	302	357	18.9	C	160
C5A	128	20	59 10	152 56	77 280	3.9	192	355	0.3	A	5.4	222	344	0.5	A	10.2	326	338	0.9	C	28.0	297	338	4.5	C	160
C6B	77	26	59 19	152 38	78 148	6.9	199	8	2.8	C	11.4	213	359	3.7	C	22.7	315	358	7.3	C	57.3	287	356	19.5	C	143
C7B	68	17	59 18	152 10	78 148	8.9	161	358	2.6	C	15.9	184	358	2.5	C	36.8	299	358	4.8	C	98.0	269	357	17.4	C	142
C8B	190	64	59 02	152 03	78 149	8.7	179	301	3.3	A	13.1	207	302	3.7	A	28.0	307	300	2.5	C	70.0	278	295	5.8	C	83
C9B	124	66	58 47	152 16	78 149	10.0	191	293	2.5	C	15.4	205	296	1.9	C	27.2	298	295	1.5	C	70.5	268	291	9.6	C	139
C10B	175	25	58 30	153 12	78 148	2.1	265	58	0.3	A	1.7	307	35	0.1	A	3.3	48	25	1.7	C	8.3	4	35	3.4	C	134
C12A	50	20	59 32	152 14	78 148	9.3	201	9	1.1	C	15.1	212	6	2.0	C	29.8	319	7	0.4	C	79.7	294	6	4.4	C	81
C13A	68	26	59 28	152 41	78 148	9.5	222	23	4.2	C	14.3	235	22	4.5	C	26.5	335	16	9.8	C	74.1	308	13	28.0	C	141
H2	110	50	55 25	157 59	77 301	4.2	179	25	2.2	C	6.9	213	35	3.8	C	6.1	298	5	2.9	C	16.3	263	358	8.4	C	129
H4	118	70	55 46	157 31	77 301	3.9	172	35	1.2	C	5.8	196	33	1.7	C	7.4	295	16	2.6	C	19.6	260	15	7.6	C	129

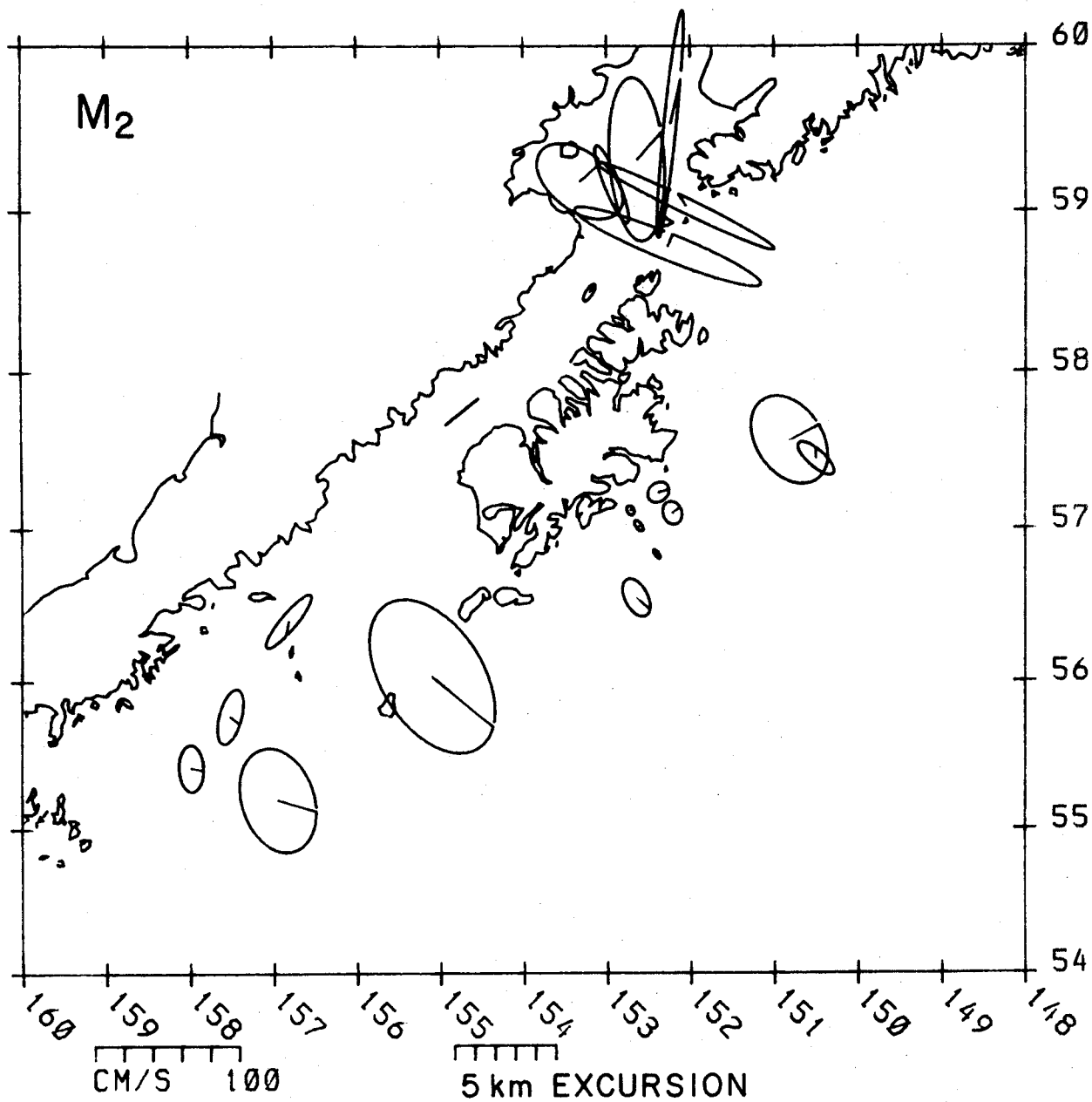


Figure 50. M_2 current ellipses for selected stations in the northwest Gulf of Alaska. Ellipses are centered at station locations; lines radiating from the centers indicate constituent current vectors when the M_2 Greenwich equilibrium phase angle is 0° .

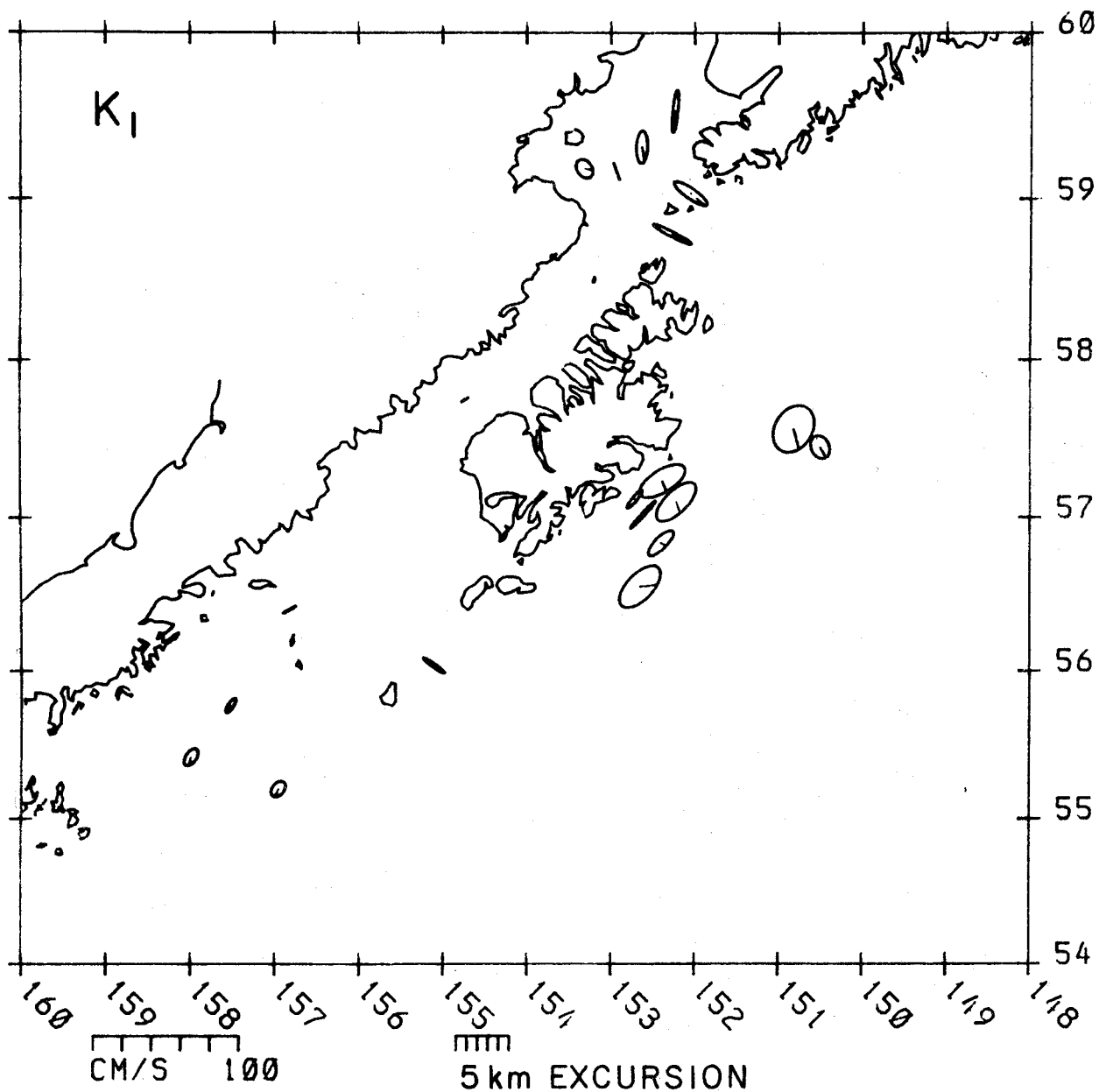


Figure 51. K_1 current ellipses for selected stations in the northwest Gulf of Alaska. Ellipses are centered at station locations; lines radiating from the centers indicate constituent current vectors when the K_1 Greenwich equilibrium phase angle is 0° .

at Middle Albatross Bank, which results in predominantly diurnal tidal currents ($F > 1.5$). Elsewhere the currents are mixed predominantly semidiurnal or regular semidiurnal ($F < .25$).

In assessing the environmental impact of pollutants, the tidal excursion is important in relation to the proximity of potential impact areas. The tidal excursion in kilometers, over one-half of a tidal period (the flood tide for instance), is:

$$H \int_0^{\pi} \cos \sigma t dt = H \frac{T}{\pi}$$

where H is the amplitude, σ is frequency and T is period. For the semidiurnal tide this is approximately $0.14H$ (H in cm sec^{-1} , and excursion in km). Thus the mean spring tide excursion, where $H = 1.05 (M_2 + S_2)$, is 20 km at C7 in eastern lower Cook Inlet, 15 km at C8 in Stevenson Entrance, 12 km at K11 southwest of Kodiak Island, and only 1.5 km at C10 in northern Shelikof Strait. At Middle Albatross Bank, where the currents are predominantly diurnal, the excursion is $.29H$, so during extreme lunar declination when $H = K_1 + O_1$, the excursion over one-half of a diurnal cycle at K7 is about 8 km.

3.4 Current Energy Partition With Frequency

In the following section, we present speed and horizontal kinetic energy (HKE) characteristics from current records collected during the bank-trough experiment (Tables 5 and 6), from North Albatross Bank (Table 7) and from the lower Cook Inlet/Shelikof Strait experiment (Table 6). Coastline and shelf-break orientation are used to define positive alongshelf and cross-shelf as 225°T and 315°T for all records from the bank-trough, north Albatross Bank (WGC series) and C10, 300°T and 030°T for C8B and C9B; and 090°T and 000°T for the lower Cook Inlet records (C3A and 3B and C4A and 4B). Velocities from 35-h filtered records were decomposed along these axes and are presented as speeds. Variance along an axis was used to determine standard deviation as well as subtidal kinetic energy. The 2.9-h filtered data were used to estimate kinetic energy in tidal frequency bands. We note that the latter estimates are averages over several bands, and as such include energy from sources other than tides. The specific tidal frequencies do not indicate seasonal trends, as noted also in Section 3.3. The following equations define our parameters:

$$\text{Kinetic energy of the mean } (\overline{KE}) = \frac{1}{2}(\bar{u})^2 + \frac{1}{2}(\bar{v})^2$$

where the bar represents mean axis speed;

$$\text{Kinetic energy of subtidal flow } (KE') = \frac{1}{2}\sigma_u \text{ or } \frac{1}{2}\sigma_v$$

where σ represent variance along each axis.

Moorings WGC2A to 2C represent conditions on North Albatross Bank (Table 7). These moorings were deployed at the shelf-break at a depth of approximately 190 m and the series WGC2D to 2F were deployed approximately 25 km shoreward in about 85 m of water. This shoreward shift in mooring location resulted in a substantial change in flow characteristics and the distribution of HKE. At the shelf-break, alongshelf \overline{KE} was dominant. At the shoaler location, flow retained some tendency to be alongshelf, however, the dominant energy was

TABLE 5

Current statistics in winter for the bank-trough region southeast of Kodiak Island, and mean alongshelf and cross-shelf wind stress for the current observation period. Mooring locations are indicated on Figure 9.

Mooring (meter depth)	Observed Speed (cm/s)		Horizontal Kinetic Energy Distribution (cm ² /s ²)					
	Alongshelf	Cross-shelf	Alongshelf			Cross-Shelf		
			Mean	Subtidal	Tidal	Mean	Subtidal	Tidal
BANK								
K6A (23m)	12.3±11.9	19.1±11.2	75.7	70.2	171.5	186.3	62.3	46.1
(65m)	10.6± 8.0	11.4± 6.4	56.2	32.0	88.5	64.8	20.7	17.4
K7A (28m)	-4.1± 8.4	10.7± 9.2	8.4	35.0	173.5	57.2	42.7	62.5
(70m)	-1.5± 4.6	8.0± 5.6	2.3	10.6	76.9	44.0	15.8	25.2
TROUGH								
K8A (25m)	24.3±12.9	-10.1± 7.2	295.3	82.7	35.5	51.0	26.4	20.8
(67m)	20.9±10.1	- 8.3± 6.3	218.4	50.8	31.2	34.5	20.1	9.9
(140m)*	10.1± 7.3	- 6.4± 5.5	51.0	26.4	18.3	20.5	15.2	5.1
K9A (25m)	4.6±10.4	- 0.6± 7.8	10.6	53.8	68.3	0.2	30.1	17.7
(148m)	0.8± 4.7	2.5± 6.2	0.3	11.0	21.4	3.1	18.5	15.1
K10A (25m)	-0.8± 9.4	8.2± 8.8	0.3	44.0	74.1	33.6	39.0	25.8
(144m)	-1.7± 4.1	5.4± 6.8	1.5	8.4	24.5	14.8	22.9	13.2
Wind Stress (dynes/cm ²)								
EB46008		0.76±1.9	0.61±2.0					

*All records 133 days except K8A (140m) which was 66 days. Observation period began in mid-October 1977.

TABLE 6

Current statistics in summer for the bank-trough region southeast of Kodiak Island, and mean alongshelf and cross-shelf wind stress for the current observation period. Mooring locations are indicated on Figure 9.

Mooring (meter depth)	Observed Speed (cm/s)		Horizontal Kinetic Energy Distribution (cm ² /s ²)					
	Alongshelf	Cross-shelf	Alongshelf		Cross-Shelf			
			Mean	Subtidal Tidal	Mean	Subtidal	Tidal	
BANK								
K6B (32m)	9.6±3.0	12.6±4.8	45.9	17.6	120.2	78.9	11.4	40.3
(72m)	6.6±3.4	5.2±2.6	21.6	1.9	63.1	13.3	3.4	18.5
K7B (29m)	-0.8±4.5	9.0±5.3	0.4	9.9	113.2	40.2	14.0	44.9
TROUGH								
K8B (30m)	17.6±7.1	-2.9±3.3	154.9	25.0	25.3	4.2	5.3	10.4
(75m)	10.8±4.5	-0.9±3.5	58.5	2.9	21.9	0.4	0.2	10.5
K9B (13m)	4.9±6.3	-0.8±8.1	11.9	19.7	81.4	0.3	32.4	43.5
(58m)	3.5±6.4	2.4±7.5	6.1	20.2	76.1	2.8	27.8	24.7
(142m)	1.5±2.4	3.7±3.1	1.1	2.8	8.8	6.9	4.8	15.8
K10B (24m)	2.1±4.6	4.3±4.9	2.2	10.4	47.9	9.1	12.1	16.2
(69m)	0.8±4.4	5.7±5.5	0.3	9.6	44.6	16.0	15.2	23.4
(149m)	-2.5±2.3	5.8±3.6	3.2	2.7	13.5	16.6	6.5	12.3
Wind Stress (dynes/cm ²)								
EB46008	-0.18±0.5	0.04±0.4						

*All records are longer than 125 days, and commenced in late May 1978.

TABLE 7

Selected winter and summer current statistics from the lower Cook Inlet region and from the banks southeast of Kodiak Island. Mooring locations are indicated on Figures 7 and 8.

Mooring (meter depth) Record Length(d):Start	Observed Speed (cm/s)		Distribution of HKE (cm ² /s ²)					
	Alongshelf	Cross-shelf	Mean	Subtidal	Tidal	Mean	Subtidal	Tidal
NORTH ALBATROSS BANK								
WGC-2A (100m) 66:75265	25.7± 6.5	-0.40±2.9	330.30	21.0	39.1	0.1	4.3	84.5
WGC-2C (24m) 90:76070	21.8±12.7	0.70±5.6	237.60	80.7	116.1	0.3	15.8	80.5
63:76070 (104m)	24.4± 7.9	4.30±3.6	297.70	21.9	31.7	9.4	6.4	74.1
WGC-2D (20m) 133:76160 (80m)	3.0± 4.6 0.9± 2.1	1.10±3.4 -0.90±1.7	4.60 0.30	10.4 2.1	244.9 90.9	0.6 0.3	5.7 1.4	378.5 136.0
WGC-2E (20m) 156:76293	2.2± 9.7	0.60±6.6	2.50	47.5	303.0	0.2	21.6	478.5
WGC-2F (20m) 167:77084 (80m)	4.7± 5.5 1.9± 2.8	-0.40±3.9 -2.00±2.1	10.90 1.90	15.0 3.8	265.5 103.0	0.1 2.0	7.6 2.2	401.0 149.9
LOWER COOK INLET AND SHELIKOF STRAIT								
C-10 (65m) 151:77278	23.8±17.3	1.90±8.4	283.20	149.4	19.6	1.8	35.3	5.2
C-10B (70) 133:78148	11.9±11.0	-0.70±8.1	70.80	60.3	12.1	0.3	8.1	3.8
C-9B (66m) 133:78150	9.6±10.8	-0.40±4.9	46.10	58.9	1600.1	0.1	11.9	69.9
C-8B (63m) 133:78150	20.4±18.2	-4.70±8.2	208.10	165.8	1953.0	11.1	33.7	100.5
C-4 (65m) 150:77280	-1.3± 6.5	-0.70±6.3	0.90	21.2	40.9	0.3	19.8	373.4
C-4B (64m) 133:78150	0.5± 6.7	-1.20±5.4	0.02	16.3	32.8	0.8	16.1	348.0
C-3 (50m) 159:77280	-1.3± 4.2	-0.90±2.9	0.90	8.9	58.5	0.4	4.1	420.0
C-3B (50m) 93:78148	0.6± 4.1	-0.06±2.8	0.20	8.2	43.1	0.0	3.9	334.0

tidal. The alongshelf speeds were consistent during the observation periods of WGC2D and 2F, whereas during winter 1976-77, alongshelf flow was weaker and more variable. Over the bank, subtidal kinetic energy indicated a threefold variation between winter (WGC2E) and nonwinter records. We attribute this to increased meteorological forcing in winter.

Records from C8, 9, and 10 are representative of the Kenai Current (Table 7). Records from C10 and C10B indicate that during October 1977 to March 1978 (C10) both \overline{KE} and KE' were substantially greater than during May to October 1978. This is consistent with our present understanding of coastal flow in the northwest Gulf of Alaska (Schumacher and Reed, 1980). A peak in baroclinic transport (and speed) occurred sometime in October-November; during this period, 7-day average flow down the axis of Shelikof Strait was observed to be as high as $\sim 70 \text{ cm sec}^{-1}$. In December 1977 through February 1978, observed mean wind stress was $\sim 1.2 \text{ dyne cm}^{-2}$ in an along-shore direction. The resulting set-up and barotropic transport (and speed) resulted in 7-day average axial speeds in Shelikof Strait of 20 to 50 cm sec^{-1} . Winds from June-September 1978 did not contribute appreciably to transport, and the baroclinic field suggested transports 0.1 to 0.3 of those observed during peak freshwater addition in fall. Records from the entrances to Shelikof Strait (C8B and C9B) indicate that tidal frequencies dominated HKE. However, at lower frequencies and in a mean sense, there was a significant difference between the two entrances. \overline{KE} was four times greater in Kennedy Entrance than in Stevenson Entrance. As suggested by Schumacher and Reed (1980), current records and hydrographic data indicate that the Kenai Current preferentially flows through Kennedy Entrance.

Within lower Cook Inlet proper (C3 and C4 series, Table 7), net flow was not significant in the total energy balance and tides dominated HKE

estimates. We note that subtidal frequencies at both of these locations indicate a less dramatic change from winter (October 1977-March 1978) to summer (May to October 1978) than was observed over the banks. Estimated energy due to subtidal frequencies increased by 25 to 30% in lower Cook Inlet and three- to four-fold over the banks. Orographic effects on the wind field over Lower Cook Inlet appear to diminish seasonal trends, whereas over the banks a strong seasonal change was observed.

The most striking feature of the velocity field is that seasonal differences are small in mean speed components and, in several cases, statistically insignificant. HKE in all three frequency bands is greater in winter, a combination of a more energetic regime or perhaps rotor wave-induced noise. Various authors (e.g., Mayer *et al.*, 1979; Halpern and Pillsbury, 1976) have concluded that rotor pumping can significantly affect speeds recorded by Aanderaa current meters. In order to determine whether the western Gulf current meter data set might be significantly contaminated by such wave-induced noise, successive 29-day harmonic tide analyses were performed for data from the summer (June, July, August) and winter (December, January, February). The following table shows the mean M_2 and standard deviations for those stations which had both summer and winter data at the 20-m depth.

TABLE 8

	C4	C10	WGC2	KG	K7	K8	K10	K.11
Winter Mean	35.2	4.7	30.5	7.4	6.8	2.7	3.8	45.8
S.D.**	.6	.6	.9	.7	.7	.7	.3	.6
Summer Mean	33.3	5.9	29.5	7.4	7.4	2.7	2.4	49.1*
S.D.**	2.8	1.2	2.4	.5	.4	.7	1.0	.8
Winter-Summer	1.9	-1.2	1.0	0	-.6	0	1.4	-3.3

*June-mid July only available

**S.D. = standard deviation.

mean M_2 speeds were computed by

$$A_1 = \frac{U_i^2 + V_i^2}{2}^{\frac{1}{2}}$$

where U_i is the major axis M_2 amplitude and V_i is the minor axis amplitude for time period i . Five successive analyses were done for each season, with a 14-day overlap between segments. The A_i 's were then averaged to produce the seasonal averages shown in the table.

If it is presumed that wave energy is much greater during the winter (and the windstress values shown in Tables 3 and 4 indicate that it is), then these results suggest that wave-induced noise does not significantly affect the speeds recorded from these data sets, at least on a seasonal average. The difference between these results and those of previous studies probably results from the fact that the subsurface float in our studies was deep enough (usually greater than 20 m) to prevent significant contamination by wave noise.

Over Middle Albatross Bank, HKE was greater near-shore (K6) than over mid-bank (K7), and cross-shelf mean HKE dominated in both seasons (Tables 5-6). Over Kiliuda Trough, a similar pattern occurred; however, the along-shelf mean HKE was dominant. Seaward of K8, current records suggest a dramatic change in velocity-field characteristics. Both tidal and sub-tidal HKE were larger than mean HKE.

3.5 Wind Observations

Winds over the ocean can be computed from surface pressure maps in conjunction with a boundary layer model. In general, surface winds are weaker than and aligned to the left of the computed geostrophic wind. Researchers have applied this technique with various degrees of sophistication and success. Agreement between computed winds and measured winds from data buoys are generally good except near the coastline, where a variety of additional physical processes become significant. For example, air flow in Lower Cook Inlet is predominantly down-gradient, that is, at right angles to the left of the geostrophic wind.

In the region of Albatross Bank, east of Kodiak, we found measurements from a data buoy approximately 60 km offshore agreed with calculations. We conclude that coastal influence on winds is not seen that far offshore. Lower Cook Inlet winds were completely dominated by the surrounding mountains.

3.5.1 Orographic Control

We have examined data from buoys located off the northeast Gulf of Alaska coast (EB33, EB45, EB72), Kodiak Island (EB46008, formerly EB49), and lower Cook Inlet (EB46007, formerly EB39), and found that within 50-100 km from shore the winds begin to align with the coastal mountains. The size of the mountain range affects this distance. Within about 25 km of the coast, smaller scale features, such as drainage winds, are felt.

The east coast of Kodiak Island is dominated by mountainous estuaries. Wind measurements from Kodiak and Kiliuda Bay confirm the presence of strongly bimodal winds aligned with the estuary axes. In the winter, these winds are predominantly offshore. However, NDBO buoy EB46008, located 60 km offshore, showed little coastal effect; its measurements agreed quite well with surface winds which were computed by the Fleet Numerical Weather Central

facility. As the mountains of Kodiak are not particularly high, we expect their offshore effect to be correspondingly reduced; however, without other measurements we cannot determine the extent of reduction.

The wind field over lower Cook Inlet, on the other hand, is completely dominated by mountains. We have made a concentrated study of this region to better understand the processes active in such orographically controlled estuaries.

3.5.2 Lower Cook Inlet Meteorology

The mountainous borders of lower Cook Inlet form natural channels for the flow of air (Fig. 52). The major orographic axis extends from the Susitna Valley in upper Cook Inlet southward and into Shelikof Strait, and is oriented at about 30° T. This channel is bounded on the east by the Talkeetna and Kenai mountains and lesser ranges on Kodiak and Afognak islands. It is bounded on the west by the Alaska and Aleutian ranges. The only breaks in this mountainous barrier to air flow occur at Kennedy and Stephenson Entrances and at the Kamishak Gap, a region of relatively low elevation about 50 km wide between Lake Iliamna and Kamishak Bay.

Orographic Channelling. The prevalence of orographic channelling of winds in lower Cook Inlet is clearly seen in wind fabric diagrams (Davis and Ekern, 1977) constructed using data from environmental buoy EB-46007 (cf. Fig. 52 for buoy location). These diagrams are contoured plots indicating the relative concentrations of observations of wind speed and the direction from which the wind blows during a given month. The observations are 8-min means acquired once every 3 hours. Fabric diagrams for four representative months in 1978 are shown in Fig. 53. Lines have been drawn on the diagrams to indicate the directions of the four major orographic axes as seen from the

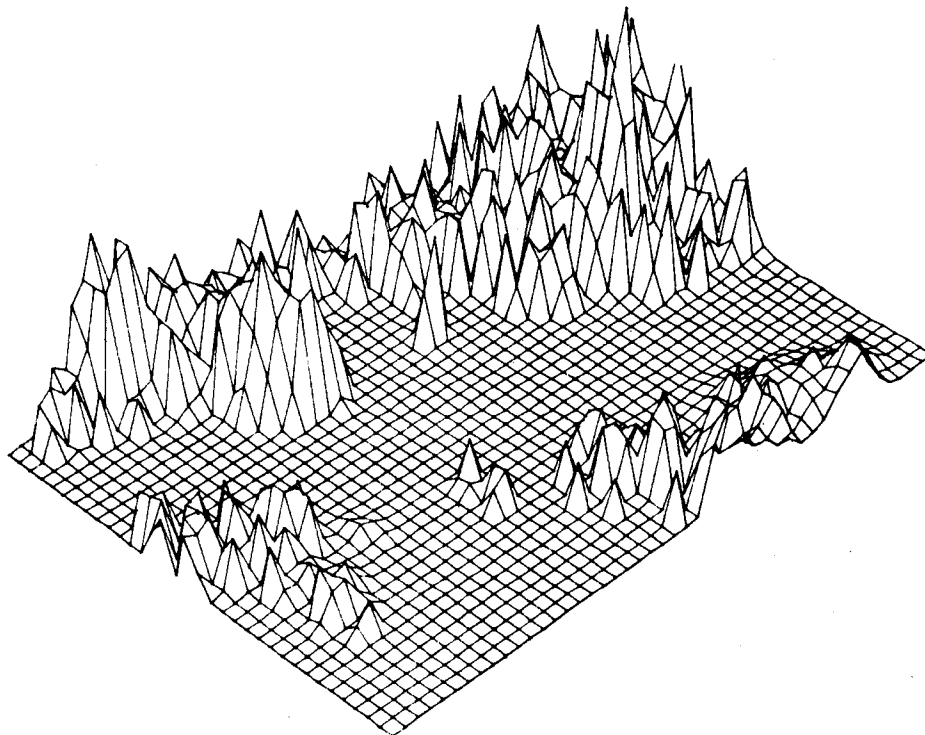
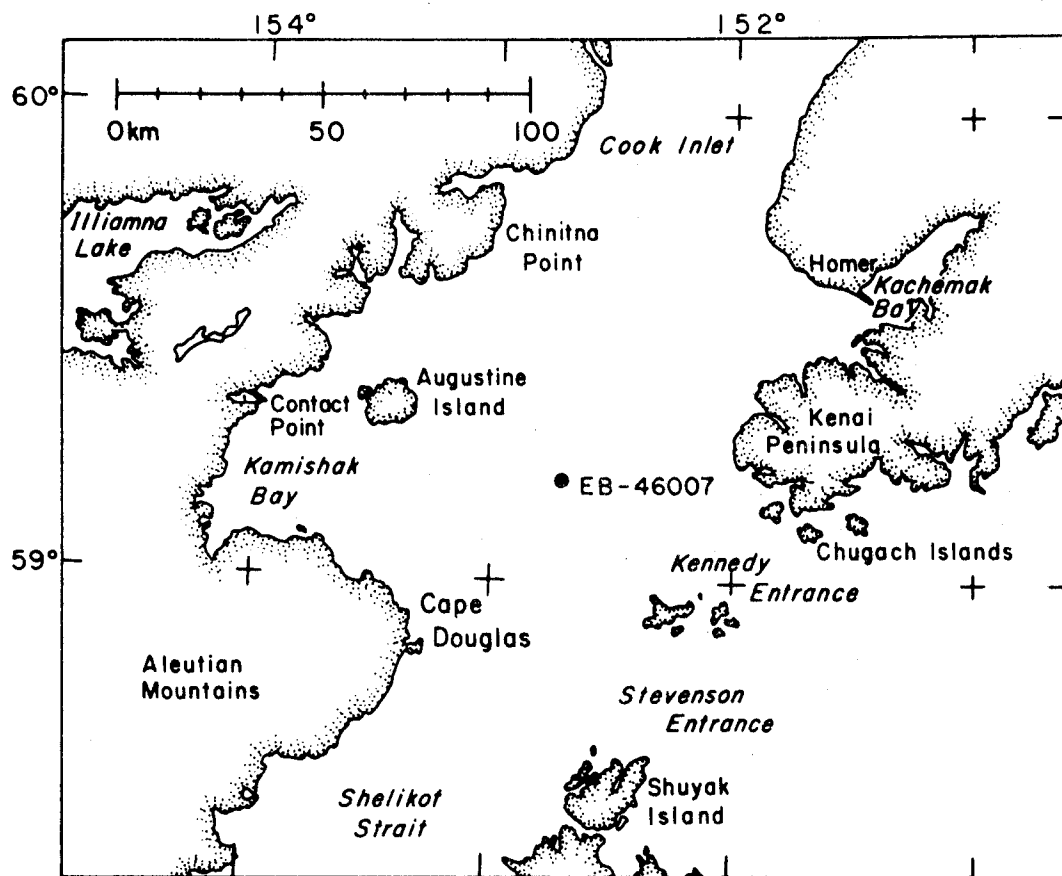


Figure 52. Geographical locations in the lower Cook Inlet region and (lower) a relief map of the same area. The black dot indicates the location of environmental buoy EB-46007.

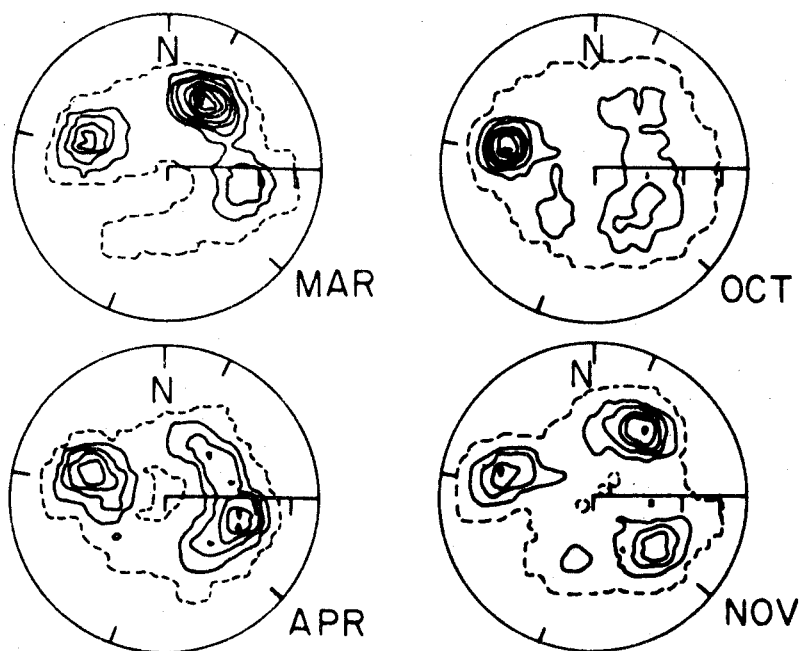


Figure 53. Wind fabric diagrams for EB-46007 in lower Cook Inlet for four months in 1978. The four tic marks on each circle represent the directions of the four channel axes: upper Cook Inlet; Kennedy and Stevenson entrances; Shelikof Strait; and the Kamishak Gap.

buoy. The contours are in intervals of 2% of the observations per percent of the plot area. In March winds were persistently from upper Cook Inlet and closely aligned with the Inlet axis. In April winds blew in both directions through the Kamishak Gap-Kennedy Entrance channel and to a lesser extent from Kachemak Bay and the upper Cook Inlet. In October, winds were almost exclusively from the Kamishak Gap; in November winds originated from all four of the intersecting channels. Little wind was observed from the northwest or southwest, due to the blocking action of the Alaskan and Aleutian ranges.

Though the 4 months that are shown exhibit orographic channeling particularly well, all data obtained show this channeling effect. Given the four major intersecting channels, it is possible to define a minimum of 16 possible flow patterns. Of these, the two which appear most likely to occur are those resulting from the synoptic scale pressure distribution and from interior drainage winds, especially from the Susitna Valley which enters upper Cook Inlet.

Pressure Gradient Forcing. The Geostrophic wind is given by

$$u_g = - \frac{1}{\rho f} \frac{\partial p}{\partial y}$$

$$v_g = \frac{1}{\rho f} \frac{\partial p}{\partial x}$$

where u_g and v_g are the east-west and north-south components of the geostrophic wind, ρ is the air density, f is the Coriolis parameter, and $\frac{\partial p}{\partial x}$ and $\frac{\partial p}{\partial y}$ are the east-west and north-south pressure gradients.

At least three stations are needed to establish the two-dimensional pressure gradient. If more stations are available a plane may be fitted to

the observations using multiple regression techniques. The equation

$$p = ax + by + c$$

is fit where x and y are the positions of each station. The pressure gradients are then

$$\frac{\partial p}{\partial x} = a \quad \text{and} \quad \frac{\partial p}{\partial y} = b$$

If curvature in the pressure field is judged significant, higher order equations may be used. The second order equation is

$$p = a_0 + a_1x + a_2y + a_3x^2 + a_4y^2 + a_5xy,$$

for which a minimum of six stations are required. However, for most applications many more than six stations are needed to adequately define the second order pressure field.

In this study we have used a first-order fit with only three stations: Anchorage, Kodiak, and King Salmon. We would have liked to have used Iliamna, but it reports irregularly and, in addition, a 2-mb bias was found in pressure readings reported for March-June 1978. It was felt that the three chosen stations were spaced around the lower Cook Inlet (Fig. 12) to give a reliable and representative network for determining the regional pressure gradient. There are undoubtedly small-scale gradients that are unresolved by such a widely spaced network. These three stations will also be inadequate when the pressure field is highly curved, for we are assuming that it is well represented by a plane.

The geostrophic wind was determined for 7 months in 1978 and 1979. The hourly pressure readings were filtered with a 3-h triangular filter and sampled every 3 hours. These pressures were then fit with a plane to determine the pressure gradients.

In Figure 54 the direction of the geostrophic wind is plotted against that of EB-46007 for the spring (March through June) and for the winter (November through January). Only points for which the geostrophic wind is

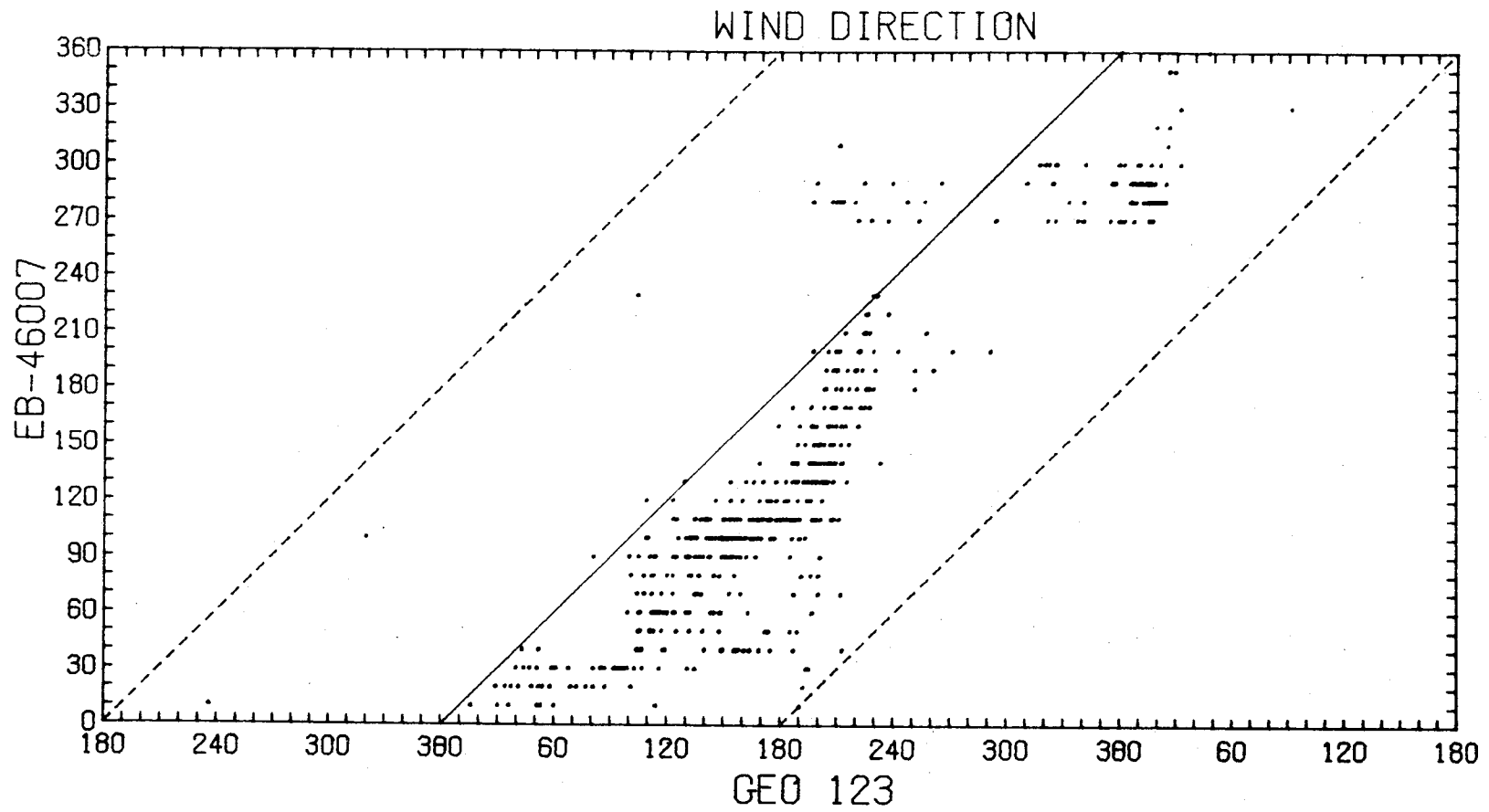


Figure 54. Wind direction at environmental buoy EB-46007 in lower Cook Inlet compared to direction of the geostrophic wind for cases where the geostrophic wind speed was greater than 5 m sec^{-1} .

greater than 5 m sec^{-1} are plotted. The solid line indicates winds which are from the same direction (i.e., the buoy winds are parallel to the isobars); points to the right of the line indicate a component of buoy winds down the pressure gradient, while those to the left indicate a countergradient component.

These figures show clearly the ambiguity often seen in the relation between geostrophic and surface winds in orographically dominated sites; a wide range of surface winds is observed for a given geostrophic wind. For example, with the geostrophic wind from 180° the observed buoy wind can come from virtually any direction. The apparent countergradient flow out of Kamishak Gap may be the result of poor estimation of the local pressure gradient from the three widely spaced stations. Alternately, the pressure field in the Bering Sea could drive air through the Iliamna Gap into lower Cook Inlet and against the pressure gradient there. We have not found that the regional pressure gradient is a good predictor of the local winds. It should be noted, however, that in virtually all cases when the geostrophic wind direction was from $270^\circ-0^\circ$ in the March-June period or from $240^\circ-40^\circ$ in the November-December period, westerlies from the Iliamna Gap occurred.

Drainage Winds. Given the presence of adjacent continental land masses whose interior regions are occupied during winter by cold dense air masses, we suspect that drainage or katabatic winds might play an important role in the local wind field in lower Cook Inlet. The magnitude of such winds is dependent upon the cold air reservoir, the external large-scale pressure field and local topographic focussing. These flows are generally colder than the surrounding air and therefore flow beneath the ambient air overlying the water. The distance offshore to which the flow persists depends

upon the water-air heat flux and upon the stability of the overlying air. By far the major winter wind feature in lower Cook Inlet is the drainage wind from the Susitna Valley (Fig. 53), which is supplied by a dominant inland high pressure region to the north.

On a smaller scale, drainage winds appear off virtually every glacier and river valley which enters lower Cook Inlet. An example of such a flow was observed in the vicinity of Cape Douglas (Fig. 55), with the wind originating from 2100-m Mt. Douglas and funneling out of a small valley. Width of both the valley mouth and the flow offshore was about 2 km. Vertical potential temperature profiles obtained within this flow and from nearby undisturbed air over northern Shelikof Strait showed similar structure above about 300 m (Fig. 56). The profile off Cape Douglas exhibited, however, a stable layer which was eroded by sea-air heat flux from the surface to a height of 200 m during its passage from the coastline to a point about 10 km offshore. Environmental buoy EB-46007, located about 40 km off this valley, did not reflect the presence of this flow. In general, the buoy data suggest that katabatic flow seldom, if ever, attains the central part of lower Cook Inlet.

Kachemak Bay, across the lower inlet from Cape Douglas, often exhibits drainage winds because several glaciers terminate at its head. At times, these drainage winds resulted in strong ENE winds at Homer, while winds observed at EB-46007 in the lower inlet were westerly. Shipboard observations suggest that the drainage winds in Kachemak Bay are confined to the southern portion of the bay mouth and seldom persist beyond about 20 km from the bay mouth.

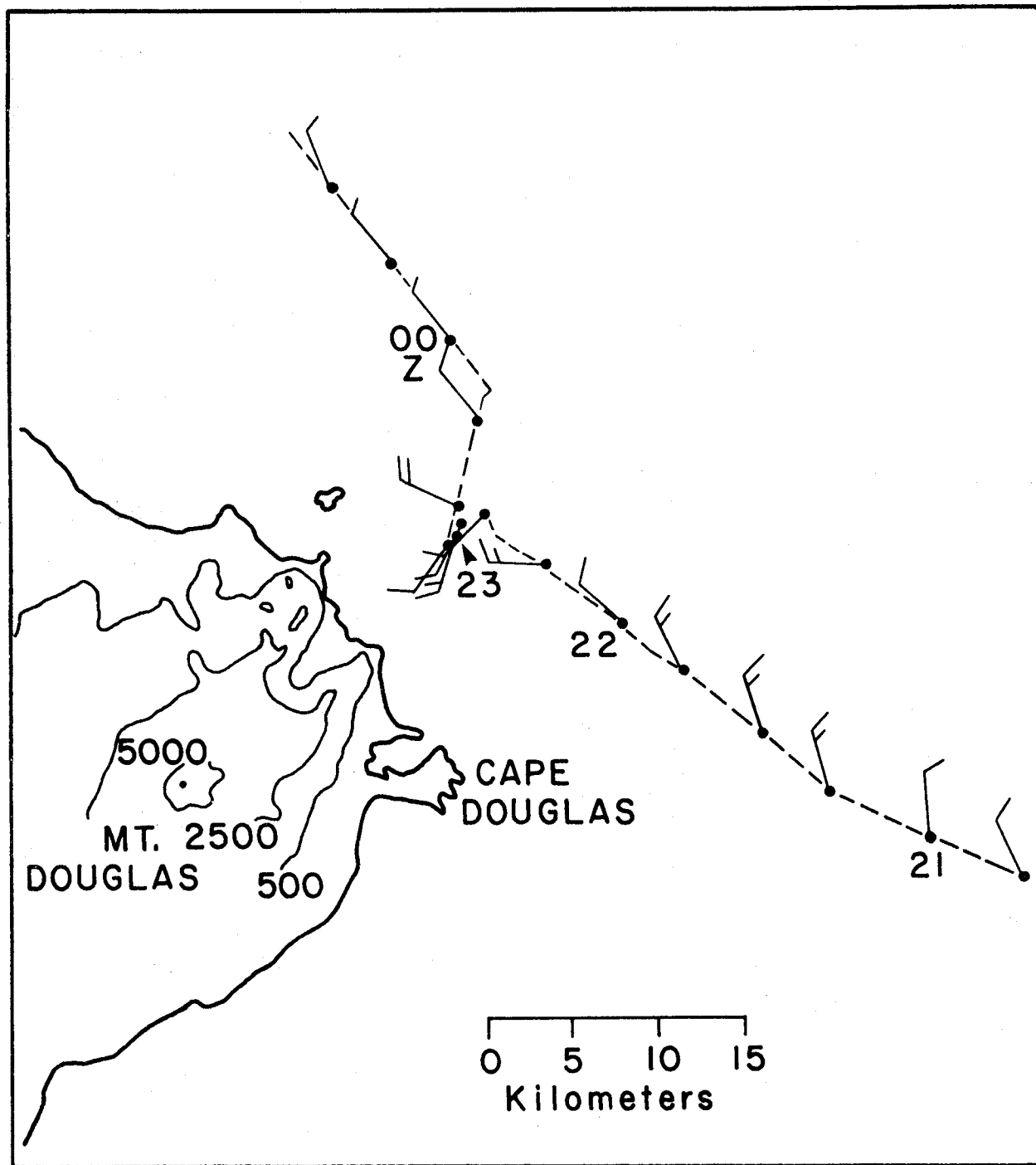


Figure 55. Observations of surface wind velocity in the vicinity of Cape Douglas, lower Cook Inlet, on 17-18 March 1978. Katabatic flow extended offshore from a mountain valley. Elevation contours are in feet above mean sea level.

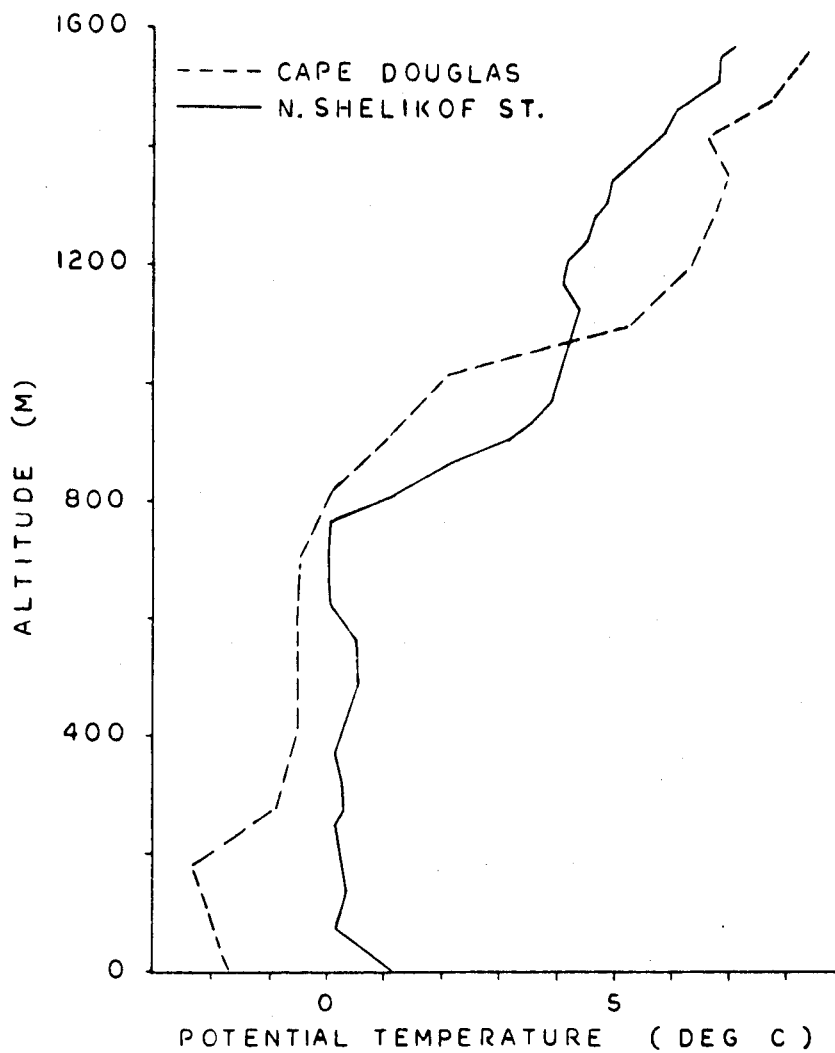


Figure 56. Comparison of vertical potential temperature profiles from airsonde ascents near Cape Douglas and over northeastern Shelikof Strait. A remnant katabatic layer was evident below about 300 m in the sounding from Cape Douglas.

Wake Effects. Given the large vertical relief of land masses surrounding lower Cook Inlet, we would a priori expect to see localized effects of certain of these masses on the air flow. An exceptional example is provided by Augustine Island, which presents a 1300-m high cone-shaped obstacle to local air flow at the eastern edge of Kamishak Bay (Fig. 52). Theoretical and laboratory studies of flow past a cylinder (Hinze, 1959; Batchelor, 1967) have shown that the imposed pressure and velocity distributions generate vortical flow in the lee of the cylinder. Flow on the lee side of an isolated mountain would be expected to show similar characteristics. This supposition was borne out by Scorer (1967), who found that wake effects were present and that the arc sector defining the wake within which lee waves are apparent may vary from 10° - 70° . Amplitude of the lee wave disturbances decreases rapidly with increasing height and with distance downstream from the obstacle.

During a period of NNW winds in the lower Inlet, the free stream wind had speeds from 3 to 8 m sec⁻¹ and directions from 320-020°T. Assuming a disturbed downstream arc sector of 70° and considering the directional range of the free stream winds, all observed winds to 03 GMT depicted on Figure 57 could be categorized as wake flow. No such confused flow was encountered prior to a station occupation at about 02 GMT some 4 km offshore. Here, in an hour's time and within an area of 2 km², wind direction was observed to vary over nearly 360° , suggesting the presence of vortical flow induced by the mountain.

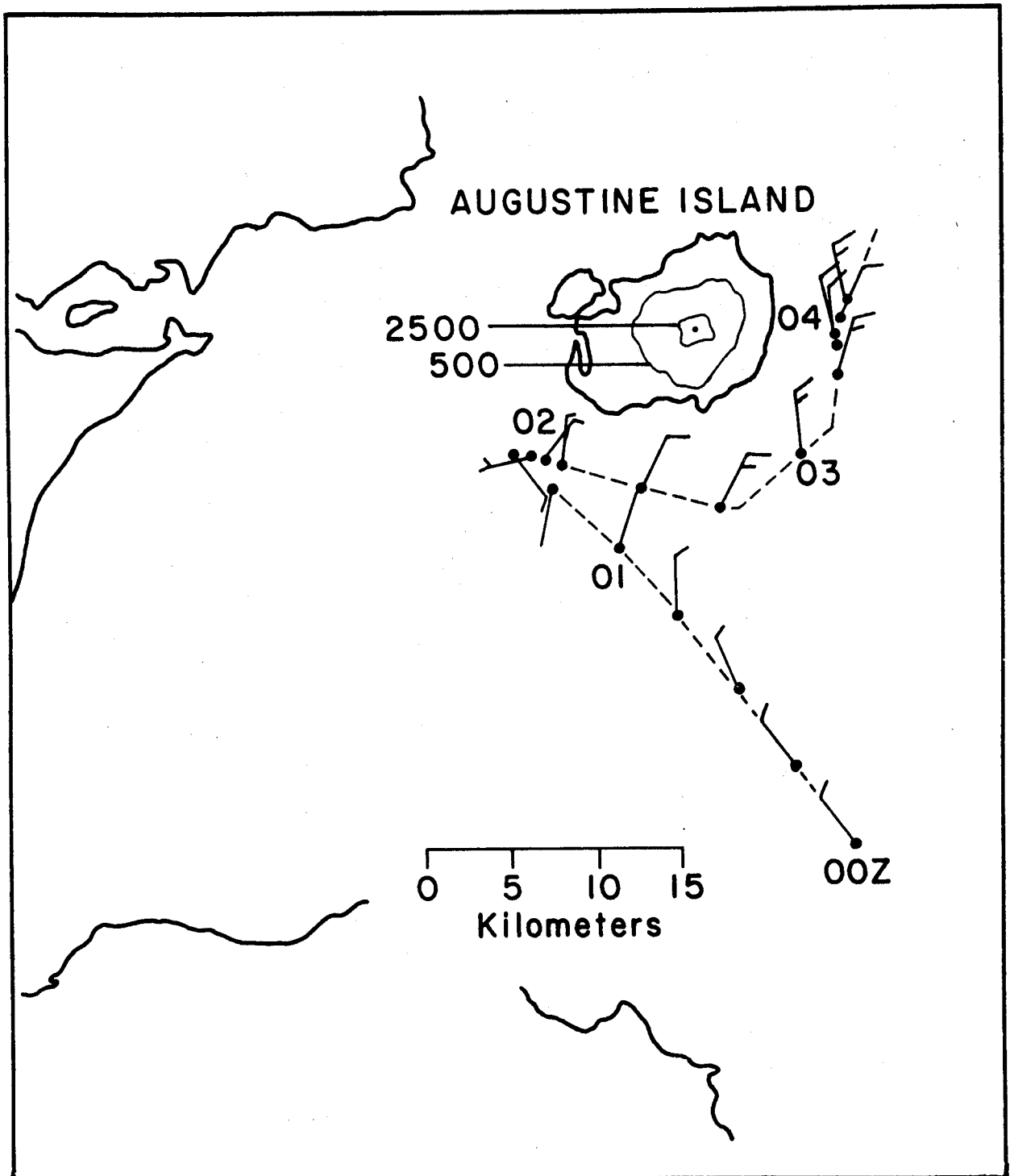


Figure 57. Observations of surface wind velocity in the vicinity of Augustine Island on 18 March 1978. Variable winds at about 02 Z suggest that vortical flow was present in the lee of Mt. Augustine. A quarter flag on the vector shaft designates wind speed below 1.5 m sec^{-1} .

Summary and Conclusion. Winds in lower Cook Inlet are orographically funneled through two perpendicularly oriented channels defined by upper Cook Inlet-Shelikof Strait and Kamishak Bay-Stevenson Entrance. Specific flow patterns appear in most cases to be triggered by the larger scale pressure gradient, though the relationship between geostrophic winds and observed winds is weak and poorly understood at present. Within 20 km of shore, drainage winds emanate from glacier and river valleys. These winds are nearly continuously occurring, but are quickly eroded over water by the sea-air heat exchange. On a yet smaller scale, vortical circulation has been observed in the lee of Augustine Island, a major, centrally located topographic feature in the lower Inlet.

In an effort to provide a more realistic wind input to oil spill trajectory models, we drew surface wind patterns for the lower Cook Inlet based on the weather types of Putnins (1966). Putnins determined 22 different generalized weather classifications for Alaska based on 18 yr of daily synoptic weather charts. For each type he reproduced a representative surface weather chart. For each weather chart, we drew a sketch of what our interpretation of the wind patterns in the lower Cook Inlet would be. This interpretation was based on the data we have analyzed and on our experience in the area. It was, of necessity, tentative and subjective.

The twenty-two wind patterns could be reduced reasonably to five. These five patterns, labeled I through V, are found in Figures 58-62. The wind speeds are indicated in m sec^{-1} . The major guiding principle in the formulation of these patterns is that the wind is predominantly channeled by the orography of the region. We have good evidence that this is true from EB-46007. We have also noted examples where this was not apparently the case, in which the winds seem to be passing across the Kenai Mountains.

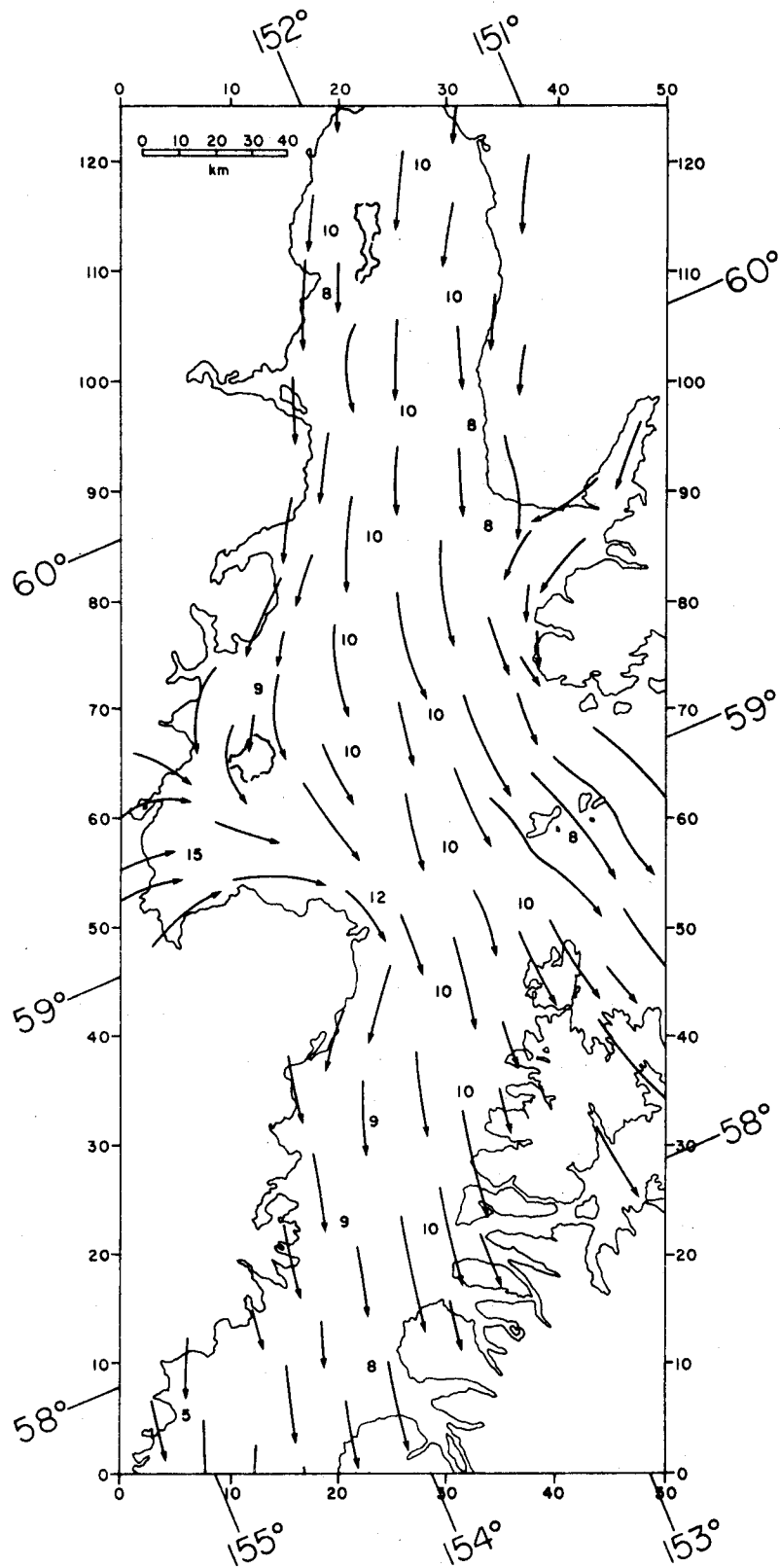


Figure 58. Map I of Putnins' wind type for lower Cook Inlet.

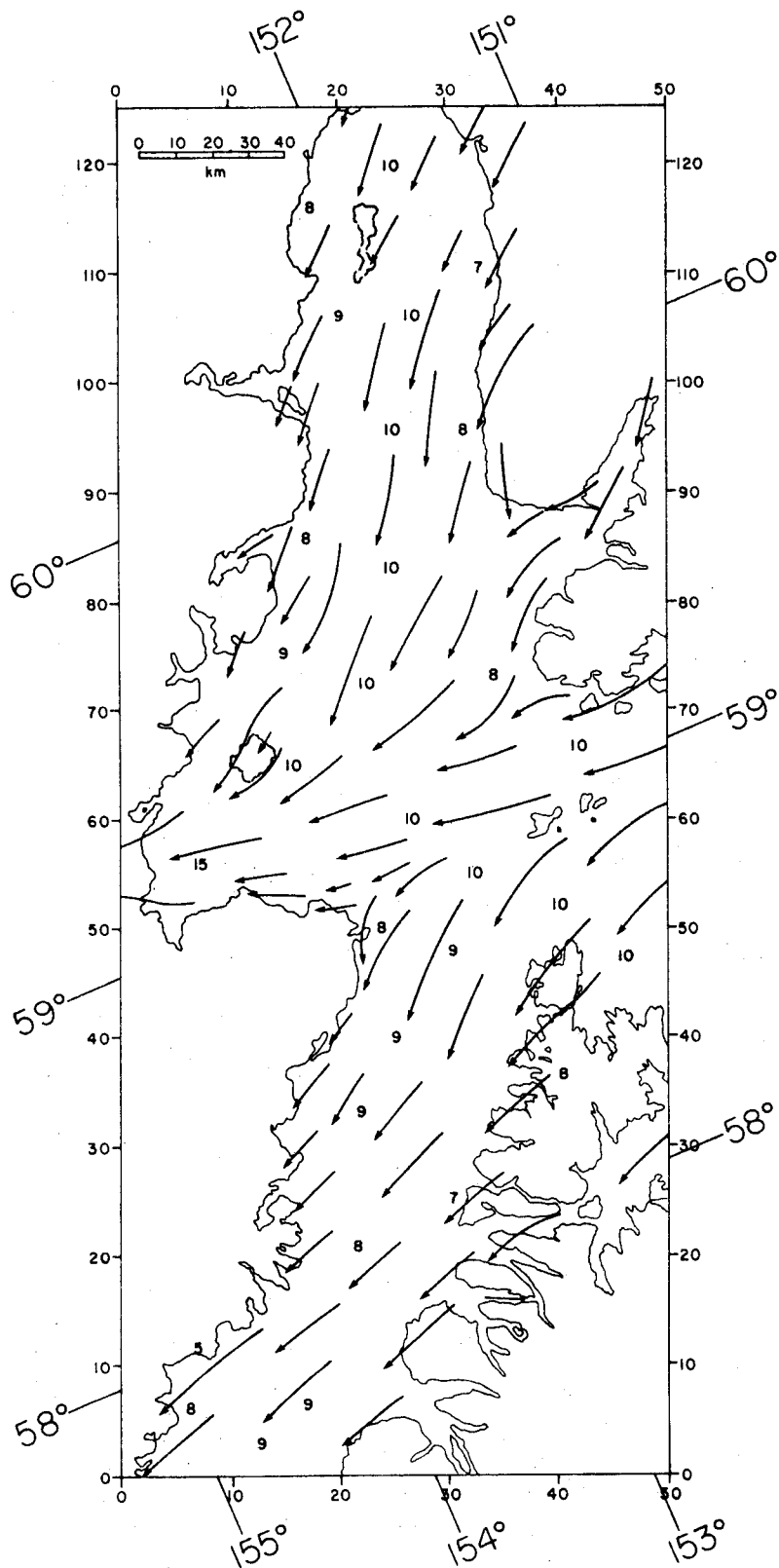


Figure 59. Map II of Putnins' wind type for lower Cook Inlet.

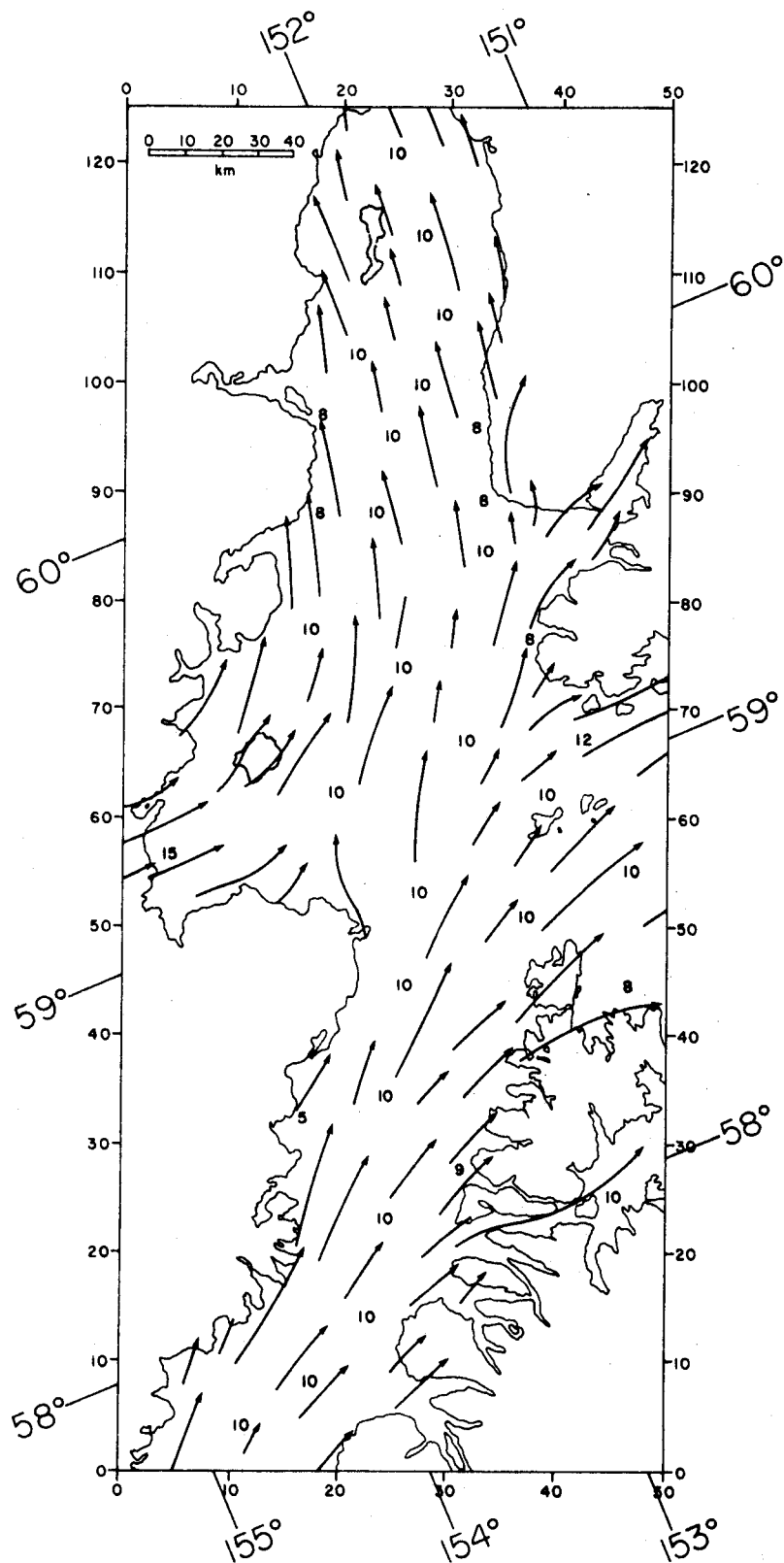


Figure 60. Map III of Putnins' wind type for lower Cook Inlet.

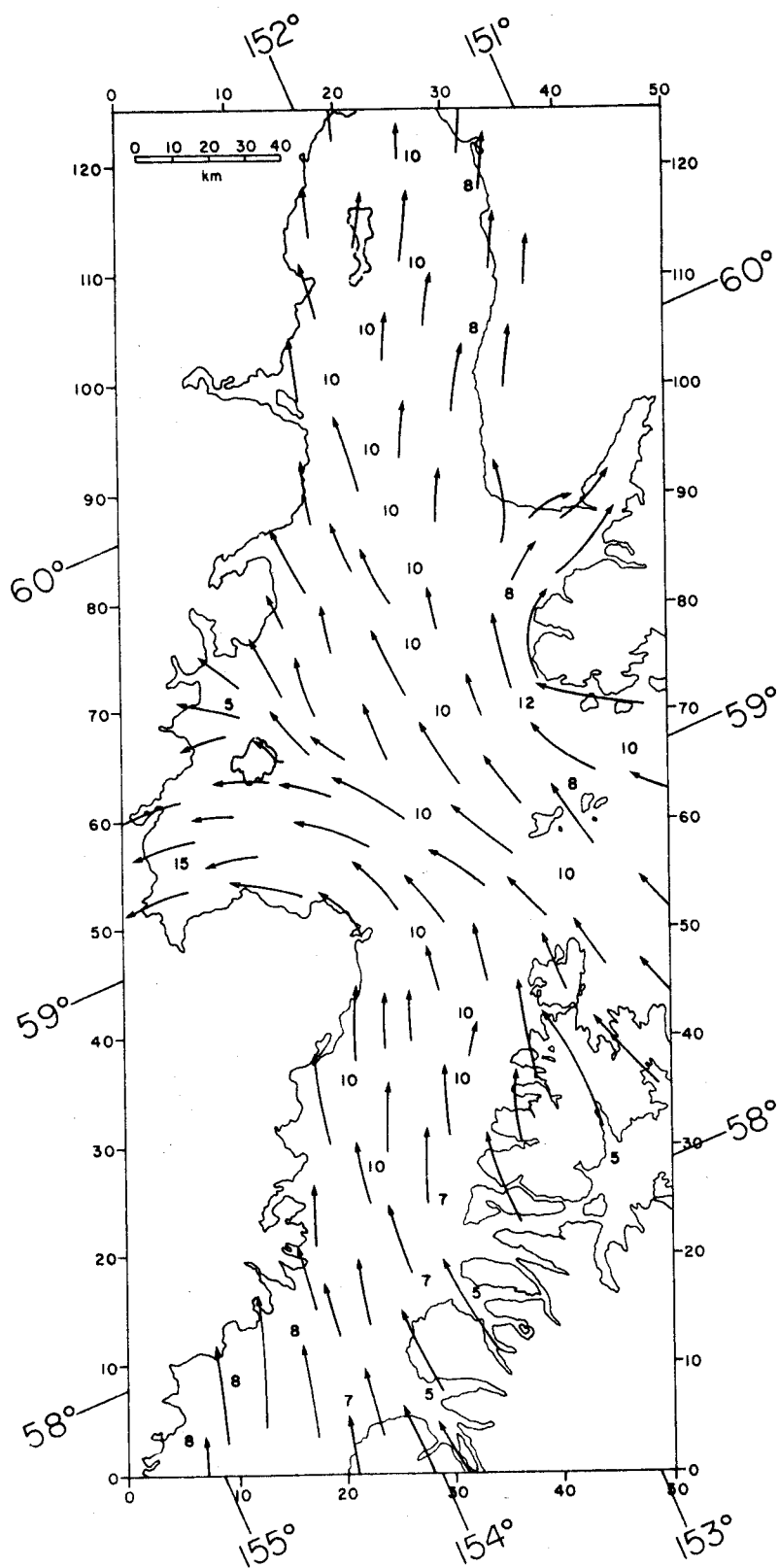


Figure 61. Map IV of Putnins' wind type for lower Cook Inlet.

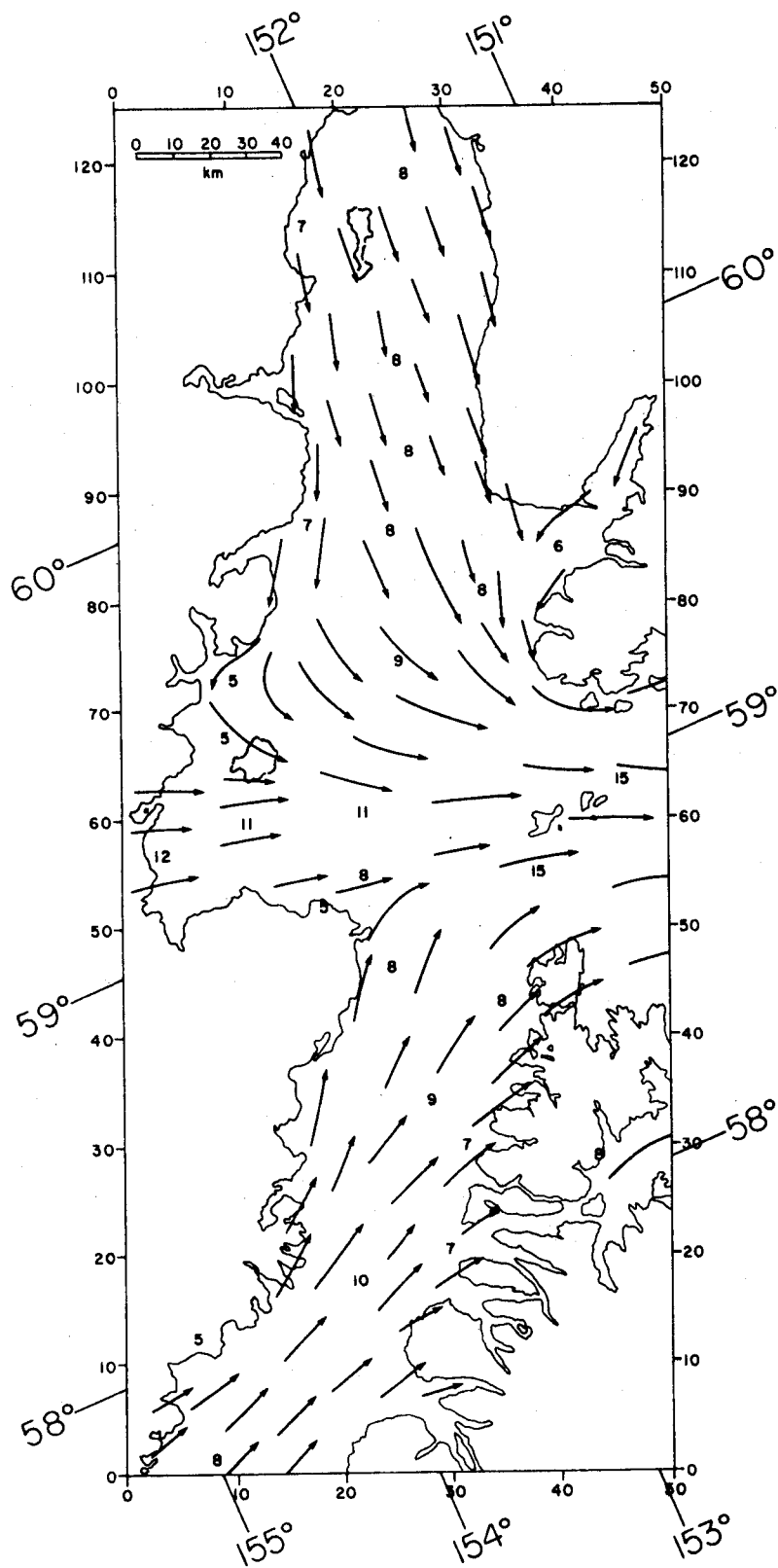


Figure 62. Map V of Putnins' wind type for lower Cook Inlet.

There are undoubtedly many situations which would not be well approximated by one of the five patterns, but nevertheless we feel these patterns show the dominant winds.

Each of Putnins' types is assigned a wind pattern map and a scaling factor for the wind speeds in Table 9. In Table 10 the Putnins types associated with each map are listed with their annual percentage occurrence and the total annual percentage occurrence for each map.

An approximate transition matrix was compiled from Putnins' report. He lists the number of times each classification was followed by each of the other classifications on a month-by-month basis for the 18 yr of records. For example, in January type D (101 occurrences) was repeated 73 times, when followed by type E₁ 6 times, by type E 5 times, and by type H 4 times. The compilation was somewhat incomplete in that Putnins ignored sequences that occurred rarely. We summed these monthly figures to give the total number of occurrences of each sequence for the whole 18 yr of record. This matrix was then normalized to give the percent probability of each type following each other type (Table 11).

The above scheme provided a transition matrix based on a long historical record. The study by Putnins was the only one available. There are, however, a number of weaknesses to this approach, especially when applied to the lower Cook Inlet region alone. First, each of Putnins' classifications includes a broad range of different weather situations that may produce quite different local winds. The synoptic map reproduced by Putnins for each type is nothing more than a representative sample, and it cannot be presumed that all situations of the same type will produce similar winds in lower Cook Inlet even though that is our working assumption. It is a bit disheartening to note that the most common type, A', has the least well defined pressure gradients

TABLE 9

Assignment of Putnins' wind types according to patterns
(cf. Fig. 58-62), and scaling factors for wind speeds

<u>Type</u>	<u>Map</u>	<u>Scaling Factor</u>
A	II	1.5
A	II	1.5
A ^c	V	1.0
A''	III	1.0
A'''	IV	1.0
A ₁	I	1.5
A ₂	IV	1.0
A ₃	III	0.3
B	I	1.0
C	II	0.5
D	II	1.0
D'	I	1.5
D ₁	II	1.0
E	IV	0.5
E'	IV	0.5
E''	II	0.5
E ₁	V	0.5
E' ₁	IV	0.5
F	III	1.2
F ₁	II	1.0
G	V	1.0
H	I	1.0

TABLE 10

Putnins' wind types associated with each map (Fig. 58-62), annual percentage occurrence of each type, and total annual percentage occurrence for each map

<u>Map</u>	<u>Types and % Annual Occurrence</u>							<u>Total %</u>
I	A ₁ 6.7	B 1.0	D' 1.2	H 7.1				16.0
II	A 7.5	A ₃ 3.7	C 1.3	D 6.3	D ₁ 3.6	E'' 0.8	F ₁ 0.7	23.9
III	A'' 5.2	A ₃ 1.1	F 1.1					7.4
IV	A''' 1.6	A ₂ 5.9	E 6.3	E' 8.2	E' ₁ 5.3			27.3
V	A' 23.2	G 1.0	E ₁ 1.0					25.2

TABLE 11

Normalized matrix showing the percent probability of each of the Putnins' wind types following each other type.

	A	A'	A''	A'''	A ₁	A ₂	A ₃	A _c	B	C	D	D'	D ₁	E	E'	E''	E ₁	E' ₁	F	F ₁	G	H		
A	51.7	36.0	4.1		1.1			1.9					1.4	0.5	1.1			2.2						
A'	3.8	68.2	6.0	0.4	7.4	4.5	0.5	1.0						0.7	1.5			1.2					4.8	
A''			13.0	39.1		15.3				10.8		4.3	6.6	10.9										
A'''			13.0	39.2		15.2				10.9		4.3		6.5	10.9									
A ₁		15.5			50.3	0.7			0.7	5.5	6.9		1.4		3.8			0.7		1.4			13.1	
A ₂	4.2	21.8	1.9		1.9	49.8		1.2			1.2			1.9	13.8			0.8					1.5	
A ₃		14.3				20.0	65.7																	
A _c	3.5	34.5			6.5	1.7		50.4														1.7	1.7	
B		25.0	35.0						20.0						20.0									
C		22.5		6.5	10.0	6.4			6.4	35.4				6.4										
D							0.6				71.4		1.9	8.2	8.2			5.0		1.6			3.1	
D'			5.7		5.7	5.7					11.4	48.6	8.6	8.6	5.7									
D ₁	11.4	3.6			1.8								59.6		2.5			1.8					19.3	
E	10.0	13.7	4.7	2.3		2.0								40.5	17.4			9.4						
E'	1.7	4.1	1.2		0.5	7.0					6.0		1.2	19.2	54.0	0.5		4.6						
E''																50.0		25.0					25.0	
E ₁		42.9															57.1							
E' ₁	18.2	24.0				1.8		3.1					1.3	7.6	5.8			38.2						
F					26.7	13.4							13.4						46.5					
F ₁	50.0																		50.0					
G					100.0																			
H	1.7	16.1			5.8	1.6		5.0					9.8		1.7			3.6					54.7	

in the lower Cook Inlet area and is most subject to allowing small changes in the positions of low pressure centers to produce large local wind changes. Furthermore, we have only a limited basis for assigning local wind conditions based on a specific baric situation. Finally, and of the least consequence, the transition matrix determined from Putnins' compilation of monthly sequences was not complete and produced some distortion of the overall frequency of occurrence. For example, type A' occurred 23.2% of the time, while the transition matrix is based on an occurrence of 27.3% of the time.

6. ACKNOWLEDGEMENTS

We acknowledge the aid of a large number of persons, not only in the preparation of this document but in carrying out the field work and analyses which have led to its existence. Of these, special thanks must go to the officers and crews of the research vessels DISCOVERER, SURVEYOR, ACONA, MOANA WAVE and MILLER FREEMAN for laboring under less than ideal conditions to carry out an ambitious field program; the first of this magnitude ever undertaken in these stormy waters. Lynn Long, Sharon Wright, Sally Dong, Cindy Loitsch, Jean Chatfield, Phyllis Hutchens, Joy Golly, and Gini May Flake of NOAA/PMEL are due thanks, also, for their help in analyzing the data and preparing the document. Dr. Tom Royer of the University of Alaska and Mr. Ronald K. Reed of PMEL/NOAA have contributed suggestions which have aided preparation of the manuscript. This study was supported in part by the Bureau of Land Management through interagency agreement with the National Oceanic and Atmospheric Administration, under which a multiyear program responding to needs of petroleum development of the Alaskan continental shelf has been managed by the Outer Continental Shelf Environmental Assessment Program (OCSEAP) Office.

7. REFERENCES

- Barrick, D. E., M. W. Evans, and B. L. Weber (1977): Ocean surface currents mapped by radar. Science, Vol. 198, 138-144.
- Batchelor, G. K. (1967) An Introduction to Fluid Dynamics. University Press, New York, N.Y., 615 pp.
- Brower, W.A., Jr., H. F. Diaz, A. S. Prechtel, H. W. Searby, and J. L. Wise (1977) Climatic Atlas of the Outer Continental Shelf Waters and Coastal Regions of Alaska, Vol. 1, Gulf of Alaska. NOAA/OCSEAP Final Rept. Ru No. 347 (unpublished manuscript). 439 pp.
- Burbank, D. C. (1977) Circulation studies in Kachemak Bay and lower Cook Inlet, Alaska. Dept. of Fish and Game, Anchorage, AK (unpublished manuscript). 207 pp.
- Charnell, R. L. and G. A. Krancus (1976) A processing system for Aanderaa current meter data. NOAA Tech. Memo. ERL-PMEL 6, NOAA, Boulder, CO. 50 pp.
- Davis, B. L. and M. W. Ekern (1977) Wind fabric diagrams and their application to wind energy analysis. J. Appl. Meteor., 16: 522-531.
- Dodimead, A. J., F. Favorite and T. Hirano (1963) Review of oceanography of the subarctic Pacific region. Bull. Int. N. Pacific Fish. Comm., 13: 1-195.
- Favorite, F. (1964) Drift bottle experiments in the northern North Pacific Ocean, 1962-1964. J. Oceanog. Soc. Japan, 20: 160-167.
- Favorite, F. (1967) The Alaskan Stream. Bull. 21, Int. N. Pac. Fish. Comm., Vancouver, B. C. 1-20.
- Favorite, F. and D. M. Fisk (1971) Drift bottle experiments in the North Pacific Ocean and Bering Sea 1957-60, 1962, 1966, and 1970. NOAA/ NMFS Data Rep. 67, U.S.D.O.C., Washington, D. C. 20 pp.
- Favorite, F., A. J. Dodimead and K. Nasu (1976) Oceanography of the subarctic Pacific region, 1960-1972. Bull. Int. N. Pacific Fish. Comm., 33: 1-187.
- Favorite, F. and W. J. Ingraham (1977) On flow in the northwestern Gulf of Alaska, May 1972. J. Oceanog. Soc. Japan, 33: 67-81.
- Gatto, L. W. (1976) Baseline data on the oceanography of Cook Inlet, Alaska. Rept. 76-25, U. S. Army Cold Regions Res. and Eng. Lab., Hanover, N.H. 84 pp.
- Halpern, D., and R. D. Pillsbury (1976) Influence of surface waves on subsurface current measurements in shallow water. Limnol. and Oceanog., 21: 611-616.

- Hayes, S. P. (1979) Variability of current and bottom pressure across the continental shelf in the Northeast Gulf of Alaska. J. Phys. Oceanog., 9: 88-103.
- Hayes, S. P. and J. D. Schumacher (1976) Description of wind, current and bottom pressure variations on the continental shelf in the northeast Gulf of Alaska from February to May 1975. J. Geophys. Res., 81: 6411-6419.
- Hinze, J. O. (1959) Turbulence. McGraw-Hill, New York, N.Y., 586 pp.
- Holbrook, J. R., R. D. Muench and G. A. Cannon (1979) Seasonal observations of low-frequency atmospheric forcing in the Strait of Juan de Fuca. Proc. Fjord Oceanog. Workshop, Plenum Press, New York, 305-317.
- Ingraham, W. J., A. Bakun and F. Favorite (1976) Physical oceanography of the Gulf of Alaska. Environmental Assessment of the Alaskan Continental Shelf, 11, NOAA/ERL, Boulder, CO. (unpublished manuscript).
- International Hydrographic Bureau (1966) Tides, Harmonic Constants. Spec. Publ. No. 26, Monaco. 260 pp.
- Jacobs, W. C. (1951) The energy exchange between the sea and atmosphere and some of its consequences. Bull. Scripps Inst. Oceanog., 6: 27-122.
- Kinney, P. J., D. K. Button, D. M. Schell, B. R. Robertson and J. Groves (1970a) Quantitative assessment of oil pollution problems in Alaska's Cook Inlet. Rept. R-169, Inst. Mar. Sci., Univ. of Alaska, Fairbanks. 125 pp.
- Kinney, P. J., J. Groves and D. K. Button (1970b) Cook Inlet environmental data, R/V Acona cruise 065 - May 21-28, 1968. Rept. R70-2, Inst. Mar. Sci., Univ. of Alaska, Fairbanks. 120 pp.
- Knull, J. R. and R. Williamson (1969) Oceanographic survey of Kachemak Bay, Alaska. Man. Rept. 60, Bur. Comm. Fish. Lab., Auke Bay, Alaska. 54 pp.
- Levanon, N. (1975) (Editor) Special issue on data collection from multiple earth platforms. IEEE Trans. on Geoscience Electronics, Vol. 13.
- Luther, D. S. and C. Wunsch (1975) Tidal Charts of the Central Pacific Ocean. J. Phys. Oceanog., 5: 222-230.
- Matthews, J. B. and J. C. Mungall (1972) A numerical tidal model and its application to Cook Inlet, Alaska. J. Mar. Res., 30: 27-38.
- Mayer, D. A., D. V. Hansen, and D. A. Ortman (1979) Long-term current and temperature observations on the middle Atlantic shelf. J. Geophys. Res., 84: 1776-1792.
- McEwen, G. F., T. G. Thompson and R. Van Cleve (1930) Hydrographic sections and calculated currents in the Gulf of Alaska, 1927 to 1928. Rept. Int. Fish. Comm., No. 4. 36 pp.

- Muench, R. D., H. O. Mofjeld and R. L. Charnell (1978) Oceanographic conditions in lower Cook Inlet; spring and summer 1973. J. Geophys. Res., 83: 5090-5098.
- Muench, R. D. and J. D. Schumacher (1980) Some observations of physical oceanographic conditions on the northeast Gulf of Alaska continental shelf. NOAA Tech. Memo. ERL PMEL-17, NOAA/ERL, Boulder, CO. 84 pp.
- Munk, W. H. and D. Cartwright (1966), Tidal Spectroscopy and Prediction. Phil. Trans. Roy. Soc. London A, 259, 533-581.
- Pearson, C. A. (1973) Deep sea tide and current observations in the Gulf of Alaska and northeast Pacific. NOAA Tech. Memo. NOS16, NOAA/NOS, Rockville, MD. 18 pp.
- Pietrafesa, L. J. and G. S. Janowitz (1979) On the effects of buoyancy flux on continental shelf circulation. J. Phys. Oceanog., 9: 911-918.
- Putnins, P. (1966) Studies on the Meteorology of Alaska: First Interim Report (The sequences of baric weather patterns over Alaska). U. S. Dept. Commerce, ESSA/EDS, Silver Spring, MD (unpublished manuscript).
- Rapatz, W. J. and W. S. Huggett (1977) Pacific Ocean offshore tidal program. Proc. XV Int. Cong. Surv., Stockholm. 47-80.
- Reed, R. K. (1980) Direct measurement of recirculation in the Alaskan Stream. J. Phys. Oceanog., Vol. 10 (in press).
- Reed, R. K. and N. E. Taylor (1965) Some measurements of the Alaska Stream with parachute drogues. Deep-Sea Res., 12: 777-784.
- Reed, R. K., R. D. Muench and J. D. Schumacher (1980) On baroclinic transport of the Alaskan Stream near Kodiak Island. Deep-Sea Res., Vol. 27 (in press).
- Roden, G. I. (1969) Winter circulation in the Gulf of Alaska. J. Geophys. Res., 74: 4523-4534.
- Royer, T. C. (1975) Seasonal variations of waters in the northern Gulf of Alaska. Deep-Sea Res., 22: 403-416.
- Royer, T. C. and R. D. Muench (1977) On the ocean temperature distribution in the Gulf of Alaska, 1974-1975. J. Phys. Oceanog., 7: 92-99.
- Royer, T. C. (1979) On the effect of precipitation and runoff on coastal circulation in the Gulf of Alaska. J. Phys. Oceanog., 9: 555-563.
- Royer, T. C., D. V. Hansen and D. J. Pashinski (1979) Coastal flow in the northern Gulf of Alaska as observed by dynamic topography and satellite-tracked drogued drift buoys. J. Phys. Oceanog., 9: 785-801.

- Scorer, R. S. (1967) Causes and consequences of standing waves. Proc. Symp. on Mountain Meteorology, Atmos. Sci. Paper 122, Colorado State Univ., Fort Collins, CO, 75-101.
- Schumacher, J. D., R. Sillcox, D. Dreves and R. D. Muench (1978) Winter circulation and hydrography over the continental shelf of the northwest Gulf of Alaska. NOAA Tech. Rept. ERL 404-PMEL 31, NOAA, Boulder, CO. 16 pp.
- Schumacher, J. D., R. K. Reed, M. Grigsby and D. Dreves (1979) Circulation and hydrography near Kodiak Island, September to November 1977. NOAA Tech. Memo. ERL-PMEL-13, NOAA, Boulder, CO. 49 pp.
- Schumacher, J. D. and R. K. Reed (1980) Coastal flow in the northwest Gulf of Alaska: the Kenai Current. J. Phys. Oceanog., 85 (in press).
- Thomson, R. E. (1972) On the Alaskan Stream. J. Phys. Oceanog., 2: 363-371.
- Wang, D. P. and A. J. Elliott (1978) Non-tidal variability in the Chesapeake Bay and Potomac River: evidence for non-local forcing. J. Phys. Oceanog., 8: 225-232.
- Wang, D. P. (1978) Subtidal sea level variations in the Chesapeake Bay and relations to atmospheric forcing. J. Phys. Oceanog., 8: 413-421.
- Winant, C. D. and R. C. Beardsley (1979) A comparison of some shallow wind-driven currents. J. Phys. Oceanog., 9: 218-220.
- Wright, F. F., G. D. Sharma, and D. C. Burbank (1973) Ertis-1 observation of sea surface circulation and sediment transport, Cook Inlet, Alaska. Proc. Symp. on Significant Results Obtained from the Earth Resources Technology Satellite-1, NASA, Washington, D. C., 1315-1322.

Appendix A. Current meter statistics for northwest Gulf of Alaska moorings.

Mooring	"In" Water OBS		2.86 hr. Net Drift		35 hr. Net Drift		2.86 Mean		35 Mean		Temp.	Pressure		Salinity							
	Lat.	Long.	Speed	Dir.	Speed	Dir.	Speed	Dir.	Speed	Dir.		Mean	Var.	Mean	Var.						
C1A	59.18	153.30	20	42	77-279	160	1810	16.26	198.8	15.94	198.7	38.94	16.93	247.18	90.82	4.52	4.91	26.12	1.48	31.12	0.36
C1B	59.18	153.31	18	40	78-148	87	2504	9.15	202.4	9.34	203.5	31.54	10.38	162.59	27.72	8.64	2.77	20.39	1.48	31.40	0.31
C1A	59.18	153.30	34	42	77-279	160	2512	9.04	198.4	8.98	198.7	25.07	10.73	146.52	51.81	4.66	4.65	40.41	1.85	31.08	0.25
C1B	59.18	153.31	35	40	78-148	143	3286	4.36	193.5	4.34	192.7	18.15	6.22	83.56	15.04	9.04	2.21	38.03	1.02	30.45	0.78
C2A	59.23	153.03	20	64	77-279	128	2355	8.18	226.6	8.14	226.6	35.45	11.64	256.60	65.48	5.79	3.72	28.59	1.70	31.37	0.25
C2B	59.23	153.13	18	62	78-148	143	3176	14.64	218.3	14.57	218.4	40.81	17.42	416.01	83.94	9.07	2.07	18.53	1.60	30.33	1.92
C2A	59.23	153.03	50	64	77-279	21	2498	8.03	196.4	10.04	197.1	25.15	18.39	163.79	79.10	8.55	0.12	58.47	2.38	31.52	0.11
C2B	Bad data		48				2505														
C3A	59.40	152.89	20	59	77-280	159	2494	8.21	234.2	8.30	233.6	46.35	9.51	380.48	27.25	5.23	3.68	25.43	2.19	31.42	0.26
C3B	59.41	152.89	25	64	78-148	143	598	17.14	231.8	17.25	231.8	52.14	18.82	603.78	54.93	9.10	1.98	23.49	1.77	0.00	0.00
C3A	59.40	152.89	50	59	77-280	159	2359	1.59	230.9	1.70	229.7	28.42	4.49	212.49	8.86	5.32	3.26	53.89	2.41	31.38	0.11
C3B	59.41	152.89	55	64	78-148	97	3180	0.58	109.8	0.64	94.9	24.56	4.09	179.98	7.89	8.15	1.38	51.08	1.82	30.96	0.76
C4A	59.28	152.90	20	84	77-280	159	1452	3.19	272.9	3.15	273.1	40.11	9.03	317.37	48.24	5.80	2.94	19.32	1.87	31.43	0.26
C4B	59.28	152.92	19	83	78-153	138	3294	2.90	243.7	2.97	245.7	26.40	5.56	551.80	27.38	0.00	0.00	0.00	0.00	0.00	0.00
C4A	59.28	152.90	65	84	77-280	159	1672	1.56	241.3	1.55	238.8	26.35	7.07	217.17	33.56	5.95	2.68	65.14	2.97	31.65	0.07
C4B	59.28	152.92	64	83	78-150	141	3290	1.41	166.4	1.33	157.8	26.95	6.61	199.31	29.01	8.27	1.26	62.69	1.50	31.13	0.48
C5A	59.17	152.94	20	128	77-280	159	1804	20.77	249.8	20.96	250.3	34.95	23.93	269.56	162.62	6.04	2.59	17.49	1.46	31.52	0.25
C5B	59.17	152.90	27	135	78-148	115	2156	18.96	251.6	19.06	251.8	44.81	23.14	796.84	258.46	8.40	1.68	0.00	0.00	28.63	1.68
C5A	59.17	152.94	65	128	77-280	159	1981	16.15	240.1	16.29	240.1	30.61	19.03	148.49	87.95	6.10	2.27	62.33	2.09	31.73	0.08
C5B	Bad data		72				3184														
C5A	Bad data		122				2168														
C5B	59.17	152.90	127	135	78-148	123	1815	2.35	199.1	2.46	199.8	15.05	6.18	85.25	23.02	7.00	0.54	128.55	1.78	32.06	0.07
C6A	59.30	152.64	20	71	77-280	162	1817	2.41	280.5	2.48	275.0	46.34	9.09	444.15	66.96	5.96	3.00	21.72	2.16	31.57	0.23
C6B	59.31	152.63	26	77	78-148	142	3173	0.88	256.9	0.65	256.1	46.31	7.49	518.61	38.89	8.84	2.01	0.00	0.00	25.74	1.81
C6A	Bad data		65				1818														
C6B	59.31	152.63	71	77	78-148	143	3295	3.09	119.2	3.22	118.7	25.38	5.44	193.44	11.60	8.41	1.33	70.82	1.81	30.89	0.75
C7A			20				Not recovered														
C7B	59.31	152.18	17	68	78-148	142	2249	4.19	310.0	4.17	310.0	71.69	7.48	1505.49	42.07	6.61	1.84	31.39	0.39	21.87	1.82
C7A	59.32	152.20	65	71	78-281	118	1986	1.48	343.0	1.52	352.8	53.43	4.16	902.31	7.52	6.59	2.13	63.02	2.25	0.00	0.00
C7B	59.31	152.18	62	68	78-148	142	2500	1.80	237.3	1.81	237.2	38.91	3.56	598.15	4.68	8.31	1.16	67.52	1.68	31.86	0.21
C8A	Lost		20				1806														
C8B	59.0	152.06	63	190	78-149	138	3179	22.26	287.3	22.09	287.4	61.54	23.50	1607.82	353.61	7.79	0.82	63.53	5.67	31.96	0.04
C8A	59.04	152.06	65	191	77-277	19	1681	28.10	295.9	27.34	294.0	52.83	29.34	866.77	96.04	8.12	0.17	72.07	61.37	32.05	0.04
C8B	59.03	152.06	64	190	78-149	82	2252	14.24	284.2	14.21	283.8	51.96	15.55	978.58	70.36	7.26	0.57	63.96	3.85	31.95	0.03
C8A	Inst. Failed		180				1680														
C8B	59.03	152.06	179	190	78-149	138	1682	7.84	258.3	7.84	258.7	39.83	8.63	262.40	20.18	6.65	0.27	179.39	1.63	32.39	0.03
C9A	Lost		20																		
C9B	58.78	152.27	66	124	78-149	138	1973	10.84	299.9	10.58	299.6	52.51	13.18	965.86	102.87	6.78	0.47	66.82	1.69	32.22	0.05
C9A	Lost		65																		
C9B	58.77	152.27	67	124	78-149	138	2501	10.64	297.3	10.38	296.8	52.11	13.05	976.83	104.88	6.76	0.46	68.24	1.89	32.28	0.05
C9A	Lost		107																		
C9B	58.78	152.27	114	124	78-149	138	2248	11.68	300.3	11.35	300.5	34.38	12.04	362.54	74.83	6.09	0.33	115.55	1.13	32.41	0.07
C10A	58.50	153.19	20	170	77-278	159	1683	27.66	228.9	27.80	229.6	33.20	31.01	470.82	382.87	5.82	1.69	26.44	1.66	31.92	0.21
C10B	58.50	153.20	25	175	78-148	134	3171	14.70	221.4	14.43	221.6	20.08	17.67	182.55	118.26	8.59	1.77	21.26	2.00	31.19	1.07
C10A	58.50	153.19	65	170	77-278	159	1982	23.34	228.8	23.43	229.4	27.29	25.73	294.65	254.31	5.87	1.06	72.26	1.46	32.15	0.05
C10B	58.50	153.20	70	175	78-148	134	3175	12.48	221.3	11.95	221.4	17.15	15.28	119.84	94.07	7.36	0.97	66.25	2.14	31.52	0.78
C10B	Bad data		157				1824														
C10B	58.50	153.20	165	175	78-148	134	1669	4.77	201.8	4.28	200.4	11.13	9.29	67.06	49.37	5.42	0.26	18.08	0.39	32.49	0.03
C11A	Lost		34																		
C11B	59.56	151.66	82.4	87	78-149	20	1451	1.37	336.4	1.39	333.7	10.23	1.61	13.72	0.77	5.54	0.04	80.01	2.78	32.04	0.00
C12A	59.53	152.23	20	50	78-148	81	2358	4.03	41.4	3.85	42.4	54.82	4.55	990.82	4.21	7.93	1.31	19.98	2.80	31.76	0.14
C13A	59.47	152.68	26	68	78-148	141	3293	5.14	190.6	5.15	189.2	59.65	8.92	704.34	22.41	8.92	1.79	22.21	1.50	31.08	0.23
C12A	59.53	152.23	46	50	78-148	141	3291	4.02	31.0	3.97	30.1	42.81	4.60	651.61	4.25	8.73	1.71	46.71	2.14	30.58	1.47
C13A	Bad data		56.6				2356														

Appendix A. Continued

Mooring	Lat.	Long.	Meter Depth	Bott. Depth	Date	"In" Water OBS.	Per. Meter 'Days' #	2.86 hr. Wet Drift		35 hr. Wet Drift		2.86 Mean		35 Mean		Temp.		Pressure		Salinity	
								Speed	Dirac.	Speed	Dirac.	Speed	Var.	Speed	Var.	Mean	Var.	Mean	Var.	Mean	Var.
K1A	Inst. failed		20				1988														
K1A	57.75	154.73	100	228	76-290	164	1820	27.12	237.8	27.55	237.3	32.87	31.05	247.26	135.66	6.47	0.35	108.94	1.00	32.15	0.03
K2A	58.62	153.08	20	164	76-290	165	1975	41.92	214.3	42.50	214.0	46.17	43.96	588.39	408.45	6.52	0.80	29.24	2.03	31.80	0.12
K2A	58.62	153.08	100	164	76-290	165	2163	26.21	223.2	26.73	228.0	30.19	28.55	249.26	180.05	6.46	0.42	111.02	1.62	32.06	0.03
K3A	58.76	152.17	20	198	76-289	37	1451	33.34	296.6	32.38	296.8	61.12	33.58	1352.74	266.94	7.41	0.35	24.82	3.32	31.88	0.14
K3A	Bad data		100				1806														
K4A	Lost mooring						1816														
K4A	Lost mooring						1976														
K5A	56.55	152.66	20	95	76-292	157	2359	14.73	191.9	15.04	192.1	29.75	18.11	140.44	73.29	10.75	0.43	0.00	0.00	28.20	0.01
K5A	56.55	152.66	80	95	76-292	157	1809	13.30	184.0	13.49	184.2	19.04	14.49	110.78	67.47	5.72	0.15	92.23	0.25	32.70	0.05
K6A	57.22	152.43	23	75	77-292	141	2249	21.63	282.6	21.52	282.9	33.17	24.32	178.69	145.05	5.02	1.41	23.47	0.52	32.40	0.06
K6B	57.23	152.39	32	82	78-141	137	3296	15.72	278.1	15.63	278.0	23.14	16.21	117.14	41.39	7.77	1.38	31.03	0.75	31.38	1.75
K6A	57.22	152.43	65	75	77-292	141	2248	14.67	272.5	14.53	272.5	21.23	16.18	91.98	62.67	5.27	1.21	66.25	0.32	32.43	0.03
K6B	57.23	152.39	72	82	78-141	137	1676	8.31	263.1	8.26	263.0	14.27	8.57	55.76	13.12	0.00	0.00	70.14	2.32	0.00	0.00
K7A	57.06	152.30	28	80	77-292	142	2245	10.52	336.7	10.59	337.1	25.27	13.96	133.08	72.35	5.20	1.01	22.97	0.68	32.40	0.05
K7B	57.09	152.22	29	84	78-141	135	2513	8.77	318.9	8.99	318.8	19.79	10.11	71.32	26.63	7.99	1.21	28.70	0.59	32.11	0.05
K7A	57.06	152.30	70	80	77-292	142	1984	7.65	325.5	7.66	325.8	16.58	9.25	46.92	26.84	5.20	0.75	70.14	0.66	33.00	0.05
K7B	Bad data		74				1675														
K8A	57.12	152.75	25	150	77-292	141	2500	25.04	201.6	25.08	201.8	29.64	26.47	176.69	156.64	5.14	1.53	22.52	0.77	32.36	0.07
K8B	57.11	152.72	30	155	78-141	135	3174	17.90	216.3	17.87	216.1	19.82	18.23	86.12	47.23	8.36	1.63	27.16	0.64	32.14	0.12
K8A	Incomplete		67				1829														
K8B	57.11	152.72	75	155	78-141	135	1827	10.52	220.7	10.66	220.5	13.87	11.36	35.21	16.72	0.00	0.00	0.00	0.00	0.00	0.00
K8A	57.12	152.75	140	150	77-292	65	1827	11.47	199.8	12.22	199.3	15.85	14.04	103.59	67.87	0.00	0.00	143.57	1.30	0.00	0.00
K9A	Incomplete		25				2505														
K9B	56.99	152.56	13	146	78-141	137	3172	4.82	218.1	5.04	221.5	19.47	9.81	77.42	35.93	9.53	1.99	11.04	0.76	31.77	0.56
K9A	57.01	152.62	67	86	77-292	141	1978	0.00	150.1	0.00	150.1	0.00	0.00	0.00	0.00	5.17	1.03	67.89	2.71	32.50	0.02
K9B	56.99	152.56	58	146	78-141	137	3185	4.38	260.3	4.35	260.4	17.97	9.09	60.70	30.33	6.37	0.37	56.78	0.44	32.49	0.01
K9A	57.01	152.62	148	86	77-292	141	1808	2.81	300.2	2.79	299.7	10.80	6.86	29.64	17.46	0.00	0.00	152.55	0.73	0.00	0.00
K9B	56.99	152.56	142	146	78-141	137	2498	3.77	292.8	3.84	293.0	8.49	4.72	20.09	7.54	4.93	0.02	142.30	0.56	32.89	0.02
K10A	Incomplete		25				1811														
K10B	56.83	152.39	24	153	78-141	136	2512	4.60	291.5	4.74	291.0	13.57	6.91	38.16	18.24	8.68	1.88	23.74	0.53	32.31	0.03
K10A	56.85	152.43	144	154	77-292	141	1987	5.62	332.0	5.57	332.1	11.64	7.75	45.80	31.55	5.21	0.07	143.87	0.18	33.02	0.09
K10B	56.83	152.39	69	153	78-141	136	2502	5.78	307.9	5.82	306.8	14.56	7.93	32.58	18.73	5.86	0.08	69.03	0.19	32.43	0.01
K10B	56.83	152.39	149	153	78-141	136	3287	6.21	338.3	6.30	338.6	9.89	6.69	27.41	12.82	4.82	0.03	149.50	0.42	0.00	0.00
K11A	Incomplete		31				598														
K11B	56.03	155.10	25	60	78-142	67	2355	10.02	224.6	10.12	223.9	54.85	10.70	370.86	33.60	6.38	0.39	23.97	0.55	32.46	0.01
K12A	55.99	156.30	18	213	77-297	135	1815	24.30	201.5	24.59	202.6	45.26	32.36	437.94	354.75	4.72	1.36	16.69	1.85	31.86	0.09
K12B	Bad data		24				3183														
K12A	55.99	156.30	203	213	77-297	135	1673	6.45	179.1	6.86	181.6	21.31	14.71	158.53	64.59	5.04	0.05	202.84	0.24	33.29	0.24
K12B	Bad data		208				1671														
K13A	Not deployed						1988														
K13B	56.40	156.82	28	115	78-142	138	3178	13.62	221.1	13.88	220.4	25.17	16.50	234.33	72.66	8.13	2.61	32.69	1.14	31.44	0.35
K13A	Incomplete		102				2356														
K13B	56.40	156.82	111	115	78-142	138	3289	2.65	200.7	2.68	201.5	12.67	5.82	42.50	8.65	5.79	0.78	114.94	0.18	32.02	0.02
HI-A	55.79	158.65	51	71	77-301	130	2504	15.87	219.0	16.07	219.0	21.82	17.88	123.58	89.41	4.67	2.34	55.25	0.73	31.61	0.10
HI-B	Incomplete		50				1833														
HI-D	55.76	157.52	50	118	77-301	16	1826	12.19	318.1	11.24	314.1	20.95	12.18	93.63	22.46	7.25	0.07	56.47	0.45	31.34	0.02
HI-B	55.42	157.98	90	110	77-301	129	2501	7.44	29.2	7.27	28.6	17.27	10.36	96.14	50.47	5.08	1.46	92.76	0.50	32.18	0.04
HI-D	55.76	157.52	90	118	77-301	33	2502	10.09	320.3	10.13	320.7	18.72	11.41	104.51	18.27	6.90	0.42	97.32	0.21	31.70	0.03
HI-D	55.76	157.52	70	118	77-301	129	603	10.65	323.5	10.64	323.6	21.05	12.91	109.45	39.88	4.81	1.71	73.39	0.00	32.10	0.06

Appendix A. Continued

Mooring	"In" Water OBS.				2.86 hr. Net Drift		35 hr. Net Drift		2.86	35	Temp.		Pressure		Salinity						
	Lat.	Long.	Meter Depth	Bott. Depth	Date	Per. Meter 'Days' #	Speed	Dir.ec.	Speed	Dir.ec.	Speed	Var.	Var.	Mean	Var.	Mean	Var.				
WGC-1A	54.03	163.0	20	188	75-248	57 1678	27.13	263.6	27.17	263.6	35.67	29.54	206.10	184.94	7.97	0.78	19.23	0.37	31.93	0.03	
WGC-1B	54.02	163.0	20	194	75-306	131 1455	11.94	243.0	12.22	243.0	17.58	15.68	176.55	138.38	4.31	0.51	0.00	0.00	0.00	0.00	
WGC-1A	54.03	163.0	103	188	75-248	57 1677	15.22	256.8	14.93	257.2	21.15	16.22	57.55	65.51	5.41	0.33	100.47	1.04	32.94	0.06	
WGC-1B	54.02	163.0	100	194	75-306	58 645	20.99	262.8	21.47	262.8	28.07	23.95	330.86	348.98	5.10	0.84	112.50	2.21	32.13	3.83	
WGC-1C	54.02	163.0	20	186	76-073	90 1982	25.33	253.8	25.13	253.5	32.48	26.73	162.34	123.85	2.68	0.99	11.55	0.42	32.23	0.07	
WGC-1D	54.02	163.0	20	89	76-164	110 1973	11.15	253.2	11.17	252.9	22.20	12.97	88.94	59.20	8.02	1.61	17.41	0.30	32.04	0.04	
WGC-1C	54.02	163.0	50	186	76-073	90 1978	24.36	254.7	24.42	254.1	30.77	25.38	102.88	110.13	2.73	0.51	42.03	0.43	32.38	0.11	
WGC-1D	54.02	163.0	50	89	76-164	110 598	10.23	254.6	10.33	254.6	20.48	11.66	53.53	39.50	4.57	1.32	49.97	20.87	31.87	0.01	
WGC-1C	54.02	163.0	100	186	76-073	90 1985	18.98	243.1	19.06	242.8	24.19	19.99	58.98	76.47	3.07	0.22	91.96	0.32	33.06	0.06	
WGC-1C	54.02	163.0	175	186	76-073	90 1832	7.56	225.3	7.66	225.2	11.37	9.06	52.71	37.02	4.57	0.27	171.19	14.87	32.13	0.07	
WGC-1E	54.05	163.1	18	88	76-275	209 2245	23.32	258.5	23.63	258.2	39.41	28.74	227.11	162.84	5.57	2.08	0.00	0.00	31.59	0.04	
WGC-1F	54.06	163.1	20	88	77-120	131 1825	16.29	261.5	16.16	262.1	26.31	17.58	98.07	61.92	8.00	5.41	11.19	0.36	31.56	0.06	
WGC-1E	54.05	163.1	78	88	76-275	78 2249	12.46	250.5	12.19	250.3	19.42	14.05	81.49	45.25	6.72	0.42	0.00	0.00	0.00	0.00	
WGC-1F	54.06	163.10	76	88	77-119	131 1973	6.86	249.6	7.07	248.8	12.65	8.50	33.49	12.78	5.54	0.78	75.55	0.16	32.09	0.04	
WGC-2A	57.45	150.49	20	185	75-265	56 1684	32.96	226.8	33.51	226.5	43.29	34.16	270.82	74.74	7.24	1.87	16.73	0.64	32.14	0.07	
WGC-2B	Lost mooring																				
WGC-2A	57.45	150.49	100	185	75-265	56 1683	25.64	224.3	25.73	224.1	30.16	25.91	109.46	41.70	5.31	0.07	96.84	0.33	33.04	0.09	
WGC-2B	Lost mooring																				
WGC-2C	57.45	150.49	24	185	76-070	90 1977	21.63	226.6	21.80	226.9	30.10	23.41	160.37	119.84	4.86	0.82	19.20	0.81	32.40	0.05	
WGC-2D	57.56	150.82	20	92	76-160	132 1678	3.27	242.4	3.23	244.6	33.79	5.52	223.78	12.10	7.85	1.44	21.02	0.72	31.23	3.47	
WGC-2C	57.45	150.49	54	185	76-070	90 1825	23.83	232.3	24.06	232.2	30.21	25.08	122.38	100.38	4.53	0.38	49.15	0.33	32.56	0.01	
WGC-2D	57.56	150.82	50	92	76-160	132 1808	3.81	234.0	3.69	235.4	31.62	4.89	177.03	8.06	6.92	0.76	47.99	0.71	31.90	0.91	
WGC-2C	57.45	150.49	104	185	76-070	61 1818	25.54	235.3	24.80	235.0	30.19	25.13	164.33	60.17	4.28	0.16	98.87	0.53	32.78	0.02	
WGC-2D	57.56	150.82	80	92		1455	1.19	181.1	1.20	181.0	19.77	2.52	104.14	2.10	6.63	0.50	0.00	0.00	32.18	0.20	
WGC-2C	57.45	150.49	179	185	76-070	90 1837	12.77	182.5	13.05	182.3	25.36	15.07	195.43	55.97	4.76	0.10	175.05	0.27	33.17	0.07	
WGC-2E	57.56	150.82	20	90	76-293	155 1807	2.49	239.5	2.31	240.6	41.13	10.43	219.60	33.93	6.06	0.80	17.24	0.85	32.27	0.16	
WGC-2F	57.57	150.83	20	90	77-084	167 1815	34.08	7.04	246.27	17.75	4.68	218.7	4.69	22.04	7.46	5.06	18.89	0.51	31.97	0.27	
WGC-2E	57.56	150.82	80	90		1814	0.05	280.7	0.05	287.05	1.47	0.29	0.01	0.05	2.46	0.29	78.23	0.84	36.10	0.02	
WGC-2F	57.57	150.83	80	90	77-084	167 1826	2.83	178.3	2.80	178.6	20.38	3.93	114.56	4.36	6.06	0.90	77.96	0.61	32.12	0.09	
WGC-3A	Lost mooring																				
WGC-3B	55.19	156.97	20	111	76-162	129 1817	21.35	255.0	21.41	255.7	43.78	22.95	412.01	101.55	8.17	2.21	18.28	0.37	32.90	0.16	
WGC-3C	55.20	156.95	28	112	76-292	138 1829	26.19	239.7	26.07	238.8	50.46	33.50	485.54	219.17	6.17	0.60	20.77	34.00	0.00	0.00	
WGC-3B	Inst. failed																				
WGC-3C	55.20	156.95	90	112	76-292	153 2168	19.59	231.8	19.81	231.6	34.96	20.79	242.37	131.11	6.00	0.37	99.75	0.16	32.90	0.11	
WGC-3B	Inst. failed																				
WGC-3D	55.20	156.96	20	112	77-191	131 1682	23.82	254.6	24.11	254.9	43.29	25.71	401.53	87.75	7.79	5.57	9.82	0.13	32.06	0.16	
WGC-3D	Inst. failed																				

Appendix B. Release and recovery information for drift cards released in the Kodiak Island region during 1978.

RELEASED -----	R E C O V E R E D				
	CARD -----	DATE -----	LATITUDE -----	LONGITUDE -----	COMMON NAME -----
101 - 200	107	05/20/78	57 24.0N	156 22.0W	SLAUGHTER ISL
03/05/78	123	07/24/78	59 0.0N	153 37.0W	KAMISHAK BAY
59 4.6N	155	07/24/78	59 0.0N	153 37.0W	KAMISHAK BAY
150 39.4W	171	05/30/79	59 4.0N	153 44.0W	CAPE DOUGLAS
201 - 300	214	04/10/78	58 37.8N	152 27.5W	CARSHAN PT
03/06/78	245	06/18/78	58 22.4N	152 6.5W	SEAL BAY
58 31.8N	250	07/08/78	58 23.3N	152 7.5W	TOLSTOI PT
150 45.0W	263	05/15/78	57 50.2N	152 21.0W	MILLER PT
	268	07/24/78	57 5.2N	153 11.7W	OCEAN BAY
	292	07/08/78	58 23.3N	152 7.5W	TOLSTOI PT
301 - 400	306	07/22/78	57 18.1N	153 0.0W	KILUDA BAY
03/06/78	319	04/09/78	57 27.8N	152 27.0W	PASAGSHAK BAY
58 15.2N	325	05/08/78	57 27.8N	152 27.0W	PASAGSHAK BAY
149 52.0W	342	04/22/78	57 5.3N	153 11.0W	OCEAN BEACH
	343	04/09/78	57 27.8N	152 27.0W	PASAGSHAK BAY
	352	07/22/78	57 10.0N	153 8.5W	PORT HOBRON
	365	07/01/78	56 29.3N	154 35.0W	TUGIDAK ISL
	366	04/05/79	57 31.0N	152 56.0W	HIDDEN BASIN
	371	06/04/78	57 18.0N	153 3.0W	KILUDA BAY
	372	10/10/78	57 9.0N	153 11.0W	PORT HOBRON
	380	07/22/78	57 1.0N	153 36.0W	KTAVAK BAY
	388	05/13/79	57 31.5N	152 16.6W	SACRAMENTO RIVER
	392	03/27/79	57 12.0N	153 10.0W	MCCORD RANCH
	395	04/26/78	57 17.9N	153 3.0W	KILUDA BAY
401 - 500	454	10/14/78	54 52.0N	158 54.0W	STROGNOFF PT
03/06/78	454	06/12/79	59 41.7N	140 17.5W	POINT MANFY
58 3.6N					
149 10.3W					
501 - 600					
03/10/78					
58 27.6N					
151 50.0W					
601 - 700	609	07/22/78	57 12.5N	153 16.0W	OLD HARBOR
03/10/78	625	08/03/78	57 26.0N	152 43.0W	EAGLE COVE
57 58.3W	628	02/22/79	57 12.0N	153 10.0W	MCCORD RANCH
150 44.6W	630	04/09/78	57 27.8N	152 27.0W	PASAGSHAK BAY
	634	10/09/78	57 25.2N	152 43.0W	FAGLE HARBOR
	644	04/29/78	57 17.9N	153 3.0W	KILUDA BAY
	664	04/12/78	57 27.8N	152 27.0W	PASAGSHAK BAY
	671	09/12/78	57 9.0N	153 11.0W	MCCORD RANCH
	695	03/27/79	57 12.0N	153 10.0W	MCCORD RANCH

Appendix B. Continued

RELEASED	RECOVERED				
-----	CARD	DATE	LATITUDE	LONGITUDE	COMMON NAME
-----	-----	-----	-----	-----	-----
701 - 800	743	07/24/78	56 24.0N	154 45.0W	TUGIDAK ISL
03/13/78	777	10/01/78	56 30.0N	160 0.0W	PORT HEIDEN
57 25.8N	798	05/05/79	59 21.0N	146 25.0W	MIDDLETON ISL
151 25.8W					
801 - 900					
03/14/78					
57 16.3N					
151 42.2W					
901 -1000	904	11/23/78	57 51.0N	152 38.0W	CANNONS BEACH
03/10/78	908	04/20/78	58 8.8N	153 16.8W	NORTH BEACH
58 21.4N	910	05/17/78	57 24.0N	156 22.0W	WIDE BAY
151 6.9W	920	11/06/78	57 52.0N	153 50.0W	CP UGAT
	958	07/11/78	57 44.0N	153 30.0W	PACKERS SPIY
	966	04/20/78	58 8.8N	153 16.8W	NORTH BEACH
	973	08/02/79	58 0.0N	153 17.0W	OUTLET CAPE
	985	06/19/78	57 39.0N	154 7.0W	7 MILE BEACH
	998	10/22/78	58 7.0N	153 2.0W	
1001-1100	1010	06/30/78	56 32.0N	154 8.0W	SITKINAK ISL
03/14/78	1022	07/22/78	56 53.0N	154 12.0W	LAZY BAY
57 3.1N	1046	07/01/78	56 29.3N	154 35.0W	TUGIDAK ISL
152 7.8W	1062	05/02/78	56 56.1N	154 10.0W	AKHIOK VILLAGE
1101-1200	1133	11/10/78	54 36.0N	164 52.0W	CAPE SARICHEF
03/14/78	1165	07/04/79	55 49.5N	155 32.0W	CHIRIKOF ISL
56 53.6N					
152 33.0W					
1201-1300	1242	10/01/78	56 30.0N	160 0.0W	PORT HEIDEN
03/14/78	1243	10/17/79	53 27.0N	166 55.0W	SW. UNALASKA ISL
56 53.6N					
152 33.0W					
1301-1400	1322	08/15/79	52 56.0N	168 54.0W	NIKOLSKI
03/16/78					
56 7.5N					
153 56.2W					
1401-1500	1413	05/05/79	56 0.0N	161 16.0W	NELSON LAGOON
03/10/78	1423	05/03/78	58 18.1N	153 2.0W	CP PARAMANOF
58 50.0N	1448	05/02/78	58 18.4N	153 2.7W	CP PARAMANOF
151 39.0W	1452	04/20/78	58 8.8N	153 16.8W	NORTH BEACH
	1464	05/14/78	58 18.4N	153 2.7W	CP PARAMANOF
	1486	06/26/78	57 39.1N	154 7.0W	7 MILE BEACH
	1495	07/26/78	58 17.0N	152 55.5W	CP PARAMANOF

Appendix B. Continued

RELEASED	RECOVERED				
	CARD	DATE	LATITUDE	LONGITUDE	COMMON NAME
3001-3100 05/23/78 58 48.3N 149 36.1W	3036	07/04/78	57 39.1N	154 7.0W	7 MILE BEACH
	3058	07/30/78	57 40.0N	152 28.0W	MIDDLE BAY
3101-3200 05/23/78 59 20.3N 150 7.3W	3102	08/01/78	59 32.0N	153 46.2W	URSUS COVE
	3107	07/03/78	60 21.0N	152 0.0W	KALGIN ISL
	3111	07/25/78	59 18.4N	154 6.0W	AMAKDORI PEACH
	3144	03/27/79	57 12.0N	153 10.0W	MCCHORD RANCH
	3156	07/01/78	59 20.0N	153 22.0W	ST AUGUSTINE
3201-3300 05/23/78 58 51.3N 149 45.4W	3203	12/31/78	58 12.0N	152 21.0W	KITOI BAY
	3221	06/21/79	56 57.0N	153 41.0W	JAP BAY
	3221	06/21/79	56 57.0N	153 41.0W	UPPER JAP BAY
	3228	09/19/78	57 25.5N	152 20.0W	NARROW CAPE
	3242	11/01/78	58 16.0N	151 16.0W	MARMOT ISL.
	3267	07/25/78	59 18.4N	154 6.0W	AMAKDEDGRI BEACH
	3276	10/29/78	58 9.0N	152 6.0W	PILLAR CAPE
	3278	07/25/78	59 18.4N	154 6.0W	AMAKDEDORI BEACH
	3294	07/31/78	57 40.0N	152 28.0W	MIDDLE BAY
	3297	09/22/78	58 29.3N	152 33.9W	DAYLIGHT HRP
	3297	09/22/78	58 29.3N	152 33.9W	DAYLIGHT HRP
3301-3400 05/23/78 58 59.9N 149 56.7W	3322	11/12/78	57 52.6N	152 41.2W	CRAG PT
	3346	11/01/78	57 51.0N	153 51.0W	CAPE UGAT
	3351	08/22/78	57 57.0N	152 28.0W	SPRUCE ISLAND
	3366	09/04/78	58 17.0N	154 8.0W	KAMISHAK
3401-3500 05/23/78 59 4.6N 149 54.4W	3402	07/25/78	59 18.4N	154 6.0W	AMAKDEDORI B
	3405	07/23/78	58 39.0N	152 26.0W	MIDDLE BAY
	3408	07/31/78	57 56.0N	152 25.0W	PINAPPLE COVE
	3409	08/11/78	57 55.0N	153 42.0W	MINERS PT
	3416	04/18/79	57 6.0N	156 30.0W	PORT WRANGLE
	3446	06/27/78	57 10.5N	154 32.5W	AGAKULIK RIVER
	3480	07/12/78	57 40.0N	152 26.5W	MIDDLE BAY
3501-3600 05/23/78 58 44.7N 149 27.5W	3507	08/18/78	57 54.8N	152 59.5W	DRY SPRUCE BAY
	3508	07/25/78	59 18.4N	154 6.0W	AMAKDEDORI P
	3511	07/31/78	57 56.0N	152 25.0W	PINAPPLE COVE
	3520	08/13/78	59 32.0N	153 46.2W	URSUS COVE
	3527	06/22/79	56 33.0N	157 9.0W	SUTWIK ISL
	3535	04/15/79	57 40.0N	152 28.0W	
	3546	09/21/78	56 57.5N	153 35.5W	KNOLL BAY
	3583	09/06/78	59 30.0N	153 44.0W	URSUS COVE
	3585	08/21/78	57 27.5N	152 27.0W	PASAGSHAK BAY

Appendix B. Continued

RELEASED	RECOVERED				
-----	CARD	DATE	LATITUDE	LONGITUDE	COMMON NAME
-----	----	-----	-----	-----	-----
3601-3700	3610	07/19/78	59 12.5N	154 8.1W	CHENIK LAGOON
05/23/78	3657	09/09/79	57 46.9N	152 21.5W	WOODY ISL
58 37.8N	3673	10/11/78	57 56.5N	152 29.0W	W SIDE SPRUCE ISL
149 7.5W	3684	08/05/78	59 21.3N	153 57.5W	CONTACT PR
	3686	06/25/78	60 11.0N	151 26.0W	CLAM GULCH
	3689	07/25/78	59 18.4N	154 6.0W	AMAKDEDORI R
	3690	07/24/78	59 30.8N	154 45.3W	URSUS COVE
	3691	07/14/78	59 18.0N	154 6.7W	AMAKDEDORI P
	3698	08/11/78	59 23.0N	153 31.0W	W ST AUGUSTINE
	3700	07/25/78	59 18.8N	154 6.0W	AMAKDEDORI P
3701-3800	3710	08/02/78	57 5.3N	153 11.0W	OCEAN BAY
05/23/78	3792	09/09/79	56 32.5N	154 39.0W	TUGIDAK ISL
58 24.5N	3794	03/25/79	57 4.0N	153 34.0W	KAISIGNAK BAY
148 27.0W	3800	08/03/78	57 53.7N	153 48.0W	RINER CREEK
3801-3900	3812	07/01/78	56 57.0N	154 9.0W	MOSER BAY
05/23/78	3823	10/22/78	57 56.5N	152 29.0W	SPRUCE ISLAND
59 10.3N	3826	06/12/78	57 45.0N	155 36.5W	PAULF BAY
150 .7W	3841	10/28/78	57 17.5N	154 45.0W	GURNEY BAY
	3842	07/21/78	57 39.1N	154 7.0W	7 MILE BEACH
	3873	06/26/78	57 56.5N	153 16.0W	VIEKODA BAY
3901-4000	3902	10/14/78	57 36.0N	152 16.0W	LONG ISL
05/23/78	3904	08/10/78	59 32.0N	153 46.2W	URSUS COVE
58 32.0N	3906	08/01/78	59 32.0N	153 46.2W	URSUS COVE
148 48.2W	3913	08/09/78	58 11.2N	152 22.0W	KITIO BAY
	3914	08/29/78	58 31.0N	153 54.0W	CHINIAK BAY
	3915	07/13/78	59 29.0N	153 42.8W	ROCKY COVE
	3943	08/01/78	59 32.0N	153 46.2W	URSUS COVE
	3945	06/27/78	59 50.0N	151 48.0W	WHISKEY GULCH
	3960	07/08/78	57 47.8N	152 21.8W	MISSION BEACH
	3978	09/26/78	56 52.0N	154 14.0W	CAPE AKHIOK
	3982	06/09/79	57 12.0N	153 10.0W	PORT HOBRON
	3987	07/25/78	59 18.4N	154 6.0W	AMAKDEDORI R
4001-4100	4027	09/17/79	57 12.0N	153 10.0W	SITKALIDAK
10/03/78	4030	10/07/78	57 1.6N	153 23.8W	NATALIA PENN
57 5.6N	4031	10/07/78	57 1.6N	153 23.8W	NATALIA PENN
152 12.9W	4046	07/10/79	57 12.0N	153 10.0W	PORTHOBRON
	4051	10/07/78	57 1.6N	153 23.8W	NATALIA PENN
	4065	10/07/78	57 1.6N	153 23.8W	NATALIA PENN
	4077	10/07/78	57 1.6N	153 23.8W	NATALIA PENN
	4078	10/07/78	57 1.6N	153 23.8W	NATALIA PENN
	4087	10/07/78	57 1.6N	153 23.8W	NATALIA PENN
	4091	10/07/78	57 1.6N	153 23.8W	NATALIA PENN

Appendix B. Continued

RELEASED	RECOVERED				
-----	CARD	DATE	LATITUDE	LONGITUDE	COMMON NAME
-----	-----	-----	-----	-----	-----
4101-4200 10/04/78 56 49.4N 152 24.3W					
4201-4300 10/04/78 57 6.4N 152 43.9W	4239 4269 4276 4277 4288 4292	11/05/78 04/05/79 11/03/78 11/08/78 11/04/78 04/07/79	57 .2N 57 .3N 57 .2N 57 .2N 57 .2N 57 .3N	153 33.0W 153 33.0W 153 33.0W 153 33.0W 153 33.0W 153 33.0W	KIAVAK BAY KIAVAK BAY KIAVAK BAY KIAVAK B KIAVAK BAY KIAVAK BAY
4301-4400 10/04/78 56 59.6N 152 34.0W	4338 4340	03/17/79 08/26/79	56 34.0N 55 44.0N	169 38.0W 159 54.0W	ST GEORGE ISL DEPT POINT
4401-4500 10/05/78 57 13.6N 152 23.1W					
4501-4600 10/07/78 56 13.2N 154 59.0W	4549	08/15/79	56 43.0N	154 4.0W	ATAKALIK ISL
4601-4700 10/07/78 56 8.5N 155 9.6W	4677	03/26/79	56 34.0N	169 38.0W	ST GEORGE ISL
4701-4800 10/08/78 56 3.9N 155 16.3W					
4801-4900 10/08/78 55 58.4N 155 25.8W					
4901-5000 10/07/78 56 .7N 155 5.1W	4950	07/07/79	55 49.5N	155 32.0W	CHIRICOF ISL

Appendix B. Continued

RELEASED	RECOVERED				
	CARD	DATE	LATITUDE	LONGITUDE	COMMON NAME
5001-5100	5011	01/14/79	57 35.5N	152 27.5W	KALSIN BECH
10/10/78	5013	11/01/78	57 51.0N	153 51.0W	UGAT CAPE
59 2.8N	5019	10/30/78	57 42.2N	153 50.2W	SPIRIDON BAY
150 57.2W	5053	10/30/78	57 42.2N	153 50.2W	SPIRIDON BAY
	5064	07/08/79	56 54.0N	154 18.0W	ALITAK LAGOON
	5080	10/30/78	57 42.2N	153 42.2W	SPIRIDON BAY
	5099	01/17/79	57 12.0N	153 10.0W	MCCHORD RANCH
5101-5200	5134	10/30/78	57 42.2N	153 50.2W	SPIRIDON BAY
10/10/78	5180	10/30/78	57 42.2N	153 50.2W	SPIRIDON BAY
58 50.1N	5188	10/30/78	57 42.2N	153 50.5W	SPIRIDON BAY
150 56.2W	5200	10/30/78	57 42.2N	153 50.2W	SPIRIDON BAY
5201-5300	5203	10/30/78	57 42.2N	153 50.2W	SPIRIDON BAY
10/10/78	5208	06/06/79	57 38.0N	154 21.0W	CAPE UYAT
58 51.6N	5235	12/14/78	57 42.2N	153 50.5W	SPIRIDON BAY
150 53.0W	5278	10/30/78	57 42.2N	153 50.2W	SPIRIDON BAY
5301-5400	5323	11/10/78	58 3.5N	153 14.0W	ONION BAY
10/10/78	5328	11/08/78	59 21.2N	151 55.3W	ENGLISH BAY
58 44.9N					
150 51.6W					
5401-5500	5467	03/18/79	57 25.5N	152 20.0W	
10/10/78					
58 38.6N					
150 48.0W					
5501-5600	5516	05/10/79	57 30.0N	152 44.0W	SALTRY COVE
10/10/78					
58 32.3N					
150 44.9W					
5601-5700	5636	06/27/79	55 47.0N	155 41.0W	S. CHIRIKOF ISL
10/10/78	5615	03/21/79	57 49.0N	152 26.0W	MONASHKA BAY
58 24.5N	5649	01/06/79	57 46.8N	152 26.5W	GIBSON COVE
150 49.0W	5675	05/01/79	58 55.8N	152 12.4W	USHAGAT ISL
	5683	01/20/79	57 38.5N	152 26.0W	PRCAD PT
5701-5800	5732	12/27/78	57 24.2N	152 30.0W	CAPE CURRENT
10/10/78	5742	07/08/79	55 20.0N	160 26.0W	POPOFF ISL
58 18.8N	5748	03/27/79	57 12.0N	153 10.0W	MCCHORD RANCH
150 37.8W	5782	04/12/79	57 40.0N	152 29.0W	MIDDLE BAY
5801-5900	5807	05/27/79	57 12.0N	153 10.0W	PORT HOBORN
10/10/78	5819	01/15/79	58 56.0N	152 15.0W	USHAGAT ISL
58 11.3N	5851	03/18/79	57 25.5N	152 20.0W	
150 25.6W					

Appendix C. Release and recovery information for seabed drifters, including returns through February, 1980.

Cruise Number	Date Released	Release Location		Recovery Date	Recovery Location	
		Latitude N	Longitude W		Latitude N	Longitude W
4MF 77	5 Nov 77	58°02'	151°38'	Jan 79	Nataliu Bay	
	5 Nov 77	56°53'	153°04'	8 Jan 78	56°50'	153°18'
	2 Nov 77	57°37'	151°55'	-	57°03'	152°48'
4DI 78	9 Apr 78	57°07'	153°00'	Jan 79	Nataliu Bay	
	8 Apr 78	57°47'	151°41'	19 May 78	57°25'	152°30'
	9 Apr 78	57°28'	152°10'	30 Sep 78	57°32'	151°42'
	29 Mar 78	58°04'	151°45'	-	-	-
	29 Mar 78	58°04'	151°45'	23 Sep 79	Chiniak Gulley	
2MF 78	24 Jun 78	56°55'	153°22'	29 Jan 79	57°08'	153°25'
	24 Jun 78	57°04'	153°03'	11 Nov 78	Ocean Bay, Sitkalidak Isl.	
	26 Jun 78	57°16'	151°17'	18 Sep 78	57°34'	151°51'
	26 Jun 78	56°59'	152°55'	17 Sep 78	57°08'	152°44'
	24 Jun 78	56°55'	153°22'	17 Nov 78	57°05'	153°26'
	26 Jun 78	57°16'	151°17'	6 Dec 78	57°38'	151°52'
	26 Jun 78	57°16'	151°17'	28 Sep 78	57°32'	151°42'
	22 Jun 78	57°36'	151°48'	21 Sep 78	57°32'	151°40'
	22 Jun 78	57°36'	151°48'	24 Sep 78	57°25'	151°26'
	27 Jun 78	57°43'	150°54'	26 Sep 78	57°22'	151°22'
	24 Jun 78	57°12'	152°44'	27 Sep 78	56°52'	153°26'
	24 Jun 78	57°19'	152°24'	27 Oct 78	57°24'	152°24'
	24 Jun 78	56°55'	153°22'	15 Sep 78	57°03'	153°25'
	24 Jun 78	56°55'	152°22'	23 Sep 78	57°03'	153°25'
	26 Jun 78	57°00'	151°55'	29 Sep 78	57°03'	152°30'
	26 Jun 78	57°16'	151°17'	29 Sep 78	57°38'	151°58'
	21 Jun 78	58°03'	151°25'	20 Jan 79	57°40'	151°50'
	24 Jun 78	56°55'	153°22'	6 Dec 78	57°05'	153°26'
	24 Jun 78	56°55'	153°22'	23 Oct 78	57°05'	153°26'
	27 Jun 78	57°43'	150°54'	-	-	-
	24 Jun 78	57°04'	153°03'	18 Feb 79	Ocean Bay, Sitkalidak Isl.	
	22 Jun 78	57°37'	151°47'	18 Feb 79	57°21'	152°33'
	21 Jun 78	58°03'	151°25'	11 Feb 79	57°31'	152°17'
	24 Jun 78	56°55'	153°22'	28 Feb 79	57°10'	153°20'
	24 Jun 78	56°55'	153°22'	26 Feb 79	57°10'	153°19'
	24 Jun 78	56°55'	153°22'	24 Feb 79	57°09'	153°21'
	22 Jun 78	58°18'	150°12'	8 Jan 79	-	-
	30 Jun 78	56°26'	153°44'	11 Apr 79	-	154°32'
	24 Jun 78	57°04'	153°03'	3 Feb 80	56°37'	153°06'
	27 Jun 79	57°43'	150°55'	20 Nov 79	57°43'	152°20'
27 Jun 78	57°43'	150°55'	27 Oct 79	Cape Chiniak on NE Side Kodiak		
22 Jun 78	58°18'	150°12'	4 Jul 79	57°16'	150°46'	
22 Jun 78	58°18'	150°12'	19 Oct 79	Chiniak Gully		

Appendix C. Continued

1WE 78	28 Oct 78	56°55'	153°22'	17 Mar 79	57° -	153°25'
	28 Oct 78	57°16'	151°17'	2 Feb 79	Silver Bay,	Cape Chiniak
	1 Nov 78	57°36'	151°46'	5 Jan 79	57°25'	152°00'
	28 Oct 78	56°55'	153°22'	28 Jan 79	57°07'	153°25'
	27 Oct 78	57°29'	152°07'	19 Jan 80	56°53'	152°35'
	2 Nov 78	58°03'	151°27'	6 Jan 80	57°32'	151°44'
	1 Nov 78	57°45'	151°28'	3 Jan 80	Cap Chiniak	
	1 Nov 78	58°18'	150°12'	31 Dec 79	57°34'	151°49'
	1 Nov 78	57°37'	151°47'	29 Dec 79	57°33'	151°48'
	1 Nov 78	58°18'	150°12'	24 Nov 79	57°38'	152°20'
1MF 79	15 Feb 79	57°04'	153°04'	29 Mar 79	Ocean Bay,	Sitkalidak Isl.
	15 Feb 79	57°04'	153°04'	29 Mar 79	"	"
	18 Feb 79	57°45'	151°28'	25 Mar 79	57°56'	151°57'
	15 Feb 79	57°04'	153°04'	4 Apr 79	Ocean Bay,	Sitkalidak Isl.
	15 Feb 79	57°04'	153°04'	4 Apr 79	"	"
	15 Feb 79	57°04'	153°04'	4 Apr 79	"	"
	15 Feb 79	57°04'	153°04'	4 Apr 79	"	"
	18 Feb 79	57°45'	151°28'	23 Sep 79	"	"
	15 Feb 79	57°04'	153°02'	12 Jan 80	56°58'	153°29'
	22 Feb 79	58°04'	151°24'	19 Jan 80	57°08'	152°31'
	22 Feb 79	58°04'	151°24'	29 Dec 79	57°20'	152°30'
	18 Feb 79	57°29'	152°06'	31 Oct 79	57°14'	152°54'
	15 Feb 79	57°04'	151°02'	11 Nov 79	56°46'	153°29'
	7 Mar 79	58°18'	150°12'	2 Nov 79	Loran:31402-11697-7960	
					32070-43168-9990	
	15 Feb 79	57°04'	153°02'	12 Oct 79	Newman Bay	
					Loran-31228-32535	

Appendix D. CTD stations used in NWGOA program, listed by cruises.

<u>Cruise ID</u>	<u>Vessel</u>	<u>Dates</u>	<u>No. Casts</u>
RP4-DI77C2	<u>Discoverer</u>	4-12 Oct 77	186
RP4-DI77C3	<u>Discoverer</u>	13-21 Oct 77	97
RP4-DI77C4	<u>Discoverer</u>	27 Oct-5 Nov 77	127
RP4-SU77B5	<u>Surveyor</u>	6-15 Sep 77	130
RP4-SU77C2	<u>Surveyor</u>	4-17 Nov 77	46
RP4-DI77A2	<u>Discoverer</u>	2-10 Mar 77	58
Acona 245	<u>Acona</u>	30 June-16 Jul 77	109
RP4-DI76A	<u>Discoverer</u>	13 May-2 June 76	130
RP-DI76BL6	<u>Discoverer</u>	14-23 Oct 76	39
RP4-DI77A3	<u>Discoverer</u>	15 Mar-1 Apr 77	141
RP4-DI77A4	<u>Discoverer</u>	5-22 Apr 77	106
RP4-DI76A	<u>Discoverer</u>	7-13 Apr 76	27
DS5	<u>Discoverer</u>	9-16 Nov 77	94
Acona 205	<u>Acona</u>	13 Feb 75	3
814	<u>Uncertain</u>	30 Oct-13 Nov 75	116
MW3	<u>Moana Wave</u>	20 Apr-1 May 76	99
RP4-SU78A2	<u>Surveyor</u>	4-17 Mar 78	179
RP4-DI78A1	<u>Discoverer</u>	6-24 Mar 78	180
RP4-DI78A2	<u>Discoverer</u>	14-20 Apr 78	26
RP4-DI78A4	<u>Discoverer</u>	26 May-7 June 78	135
OP 343603	<u>Silas Bent</u>	1-26 Sep 75	127
MW4	<u>Moana Wave</u>	7-20 May 76	94
MW5	<u>Moana Wave</u>	22 Jul-1 Aug 76	69
RP4-DI78A2	<u>Discoverer</u>	28 Mar-14 Apr 78	91
RP4-DI78B4	<u>Discoverer</u>	6-22 Oct 78	171
RP4-MF77A4	<u>Miller Freeman</u>	3-7 April 77	25
RP4-MF78A4	<u>Miller Freeman</u>	20 Jun-5 Jul 78	106
RP4-SU78A3	<u>Surveyor</u>	24-27 Mar 78	21
RP4-DI78A3	<u>Discoverer</u>	25 Apr-5 May 78	42
RP4-MF78A1	<u>Miller Freeman</u>	9-12 May 78	20
RP4-MF78A5	<u>Miller Freeman</u>	13-18 Jul 78	53
RP4-SU78B1	<u>Surveyor</u>	14-18 Aug 78	36
RP4-MF78A3	<u>Miller Freeman</u>	7-11 June 78	49
Wekoma-78	<u>Wekoma</u>	27 Oct-13 Nov 78	94
RP4-MF78A	<u>Miller Freeman</u>	20-30 May	107
RP4-SU79B	<u>Surveyor</u>	5-14 Aug	79
RP4-SU79A	<u>Surveyor</u>	23 Mar-3 Apr 79	141
248IMS	<u>Acona</u>	10-16 Aug 77	20
SU4IMS	<u>Surveyor</u>	21 Sep-2 Oct 76	79
IMS79A	<u>Surveyor</u>	9-21 Feb 79	133
241IMS	<u>Acona</u>	24 Apr 77	5
FN9IMS	<u>Miller Freeman</u>	29 Mar-2 Apr 77	32
254IMS	<u>Acona</u>	28 Nov-2 Dec 77	9
FN8IMS	<u>Miller-Freeman</u>	12-18 Nov 76	87
FN7IMS	<u>Miller Freeman</u>	10-19 Nov 76	24
IMS812	<u>Discoverer</u>	10-15 Oct 75	24
MW6	<u>Moana Wave</u>	13-19 Oct 76	22

FINAL REPORT--TASK 1
OIL SPILL TRAJECTORY SIMULATION
LOWER COOK INLET - SHELIKOF STRAIT, ALASKA
BERING SEA - GULF OF ALASKA PROJECT OFFICE
OUTER CONTINENTAL SHELF ENVIRONMENTAL
ASSESSMENT PROGRAM

JOB NO. 06797-014-88
June 13, 1980

LOS ANGELES, CALIFORNIA

June 13, 1980

Outer Continental Shelf Environmental
Assessment Program
Bering Sea - Gulf of Alaska Project Office
Post Office Box 1808
Juneau, Alaska 99802

Attention: Herbert E. Bruce, Ph.D.
OCSEAP Project Manager

Gentlemen:

Final Project Report
Oil Spill Trajectory Simulation
Lower Cook Inlet and Shelikof Strait, Alaska
For National Oceanic and Atmospheric Administration

We are pleased to submit our final project report on oil spill trajectory simulation in Lower Cook Inlet and Shelikof Strait, Alaska. This report has incorporated and responded to comments received from your Juneau staff, as well as the Bureau of Land Management (BLM) in Anchorage, Alaska, and the United States Geological Society (USGS) in Reston, Virginia.

We wish to express our appreciation to the Pacific Marine Environmental Laboratory (PMEL) in Seattle, Washington for their assistance during the meteorological and oceanographic data collection phase of this project.

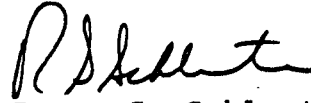
An Executive Summary has been prepared which presents the essential results and conclusions of this study. This Executive Summary is designed to be self-sufficient documentation of the project for those who may not be interested in the full, detailed report.

National Oceanic and Atmospheric
Administration
June 13, 1980
Page 2

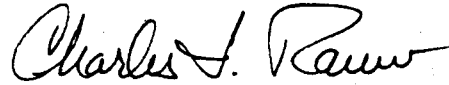
It has been a pleasure to work on this phase of our 1980 fiscal year contract with your Juneau staff. Please do not hesitate to contact us if you have questions regarding the contents or findings of this study.

Very truly yours,

DAMES & MOORE
Marine Services Group



Roger S. Schlueter, Ph.D.
Managing Principal-in-Charge



Charles I. Rauw
Project Manager

RSS:CIR:sms

PREFACE

This report describes a study of oil spill trajectory simulation in Lower Cook Inlet and Shelikof Strait, Alaska. The work was performed under Contract No. NA80RAC00075 between Dames & Moore and the National Oceanic and Atmospheric Administration.

This study was supported by the Bureau of Land Management through through interagency agreement with the National Oceanic and Atmospheric Administration, under which a multi-year program responding to needs of petroleum development of the Alaskan continental shelf is managed by the Outer Continental Shelf Environmental Assessment Program (OSCEAP) Office.

Executive Summary

The primary objective of this study, one of a continuing series focusing on the behavior of spilled oil, was to perform trajectory simulations of spilled oil in Lower Cook Inlet and Shelikof Strait, Alaska. Trajectories of the centroid of hypothetical surface slicks originating from selected launch sites throughout the study area represented slick behavior. Physico-chemical processes such as spreading, evaporation, and sinking were neglected. Trajectory driving forces included winds, tidal and net currents.

A total of 38 hypothetical launch sites were specified by the U.S. Geological Survey (USGS) as representing locations of potential transportation routes, drilling and production sites within the study area. Also included in these sites were five open water boundary launch sites which allowed the results presented here to be interfaced with a complementary USGS Gulf of Alaska trajectory model.

Wind fields in the area of interest were defined by five spatially dependent flow patterns and six intensity factors. These patterns were prepared by the Pacific Marine Environmental Laboratories (PMEL, 1980) and represent refinements to the five primary wind fields developed and presented in Dames & Moore, 1979. The wind patterns and intensity factors were correlated by PMEL to the 22 baric weather patterns developed in Putnins, 1966a. A catalog of approximately 19 continuous years of daily baric weather patterns (Putnins, 1966b) was converted to a corresponding wind pattern and intensity catalog.

Surface currents were divided into two spatially varying components, a time-dependent tidal flow and a constant net surface circulation. The tidal flow field for Lower Cook Inlet was the same as that developed in Dames & Moore, 1979 and represents average tidal current velocities based on harmonic analyses of current measurements in combination with the results of a tidal flow hydrodynamic model. The tidal flow field was expanded to include Shelikof Strait using harmonic analyses of current measurements from two moorings within the strait.

The net surface circulation was represented by winter and summer net current patterns derived from analyses of current measurements, published literature, and a previously developed net circulation pattern (Dames & Moore, 1979).

In order to obtain a statistically significant sample of trajectory impact locations for subsequent risk analyses by the USGS, 200 trajectories were initiated at each launch site for both summer and winter seasons for a total of 15,200 trajectories. The winter season was defined from October through March and the summer season was defined from April through September. The basis for the seasonal designation was limited by the knowledge of the seasonal variation of net surface currents.

Each trajectory was initiated by randomly selecting a day/month/year within the desired season and entering the converted wind catalog for that date. The wind field was then sequenced from the initial starting date, every 24 hours according to the following observed weather pattern. The net current pattern for that season was held constant for the duration of

trajectory simulation. The tidal current pattern was time dependent with the initial tidal phase incremented 30 degrees for each sequential trajectory.

A limited analysis was performed on the trajectory impact locations by season for all sites combined and for two selected sites individually. The results are presented in terms of the percent frequency of boundary impact per kilometer along discrete reaches of the shorelines of Lower Cook Inlet and Shelikof Strait.

The primary results from the present oil spill trajectory simulation were the 15,200 trajectories delivered to the USGS for use in their oil spill risk assessment study (LaBelle, 1980). These trajectories represent the most comprehensive set of descriptors of surface transport behavior available in Lower Cook Inlet and Shelikof Strait.

Two major improvements in the data base allowed consideration of seasonal effects on trajectory movement to be made for the first time. The availability of processed and analyzed winter net current data resulted in the ability to estimate winter and summer net current patterns. In addition, the use of Putnins' continuous daily weather catalog coupled to revised local wind fields over Lower Cook Inlet and Shelikof Strait also provided the ability to evaluate seasonal effects of the meteorological component of the trajectory driving forces.

The inclusion of variability of the wind fields resulted in complex trajectory behavior considering each trajectory independently. However, collectively the trajectories moved and/or

impacted the shoreline in preferred directions or locations based primarily on launch site and season. Considering all sites combined and ignoring impacts along open water boundaries, the following areas experienced relatively high frequencies of shoreline impacts:

1. The northern and central shorelines of Shelikof Strait
2. Augustine Island
3. The Barren Islands
4. Kalgin Island
5. The western shoreline of Kamishak Bay
6. The western shoreline of Lower Cook Inlet between Iniskin Bay and Chisik Island
7. The shoreline of Lower Cook Inlet directly west of Kalgin Island
8. The eastern shoreline of Lower Cook Inlet between Anchor Point and Ninilchik

The major overall seasonal effect observed in the trajectories was a northward shift of the paths and impact locations during the summer season. This is a direct result of the decreased magnitude of the net current through Shelikof Strait and the increased frequency of northerly wind fields during the summer.

Further improvements in trajectory simulation for Lower Cook Inlet and Shelikof Strait using the deterministic approach taken in Dames & Moore (1976, 1979), and the present study should focus primarily on refining the temporal and spatial accuracy of the data bases. Incorporating diurnal variations in the wind fields would add to the dispersion of trajectories observed in the present study and would increase the ability to realistically model the meteorological forcing of surface transport.

The knowledge and accuracy of net surface currents in northern Lower Cook Inlet has not been improved over those used

in the 1979 study. Unprocessed current meter records exist and analysis of these records would significantly improve the accuracy and reliability of the resulting trajectories in this portion of the study area. The variability of the net surface currents over periods of time as short as 24 hours have been observed to be significant both in terms of magnitude and direction. Incorporation of this effect would also add to the dispersive nature of trajectory paths and impact locations and would also increase the ability to realistically model the forcing fields.

These and other improvements would require significant commitments of time and resources to perform field programs and data analyses. With the exception of the currents in northern Lower Cook Inlet, it is questionable whether the improvements if incorporated would provide cost effective increases in the present knowledge of surface transport characteristics in Lower Cook Inlet and Shelikof Strait. If the emphasis shifts from large regional studies of trajectory behavior to those local areas of concern identified by the regional studies, then those improvements in the data base would become mandatory. Local effects, such as a diurnal sea breeze, drainage winds, near coast circulation features, would need to be examined in detail as well as the variability of these features on a shorter time interval. This is a direct result of the fact that as the length scale of the area of interest becomes smaller, the time scale of the features modeled must be decreased (if the magnitudes of the forcing functions remain relatively constant) to provide the

level of detail necessary to accurately evaluate the resulting trajectory movement.

It is also concluded that continued studies on a regional level of the behavior of spilled oil should begin to examine the physical characteristics of spills such as spreading, weathering, sinking and interactions with winds, waves and ice. These studies will provide more specific information from which environmental effects of spilled oil can be assessed.

CONTENTS

	<u>Page</u>
I. Introduction	244
Purpose	244
Scope	244
Objectives	245
II. Modeling Approach	246
Oil Spill Model	246
Grid Coverage	247
Oil Spill Scenarios	248
III. Input Data Development and Application	250
General	250
Putnins' Weather Catalog	251
Wind Fields	254
Net Current Patterns	255
Tidal Current Pattern	260
IV. Simulation Results	262
V. Conclusions and Recommendations	273
Bibliography	277
Appendix A - Wind Field & Intensity Catalog Input Data File	318
Appendix B - Wind Field Input Data File	323
Appendix C - Net Current Field Input Data File	334
Appendix D - Tidal Current Field Input Data File	342

LIST OF FIGURES

Figure

		279
1	Grid System	279
2	Trajectory Launch Sites	280
3	Wind Field 1	281
4	Wind Field 2	282
5	Wind Field 3	283
6	Wind Field 4	284
7	Wind Field 5	285
8	Winter Net Current Pattern	286
9	Summer Net Current Pattern	287
10	Tidal Current Phase Distribution	288
11	Tidal Current Pattern - Phase = 0°	289
12	Tidal Current Pattern - Phase = 90°	290
13	Tidal Current Pattern - Phase = 180°	291
14	Tidal Current Pattern - Phase = 270°	292
15-18	Sample Trajectories, Site P7, Winter	293 - 296
19-22	Sample Trajectories, Site P7, Summer	297 - 300
23-26	Sample Trajectories, Site P3, Winter	301 - 304
27-30	Sample Trajectories, Site P3, Summer	305 - 308
31-32	Base Case Trajectories, Site 8, Dames & Moore (1979)	309 - 310
33	Boundary Impact Frequency, Site P7, Winter	311
34	Boundary Impact Frequency, Site P7, Summer	312
35	Boundary Impact Frequency, Site P3, Winter	313
36	Boundary Impact Frequency, Site P3, Summer	314
37	Annual Percent Probability of Exposure, Site 8, Dames & Moore (1979)	315
38	Boundary Impact Frequency, All Sites, Winter	316
39	Boundary Impact Frequency, All Sites, Summer	317

LIST OF TABLES

Table

I	Conversion Factors From Putnins' Weather Typology to PMEL's Wind Field and Intensity Factors	252
II	Wind Field Frequency of Occurrence	256
III	Wind Field Frequency of Occurrence Accounting For Intensity	257
IV	Percentage of Trajectories Exceeding Upper Time Limit of 10 Days	271

I. Introduction

Purpose

This study was initiated by the Outer Continental Shelf Environmental Assessment Program (OCSEAP) on behalf of the Bureau of Land Management. Two previous oil spill trajectory analyses covering the Lower Cook Inlet area were performed for the OCSEAP (Dames & Moore, 1976; Dames & Moore, 1979). These studies provided information on probable shoreline impact areas and associated time to impact of hypothetical oil spills originating from a total of 21 selected point spill locations within Lower Cook Inlet.

The present study extended the areal coverage to include Shelikof Strait and provided significant improvements in the environmental data fields. The calculated trajectories were supplied to the USGS for their use in an oil spill risk assessment study (LaBelle, 1980).

Scope

This study was conducted in accordance with the scope of services for Task I detailed in the Dames & Moore proposal, "Oil Dispersion Analysis, Lower Cook Inlet and Shelikof Strait, Alaska," RFX41-436-2905, for National Oceanic and Atmospheric Administration, July 19, 1979 and "Proposal Addendum, Oil Spill Dispersion Analysis," RFX41-436-2905, October 15, 1979, subsequently amended in a letter dated February 4, 1980.

Objectives

The primary elements of the scope of services for Task 1 presented in the above documents are summarized below:

1. Expand the areal coverage of the modeling effort to incorporate Shelikof Strait.
2. Update and extend the net and tidal current fields based on information supplied by Pacific Marine Environmental Laboratories (PMEL).
3. Revise and extend surface wind patterns developed by PMEL corresponding to specific baric weather patterns identified by Putnins (1966a and 1969).
4. Calculate trajectories from sites specified by the USGS using a daily sequence of wind patterns corresponding to historically observed baric weather patterns (Putnins, 1966b).
5. Provide trajectory information to the USGS in a computer compatible format as input to a risk assessment study.
6. Evaluate the applicability of a first order wind field transition matrix to represent historically observed sequences and variability of wind fields as applied to trajectory simulation.

Elements 1-5 are reported upon here; results of the analyses conducted under element 6 are in preparation and will be reported in a separate submittal.

II. Modeling Approach

Oil Spill Model

The theoretical basis of the oil spill model used in this study is the same as employed in the two previous OCSEAP oil spill trajectory analyses performed for the Lower Cook Inlet area (Dames & Moore, 1976; 1979). Modifications to the computer program embodying the model were necessitated to allow implementation on a UNIVAC 90/60 computer. Additional modifications were performed to facilitate an increased efficiency in handling input/output requirements that were significantly larger due to expanded grid coverage, time variability of the wind fields and increased number of trajectory runs. Model verification was performed and was in agreement with the verification reported in Appendix A of Dames & Moore, 1979.

Movement of the spill centroid in the Dames & Moore model was considered to be governed by the independent effects of wind and water currents. Second-order forces such as waves and wind-wave current interaction were neglected. The wind-induced velocity vector of the trajectory centroid was taken to be colinear with the wind vector and proportional to the wind speed. The proportionality constant has been experimentally found in the range from 1 to 5 percent (Oceanographic Institute of Washington, 1977) and was taken to be 3 percent for this study. There is some question as to whether the wind and slick vectors should be colinear due to the considerable scatter in relevant field data. However, the evidence is not conclusive on this issue and, hence, this study assumed colinearity.

In the absence of winds, the slick centroid was modeled to move at the same velocity as the underlying current. As with the wind-driven component, there is no conclusive set of evidence which documents that this is the best approach. However, alternative schemes (i.e., Swartzberg, 1971) have major flaws or have been subjected to limited validation.

For this study, the current field was divided into two components, a net surface component and a tidal component. Hence, the centroidal velocity vector can be written as:

$$\bar{U}_{oil} = 0.03 \bar{U}_{wind} + \bar{U}_{tidal} + \bar{U}_{net} \quad (1)$$

With input data available to the model, a trajectory was generated by evaluating Equation (1) over a sequence of finite time steps ($\Delta t = 30$ minutes) until the centroid reached a boundary or exceeded an upper limit on time.

Grid Coverage

Operational implementation of the oil spill model was based on a grid system that overlapped the area of interest as illustrated in Figure 1. The grid system served multiple purposes: (1) definition of the Cook Inlet and Shelikof Strait geometry, (2) input of wind and current information, and (3) definition of shoreline impact locations.

This grid system was oriented along the main axis of Lower Cook Inlet and Shelikof Strait with each grid cell being 3 km on a side. Characteristic features required by the model, such as land and water areas and open water boundaries, were prescribed by assigning to each cell an index that defined the predominant

feature of that cell. Land boundaries were chosen to represent the best approximation of the geometric extent of the inlet.

The boundary of the grid system shown in Figure 1 ignored those bays, inlets and channels that were not considered major features of the Lower Cook Inlet and Shelikof Strait system. The surface winds and water motions within these areas are dominated by local effects that cannot be determined from the regional wind and flow patterns developed for the larger open water areas of Lower Cook Inlet and Shelikof Strait. Without detailed oceanographic and meteorological data in each embayment, inlet, or channel, it was not possible to accurately simulate the movement of a spill centroid for these areas. Therefore, for those cases where the trajectory intersected one of these boundary conditions, the trajectory was terminated. It was concluded that oil would have entered the bay, inlet, or channel, but its subsequent behavior is unknown.

Oil Spill Scenarios

The locations of oil spill launch sites for the trajectory study were specified by the USGS since the results of the trajectory analysis were to be used by the USGS in an oil spill risk assessment (LaBelle, 1980). The launch sites specified were substantially different from those used in the previous trajectory analyses (Dames & Moore, 1979; 1976). Except for one point site, all launch sites were designated as line sources as shown in Figure 2. These line sources represent launch sites that cover potential platform locations, tanker or pipeline transportation routes, or water grid boundaries. The water grid boundary

launch sites were selected by USGS to allow them to pick up a trajectory moving out of the boundary and continue the trajectory simulation beyond the Dames & Moore grid system.

From each launch site shown in Figure 2, 400 trajectories were initiated. For the line sources, the trajectory starting locations were evenly distributed along the total length of the line. Two hundred trajectories were launched from each site during a summer and winter season for a total of 400 trajectories per site. The number of trajectories per site per season was specified by the USGS as being the minimum number of trajectories required to obtain statistical significance for their risk assessment. The total number of trajectories that were calculated for the Lower Cook Inlet and Shelikof Strait area was 15,200 (38 sites x 200 trajectories per site per season x 2 seasons). This represented an increase of approximately 20 times the number of trajectories that were run in the 1979 Dames & Moore trajectory analysis. The results of these trajectories were supplied on computer compatible magnetic tape to the USGS.

III. Input Data Development and Application

General

The primary emphasis on input data development for the present study was to improve the wind fields and implement a technique that would realistically approximate their variability. Recommendations made at the conclusion of the 1979 trajectory analysis recognized this simulation deficiency and concluded, "the results of this project indicate that the wind fields and their simulated behavior are the most limiting aspect of the environmental data base" (Dames & Moore, 1979).

Secondary emphasis was placed on improvements in the net current field made possible by the availability of analyzed winter current measurements and ongoing studies of the general circulation features of the Lower Cook Inlet and Shelikof Strait system. The availability of winter current data provided the potential for development of at least two seasonal net current patterns, winter and summer. The ongoing circulation studies provided information that would allow refinement of the spatial features of the previously developed net circulation pattern.

Due to the inclusion of Shelikof Strait, which increased the study area nearly two-fold, another aspect of input data development was to collect and analyze the necessary information to expand both the wind and current fields to cover Shelikof Strait.

All of the above input data improvements were to be extracted from available OCSEAP reports. However, during the course of the study, certain data was not available in the requisite format. This necessitated additional data analyses to

develop the required fields. Detailed discussion of the input data development is provided in the following sections.

Putnins' Weather Pattern Catalog

The original intent of the meteorological input data was to utilize variable wind fields with improved spatial resolution developed by PMEL. The variability of the wind fields was to be prescribed by a transition matrix also developed by PMEL based on their meteorological data and analyses in the Lower Cook Inlet and Shelikof Strait area. Based on a preliminary meeting, it became apparent that these data products were not going to be available in time to incorporate them into the trajectory analysis. It was agreed that PMEL would revise the Putnins' wind fields used in the previous trajectory studies (Dames & Moore, 1979; 1976) and provide a transition matrix based on Putnins' work (Putnins, 1966a; 1969). Review of the Putnins' transition matrix provided by PMEL revealed that it was incomplete and overemphasized the more frequently occurring weather patterns. A solution to this problem was obtained by utilization of Putnins' unpublished tabulations of approximately 19 years of daily baric weather patterns (Putnins, 1966b).

Putnins developed 22 specific baric weather patterns describing mesoscale weather situations over Alaska. These 22 baric weather patterns were related to 5 wind fields and 6 wind field intensities as developed by PMEL and shown in Table I (PMEL, 1980). These wind patterns and intensity conversions allowed two approaches to the utilization of Putnins' catalog of daily baric weather patterns. The first approach was to use the

TABLE I
 CONVERSION FACTORS FROM PUTNINS' WEATHER TYPOLOGY
 TO PMEL'S WIND FIELD AND INTENSITY FACTORS

<u>Putnins</u> <u>Type</u>	=	<u>PMEL</u> <u>Type</u>	(<u>PMEL Type</u> <u>Wind Field</u> / <u>Intensity Factor</u>)
A	=	25	1 = Figure 3 1 = 0.3
A _C	=	25	2 = Figure 4 2 = 0.5
A'	=	53	3 = Figure 5 3 = 1.0
A"	=	33	4 = Figure 6 4 = 1.2
A'''	=	43	5 = Figure 7 5 = 1.5
A ₁	=	15	6 = 0.7
A ₂	=	43	
A ₃	=	31	
B	=	16	
C	=	22	
C ₁	=	42	
D	=	23	
D'	=	15	
D ₁	=	23	
E	=	45	
E'	=	42	
E"	=	26	
E ₁	=	22	
F	=	43	
F ₁	=	23	
G	=	53	
H	=	14	

Example: PMEL Type 45 represents wind field number 4 as shown in Figure 6 with all magnitudes increased by a factor of 1.5 as denoted by the intensity factor index 5. PMEL Type 45 is equivalent to Putnins' Weather Type E.

catalog directly, entering with a random date and historically sequencing the wind fields as converted by Table I from the weather types given in the catalog. The second approach was to use the catalog to calculate a first order transition matrix and use this matrix to sequence the wind fields. The former method was selected for this trajectory study because certain unresolved questions remained regarding the applicability of a first order transition matrix to the accurate sequencing of weather patterns in Alaska. These questions are currently under study with the results to be presented in a succeeding report.

Seasonal variability of the full suite of trajectory driving forces was limited by the ability to define the seasonal characteristics of the net current pattern. Since only "winter" and "summer" net current patterns could be developed from the data sources, the wind fields were also applied seasonally by "winter" and "summer" conditions defined by the chosen starting date of the catalog. Winter conditions were defined as occurring from October through March, and summer conditions defined as occurring from April through September.

The wind field catalog includes all days from January 1, 1945 through March 31, 1963. The wind field sequencing was initiated by randomly selecting a day, month and year. As the trajectory simulation proceeded, the wind fields were sequenced every 24 hours corresponding to the observed sequence in the catalog. This sequencing continued until the trajectory impacted a boundary or exceeded a time limit of 10 days. The daily catalog

of wind fields and intensities that were used for the trajectory simulation is presented in Appendix A.

Wind Fields

As briefly discussed in the previous section, the original intent regarding preparation of the meteorological input data was for PMEL to develop representative wind fields over Lower Cook Inlet and Shelikof Strait as a direct result of their ongoing meteorological programs. The required products were not available within the schedule limitations of the trajectory simulation study. This necessitated a less rigorous treatment of the wind fields and it was agreed that PMEL would provide revisions to wind fields previously developed by Dames & Moore for use with Putnins' typology. PMEL's direct exposure to local wind characteristics, derived during their meteorological field measurement program and data analysis, would provide added confidence in the wind field development. The five wind fields developed by PMEL were reviewed in Anchorage, Alaska on February 6, 1980 during a combined meeting with PMEL, Dames & Moore and local meteorologists.

The revised wind fields included the spatial variability of wind speed and direction over Lower Cook Inlet and Shelikof Strait. In addition, wind intensity scaling factors were assigned to each wind field to account for the relative strength or weakness of the wind pattern as related to a particular Putnins' baric weather pattern. The intensity scaling factors that were applied to each wind field essentially multiplied all

speeds by a constant factor; the direction was unaffected by this scaling process.

The five basic wind fields are shown on Figures 3 through 7, and the relationship between intensity, wind field and baric weather pattern is presented in Table I. The digitized input data files for the five basic wind fields are presented in Appendix B. Table II presents the percent frequency of occurrence for the five basic wind fields for summer, winter and annual conditions. These frequencies were derived from the 19 years of converted daily weather catalog data. Table III presents the percent frequency of occurrence for the 13 specific combinations of wind fields and intensity factors for summer, winter and annual conditions. A comparison of the summer and winter frequencies of occurrence indicates that seasonal variations in percentages are significant.

Net Current Patterns

The net current pattern utilized in the 1979 trajectory analysis (Dames & Moore, 1979) was developed primarily from current measurement data taken by PMEL and NOS during summer months from May to August. Thus, the pattern was representative of summer conditions and seasonal variations of the net surface circulation were not included in the 1979 trajectory analysis.

The objective of developing updated current patterns for the present study was to include seasonal variations based on published information from PMEL. Winter current meter data had been processed and analyzed by PMEL and thus afforded an opportunity to estimate at least a representative average summer and

TABLE II
WIND FIELD FREQUENCY OF OCCURRENCE

<u>PMEL Type</u> <u>(Wind Field)</u>	<u>Percent Frequency of Occurrence</u>		
	<u>Summer</u> <u>(April-Sept)</u>	<u>Winter</u> <u>(Oct-March)</u>	<u>Annual</u>
1	11.60	20.21	15.95
2	17.15	32.33	24.83
3	9.71	2.61	6.12
4	36.40	21.04	28.64
5	25.14	23.81	24.46

TABLE III
WIND FIELD FREQUENCY OF OCCURRENCE
ACCOUNTING FOR INTENSITY

PMEL Type (Wind Field/Intensity Factor)	<u>Percent Frequency of Occurrence</u>		
	Summer (April-Sept)	Winter (Oct-March)	Annual
14	3.83	10.42	7.16
15	6.44	9.11	7.79
16	1.34	0.68	1.01
22	2.00	2.73	2.37
23	6.65	14.37	10.55
25	8.29	14.28	11.32
26	0.36	1.10	0.74
31	1.37	0.65	1.01
33	8.35	1.96	5.12
42	15.94	11.07	13.48
43	12.72	5.02	8.82
45	7.74	4.96	6.33
53	24.97	23.67	24.30

winter net surface circulation pattern. Temporal variations of each pattern were not able to be specified from the available data base. The area of coverage was expanded to include Shelikof Strait.

The published reports that were used to develop the winter and summer net current patterns included Muench, et al. (1978, 1980); Schumacher, et al. (1978, 1979); and Reed, et al. (1979). In addition, a visit was made to PMEL to obtain clarification of certain data and results and to extract newly analyzed and unpublished data (Muench, 1979). These data sources were used to modify and expand the representative average net summer circulation pattern presented in Dames & Moore, 1979. An average net winter circulation pattern was also developed from the above data sources. Major features of both the summer and winter net circulation patterns are in agreement with the circulation pattern presented in Muench, et al. (1980). Flow patterns in the northern portion of Lower Cook Inlet, not covered by the pattern presented in Muench, et al. (1980), were extracted from the pattern presented in Dames & Moore (1979). The net circulation pattern for northern Lower Cook Inlet was described in Dames & Moore (1979) as being at best a rough estimate. No new data or analyses were found in the publications used to develop the patterns for this study that would increase the confidence or accuracy of the net circulation pattern in this area of Lower Cook Inlet.

The net surface circulation patterns for representative winter and summer conditions are shown on Figures 8 and 9, respectively and are presented in digitized form in Appendix C.

Winter is defined as that period from October through March, and summer is defined as that period from April through September.

One important aspect of the net current input data that could not be addressed with the information contained in the publications used to develop the net current patterns is their variability with time. The spatial distribution of current meter moorings within Lower Cook Inlet and Shelikof Strait was not adequate to represent the current variability by using standard deviations of the mean. This technique was used in a limited analysis in conjunction with an assumed normal distribution for selected areas with dense current meter coverage in Lower Cook Inlet for the Dames & Moore 1979 study. For the present study, two current meter moorings are used to describe the currents in Shelikof Strait, and none are available to characterize the surface current variability in northern Lower Cook Inlet. For the present trajectory simulation analysis, the current variability would need to be specified over the entire area of coverage.

The variability of the magnitude and direction of measured currents in Lower Cook Inlet and Shelikof Strait has been discussed in Muench, et al. (1980); Muench, et al. (1978); and Schumacher, et al. (1978). In summary, these publications characterize the current variability in Lower Cook Inlet and Shelikof Strait as having speed and direction fluctuations with time scales of 2 to 7 days. Shelikof Strait has a strong mean flow and experiences fluctuations in speed and direction that are smaller relative to the mean flow compared to regions of weak mean flow, such as in central Lower Cook Inlet, where the

fluctuations become the dominant flow characteristic. Attempts to correlate the fluctuations observed from the various current moorings generally revealed a poorly related sequence of flow events. The one exception occurred between the two current meter stations located within Shelikof Strait. This was expected in that Shelikof Strait has confining lateral boundaries which, due to continuity considerations, suggest that a fluctuation at one end would generate a compensating fluctuation at the other end.

Tidal Current Pattern

The tidal current pattern developed in Dames & Moore (1979) was expanded to cover Shelikof Strait. The semidiurnal tide has a standing wave characteristic within Shelikof Strait as a result of the progressive tidal wave entering the strait from both the north and south end as it passes Kodiak Island. This results in an antinode, where no semidiurnal tidal current component would exist, located in the upper third of the strait.

The semidiurnal component of tidal current was selected to represent average tidal current conditions to be consistent with the analyses present in Dames & Moore (1979). The magnitude of both the ebb and flood M_2 tidal current constituent were assumed equal. The spatial distribution of the M_2 tidal current constituent in Lower Cook Inlet was interpolated in the Dames & Moore (1979) study with the aid of a two-dimensional hydrodynamic tidal model (Mungall and Matthews, 1973; and Mungall, 1973). Application of this model over the expanded study area was not conducted since it was believed that the tidal currents within the strait

could adequately be interpolated from existing measurements and harmonic analyses by applying basic hydrodynamic principles.

Therefore, the tidal current pattern developed for the present study was based on the pattern developed in Dames & Moore (1979) and expanded to cover Shelikof Strait by interpolating the results of harmonic analyses of current meter data from two mooring locations in Shelikof Strait. Likewise, the spatial distribution of the tidal current phase angle was based on that presented in Dames & Moore (1979) and expanded to cover Shelikof Strait by interpolating the phase relationships of the harmonic analyses of current meter data given in Muench, et al. (1980) and as discussed with Muench (1979). The resulting tidal current phase distribution for the entire study area is shown in Figure 10. Tidal current vector patterns for phase angles of 0, 90, 180 and 270 degrees are shown in Figures 11 through 14, respectively. The zero phase angle was arbitrarily defined for the southern portion of Lower Cook Inlet on a line between Cape Douglas and Cape Elizabeth. The phase relationships shown are representative of peak tidal currents occurring during a mean tidal range with a single value corresponding to an average of the peak ebb and flood tidal current phases. The digitized tidal current field input data file is presented in Appendix D.

IV. Simulation Results

The primary results from the trajectory simulation for Lower Cook Inlet and Shelikof Strait were the computer tapes containing the 15,200 trajectories. These tapes were delivered to the USGS for subsequent use in an oil spill risk assessment. Therefore, no attempt was made to perform a complete trajectory analysis. However, a limited analysis was conducted in order to highlight the major findings, comparisons, and conclusions as a result of the present trajectory simulation study.

The most significant improvement over the trajectory simulation presented in Dames & Moore, 1979 is the inclusion of wind field variability. The 24 hour sequencing of wind fields in the present study more realistically represents the temporal variability of surface winds than the assumed 150 hour constant wind fields used in the 1979 study.

Examples of trajectories calculated in the present study are shown in Figures 15 through 30. These figures present sample trajectories from two launch sites, P7 and P3, for a variety of wind sequences on a seasonal basis. Comparison of these figures with Figures 31 and 32 (reproduced from Figures B-35 and B-53 presented in Dames & Moore, 1979) reveals a significant change in the behavior of a majority of the trajectories calculated in the present study. While persistence of the wind fields is evident for some of the trajectories presented in Figures 15 through 30, total reversals and major changes in direction are observed for the majority of the trajectories. Thus, the results of modeling the variability of the wind fields in the present study

reinforces the conclusion reached in the 1979 study that the wind dominates trajectory movement. This conclusion should bear in mind that the variability of the other forcing fields, net and tidal currents, was not incorporated in the trajectory modeling effort for the present study. It would be reasonable to assume that the wind would dominate trajectory movement even if these effects were realistically modeled.

Figures 15 through 18 show sample trajectories from launch site P7 during the winter season. Ten trajectories are plotted on each figure. The trajectories exhibit two preferred directions; to the west into Kamishak Bay and to the southwest into Shelikof Strait. These directions were primarily a result of the vectorial combinations of the winter net current pattern and wind fields 1, 2 and 4. These wind fields occurred approximately 74% of the time during the winter season as shown on Table II. Therefore, trajectories with directions other than into Kamishak Bay and Shelikof Strait would be the exception rather than the rule.

Travel time to impact varied widely depending on many parameters so that no attempt was made to evaluate the elapsed time to impact in detail. The elapsed time to impact for trajectories from launch site P7 during winter conditions ranged from 12 hours up to the simulation time limit of 240 hours (10 days).

Figures 19 through 22 present sample trajectories from launch site P7 during the summer season. Ten trajectories are plotted on each figure. Comparison of the winter and summer trajectories showed a significant shift of overall trajectory movement. The

summer trajectories penetrated further up into Lower Cook Inlet than the winter trajectories. This occurred even though the summer net current magnitude in Lower Cook Inlet was greater than in winter. Wind fields 3 and 4 would combine vectorially with the net current field to generate movement up into Lower Cook Inlet. These two wind fields occurred approximately twice as frequently in summer as in winter (46% to 26% of the time) which resulted in the observed change in overall trajectory movement up into Lower Cook Inlet during summer conditions. The elapsed time to impact for trajectories from launch site P7 during summer conditions ranged from 14 to 240 hours.

Trajectories were also examined from site P3. As shown in Figure 2, site P3 is a point source site and was located in very nearly the same location as site 8 from the 1979 study. The selection of site P3 for trajectory analysis in the present study allowed limited qualitative comparisons to be made between the results of the two studies. Sample trajectories are provided in Figures 23 through 30. There are ten sample trajectories plotted on each figure and four figures presented for each season.

Site P3 was located near the north end of Shelikof Strait where the flows from Lower Cook Inlet and through Kennedy and Stevenson Entrances converged to form a strong southwesterly net flow. Based on this net flow and the dominant winter wind fields it would be expected that the primary trajectory movement would be to the southwest into Shelikof Strait during the winter season. In fact, this conclusion was shown to be true for those trajectories presented in Figures 23 through 26. These sets of

figures represent sample trajectories calculated during winter conditions. None of the sample trajectories presented in these figures showed movement into Lower Cook Inlet northward of Augustine Island. The elapsed time to impact for trajectories from launch site P3 during winter conditions ranged from 30 to 240 hours.

During summer conditions the net flow into and through Shelikof Strait weakened and the frequency of wind fields 3 and 4, which have north-northeasterly flow in the vicinity of P3, increased significantly. The combination of these two factors should have resulted in an overall shift of trajectories northward with some increase in transport into Lower Cook Inlet. Also, the reduced net current magnitudes through Kennedy and Stevenson Entrances during the summer should have allowed an increase in trajectory movement toward the Barren Islands from site P3. Figures 27 through 30 show in a qualitative sense that the above features were, in fact, observed. These figures show an increase of trajectories moving into Kamishak Bay and around the Barren Islands over that observed during winter. Some trajectories moved north of Augustine Island basically keeping to the middle or western side of Lower Cook Inlet. The elapsed time to impact for trajectories from launch site P3 during summer conditions ranged from 23 to 240 hours.

Since it was not feasible to meaningfully present all trajectories from one site, much less all sites, summary figures were developed showing percent frequency of boundary impact per kilometer of boundary. The shoreline and water boundaries were

segmented into representative reaches and the frequency of trajectory impact was calculated for each reach for winter and summer conditions. The frequency of impact per kilometer of reach was displayed by the width of each line segment. This technique provided a qualitative visual aid in evaluating trajectory impact distribution.

Figure 33 presents the percent frequency of boundary impact per kilometer of reach for site P7 for winter conditions. The most obvious feature was the high frequency of impact which occurred near Chenik Head along the west side of Kamishak Bay. This was due primarily to wind fields 2 and 4 which occurred over 53% of the time during winter and had westerly flows that would clearly dominate trajectories in the weak net and tidal current fields existing in Kamishak Bay. Relatively large frequencies of impact also occurred along the western reach of Augustine Island and the northern exposed reach of Uganik Bay. Both shorelines of middle and northern Shelikof Strait were impacted with regular frequency. Other areas that had significant impact frequencies included the Barren Islands and the western shoreline of Lower Cook Inlet from Ursus Cove to just below Chisik Island. No impacts were recorded north of Chisik Island nor along the eastern shoreline of Lower Cook Inlet. This area included Kachemak Bay southward around Cape Elizabeth to the Chugach Islands.

Figure 34 presents the percent frequency of boundary impact per kilometer of reach for site P7 for summer conditions. The high impact frequency near Chenik Head was again apparent, but

was lesser in magnitude than that observed during winter conditions. This was presumably due to the stronger southwesterly net flow in central Lower Cook Inlet during the summer conditions as wind fields 2 and 4 maintained a strong 53% combined frequency of occurrence during the summer conditions. The shift in impact location toward the north during summer was evident in this figure. Impacts along both shorelines of Shelikof Strait were observed to diminish during summer. Augustine Island had an increase in impact frequency as did the Barren Islands. Most notably the western shoreline of Lower Cook Inlet from Iniskin Bay to just north of Chinitna Bay displayed a dramatic increase in impact frequency. The northern portion of Lower Cook Inlet was again void of any trajectory impacts, but some trajectories now impacted the eastern shoreline near Anchor Point in Kachemak Bay and along Cape Elizabeth. Rather significant frequency of impacts occurred along the water boundaries of Kennedy and Stevenson Entrances suggesting possible transport into the Gulf of Alaska northeast of Kodiak Island. Impacts also occurred at a lesser frequency along the water boundary between the southern tip of Kodiak Island and the Alaska Peninsula, indicating transport south of Kodiak Island.

Figures 35 and 36 present the percent frequency of boundary impact per kilometer of reach for site P3 for winter and summer conditions, respectively. The winter figure indicated a rather even distribution along the western shoreline of Kamishak Bay and southward along both shorelines of Shelikof Strait. No impacts were recorded north of Augustine Island and the largest impact

frequencies occurred along the shorelines in the central portion of Shelikof Strait. This portion of Shelikof Strait, between Cape Gull and Uganik Bay represents the narrowest width of the strait. In addition, this area marks a transition in a slight alignment change between upper and lower Shelikof Strait. Therefore, it would be expected that this region would experience a greater frequency of impact from trajectories moving up or down the strait due to the narrow width and slight change in geometric alignment.

Figure 36 reveals that summer conditions again result in a general northward shift of impact locations compared to those observed during winter conditions. The frequency distribution along the shorelines of Shelikof Strait had lessened in magnitude and extent. The frequency of impacts which occurred along the western shoreline of Kamishak Bay dramatically increased over that observed during winter conditions. The Barren Islands had a high frequency of impact primarily along the western and southern exposure of their shorelines. Impacts also occurred along the southern shoreline of Augustine Island and the western shoreline of Lower Cook Inlet from Iniskin Bay northward beyond Chinitna Bay. A relatively high frequency of impacts occurred along the water boundary of Kennedy and Stevenson Entrances for both winter and summer conditions. However, only winter conditions indicated trajectory movement as far south as the boundary between the southern tip of Kodiak Island and the Alaska Peninsula.

Although a direct comparison of trajectory impact cannot be made for site P3 in the present study and site 8 in the 1979

study, Figure 37 is presented for a qualitative discussion. Figure 37 is reproduced from Figure B-89 of Dames & Moore, 1979, and presents the annual percent probability of shoreline exposure for trajectory impacts from site 8 of that study. Three regions were shown to have high probabilities of trajectory impact. These were the southern shoreline of Augustine Island, Cape Douglas and the northern and western shoreline of Shuyak Island. Also impacted, but to a lesser extent was the shoreline south of Chinitna Point and the shoreline near Anchor Point. The present study agreed with the high frequency of impacts along Shuyak Island and Cape Douglas, but did not indicate as high a relative frequency of impacts on Augustine Island. Within the same areal coverage as the 1979 study, the present study indicated high impact frequencies occurred among the Barren Islands and along the western shoreline of Kamishak Bay. These were areas that the 1979 study did not show as being impacted. The results of the two studies were in agreement with respect to the low frequency of impacts which occurred north of Augustine Island. Both studies showed no impacts near Kachemak Bay.

Figures 38 and 39 present the percent frequency of boundary impact per kilometer of reach for all sites for winter and summer conditions respectively. Again, the most general trend observed was a shift of trajectory impact location from the south to the north when comparing winter to summer conditions. Areas of high frequency of impact included the western shoreline of Kamishak Bay, Augustine Island, the Barren Islands, the western shoreline of Lower Cook Inlet from Iniskin Bay to north of Chinitna Bay and

the central and northern shorelines of Shelikof Strait. The relatively high impact frequencies for the water boundary of Kennedy and Stevenson Entrances and the water boundary between the southern tip of Kodiak Island and the Alaska Peninsula were somewhat misleading. This was due to the fact that these boundaries were also used as launch sites for a significant number of the total trajectories simulated. Therefore, the frequencies along these boundaries were expected to be relatively high. Kamishak Bay is shown on both Figures 38 and 39 to have had very low frequencies of impacts. The southern shorelines of Shelikof Strait also had relatively low frequencies of impacts.

These figures provide a visual summary description of the trajectory simulation from a boundary impact viewpoint. However, the location of all launch sites should be kept in mind as they have just as direct an influence of impact location as the forcing fields used to drive the trajectories.

The percentage of trajectories that did not impact a boundary prior to exceeding the upper time limit of 10 days is presented in Table IV for sites P7, P3 and all sites combined for winter and summer conditions. This table shows that the time limitation of 10 days affected only a minor portion of the total number of trajectories run. In addition, the table shows the percentages for summer slightly and consistently higher than those for winter. This may be attributed to the stronger flows throughout most of the study area that occur in winter as well as an increased percent frequency of occurrence of wind fields with higher intensity factors during winter conditions.

TABLE IV
 PERCENTAGE OF TRAJECTORIES REACHING UPPER
 TIME LIMIT OF 10 DAYS

<u>Site</u>	<u>Percent of Trajectories</u>	
	<u>Winter</u>	<u>Summer</u>
P7	6.5	8.5
P3	6.0	9.0
All Sites	6.8	8.2

A brief qualitative discussion of some aspects of the results of this trajectory analyses has been presented to help clarify the methodology and approach. The quantitative aspects of the results are the subject of the USGS risk assessment study (LaBelle, 1980). Tapes of all trajectory runs are being maintained by Dames & Moore if additional analyses are desired.

V. Conclusions and Recommendations

A brief discussion and samples of the results of this trajectory study were presented in the previous section. Without performing a detailed analysis of the trajectory results, only general conclusions can be drawn from this study.

Implementation of wind field variability was one of the primary objectives of this study. The persistence of the wind fields as well as the variability was incorporated through the use of Putnins' weather catalog and marks a significant improvement over the methodology employed in the 1979 study. The second significant improvement was the development and implementation of two seasonal (winter and summer) net current patterns. This allowed, for the first time in Lower Cook Inlet, trajectories to be computed on a seasonal basis. The primary difference was a general shift in trajectories toward the north during summer conditions. Weaker fields occurred during summer conditions which resulted in a slight increase in the number of trajectories that exceeded a 10 day upper limit on trajectory simulation time. It does not appear feasible, considering existing data and planned field efforts, to refine seasonal net current patterns beyond the two seasons developed in this study. The existence of Putnins' daily weather catalog and the coupled wind fields and intensity factors would allow any detail of seasonal breakdown.

The sample results of the trajectory simulation examined in this study once again suggest that the wind drift component of flow dominated trajectory movement. The variability of the wind fields added to this dominance in that the trajectory movement

was altered significantly by each shift in the wind field. The seasonal variability of the net current patterns was observed in specific examples to result in an overall shift of trajectories somewhat northward during summer conditions. However, the net current patterns had a secondary (compared to the wind fields) effect on overall trajectory movement. The effect of the tidal current component was important in certain specific trajectories, but overall preferred movement was not significantly affected. It can be concluded that the tidal current component added a measure of dispersion to trajectory movement and impact location and should be included in trajectory simulation for an enclosed coastal region such as Lower Cook Inlet and Shelikof Strait.

If further trajectory simulations using deterministic environmental forcing fields are desired for this area, certain improvements can be suggested as a result of the present study and knowledge of the existing data base. One area of improved simulation would be to account for the diurnal land-sea interaction on the wind fields. Since this is primarily an onshore-offshore effect and would vary with location, the resulting trajectory behavior may be significant; as an example, shorter times to shoreline impact would be expected.

If improved deterministic trajectory simulation is desired, it is recommended that the variability of the net current pattern both in terms of magnitude and direction be evaluated in greater detail. This is particularly important where the variability has been shown to be significant. As discussed in Muench, 1980, flow pulses have been observed with current magnitudes twice as large

as the mean and with complete reversals in direction at current moorings located at the northern end of Shelikof Strait. It is doubtful that the existing data base can provide the required spatial and temporal coverage for the parameters needed to specify the current variability. However, the effect of this variability could be examined in an area where adequate coverage existed and recommendations formulated from the results. It is further recommended that the unprocessed NOS current meter records from northern Lower Cook Inlet taken in 1973 be analyzed as the patterns utilized in this study are still uncertain in this area.

While the tidal current pattern used in the present study does not simulate the elliptical nature and lunar phasing of tidal current strength, it is not believed necessary to add these characteristics based on the results of this study as well as those of the 1979 study. A reasonable approximation can be implemented to account for these effects if so desired and would provide an additional source of time and spatial variability to trajectory simulations.

In summary, there are limited improvements that can be made to trajectory simulation using empirical, deterministic environmental forcing fields in the Lower Cook Inlet and Shelikof Strait area from existing data bases. Major improvements would require significant commitments of time and resources to conduct and collect the appropriate field programs and data. Such programs might examine the directional and angular coupling of the wind drift component on an actual oil slick. Other field studies may

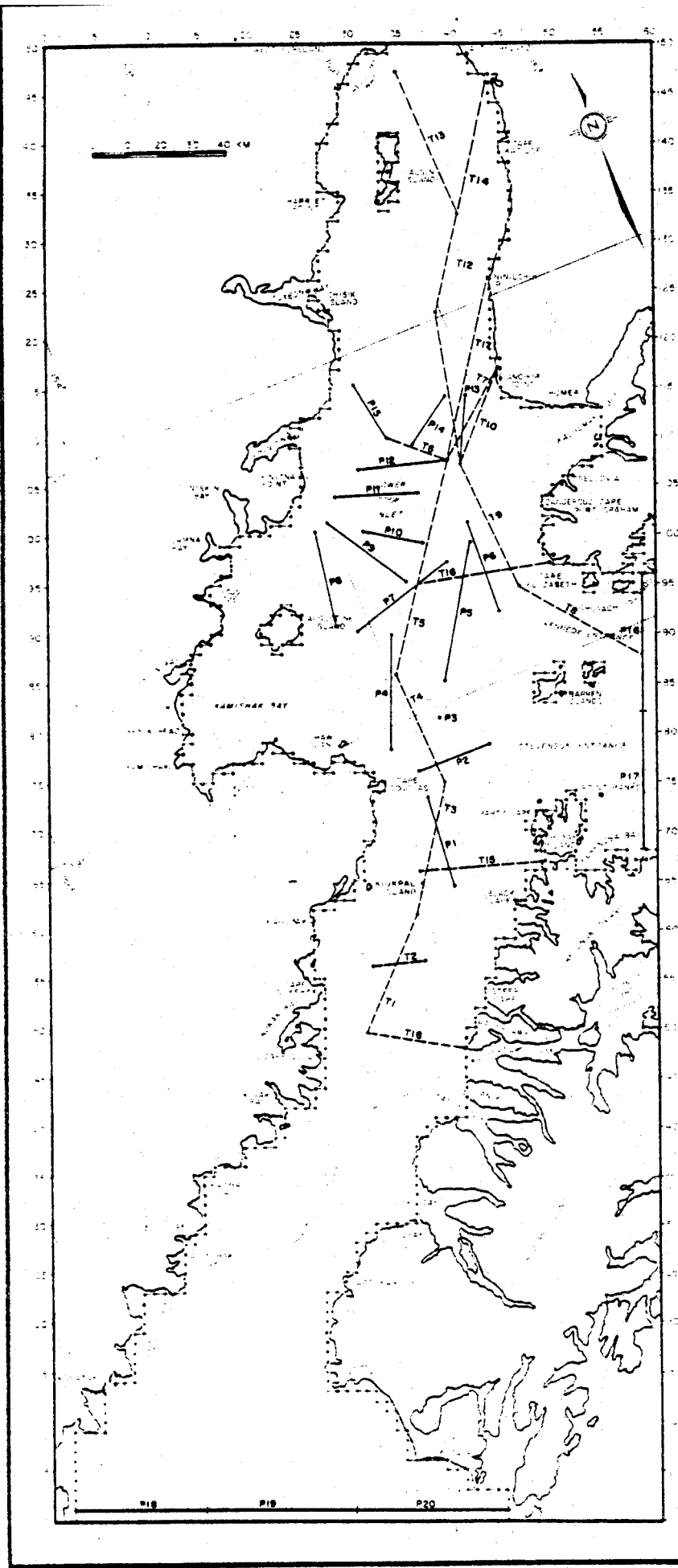
be desired in order to define the surface transport existing in the various embayments and channels that are currently excluded from this grid system.

However, it is recommended that future efforts now begin to focus on those aspects of oil movement beyond the centroidal transport of a hypothetical slick. Mechanisms such as spreading and weathering are believed to be a more important consideration in oil spill assessment than the increased accuracy possibly obtainable in continued trajectory simulations.

BIBLIOGRAPHY

- Dames & Moore, 1976. Report, Oil Spill Trajectory Analysis, Lower Cook Inlet, Alaska, for National Oceanic and Atmospheric Administration, Job Number 6797-003-20.
- _____, 1979. Report, Oil Spill Trajectory Analysis, Lower Cook Inlet, Alaska, for National Oceanic and Atmospheric Administration, Job Number 6979-011-02.
- LaBelle, R.P., W.B. Samuels, K.J. Lanfear, 1980. An Oil Spill Risk Analysis for Cook Inlet and Shelikof Strait (Proposed Sale 60) Outer Continental Shelf Lease Area; U.S. Geological Survey Open File Report 80 - in preparation .
- Muench, R.D., H.O. Mofjeld, and R.L. Charnell, 1978. Oceanographic Conditions in Lower Cook Inlet: Spring and Summer 1973. J. Geophys. Res. 83(C10): 5090-5098.
- Muench, R.D., 1979. Personal communication. Current meter data, circulation patterns and tidal current harmonics for Lower Cook Inlet and Shelikof Strait.
- Muench, R.D., J.D. Schumacher, and R. Sillcox, 1979. Northwest Gulf of Alaska Shelf Circulation, Annual Report, Research Unit #138, U.S. Dept. of Commerce, NOAA/OCSEAP.
- Muench, R.D., and J.D. Schumacher, 1980. Physical Oceanographic Conditions in the Northwest Gulf of Alaska, Northwest Gulf of Alaska Synthesis Report for U.S. Dept. of Commerce, NOAA/OCSEAP (in press).
- Mungall, J.C.H., and J.B. Matthews, 1973. Numerical Tidal Models with Unequal Grid Spacings. Tech. Rep. R73-2. Institute of Marine Science, Univ. of Alaska, Fairbanks, Alaska.
- Mungall, J.C.H., 1973. Cook Inlet Tidal Stream Atlas. Tech. Rep. R73-2. Institute of Marine Science, Univ. of Alaska, Fairbanks, Alaska.
- Oceanographic Institute of Washington, 1977. Modeling Methods for Predicting Oil Spill Movement, Oceanographic Commission of Washington, Seattle, Washington, March.
- Pacific Marine Environmental Laboratories, 1980. Personal communication. Development of local wind fields corresponding to regional synoptic weather patterns after Putnins, 1966a, R.M. Reynolds, Marine Meteorological Studies Group, NOAA.
- Putnins, P., 1966a. Studies on the Meteorology of Alaska: First Interim Report (The sequences of baric weather patterns over Alaska). U.S. Dept. Commerce, ESSA/EDS, Silver Spring, Maryland.

- _____, 1966b. Unpublished tabulation of daily baric weather types for Alaska from January 1, 1945 to March 31, 1963, University of Alaska.
- _____, 1969. Studies on the Meteorology of Alaska: Final Report (Weather situations in Alaska during the occurrences of specific baric weather), U.S. Department of Commerce, ESSA, Research Laboratories, Boulder, Colorado, 80302, 267 p.
- Reed, R.K., R.D. Muench, and J.D. Schumacher, 1979. On Baroclinic Transport of the Alaskan Stream near Kodiak Island. (in preparation for submission to Deep-Sea Res.)
- Schumacher, J.D., R. Sillcox, D. Dreves, and R.D. Muench, 1978. Winter Circulation and Hydrography Over the Continental Shelf of the Northwest Gulf of Alaska. NOAA Technical Report ERL 404-PMEL 31, 16 p.
- Schumacher, J.D., R.K. Reed, M. Grigsby, and D. Dreves, 1979. Circulation and Hydrography Near Kodiak Island; September - November 1977. (Submitted for publication as an ERL Technical Report.)
- Swartzberg, H.G., 1971. "The Movement of Oil Spills," Proc. of the Jt. Conf. on Prev. and Cont. of Oil Spills, published by Amer. Petrol. Inst., Washington, D.C., pp. 489-494.



LEGEND:

P1 - P15 PLATFORM LOCATIONS

P16 - P20: WATER GRID BOUNDARIES

T1 - T18: PIPELINE OR TANKER ROUTES

FIGURE 2: TRAJECTORY LAUNCH SITES

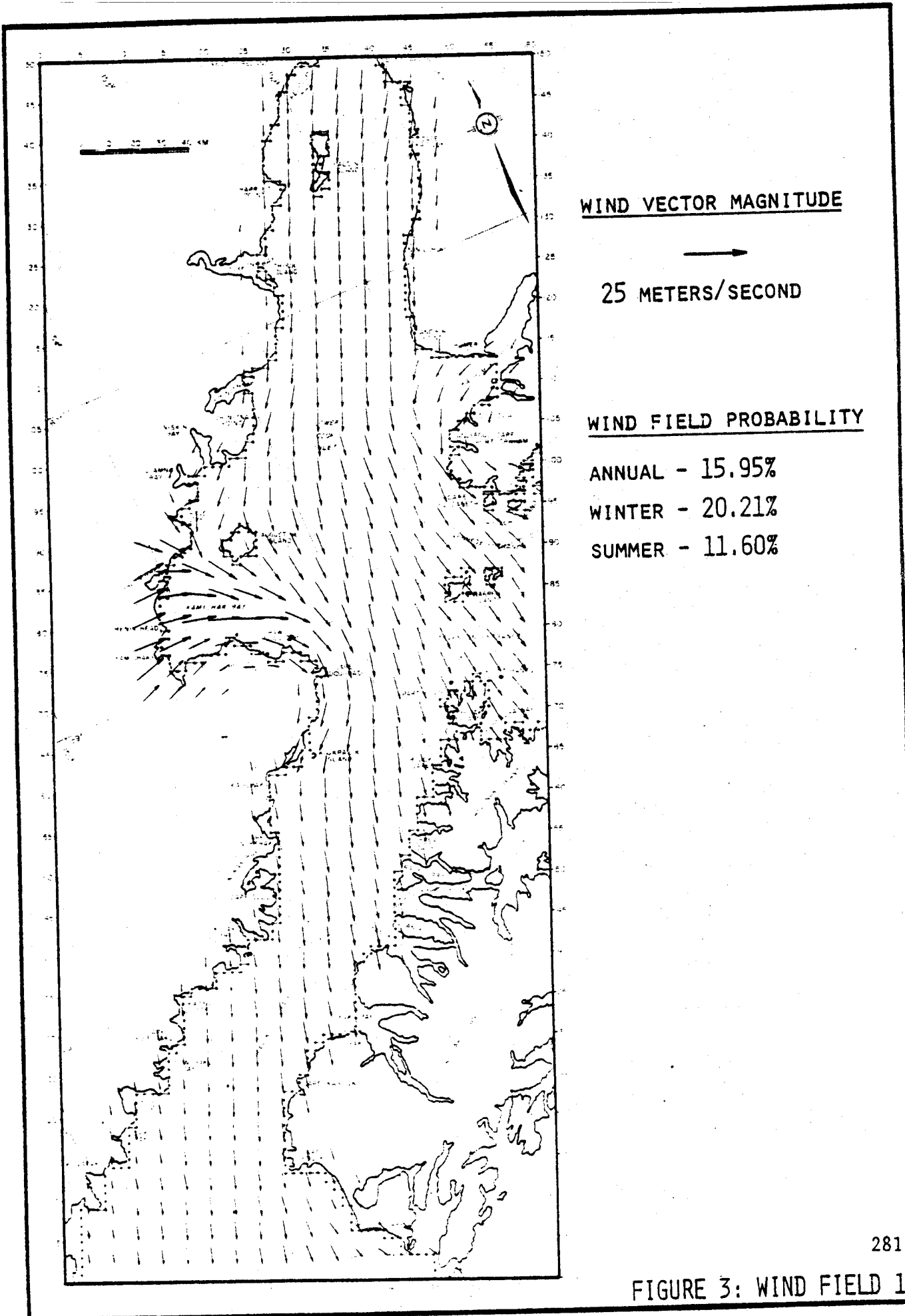
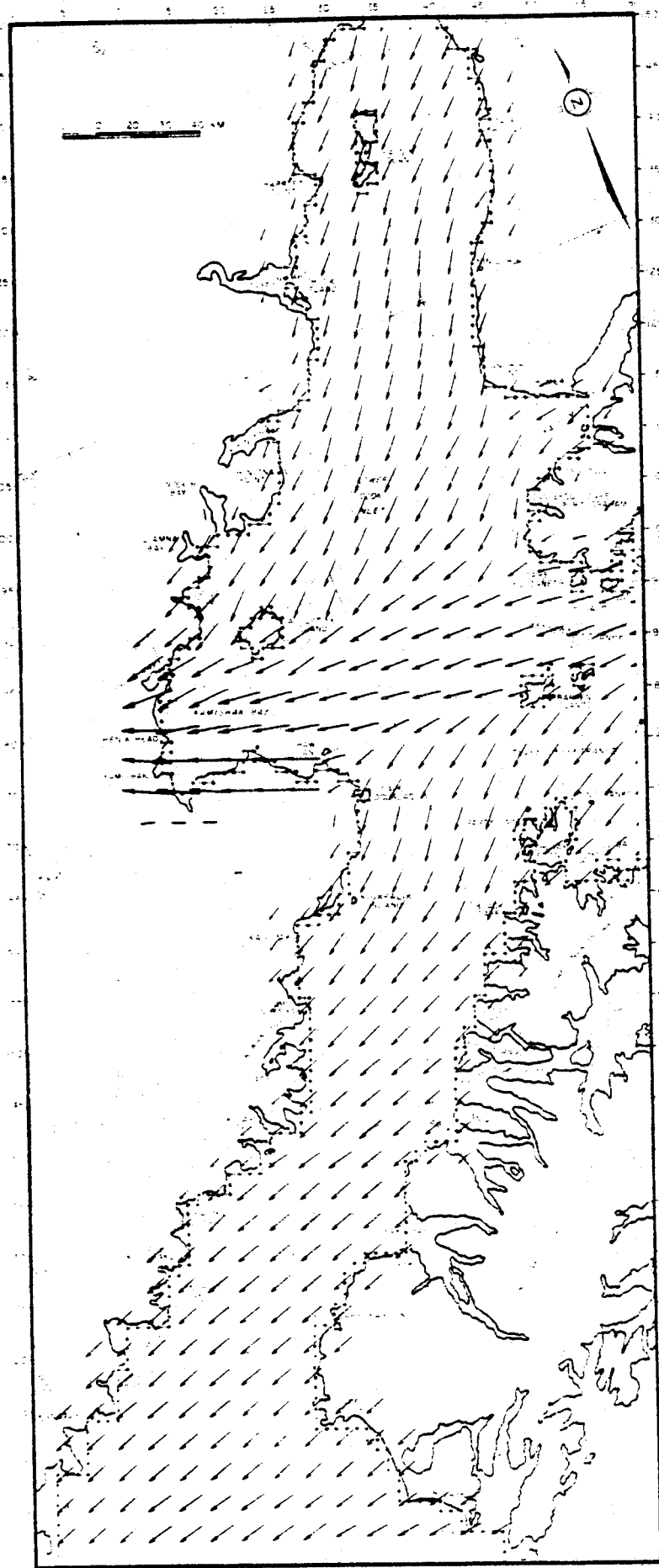


FIGURE 3: WIND FIELD 1



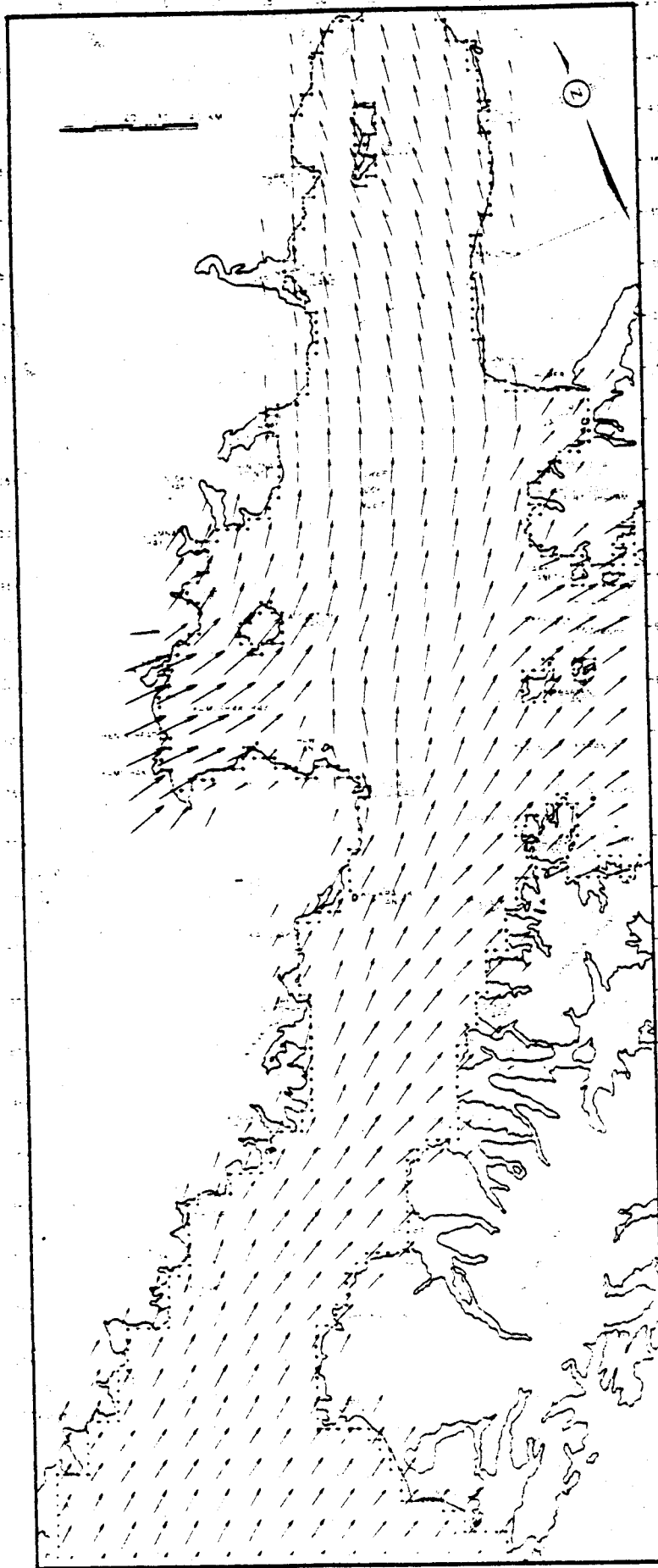
WIND VECTOR MAGNITUDE

→
25 METERS/SEC

WIND FIELD PROBABILITY

- ANNUAL - 24.83%
- WINTER - 32.33%
- SUMMER - 17.15%

FIGURE 4: WIND FIELD 2



WIND VECTOR MAGNITUDE



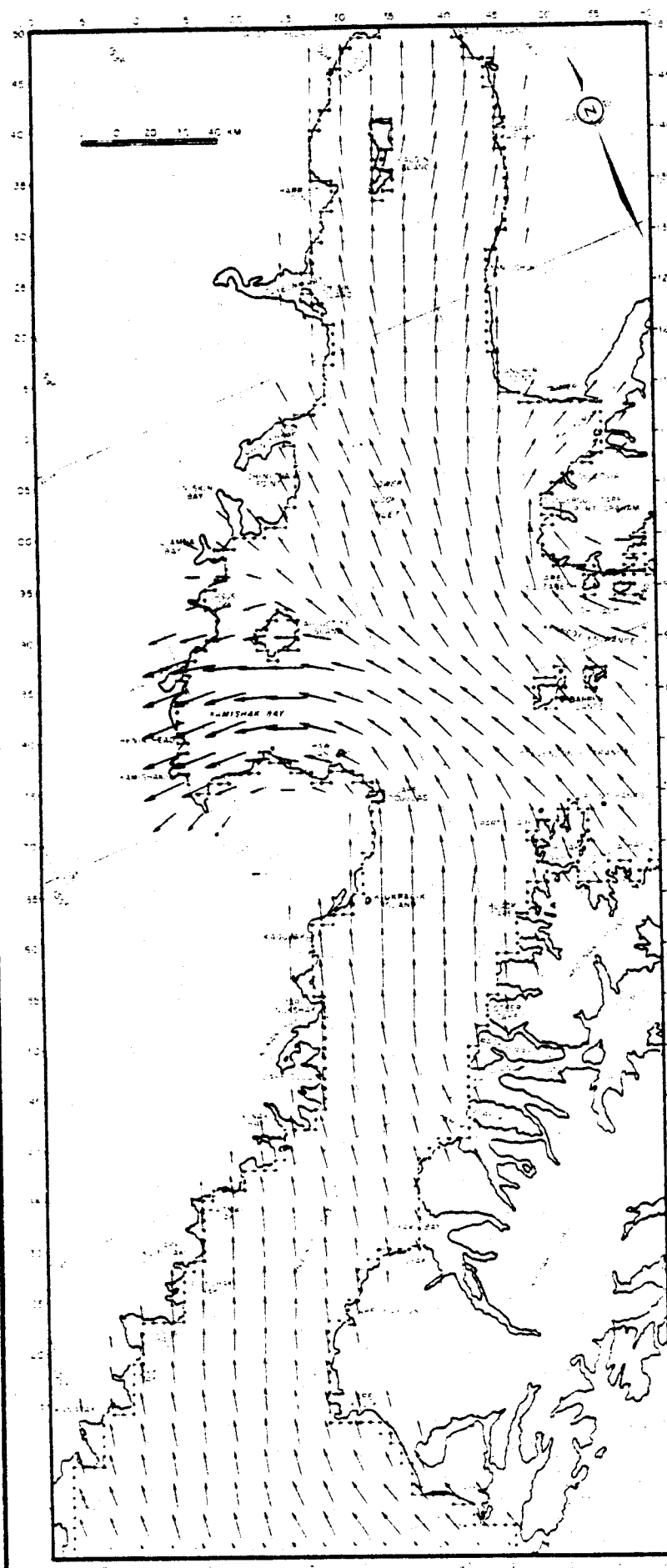
25 METERS/SEC

WIND FIELD PROBABILITY

ANNUAL - 6.12%

WINTER - 2.61%

SUMMER - 9.71%



WIND VECTOR MAGNITUDE

→
25 METERS/SEC

WIND FIELD PROBABILITY

ANNUAL - 28.64%
 WINTER - 21.04%
 SUMMER - 36.40%

FIGURE 6: WIND FIELD 4

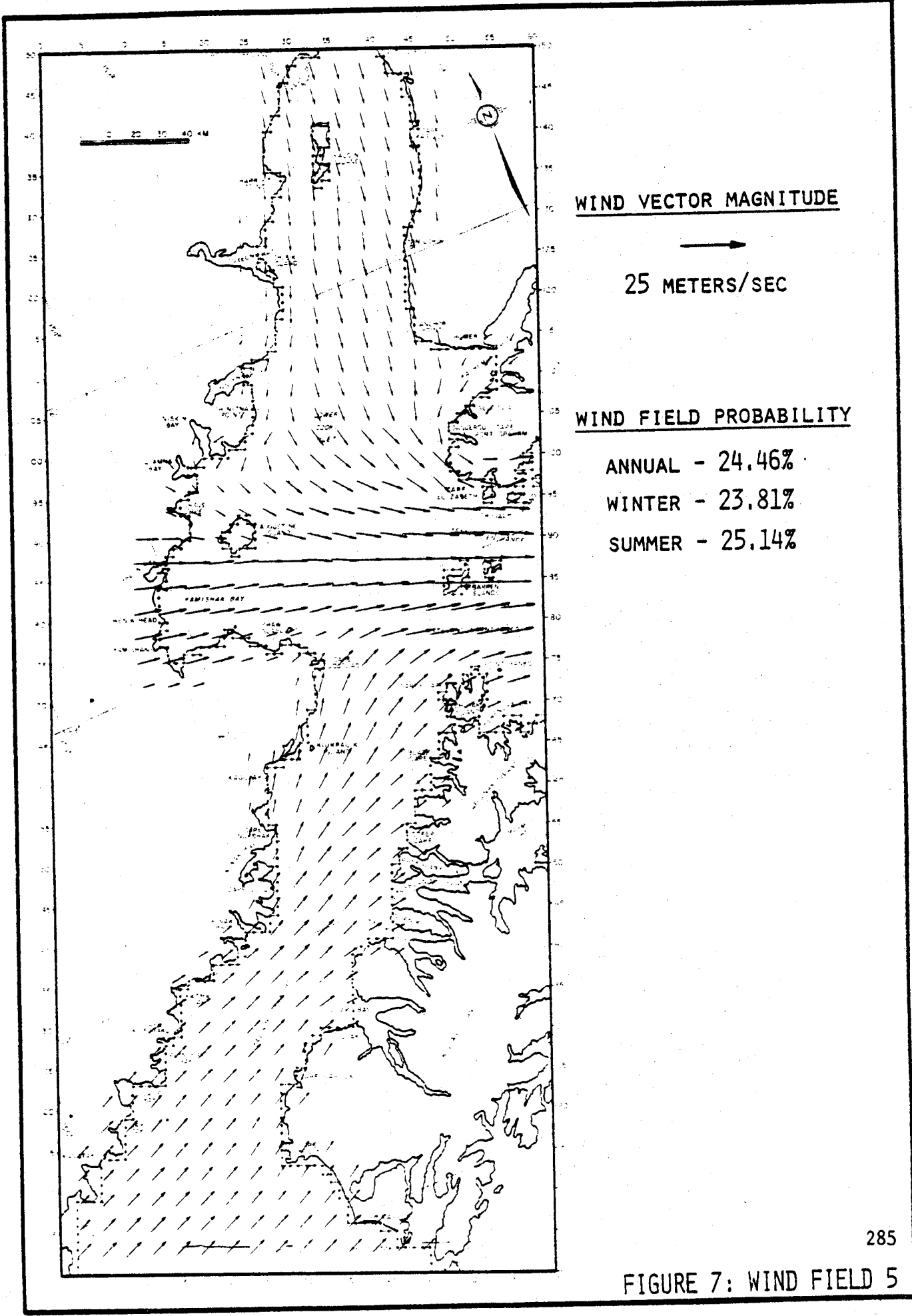


FIGURE 7: WIND FIELD 5

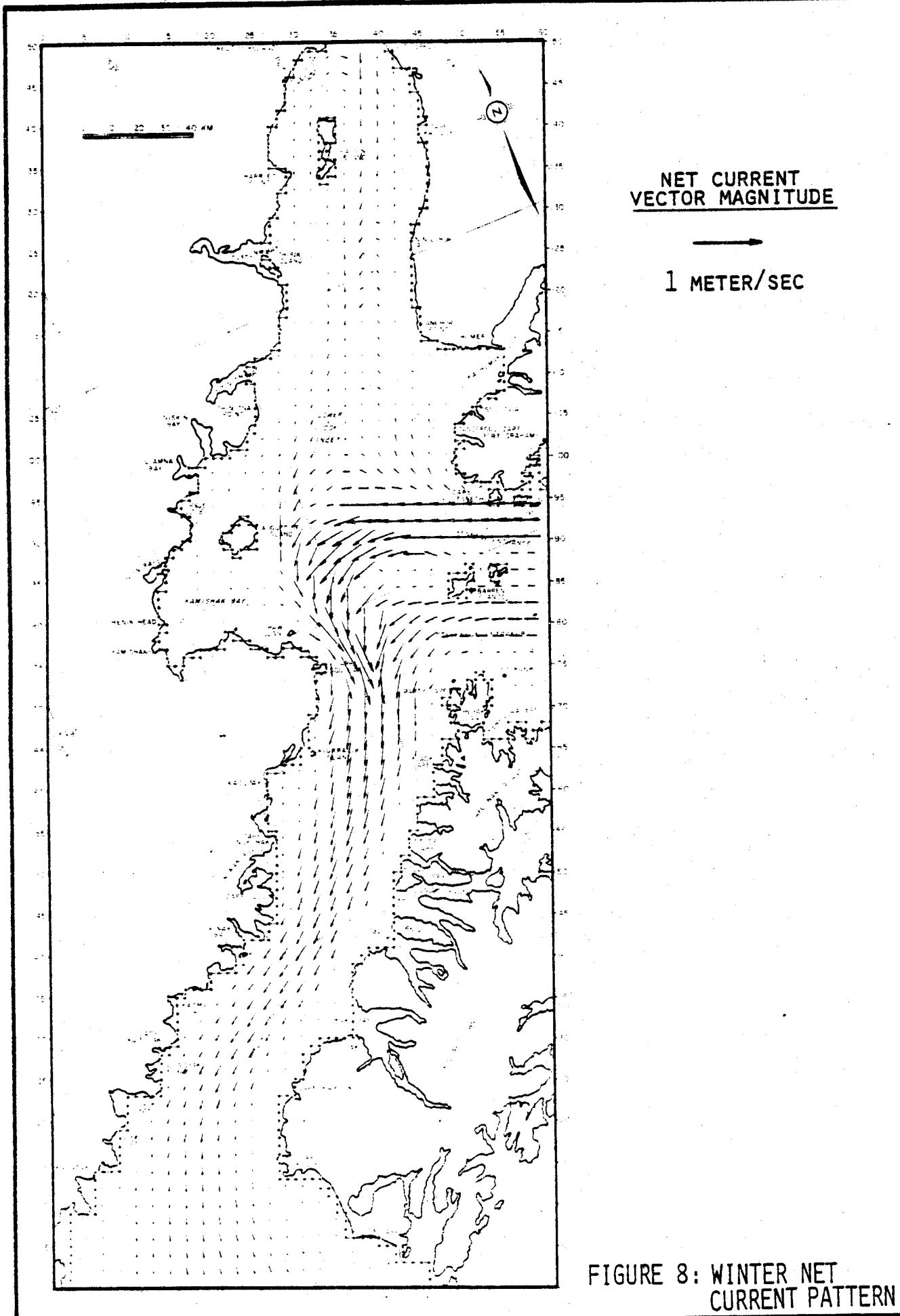
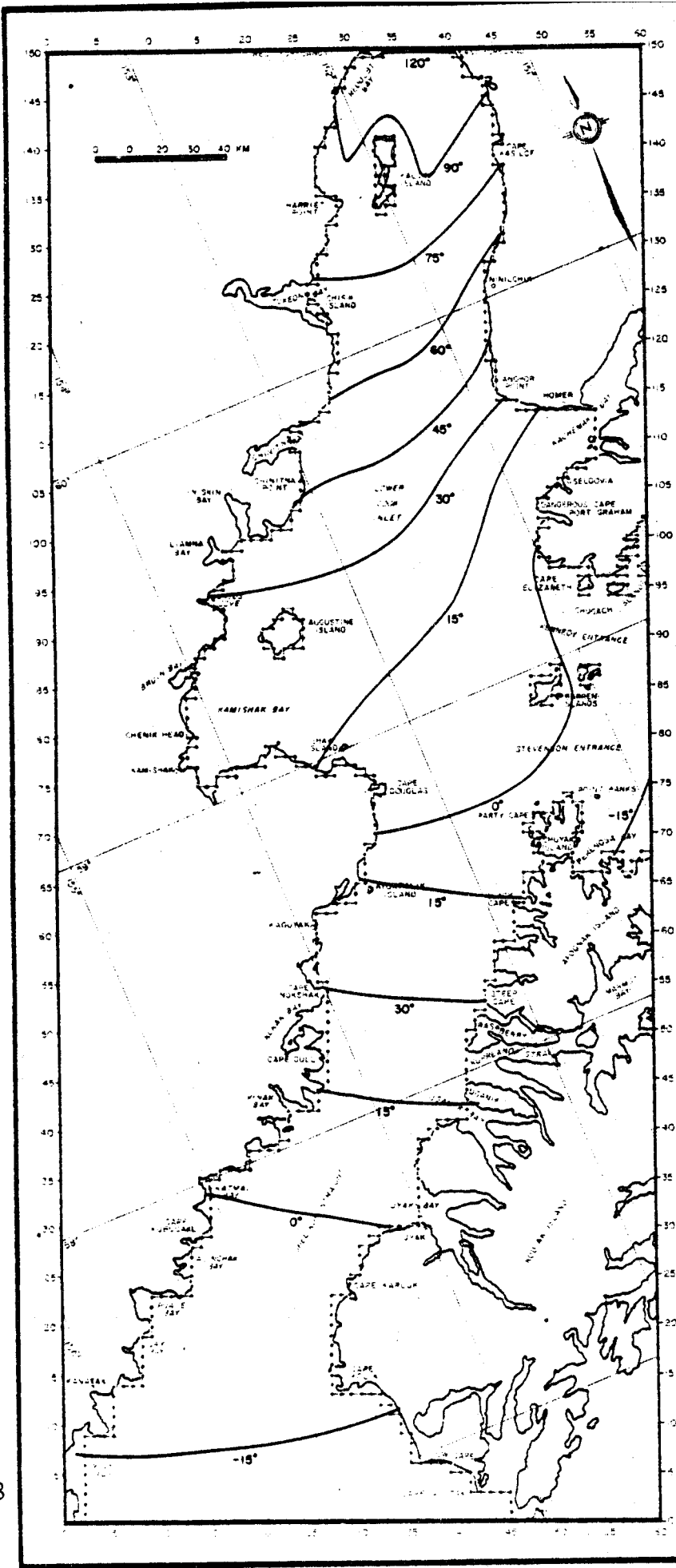
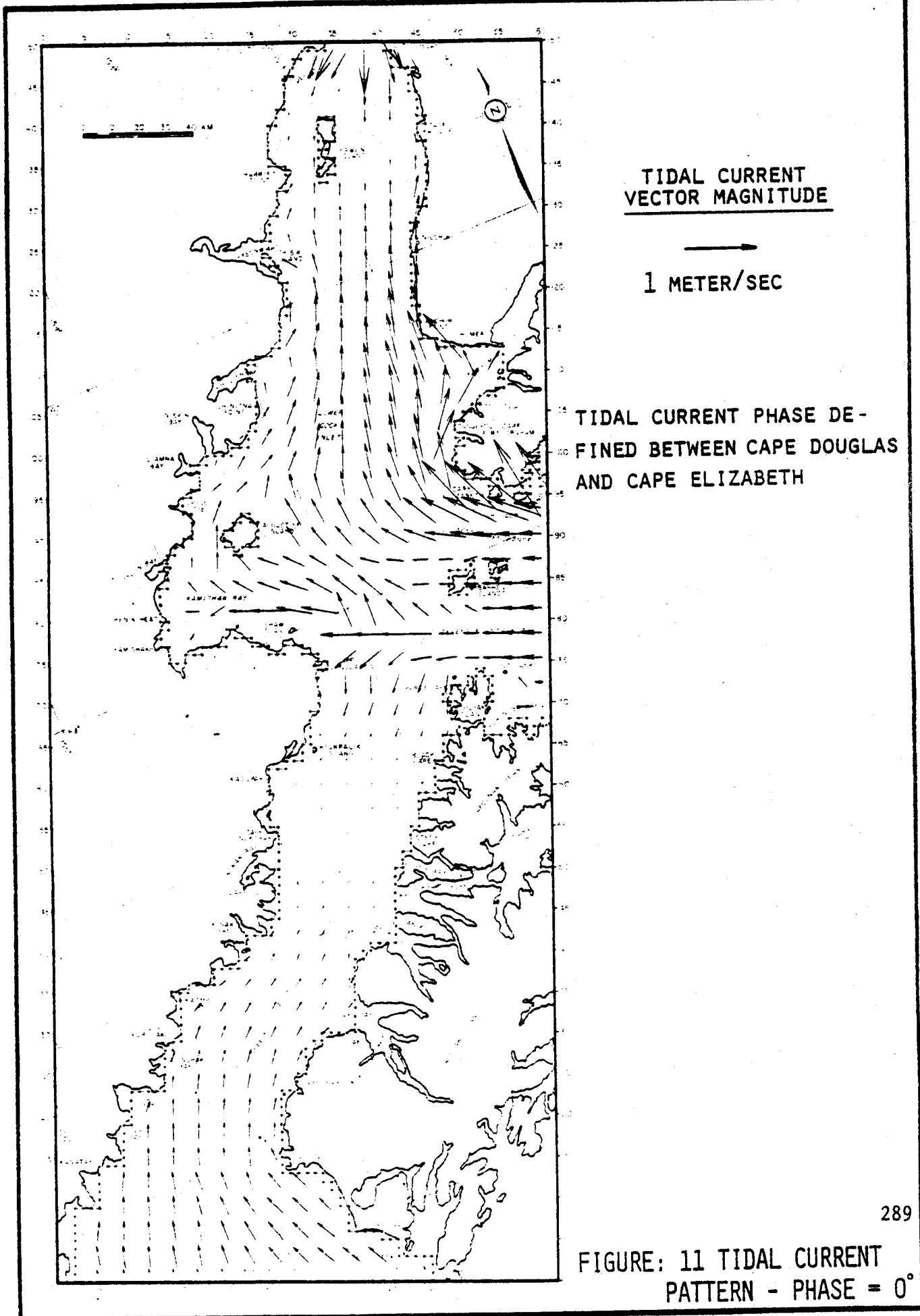


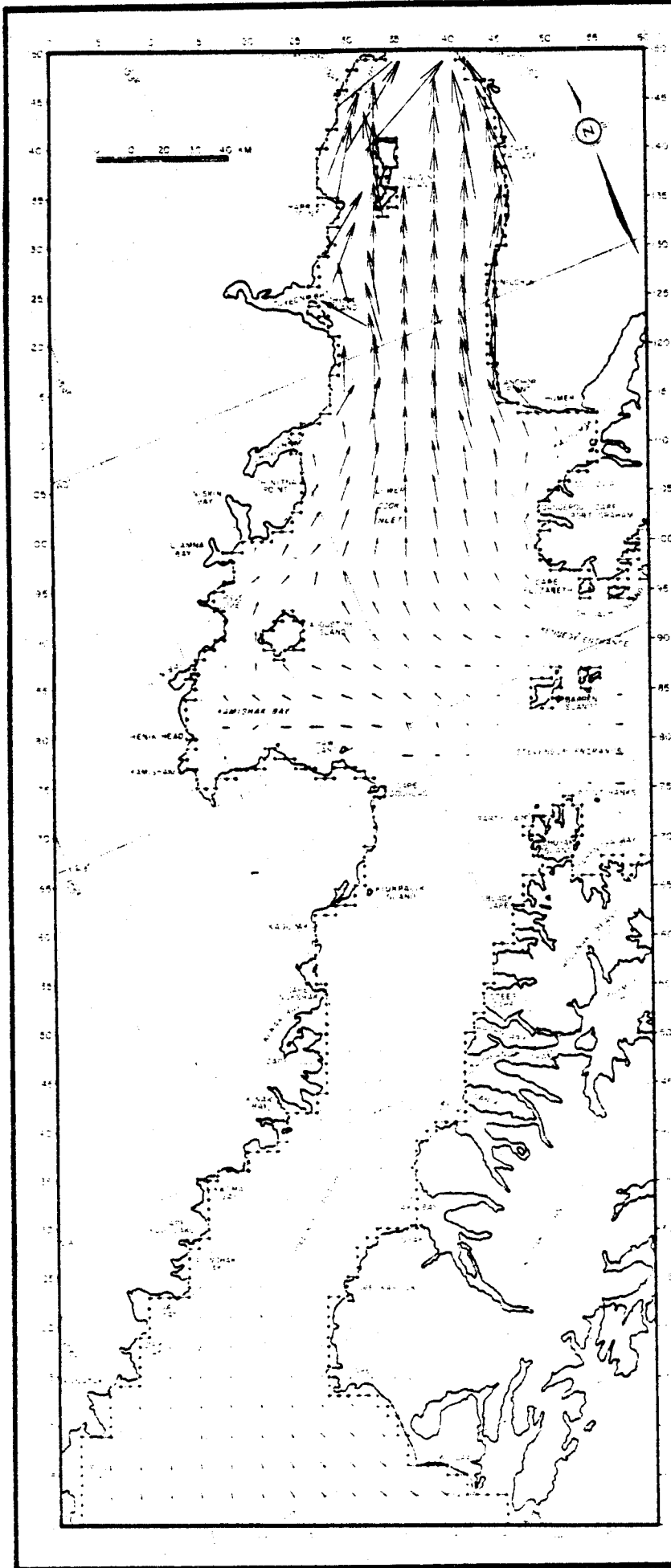
FIGURE 8: WINTER NET CURRENT PATTERN



PHASE GIVEN IN DEGREES
 RELATIVE TO TIDAL CUR-
 RENTS AT ENTRANCE TO
 LOWER COOK INLET.
 (360° = 12.4 HOURS)

FIGURE 10: TIDAL CURRENT
 PHASE DISTRIBUTION





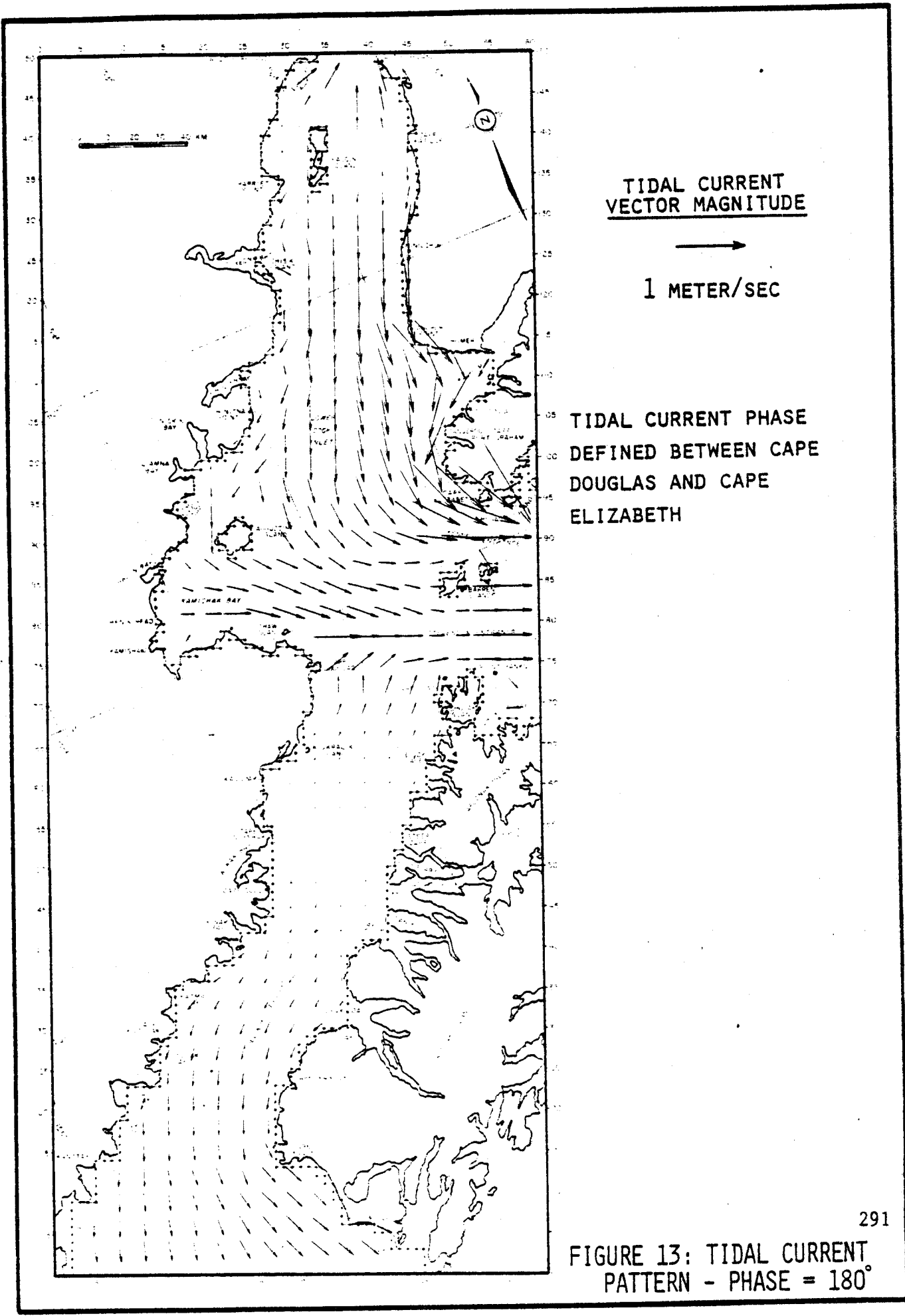
**TIDAL CURRENT
VECTOR MAGNITUDE**



1 METER/SEC

**TIDAL CURRENT PHASE
DEFINED BETWEEN CAPE
DOUGLAS AND CAPE
ELIZABETH.**

**FIGURE 12: TIDAL CURRENT
PATTERN - PHASE = 90°**



**TIDAL CURRENT
VECTOR MAGNITUDE**



1 METER/SEC

**TIDAL CURRENT PHASE
DEFINED BETWEEN CAPE
DOUGLAS AND CAPE
ELIZABETH**

**FIGURE 13: TIDAL CURRENT
PATTERN - PHASE = 180°**

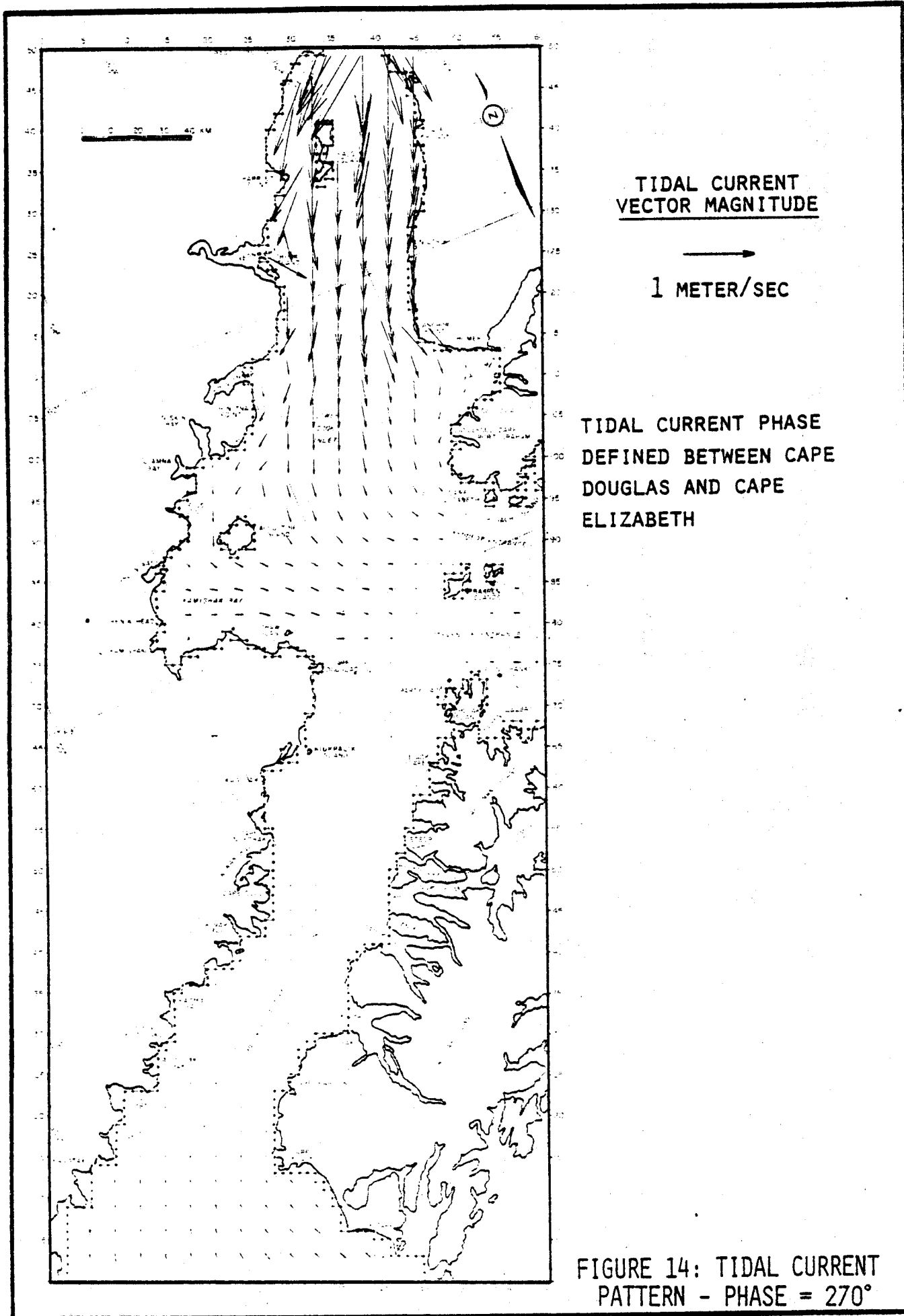


FIGURE 14: TIDAL CURRENT PATTERN - PHASE = 270°

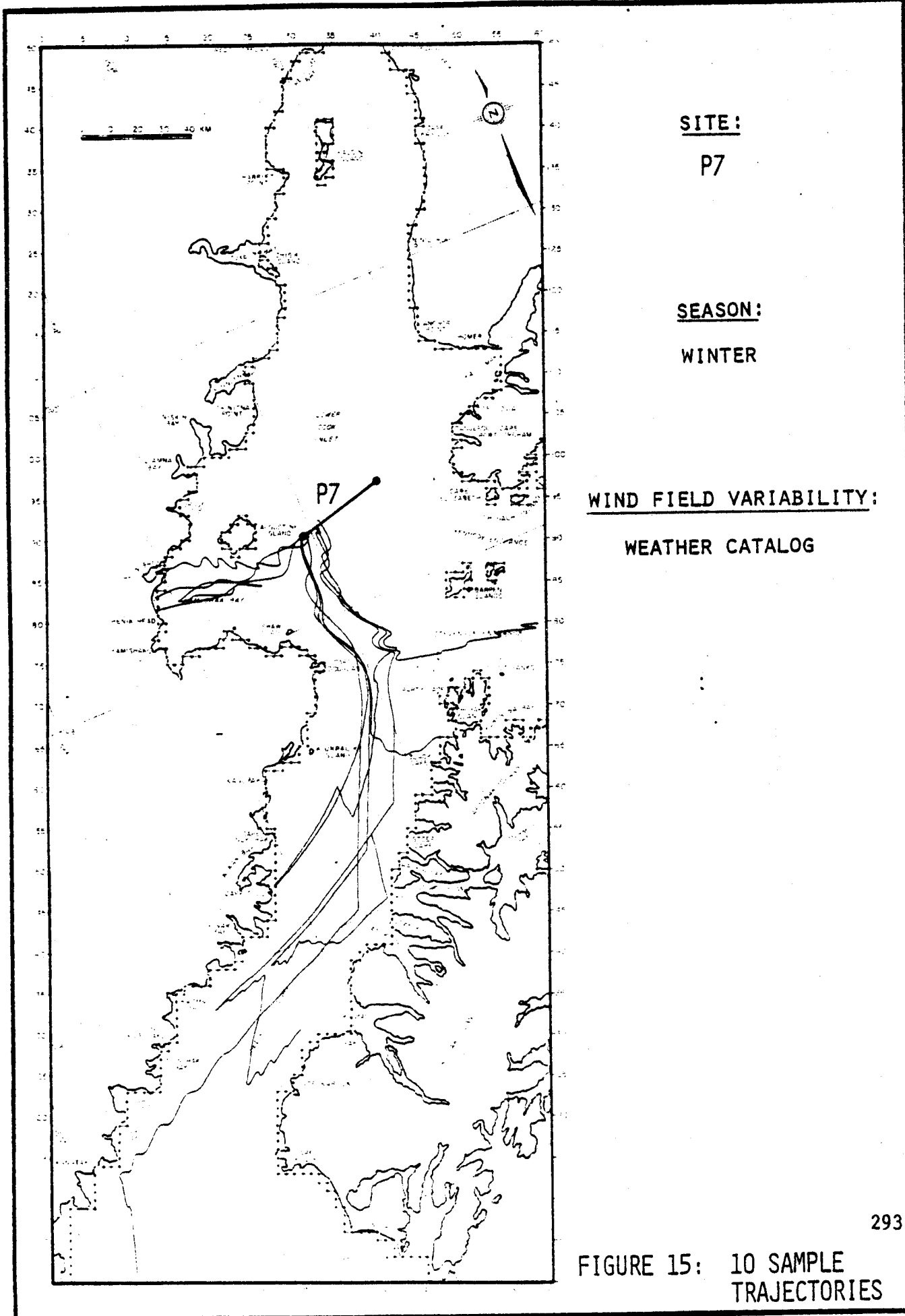


FIGURE 15: 10 SAMPLE TRAJECTORIES

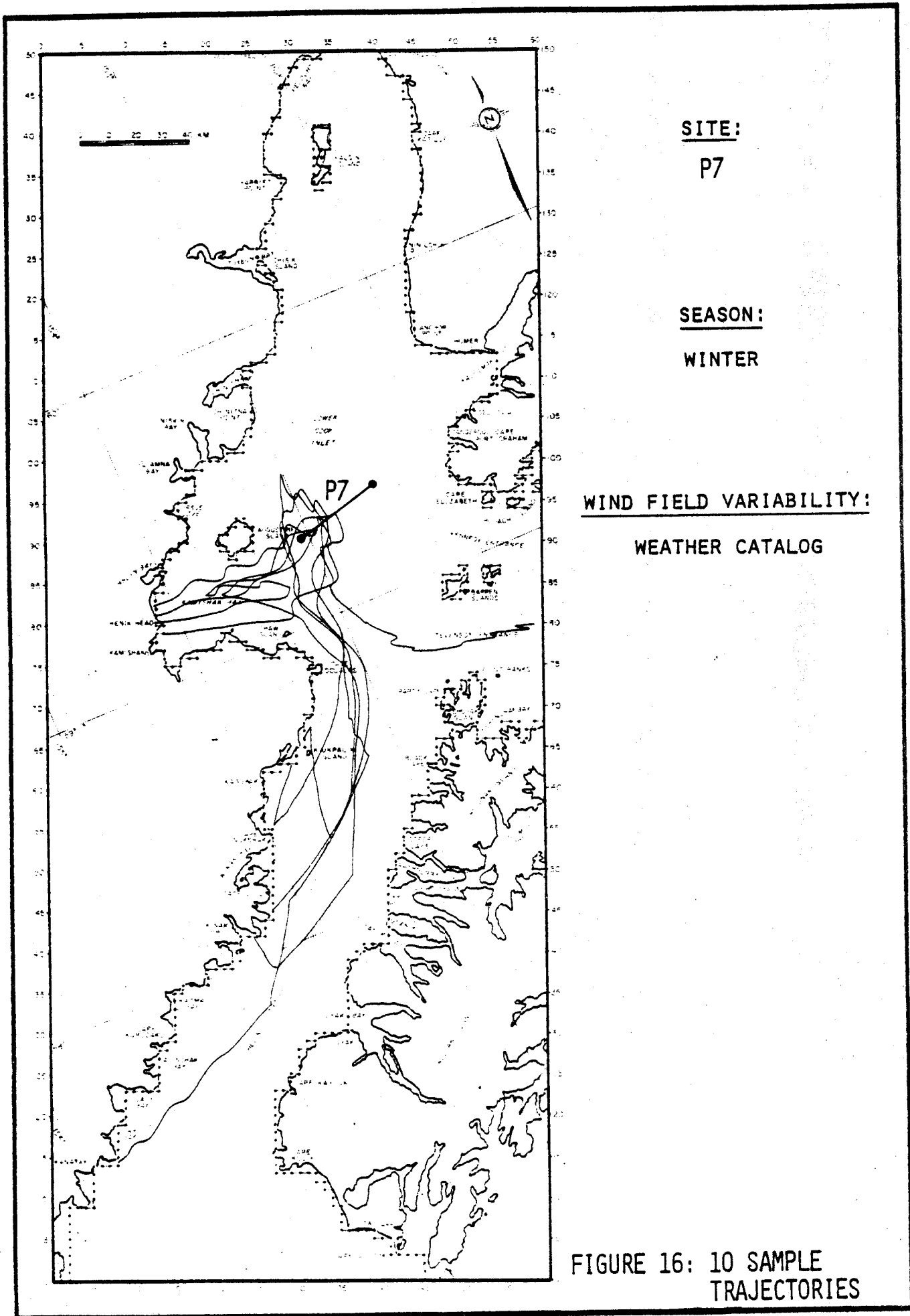
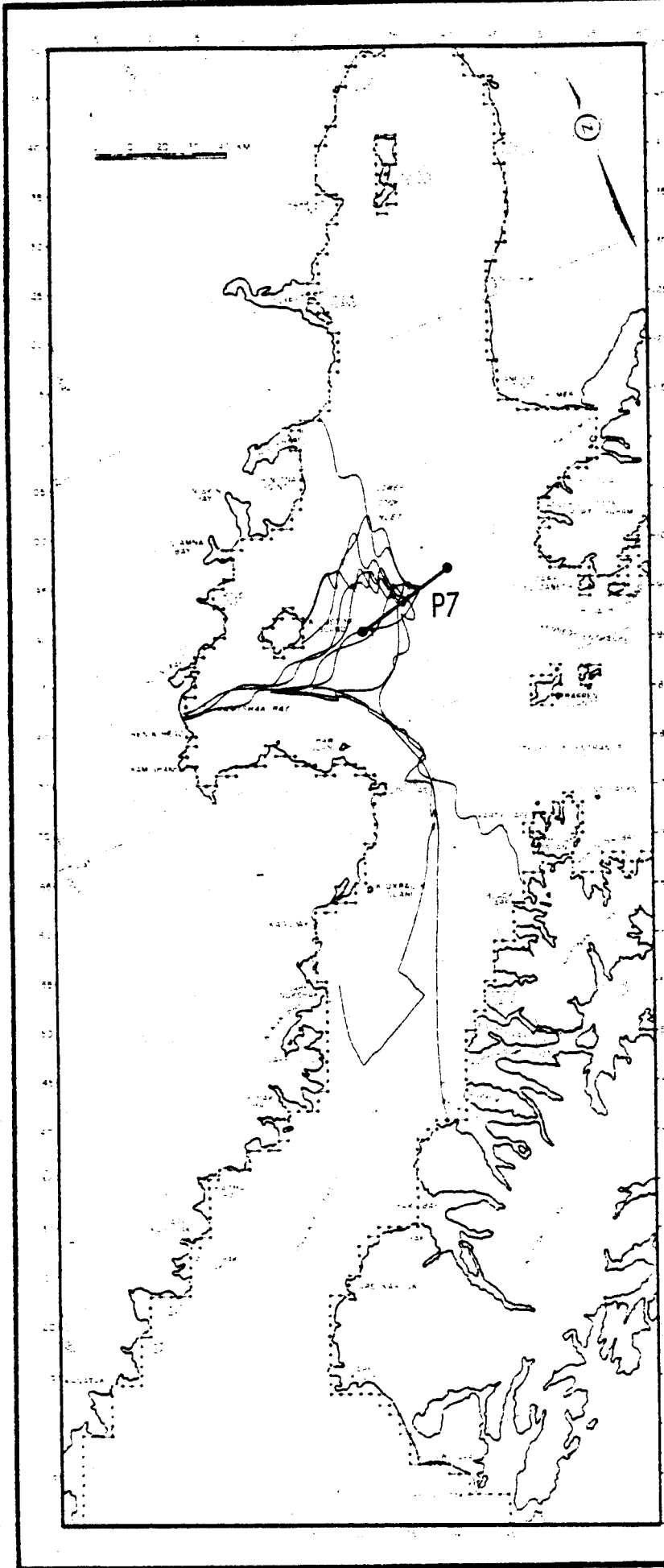


FIGURE 16: 10 SAMPLE TRAJECTORIES



SITE:

P7

SEASON:

WINTER

WIND FIELD VARIABILITY:

WEATHER CATALOG

FIGURE 17: 10 SAMPLE
TRAJECTORIES

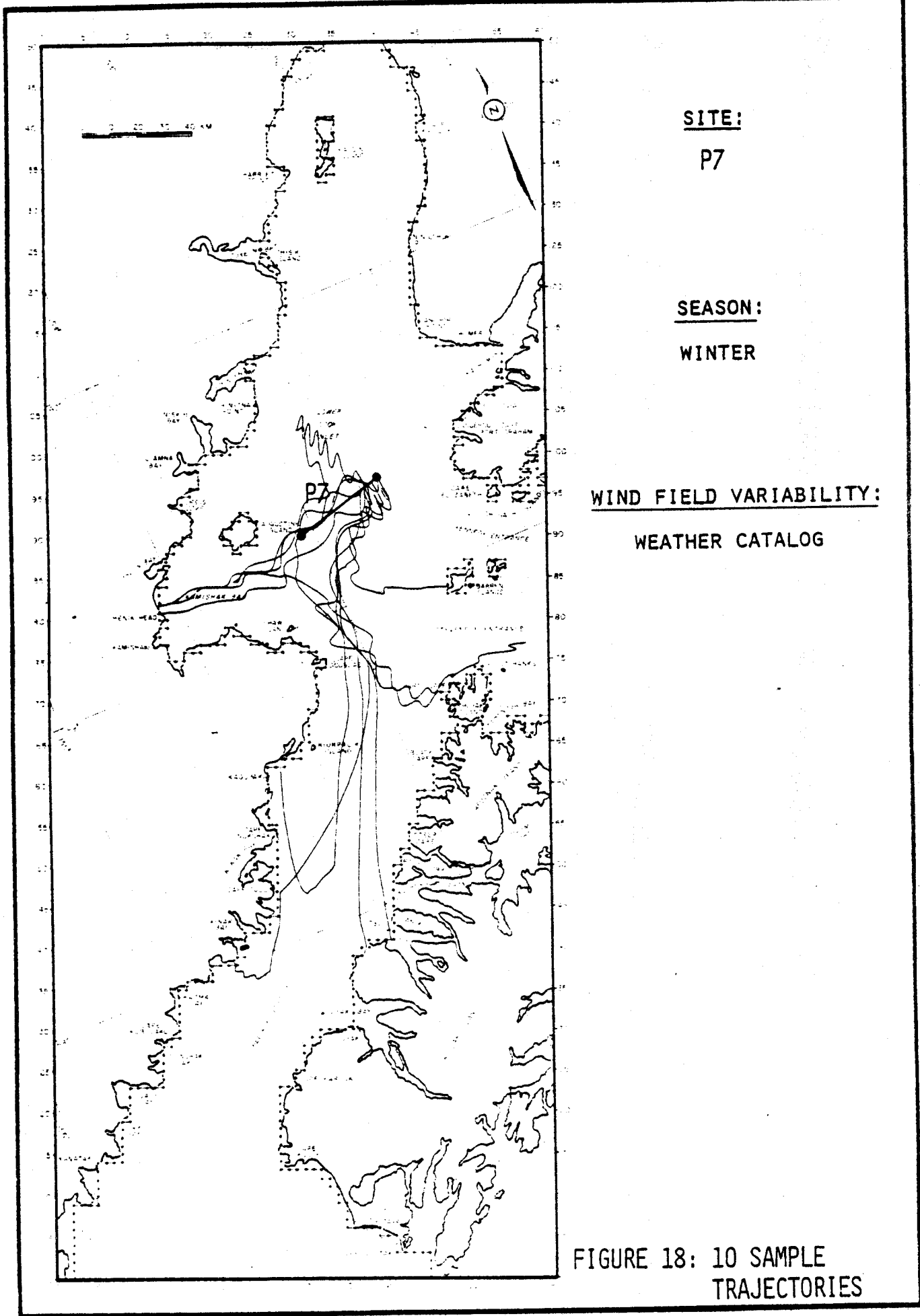


FIGURE 18: 10 SAMPLE TRAJECTORIES

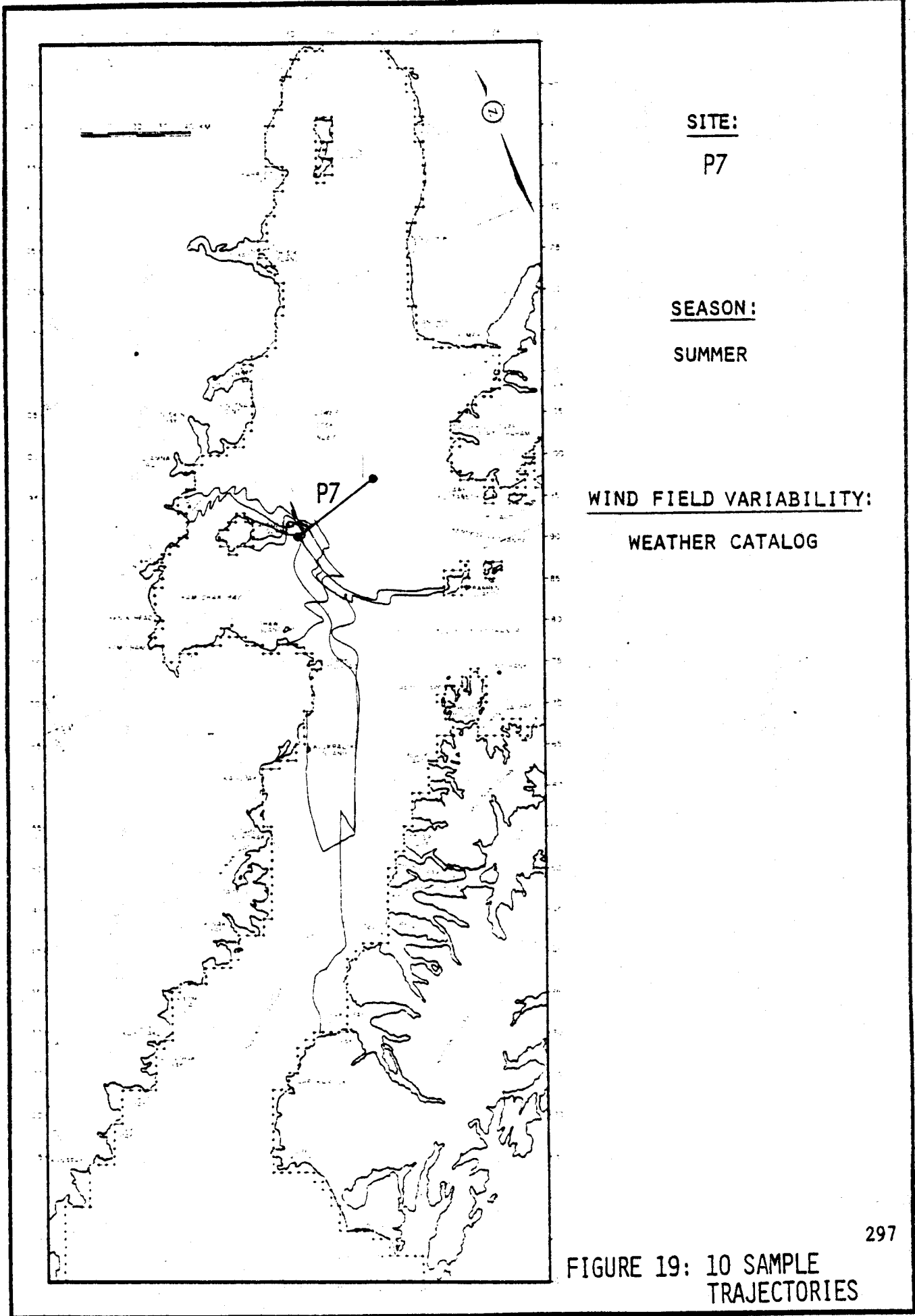
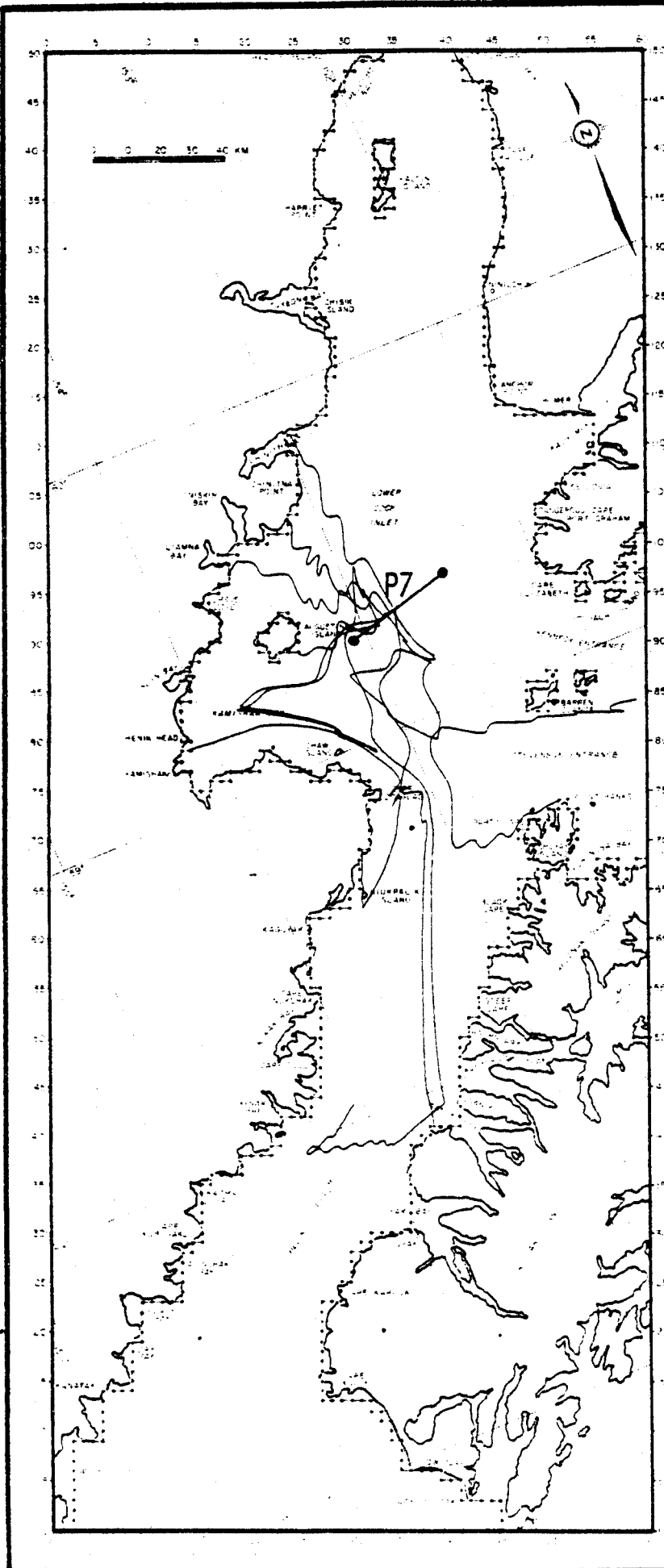


FIGURE 19: 10 SAMPLE TRAJECTORIES



SITE:

P7

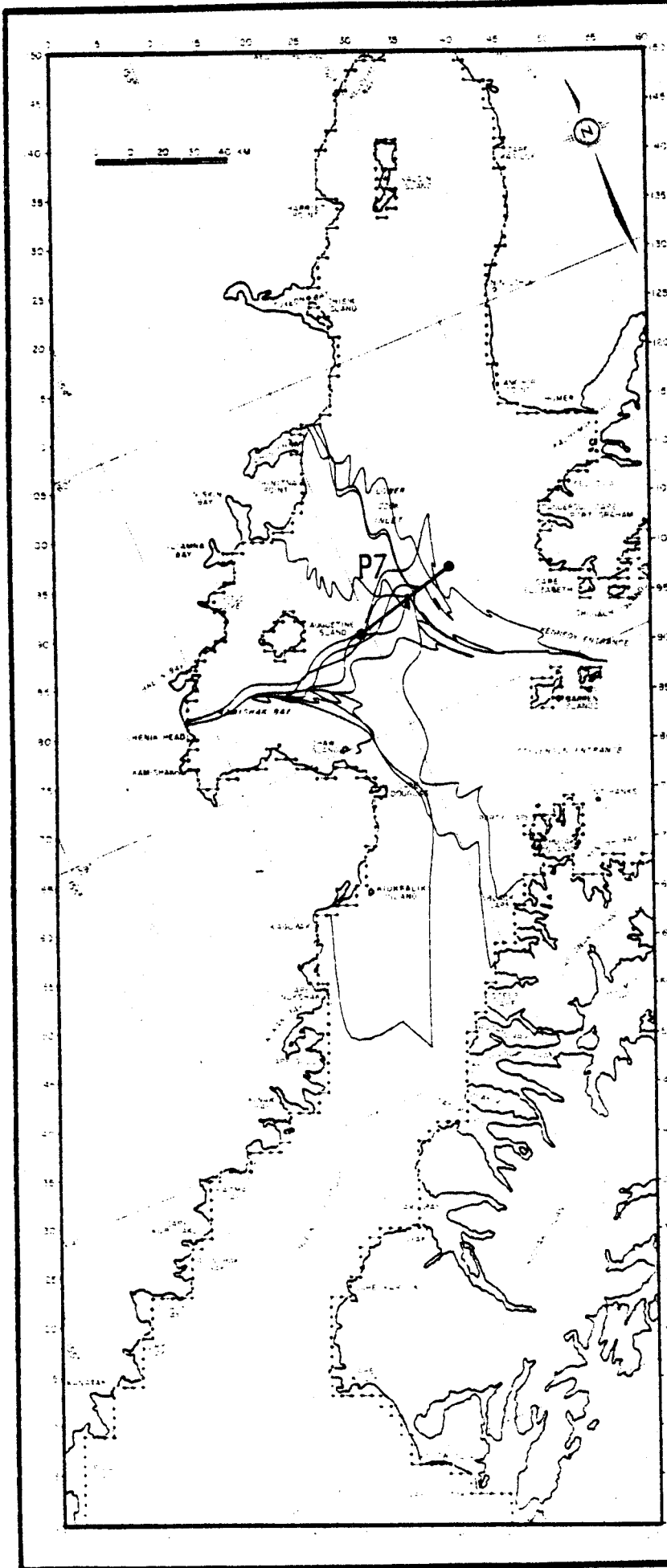
SEASON:

SUMMER

WIND FIELD VARIABILITY:

WEATHER CATALOG

FIGURE 20: 10 SAMPLE TRAJECTORIES



SITE:

P7

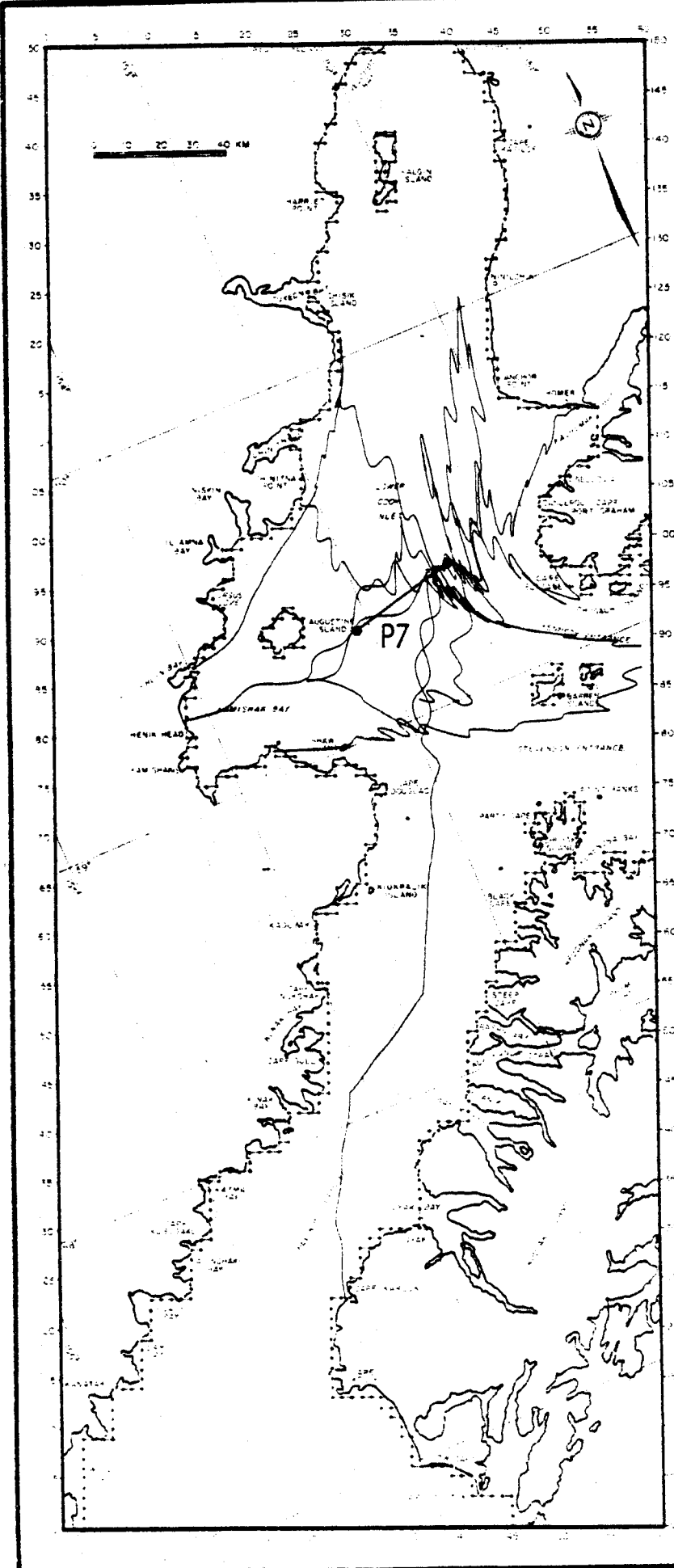
SEASON:

SUMMER

WIND FIELD VARIABILITY:

WEATHER CATALOG

FIGURE 21: 10 SAMPLE TRAJECTORIES



SITE:

P7

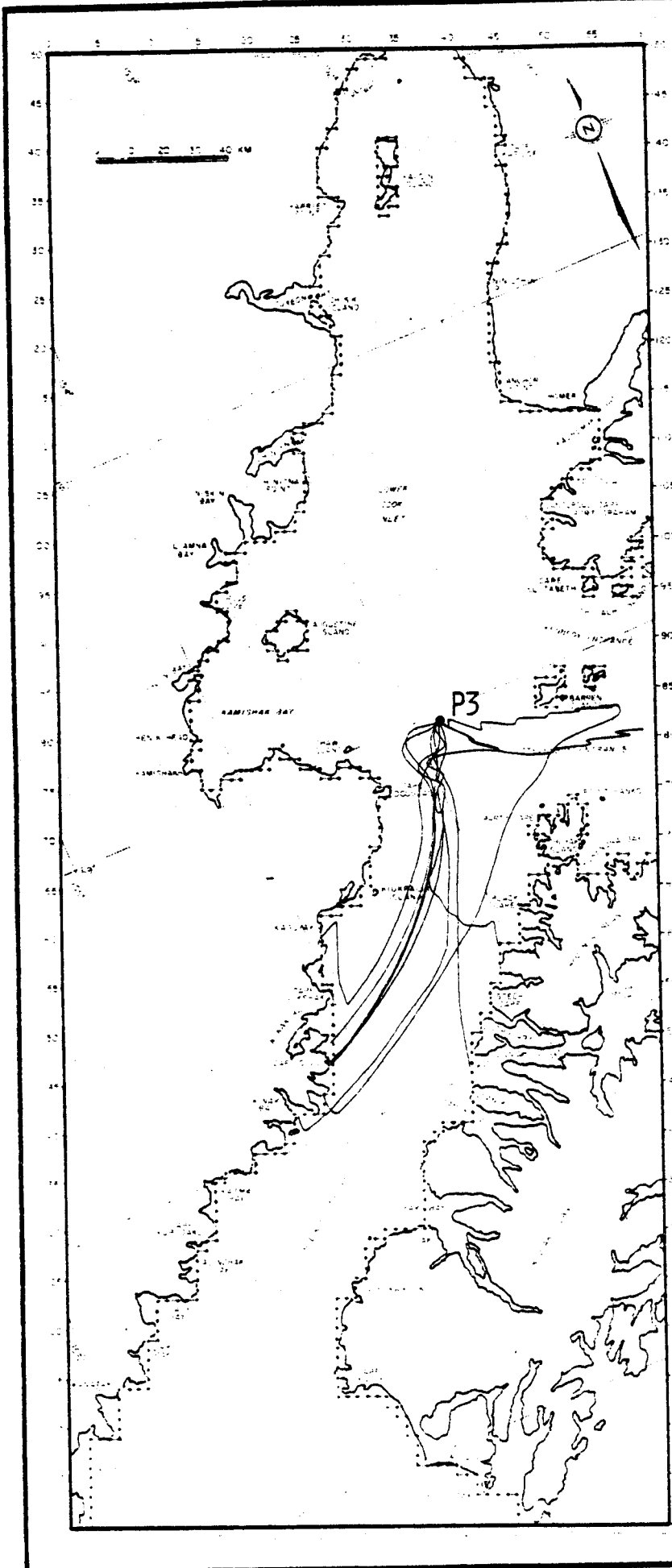
SEASON:

SUMMER

WIND FIELD VARIABILITY:

WEATHER CATALOG

FIGURE 22: 10 SAMPLE TRAJECTORIES



SITE:

P3

SEASON:

WINTER

WIND FIELD VARIABILITY:

WEATHER CATALOG

FIGURE 23: 10 SAMPLE
TRAJECTORIES

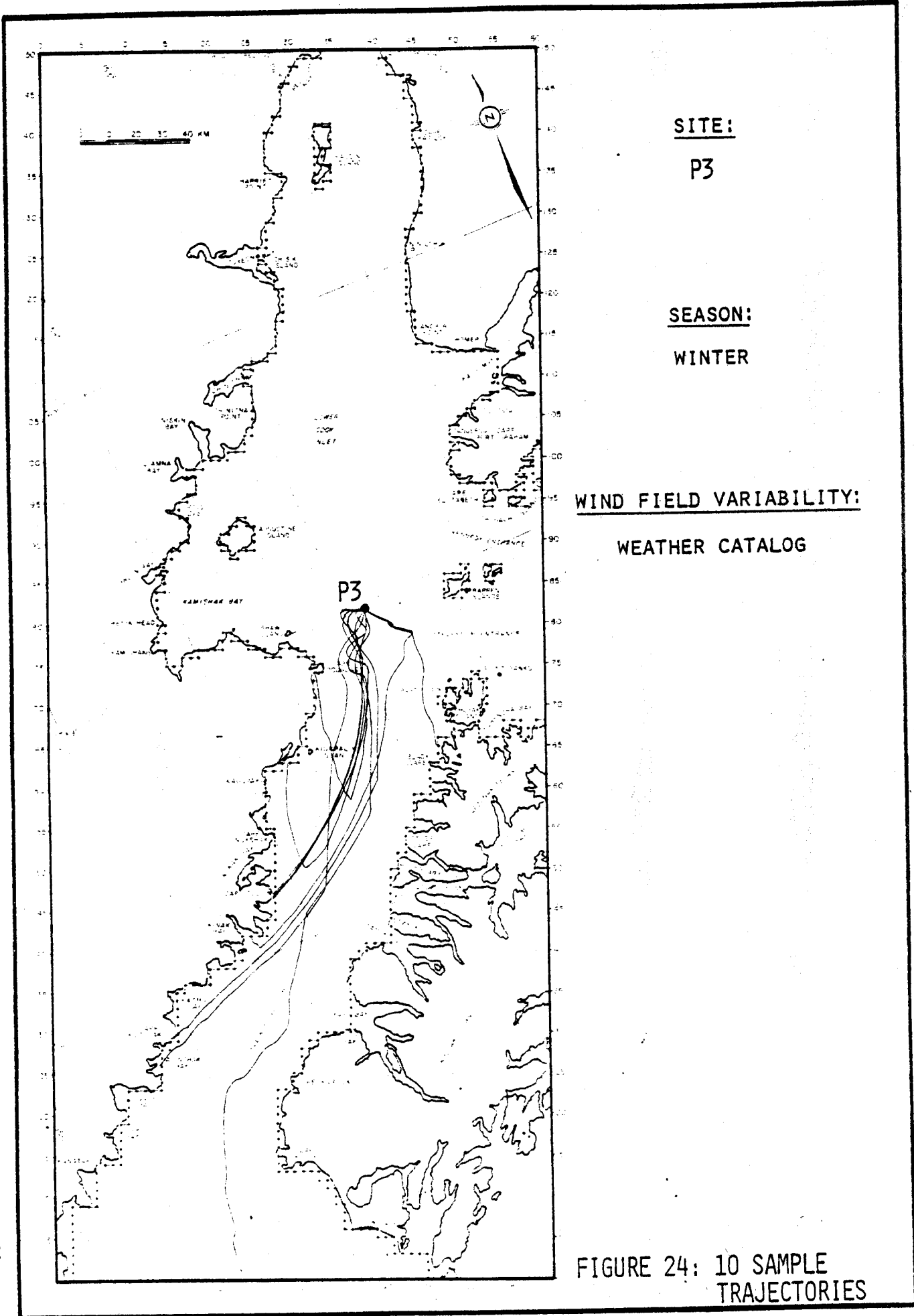
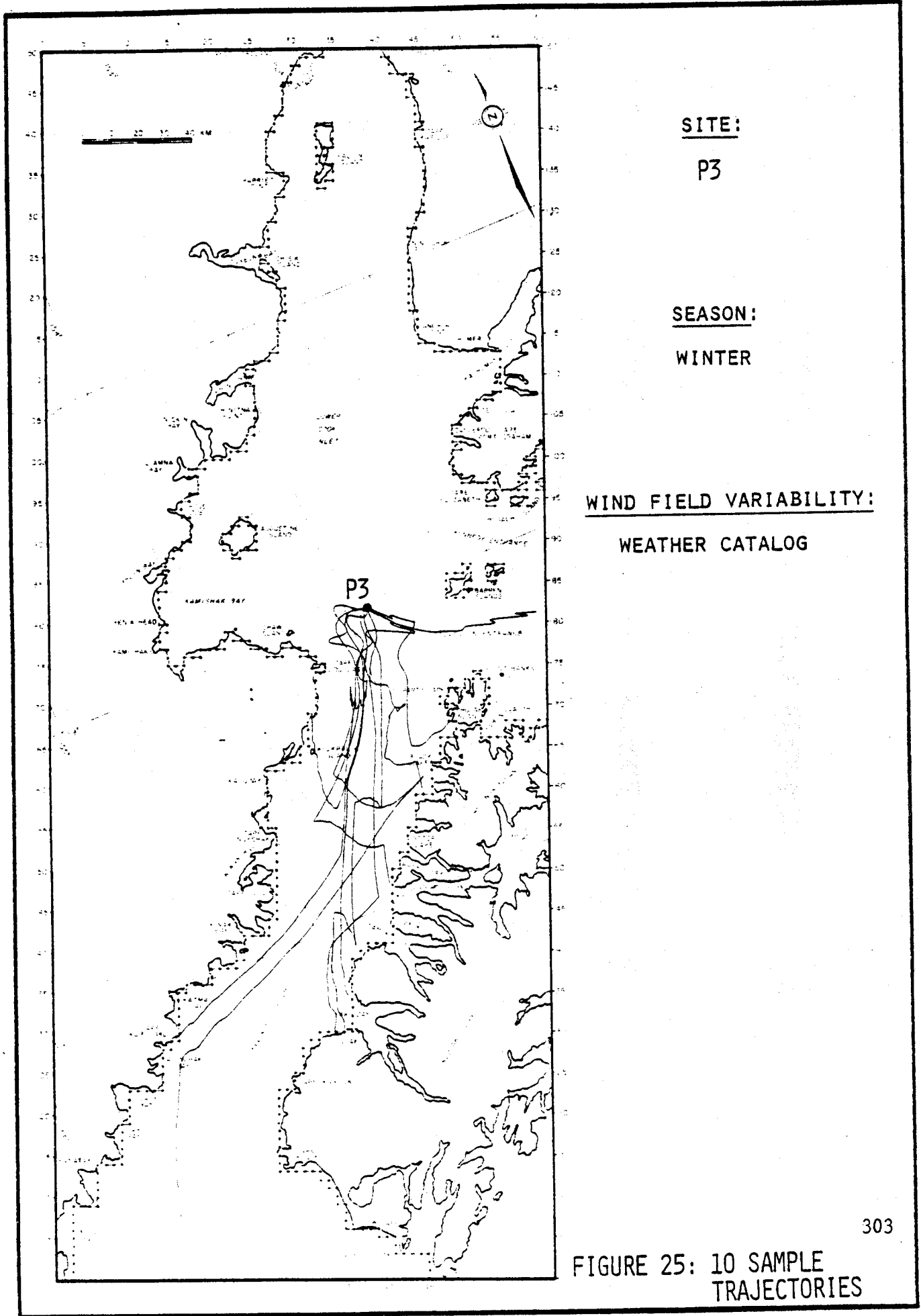
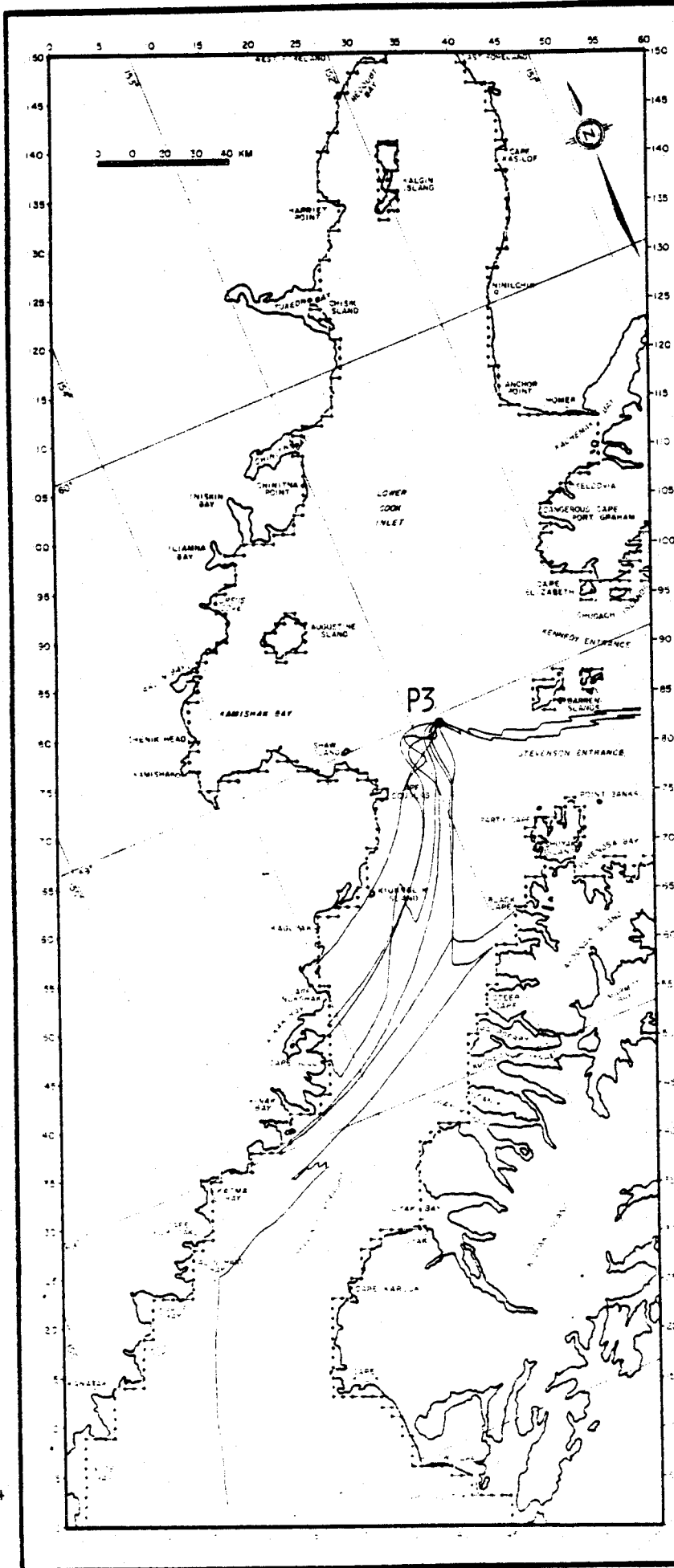


FIGURE 24: 10 SAMPLE TRAJECTORIES





SITE:

P3

SEASON:

WINTER

WIND FIELD VARIABILITY:

WEATHER CATALOG

FIGURE 26: 10 SAMPLE TRAJECTORIES

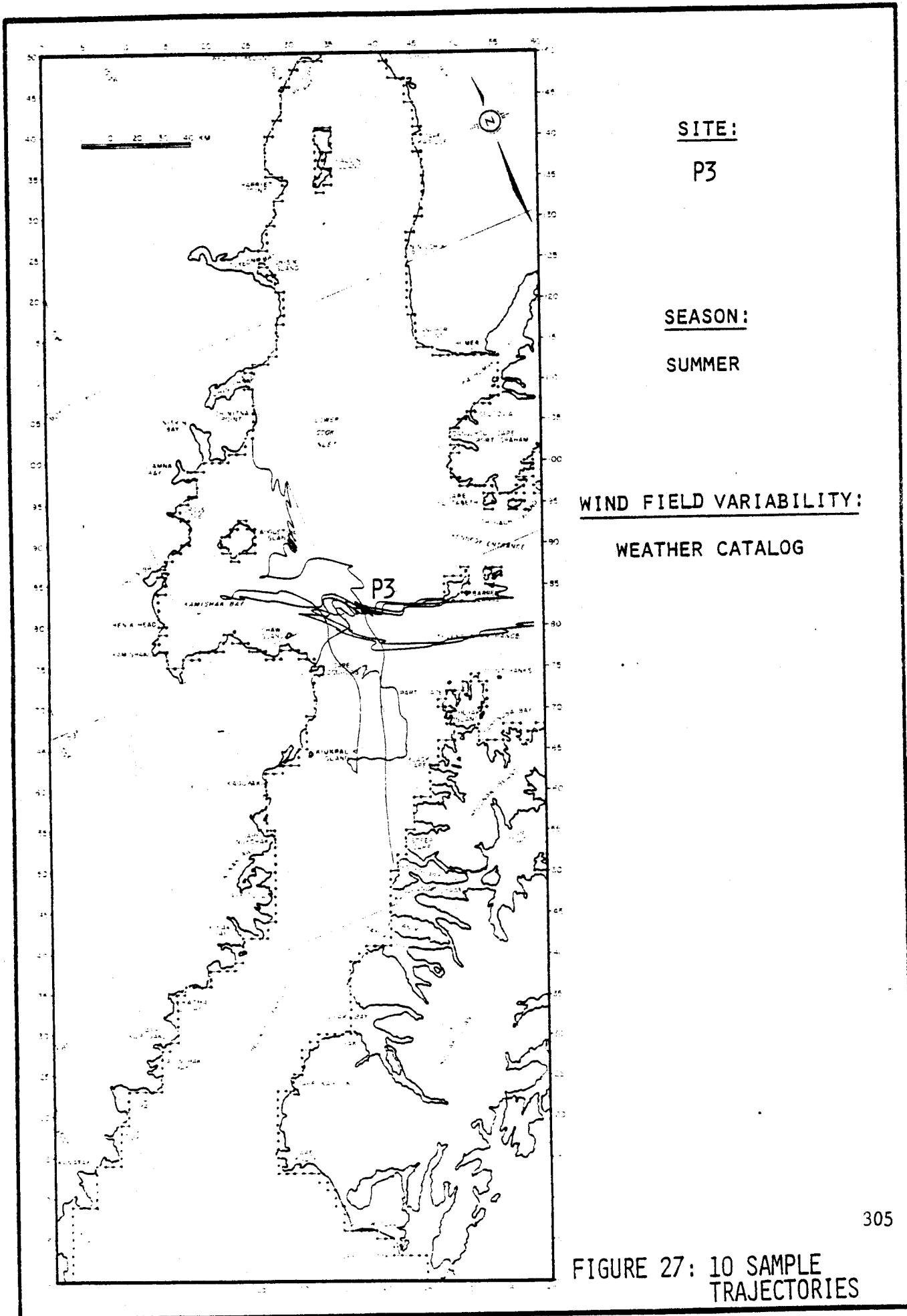
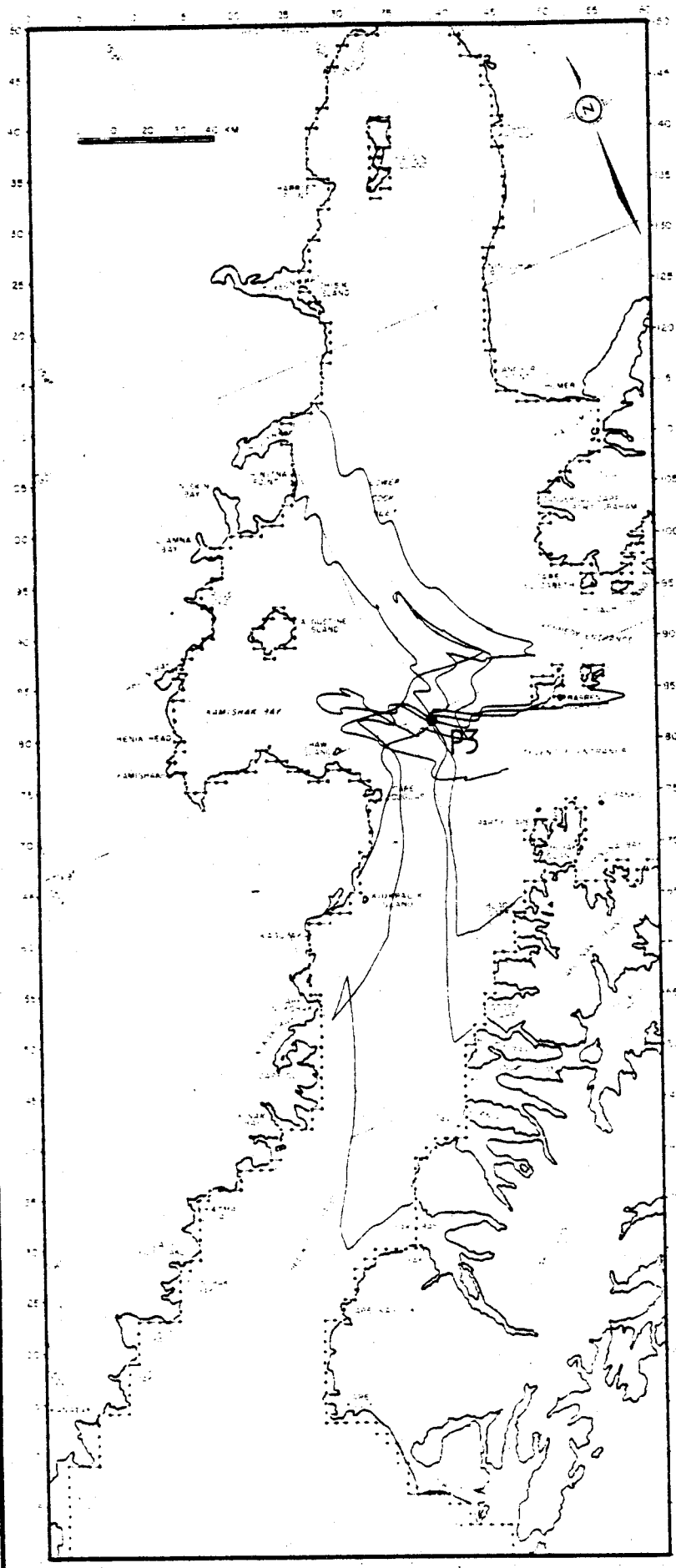


FIGURE 27: 10 SAMPLE TRAJECTORIES



SITE:

P3

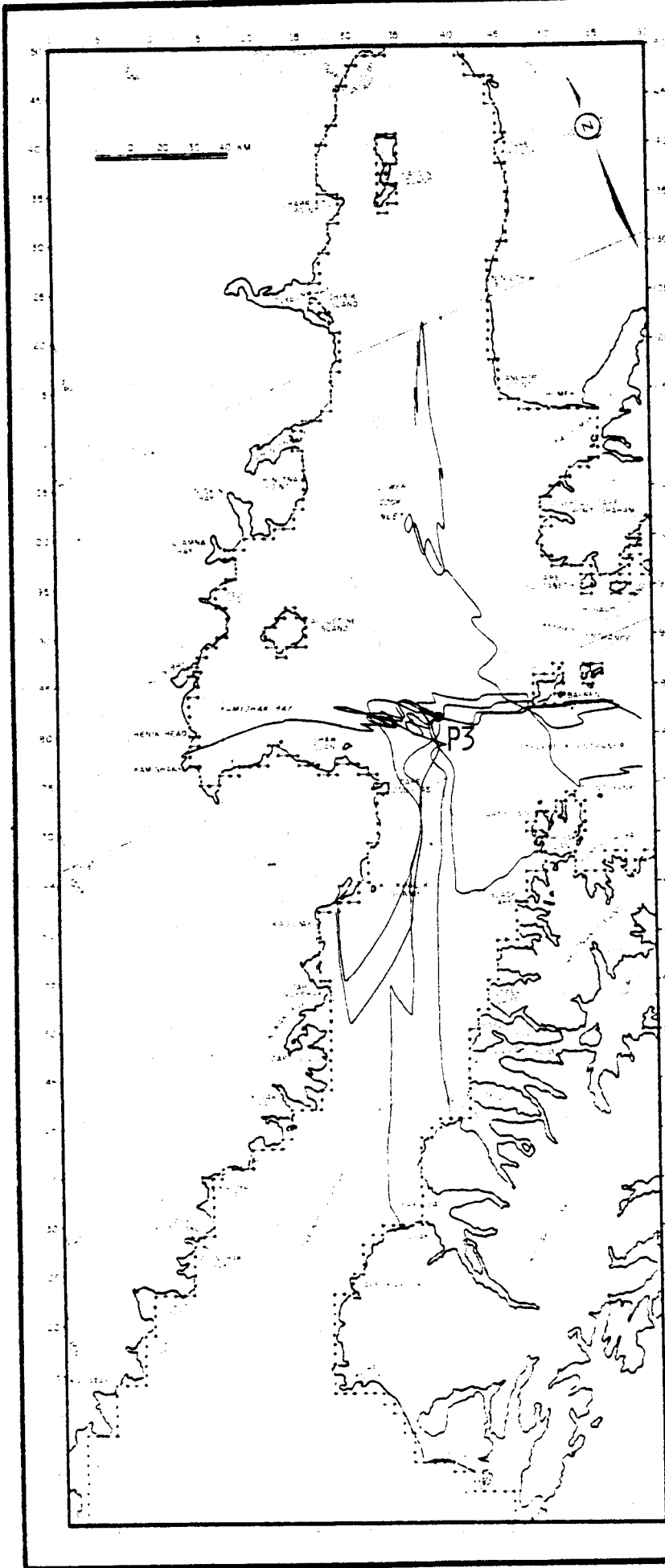
SEASON:

SUMMER

WIND FIELD VARIABILITY:

WEATHER CATALOG

FIGURE 28: 10 SAMPLE TRAJECTORIES



SITE:

P3

SEASON:

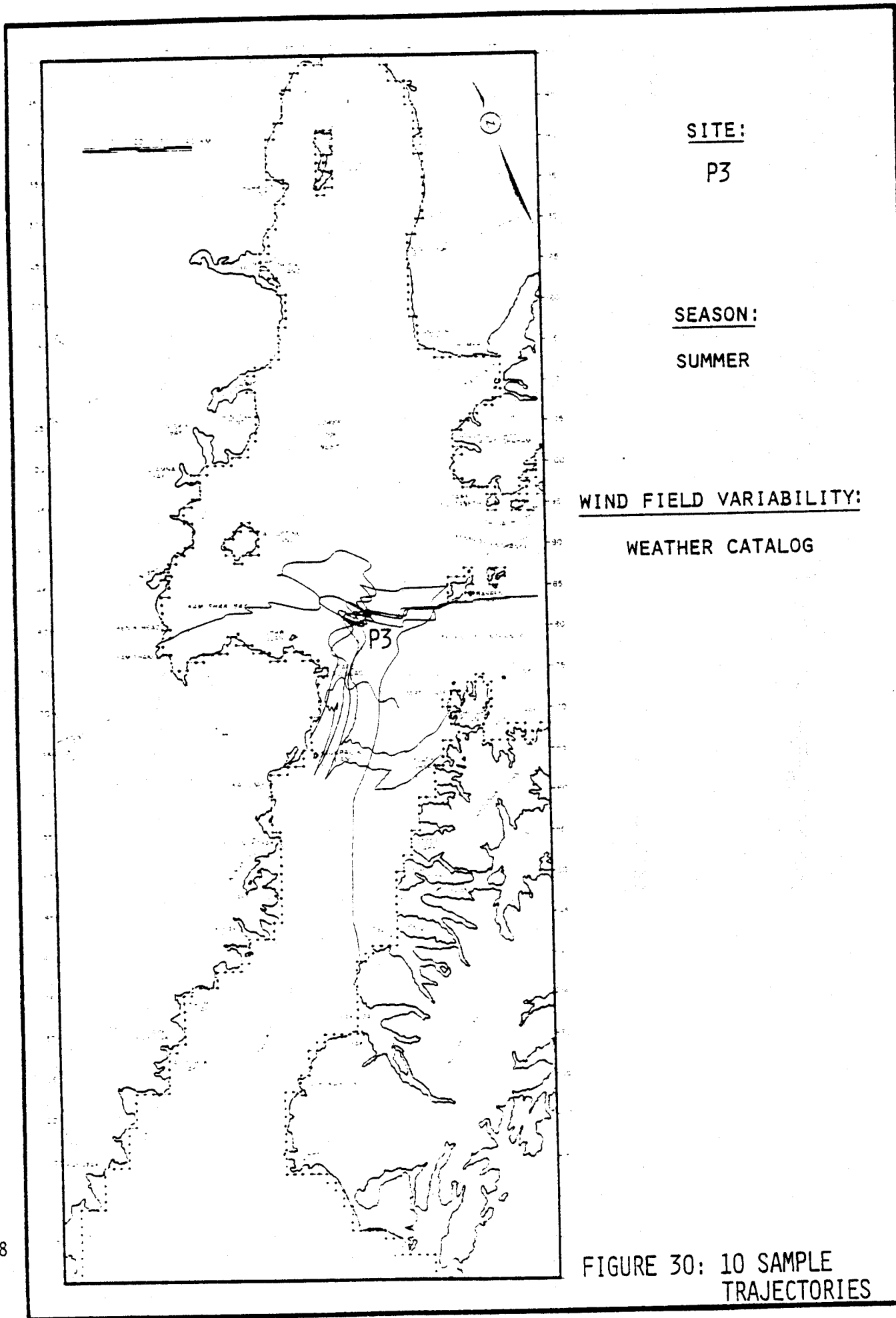
SUMMER

WIND FIELD VARIABILITY:

WEATHER CATALOG

307

FIGURE 29: 10 SAMPLE TRAJECTORIES



SITE:
P3

SEASON:
SUMMER

WIND FIELD VARIABILITY:
WEATHER CATALOG

FIGURE 30: 10 SAMPLE TRAJECTORIES

WIND
4

SITE
8

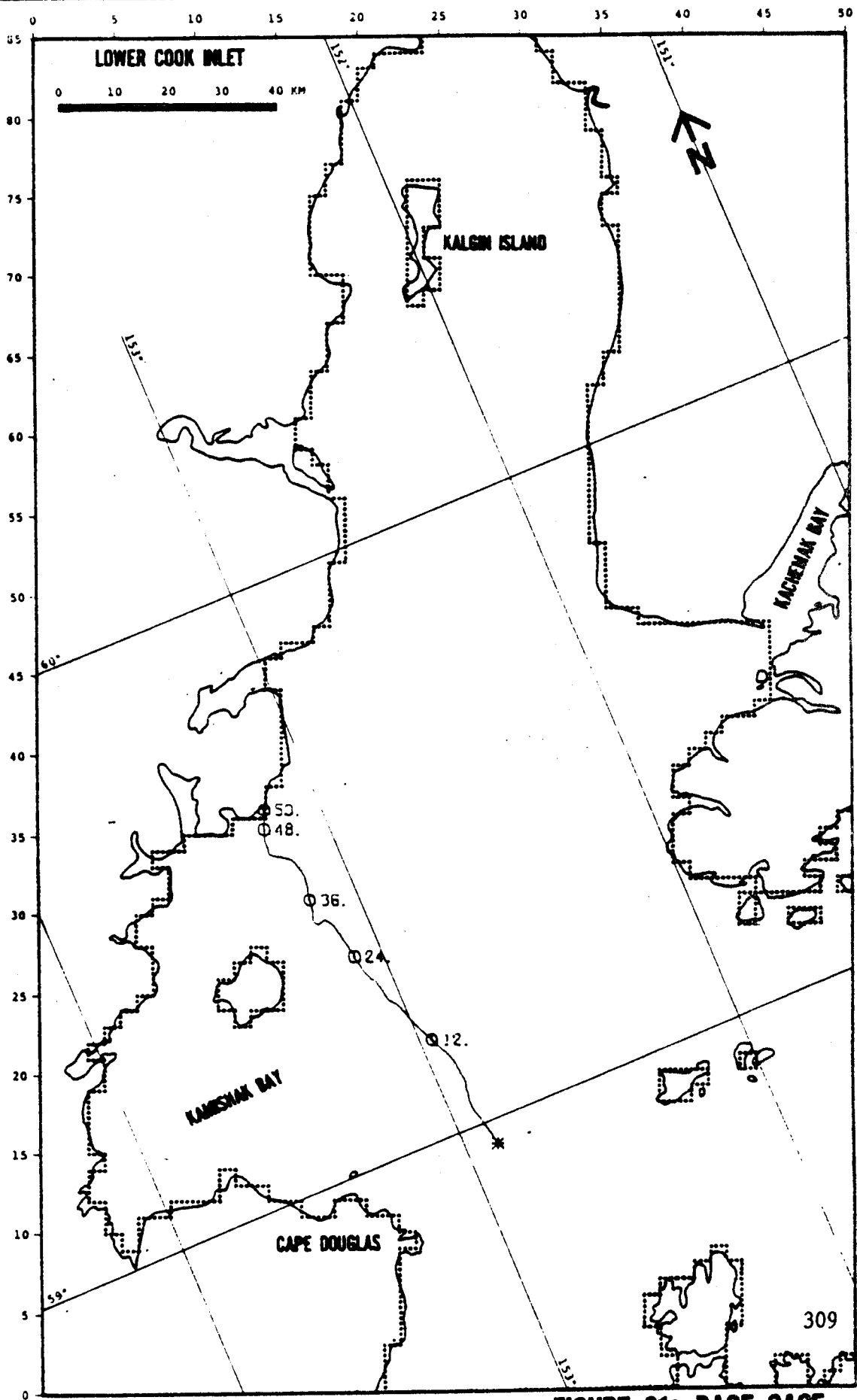


FIGURE 31: BASE CASE
(FROM DAMES & MOORE, 1979)

WIND
6

SITE
3

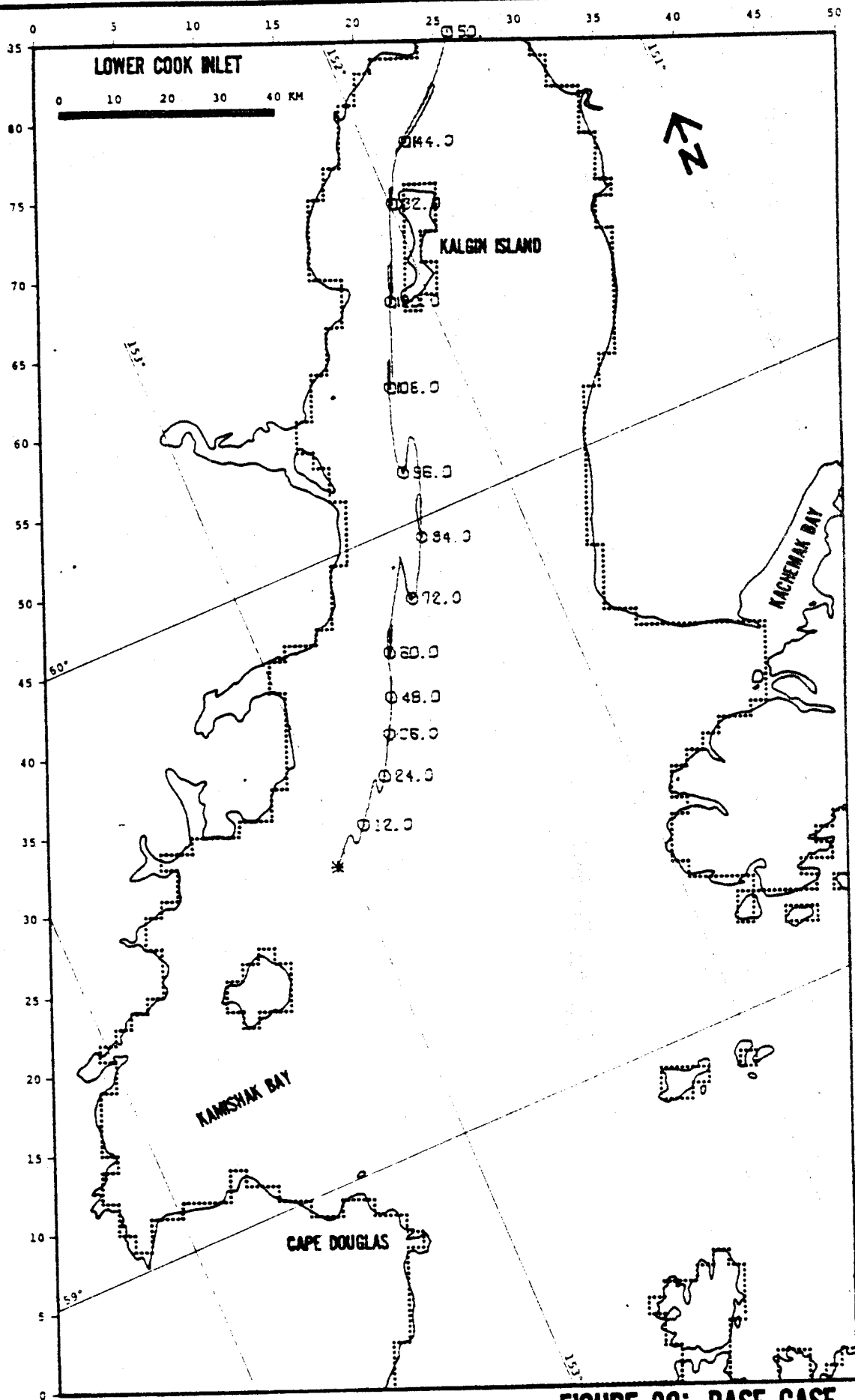
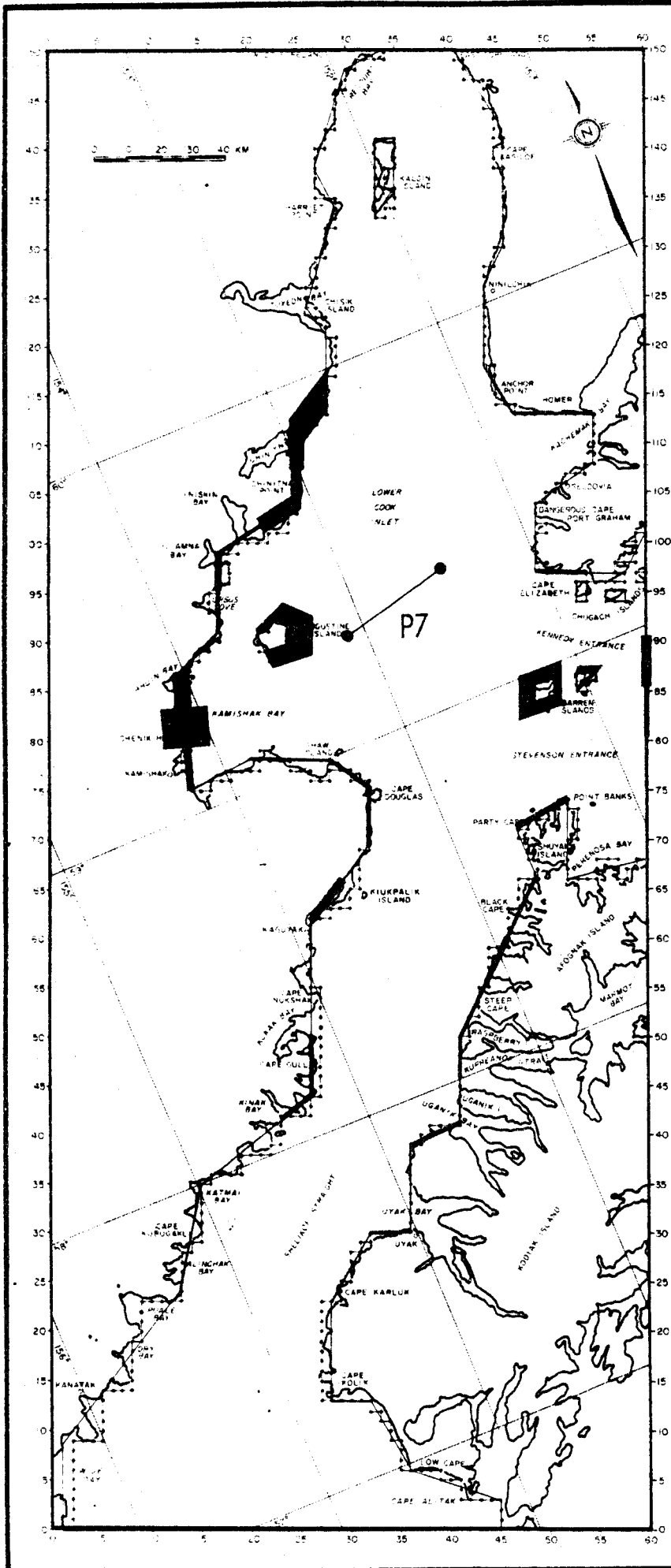


FIGURE 32: BASE CASE

(FROM DAMES & MOORE, 1979)



SITE:

P7

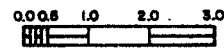
SEASON:

SUMMER

WIND FIELD VARIABILITY:

WEATHER CATALOG

PERCENT FREQUENCY OF
BOUNDARY IMPACT PER
KILOMETER OF REACH



NOTE: WIDTH OF SHADING
ALONG SEGMENTED REACHES
REPRESENTS MAGNITUDE OF
PERCENT FREQUENCY OF
BOUNDARY IMPACT

FIGURE 34: BOUNDARY IMPACT
FREQUENCY

PROBABILITY RANGES:

- 0-10%
- ▣ 10-20%
- 20-30%

SITE 8

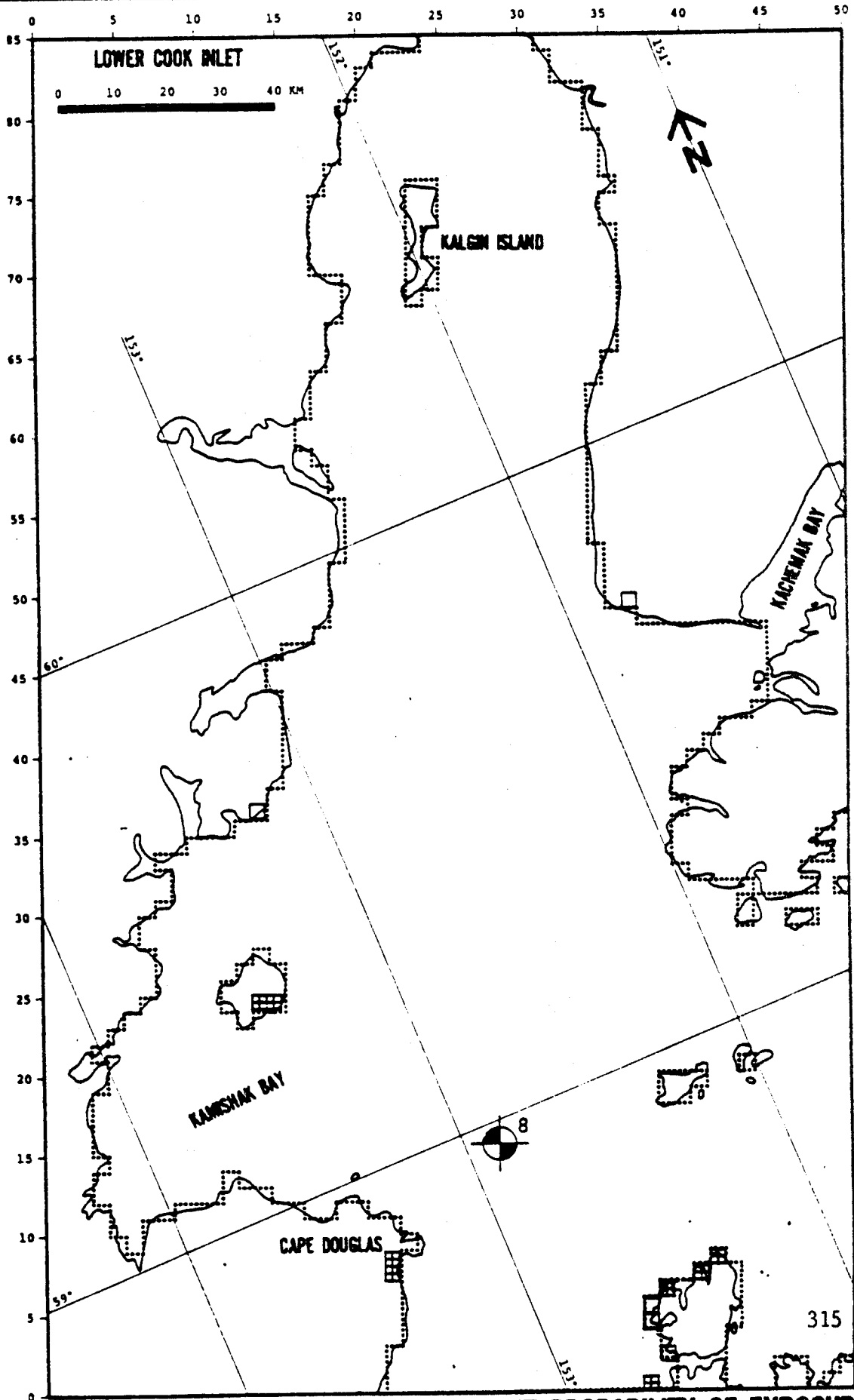


FIGURE 37: ANNUAL PERCENT PROBABILITY OF EXPOSURE
(FROM DAMES & MOORE, 1979)

50 11 0053531523222243224545431543232323262645252222151526222215434300
50 12 0053531515225353142543452553532626142323231414142345252522144353
51 1 0053141442422525255353435315151414141553151515152623232323232342
51 2 0014141414142314142323454245424225535315424225252322251643000000
51 3 00232323232623232314532553532653151423534314535325255353141442
51 4 0042255353252525532315154342424242452623234242144325252525255300
51 5 00434342422323232323232314532553452525252553535342424242454242
51 6 00424242424242434314535353535345454542454243434343234242454300
51 7 0042424242333342452323424223434245434233535353151543434315155331
51 8 0015535353454545434242252525535331534342225353334242252525434323
51 9 0023235325535353235353255353534515252542454223232314145322535300
51 10 0053333353535353531414151522232323234242424223425333342424242
51 11 0025535325455325251442535322334316532545424242532525255353532500
51 12 0053535353151514142342432323532223234253334242432342434342452525
52 1 0033432553141514151523425342234253154343431414231425252542142323
52 2 0053535314234242422525151414141442424245425342535314454543450000
52 3 00452314141442424243454253254553531515141442532525535353151515
52 4 001515151542424242255315535353532525534325255353422553434532200
52 5 0022434333535315144323141553434226422533335315434343454225434353
52 6 0053535333343454542424223434343432314434343434343434343434300
52 7 0053433345454253334242424225331543432515422342424243424343334316
52 8 0016454345454242424245431515151543535353531516533343141442424225
52 9 0053421515151542425353155353141414535322451514232325252553531400
52 10 0014144242535343434353531522454553332253532514532345162242255314
52 11 0053535342424242252553532553142525252553422543254545422314231400
52 12 0014252514535353535353535353535353152523232525252525252553255353
53 1 0053534242424542232323141423141423232553535353152314231414141414
53 2 005353534314141425254342254225535353422525434242252542252500000
53 3 00534214141414151514143126452525353531453252523535353535315
53 4 00425353535315152323232314144253254225535343432325252525231400
53 5 0023142314431414535343145353435323255353252543434342424243424242
53 6 00422342231453434343435343454553431515151515151515151523434300
53 7 0043434343434331535343151515535315333343434242424223234242424242
53 8 00425353534343433343333343434353531543224343453333333333353535353
53 9 00431616535353534226265353534242535333335353535353535353531515232300
53 10 00141414142525535353535325255353535353535353535353531453531414141453
53 11 0053531553262622422232325535353535314224223142323234225532553421414235314
53 12 004525353535353535353535314224223142323234225532553421414235314
54 1 0053141414145353535343262626232323232323232323232323232323231443435353
54 2 004253532525533332323232314141523144343163131435315151442000000
54 3 004253162332225531553535315154522151545454343151523232323232323
54 4 0023231543152343151423155333535353434314141515151523234545252500
54 5 002225255322252542454242424342323232325434315141433144325255323
54 6 005353434242454242452543535353533342234516333333333435331454200
54 7 0042423534343433131334333224242535331535333434343424245455343155
54 8 0031313131424245454553535343433143434545434345454343164533424533
54 9 0045453325313116224343151442454243314343435353535315434242454200
54 10 0042422323231414252553533325252525535353535345455322534225252553
54 11 005343255353534223141423231414535353535353535353535353164531154200
54 12 0053431526435353532525535315533131312315535353151515151443313122
55 1 0043255315142542452553424242532514142525532553532525424242141414
55 2 0042535325151515144223535315531543434343432342424242421523000000
55 3 00154242252525154253531523424245534533424222424242424225255353142525
55 4 0015144215151515535353222214531545423353535353535314141442532500
55 5 0042423142532553435353434242424225535353434245252525535343434242
55 6 005343155333422325535353333333343314343422531254242535353534300
55 7 004245454343434342252553534543453333342424342424545535353431515
55 8 004243434353535353255353435322535315433133334325255333333332325
55 9 00255333154242424242535353535353222224242424545534323454553252500
55 10 0022252553535353151553255333535353535353535353535353535353531515151523
55 11 0023232343431553531542424214141415151553531423264242262642535300
55 12 0053141414232314255315264543234242532323231516152343264331151525
56 1 0015265315232253221523232323232315154315252525251523234245452215
56 2 002553424243434353151515232342252553151523234553535353252515530000
56 3 0015151515141515152342454542532525252542424225251523142214141443
56 4 00145353531514145325252553535342255353232323454242424242424200
56 5 0025254223234253535353534253535353535314535353534245452543535343
56 6 00535345455353532525434343423353155353255331313115155343422300
56 7 00232331313131431515232323232331151553425353422323234543434343
56 8 00153333151643223123424242225255353535353535353535353535353535343
56 9 004342424253422542424542454533232243535353535343141442452255300

56 10 005353535353532222225353432553535315532253141414222243255353151515
56 11 0016255353152314145353151514434353142553252553534242255325162300
56 12 0015232323232342151415232323422323141525144343313131314242535323
57 1 002325424315152342232323232323232323422323232342232323454242452323
57 2 0023424242424343535315152325431514424242232323232525254325000000
57 3 0043251425141414142525151514434242255333334315151414331423232323
57 4 0025161523424245454242454545154542424223421414144253535314232300
57 5 0023232342424223234242232323144225252525255343434323141453431442
57 6 0042424242232323254342252525333316252515151553533325165353434300
57 7 00434333333333163325454245332545454545333343433535343432215151542
57 8 00424245453333154242434353534242422333333151515234242425333325
57 9 0042452542255343434343422533454223422553434315235315155353531500
57 10 0016422342424523432516165333424242421553234545452243432325253343
57 11 0025252525334545232323252525254242252545454214425353255325255300
57 12 0025253325252525334545333333535314141414252525255315142525141553
58 1 0015231443252525331414232323232323231414232323232525232323232323
58 2 004242422323232323232323141423232323252523232325231442000000
58 3 0042254315453314141442424523162323232345535322531414141414142525
58 4 0025141423424223142323255325252553535322432323454545452323234200
58 5 00141453535353535353142314535325434545452525424242232323232342
58 6 00424242424242424242424232525253342533323424225333334343333333300
58 7 0053165342424242534353434225333315534253533325535323232525333343
58 8 004353535353535342435325252525535353535315425353535334322333333
58 9 003345531516163322424243423353151533535353533252534315154200
58 10 00252534343333342222151522455353532525151545142225531522532553
58 11 0053535325252553531515151515454525535315152245424242252531231400
58 12 0053534542232323232323144223232323232323252525255353234315151515
59 1 00232353535315151515151523231515152323232314141414142525424242
59 2 00252545431523424323435323454545254253534343152525252553000000
59 3 00432515141453535315151515151553531515153153141414235325535325
59 4 002525531553151525255325424343151443141414232345425353333454500
59 5 0045454542251425255353314141425252525231515424543422342434343
59 6 002525435353252515152215424245424542323235353333315155333432200
59 7 00335353253343222233335353535353535322224353535343334343435353
59 8 0043231515155333315334223454325144545455353333434342454353535353
59 9 0053435353535343232515152245425353141414314343254353434245252500
59 10 0033342232323232314141453535343162323234225252534225342253254353
59 11 003314424253535333323234542454542252525535325534242422525532500
59 12 0053534215155353435353534325252515222514535353535315534325534242
60 1 00424242252553434553535353535353532542422323231423232342232325252
60 2 00532525252525252553535353252525454545222242454242232323230000
60 3 0023232323231515152353531415532525255315232314421414151423231425
60 4 00535315155353424253534325252525353155353535343535353232323141400
60 5 0023421415232325533316252525251423232353252345252525142523315353
60 6 00534333232342434343535333335353531543421422224542253252535300
60 7 0053535353535333424215152323232553535333424242424343435353533333
60 8 003353533325333343151542424242435353535333453333345254553531553
60 9 0043252525155322434353252525434525532542424225252533534543234500
60 10 00333332525435343425314141425252542232226252525252525253252525
60 11 005353142553532342422614141414145325252525535315151515224222532600
60 12 0026333314424225252525532553424242422323232525252526424242255314
61 1 0014252525255314141423232325252525422342424242454545142323232322
61 2 005353535325535353535314141414141414141414141414231425154353252500000
61 3 00255314232325252323252543155353532525232314141414141423232525
61 4 005353144343425343453333343535325535353434245424545531514232300
61 5 0023234223424223262345532214144553532553535314535342425353534242
61 6 004253335353252553152525255353151515155353314353535353342424200
61 7 0043535353531653535322433343533345535353334343454245424542424245
61 8 0043334525535353534245425315433353424545455353533333535325532553
61 9 005353533345252553454525255353535353534233252525252533234545535300
61 10 005353535353422525151415151515154535345452553535353535353254315
61 11 0045451442534315535353532225434225535342535353154253532623422500
61 12 0025535315434215454545252525152515152323261415141515531543432325
62 1 0025162522151523234222152345224515232323232345432315231515151525
62 2 005353234242424242535353531423232323234545421542234242232323000000
62 3 0023422242454553534542231415531415155343151515232525142525422342
62 4 0045421425151522431553161515155343151525251553153333335343434300
62 5 0015151542422342454245422553434225334542333345333345452515151533
62 6 0033335343535333334542454533254343431515151543253353533333534200
62 7 0042234243424542424525255353425342424242532214424245424242424245

62 8 0045422553534345333315254242452342434325253333535333454542451643
62 9 004253534215144215331633335353535342232525252522533353152500
62 10 0053331633334225251515151514142553333353533345424225532325232323
62 11 0023424242252325252525151523231442422525435353232525531553252500
62 12 0053532515155323232342252525252553145353252323452315232323232323
63 1 0023432515251543432323424222454545442424223424242232323232323
63 2 0023151515252525251543232323231515422525252525252325252525000000
63 3 0025234253254242425345154253153314252553152233152245431515232323

Input Data File Format: Wind Fields

323

Grid Coord.	Wind Parameters for (Y,X)		Wind Parameters for (Y,X+3)		Wind Parameters for (Y,X+6)		Wind Parameters for (Y,X+9)		Wind Parameters for (Y,X+12)		Wind Parameters for (Y,X+15)		Wind Parameters for (Y,X+18)	
N Y X	V	θ	V	θ	V	θ	V	θ	V	θ	V	θ	V	θ
XXXXXX	XX.	XXX.	XX.	XXX.	XX.	XXX.	XX.	XXX.	XX.	XXX.	XX.	XXX.	XX.	XXX.

N - WIND FIELD NUMBER

(Y,X) - GRID CELL LOCATION FOR WIND FIELD DATA

V - WIND VELOCITY AT (Y,X) IN METERS/SEC

θ - DIRECTION OF WIND VELOCITY AT (Y,X) IN DEGREES (MEASURED CLOCKWISE FROM NORTH)

100000	05.	170.	05.	170.	05.	170.	07.	170.	07.	175.	08.	175.	08.	175.
100021	08.	175.	09.	170.	09.	165.	09.	160.	08.	155.	08.	145.	06.	140.
100042	05.	130.	05.	130.										
100300	05.	170.	05.	170.	05.	170.	07.	175.	07.	175.	08.	175.	08.	175.
100321	08.	175.	09.	170.	09.	170.	08.	160.	08.	155.	05.	140.	05.	130.
100342	05.	130.	05.	130.										
100600	05.	170.	05.	170.	05.	170.	07.	175.	07.	175.	08.	175.	08.	175.
100621	09.	175.	09.	175.	09.	170.	08.	160.	06.	145.	05.	140.	05.	135.
100642	05.	130.												
100900	05.	170.	05.	170.	05.	170.	07.	175.	07.	175.	08.	175.	09.	175.
100921	09.	175.	10.	170.	09.	165.	07.	160.	05.	155.	05.	150.		
100942														
101200			05.	170.	05.	170.	06.	170.	07.	170.	08.	170.	09.	175.
101221	09.	175.	10.	175.	08.	170.	07.	165.	05.	160.	05.	155.		
101242														
101300			05.	170.	05.	170.	05.	170.	05.	170.	08.	175.	09.	175.
101521	09.	175.	10.	175.	06.	175.	06.	170.	05.	165.				
101542														
101800				05.	170.	05.	170.	06.	170.	08.	175.	08.	175.	
101821	09.	175.	10.	175.	08.	175.								
101842														
102100				05.	170.	05.	170.	05.	170.	06.	175.	08.	180.	
102121	09.	180.	09.	180.	09.	175.	07.	170.						
102142														
102400							05.	170.	05.	170.	05.	175.	08.	180.
102421	08.	180.	09.	180.	09.	175.	07.	170.						
102442														
102700									05.	170.	05.	170.	08.	180.
102721	08.	180.	08.	180.	09.	175.	10.	170.	08.	170.				
102742														
103000									05.	170.	05.	170.	08.	180.
103021	07.	180.	08.	180.	08.	175.	10.	170.	08.	170.	05.	170.		
103042														
103300											05.	175.	05.	180.
103321	07.	180.	08.	175.	08.	175.	10.	175.	08.	170.	05.	170.		
103342														
103600											05.	180.	05.	180.
103621	05.	175.	08.	175.	08.	175.	08.	175.	08.	170.	05.	170.		
103642														
103900													05.	180.
103921	05.	175.	05.	170.	07.	175.	08.	180.	08.	175.	09.	170.	10.	170.
103942	05.	170.												
104200														
104221	05.	175.	05.	170.	06.	175.	09.	175.	09.	175.	10.	170.	10.	170.
104242	05.	170.												
104500														
104521			05.	170.	05.	170.	08.	175.	10.	175.	10.	170.	08.	170.
104542	05.	170.												
104800														
104821					05.	170.	07.	170.	10.	175.	10.	170.	08.	170.
104842	06.	170.												
105100														
105121					06.	170.	08.	170.	10.	170.	10.	170.	08.	170.
105142	06.	170.	05.	170.										
105400														
105421			05.	170.	06.	170.	08.	170.	09.	175.	10.	175.	10.	170.
105442	07.	170.	05.	170.										
105700														
105721			05.	170.	05.	170.	08.	175.	09.	175.	10.	175.	10.	170.
105742	05.	170.	05.	170.	05.	170.								
106000														
106021			05.	170.	05.	170.	07.	180.	09.	180.	10.	175.	10.	175.
106042	10.	175.	08.	165.	05.	165.								
106300														
106321			05.	170.	05.	170.	08.	200.	09.	190.	10.	180.	10.	175.
106342	10.	175.	08.	165.	05.	165.								
106600														
106621							08.	205.	11.	205.	11.	190.	10.	180.
106642	09.	175.	05.	165.	05.	165.	05.	160.	08.	145.	08.	140.	10.	140.
106900														
106921							08.	190.	11.	195.	11.	190.	10.	180.
106942	09.	170.	09.	165.	08.	160.	08.	155.	10.	150.	10.	140.	10.	140.
107200									10.	045.	08.	045.	06.	045.
107221	04.	050.					05.	180.	08.	175.	10.	175.	12.	170.
107242	10.	165.	10.	160.	10.	155.	10.	150.	10.	145.	10.	140.	10.	140.

107500										15.	050.	10.	045.	08.	045.		
107521	05.	060.	05.	090.	05.	100.	10.	130.	12.	155.	12.	165.	12.	170.			
107542	10.	165.	10.	165.	10.	155.	10.	150.	10.	150.	10.	145.	10.	145.			
107800											15.	070.	15.	065.	10.	065.	
107821	08.	075.	08.	090.	10.	110.	11.	120.	12.	140.	12.	155.	11.	165.			
107842	10.	165.	10.	165.	10.	155.	10.	145.	10.	140.	10.	145.	10.	145.			
108100											15.	065.	15.	075.	15.	080.	
108121	14.	085.	13.	090.	13.	095.	12.	115.	11.	140.	11.	160.	10.	170.			
108142	10.	160.	10.	155.	08.	140.	08.	140.	10.	145.	10.	150.	10.	150.			
108400											15.	065.	15.	085.	15.	095.	
108421	14.	110.	13.	110.	13.	120.	12.	145.	11.	150.	10.	170.	10.	170.			
108442	10.	165.	10.	160.	08.	140.	08.	145.	10.	145.	10.	150.	10.	150.			
108700											15.	060.	15.	070.	15.	115.	
108721	15.	125.	10.	130.	13.	145.	12.	150.	10.	155.	10.	170.	10.	170.			
108742	10.	160.	10.	155.	10.	145.	10.	140.	10.	140.	10.	145.	10.	145.			
109000											13.	110.	13.	120.	11.	160.	
109021	08.	170.	05.	160.	10.	150.	10.	155.	10.	160.	10.	170.	10.	170.			
109042	10.	160.	10.	150.	10.	140.	10.	135.	10.	140.	10.	135.	09.	130.			
109300												11.	145.	09.	180.		
109321	08.	200.	09.	165.	10.	165.	10.	165.	10.	170.	10.	165.	10.	165.			
109342	10.	165.	10.	160.	10.	150.	10.	140.	10.	130.	10.	110.	10.	100.			
109600												05.	160.	05.	200.		
109621	09.	200.	09.	190.	09.	180.	10.	170.	10.	170.	10.	170.	10.	170.	10.	160.	
109642	10.	160.	10.	160.	10.	160.	10.	130.	08.	090.	08.	090.	08.	090.			
109900												05.	200.	05.	210.		
109921	08.	200.	09.	185.	09.	180.	10.	175.	10.	175.	10.	165.	10.	160.			
109942	10.	160.	11.	165.	12.	145.	08.	145.	06.	130.	06.	110.	06.	090.			
110200														05.	210.		
110221	05.	210.	05.	205.	09.	190.	10.	180.	10.	175.	10.	165.	10.	165.			
110242	10.	165.	10.	155.	10.	180.	05.	170.			05.	090.	05.	090.			
110500																	
110521			05.	205.	09.	195.	10.	185.	10.	180.	10.	180.	10.	175.			
110542	10.	170.	10.	165.	08.	185.	06.	195.	05.	195.							
110800																	
110821			05.	190.	10.	195.	10.	190.	10.	180.	10.	180.	10.	175.			
110842	10.	175.	08.	195.	08.	200.	08.	215.	06.	215.	05.	215.					
111100																	
111121			05.	190.	08.	185.	10.	185.	10.	180.	10.	180.	10.	180.			
111142	10.	180.	09.	195.	07.	210.	07.	225.	07.	225.	06.	225.					
111400																	
111421			05.	185.	08.	185.	10.	185.	10.	180.	10.	180.	10.	180.			
111442	10.	180.	08.	180.	05.	180.	05.	250.	05.	235.	05.	210.					
111700																	
111721					05.	180.	08.	185.	10.	180.	10.	180.	10.	180.			
111742	10.	180.	08.	170.													
112000																	
112021					05.	180.	08.	180.	09.	175.	10.	180.	10.	180.			
112042	10.	180.	08.	180.													
112300																	
112321			04.	185.	05.	180.	07.	175.	09.	175.	10.	180.	10.	180.			
112342	10.	180.	08.	180.													
112600																	
112621			04.	185.	05.	185.	08.	180.	09.	180.	10.	180.	10.	180.			
112642	10.	180.	10.	185.													
112900																	
112921			04.	190.	06.	180.	09.	185.	10.	185.	10.	180.	10.	180.			
112942	10.	180.	10.	185.	06.	185.											
113200																	
113221					06.	180.	09.	180.	08.	180.	10.	180.	10.	180.			
113242	10.	180.	10.	180.	06.	185.											
113500																	
113521					06.	180.	09.	180.	08.	180.	10.	180.	10.	180.			
113542	10.	185.	08.	185.	06.	185.											
113800																	
113821					06.	180.	10.	180.	06.	180.	10.	185.	10.	185.			
113842	10.	190.	08.	190.	06.	190.											
114100																	
114121					06.	180.	10.	180.	06.	180.	10.	185.	10.	185.			
114142	10.	190.	08.	190.	06.	190.											
114400																	
114421					06.	180.	08.	180.	10.	185.	10.	185.	10.	185.			
114442	10.	190.	08.	190.	06.	190.											
114700																	
114721					06.	180.	08.	180.	10.	185.	10.	185.	10.	185.			
114742	10.	185.	06.	185.													
115000																	
115021							06.	180.	08.	185.	10.	185.	10.	185.			
115042	08.	185.															

200000	08.	230.	08.	230.	08.	230.	08.	230.	08.	230.	08.	230.	10.	230.	
200021	10.	230.	10.	235.	10.	240.	10.	240.	10.	240.	10.	240.	10.	240.	
200042	10.	240.	10.	245.											
200300	08.	230.	08.	230.	08.	230.	08.	230.	10.	235.	10.	235.	10.	235.	
200321	10.	235.	10.	235.	10.	235.	08.	240.	08.	240.	08.	240.	08.	240.	
200342	08.	240.	08.	240.											
200600	08.	230.	08.	230.	08.	230.	08.	230.	10.	235.	10.	235.	10.	235.	
200621	10.	235.	08.	235.	08.	235.	08.	235.	08.	235.	08.	235.	08.	235.	
200642	08.	235.													
200900	08.	230.	08.	230.	08.	230.	08.	230.	09.	230.	09.	230.	09.	230.	
200921	09.	230.	08.	230.	08.	230.	08.	230.	08.	230.	08.	230.			
200942															
201200			08.	230.	08.	230.	08.	230.	09.	230.	09.	230.	09.	230.	
201221	08.	230.	08.	230.	08.	230.	08.	230.	08.	230.	08.	230.			
201242															
201500			08.	230.	08.	230.	09.	230.	09.	230.	09.	230.	09.	230.	
201521	08.	230.	08.	230.	08.	230.	08.	230.	08.	230.					
201542															
201800					08.	230.	08.	230.	08.	230.	08.	230.	09.	230.	
201821	09.	230.	09.	230.	08.	230.									
201842															
202100					08.	230.	08.	230.	08.	230.	08.	230.	09.	230.	
202121	09.	230.	09.	230.	08.	230.	08.	230.							
202142															
202400							08.	230.	08.	230.	08.	230.	09.	230.	
202421	09.	230.	09.	230.	09.	230.	08.	230.							
202442															
202700									08.	230.	08.	230.	09.	230.	
202721	09.	230.	09.	230.	09.	230.	08.	230.	08.	230.					
202742															
203000									08.	230.	08.	230.	08.	230.	
203021	09.	230.	09.	230.	09.	230.	09.	230.	08.	230.	08.	230.			
203042															
203300												05.	225.	08.	225.
203321	09.	230.	09.	230.	09.	230.	09.	230.	08.	230.	08.	230.			
203342															
203600												05.	225.	08.	225.
203621	09.	230.	09.	230.	09.	230.	09.	230.	09.	230.	08.	230.			
203642															
203900														05.	225.
203921	05.	230.	08.	235.	09.	235.	10.	235.	09.	230.	08.	230.	06.	230.	
203942	06.	230.													
204200															
204221	05.	230.	05.	230.	08.	230.	08.	230.	10.	230.	08.	230.	07.	230.	
204242	06.	230.													
204500															
204521			05.	230.	08.	230.	08.	230.	09.	230.	08.	230.	07.	230.	
204542	06.	230.													
204800															
204821					08.	230.	09.	230.	09.	230.	09.	230.	08.	230.	
204842	07.	230.													
205100															
205121					08.	225.	10.	225.	10.	225.	09.	225.	08.	225.	
205142	07.	225.	06.	225.											
205400															
205421			05.	225.	08.	225.	09.	225.	09.	225.	08.	225.	08.	225.	
205442	07.	225.	05.	225.											
205700															
205721			06.	225.	08.	225.	09.	220.	09.	220.	09.	220.	08.	225.	
205742	08.	225.	07.	225.	05.	225.									
206000															
206021			05.	220.	08.	220.	09.	215.	09.	215.	09.	220.	09.	220.	
206042	09.	225.	08.	225.	05.	225.									
206300															
206321			05.	220.	05.	220.	08.	220.	09.	210.	09.	210.	09.	215.	
206342	09.	205.	08.	205.	06.	210.									
206600															
206621							08.	220.	09.	210.	09.	205.	09.	205.	
206642	09.	200.	10.	205.	08.	220.	08.	230.	08.	230.	08.	230.	08.	230.	
206900															
206921							06.	215.	08.	205.	09.	200.	09.	195.	
206942	09.	200.	10.	205.	10.	210.	08.	235.	08.	230.	10.	230.	10.	230.	
207200									05.	260.	05.	270.	05.	270.	
207221							05.	190.	08.	195.	09.	195.	09.	195.	
207242	09.	200.	09.	200.	09.	210.	10.	215.	10.	220.	10.	220.	10.	220.	

207500									17.	275.	15.	275.	14.	275.
207521	13.	270.	12.	270.	11.	270.	05.	240.	08.	210.	09.	210.	09.	210.
207542	09.	210.	10.	205.	10.	205.	10.	215.	10.	220.	10.	220.	10.	220.
207800									17.	275.	17.	270.	15.	270.
207821	14.	270.	13.	270.	12.	270.	08.	255.	08.	230.	10.	215.	10.	215.
207842	10.	215.	10.	210.	10.	210.	10.	215.	10.	220.	10.	220.	10.	220.
208100									17.	270.	15.	260.	15.	260.
208121	15.	260.	13.	260.	12.	260.	11.	260.	10.	255.	10.	245.	10.	240.
208142	10.	235.	10.	225.	10.	220.	10.	220.	10.	220.	10.	220.	10.	220.
208400									17.	250.	15.	240.	15.	245.
208421	15.	255.	15.	255.	12.	255.	10.	255.	10.	255.	10.	255.	10.	255.
208442	10.	255.	10.	255.	08.	255.	08.	235.	08.	235.	10.	235.	10.	230.
208700									15.	235.	15.	240.	13.	240.
208721	11.	250.	11.	245.	11.	235.	10.	250.	10.	250.	10.	250.	10.	250.
208742	10.	250.	10.	255.	10.	255.	10.	255.	10.	250.	10.	245.	10.	245.
209000									10.	230.	10.	230.	12.	220.
209021	08.	220.	08.	235.	10.	235.	10.	235.	10.	240.	10.	245.	10.	250.
209042	10.	250.	10.	250.	10.	250.	10.	250.	10.	250.	10.	250.	10.	250.
209300											10.	225.	12.	225.
209321	12.	205.	10.	215.	10.	205.	10.	200.	10.	220.	10.	225.	10.	240.
209342	10.	245.	10.	245.	10.	250.	09.	255.	09.	255.	09.	250.	09.	250.
209600											08.	220.	08.	220.
209621	10.	215.	10.	215.	10.	215.	10.	205.	10.	210.	10.	220.	10.	230.
209642	10.	230.	10.	215.	08.	235.	08.	260.	08.	260.	08.	250.	08.	235.
209900											06.	215.	08.	215.
209921	08.	210.	09.	220.	10.	215.	10.	205.	10.	205.	10.	210.	10.	220.
209942	10.	225.	10.	210.	07.	190.	05.	240.	05.	255.	05.	240.	08.	235.
210200													05.	170.
210221	06.	205.	08.	210.	09.	215.	10.	205.	10.	205.	10.	205.	10.	210.
210242	10.	205.	10.	200.	08.	190.	05.	200.			05.	225.	05.	230.
210500														
210521			08.	205.	08.	210.	09.	200.	10.	200.	10.	205.	10.	210.
210542	10.	205.	10.	205.	08.	205.	05.	210.	05.	210.				
210800														
210821			06.	200.	08.	205.	10.	195.	10.	195.	10.	200.	10.	205.
210842	10.	210.	09.	205.	10.	210.	08.	220.	05.	235.	05.	240.		
211100														
211121			05.	240.	08.	205.	10.	200.	10.	195.	10.	195.	10.	200.
211142	10.	200.	09.	195.	05.	230.	08.	240.	10.	225.	05.	220.		
211400														
211421			05.	240.	06.	210.	08.	200.	10.	195.	10.	195.	10.	190.
211442	09.	195.	08.	190.	05.	210.	05.	245.	05.	240.	08.	210.		
211700														
211721					06.	205.	08.	200.	10.	195.	10.	195.	10.	190.
211742	09.	190.	08.	190.										
212000														
212021					08.	195.	08.	195.	10.	195.	10.	190.	10.	185.
212042	09.	190.	08.	200.										
212300														
212321			05.	200.	07.	200.	08.	195.	10.	190.	10.	190.	10.	185.
212342	09.	190.	08.	205.										
212600														
212621			05.	200.	08.	200.	09.	200.	10.	195.	10.	190.	10.	185.
212642	09.	190.	08.	205.										
212900														
212921			05.	205.	08.	200.	09.	200.	10.	195.	10.	195.	10.	195.
212942	09.	195.	08.	210.	05.	210.								
213200														
213221					05.	200.	09.	200.	08.	200.	10.	195.	10.	195.
213242	10.	195.	07.	215.	05.	215.								
213500														
213521					08.	205.	09.	205.	08.	205.	08.	205.	10.	205.
213542	10.	205.	07.	210.	05.	210.								
213800														
213821					08.	205.	09.	205.	08.	205.	08.	205.	10.	205.
213842	08.	205.	07.	205.	05.	210.								
214100														
214121					08.	205.	10.	205.	08.	205.	08.	205.	10.	205.
214142	08.	205.	07.	205.	05.	210.								
214400														
214421					06.	206.	08.	200.	10.	195.	10.	195.	10.	205.
214442	10.	205.	07.	205.	05.	205.								
214700														
214721					06.	200.	08.	200.	10.	195.	10.	195.	10.	205.
214742	10.	205.	07.	205.										
215000														
215021							08.	200.	10.	195.	11.	195.	11.	205.
215042	08.	205.												

300000	08.	030.	09.	030.	10.	030.	10.	030.	10.	030.	10.	030.	10.	030.	
300021	10.	030.	10.	035.	10.	035.	09.	035.	08.	035.	08.	040.	08.	040.	
300042	08.	040.	09.	040.											
300300	08.	030.	08.	030.	09.	030.	10.	030.	10.	030.	10.	030.	10.	030.	
300321	10.	030.	10.	035.	10.	035.	09.	035.	08.	040.	08.	040.	08.	040.	
300342	08.	040.	08.	040.											
300600	08.	030.	08.	030.	08.	030.	09.	030.	10.	030.	10.	030.	10.	030.	
300621	10.	030.	10.	035.	10.	035.	09.	035.	08.	040.	08.	040.	08.	040.	
300642	08.	040.													
300900	08.	030.	08.	035.	08.	035.	09.	035.	10.	035.	10.	035.	10.	035.	
300921	10.	035.	10.	035.	09.	035.	08.	035.	08.	035.	08.	035.			
300942															
301200			08.	035.	08.	035.	09.	035.	10.	035.	10.	035.	10.	035.	
301221	10.	035.	08.	035.	08.	035.	08.	035.	08.	035.	08.	035.			
301242															
301500			08.	030.	08.	030.	08.	030.	09.	030.	10.	030.	10.	030.	
301521	10.	030.	09.	030.	08.	030.	08.	030.	08.	030.					
301542															
301800					08.	030.	08.	030.	08.	030.	10.	030.	10.	030.	
301821	10.	030.	09.	030.	08.	030.									
301842															
302100					07.	030.	07.	030.	08.	030.	10.	030.	10.	030.	
302121	10.	030.	10.	030.	08.	030.	08.	030.							
302142															
302400							07.	025.	07.	025.	08.	025.	10.	025.	
302421	10.	030.	10.	035.	08.	040.	08.	045.							
302442															
302700									07.	020.	08.	020.	10.	025.	
302721	10.	035.	10.	040.	09.	040.	08.	045.	08.	045.					
302742															
303000											08.	020.	10.	020.	
303021	10.	025.	10.	035.	10.	040.	09.	045.	08.	045.	08.	045.			
303042															
303300											06.	020.	08.	020.	
303321	10.	030.	10.	040.	10.	040.	10.	040.	09.	040.	08.	045.			
303342															
303600											06.	020.	06.	020.	
303621	08.	035.	10.	035.	10.	040.	10.	040.	10.	045.	08.	045.			
303642															
303900													06.	020.	
303921	06.	020.	08.	030.	10.	035.	10.	035.	10.	040.	09.	050.	08.	050.	
303942	05.	045.													
304200															
304221	05.	035.	06.	030.	08.	030.	10.	030.	10.	035.	10.	045.	08.	045.	
304242	05.	045.													
304500															
304521			05.	025.	05.	025.	09.	025.	10.	030.	10.	035.	08.	045.	
304542	05.	065.													
304800															
304821					08.	020.	09.	025.	10.	030.	10.	035.	09.	040.	
304842	08.	045.													
305100															
305121					08.	015.	09.	025.	10.	035.	10.	040.	09.	040.	
305142	05.	045.	05.	045.											
305400															
305421			05.	025.	05.	015.	09.	020.	09.	025.	10.	040.	10.	040.	
305442	05.	045.	05.	045.											
305700															
305721			05.	030.	05.	030.	08.	020.	09.	020.	10.	040.	10.	040.	
305742	08.	045.	08.	045.	05.	045.									
306000															
306021			05.	030.	08.	030.	09.	025.	09.	020.	10.	030.	10.	040.	
306042	09.	045.	08.	045.	05.	045.									
306300															
306321			05.	030.	05.	030.	08.	030.	10.	025.	10.	025.	10.	035.	
306342	10.	045.	10.	045.	05.	055.									
306600															
306621							08.	030.	09.	030.	10.	025.	10.	025.	
306642	10.	045.	10.	045.	09.	040.	08.	065.	08.	070.	08.	075.	08.	080.	
306900															
306921							08.	030.	09.	030.	10.	020.	10.	025.	
306942	10.	035.	10.	045.	09.	045.	08.	045.	08.	055.	08.	070.	08.	080.	
307200										15.	050.	10.	040.	08.	030.
307221							05.	020.	05.	010.	10.	015.	10.	025.	
307242	10.	030.	10.	040.	10.	045.	08.	045.	08.	050.	08.	060.	08.	070.	

307500										15.	055.	15.	060.	05.	060.
307521	05.	060.	05.	050.	05.	030.	05.	000.	08.	345.	10.	000.	10.	025.	
307542	10.	030.	10.	035.	10.	040.	10.	045.	08.	050.	10.	055.	10.	055.	
307800										15.	065.	15.	065.	12.	065.
307821	10.	065.	05.	045.	05.	025.	05.	340.	08.	350.	10.	000.	10.	015.	
307842	10.	020.	10.	030.	10.	040.	10.	050.	10.	050.	10.	050.	10.	055.	
308100										15.	065.	15.	065.	15.	065.
308121	12.	060.	10.	050.	05.	025.	09.	000.	10.	350.	10.	005.	10.	015.	
308142	10.	025.	10.	030.	10.	030.	10.	040.	10.	045.	10.	050.	10.	055.	
308400										15.	065.	15.	065.	14.	060.
308421	13.	055.	12.	050.	10.	040.	09.	000.	10.	005.	10.	010.	10.	015.	
308442	10.	025.	10.	030.	10.	030.	10.	040.	10.	045.	10.	050.	10.	055.	
308700										15.	070.	15.	065.	14.	055.
308721	14.	050.	13.	040.	13.	035.	09.	010.	10.	015.	10.	010.	10.	010.	
308742	10.	025.	10.	030.	10.	045.	10.	050.	10.	050.	10.	055.	10.	055.	
309000										10.	085.	10.	055.	13.	045.
309021	13.	035.	13.	040.	13.	035.	10.	025.	10.	020.	10.	015.	10.	010.	
309042	10.	015.	10.	025.	10.	050.	10.	055.	11.	060.	10.	060.	10.	055.	
309300											10.	040.	10.	035.	
309321	12.	020.	09.	025.	12.	025.	12.	015.	10.	015.	10.	010.	10.	005.	
309342	10.	010.	10.	020.	10.	035.	11.	060.	12.	060.	12.	060.	11.	060.	
309600											10.	040.	10.	030.	
309621	11.	015.	10.	020.	10.	015.	10.	010.	10.	010.	10.	015.	10.	015.	
309642	10.	010.	10.	015.	08.	025.	07.	070.	07.	070.	11.	060.	12.	060.	
309900											10.	035.	10.	025.	
309921	10.	015.	10.	015.	10.	010.	10.	010.	10.	005.	10.	005.	10.	010.	
309942	10.	010.	10.	015.	08.	015.	08.	025.	07.	050.	06.	060.	05.	060.	
310200													05.	025.	
310221	08.	015.	08.	015.	10.	010.	10.	010.	10.	005.	10.	005.	10.	010.	
310242	10.	010.	10.	015.	08.	015.	08.	030.			05.	060.	05.	060.	
310500															
310521			05.	005.	08.	000.	10.	000.	10.	000.	10.	005.	10.	005.	
310542	10.	010.	10.	015.	09.	030.	08.	035.	05.	035.					
310800															
310821			05.	000.	08.	355.	10.	000.	10.	000.	10.	000.	10.	000.	
310842	10.	000.	10.	010.	10.	015.	07.	045.	06.	045.	05.	040.			
311100															
311121			05.	000.	08.	355.	10.	355.	10.	355.	10.	350.	10.	350.	
311142	10.	355.	10.	355.	09.	000.	08.	035.	07.	035.	07.	025.			
311400															
311421			05.	000.	08.	355.	08.	355.	10.	355.	10.	350.	10.	350.	
311442	10.	350.	10.	355.	08.	350.	07.	040.	07.	040.	05.	040.			
311700															
311721					05.	355.	08.	350.	10.	350.	10.	350.	10.	350.	
311742	10.	350.	08.	000.											
312000															
312021					05.	350.	08.	350.	10.	350.	10.	350.	10.	350.	
312042	10.	350.	08.	000.											
312300															
312321			05.	350.	08.	350.	08.	350.	10.	350.	10.	350.	10.	345.	
312342	10.	345.	08.	350.											
312600															
312621			05.	350.	08.	355.	08.	355.	10.	345.	10.	345.	10.	345.	
312642	10.	345.	08.	350.											
312900															
312921			05.	350.	08.	355.	08.	355.	10.	340.	10.	340.	10.	345.	
312942	10.	345.	08.	345.	05.	345.									
313200															
313221					05.	355.	10.	350.	10.	340.	10.	340.	10.	340.	
313242	10.	345.	08.	345.	05.	345.									
313500															
313521					05.	350.	08.	345.	10.	340.	10.	340.	10.	340.	
313542	10.	345.	08.	350.	05.	350.									
313800															
313821					05.	345.	08.	340.	10.	340.	10.	340.	10.	345.	
313842	10.	350.	08.	350.	05.	350.									
314100															
314121					05.	345.	08.	340.	08.	345.	10.	345.	10.	345.	
314142	10.	350.	08.	350.	05.	350.									
314400															
314421					05.	350.	08.	350.	10.	350.	10.	345.	10.	345.	
314442	10.	345.	08.	345.	05.	345.									
314700															
314721					05.	350.	08.	350.	10.	355.	10.	345.	10.	345.	
314742	08.	345.	05.	345.											
315000															
315021							08.	355.	10.	355.	10.	345.	10.	345.	
315042	08.	345.													

400000	05.	340.	07.	340.	08.	340.	09.	340.	09.	340.	10.	340.	10.	335.	
400021	10.	335.	10.	330.	10.	330.	10.	330.	10.	325.	10.	325.	10.	325.	
400042	08.	325.	08.	325.											
400300	05.	340.	07.	340.	08.	340.	09.	340.	09.	345.	09.	345.	10.	345.	
400321	10.	345.	10.	330.	10.	335.	10.	325.	10.	320.	08.	320.	08.	320.	
400342	08.	320.	08.	320.											
400600	05.	340.	07.	340.	08.	340.	08.	345.	09.	350.	09.	355.	09.	350.	
400621	10.	345.	10.	335.	10.	335.	10.	325.	08.	320.	08.	320.	08.	320.	
400642	08.	320.													
400900	05.	340.	07.	345.	08.	345.	08.	350.	09.	350.	09.	350.	09.	350.	
400921	10.	350.	10.	345.	10.	340.	10.	335.	07.	335.	07.	335.			
400942															
401200			05.	345.	08.	350.	08.	350.	08.	350.	09.	355.	09.	350.	
401221	10.	355.	09.	350.	08.	345.	08.	345.	07.	345.	07.	345.			
401242															
401500			05.	350.	05.	350.	08.	350.	08.	350.	09.	350.	09.	350.	
401521	10.	355.	08.	350.	07.	345.	07.	345.	07.	345.					
401542															
401801					05.	350.	08.	355.	08.	355.	09.	355.	09.	355.	
401821	10.	355.	08.	355.	07.	350.									
401842															
402101					05.	350.	07.	350.	08.	355.	09.	000.	09.	000.	
402121	10.	000.	08.	355.	07.	350.	05.	350.							
402142															
402400							05.	350.	07.	355.	08.	000.	09.	000.	
402421	10.	000.	08.	000.	08.	355.	07.	350.							
402442															
402700									08.	000.	08.	000.	09.	000.	
402721	10.	000.	08.	355.	08.	355.	07.	355.	05.	355.					
402742															
403000										08.	000.	08.	000.	09.	000.
403021	09.	355.	08.	355.	08.	355.	07.	355.	07.	350.	05.	340.			
403042															
403300											08.	000.	09.	355.	
403321	09.	355.	08.	355.	08.	355.	08.	350.	08.	350.	05.	340.			
403342															
403600											05.	000.	09.	350.	
403621	08.	350.	08.	350.	08.	350.	08.	350.	07.	345.	06.	340.			
403642															
403900													05.	355.	
403921	05.	350.	08.	350.	08.	345.	08.	345.	08.	350.	07.	345.	05.	340.	
403942	05.	330.													
404200															
404221	05.	350.	08.	350.	08.	345.	08.	350.	08.	350.	07.	345.	07.	335.	
404242	05.	330.													
404500															
404521			05.	350.	08.	355.	08.	350.	08.	350.	08.	345.	07.	335.	
404542	05.	335.													
404800															
404821					10.	000.	09.	355.	08.	345.	08.	345.	07.	345.	
404842	05.	350.													
405100															
405121					10.	000.	09.	355.	09.	350.	09.	355.	08.	355.	
405142	07.	350.	05.	345.											
405400															
405421			05.	000.	10.	000.	10.	350.	10.	355.	10.	000.	09.	000.	
405442	07.	355.	05.	350.											
405700															
405721			05.	000.	10.	355.	10.	350.	10.	000.	10.	000.	10.	000.	
405742	07.	000.	05.	355.	05.	350.									
406000															
406021			05.	000.	10.	355.	10.	355.	10.	000.	10.	000.	10.	000.	
406042	10.	000.	05.	355.	05.	350.									
406300															
406321			05.	000.	10.	355.	10.	000.	10.	000.	10.	000.	10.	000.	
406342	10.	005.	07.	000.	05.	350.									
406600															
406621							08.	000.	10.	000.	10.	000.	10.	000.	
406642	10.	010.	10.	000.	08.	350.	05.	325.	05.	325.	05.	320.	05.	320.	
406900															
406921							08.	000.	10.	000.	10.	000.	10.	350.	
406942	10.	350.	10.	350.	08.	340.	08.	340.	08.	325.	10.	320.	10.	320.	
407200									10.	230.	08.	220.	05.	220.	
407221							05.	000.	08.	355.	10.	350.	10.	345.	
407242	10.	345.	10.	350.	10.	340.	10.	340.	10.	330.	10.	320.	10.	320.	

407500									15.	245.	10.	245.	08.	250.
407521	05.	250.	05.	270.	05.	290.	05.	320.	08.	340.	10.	335.	10.	330.
407542	10.	340.	10.	330.	10.	315.	10.	320.	10.	320.	10.	320.	10.	320.
407800									15.	250.	15.	250.	15.	250.
407821	08.	265.	08.	280.	10.	285.	08.	300.	10.	325.	10.	330.	10.	325.
407842	10.	315.	10.	315.	10.	315.	10.	320.	10.	320.	10.	320.	10.	320.
408100									15.	250.	15.	250.	15.	250.
408121	15.	260.	14.	270.	13.	285.	11.	295.	10.	305.	10.	315.	10.	315.
408142	10.	310.	10.	310.	10.	310.	10.	310.	10.	315.	10.	320.	10.	320.
408400									15.	250.	15.	250.	15.	255.
408421	15.	265.	14.	270.	13.	285.	11.	270.	10.	300.	10.	305.	10.	305.
408442	10.	310.	10.	310.	09.	315.	08.	325.	08.	330.	10.	320.	10.	310.
408700									15.	250.	15.	260.	15.	265.
408721	12.	270.	12.	270.	12.	280.	12.	285.	10.	300.	10.	305.	10.	310.
408742	10.	315.	09.	315.	08.	325.	08.	320.	08.	310.	10.	300.	10.	295.
409000									10.	250.	10.	255.	08.	255.
409021	08.	260.	08.	270.	10.	280.	10.	305.	10.	305.	10.	315.	10.	325.
409042	10.	330.	10.	330.	10.	315.	10.	305.	10.	295.	10.	290.	10.	290.
409300											05.	255.	05.	255.
409321	08.	255.	08.	300.	09.	310.	10.	320.	10.	335.	10.	340.	10.	330.
409342	10.	330.	10.	335.	11.	320.	11.	320.	11.	295.	11.	280.	11.	280.
409600											05.	270.	05.	275.
409621	05.	285.	08.	310.	10.	335.	10.	335.	10.	335.	10.	330.	10.	330.
409642	10.	345.	12.	345.	12.	345.	12.	330.	12.	280.	12.	270.	12.	270.
409900											05.	295.	05.	305.
409921	05.	310.	07.	325.	08.	345.	10.	345.	10.	340.	10.	340.	10.	345.
409942	10.	350.	12.	350.	13.	355.	08.	320.	06.	295.	06.	270.	06.	270.
410200													05.	310.
410221	06.	320.	08.	335.	10.	340.	10.	345.	10.	340.	10.	340.	10.	345.
410242	10.	350.	11.	350.	08.	000.	05.	000.			05.	240.	05.	240.
410500														
410521			08.	335.	09.	335.	10.	335.	10.	335.	10.	340.	10.	350.
410542	10.	350.	10.	355.	08.	030.	06.	045.	05.	045.				
410800														
410821			05.	330.	08.	330.	10.	335.	10.	335.	10.	340.	10.	350.
410842	10.	000.	10.	005.	08.	030.	06.	045.	05.	045.	05.	045.		
411100														
411121			05.	330.	08.	335.	10.	340.	10.	340.	10.	345.	10.	355.
411142	10.	000.	10.	005.	07.	025.	07.	040.	06.	035.	05.	035.		
411400														
411421			08.	330.	08.	340.	08.	345.	10.	350.	10.	000.	10.	000.
411442	10.	005.	08.	000.	07.	030.	07.	075.	07.	040.	05.	040.		
411700														
411721					06.	355.	08.	355.	10.	350.	10.	000.	10.	000.
411742	10.	005.	08.	000.										
412000														
412021					05.	000.	08.	355.	10.	345.	10.	000.	10.	005.
412042	10.	005.	08.	000.										
412300														
412321			05.	355.	08.	355.	10.	350.	10.	350.	10.	000.	10.	005.
412342	10.	005.	08.	000.										
412600														
412621			05.	355.	08.	355.	10.	350.	10.	355.	10.	000.	10.	005.
412642	10.	010.	08.	010.										
412900														
412921			05.	355.	08.	355.	10.	355.	10.	000.	10.	000.	10.	005.
412942	10.	010.	08.	010.	06.	010.								
413200														
413221					06.	355.	08.	350.	08.	000.	10.	005.	10.	010.
413242	10.	010.	08.	010.	06.	010.								
413500														
413521					06.	355.	08.	350.	08.	000.	08.	005.	10.	010.
413542	10.	010.	08.	010.	06.	010.								
413800														
413821					08.	355.	08.	355.	08.	005.	08.	010.	10.	010.
413842	10.	010.	08.	010.	06.	010.								
414100														
414121					06.	000.	08.	000.	08.	005.	08.	005.	10.	010.
414142	10.	010.	08.	010.	06.	010.								
414400														
414421					06.	000.	08.	000.	08.	000.	10.	000.	10.	005.
414442	10.	005.	08.	005.	06.	010.								
414700														
414721					06.	000.	08.	000.	08.	000.	10.	000.	10.	000.
414742	08.	000.	06.	005.										
415000														
415021							08.	000.	08.	000.	10.	000.	10.	000.
415042	08.	000.												

500000	07.	050.	08.	050.	09.	050.	07.	045.	10.	045.	10.	045.	10.	045.	
500021	10.	045.	10.	045.	10.	045.	08.	045.	08.	045.	08.	045.	08.	045.	
500042	08.	045.	08.	045.											
500300	07.	045.	08.	045.	09.	045.	09.	045.	09.	045.	09.	045.	09.	045.	
500321	09.	045.	09.	045.	08.	045.	08.	045.	08.	045.	08.	045.	08.	045.	
500342	08.	045.	07.	045.											
500600	07.	045.	07.	045.	08.	045.	09.	045.	09.	045.	09.	045.	09.	045.	
500621	09.	045.	09.	045.	09.	045.	08.	045.	08.	045.	07.	045.	07.	045.	
500642	07.	045.													
500900	07.	045.	07.	045.	07.	045.	08.	045.	09.	045.	09.	045.	09.	045.	
500921	08.	040.	08.	040.	07.	040.	07.	040.	07.	040.	07.	040.			
500942															
501200			07.	045.	07.	045.	08.	045.	09.	045.	08.	040.	08.	040.	
501221	08.	040.	08.	040.	07.	035.	07.	035.	07.	035.	07.	035.			
501242															
501500			07.	045.	07.	045.	07.	045.	08.	040.	08.	040.	08.	040.	
501521	07.	040.	07.	035.	07.	035.	07.	035.	07.	035.					
501542															
501800					07.	045.	07.	045.	07.	040.	08.	040.	08.	040.	
501821	07.	040.	07.	035.	07.	035.									
501842															
502100		0.	0.	07.	040.	07.	040.	07.	040.	07.	040.	07.	040.	07.	040.
502121	07.	040.	07.	040.	07.	040.	07.	040.							
502142															
502400							07.	040.	07.	040.	07.	045.	08.	045.	
502421	08.	045.	07.	045.	07.	035.	07.	025.							
502442															
502700									07.	045.	08.	045.	08.	045.	
502721	08.	045.	08.	045.	07.	040.	07.	025.	07.	035.					
502742															
503000									07.	055.	07.	050.	07.	045.	
503021	08.	045.	08.	045.	08.	045.	07.	040.	07.	050.	07.	060.			
503042															
503300											07.	060.	07.	055.	
503321	08.	050.	08.	045.	08.	045.	08.	050.	08.	055.	05.	065.			
503342															
503600											07.	060.	05.	060.	
503621	07.	050.	09.	045.	08.	045.	08.	050.	08.	050.	07.	055.			
503642															
503900													05.	060.	
503921	06.	050.	07.	050.	09.	045.	10.	045.	08.	045.	07.	055.	06.	055.	
503942	05.	055.													
504200															
504221	05.	050.	08.	045.	09.	040.	10.	045.	10.	045.	08.	045.	07.	060.	
504242	05.	065.													
504500															
504521			05.	030.	07.	030.	09.	040.	10.	040.	09.	040.	08.	050.	
504542	07.	060.													
504800															
504821					07.	030.	09.	040.	09.	040.	09.	040.	07.	050.	
504842	07.	055.													
505100															
505121				04.	030.	08.	025.	09.	040.	09.	045.	08.	050.		
505142	07.	050.	05.	050.											
505400															
505421			04.	015.	05.	010.	08.	025.	09.	035.	09.	045.	08.	050.	
505442	07.	055.	05.	055.											
505700															
505721			04.	010.	06.	010.	06.	020.	08.	035.	09.	040.	09.	045.	
505742	07.	050.	05.	050.	05.	050.									
506000															
506021			05.	010.	07.	010.	07.	020.	08.	030.	09.	035.	09.	045.	
506042	07.	050.	07.	050.	05.	050.									
506300															
506321			04.	010.	06.	010.	07.	015.	08.	025.	08.	030.	09.	035.	
506342	08.	045.	07.	050.	05.	050.									
506600															
506621							07.	015.	08.	020.	08.	025.	09.	030.	
506642	09.	035.	08.	045.	08.	050.	05.	055.	05.	060.	05.	060.	05.	065.	
506900															
506921							07.	010.	08.	010.	08.	020.	09.	035.	
506942	10.	040.	08.	045.	07.	045.	05.	060.	06.	065.	07.	070.	07.	075.	
507200									05.	075.	05.	075.	05.	075.	
507221							05.	020.	08.	015.	08.	025.	09.	035.	
507242	10.	045.	09.	050.	08.	055.	07.	066.	08.	070.	10.	075.	10.	080.	

507500									10.	075.	10.	075.	10.	075.	
507521	10.	075.	05.	075.	05.	075.	05.	050.	05.	035.	09.	045.	10.	045.	
507542	11.	050.	11.	055.	11.	060.	10.	065.	10.	075.	12.	080.	12.	085.	
507800										12.	080.	12.	080.	10.	075.
507821	10.	075.	05.	075.	05.	075.	05.	075.	05.	070.	08.	055.	10.	065.	
507842	12.	075.	12.	080.	12.	080.	14.	080.	14.	080.	14.	080.	14.	085.	
508100										12.	080.	12.	080.	11.	080.
508121	11.	080.	11.	080.	10.	080.	10.	080.	10.	075.	11.	080.	13.	080.	
508142	13.	080.	15.	080.	15.	080.	15.	080.	15.	080.	15.	085.	15.	085.	
508400										12.	085.	12.	085.	11.	085.
508421	11.	080.	11.	080.	11.	085.	11.	085.	11.	085.	11.	085.	12.	085.	
508442	13.	085.	14.	085.	10.	090.	10.	090.	10.	090.	12.	070.	15.	090.	
508700										12.	090.	12.	090.	12.	090.
508721	11.	085.	11.	085.	11.	090.	11.	090.	11.	095.	11.	095.	12.	090.	
508742	13.	090.	14.	090.	14.	090.	14.	090.	15.	090.	15.	090.	15.	090.	
509000										10.	090.	08.	070.	07.	100.
509021	05.	100.	05.	110.	07.	105.	10.	105.	11.	105.	11.	105.	11.	100.	
509042	12.	100.	13.	095.	14.	095.	14.	095.	15.	095.	15.	095.	15.	095.	
509300											05.	115.	05.	115.	
509321	05.	125.	06.	120.	07.	120.	08.	110.	09.	110.	10.	105.	10.	105.	
509342	11.	105.	11.	100.	11.	100.	12.	095.	12.	095.	12.	095.	12.	090.	
509600											05.	120.	05.	140.	
509621	05.	135.	07.	135.	08.	130.	09.	130.	09.	125.	10.	120.	10.	115.	
509642	10.	110.	11.	125.	10.	135.	08.	115.	09.	100.	10.	075.	10.	075.	
509900											05.	140.	05.	165.	
509921	05.	215.	07.	200.	08.	165.	09.	145.	09.	135.	09.	130.	09.	130.	
509942	10.	140.	10.	135.	10.	135.	08.	125.	06.	090.	05.	075.	05.	075.	
510200													05.	200.	
510221	05.	235.	05.	235.	07.	215.	08.	150.	09.	145.	09.	145.	09.	140.	
510242	10.	135.	10.	145.	08.	170.	05.	160.			05.	075.	05.	075.	
510500															
510521			04.	210.	06.	195.	08.	170.	08.	160.	08.	160.	08.	160.	
510542	09.	160.	09.	175.	06.	200.	06.	220.	05.	220.					
510800															
510821			04.	190.	07.	190.	07.	190.	08.	165.	08.	160.	08.	160.	
510842	08.	165.	08.	180.	07.	195.	06.	215.	05.	230.	05.	240.			
511100															
511121			04.	200.	06.	200.	07.	190.	08.	165.	08.	165.	08.	165.	
511142	08.	170.	07.	175.	06.	170.	04.	210.	05.	220.	05.	230.			
511400															
511421			04.	215.	06.	195.	07.	190.	08.	170.	08.	165.	08.	165.	
511442	08.	165.	07.	165.	06.	170.	04.	235.	04.	240.	05.	210.			
511700															
511721					05.	185.	07.	180.	08.	170.	08.	165.	08.	165.	
511742	08.	165.	06.	165.											
512000															
512021					05.	180.	07.	180.	08.	165.	08.	165.	08.	165.	
512042	08.	165.	06.	165.											
512300															
512321			04.	180.	05.	180.	07.	170.	08.	170.	08.	170.	08.	165.	
512342	08.	165.	08.	165.											
512600															
512621			04.	180.	05.	180.	07.	175.	08.	175.	08.	175.	08.	175.	
512642	08.	165.	07.	165.											
512900															
512921			04.	180.	05.	180.	07.	175.	08.	175.	08.	175.	08.	170.	
512942	08.	165.	07.	165.	05.	175.									
513200															
513221					05.	175.	07.	175.	07.	175.	08.	175.	08.	165.	
513242	08.	165.	07.	170.	05.	175.									
513500															
513521					07.	175.	07.	170.	07.	165.	07.	165.	08.	165.	
513542	08.	170.	07.	170.	05.	175.									
513800															
513821					07.	175.	07.	170.	07.	165.	07.	165.	08.	165.	
513842	08.	165.	07.	165.	05.	165.									
514100															
514121					07.	170.	07.	165.	07.	165.	08.	165.	08.	165.	
514142	08.	165.	07.	165.	05.	165.									
514400															
514421					07.	165.	07.	165.	08.	165.	08.	165.	08.	165.	
514442	07.	165.	07.	165.	05.	165.									
514700															
514721					07.	165.	07.	165.	08.	165.	08.	165.	08.	165.	
514742	07.	165.	05.	165.											
515000															
515021							07.	165.	07.	165.	08.	165.	08.	165.	
515042	08.	165.													

Input Data File Format: Net Currents

Grid Coordinates		NET CURRENT PARAMETERS FOR (Y, X)			NET CURRENT PARAMETERS FOR (Y, X+2)			NET CURRENT PARAMETERS FOR (Y, X+4)			NET CURRENT PARAMETERS FOR (Y, X+6)			NET CURRENT PARAMETERS FOR (Y, X+8)		
Y	X	V _{wint}	V _{sum}	θ	V _{wint}	V _{sum}	θ	V _{wint}	V _{sum}	θ	V _{wint}	V _{sum}	θ	V _{wint}	V _{sum}	θ
XXX	XX	X.XX	X.XX	XXX.	X.XX	X.XX	XXX.	X.XX	X.XX	XXX.	X.XX	X.XX	XXX.	X.XX	X.XX	XXX.
(Y, X) - GRID CELL LOCATION FOR NET CURRENT DATA																
V _{wint} - NET CURRENT VELOCITY FOR WINTER SEASON IN METERS/SEC																
V _{sum} - NET CURRENT VELOCITY FOR SUMMER SEASON IN METERS/SEC																
θ - DIRECTION OF NET CURRENT (IN DEGREES, CLOCKWISE FROM NORTH)																

00002	0.00	0.00	010.	0.03	0.02	010.	0.05	0.03	010.	0.01	0.01	140.	0.10	0.05	180.
00012	0.10	0.05	180.	0.12	0.06	175.	0.15	0.10	170.	0.15	0.10	170.	0.15	0.10	165.
00022	0.15	0.10	165.	0.14	0.07	160.	0.10	0.05	155.	0.10	0.05	155.	0.05	0.02	150.
00032	0.02	0.01	140.	0.01	0.01	140.	0.02	0.01	325.	0.02	0.01	325.	0.01	0.01	315.
00042	0.01	0.01	310.	0.01	0.01	310.	0.00	0.00	310.						
00052															
00102	0.00	0.00	010.	0.03	0.02	010.	0.05	0.03	010.	0.01	0.01	140.	0.10	0.05	180.
00112	0.10	0.05	180.	0.12	0.06	175.	0.15	0.10	170.	0.15	0.10	170.	0.15	0.10	165.
00122	0.15	0.10	165.	0.14	0.07	160.	0.10	0.05	155.	0.10	0.05	155.	0.05	0.02	150.
00132	0.02	0.01	140.	0.01	0.01	140.	0.02	0.01	325.	0.02	0.01	325.	0.01	0.01	315.
00142	0.01	0.01	310.	0.01	0.01	310.	0.00	0.00	310.						
00152															
00302	0.00	0.00	010.	0.03	0.02	010.	0.05	0.03	015.	0.01	0.01	140.	0.10	0.05	180.
00312	0.10	0.05	180.	0.12	0.06	175.	0.15	0.10	170.	0.15	0.10	170.	0.15	0.10	165.
00322	0.15	0.10	165.	0.13	0.06	160.	0.10	0.05	155.	0.08	0.04	150.	0.05	0.02	145.
00332	0.03	0.01	140.	0.02	0.01	320.	0.02	0.01	320.	0.01	0.01	315.	0.01	0.01	310.
00342	0.00	0.00	310.	0.00	0.00	310.									
00352															
00502	0.00	0.00	010.	0.03	0.02	010.	0.05	0.03	015.	0.01	0.01	135.	0.10	0.05	180.
00512	0.10	0.05	180.	0.12	0.06	175.	0.15	0.10	170.	0.15	0.10	170.	0.15	0.10	165.
00522	0.15	0.10	165.	0.12	0.06	160.	0.10	0.05	155.	0.06	0.03	150.	0.04	0.02	140.
00532	0.03	0.01	325.	0.03	0.01	325.	0.01	0.01	315.	0.01	0.01	290.	0.00	0.00	290.
00542															
00552															
00702	0.00	0.00	025.	0.02	0.01	030.	0.05	0.03	030.	0.01	0.01	070.	0.10	0.05	180.
00712	0.10	0.05	180.	0.12	0.06	180.	0.15	0.10	180.	0.15	0.10	175.	0.15	0.10	170.
00722	0.13	0.07	165.	0.11	0.05	160.	0.05	0.04	160.	0.05	0.02	155.	0.01	0.01	325.
00732	0.04	0.02	325.	0.02	0.01	325.	0.00	0.00	335.	0.00	0.00	290.			
00742															
00752															
00902	0.00	0.00	090.	0.00	0.00	050.	0.03	0.01	035.	0.05	0.02	035.	0.08	0.04	190.
00912	0.10	0.05	190.	0.12	0.06	185.	0.15	0.10	180.	0.15	0.10	180.	0.15	0.10	175.
00922	0.12	0.06	170.	0.10	0.05	165.	0.05	0.02	155.	0.01	0.01	330.	0.05	0.02	325.
00932	0.02	0.01	320.	0.00	0.00	320.									
00942															
00952															
01102				0.00	0.00	320.	0.02	0.01	025.	0.04	0.02	035.	0.08	0.04	190.
01112	0.10	0.05	190.	0.12	0.06	185.	0.14	0.10	180.	0.15	0.10	180.	0.16	0.11	180.
01122	0.12	0.06	175.	0.10	0.05	170.	0.05	0.02	165.	0.05	0.02	310.	0.02	0.01	300.
01132	0.01	0.01	300.	0.00	0.00	300.									
01142															
01152															
01302				0.00	0.00	060.	0.01	0.01	060.	0.02	0.01	075.	0.04	0.02	140.
01312	0.10	0.05	195.	0.13	0.07	190.	0.15	0.10	185.	0.16	0.11	185.	0.16	0.11	180.
01322	0.10	0.05	175.	0.05	0.02	170.	0.01	0.01	295.	0.00	0.00	295.	0.00	0.00	280.
01332	0.00	0.00	280.												
01342															
01352															
01502							0.00	0.00	110.	0.00	0.00	210.	0.03	0.01	200.
01512	0.10	0.05	195.	0.13	0.07	195.	0.14	0.10	190.	0.17	0.11	185.	0.14	0.10	185.
01522	0.10	0.05	180.	0.04	0.02	170.	0.01	0.01	165.	0.00	0.00	160.			
01532															
01542															
01552															
01702										0.00	0.00	175.	0.02	0.01	200.
01712	0.08	0.04	195.	0.12	0.06	195.	0.16	0.11	195.	0.18	0.12	190.	0.13	0.07	190.
01722	0.10	0.05	185.	0.05	0.02	180.	0.01	0.01	180.	0.00	0.00	180.			
01732															
01742															
01752															
01902										0.00	0.00	220.	0.01	0.01	215.
01912	0.05	0.02	205.	0.10	0.05	200.	0.15	0.10	200.	0.18	0.12	200.	0.15	0.10	195.
01922	0.10	0.05	190.	0.05	0.02	190.	0.01	0.01	180.	0.00	0.00	180.			
01932															
01942															
01952															
02102										0.00	0.00	220.	0.01	0.01	215.
02112	0.02	0.01	210.	0.10	0.05	205.	0.12	0.06	205.	0.19	0.13	200.	0.18	0.12	200.
02122	0.12	0.06	200.	0.08	0.04	195.	0.01	0.01	190.	0.00	0.00	190.			
02132															

04522						0.00	0.00	180.	0.08	0.04	205.	0.21	0.15	200.	
04532	0.27	0.18	200.	0.24	0.17	200.	0.20	0.15	200.	0.10	0.05	200.	0.01	0.01	185.
04542	0.00	0.00	270.												
04552															
04702															
04712															
04722						0.00	0.00	180.	0.08	0.04	195.	0.20	0.15	200.	
04732	0.24	0.17	200.	0.28	0.19	200.	0.23	0.16	205.	0.15	0.10	205.	0.01	0.01	180.
04742	0.00	0.00	270.												
04752															
04902															
04912															
04922						0.00	0.00	180.	0.05	0.02	195.	0.18	0.12	200.	
04932	0.24	0.17	200.	0.30	0.20	200.	0.25	0.18	205.	0.20	0.15	205.	0.01	0.01	190.
04942	0.00	0.00	180.												
04952															
05102															
05112															
05122						0.00	0.00	180.	0.05	0.02	195.	0.16	0.11	195.	
05132	0.22	0.16	195.	0.28	0.19	195.	0.28	0.19	200.	0.20	0.15	200.	0.05	0.02	200.
05142	0.00	0.00	200.												
05152															
05302															
05312															
05322						0.00	0.00	180.	0.04	0.02	190.	0.10	0.05	195.	
05332	0.20	0.15	195.	0.26	0.18	195.	0.30	0.20	200.	0.24	0.17	200.	0.16	0.11	200.
05342	0.01	0.01	200.	0.00	0.00	200.									
05352															
05502															
05512															
05522						0.00	0.00	180.	0.02	0.01	000.	0.05	0.02	195.	
05532	0.20	0.15	195.	0.25	0.17	195.	0.34	0.22	195.	0.28	0.19	195.	0.20	0.15	195.
05542	0.02	0.01	195.	0.00	0.00	200.									
05552															
05702															
05712															
05722						0.00	0.00	015.	0.05	0.02	020.	0.05	0.02	200.	
05732	0.18	0.12	195.	0.25	0.17	190.	0.36	0.24	190.	0.32	0.21	190.	0.21	0.15	195.
05742	0.04	0.02	195.	0.00	0.00	195.									
05752															
05902															
05912															
05922						0.00	0.00	020.	0.03	0.01	020.	0.04	0.02	200.	
05932	0.10	0.05	195.	0.22	0.16	190.	0.36	0.24	190.	0.35	0.23	190.	0.25	0.17	195.
05942	0.10	0.05	195.	0.00	0.00	195.									
05952															
06102															
06112															
06122						0.00	0.00	035.	0.02	0.01	035.	0.04	0.02	035.	
06132	0.06	0.03	205.	0.22	0.16	190.	0.36	0.24	190.	0.36	0.24	190.	0.30	0.20	190.
06142	0.20	0.15	195.	0.02	0.01	195.	0.00	0.00	180.						
06152															
06302															
06312															
06322									0.00	0.00	045.	0.00	0.00	045.	
06332	0.05	0.02	200.	0.21	0.15	190.	0.35	0.24	190.	0.38	0.27	185.	0.35	0.24	185.
06342	0.22	0.16	190.	0.10	0.05	190.	0.00	0.00	180.						
06352															
06502															
06512															
06522												0.00	0.00	190.	
06532	0.05	0.02	200.	0.24	0.17	200.	0.35	0.24	190.	0.40	0.30	185.	0.35	0.24	185.
06542	0.25	0.17	185.	0.14	0.08	185.	0.02	0.01	180.	0.00	0.00	160.	0.00	0.00	180.
06552	0.00	0.00	180.	0.00	0.00	325.	0.00	0.00	180.	0.00	0.00	180.	0.00	0.00	180.
06702															
06712															
06722												0.00	0.00	190.	
06732	0.03	0.01	200.	0.28	0.19	195.	0.32	0.21	190.	0.40	0.30	180.	0.40	0.30	180.
06742	0.30	0.20	180.	0.20	0.15	180.	0.02	0.01	175.	0.01	0.01	120.	0.00	0.00	090.
06752	0.01	0.01	045.	0.01	0.01	240.	0.00	0.00	270.	0.00	0.00	240.	0.00	0.00	140.

09142	0.50	0.20	270.	0.50	0.20	270.	0.50	0.20	270.	0.50	0.20	270.	0.50	0.20	270.
09152	0.50	0.20	270.	0.50	0.20	270.	0.50	0.20	270.	0.50	0.20	270.	0.50	0.20	270.
09302															
09312							0.00	0.00	180.	0.02	0.05	180.	0.02	0.05	205.
09322	0.01	0.02	215.	0.00	0.00	135.	0.02	0.05	155.	0.10	0.10	190.	0.20	0.20	210.
09332	0.10	0.20	245.	0.10	0.10	255.	0.20	0.15	270.	0.30	0.20	270.	0.30	0.20	270.
09342	0.50	0.20	270.	0.50	0.20	270.	0.50	0.20	270.	0.50	0.20	270.	0.50	0.20	270.
09352	0.50	0.20	270.	0.50	0.20	270.	0.50	0.20	270.	0.50	0.20	270.	0.50	0.20	260.
09502															
09512							0.00	0.00	180.	0.01	0.02	225.	0.04	0.04	220.
09522	0.05	0.05	210.	0.02	0.02	210.	0.02	0.05	190.	0.10	0.10	195.	0.20	0.20	205.
09532	0.10	0.20	215.	0.10	0.10	230.	0.15	0.15	260.	0.15	0.15	270.	0.15	0.15	275.
09542	0.15	0.15	280.	0.10	0.10	295.	0.10	0.10	310.	0.10	0.10	310.	0.05	0.05	315.
09552	0.05	0.05	060.	0.00	0.00	180.	0.00	0.00	230.	0.00	0.00	310.	0.00	0.00	270.
09702															
09712										0.00	0.00	180.	0.03	0.03	225.
09722	0.04	0.04	220.	0.05	0.05	215.	0.03	0.05	215.	0.07	0.10	200.	0.20	0.20	205.
09732	0.10	0.20	225.	0.10	0.10	235.	0.10	0.10	270.	0.10	0.10	295.	0.10	0.10	310.
09742	0.10	0.10	310.	0.10	0.10	320.	0.10	0.10	330.	0.05	0.05	330.	0.00	0.00	360.
09752	0.00	0.00	360.	0.00	0.00	360.	0.00	0.00	360.	0.00	0.00	360.	0.00	0.00	360.
09902															
09912										0.00	0.00	180.	0.01	0.02	210.
09922	0.02	0.02	220.	0.03	0.03	220.	0.05	0.05	220.	0.03	0.05	210.	0.15	0.15	205.
09932	0.10	0.20	215.	0.05	0.05	225.	0.05	0.05	270.	0.05	0.05	300.	0.05	0.05	330.
09942	0.10	0.10	340.	0.10	0.10	330.	0.05	0.05	330.	0.01	0.01	350.	0.00	0.00	360.
09952															
10102															
10112													0.00	0.00	180.
10122	0.00	0.00	180.	0.00	0.00	225.	0.04	0.04	225.	0.05	0.05	215.	0.10	0.10	205.
10132	0.10	0.20	210.	0.05	0.05	210.	0.05	0.05	205.	0.05	0.05	330.	0.05	0.05	340.
10142	0.10	0.10	345.	0.10	0.10	340.	0.05	0.05	330.	0.01	0.01	360.	0.00	0.00	360.
10152															
10302															
10312															
10322				0.00	0.00	180.	0.02	0.02	225.	0.04	0.05	225.	0.07	0.15	205.
10332	0.10	0.20	205.	0.05	0.05	205.	0.05	0.05	195.	0.05	0.05	355.	0.05	0.05	355.
10342	0.08	0.08	350.	0.05	0.05	340.	0.05	0.05	340.	0.01	0.01	320.	0.00	0.00	360.
10352															
10502															
10512															
10522				0.00	0.00	180.	0.01	0.02	180.	0.02	0.05	215.	0.03	0.05	225.
10532	0.10	0.20	205.	0.05	0.05	200.	0.05	0.05	205.	0.05	0.05	330.	0.05	0.05	335.
10542	0.02	0.02	355.	0.02	0.02	335.	0.02	0.01	300.	0.02	0.01	230.	0.00	0.00	225.
10552	0.00	0.00	180.												
10702															
10712															
10722				0.00	0.00	180.	0.01	0.02	175.	0.02	0.02	290.	0.02	0.04	230.
10732	0.08	0.15	205.	0.08	0.10	200.	0.04	0.07	195.	0.04	0.04	270.	0.05	0.05	305.
10742	0.02	0.02	360.	0.02	0.02	330.	0.01	0.01	330.	0.02	0.01	205.	0.01	0.01	205.
10752	0.00	0.00	220.	0.00	0.00	180.									
10902															
10912															
10922				0.00	0.00	180.	0.01	0.02	325.	0.02	0.02	330.	0.01	0.02	235.
10932	0.05	0.10	205.	0.10	0.20	200.	0.05	0.10	205.	0.02	0.02	270.	0.05	0.05	320.
10942	0.02	0.02	360.	0.02	0.02	360.	0.01	0.01	015.	0.02	0.01	155.	0.01	0.01	170.
10952	0.01	0.01	190.	0.01	0.01	225.	0.00	0.00	180.						
11102															
11112															
11122				0.00	0.00	180.	0.01	0.01	050.	0.02	0.02	025.	0.02	0.02	025.
11132	0.02	0.04	215.	0.10	0.20	200.	0.05	0.10	205.	0.02	0.02	270.	0.05	0.05	315.
11142	0.02	0.02	360.	0.02	0.02	030.	0.02	0.01	075.	0.02	0.01	140.	0.01	0.01	130.
11152	0.01	0.01	160.	0.01	0.01	180.	0.00	0.00	180.						
11302															
11312															
11322							0.00	0.00	360.	0.00	0.00	030.	0.02	0.02	030.
11332	0.02	0.03	210.	0.10	0.20	205.	0.07	0.15	200.	0.02	0.02	270.	0.05	0.05	320.
11342	0.02	0.02	360.	0.01	0.01	060.	0.01	0.01	120.	0.00	0.00	135.	0.00	0.00	180.
11352	0.00	0.00	180.	0.00	0.00	180.	0.00	0.00	180.						
11502															
11512															

11522										0.00	0.00	360.	0.01	0.01	040.
11532	0.01	0.02	060.	0.08	0.20	185.	0.10	0.20	195.	0.02	0.05	270.	0.05	0.05	320.
11542	0.02	0.02	360.	0.01	0.01	335.	0.00	0.00	360.	0.00	0.00	360.			
11552															
11702															
11712															
11722										0.00	0.00	360.	0.01	0.01	010.
11732	0.02	0.02	050.	0.05	0.08	170.	0.10	0.20	190.	0.10	0.20	225.	0.05	0.05	320.
11742	0.02	0.02	360.	0.01	0.01	360.	0.00	0.00	360.						
11752															
11902															
11912															
11922										0.00	0.00	360.	0.01	0.01	360.
11932	0.02	0.02	360.	0.05	0.07	160.	0.10	0.20	185.	0.05	0.10	235.	0.05	0.05	320.
11942	0.02	0.02	360.	0.01	0.01	360.	0.00	0.00	360.						
11952															
12102															
12112															
12122										0.00	0.00	360.	0.01	0.01	335.
12132	0.02	0.02	345.	0.05	0.06	175.	0.10	0.20	180.	0.10	0.20	215.	0.05	0.05	320.
12142	0.02	0.02	360.	0.00	0.00	360.	0.00	0.00	360.						
12152															
12302															
12312															
12322										0.00	0.00	360.	0.00	0.00	340.
12332	0.02	0.02	345.	0.03	0.05	175.	0.10	0.15	180.	0.10	0.20	215.	0.05	0.05	320.
12342	0.02	0.02	360.	0.00	0.00	360.	0.00	0.00	360.						
12352															
12502															
12512															
12522										0.00	0.00	360.	0.01	0.01	340.
12532	0.02	0.02	350.	0.05	0.05	180.	0.10	0.15	185.	0.10	0.25	215.	0.05	0.05	290.
12542	0.02	0.02	010.	0.00	0.00	360.	0.00	0.00	360.						
12552															
12702															
12712															
12722										0.00	0.00	360.	0.01	0.01	010.
12732	0.02	0.02	350.	0.05	0.05	185.	0.08	0.15	190.	0.10	0.25	205.	0.05	0.05	280.
12742	0.05	0.05	010.	0.00	0.00	010.	0.00	0.00	360.						
12752															
12902															
12912															
12922										0.00	0.00	360.	0.00	0.00	040.
12932	0.02	0.02	350.	0.05	0.05	195.	0.08	0.15	195.	0.10	0.25	200.	0.02	0.02	270.
12942	0.05	0.05	010.	0.01	0.01	020.	0.00	0.00	360.						
12952															
13102															
13112															
13122										0.00	0.00	360.	0.05	0.05	015.
13132	0.02	0.02	350.	0.03	0.03	195.	0.05	0.15	190.	0.10	0.30	195.	0.07	0.10	200.
13142	0.05	0.05	360.	0.01	0.01	010.	0.00	0.00	360.						
13152															
13302															
13312															
13322										0.00	0.00	360.	0.05	0.05	360.
13332	0.05	0.05	350.	0.00	0.00	220.	0.05	0.15	190.	0.10	0.30	190.	0.10	0.15	195.
13342	0.05	0.05	360.	0.01	0.01	360.	0.00	0.00	360.	0.00	0.00	360.			
13352															
13502															
13512															
13522										0.00	0.00	360.	0.00	0.00	330.
13532	0.05	0.05	360.	0.00	0.00	360.	0.05	0.15	185.	0.10	0.30	190.	0.10	0.15	185.
13542	0.05	0.05	350.	0.01	0.01	360.	0.00	0.00	360.	0.00	0.00	360.			
13552															
13702															
13712															
13722										0.00	0.00	360.	0.01	0.01	005.
13732	0.05	0.05	360.	0.00	0.00	360.	0.05	0.15	180.	0.10	0.35	185.	0.10	0.20	185.
13742	0.05	0.05	350.	0.01	0.01	350.	0.00	0.00	360.						
13752															

13902																				
13912																				
13922								0.00	0.00	360.	0.01	0.01	020.	0.05	0.05	020.				
13932	0.05	0.05	360.	0.00	0.00	360.	0.05	0.20	180.	0.10	0.35	180.	0.10	0.20	180.					
13942	0.05	0.05	345.	0.01	0.01	335.	0.00	0.00	360.											
13952																				
14102																				
14112																				
14122											0.00	0.00	360.	0.05	0.05	025.				
14132	0.05	0.05	030.	0.00	0.00	360.	0.05	0.20	140.	0.10	0.40	180.	0.10	0.20	175.					
14142	0.05	0.05	340.	0.01	0.01	335.	0.00	0.00	360.											
14152																				
14302																				
14312																				
14322											0.00	0.00	360.	0.02	0.02	030.				
14332	0.05	0.05	040.	0.02	0.02	050.	0.05	0.20	130.	0.15	0.40	180.	0.15	0.30	175.					
14342	0.05	0.05	330.	0.01	0.01	320.	0.00	0.00	360.											
14352																				
14502																				
14512																				
14522											0.00	0.00	360.	0.01	0.01	040.				
14532	0.05	0.05	045.	0.05	0.05	055.	0.10	0.20	115.	0.20	0.40	180.	0.10	0.30	175.					
14542	0.05	0.05	330.	0.00	0.00	320.	0.00	0.00	360.											
14552																				
14702																				
14712																				
14722																				
14732	0.03	0.03	055.	0.05	0.05	060.	0.10	0.20	110.	0.20	0.40	180.	0.05	0.30	175.					
14742	0.00	0.00	290.	0.00	0.00	360.														
14752																				
14902																				
14912																				
14922																				
14932	0.00	0.00	090.	0.00	0.00	090.	0.20	0.40	165.	0.20	0.40	180.	0.01	0.02	260.					
14942	0.00	0.00	360.																	
14952																				

Input Data File Format: Tidal Currents

342

STRETCH COORDINATES		TIDAL CURRENT PARAMETERS FOR (Y, X)				TIDAL CURRENT PARAMETERS FOR (Y, X+3)				TIDAL CURRENT PARAMETERS FOR (Y, X+6)				TIDAL CURRENT PARAMETERS FOR (Y, X+9)			
Y	X	V _{MAX}	FLOOD	EBB	PHASE	V _{MAX}	FLOOD	EBB	PHASE	V _{MAX}	FLOOD	EBB	PHASE	V _{MAX}	FLOOD	EBB	PHASE
XXX	XX	X.XX	XXX	XXX	XXX	X.XX	XXX	XXX	XXX	X.XX	XXX	XXX	XXX	X.XX	XXX	XXX	XXX
(Y, X) - GRID CELL LOCATION FOR TIDAL CURRENT DATA																	
V _{MAX} - MAXIMUM FLOOD & EBB VELOCITY IN METERS/SEC.																	
FLOOD - DIRECTION OF FLOOD CURRENT (IN DEGREES, CLOCKWISE FROM NORTH)																	
EBB - DIRECTION OF EBB CURRENT (IN DEGREES, CLOCKWISE FROM NORTH)																	
PHASE - PHASE OF TIDAL CURRENT WITH LOCATION RELATIVE TO ZERO BETWEEN GOLF DOUGLAS & CAPE ELIZABETH (IN DEGREES, 360° = 12.4 HOURS)																	

066 02									
066 14									
066 26				0.00	210	030	010	0.06	210 030 010
066 38	0.10	200	020	010	0.12	200	020	010	0.10 200 020 010
066 50	0.00	200	020	010	0.00	200	020	-15	0.00 180 360 -15
063 02									
063 14									
063 26				0.00	230	050	015	0.05	220 040 015
063 38	0.05	195	015	015	0.05	200	020	015	0.05 195 015 015
063 50									
060 02									
060 14									
060 26	0.00	205	025	022	0.03	205	025	022	0.04 195 015 022
060 38	0.04	195	015	020	0.04	200	020	018	0.03 225 025 018
060 50									
057 02									
057 14									
057 26	0.00	230	050	027	0.02	195	015	026	0.03 195 015 025
057 38	0.03	195	015	022	0.03	195	015	022	0.03 195 015 023
057 50									
054 02									
054 26	0.00	185	005	030	0.00	185	005	030	0.01 190 010 029
054 38	0.02	195	015	027	0.01	200	020	025	0.02 195 015 028
054 50									
051 02									
051 14									
051 26	0.00	000	180	024	0.01	000	180	026	0.00 005 185 029
051 38	0.00	195	015	030	0.00	195	015	030	0.00 190 010 030
051 50									
048 02									
048 14									
048 26	0.00	005	185	020	0.05	005	185	022	0.04 010 190 024
048 38	0.03	015	195	026	0.00	020	200	027	
048 50									
045 02									
045 14									
045 26	0.00	015	195	017	0.07	015	195	018	0.07 020 200 019
045 38	0.05	035	215	022	0.00	080	260	023	0.05 030 210 020
045 50									
042 02									
042 14									0.00 040 220 014
042 26	0.08	040	220	015	0.09	030	210	016	0.06 030 210 017
042 38	0.05	055	235	018	0.00	080	310	020	
042 50									
039 02									
039 14									0.00 050 230 008
039 26	0.13	020	200	010	0.12	020	200	012	0.10 050 230 008
039 38	0.00	010	190	016	0.11	025	205	014	0.10 010 190 015
039 50									
036 02									
036 14					0.00	050	230	005	0.14 040 220 006
036 26	0.15	035	215	007	0.14	035	215	008	0.12 005 185 012
036 38	0.00	005	185	012					
036 50									
033 02									
033 14	0.00	040	220	000	0.19	040	220	001	0.17 030 210 004
033 26	0.17	030	210	005	0.16	030	210	006	0.13 040 220 008
033 38	0.00	090	270	008					
033 50									
030 02									
030 14	0.00	020	200	-01	0.21	020	200	-01	0.20 025 205 000
030 26	0.18	025	205	002	0.18	030	210	002	0.10 070 250 005
030 38	0.00	120	300	006					
030 50									
027 02									0.00 020 200 -04
027 14	0.20	020	200	-03	0.23	015	195	-03	0.22 015 195 -02
027 26	0.22	015	195	-01	0.20	025	205	-01	0.00 025 205 000
027 38									
027 50									
024 02									0.00 005 185 -07

024 14	0.20 005 185 -06	0.25 005 185 -05	0.25 005 185 -05	0.24 010 190 -04
024 26	0.24 015 195 -04	0.00 015 195 -03		
024 38				
024 50				
021 02			0.00 020 200 -07	0.20 020 200 -08
021 14	0.26 000 180 -09	0.26 000 180 -07	0.25 005 185 -06	0.25 005 185 -05
021 26	0.25 010 190 -05	0.00 010 190 -05		
021 38				
021 50				
018 02		0.00 040 220 -09	0.00 040 220 -08	0.25 000 180 -08
018 14	0.27 000 180 -08	0.27 000 180 -08	0.27 000 180 -08	0.26 000 180 -08
018 26	0.26 000 180 -08	0.00 000 180 -08		
018 38				
018 50				
015 02		0.00 005 185 -10	0.00 -10 005 185	0.30 000 180 -10
015 14	0.29 000 180 -09	0.29 355 175 -09	0.28 355 175 -09	0.28 355 175 -09
015 26	0.26 335 155 -09	0.00 335 155 -10	0.00 335 155 -10	
015 38				
015 50				
012 02		0.00 010 190 -13	0.32 005 185 -12	0.32 000 180 -12
012 14	0.31 350 170 -11	0.31 340 160 -11	0.31 340 160 -11	0.31 340 160 -11
012 26	0.31 320 140 -11	0.30 315 135 -11	0.00 315 135 -12	0.00 315 135 -12
012 38				
012 50				
009 02	0.00 355 175 -13	0.00 005 185 -13	0.33 000 180 -13	0.33 355 175 -13
009 14	0.33 355 175 -13	0.33 345 165 -13	0.33 335 155 -13	0.34 325 145 -14
009 26	0.35 315 135 -14	0.34 315 135 -14	0.30 315 135 -15	0.00 315 135 -15
009 38	0.00 315 135 -15			
009 50				
006 02	0.00 355 175 -15	0.35 005 185 -15	0.35 000 180 -15	0.35 355 175 -15
006 14	0.35 350 170 -15	0.35 350 170 -15	0.35 340 160 -15	0.35 330 150 -15
006 26	0.35 320 140 -15	0.35 315 135 -16	0.35 310 130 -17	0.00 310 130 -17
006 38	0.00 310 130 -17	0.00 310 130 -17	0.00 000 180 -18	
006 50				
003 02	0.00 350 170 -17	0.37 350 170 -17	0.37 355 175 -17	0.37 355 175 -17
003 14	0.37 350 170 -17	0.37 350 170 -17	0.37 340 160 -17	0.36 330 150 -17
003 26	0.35 320 140 -18	0.35 315 135 -18	0.35 310 130 -18	0.35 310 130 -18
003 38	0.35 310 130 -18	0.00 330 150 -18	0.00 005 185 -18	0.00 005 185 -20
003 50				
000 02	0.00 320 140 -18	0.40 350 170 -18	0.40 355 175 -18	0.40 355 175 -18
000 14	0.40 350 170 -18	0.40 345 165 -18	0.40 340 160 -18	0.40 330 150 -18
000 26	0.40 325 145 -20	0.40 325 145 -20	0.40 320 140 -20	0.40 320 140 -20
000 38	0.40 320 140 -20	0.40 330 150 -20	0.40 340 160 -20	0.00 340 160 -22
000 50				

FINAL REPORT--TASK I
WIND FIELD TRANSITION MATRIX ANALYSIS
LOWER COOK INLET--SHELIKOF STRAIT, ALASKA
BERING SEA--GULF OF ALASKA PROJECT OFFICE
OUTER CONTINENTAL SHELF ENVIRONMENTAL
ASSESSMENT PROGRAM

JOB NO. 06797-014-88
OCTOBER 31, 1980

LOS ANGELES, CALIFORNIA

October 31, 1980

Outer Continental Shelf Environmental
Assessment Program
Bering Sea--Gulf of Alaska Project Office
Post Office Box 1808
Juneau, Alaska 99802

Attention: Herbert E. Bruce, Ph.D.
OCSEAP Project Manager

Gentlemen:

Final Report--Task I
Wind Field Transition Matrix Analysis
Lower Cook Inlet--Shelikof Strait, Alaska
Bering Sea--Gulf of Alaska Project Office
Outer Continental Shelf Environmental
Assessment Program

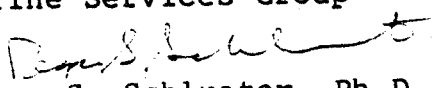
We are pleased to submit our final report on an analysis of wind field transition matrices based upon historical data for Lower Cook Inlet and Shelikof Strait, Alaska.

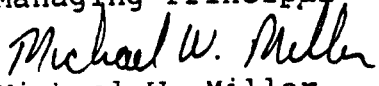
This report has incorporated and responded to comments received from your Juneau staff.

It has been a pleasure to work on this phase of our 1980 fiscal year contract with your staff. Please do not hesitate to contact us if you have questions regarding the contents of this study.

Very truly yours,

DAMES & MOORE
Marine Services Group


Roger S. Schlueter, Ph.D.
Managing Principal


Michael W. Miller
Principal Investigator

RSS:MWM:jh

CONTENTS

	<u>Page</u>
1.0 Introduction	350
1.1 Background	350
1.2 Purpose	351
1.3 Scope	351
1.4 Objectives	352
1.5 Organization	352
2.0 Data Base: Characterization of Matrices	353
2.1 Putnins' Weather Catalog	353
2.2 Accuracy of Transition Matrices	355
3.0 Auto Correlation Functions	357
4.0 Comparison of First- and Second-Order Matrices and the Weather Catalog	361
5.0 Conclusions and Recommendations	365
References	368
Appendix A: Converted Weather Catalog	369
Appendix B: Statistical Methodology--Matrix Accuracy	378

1.0 INTRODUCTION

1.1 BACKGROUND

This report describes the results of a wind field transition matrix analysis based on historical weather data used in an oil spill trajectory simulation in Lower Cook Inlet and Shelikof Strait, Alaska. The work was performed under Contract No. NA80RAC00075 between Dames & Moore and the National Oceanic and Atmospheric Administration.

This study was supported by the Bureau of Land Management through interagency agreement with the National Oceanic and Atmospheric Administration, under which a multi-year program responding to needs of petroleum development of the Alaskan continental shelf is managed by the Outer Continental Shelf Environmental Assessment Program (OSCEAP) Office.

This study was initiated by the Outer Continental Shelf Environmental Assessment Program (OCSEAP) on behalf of the Bureau of Land Management (BLM). This is one of a series of studies conducted by Dames & Moore to investigate the behavior of hypothetical oil spills within the Alaskan Outer Continental Shelf. The ability to accurately specify the variability of weather for use in an oil spill trajectory model in Lower Cook Inlet and Shelikof Strait has been a subject of continued interest for several years. The availability of a catalog of daily baric weather patterns over a 19-year period has increased the reliability that can be placed in the results of trajectory modeling in Lower Cook Inlet and Shelikof Strait. This catalog has been previously used in a hindcast mode by randomly accessing and using the observed sequences of weather patterns. This is a rather cumbersome method and does not solve the problem of specifying weather variability in a forecast mode. Simplified operations and forecast capabilities could be achieved using a transition matrix calculated

from the historical catalog. The desire to use a transition matrix led to the question of whether a first-order transition matrix adequately represents the sequencing of weather patterns in southern Alaska. The answer to this question directly influences studies conceived or being conducted for BLM/OCSEAP in Lower Cook Inlet and Shelikof Strait as well as the Bering Sea.

1.2 PURPOSE

The purpose of this study was to investigate the validity of using a first-order transition matrix to represent the time history of weather patterns in southern Alaska. Other probabilistic approaches considered were: (1) randomly accessing Putnin's 19-year catalog of daily weather patterns to obtain an observed historical sequence; or (2) using a second-order transition matrix to generate sequences of daily weather patterns.

This study dealt with three basic questions: (1) How accurate is the first-order approach? (2) Is there anything to support use of a second-order matrix? (3) Does a first-order matrix generate unrealistic sequences of weather patterns?

1.3 SCOPE

This study was conducted in accordance with the scope of services for Task I detailed in the Dames & Moore proposal, "Oil Dispersion Analysis, Lower Cook Inlet and Shelikof Strait, Alaska," RFX41-436-2905, for National Oceanic and Atmospheric Administration, July 19, 1979 and "Proposal Addendum, Oil Spill Dispersion Analysis," RFX41-436-2905, October 15, 1979, subsequently amended in a letter dated February 4, 1980.

1.4 OBJECTIVE

The primary element of the scope of services relating to the evaluation of the wind field transition matrix presented in the above documents is summarized below:

1. Evaluate the applicability of a first-order wind field transition matrix to represent historically observed sequences and variability of wind fields as applied to trajectory simulation.

1.5 ORGANIZATION

Section 2.0 investigates the accuracy of a first-order transition matrix. The approach was not to look at the matrices as a whole, but to look at individual entries, especially those associated with weather pattern sequences which occur frequently.

An evaluation of the correlation between daily weather patterns using auto correlation functions is presented in Section 3.0. This examination considered the weather patterns both with and without intensity factors.

Section 4.0 presents a comparison of a first- and second-order transition matrix and randomly accessing the weather catalog. This comparison was based on calculating the probabilities that three-day sequences would occur using the three different methods.

Finally, conclusions and recommendations are presented in Section 5.0. Significant implications with respect to oil spill modeling is discussed as well as still unresolved problem areas.

2.0 DATABASE: CHARACTERIZATION OF MATRICES

2.1 PUTNINS' WEATHER CATALOG

The oil spill trajectory studies for Lower Cook Inlet and Shelikof Strait presented in Dames & Moore (1980; 1979; and 1976) have all used the work of Putnins, (1966a) to derive wind field variability. The 1979 and 1976 studies used a deterministic approach in applying the wind fields and therefore, probabilistic wind field generation schemes were not required. One major objective of the 1980 study was to increase the variability of the wind fields used to calculate the wind drift component of surface pollutant transport. This was accomplished by randomly accessing a wind field catalog, based on the work of Putnins (1966a), and sequencing historically observed daily weather patterns. This random accessing was done enough times to provide a statistically significant sample of trajectories from each launch site examined.

Putnins (1966a) developed 22 specific baric weather patterns describing mesoscale weather situations over Alaska. These 22 baric weather patterns were related to 5 wind fields and 6 wind field intensity factors as developed by PMEL and shown in Table 2.1 (PMEL, 1980). This table was used to convert Putnins' unpublished tabulations of approximately 19 years of daily baric weather patterns (Putnins, 1966b) into a wind field catalog (Appendix A).

These wind fields and intensity factors allowed two basic approaches to be used in sequencing weather patterns during the 1980 oil spill trajectory study. The first approach was to use the wind field catalog given in Appendix A, converted from Putnins' data using Table 2.1, entering with a random date and historically sequencing the wind fields. The second approach was to use the wind field catalog to calculate first-order transition matrices (Tables A-1, A-2, A-3, A-4) and use

TABLE 2.1

CONVERSION FACTORS FROM PUTNINS' WEATHER TYPOLOGY
TO PMEL'S WIND FIELD AND INTENSITY FACTORS

Putnins Type	=	PMEL Type	PMEL Type	
			(Wind Field	/ Intensity Factor)
A	=	25	1 = Figure 3	1 = 0.3
A _C	=	25	2 = Figure 4	2 = 0.5
A'	=	53	3 = Figure 5	3 = 1.0
A"	=	33	4 = Figure 6	4 = 1.2
A"	=	43	5 = Figure 7	5 = 1.5
A ₁	=	15		6 = 0.7
A ₂	=	43		
A ₃	=	31		
B	=	16		
C	=	22		
C ₁	=	42		
D	=	23		
D'	=	15		
D ₁	=	23		
E	=	45		
E'	=	42		
E"	=	26		
E ₁	=	22		
F	=	43		
F ₁	=	23		
G	=	53		
H	=	14		

Example: PMEL Type 45 represents wind field number 4 as shown in Figure 6 with all magnitudes increased by a factor of 1.5 as denoted by the intensity factor index 5. PMEL Type 45 is equivalent to Putnins' Weather Type E.

these matrices to sequence the wind fields. The former method was used in the 1980 trajectory study because certain unresolved questions remained regarding the applicability of a first-order transition matrix. This report addresses some of the questions that have been raised regarding the accuracy of a first-order transition matrix applied to weather patterns in southern Alaska.

2.2 ACCURACY OF TRANSITION MATRICES

A transition matrix is a statistical tool used to associate probabilities of going from one "state" (in this case, wind pattern) to another "state". The question naturally arises, "How realistic are these probabilities?"

One method which can be used to analyze whether or not the database is large enough to accurately characterize first- and second-order transition matrices is to examine the individual entries in the matrices (as opposed to examining the entire matrix structure).

The problem with this approach lies in the calculation of confidence intervals for each entry. Since confidence intervals are a function of sample size and number of observations, the sampling intervals will vary from entry to entry. However, by concentrating on entries containing a relatively large sample size, i.e., number of observations, it is believed that a reasonable picture of the entire structure can be obtained. This approach is necessary because it is not possible to characterize those entries with only a few observations within reasonable confidence limits. Therefore, confidence intervals about the "major" entries will be used to examine how well the historical data characterizes the entire matrix.

Suppose that a population of three sequences is divided into two categories, those which are 14, 14, 23 and those which do not have this sequence. If in the whole population there is a proportion Θ of the above sequence, the probability that in a sample of five individuals picked at random there will be X with the 14, 14, 23 characteristic, is given by the binomial function

$$f(x) = C(5,x) \Theta^x (5-\Theta)^{5-x}$$

where

f is the probability density function

X is the observed number of 14, 14, 23s in this sample, and

Θ is the actual proportion of 14, 14, 23s in the entire population

C is the standard combinatorial notation.

The value of Θ is usually unknown, but it can be estimated from the sample, and the larger the sample, the more accurate the estimate. If p is defined as the proportion of individuals in the sample having the "characteristic" 14, 14, 23, then $p = x/s$. Obviously, if the sample s is so large that it includes the whole population, p will coincide with Θ , but for small samples p will vary from one sample to another.

The expectation of x is given by $\mu = s\Theta$, so that, since s is a fixed number (the sample size), the expectation of p is $\mu/s = \Theta$. The variance of p is:

$$\text{Var}(p) = \Theta(1-\Theta)/s$$

Hence, the variance of p naturally diminishes as the sample size increases.

If it is now assumed that x has a certain value, then the probability, that a random sample of size s will have a value of p differing from θ by any given amount, can be estimated. If the sample is large enough, i.e., (≥ 30), the normal approximation to the binomial will enable an estimate of this probability to be made quite easily. An example of this methodology is presented in Appendix B.

If the confidence limits are examined as percentages of the number of entries in the matrix rather than as a cardinal range, it is seen that there is greater statistical confidence associated with the entries of the first-order matrix as opposed to the second-order matrix.

3.0 AUTO CORRELATION FUNCTIONS

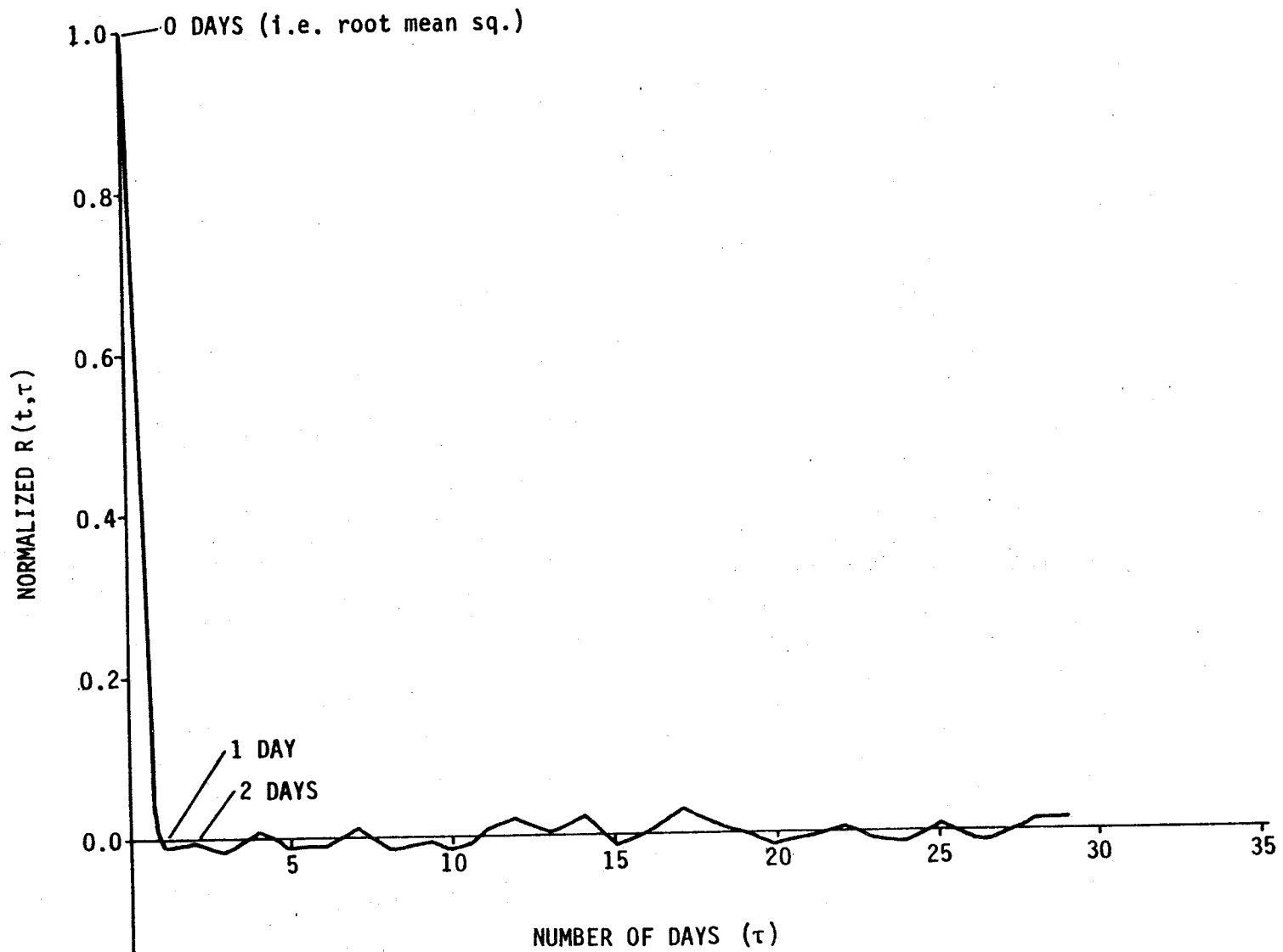
Two tests were run to investigate the correlation of daily weather patterns. Auto correlation functions were generated based upon the historical data. Since the raw data was not continuous (e.g., 14, 15, 16, 22), a simple transformation replaced each data type with an integer from 1 to 13. (Only 13 combinations of the 5 wind patterns and 6 intensities factors were correlated by PMEL to Putnins data.) The auto correlation function was generated for both the whole weather pattern (wind field and intensities) and for the pattern only (wind field only). In addition, as a point of comparison, the autocorrelation function for randomly generated weather sequences was calculated. The results are presented on Plates 3.1 through 3.3.

It is apparent from the figures that, although the correlation is small, the weather patterns are not random events. In addition, the correlation for the form only is a

BY S. Van Allen DATE 9-10-80
CHECKED BY _____

NOAA
FILE 06797-014 - (5105) 88

REVISIONS
BY _____ DATE _____



358

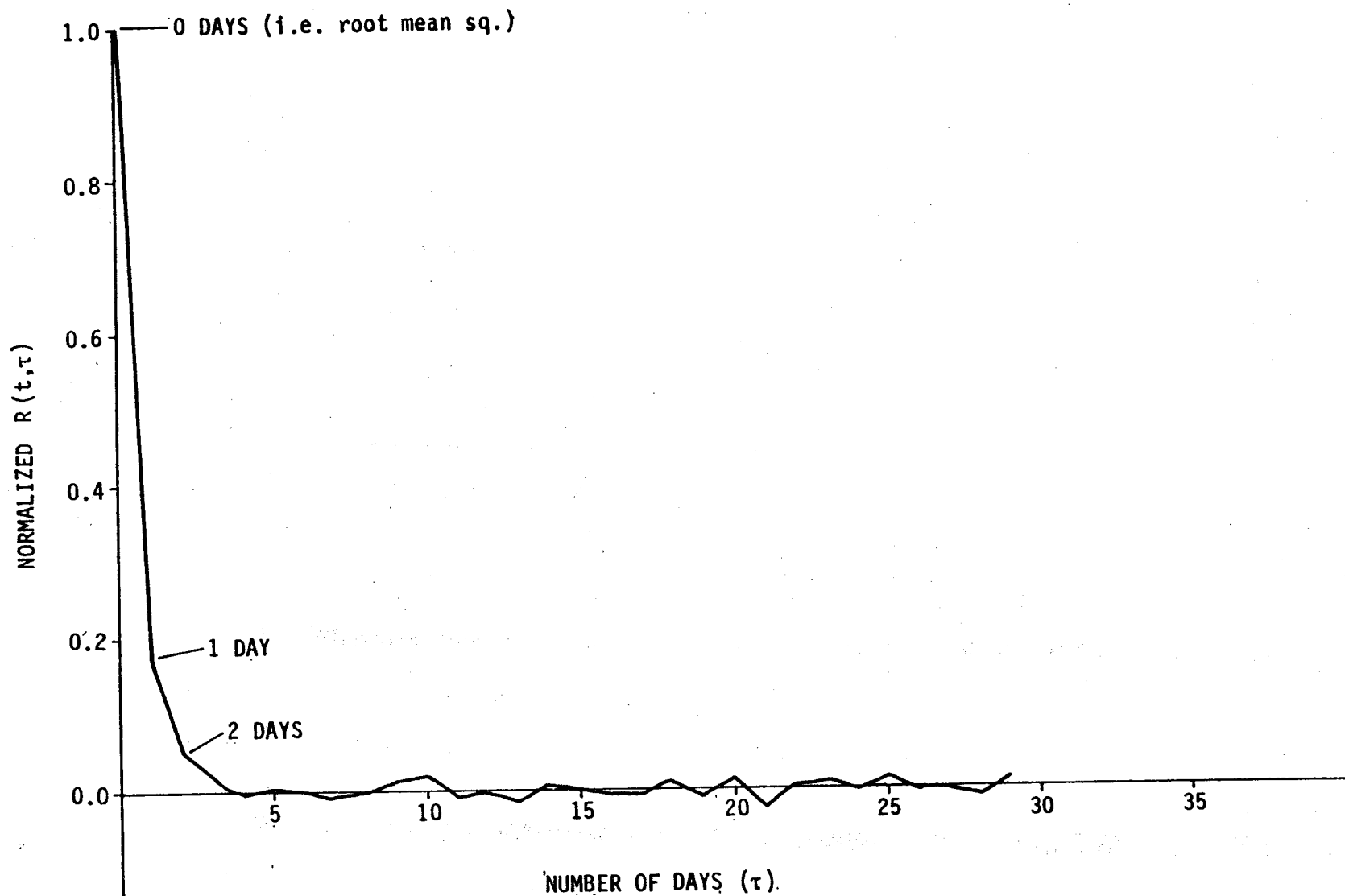
DAMES & MOORE

AUTO CORRELATION FOR RANDOM NUMBERS

BY J. Van Atta DATE 9-10-80
 CHECKED BY _____

NORR
 FILE 06T77-014-88 (5105)

REVISIONS
 BY _____ DATE _____



359

DAMES & MOORE

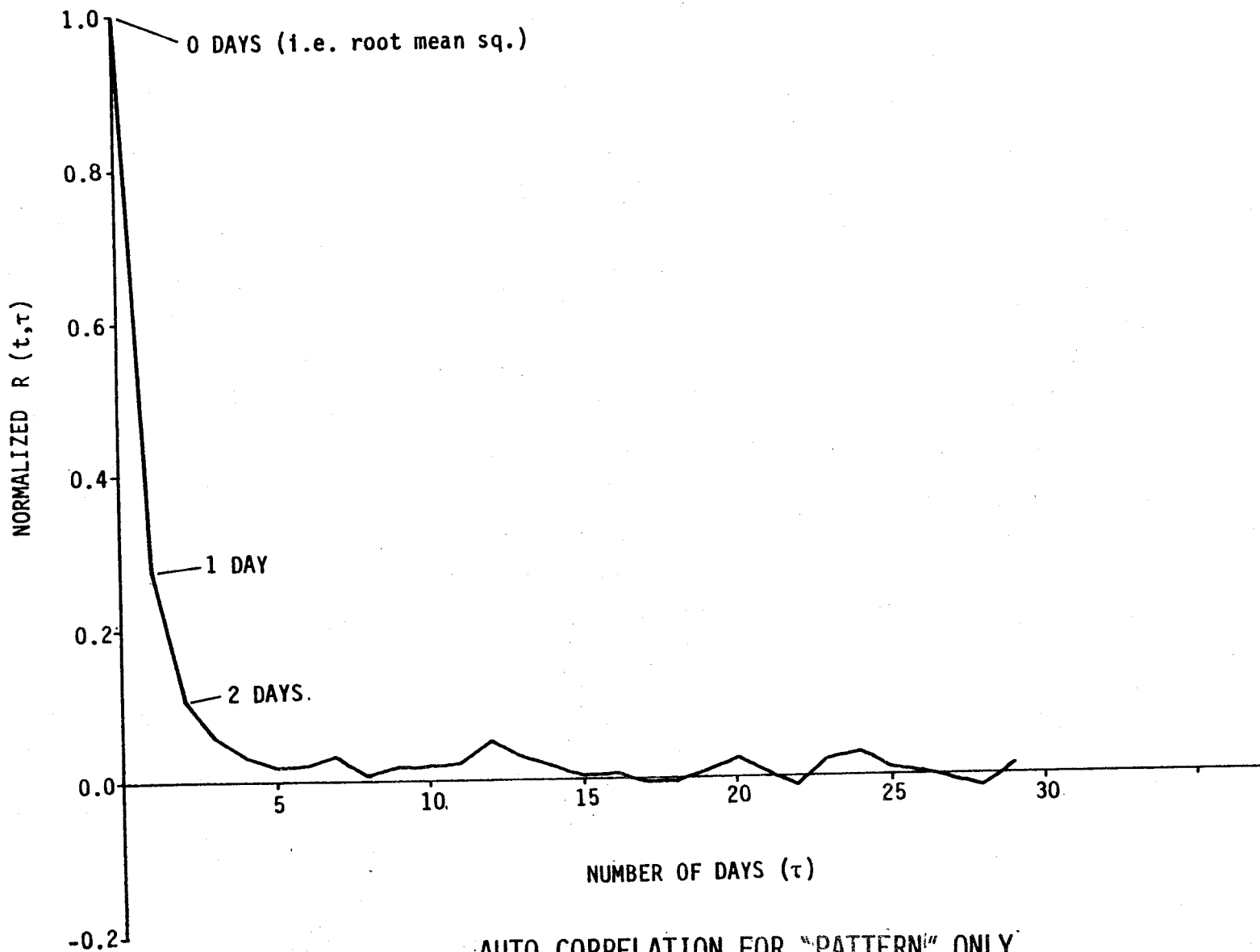
PLATE 3.2

AUTO CORRELATION FOR WEATHER CATALOG PATTERN AND INTENSITY

BY _____ DATE 9-10-80
CHECKED BY A. Van Osta

NOAA
FILE 06797-014-(5105)-88

REVISIONS
BY _____ DATE _____



little stronger than that for the form and intensity together. This seems reasonable as it can be expected that wind fields would be somewhat more stable than intensities.

The second step in the correlation analyses was to use a statistical test to determine if the occurrences of weather patterns were independent events or were correlated to the previous days' weather.

Using the first-order transition matrix as a contingency table, a chi square statistic was generated for the table using the method outlined by Freund, et al. (1960). Based upon this statistic, it was concluded that there is some correlation between the present day's weather and the previous day's weather, i.e., the null hypothesis that there is no correlation can be rejected with 95 percent confidence.

4.0 COMPARISON OF FIRST- AND SECOND-ORDER MATRICES AND THE WEATHER CATALOG

The third step in comparing the transition matrices and the weather catalog consisted of calculating the probabilities that three-day sequences would occur using three different methods.

As a first approach, each day's weather was assumed to be an independent event. The frequency of occurrence of each weather pattern was calculated from the historical data. The following analysis assumed that the initial weather pattern was 14.

A 13 x 13 matrix of probabilities was then generated using:

$$P'_{14,A,B} = P(14) \times P(A) \times P(B) \quad (4.1)$$

TABLE 4.1
PROBABILITY OF WEATHER PATTERN SEQUENCES

1 = P(14) x P(A) x P(B)
2 = P(14) x P(A/14) x P(B/A)
3 = P(14,A) x P(B/14,A)

INITIAL SEQUENCE	TYPE	14	15	16	22	23	25	26	31	33	42	43	45	53
14 14	1	.00037	.00040	.00005	.00012	.00054	.00058	.00004	.00005	.00026	.00069	.00045	.00032	.00125
	2	.01270	.00183	.00006	.00051	.00339	.00252	0.00000	.00012	.00012	.00264	.00150	.00030	.00429
	3	.01321	.00152	.00015	.00045	.00376	.00270	0.00000	.00030	.00030	.00285	.00061	.00015	.00436
14 15	1	.00040	.00043	.00006	.00013	.00059	.00063	.00004	.00006	.00029	.00075	.00049	.00035	.00136
	2	.00039	.00168	.00009	.00021	.00052	.00016	.00005	.00001	.00006	.00027	.00024	.00013	.00052
	3	.00059	.00193	0.00000	.00015	.00059	.00015	0.00000	0.00000	0.00000	.00015	0.00000	0.00000	.00074
14 16	1	.00005	.00006	.00001	.00002	.00008	.00008	.00001	.00001	.00004	.00010	.00006	.00005	.00017
	2	0.00000	.00001	.00001	.00001	.00001	.00001	0.00000	0.00000	.00002	.00001	.00001	.00001	.00003
	3	.00010	0.00000	0.00000	0.00000	0.00000	0.00000	0.00000	0.00000	0.00000	0.00000	0.00000	0.00000	0.00000
14 22	1	.00012	.00013	.00002	.00004	.00018	.00019	.00001	.00002	.00009	.00023	.00015	.00011	.00041
	2	.00008	.00011	.00003	.00020	.00005	.00008	.00002	.00002	.00007	.00011	.00014	.00012	.00019
	3	.00030	0.00000	0.00000	.00030	.00015	.00015	0.00000	0.00000	0.00000	.00030	0.00000	0.00000	0.00000
14 23	1	.00054	.00059	.00008	.00018	.00080	.00086	.00006	.00008	.00039	.00102	.00067	.00048	.00184
	2	.00076	.00029	.00001	.00011	.00441	.00049	.00007	.00005	0.00000	.00097	.00021	.00040	.00025
	3	.00150	.00045	0.00000	0.00000	.00435	0.00000	.00015	0.00000	0.00000	.00075	.00015	.00015	.00060
14 25	1	.00058	.00063	.00008	.00019	.00086	.00092	.00006	.00008	.00041	.00109	.00071	.00051	.00197
	2	.00014	.00027	.00005	.00007	.00017	.00265	.00002	.00002	.00021	.00032	.00025	.00012	.00167
	3	.00015	.00030	0.00000	0.00000	.00015	.00405	0.00000	0.00000	0.00000	.00015	.00015	0.00000	.00105
14 26	1	.00004	.00004	.00001	.00001	.00006	.00006	0.00000	.00001	.00003	.00007	.00005	.00003	.00013
	2	0.00000	0.00000	0.00000	0.00000	0.00000	0.00000	0.00000	0.00000	0.00000	0.00000	0.00000	0.00000	0.00000
	3	0.00000	0.00000	0.00000	0.00000	0.00000	0.00000	0.00000	0.00000	0.00000	0.00000	0.00000	0.00000	0.00000
14 31	1	.00005	.00006	.00001	.00002	.00008	.00008	.00001	.00001	.00004	.00010	.00006	.00005	.00017
	2	.00001	.00002	0.00000	.00001	.00002	.00001	0.00000	.00010	.00001	.00002	.00004	0.00000	.00004
	3	0.00000	0.00000	0.00000	0.00000	0.00000	0.00000	.00015	0.00000	0.00000	0.00000	.00015	0.00000	0.00000
14 33	1	.00026	.00029	.00004	.00009	.00039	.00041	.00003	.00004	.00019	.00049	.00032	.00023	.00089
	2	.00001	.00001	.00001	0.00000	.00001	.00001	0.00000	0.00000	.00010	.00002	.00003	.00002	.00005
	3	.00030	0.00000	0.00000	0.00000	0.00000	0.00000	0.00000	0.00000	0.00000	0.00000	0.00000	0.00000	0.00000
14 42	1	.00069	.00075	.00010	.00023	.00102	.00109	.00007	.00010	.00049	.00130	.00085	.00061	.00235
	2	.00016	.00008	.00001	.00007	.00051	.00063	.00005	.00002	.00009	.00280	.00041	.00075	.00066
	3	.00030	.00030	0.00000	0.00000	.00030	.00030	0.00000	0.00000	0.00000	.00330	0.00000	.00060	.00120
14 43	1	.00045	.00049	.00006	.00015	.00067	.00071	.00005	.00006	.00032	.00085	.00056	.00040	.00154
	2	.00010	.00029	.00007	.00007	.00021	.00023	.00001	.00005	.00015	.00047	.00118	.00017	.00053
	3	.00075	.00015	0.00000	0.00000	.00015	.00060	0.00000	.00015	0.00000	.00015	.00105	0.00000	.00060
14 45	1	.00032	.00035	.00005	.00011	.00048	.00051	.00003	.00005	.00023	.00061	.00040	.00029	.00110
	2	0.00000	.00001	.00001	.00002	.00003	.00007	.00001	.00001	.00004	.00014	.00006	.00022	.00009
	3	0.00000	0.00000	0.00000	0.00000	0.00000	0.00000	0.00000	0.00000	0.00000	.00014	0.00000	.00028	.00028
14 53	1	.00125	.00136	.00017	.00041	.00184	.00197	.00013	.00017	.00089	.00235	.00154	.00110	.00423
	2	.00047	.00073	.00007	.00020	.00016	.00069	.00004	.00008	.00061	.00048	.00078	.00019	.00566
	3	.00045	.00030	0.00000	.00015	.00015	.00135	0.00000	0.00000	0.00000	0.00000	.00045	.00015	.00720

TABLE 4.2
PROJECTED NUMBER OF OCCURRENCES OF GIVEN SEQUENCES
BASED UPON A 19-YEAR RECORD (6,663 DAYS)

1 = P(14) x P(A) x P(B)
2 = P(14) x P(A/14) x P(B/A)
3 = P(14,A) x P(B/14,A)

INITIAL SEQUENCE	TYPE	14	15	16	22	23	25	26	31	33	42	43	45	53
14 14	1	2.4	2.7	.3	.8	3.6	3.9	.3	.3	1.7	4.6	3.0	2.2	8.3
	2	84.6	12.2	.4	3.4	22.6	16.8	0.0	.8	.8	17.6	10.0	2.0	28.6
	3	88.0	10.1	1.0	3.0	25.0	18.0	0.0	2.0	2.0	19.0	4.0	1.0	29.1
14 15	1	2.7	2.9	.4	.9	3.9	4.2	.3	.4	1.9	5.0	3.3	2.4	9.0
	2	2.6	11.2	.6	1.4	3.4	1.1	.3	.1	.4	1.8	1.6	.8	3.5
	3	4.0	12.8	0.0	1.0	4.0	1.0	0.0	0.0	0.0	1.0	0.0	0.0	4.9
14 16	1	.3	.4	0.0	.1	.5	.5	.0	.0	.2	.6	.4	.3	1.2
	2	0.0	.1	.1	.1	.1	.1	0.0	0.0	.1	.1	.1	.1	.2
	3	.7	0.0	0.0	0.0	0.0	0.0	0.0	0.0	0.0	0.0	0.0	0.0	0.0
14 22	1	.8	.9	.1	.3	1.2	1.3	.1	.1	.6	1.5	1.0	.7	2.7
	2	.5	.7	.2	1.3	.4	.5	.1	.2	.5	.7	.9	.8	1.3
	3	2.0	0.0	0.0	2.0	1.0	1.0	0.0	0.0	0.0	2.0	0.0	0.0	0.0
14 23	1	3.6	3.9	.5	1.2	5.3	5.7	.4	.5	2.6	6.8	4.4	3.2	12.2
	2	5.1	1.9	.1	.7	29.4	3.3	.5	.3	0.0	6.5	1.4	2.7	1.7
	3	10.0	3.0	0.0	0.0	29.0	0.0	1.0	0.0	0.0	5.0	1.0	1.0	4.0
14 25	1	3.9	4.2	.5	1.3	5.7	6.1	.4	.5	2.8	7.3	4.8	3.4	13.1
	2	1.0	1.8	.3	.5	1.1	17.6	.1	.2	1.4	2.1	1.7	.8	11.1
	3	1.0	2.0	0.0	0.0	1.0	27.0	0.0	0.0	0.0	1.0	1.0	0.0	7.0
14 26	1	.3	.3	0.0	.1	.4	.4	0.0	0.0	.2	.5	.3	.2	.9
	2	0.0	0.0	0.0	0.0	0.0	0.0	0.0	0.0	0.0	0.0	0.0	0.0	0.0
	3	0.0	0.0	0.0	0.0	0.0	0.0	0.0	0.0	0.0	0.0	0.0	0.0	0.0
14 31	1	.3	.4	0.0	.1	.5	.5	0.0	0.0	.2	.6	.4	.3	1.2
	2	.1	.1	0.0	.1	.1	.1	0.0	.6	.1	.1	.3	0.0	.3
	3	0.0	0.0	0.0	0.0	0.0	0.0	1.0	0.0	0.0	0.0	1.0	0.0	0.0
14 33	1	1.7	1.9	.2	.6	2.6	2.8	.2	.2	1.3	3.3	2.2	1.5	5.9
	2	0.0	.1	0.0	0.0	.1	.1	0.0	0.0	.7	.2	.2	.1	.4
	3	2.0	0.0	0.0	0.0	0.0	0.0	0.0	0.0	0.0	0.0	0.0	0.0	0.0
14 42	1	4.6	5.0	.6	1.5	6.8	7.3	.5	.6	3.3	8.7	5.7	4.1	15.6
	2	1.1	.5	.1	.5	3.4	4.2	.3	.1	.6	18.7	2.7	5.0	4.4
	3	2.0	2.0	0.0	0.0	2.0	2.0	0.0	0.0	0.0	22.0	0.0	4.0	8.0
14 43	1	3.0	3.3	.4	1.0	4.4	4.8	.3	.4	2.2	5.7	3.7	2.7	10.2
	2	.7	2.0	.5	.5	1.4	1.5	.1	.4	1.0	3.1	7.9	1.2	3.5
	3	5.0	1.0	0.0	0.0	1.0	4.0	0.0	1.0	0.0	1.0	7.0	0.0	4.0
14 45	1	2.2	2.4	.3	.7	3.2	3.4	.2	.3	1.5	4.1	2.7	1.9	7.3
	2	0.0	.1	.1	.1	.2	.5	0.0	0.0	.3	.9	.4	1.5	.6
	3	10.0	0.0	0.0	0.0	0.0	0.0	0.0	0.0	0.0	.9	0.0	1.9	1.9
14 53	1	8.3	9.0	1.2	2.7	12.2	13.1	.9	1.2	5.9	15.6	10.2	7.3	28.2
	2	3.1	4.9	.5	1.4	1.1	4.6	.3	.5	4.1	3.2	5.2	1.3	37.7
	3	3.0	2.0	0.0	1.0	1.0	9.0	0.0	0.0	0.0	0.0	3.0	1.0	48.0

where A is the first day's weather, and
B is the second day's weather.

The second approach was to use a first-order transition matrix. Again, the initial weather pattern was assumed to be 14. A second 13 x 13 matrix was generated using:

$$P''_{14,A,B} = P(14) \times P(A/14) \times P(B/A) \quad (4.2)$$

The third approach was to use a second-order transition matrix. This time it was assumed that the initial weather conditions were specified by 14,A where A is any one of 13 patterns. The third 13 x 13 matrix was generated using

$$P''_{14,A,B} = P(14,A) \times P(B/14,A) \quad (4.3)$$

The results are presented on Tables 4.1 and 4.2.

In addition, an inquiry was made into the difference between the first- and second-order matrices with respect to the probabilities each associated with similar events. The matrices were compared in two ways. First, the mean and standard deviation were calculated for the differences between each; i.e.,

$$P''_{14,A,B} - P''_{14,A,B}.$$

Overall, the average difference between these is 0.896 days with a standard deviation of 1.462 days.

The most important finding, however, is the fact that 83 3-day sequences of weather patterns are generated by the first-order transition matrix which have not occurred in historical data or as a result of using the second-order transition matrix.

The use of a first-order transition matrix which generates non-observed patterns could have significant effects on the results of an oil spill trajectory analysis. The above finding is especially important since only the sequences beginning with "14" were examined. It is probably safe to assume that weather sequences beginning with other patterns would produce similar results; i.e., $13 \times 80 = 1,040$ sequences, or 15 percent of the total in this case, which are generated but do not occur. Since the results of the oil spill trajectory analysis are strongly related to the sequences of weather patterns, it would be important to eliminate those sequences of weather patterns which have not occurred historically. This argument becomes more critical when considering results of the auto correlation function, which showed some correlation after two days.

5.0 CONCLUSIONS AND RECOMMENDATIONS

Based upon this analysis, the following conclusions have been reached: (1) use of a first-order transition matrix is an improvement over assuming each day is a random event; (2) use of a second-order matrix is an improvement over the first-order matrix because it eliminates the generations of patterns which historically have not been observed.

There is a definite tradeoff between the accuracy with which a transition matrix can be characterized from a given data base and the number of unrealistic weather pattern sequences which are tolerable. It has been shown that a first-order matrix generates a large number of sequences which, historically, have never occurred. On the other hand, it has been demonstrated that the entries in the first-order matrix are statistically more efficient than those in a second-order matrix. Unfortunately, the question of "How much data is necessary to accurately define a transition matrix?" has not been resolved. However, it has been demonstrated that

if enough data is available, a second-order matrix is much preferable to a first-order matrix, simply because of the unrealistic sequences generated by the first-order matrix and the possible effects this may have on oil spill trajectories.

This last conclusion should be tempered with the type of oil spill trajectory study being conducted and the relative importance of other environmental factors. For example, if a first-order transition matrix generates unobserved wind field sequences, the total wind-drift vector will be the same for an observed sequence having the same wind fields. The question still remains as to whether or not unobserved sequences would generate significantly different oil spill trajectory results. If an oil spill trajectory study were conducted in a hindcast-stochastic mode, then the possibility exists that only minor differences would result from using a first- or second-order wind field transition matrix. Where the difference becomes critical would be the use of a first-order transition matrix in a forecasting-stochastic mode where unobserved sequences would give, over the short-term (2 to 3 days), erroneous probabilities and locations for trajectory movement.

If the environmental fields other than wind (tides and net currents) are significant, then unobserved wind field sequences could lead to trajectory end points different than those produced by observed sequences containing the same wind fields. The wind drift vector would combine with net and tidal currents having different gradients and phasing in strength and direction and could result in radically different paths and end points.

The trajectory study presented in Dames & Moore (1980) used historically observed sequences and, therefore, is not subject to the concerns expressed above. However, the methodology used was cumbersome and really only applicable to the hindcast-stochastic mode of operation required for the risk

assessment study. In order to take advantage of the efficiency afforded by a transition matrix approach and to be able to operate in a forecasting-stochastic mode, the following recommendations are made:

- o Perform a comparison between the end-point locations of trajectories calculated using a first- and second-order wind field transition matrix, as well as those calculated using a random access to historically sequence observed wind fields.
- o These comparisons should be performed from launch sites in at least two areas characterized by relatively strong and weak net and tidal current strength and gradients.
- o Investigate the frequency of occurrence and wind drift differential associated with 2- or 3-day forecasts containing unobserved sequences generated by a first-order transition matrix compared to a second-order transition matrix.

Completion of the above recommended studies will provide answers to key remaining questions and will lead to more accurate implementation of wind field variability in future oil spill trajectory and/or dispersion studies. The results should also aid in developing simplified strategies in implementation of oil spill contingency plans through knowledge of the relative strength of environmental fields and their resultant effect on surface transport.

REFERENCES

- Dames & Moore, 1980. Final Report, Task I, Oil Spill Trajectory Simulation, Lower Cook Inlet and Shelikof Strait, Alaska, for the Bering Sea, Gulf of Alaska Project Office, Outer Continental Shelf Environmental Assessment Program, Job Number 06797-014-88.
- _____, 1979. Report, Oil Spill Trajectory Analysis, Lower Cook Inlet, Alaska, for National Oceanic and Atmospheric Administration, Job Number 06979-011-02.
- _____, 1976. Report, Oil Spill Trajectory Analysis, Lower Cook Inlet, Alaska, for National Oceanic and Atmospheric Administration, Job Number 06797-003-20.
- Freund, John E., Paul E. Livermore, and Irwin Miller, 1960. Manual of Experimental Statistics. Prentice-Hall Mathematics Series, Prentice Hall Inc.
- Putnins, P., 1966a. Studies on the Meteorology of Alaska: First Interim Report (The sequences fo baric weather patterns over Alaska). U.S. Dept. of Commerce, ESSA/EDS, Silver Spring, Maryland.
- _____, 1966b. Unpublished tabultion of daily baric weather types for Alaska from January 1, 1945 to March 31, 1963, University of Alaska.
- _____, 1969. Studies on the Meteorology of Alaska: Final Report (Weather situations in Alaska during the occurrences of specific baric weather), U.S. Department of Commerce, ESSA, Research Laboratories, Boulder Colorado, 80302, 267 p.

45 1 00532223422314532542532553535314232342422525232542424225254253
45 2 0023232314535353435353531523424242454553435343452253424245000000
45 3 00454242534353535353535343535353145353535353532214535353534542
45 4 0023232315151545452245452253152323535314151522162315151414535300
45 5 003153532323232323231453535353234242424242424343424242424342
45 6 004353535342422525252553332323262642425353533533333163353535300
45 7 0053422323232323232315535353334245224353533353535316535345453323
45 8 00234242431516533333535353435353534343234242454353535343434242
45 9 0053335353535343452253535345534343221523234545424242424553535300
45 10 0053312525535353535353535315353163325255353532525151523452525253
45 11 00225315154242422522432314142314145353532222535353531515151500
45 12 005315141515141423232525221414424242424223231453535353531414
46 1 0053255353531414141442452323424253534245255333454242424342251453
46 2 0053141415151515151542422553532525534253142315232314141425000000
46 3 0053422525152253535314535314252553531453535353535353535353535300
46 4 00431445535353531414531453535353535353535353535353535353535300
46 5 0053454353534242454545453153535353424542424243144343421414154223
46 6 0042421542424242424343424245452222242424242425315424242424200
46 7 0042333434342234242455345154533154343434242454343532245535316
46 8 00335343434333333454545535454553534322223131434545453131224542
46 9 0031312323454345454523255353532325255353531516531414431522151400
46 10 0014535345255353343535353424245425353535353535353535353535353
46 11 00252535353335353535343535315232323232323232345455323231522431600
46 12 0053151522535315152215152315151443535353434325155342424214151445
47 1 0042532225432526154533154243255353145353141453531515152323232323
47 2 0014141414144242422323232314144245454545421442424245454223000000
47 3 0023232353535314141614145353531423234242535353532242255323141414
47 4 002323141453252553535342424242232315144353534314535353535300
47 5 00253342452553252553142343535353435353424345452545454242422323
47 6 0014141453434223235353422553333333535343434333453333154343531500
47 7 00435343424343434343154545454242424242424242434333423353434553
47 8 00534343424226424542434543424343434242431523232342535353535353
47 9 005353433353
47 10 0053221645454253
47 11 00433342434353334553435353535353535353534242422542452553424253434200
47 12 00424242532553535353535353531453532525535353535353535353535353
48 1 0025253535353535353535314421414252542422525252525254245535315142525
48 2 00454323232323232342424232323531423232323231414235353141425250000
48 3 0014231514142323234515535325255353535353535353535353535353535353
48 4 0023232343434315234342434543431515222243225353155343434316151500
48 5 00535314145353531425255353151553145353535333335315254545534343
48 6 00535343224553534223424342424242424543434343424243533333433300
48 7 003333342455343164343535345424242424553535343435353335353535353
48 8 0045454553333534342424343454543334343424243431642161631313143
48 9 005322335353534216533343424242335353535325255343255342454542500
48 10 00253535333353
48 11 0042535343434343334253
48 12 005315222214141422425353264553534253333434353154525535353535353
49 1 001414255325154245424243434332525424545164245262626422642454245
49 2 0015232343531443141523424343431515232342421414234242421414000000
49 3 00142525254243424542454523
49 4 005353535353535315161553141443145353535353535315141414535353535300
49 5 005353535315532323141453533333454245424242424242434342424243535353
49 6 0025253333155333221633255333334242435353535343432343161653153300
49 7 00434343434342452642424253333454245433333333333343535333431653
49 8 005316222233333533353435315163333534342422525334533532542425353
49 9 00535353535343434223454253
49 10 0045452525535314252553535353454545264525535345535353535353535353
49 11 0053531515222243434545431543232323232345255353151545454515434300
49 12 0015431515225353225343425353222323232323231414144225252222141453
50 1 004542432523234343232323452323232331232323232323432323232323232323
50 2 004323232222151514141414141414141422232222314231141414144242000000
50 3 00252553534342
50 4 00141522264516454553252553333335353535353535353535353535353535353
50 5 0053155353335325255353535353531414435333333343425353535333333315
50 6 001515164242423333433314424242425342452542533423353432216161500
50 7 0042424242234214424245454342144242434332223224253333333333334343
50 8 00434245334242424242264223232342452342424225252525535353333326
50 9 005352553533532525453333424242425255353425353533334545452500
50 10 0025252525232314432553535353455342224525535345535333335353535353

62 8 0045422553534345333315254242452342434325253333535333454542451643
62 9 00425353421514421533163333535353535342232525252522533333152500
62 10 005333163333422525151515151414255333335333345424225532325232323
62 11 0023424242252325252525151523231442422525435353232525531553252500
62 12 0053532515155323232342252525252553145353252323452315232323232323
63 1 002343251525154343232342422245454542424223424242232323232323
63 2 0023151515252525251543232323231515422525252525252325252525000000
63 3 0025234253254242425345154253153314252553152233152245431515232323

TABLE A-1

ANNUAL 13 x 13 WIND FIELD TRANSITION MATRIX

<u>Given Wind Field</u>	<u>Probability of Listed Wind Field Following Given Wind Field</u>												
	<u>14</u>	<u>15</u>	<u>16</u>	<u>22</u>	<u>23</u>	<u>25</u>	<u>26</u>	<u>31</u>	<u>33</u>	<u>42</u>	<u>43</u>	<u>45</u>	<u>53</u>
14	0.423	0.061	0.002	0.017	0.113	0.084	0.000	0.004	0.004	0.088	0.050	0.010	0.143
15	0.089	0.389	0.021	0.048	0.119	0.037	0.012	0.002	0.015	0.062	0.056	0.029	0.121
16	0.015	0.104	0.104	0.060	0.060	0.060	0.000	0.030	0.149	0.060	0.060	0.090	0.209
22	0.063	0.089	0.025	0.165	0.044	0.063	0.013	0.019	0.057	0.089	0.114	0.101	0.158
23	0.095	0.036	0.001	0.014	0.550	0.061	0.009	0.006	0.000	0.121	0.026	0.050	0.031
25	0.024	0.046	0.008	0.012	0.028	0.444	0.003	0.004	0.036	0.053	0.042	0.020	0.280
26	0.082	0.020	0.000	0.041	0.122	0.020	0.245	0.000	0.020	0.204	0.041	0.122	0.082
31	0.030	0.075	0.015	0.030	0.075	0.030	0.015	0.343	0.030	0.060	0.149	0.015	0.134
33	0.026	0.044	0.018	0.015	0.029	0.050	0.003	0.000	0.355	0.085	0.109	0.076	0.191
42	0.026	0.013	0.002	0.011	0.081	0.101	0.008	0.003	0.014	0.448	0.066	0.120	0.106
43	0.029	0.083	0.020	0.020	0.058	0.065	0.003	0.015	0.041	0.133	0.333	0.049	0.150
45	0.007	0.021	0.012	0.028	0.036	0.104	0.009	0.009	0.062	0.194	0.083	0.308	0.126
53	0.046	0.072	0.007	0.020	0.016	0.068	0.004	0.008	0.060	0.047	0.077	0.019	0.557

TABLE A-2

WINTER 13 x 13 WIND FIELD TRANSITION MATRIX

<u>Given Wind Field</u>	<u>Probability of Listed Wind Field Following Given Wind Field</u>												
	<u>14</u>	<u>15</u>	<u>16</u>	<u>22</u>	<u>23</u>	<u>25</u>	<u>26</u>	<u>31</u>	<u>33</u>	<u>42</u>	<u>43</u>	<u>45</u>	<u>53</u>
14	0.462	0.066	0.003	0.020	0.114	0.100	0.000	0.003	0.003	0.080	0.034	0.006	0.111
15	0.104	0.404	0.010	0.055	0.153	0.039	0.020	0.003	0.003	0.042	0.042	0.033	0.091
16	0.043	0.087	0.043	0.087	0.130	0.087	0.000	0.043	0.087	0.087	0.043	0.130	0.130
22	0.076	0.109	0.011	0.152	0.065	0.076	0.011	0.011	0.033	0.098	0.076	0.087	0.196
23	0.101	0.033	0.002	0.014	0.597	0.054	0.008	0.002	0.000	0.101	0.021	0.041	0.025
25	0.025	0.054	0.008	0.015	0.033	0.464	0.004	0.002	0.019	0.050	0.040	0.019	0.268
26	0.108	0.027	0.000	0.054	0.108	0.027	0.270	0.000	0.027	0.135	0.054	0.135	0.054
31	0.045	0.091	0.000	0.045	0.136	0.045	0.045	0.318	0.000	0.091	0.045	0.000	0.136
33	0.091	0.030	0.015	0.030	0.030	0.061	0.000	0.000	0.273	0.136	0.091	0.076	0.167
42	0.038	0.016	0.000	0.021	0.088	0.147	0.008	0.003	0.000	0.413	0.043	0.088	0.134
43	0.024	0.130	0.024	0.006	0.112	0.142	0.012	0.018	0.018	0.077	0.225	0.036	0.178
45	0.018	0.030	0.012	0.036	0.054	0.138	0.012	0.006	0.030	0.186	0.054	0.299	0.126
53	0.069	0.087	0.006	0.023	0.019	0.087	0.008	0.005	0.029	0.045	0.044	0.019	0.561

TABLE A-3

SUMMER 13 x 13 WIND FIELD TRANSITION MATRIX

<u>Given Wind Field</u>	<u>Probability of Listed Wind Field Following Given Wind Field</u>												
	<u>14</u>	<u>15</u>	<u>16</u>	<u>22</u>	<u>23</u>	<u>25</u>	<u>26</u>	<u>31</u>	<u>33</u>	<u>42</u>	<u>43</u>	<u>45</u>	<u>53</u>
14	0.317	0.048	0.000	0.008	0.111	0.040	0.000	0.008	0.008	0.111	0.095	0.024	0.230
15	0.066	0.368	0.038	0.038	0.071	0.033	0.000	0.000	0.033	0.090	0.075	0.024	0.165
16	0.000	0.114	0.136	0.045	0.023	0.045	0.000	0.023	0.182	0.045	0.068	0.068	0.250
22	0.045	0.061	0.045	0.182	0.015	0.045	0.015	0.030	0.091	0.076	0.167	0.121	0.106
23	0.082	0.041	0.000	0.014	0.447	0.078	0.009	0.014	0.000	0.164	0.037	0.068	0.046
25	0.022	0.033	0.007	0.007	0.018	0.410	0.000	0.007	0.066	0.059	0.048	0.022	0.300
26	0.000	0.000	0.000	0.000	0.167	0.000	0.167	0.000	0.000	0.417	0.000	0.083	0.167
31	0.022	0.067	0.022	0.022	0.044	0.022	0.000	0.356	0.044	0.044	0.200	0.022	0.133
33	0.011	0.047	0.018	0.011	0.029	0.047	0.004	0.000	0.375	0.073	0.113	0.076	0.196
42	0.017	0.011	0.004	0.004	0.076	0.069	0.008	0.004	0.025	0.472	0.082	0.143	0.086
43	0.031	0.064	0.019	0.026	0.036	0.033	0.000	0.014	0.050	0.155	0.377	0.055	0.138
45	0.000	0.016	0.012	0.024	0.024	0.082	0.008	0.012	0.082	0.200	0.102	0.314	0.125
53	0.024	0.057	0.007	0.018	0.013	0.050	0.000	0.011	0.091	0.049	0.108	0.018	0.553

TABLE A-4

ANNUAL 5 x 5 WIND FIELD TRANSITION MARIX

<u>Given Wind Field</u>	<u>Probability of Listed Wind Field Following Given Wind Field</u>				
	1	2	3	4	5
1	0.476	0.212	0.024	0.151	0.137
2	0.111	0.530	0.029	0.174	0.157
3	0.093	0.107	0.359	0.261	0.180
4	0.069	0.178	0.041	0.587	0.125
5	0.125	0.105	0.069	0.142	0.560

APPENDIX B

The methodology used in calculating the probability, p , that a random sample of size s will have a value of p differing from the true value, Θ , by any given amount is developed in the following paragraphs. Suppose the hypothesis, "The probability of occurrence of the sequence 14, 14, 23 is 0.124 within a 95 percent confidence," is to be tested. These limits are calculated using the normal approximation to the binomial distribution. It is known that $Z = (sp - s\Theta) / [s\Theta(1-\Theta)]^{1/2}$ is approximately $N(0,1)$ and that the two symmetrical values of Z (95 percent of the whole area of the normal distribution is included between these values) are ± 1.96 . (The area of the tails beyond $Z = \pm 1.96$ is 0.05.) If Θ is the true value of the parameter, then the following inequality exists with a probability of 0.95:

$$-1.96 \leq \frac{sp - s\Theta}{[s\Theta(1-\Theta)]^{1/2}} \leq 1.96 \quad (2.1)$$

Equation (2.1) can be written as:

$$(sp - s\Theta)^2 \leq (1.96)^2 s\Theta(1-\Theta) \quad (2.2)$$

or

$$s(p - \Theta)^2 \leq 3.84\Theta(1-\Theta) \quad (2.3)$$

Collecting the terms in Θ and Θ^2 , Equation (2.3) can be written as:

$$\Theta^2 (s + 3.84) - \Theta(2ps + 3.84) + sp^2 \leq 0 \quad (2.4)$$

For this example, $s = 202$, $p = 0.124$:

$$\Theta^2 (205.84) - \Theta((2(0.124)202) + 3.84) + 202 (0.124)^2 = 0 \quad (2.5)$$

$$205.84 \Theta^2 - 53.936 \Theta + 3.106 = 0 \quad (2.6)$$

Using the quadratic equation:

$$r = \frac{(53.936 \pm \sqrt{(53.936)^2 - 4(205.84) 3.106})}{2 (205.84)} \quad (2.7)$$

With 95 percent confidence, the true value of Θ is calculated to be between 0.0854 and 0.262. This means that given the same sample size (202), the number of occurrences could have ranged between 17 and 53 with 95 percent confidence.

Based on the converted weather catalog, there are a total of 477 sequences beginning with 14 and of these there are 40 occurrences of the sequence 14, 25. Using the methodology presented in Equation (2.5), the following relation is obtained for estimating the range of occurrences of 14, 25 that might be expected within a 95 percent confidence interval.

$$\Theta^2(477+3.84) - \Theta(2(0.0838)477 + 3.84) + 477 (0.0838)^2 \quad (2.8)$$

This, in turn leads to the results

$$r_1 = 0.0621 \quad r_2 = 0.1121 \quad (2.9)$$

I.e., $29 \leq 40 \leq 53$ with 95 percent confidence.

A similar process is carried out for a second-order matrix. Taking a sample size of 29 corresponding to the

sequence 14 25, and looking at the occurrence of the sequence 14 25 is such that $x = 13$

$$\Rightarrow p = 0.448$$

$$\Theta^2(29 + 3.84) - \Theta(2(0.448) 29 + 3.84) + 29 (0.448)^2 = 0 \quad (2.10)$$

with the results

$$r_1 = 0.2839 \quad r_2 = 0.624$$

Thus, given the sample size of 29, the number of occurrences of the sequence 14, 15, 15 could vary between 8 and 18 with 95 percent confidence, i.e., $8 \leq 13 \leq 18$.

FINAL REPORT--TASK II
EVALUATION OF CODAR DATA
LOWER COOK INLET, ALASKA
BERING SEA-GULF OF ALASKA PROJECT OFFICE
OUTER CONTINENTAL SHELF ENVIRONMENTAL
ASSESSMENT PROGRAM

JOB NO. 06797-014-88
October 31, 1980

Los Angeles, California

October 31, 1980

Outer Continental Shelf Environmental
Assessment Program
Bering Sea - Gulf of Alaska Project Office
Post Office Box 1808
Juneau, Alaska 99802

Attention: Herbert E. Bruce, Ph.D.
OCSEAP Project Manager

Gentlemen:

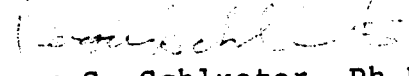
Final Report--Task II
Evaluation of CODAR Data
Lower Cook Inlet, Alaska
Bering Sea - Gulf of Alaska Project Office
Outer Continental Shelf Environmental
Assessment Program

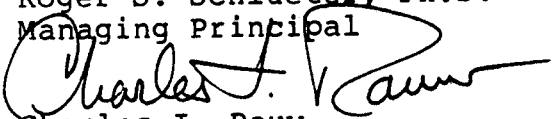
We are pleased to submit our final report on an evaluation of CODAR data taken in Lower Cook Inlet, Alaska. This report has incorporated and responded to comments received from your Juneau staff, as well as the Wave Propagation Laboratory in Boulder, Colorado.

It has been a pleasure to work on this phase of our 1980 fiscal year contract with your Juneau staff. Please do not hesitate to contact us if you have any questions regarding the contents or findings of this study.

Very truly yours,

DAMES & MOORE
Marine Services Group


Roger S. Schlueter, Ph.D.
Managing Principal


Charles I. Rauw
Project Manager

RSS:CIR:sms

CONTENTS

<u>Section</u>	<u>Page</u>
1.0 INTRODUCTION	385
1.1 BACKGROUND	385
1.2 PURPOSE	385
1.3 SCOPE	386
1.4 OBJECTIVES	386
2.0 EVALUATION OF CODAR DATA	388
2.1 CODAR SYSTEM DESCRIPTION	388
2.2 DATA AND ANALYSES	389
3.0 RESULTS AND CONCLUSIONS	394
3.1 SURFACE DRIFT COMPARISON	394
3.2 TRAJECTORY COMPARISON	395
3.3 CONCLUSIONS	397
REFERENCES	399
APPENDIX A: METEOROLOGICAL DATA	414

LIST OF FIGURES

1.	Current Meter Array Location and Range of CODAR Mapping	401
2.	24 hour Mean Surface Current Vectors for July 1, 1978	402
3.	24 hour Mean Surface Current Vectors for July 2, 1978	403
4.	24 hour Mean Surface Current Vectors for July 3, 1978	404
5.	24 hour Mean Surface Current Vectors for July 4, 1978	405
6.	24 hour Mean Surface Current Vectors for July 5, 1978	406
7.	24 hour Mean Surface Current Vectors for July 6, 1978	407
8.	24 hour Mean Surface Current Vectors for July 7, 1978	408
9.	Tidal Current Ellipses for M_2 Constituent	409
10.	Tidal Current Ellipses for K_1 Constituent	410
11.	Tidal Current Ellipses for O_1 Constituent	411
12.	Comparison of C-2 Data with CODAR Data	412
13.	Comparison of C-5 Data with CODAR Data	413

LIST OF TABLES

I.	24 Hour Mean Wind Drift Estimates	392
II.	24 Hour Mean Net Current Data	393

1.0 INTRODUCTION

1.1 BACKGROUND

This report describes a limited evaluation of CODAR data acquired in Lower Cook Inlet, Alaska during the period July 1-8, 1980.

This work was performed under Contract No. NA80RAC00075 between Dames & Moore and the National Oceanic and Atmospheric Administration. In addition to the study reported herein, other studies performed under Contract No. NA80RAC00075 include an oil spill trajectory analysis for Lower Cook Inlet and Shelikof Strait, a conceptual oil spill modeling study for Lower Cook Inlet and Shelikof Strait, and a wind transition matrix analysis. These studies have been submitted under separate cover to OCSEAP.

This study was supported by the Bureau of Land Management through interagency agreement with the National Oceanic and Atmospheric Administration, under which a multi-year program responding to needs of petroleum development of the Alaskan continental shelf is managed by the Outer Continental Shelf Environmental Assessment Program (OCSEAP) Office.

1.2 PURPOSE

This study was initiated by the Outer Continental Shelf Environmental Assessment Program (OCSEAP) on behalf of the Bureau of Land Management (BLM). This is one of a series of studies conducted by Dames & Moore to investigate the behavior of hypothetical oil spills within the Alaskan Outer Continental Shelf. One class of information that BLM has requested OCSEAP to consider is the identification and development of new monitoring techniques.

One of the more promising and newly emerging oceanographic monitoring technologies, with direct application to pollutant transport patterns and oil spill modeling, is the Coastal Ocean Dynamics Application Radar (CODAR). This technology permits mapping of surface currents over rather large geographical areas of water. The advantage of this technology over more conventional means of determining surface currents for studies of pollutant transport and oil spill modeling is obvious. This study presents a limited comparison of CODAR generated data to traditionally measured data and their subsequent application in predicting resultant surface drift.

1.3 SCOPE

This study was conducted in accordance with the scope of services for Task II detailed in the Dames & Moore proposal, "Oil Dispersion Analysis, Lower Cook Inlet and Shelikof Strait, Alaska," RFX41-436-2905, for National Oceanic and Atmospheric Administration, July 19, 1979, "Proposal Addendum, Oil Spill Dispersion Analysis," RFX41-436-2905, August 22, 1979, and "Proposal Addendum, Oil Spill Dispersion Analysis," RFX41-436-2905, October 14, 1979, subsequently amended in a letter dated February 4, 1980.

1.4 OBJECTIVES

The primary elements of the scope of services relating to the evaluation of CODAR data presented in the above documents are summarized below:

1. Process CODAR data taken in Lower Cook Inlet during the period July 1-8, 1978 between Augustine Island and Cape Douglas to yield digital data products and vector diagrams of net and tidal surface current components.

2. Compare CODAR data to other directly measured current data and to the seasonally averaged patterns developed in Task I (Dames & Moore, 1980); include a discussion of computer trajectories in light of the CODAR data.

The comparison of CODAR data to local current meter data was performed to provide an indication of the validity of deriving surface currents from Eulerian, submerged meter data. In addition, a qualitative discussion comparing trajectories calculated using the seasonal patterns and those that might have been calculated using CODAR data was to be provided. The above objectives have been met and are reported on in the following sections of this report.

2.0 EVALUATION OF CODAR DATA

2.1 CODAR SYSTEM DESCRIPTION

CODAR is the acronym for Coastal Ocean Dynamics Application Radar which is a method of surface-current measurement and mapping using a shore-based high frequency (HF) radar system. In early 1975, Dr. Donald Barrick of the Sea State Studies Branch of the Wave Propagation Laboratories (WPL) obtained initial funding from the joint NOAA/BLM Outer Continental Shelf Environmental Assessment Program (OCSEAP) to design the CODAR system. During the summer and fall of 1976 initial field tests of the system were carried out in the Miami-Ft. Lauderdale area. The feasibility and utility of the HF radar system for operational near real-time mapping of surface currents in remote coastal locations was demonstrated in subsequent field tests conducted during 1977 and 1978. One of those field tests was conducted in the Augustine Island-Cape Douglas area during late June and early July, 1978 (see Figure 1). It is data from this period of operation that is discussed here.

The operation of the HF radar system is based on the theories of sea scatter physics involving the backscatter from moving ocean waves, which in turn are being transported by an underlying current field. The wave and current motions are detected by radar as frequency displacements of the received echo from the transmitted signal ("Doppler" shifts). The surface current is determined from analysis of the spectrum reflected from the ocean surface. The details of the theory, development, and application of CODAR are presented in the following representative sample of references; Barrick and Peake (1967), Barrick and Lipu (1979), Barrick, et al., (1977), Evans (1978).

2.2 DATA AND ANALYSIS

Processed CODAR data was obtained from WPL for the period from July 1 through July 8, 1978 (Frisch, 1980). These data consisted of vector plots of 24 hour mean surface currents provided at approximate 12 hour intervals. Reproduction of the eight 24 hour mean surface current maps are provided in Figures 2 through 8. In addition to mean currents, tidal current ellipses were also calculated from the processed CODAR data for the M_2 , O_1 , and K_1 constituents. These ellipses are presented in Figures 9 through 11.

The CODAR data was taken during the same period of time that intense meteorological and oceanographical field programs were being conducted by the Pacific Marine Environmental Laboratories (PMEL) in Lower Cook Inlet. Concurrent wind and current meter data was obtained from Reynolds (1980) and Schumacher (1980) and forms the basis for this limited comparison study.

Figure 1 shows the location of five of the nearest operational current meter arrays deployed by PMEL during the same period of time. Data from each near surface meter was reduced to daily (24 hr) mean net currents and tidal current constituents based on 29 day analyses. For subsequent analyses, the net current data was assumed to be void of any wind drift component. This allowed the surface drift component to be estimated using an empirical relationship based on the surface wind velocity. Vectorially adding the current meter net velocity gave an overall net surface velocity which was then compared to the CODAR generated net surface velocity (which presumably contained both the wind drift and non-wind drift components of net surface flow).

The meteorological data used in this analysis was supplied by PMEL and is included as Appendix A. Although

meteorological station coverage was good in this area of Lower Cook Inlet during July 1-8, 1978, data recovery was rather spotty. Thus, the derived wind fields are not as reliable as one would want for a comparison such as this. The following paragraph presents a general discussion of the wind patterns that existed during the period of CODAR measurements and was, in part, extracted from Reynolds (1980).

Just preceding July 1-8, 1978, the local wind flow was influenced by air moving from the Bering Sea and across Iliamna Gap. This situation created winds blowing up Shelikof Strait and from the west-northwest across Kamishak Bay (see Appendix A) and is very similar to wind field 5 presented in Dames & Moore (1980). On the first and second of July, the weather pattern changed suddenly and the geostrophic wind direction turned southwesterly with a pressure force directed approximately down Shelikof Strait. Winds in Lower Cook Inlet suddenly switched to an easterly direction down the pressure gradient within the limits of topographic constraint. In Shelikof Strait the winds also blew down the pressure gradient switching to a northeasterly direction. This latter flow pattern basically persisted throughout the duration of the CODAR measurements. Appendix A presents the flow field for this weather pattern which is very similar to wind field 2 presented in Dames & Moore (1980).

Meteorological station data obtained from PMEL consisted of wind speed and direction for stations located on Shuyak Island and near Iliamna Lake, and direction only for the station on Augustine Island. Unfortunately, Data Buoy EB 46007, which was located in the middle of Lower Cook Inlet, near the area of CODAR coverage, was not operational during this period of time. Since no data was available to provide direct wind speed over the area of interest, a simplified approach was used to estimate the wind speed based on the wind speeds measured at Shuyak Island and Iliamna Lake. That is,

relationships were derived from the relative magnitudes of the wind vectors presented in wind fields 2 and 5 from Dames & Moore (1980). It is readily apparent that this approach can be considered only a rough approximation as many factors affecting the local wind speed have not been considered.

Although many theoretical and empirical relationships have been developed for describing the surface drift due to wind stress, the approach used in Dames & Moore (1980) will be adopted for this study. This approach assumes that the wind drift component is colinear in the direction of the wind and has a magnitude of 3.0 percent of the wind speed. These relationships were assumed for two reasons: first, to allow trajectory comparisons to be made consistent with the approach used in Dames & Moore (1980), and secondly, the data base available did not justify utilization of more sophisticated techniques. Table I presents 24 hour mean wind drift surface currents derived from the data and techniques described above. The component wind drift speeds are given for north-south and east-west directions. These components were added to the 24 hour mean net current components derived from the current meter data as an estimate of the overall net surface flow.

Table II presents the 24 hour mean net velocity components of speed and direction from the near surface current meter at each of the five arrays examined. The mean net velocity vectors of these five current meter locations were added to the daily mean wind drift vector from Table I to obtain a daily mean overall surface current vector. These were plotted on the CODAR surface current map corresponding to that particular day. These vectors are shown in Figures 2 through 8.

TABLE I
24 HOUR MEAN WIND DRIFT ESTIMATES

Da/Mo/Yr	Direction (° True)	Speed (cm/s)	Component North (cm/s)	Speeds East (cm/s)
29/06/78	280	31.5	-5.5	31.0
30/06/78	295	24.0	-10.1	21.8
01/07/78	140	18.0	13.8	-11.6
02/07/78	110	18.0	6.2	-16.9
03/07/78	100	30.0	5.2	-29.5
04/07/78	100	21.0	3.6	-20.7
05/07/78	110	21.0	7.2	-19.7
06/07/78	105	27.0	7.0	-26.1
07/07/78	115	18.0	7.6	-16.3

TABLE II
24 HOUR MEAN NET CURRENT DATA

Mooring	C-1B		C-2B		C-3B		C-4B		C-5B	
Lat.	59° 10.70'N		59° 13.50'N		59° 24.40'N		59° 16.70'N		59° 09.90'N	
Long.	153° 18.80'W		153° 07.70'W		152° 53.60'W		152° 54.90'W		152° 53.90'W	
Bottom Depth	40 m		62 m		64 m		83 m		135 m	
Meter	2504		3176		598		3294		2156	
Depth	18 m		18 m		25 m		19 m		27 m	

Date	Net Speed	Direction								
(Da/Mo/Yr)	(cm/s)	(° True)								
29/06/78	0.53	124	15.03	201	16.53	247	2.04	113	5.78	239
30/06/78	5.06	14	11.43	204	14.82	264	3.97	46	9.08	278
01/07/78	4.14	339	12.54	229	17.37	256	6.12	10	8.90	278
02/07/78	3.06	340	13.91	207	18.57	255	5.18	324	11.37	209
03/07/78	7.09	154	15.46	152	17.16	250	9.09	38	--	--
04/07/78	14.57	226	22.78	200	20.71	228	2.42	272	--	--
05/07/78	10.97	198	27.45	212	23.73	225	2.45	299	--	--
06/07/78	4.69	202	24.59	202	23.91	230	7.92	242	--	--
07/07/78	3.79	200	22.58	212	17.54	228	2.08	270	--	--
08/07/78	2.03	166	16.87	208	16.23	230	3.41	51	--	--

393

3.0 RESULTS AND CONCLUSIONS

3.1 SURFACE DRIFT COMPARISON

As shown in Figure 1, two of the current meter arrays, C-2B and C-5B, were located directly in the area of CODAR mapping coverage. Thus, it was possible to perform a direct comparison of speed and direction between the CODAR generated surface currents and the surface currents calculated at current meter locations, C-2B and C-5B. Figures 12 and 13 present these comparisons for current meter locations C-2B and C-5B, respectively.

Figure 12 shows a reasonable agreement in the direction of the surface current between the CODAR generated currents and those calculated at C-2B. The comparison of speed is not as good, but in general the data are the same magnitude and only show one day of radical departure, July 7th. The wind drift component is the dominant component when comparing the data presented in Tables I and II. Since the wind drift directional data was measured at Augustine Island, while the speed was estimated from data measured at Shuyak Island and Iliamna Lake, it is not surprising to find closer agreement between the directional data compared to the speed data.

Figure 13 shows a similar comparison for the location of current meter array C-5B. The near surface meter at C-5B produced only two overlapping days of data with the CODAR measurements. Thus, although the comparison is quite limited, close agreement was found between the CODAR and calculated surface currents.

Figures 2 through 8 show the calculated surface currents at the current meter locations plotted over the CODAR generated surface current maps. Although only two current meter locations overlap the area of CODAR coverage, the additional

vectors at the other current meter locations help provide a general picture of the overall localized flow pattern from the current meter measured data. With the exception of the July 1st map (which was a transition period between weather patterns), the agreement in vector magnitudes and directions is remarkably good. This is especially true considering the manner in which the wind drift current component was calculated.

Both the CODAR generated surface currents and the surface currents calculated in a manner consistent with the approach used in Dames & Moore (1980) indicate the importance, if not major dominance, of the wind drift surface component over the net flow component. This is clearly evident in Figures 2 through 8 which cover a region where the net (non-wind drift) flow is relatively strong (compared to magnitudes of this component in other areas of Lower Cook Inlet) and has a dominant south and southwesterly flow.

Within the limits of available data, the treatment and calculation of the wind drift component is supportive of the approach taken in previous trajectory studies presented in Dames & Moore (1980, 1979, and 1976). The assumption of the wind drift current equal to 3.0 percent of the wind speed and colinear to the wind direction has not been refuted in this limited analysis. Based on the directional comparison presented in Figure 12 for the location of current meter C-2B, a deflection angle on the order of 15 to 20 degrees to the right of the wind vector would provide a general overall better fit of the data. However, this is a single point source conclusion and the effect on the overall flow pattern is difficult to evaluate with the limited data available.

3.2 TRAJECTORY COMPARISON

Trajectories calculated using the CODAR data for this period of time would be similar to trajectories calculated

using wind field 2 and intensity factor 3 and the net and tidal fields as specified in Dames & Moore (1980). Typical values of the wind speed in the study area from wind field 2 and intensity factor 3 (Dames & Moore, 1980) range from 8 to 10 meters/sec. The direction of wind field 2 in this area is from 60 to 100 degrees (true). This would result in surface wind drift velocities calculated to be in the range of 25 to 30 cm/sec with the same directional characteristics.

The net current magnitudes in this vicinity for the summer net current pattern presented in Dames & Moore (1980) range from 5 to 30 cm/s, which is generally consistent with the measurements presented in Table II. The directions of the net currents used in Dames & Moore (1980) for this area of Lower Cook Inlet range from 100 to 220 degrees (true), which is also consistent with the direction of the stronger flows presented in Table II. (The weaker velocities have little influence on the resultant velocity vector magnitude or direction.)

The vectoral combination of the wind drift component with the net component of surface flow from the Dames & Moore (1980) fields would result in net trajectory movement with speeds ranging from 20 to 50 cm/s and directions ranging from 240 to 280 degrees (true). Similar ranges of speed and direction are observed for the majority of vectors of CODAR measured 24 hour mean surface currents presented on Figures 2 through 8. Thus, for this period of time, the general net movement of trajectories predicted by CODAR and the approach used in Dames & Moore (1980) would be very similar. The fluctuations caused by tidal excursions is difficult to quantitatively assess without actual application, but the following comments address some of the comparative aspects.

Although the tidal currents presented in Figures 9 through 11 are generally rotary in nature, the component in

the direction of the minor axis is relatively small and would result in minor excursions in these directions. With the exception of a few boundary locations, the M2 constituent of the tidal current is shown in Figure 9 to be the primary tidal current constituent. The M2 tidal current constituent was assumed in Dames & Moore (1980 and 1979) to represent "average" tidal current conditions in Lower Cook Inlet and Shelikof Strait. Representative values in Dames & Moore (1980) for the M2 tidal constituent in this region of Lower Cook Inlet have magnitudes ranging from 40 to 60 cm/sec with ebb directions of 100 to 110 degrees (true) and flood directions of 270 to 290 degrees (true). The CODAR generated data have M2 tidal current constituents typically in the range of 30 to 50 cm/sec with ebb directions ranging from 90 to 140 degrees (true) and flood directions ranging from 290 to 320 degrees (true). The CODAR generated data naturally have a wider range of variability (due to the greater spatial resolution), but the typical values are not so different that they would result in radically different trajectories if this data set were utilized in such an analysis. It should also be recognized that the CODAR generated tidal current constituents were calculated based on a time series less than that necessary to provide accurate tidal constituent predictions.

3.3 CONCLUSIONS

It is concluded, based on a comparison of CODAR generated surface currents (24 hour means) with surface currents calculated from a measured daily mean net and daily mean wind drift current, that the approach used to calculate surface transport in Dames & Moore (1980, 1979, and 1976) is a valid and reasonably accurate approach (assuming the CODAR generated surface currents are taken as ground truth). There is some evidence to suggest a wind drift deflection angle of approximately 15-20 degrees to the right, but in general, overall flow patterns are reasonably well represented using a colinear

wind-drift surface current direction. Tidal current constituents calculated using the CODAR generated data reinforce and support the approach used in previous studies in which the M_2 tidal current constituent was found to be dominant and was assumed to reasonably represent "average" tidal current conditions.

The question of whether near surface current meter records (15 to 20 meters below the surface) can be used to represent net currents (minus wind drift component) could not be adequately resolved with the given data set. In general, the net currents were smaller than the calculated wind drift component and the vectoral sum was therefore dominated by the wind drift component. In other words, the vectoral sum would be little affected whether or not the net component was considered at all. In addition, the accuracy of the wind speed near Augustine Island is suspect given the rather crude methodology by which it was estimated.

References

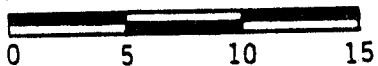
- Barrick, D.E., and R.J. Lipa, 1979. A compact transportable HF radar system for directional coastal wavefield measurements, in Ocean Wave Climate, M.D. Earle and A. Malahoff (Eds.), Plenum, New York.
- Barrick, D.E., J.M. Headrick, R.W. Bogle, and D.D. Crombie, 1974. Sea back-scatter at HF: interpretation and utilization of the echo, Proc. IEEE, Vol., 62, pp. 673-680.
- Barrick, D.E., 1972. First-order theory and analysis of MF/HF/VHF scatter from the Sea, IEEE Transactions on Antennas and Propagation, Vol. AP-20, pp. 2-10.
- Barrick, D.E., and W.H. Peake, 1967. Scattering from surfaces with different roughness scales: analysis and interpretation, Battelle Research Report, BAT-197A-10-3, Columbus, Ohio.
- Barrick, E.W., M.W. Evans, and B.L. Weber, 1977. Ocean surface currents mapped by radar, Science, 198: 138-144.
- Evans, M.W., 1978. Surface current mapping radar: Theory and application, presented at Energy/Environment '78, a Symposium on Energy Development Transports.
- Frisch, S., 1980. Personal communication, CODAR data for July 1, 1978 to July 8, 1978, Cape Douglas - Augustine Island, Alaska; 24 hr mean currents and tidal harmonic constituents (M_2 , O_1 , K_1), Wave Propagation Laboratory, NOAA.
- Dames & Moore, 1980. Final Report--Task 1, Oil spill trajectory simulation, Lower Cook Inlet-Shelikof Strait, Alaska, for the Bering Sea-Gulf of Alaska Project Office, Outer Continental Shelf Environmental Assessment Program, Job number 06797-014-88.
- _____, 1979. Final Draft, Oil spill trajectory analysis, Lower Cook Inlet, Alaska, Bering Sea-Gulf of Alaska Project Office, Outer Continental Shelf Environmental Assessment Program, Job number 06796-011-02.
- _____, 1976. Report, Oil spill trajectory analysis, Lower Cook Inlet, Alaska. For NOAA, Job number 06797-003-20.
- Reynolds, M., 1980. Personal communication, Meteorological data from Iliamna Lake, Shuyak Island, and Augustine Island for late June and July, 1978, Pacific Marine Environmental Laboratory, NOAA.

References (cont.)

Schumacher, J.D., 1980. Personal communication, Current data summaries from near-surface current meters for C-1B, C-2B, C-3B, C-4B, and C-5B arrays, Pacific Marine Environmental Laboratory, NOAA.

- ▽ -RADAR DEPLOYMENT LOCATION
- -PMEL CURRENT METER ARRAY LOCATION
- -RANGE OF CODAR SURFACE CURRENT MAPPING

SCALE (IN KM)

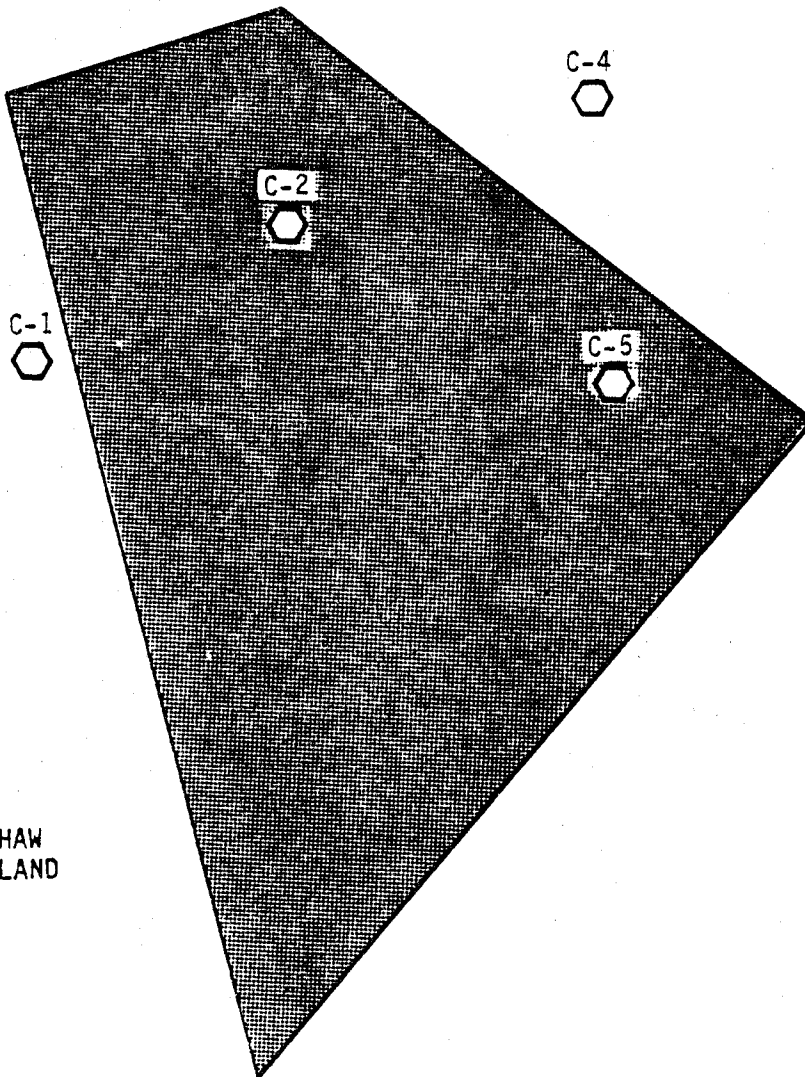


REVISIONS
BY _____ DATE _____

BY _____ DATE _____
CHECKED BY _____ FILE _____



AUGUSTINE ISLAND



SHAW ISLAND

CAPE DOUGLAS

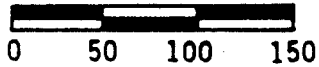


FIGURE 1 : CURRENT METER ARRAY LOCATION AND RANGE OF CODAR MAPPING

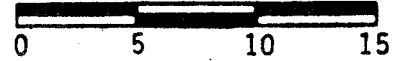
➔ -SURFACE VELOCITY VECTOR AT
CURRENT METER LOCATIONS

➤ -CODAR GENERATED SURFACE
VELOCITY VECTOR

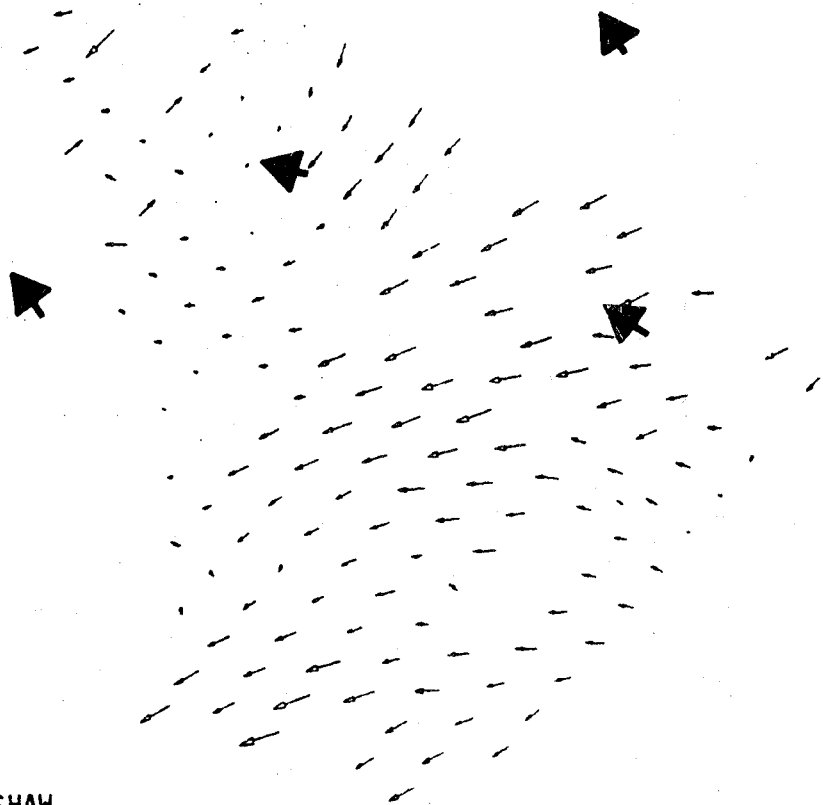
VECTOR MAGNITUDE (CM/S)



SCALE (IN KM)



AUGUSTINE
ISLAND



SHAW
ISLAND

CAPE
DOUGLAS

FIGURE 2: 24 HOUR MEAN SURFACE
CURRENT VECTORS FOR
7/01/78

REVISIONS
BY _____ DATE _____

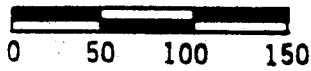
FILE _____

BY _____ DATE _____
CHECKED BY _____

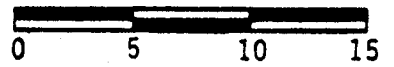
→ -SURFACE VELOCITY VECTOR AT
CURRENT METER LOCATIONS

⇨ -CODAR GENERATED SURFACE
VELOCITY VECTOR

VECTOR MAGNITUDE (CM/S)



SCALE (IN KM)



REVISIONS
BY _____ DATE _____

FILE _____

BY _____ DATE _____
CHECKED BY _____



AUGUSTINE
ISLAND

SHAW
ISLAND

CAPE
DOUGLAS

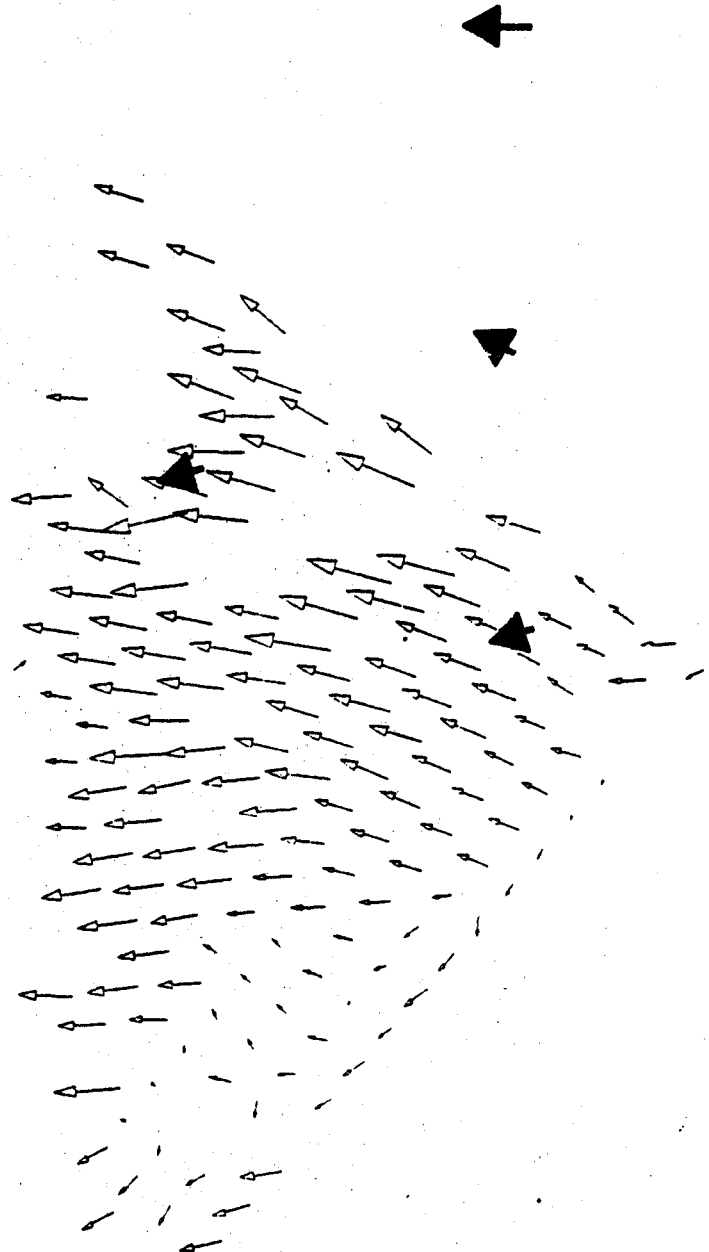


FIGURE 3 : 24 HOUR MEAN SURFACE
CURRENT VECTORS FOR

7/02/78 403

REVISIONS
BY _____ DATE _____

FILE _____

BY _____ DATE _____
CHECKED BY _____

- ➔ -SURFACE VELOCITY VECTOR AT CURRENT METER LOCATIONS
- -CODAR GENERATED SURFACE VELOCITY VECTOR

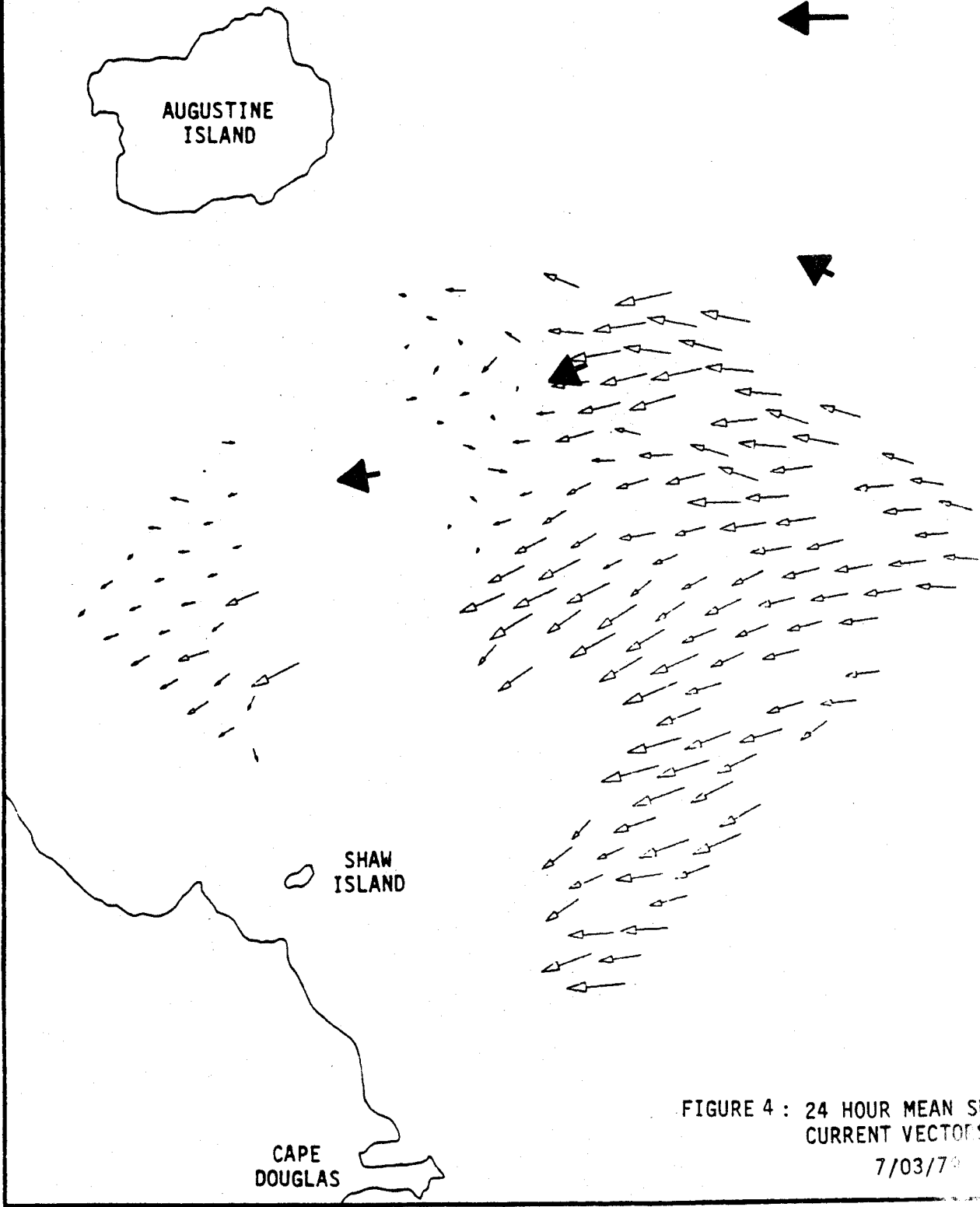
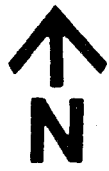
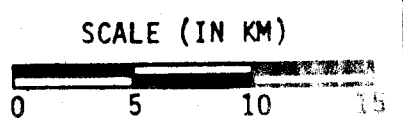
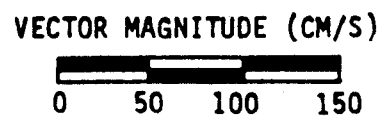
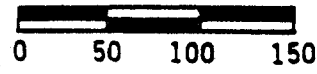


FIGURE 4 : 24 HOUR MEAN SURFACE CURRENT VECTORS FOR 7/03/79

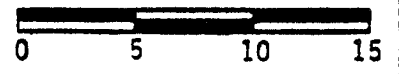
➔ -SURFACE VELOCITY VECTOR AT CURRENT METER LOCATIONS

➤ -CODAR GENERATED SURFACE VELOCITY VECTOR

VECTOR MAGNITUDE (CM/S)



SCALE (IN KM)



REVISIONS BY _____ DATE _____

FILE _____

BY _____ DATE _____
CHECKED BY _____

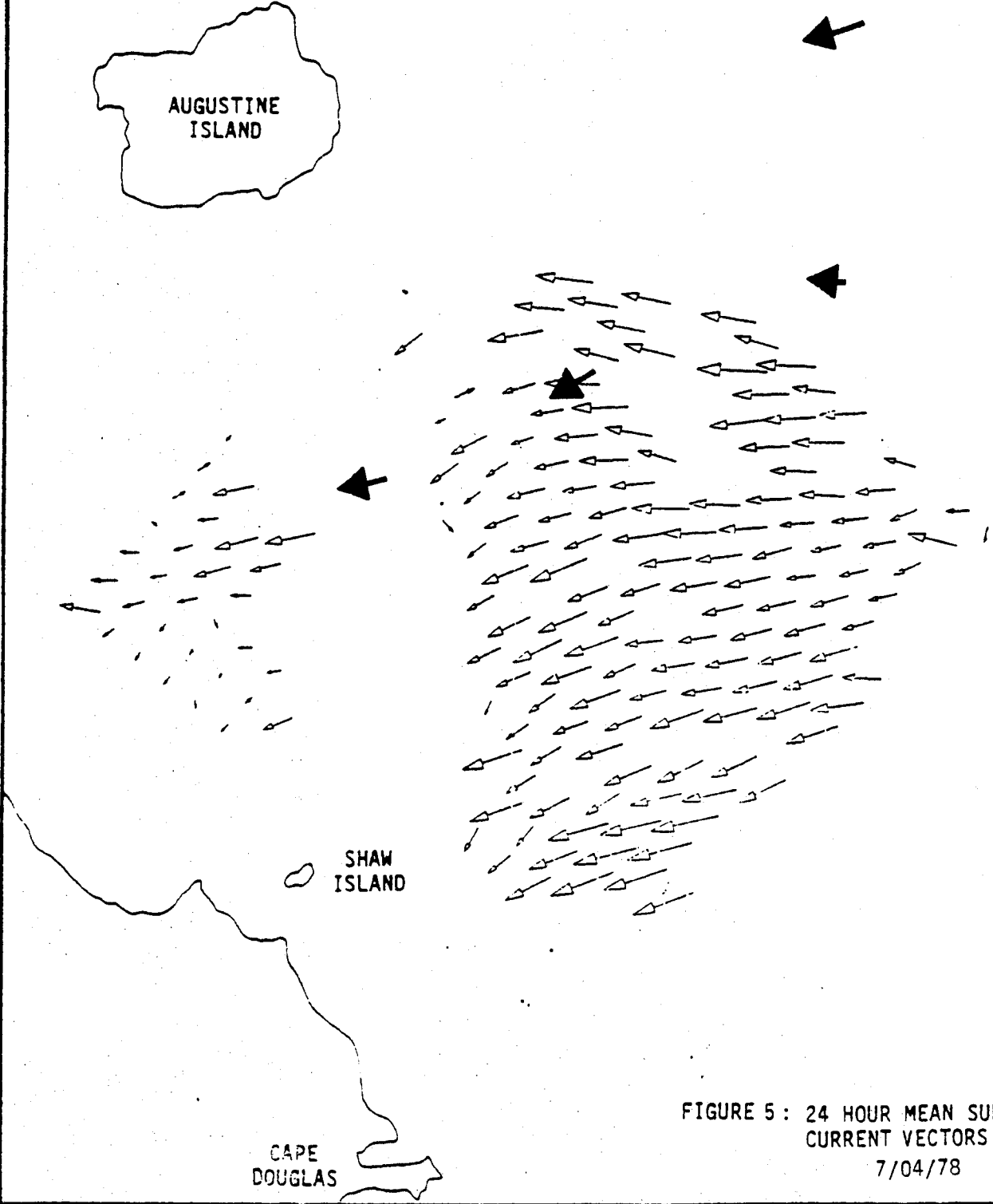


FIGURE 5 : 24 HOUR MEAN SURFACE CURRENT VECTORS FOR 7/04/78 405

REVISIONS
BY _____ DATE _____

FILE _____

BY _____ DATE _____
CHECKED BY _____

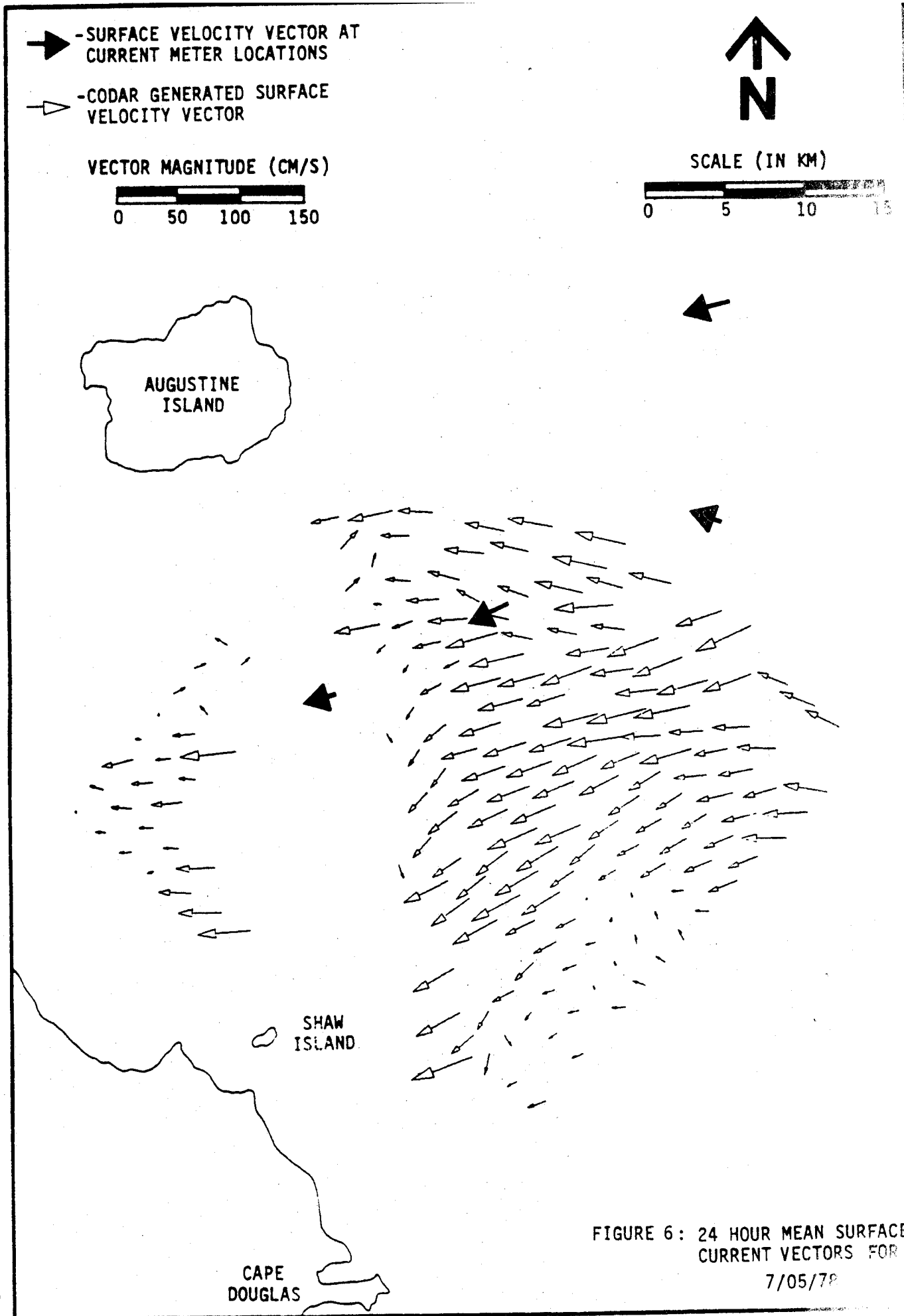
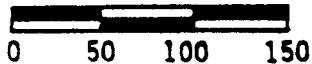


FIGURE 6: 24 HOUR MEAN SURFACE
CURRENT VECTORS FOR
7/05/78

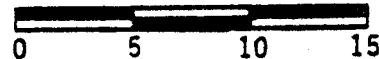
➔ -SURFACE VELOCITY VECTOR AT CURRENT METER LOCATIONS

➤ -CODAR GENERATED SURFACE VELOCITY VECTOR

VECTOR MAGNITUDE (CM/S)



SCALE (IN KM)



REVISIONS BY _____ DATE _____

BY _____ DATE _____
CHECKED BY _____ FILE _____



AUGUSTINE ISLAND

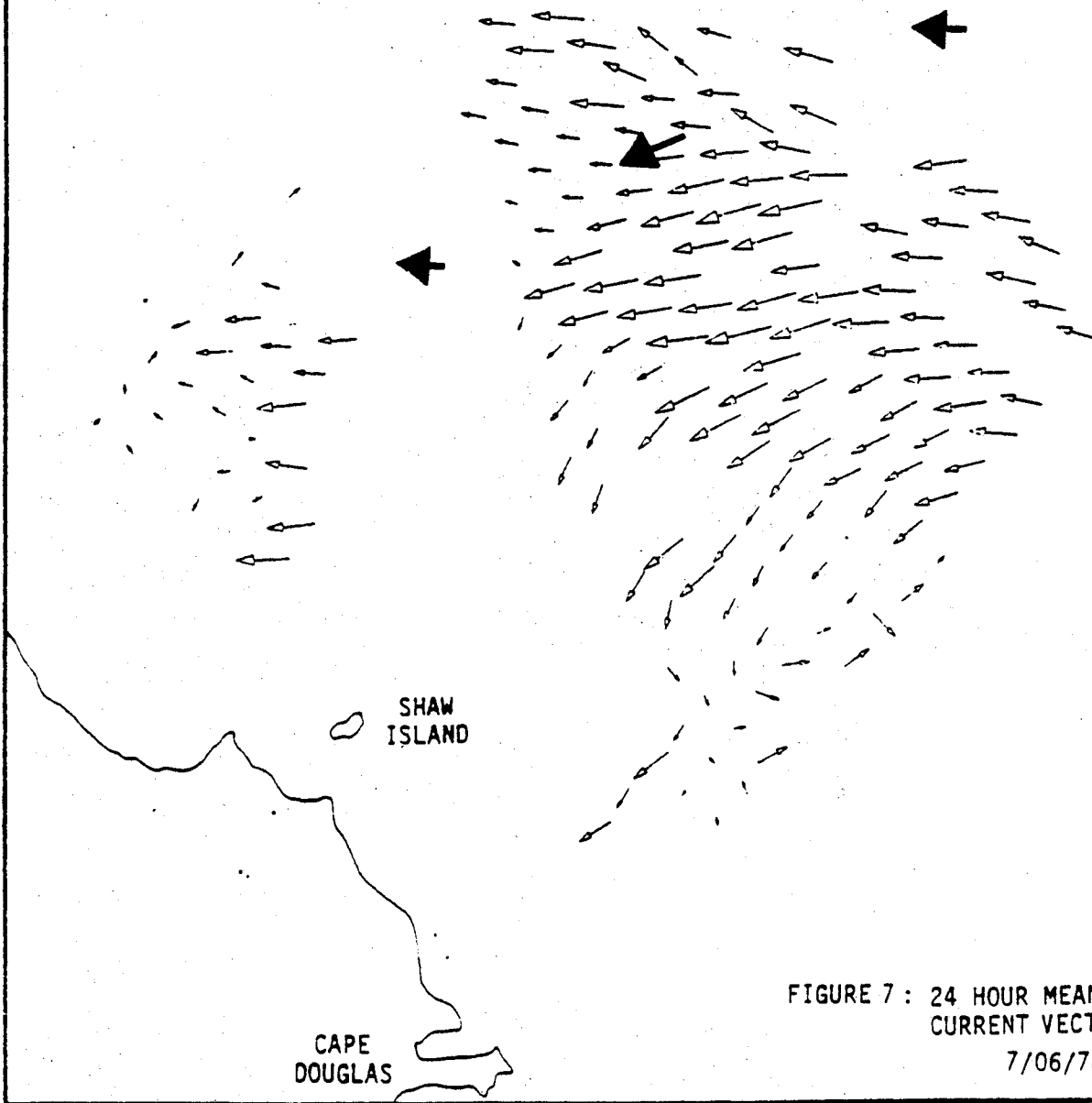


FIGURE 7 : 24 HOUR MEAN SURFACE CURRENT VECTORS FOR

7/06/78 407

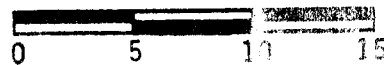
➔ -SURFACE VELOCITY VECTOR AT
CURRENT METER LOCATIONS

➤ -CODAR GENERATED SURFACE
VELOCITY VECTOR

VECTOR MAGNITUDE (CM/S)



SCALE (IN KM)



AUGUSTINE
ISLAND

SHAW
ISLAND

CAPE
DOUGLAS

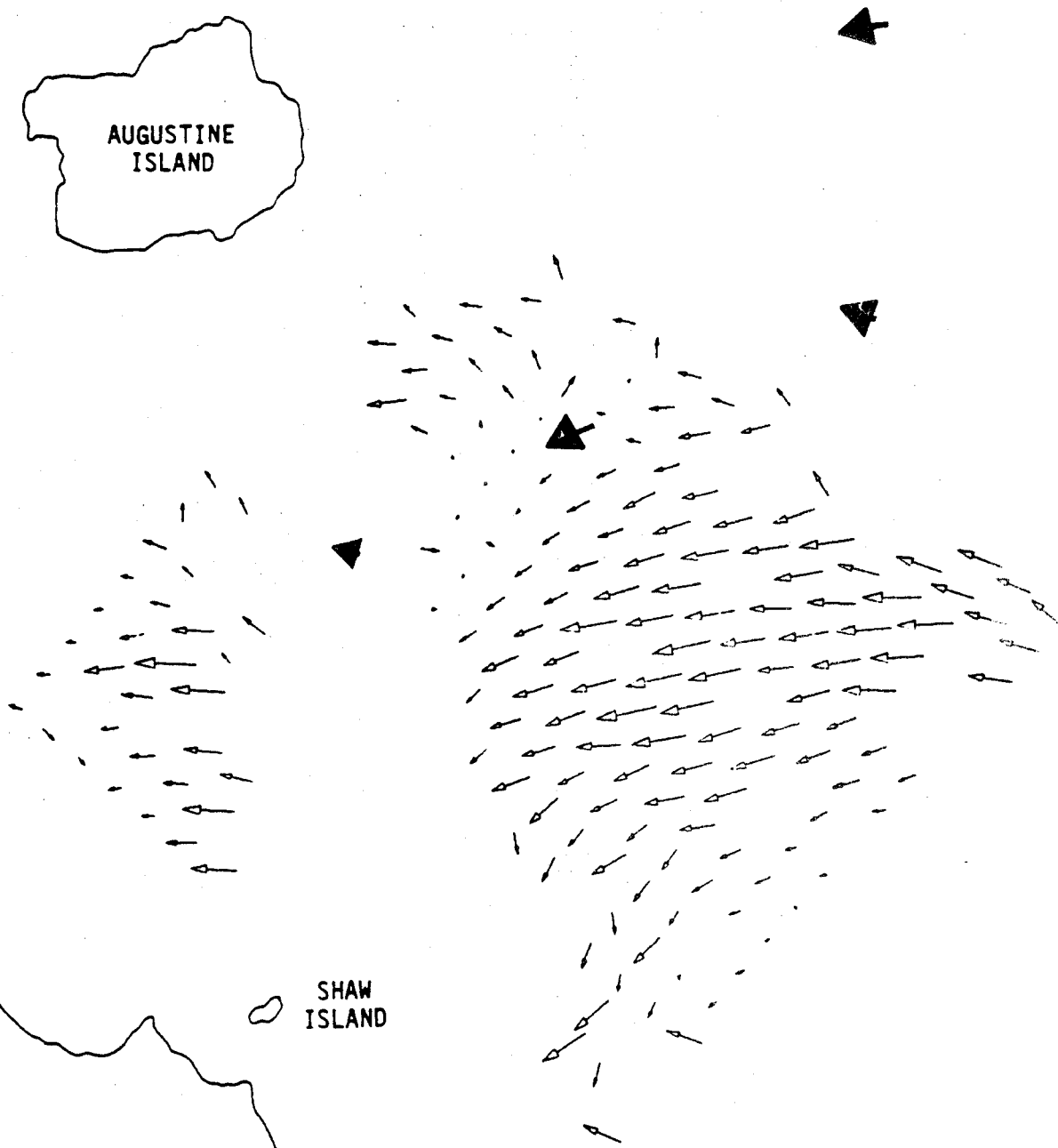


FIGURE 8 : 24 HOUR MEAN SURFACE
CURRENT VEC

7/07

REVISIONS
BY _____ DATE _____

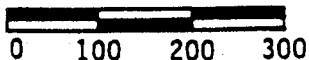
FILE _____

BY _____ DATE _____
CHECKED BY _____

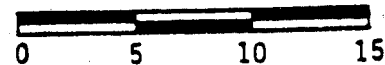
NOTE: TIDAL CURRENT VECTOR MEASURED FROM FROM CENTER OF ELLIPSE TO ANY POINT ON CURVE CORRESPONDING TO DESIRED TIDAL PHASE.



CURRENT VECTOR MAGNITUDE (CM/S)



SCALE (IN KM)

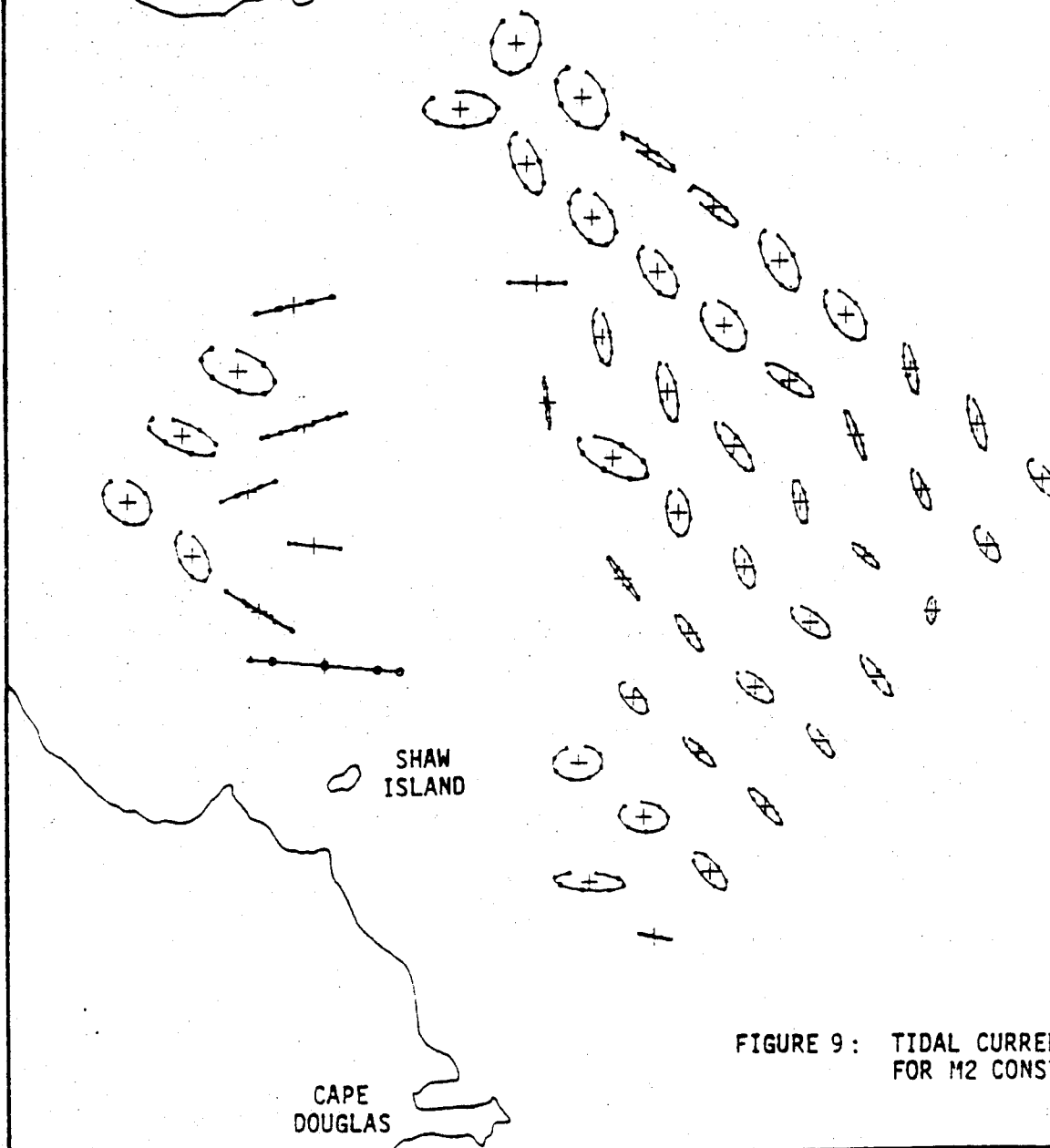


REVISIONS
BY _____ DATE _____

BY _____ DATE _____
CHECKED BY _____ FILE _____



AUGUSTINE ISLAND



SHAW ISLAND

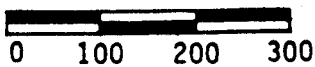
CAPE DOUGLAS

FIGURE 9: TIDAL CURRENT ELLIPSES FOR M2 CONSTITUENT

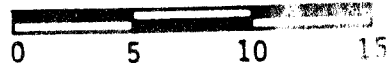
NOTE: TIDAL CURRENT VECTOR MEASURED FROM FROM CENTER OF ELLIPSE TO ANY POINT ON CURVE CORRESPONDING TO DESIRED TIDAL PHASE.



CURRENT VECTOR MAGNITUDE (CM/S)



SCALE (IN KM)



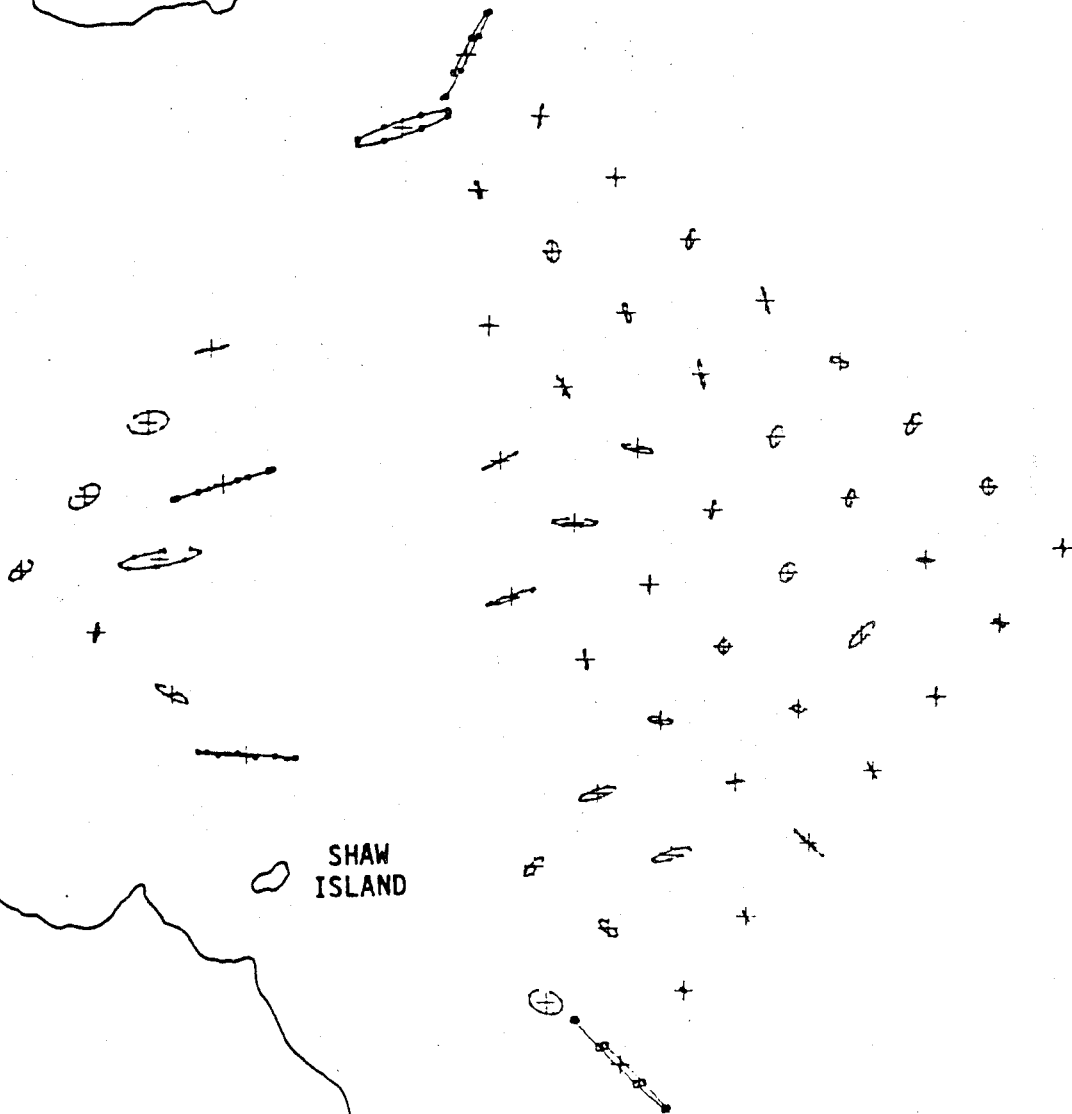
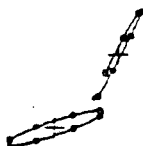
REVISIONS
BY _____ DATE _____

FILE _____

BY _____ DATE _____
CHECKED BY _____



AUGUSTINE
ISLAND



SHAW
ISLAND

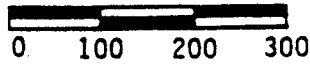
CAPE
DOUGLAS

FIGURE 10: TIDAL CURRENT ELLIPSES FOR K1 CONSTITUENT

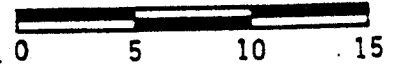
NOTE: TIDAL CURRENT VECTOR MEASURED FROM
FROM CENTER OF ELLIPSE TO ANY POINT
ON CURVE CORRESPONDING TO DESIRED
TIDAL PHASE.



CURRENT VECTOR MAGNITUDE (CM/S)



SCALE (IN KM)



REVISIONS
BY _____ DATE _____

FILE _____

CHECKED BY _____ DATE _____



AUGUSTINE
ISLAND

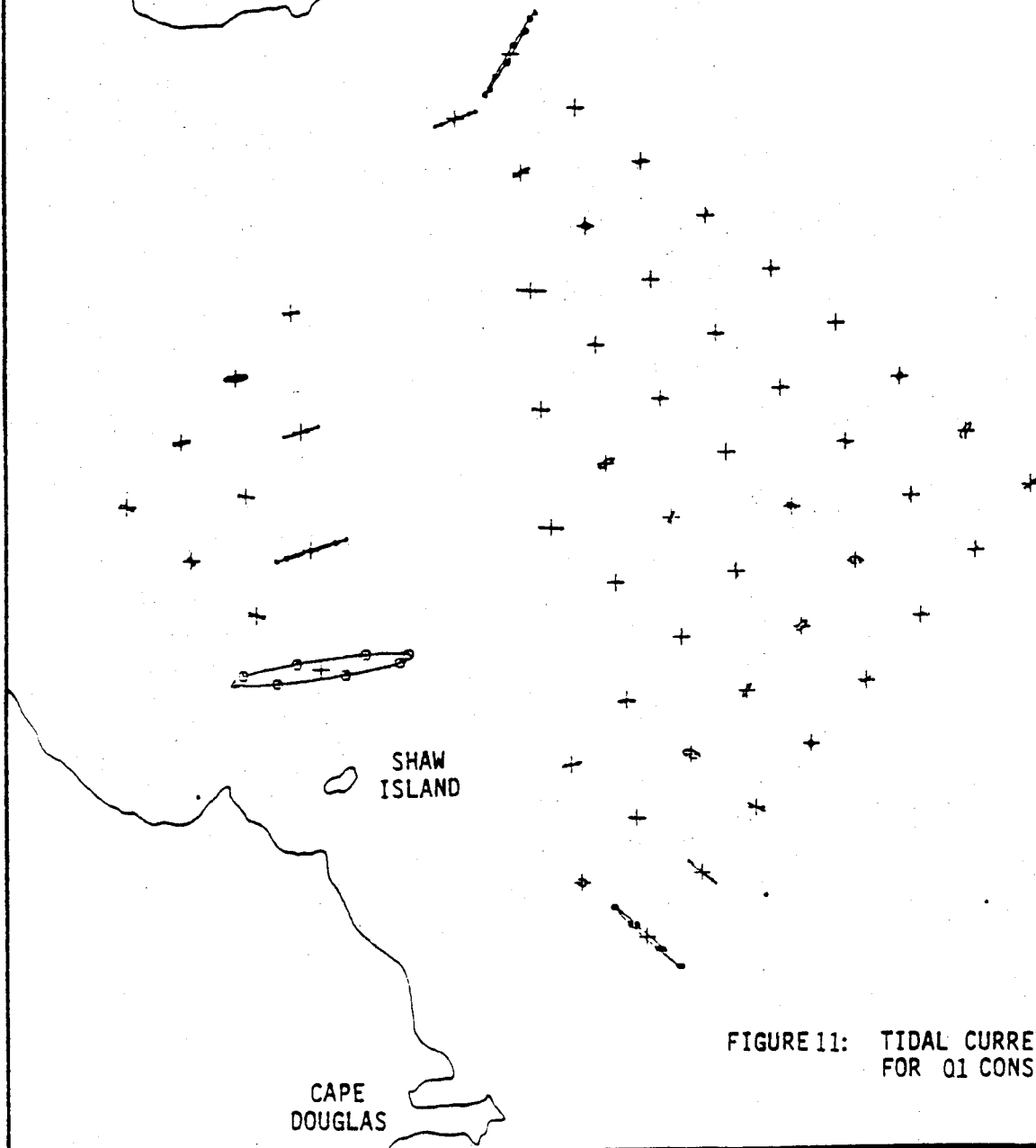


FIGURE 11: TIDAL CURRENT ELLIPSES
FOR Q1 CONSTITUENT

REVISIONS _____
 BY _____ DATE _____
 FILE _____
 BY _____ DATE _____
 CHECKED BY _____

——— C-2 DATA
 - - - CODAR DATA

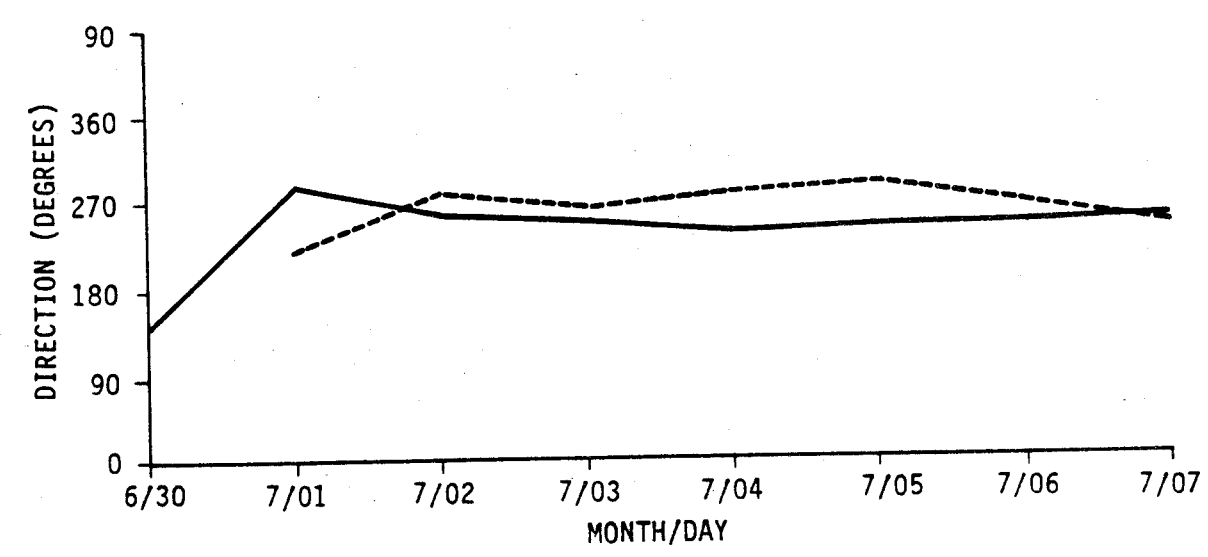
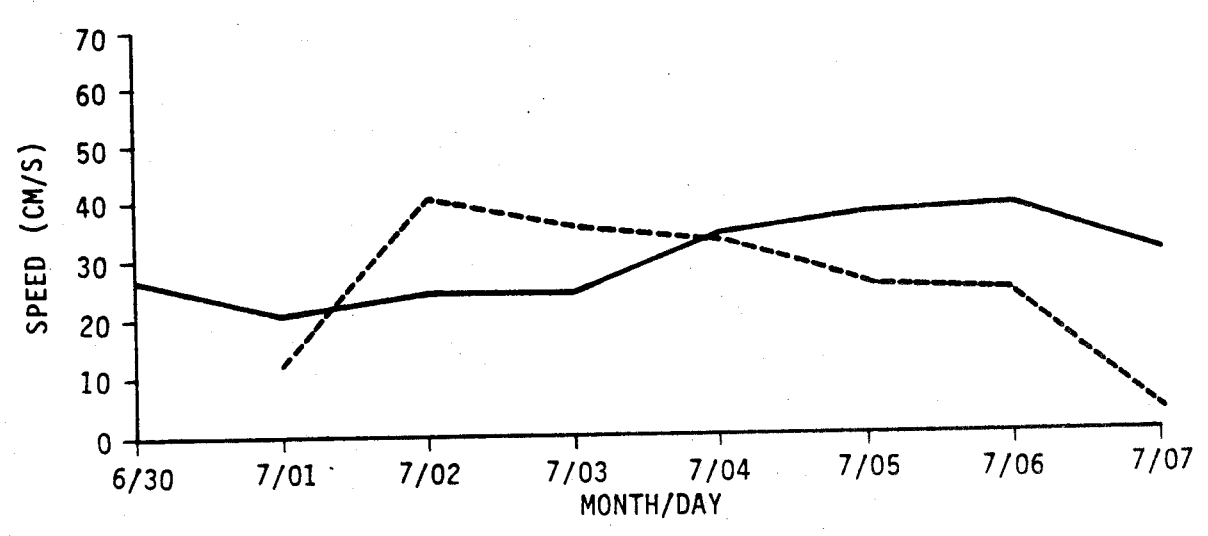


FIGURE 12: COMPARSON OF C-2 DATA WITH CODAR DATA

BY _____ DATE _____
CHECKED BY _____ FILE _____
REVISIONS BY _____ DATE _____

— C-5 DATA
- - - CODAR DATA

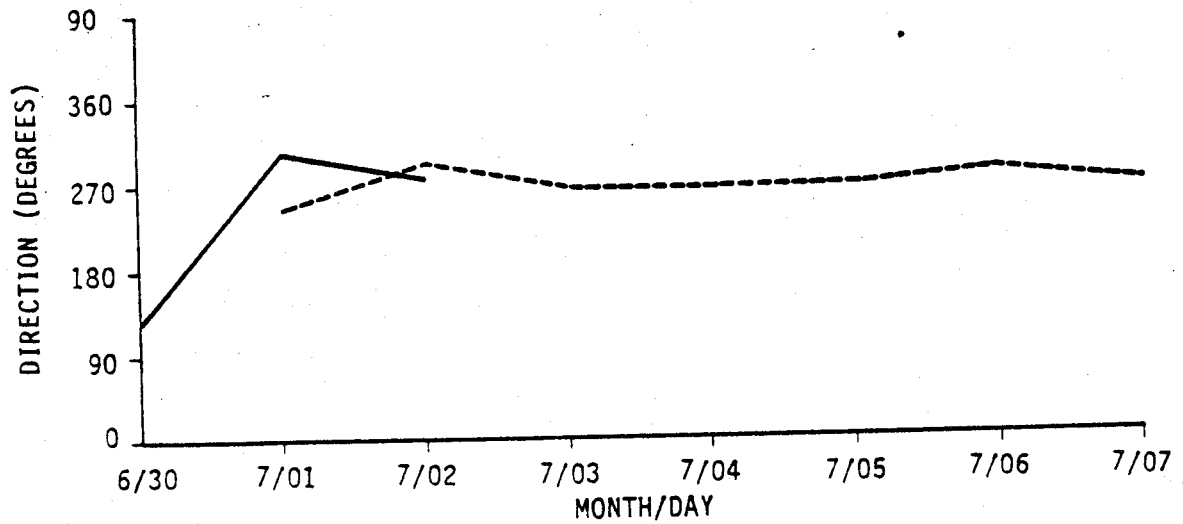
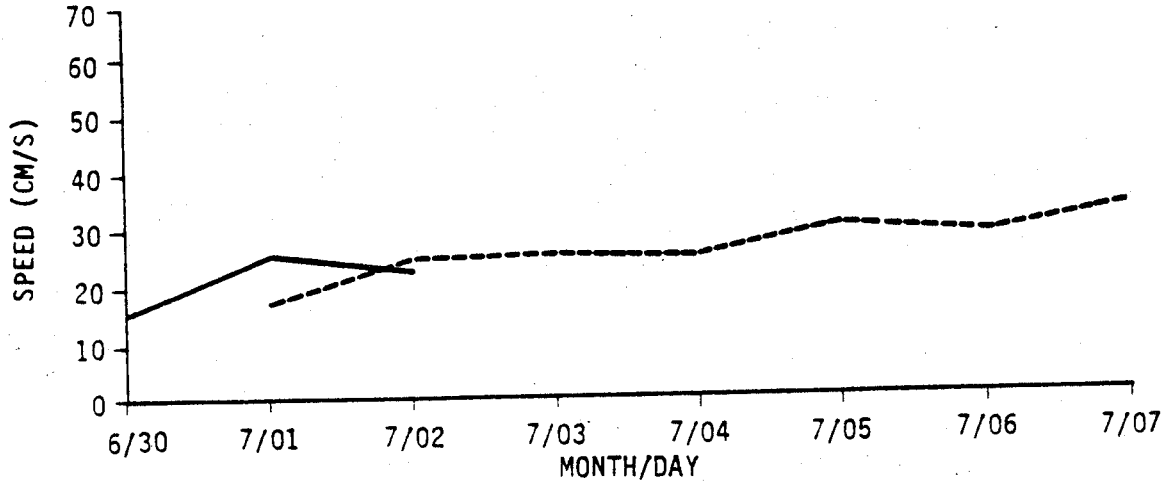


FIGURE 13: COMPARISON OF C-5 DATA WITH CODAR DATA

Appendix A

Meteorological Data

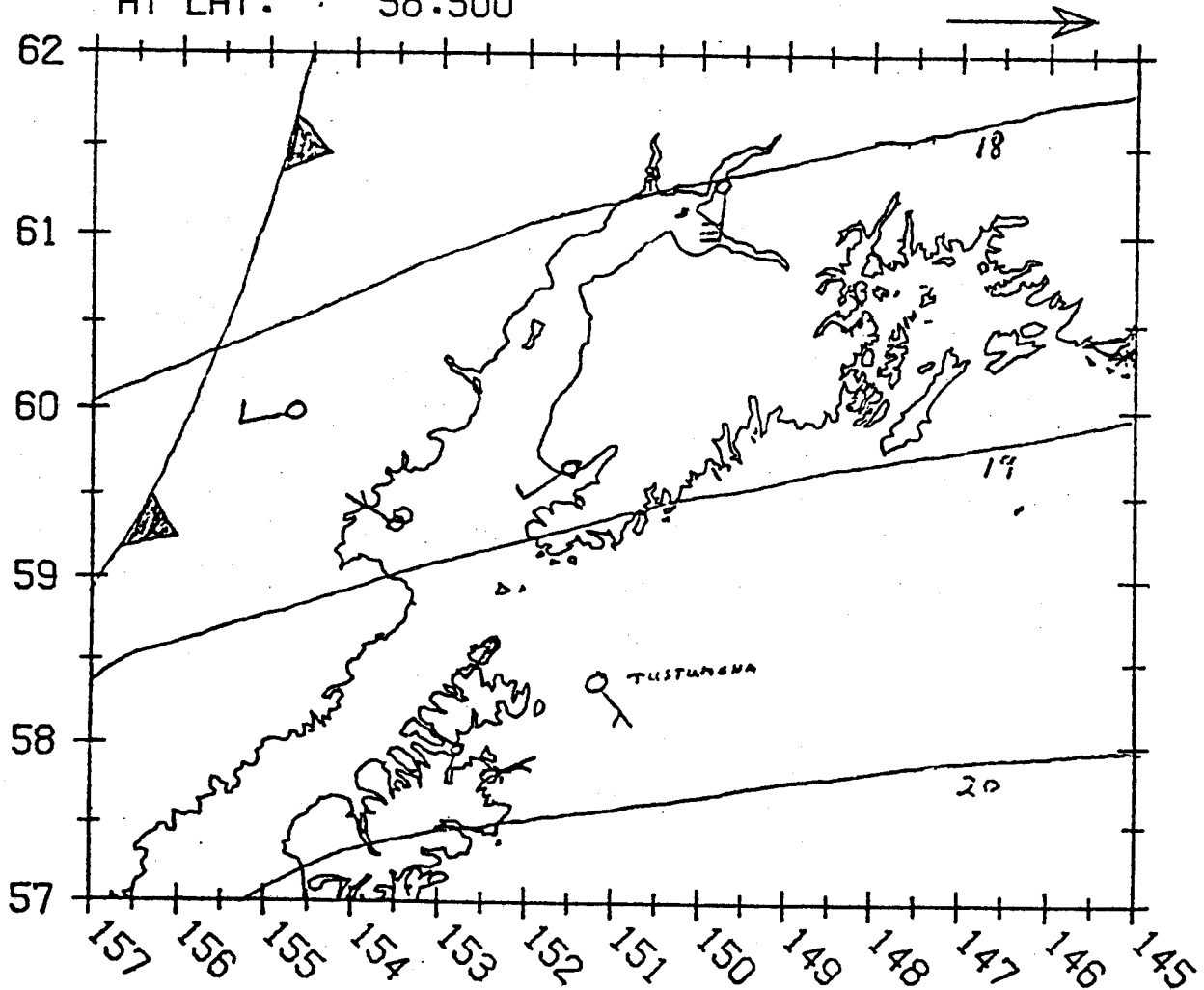
WIND OBSERVATIONS

TIME- 1800Z 29 JUNE 1978
00***0*Z

SCALE 5000000

AT LAT. 58.500

10 METERS/ SEC



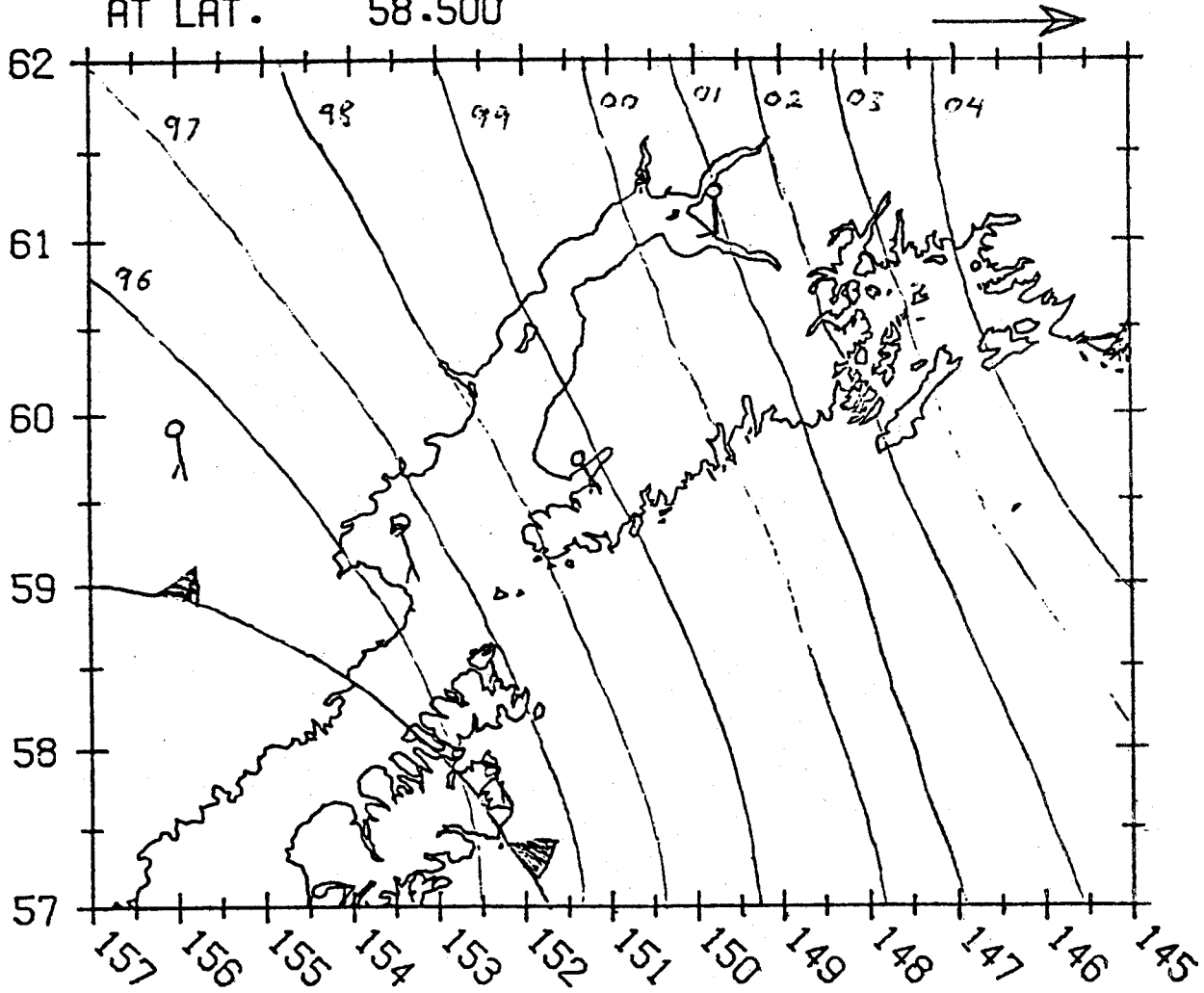
WIND OBSERVATIONS

TIME- ^{1201Z} ^{1 JULY 1975} ***0***0***0**Z

SCALE 5000000

AT LAT. 58.500

10 METERS/ SEC



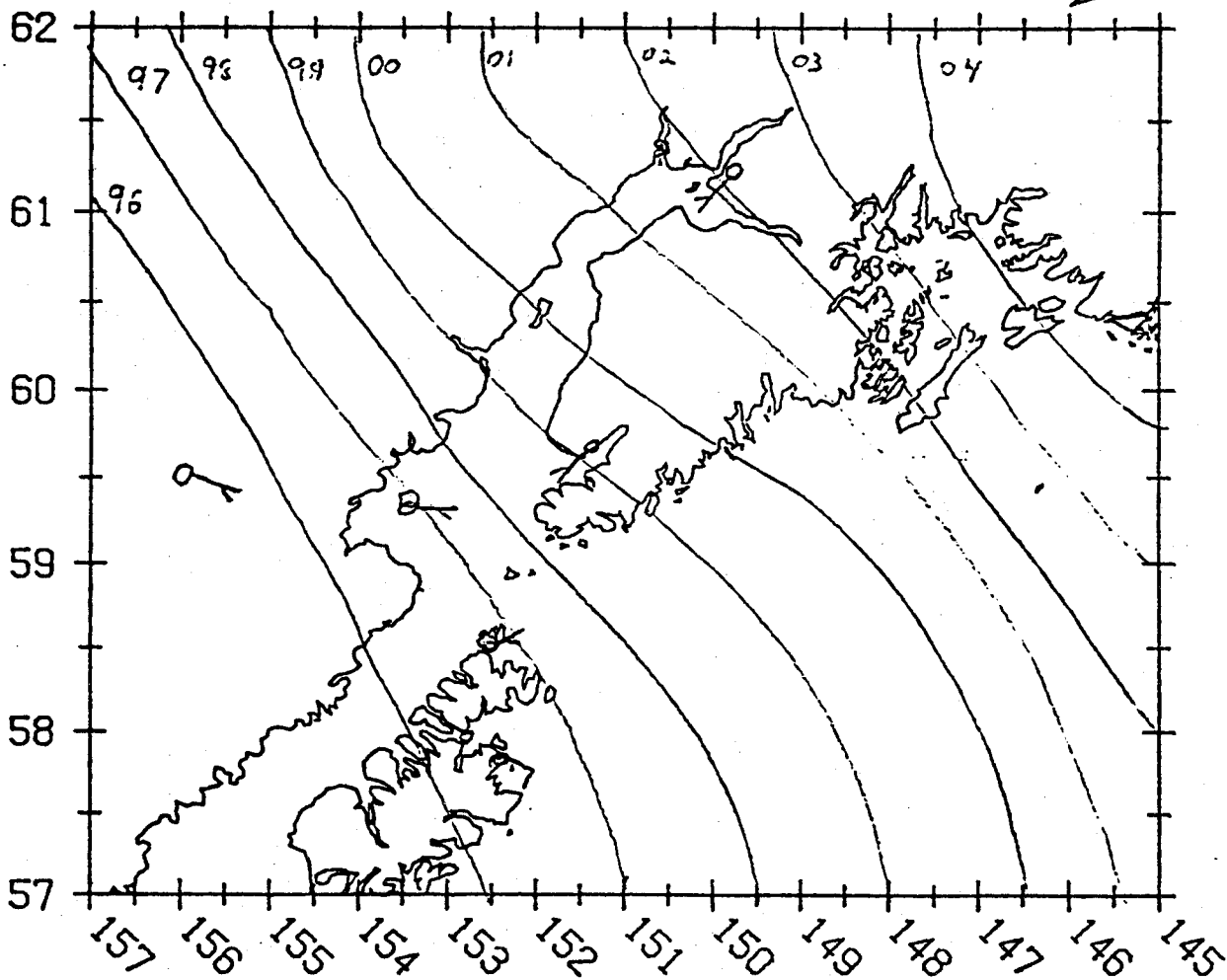
WIND OBSERVATIONS

TIME- ^{1200Z} ~~0000Z~~ ^{2 JUL 1929} ~~0000Z~~

SCALE 5000000

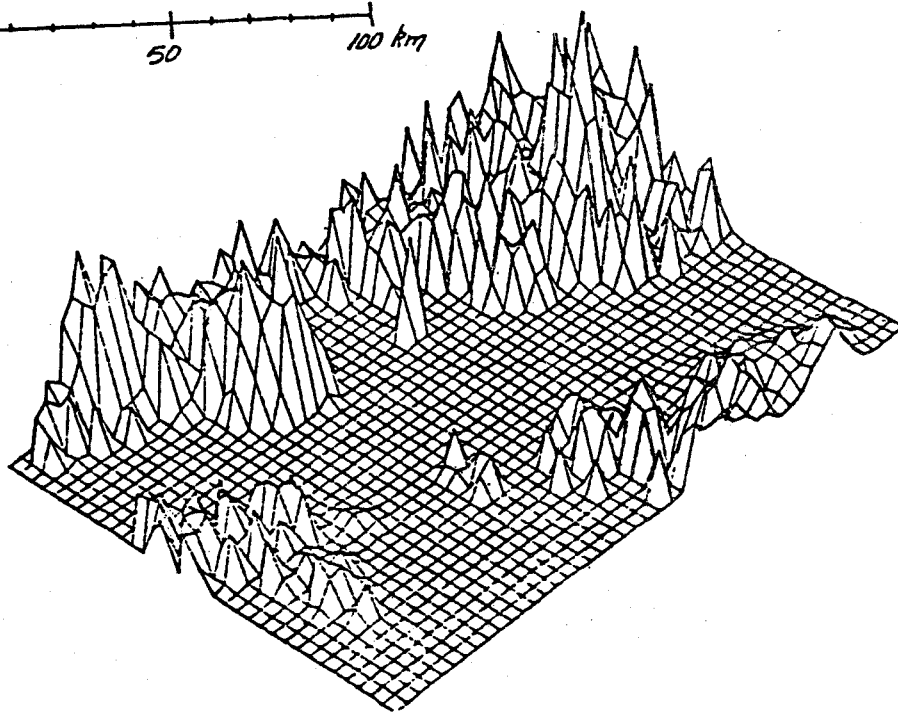
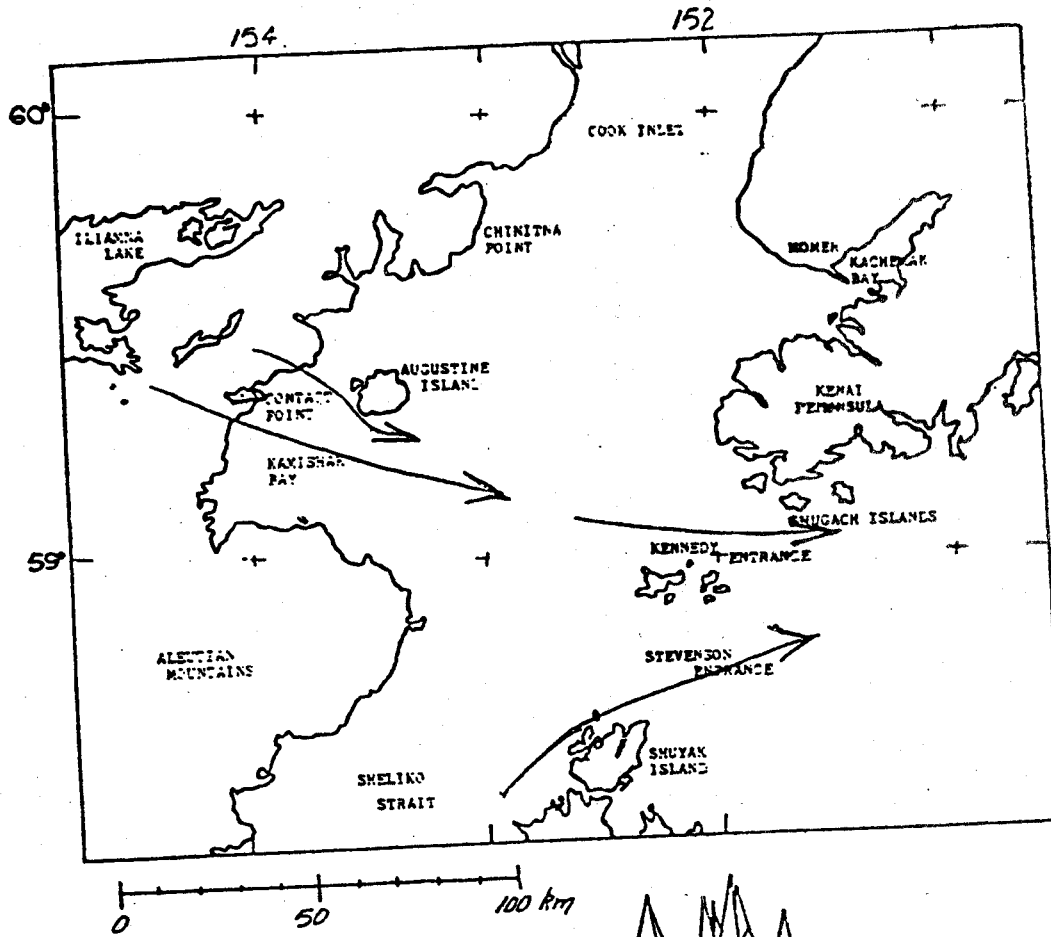
AT LAT. 58.500

10 METERS/ SEC

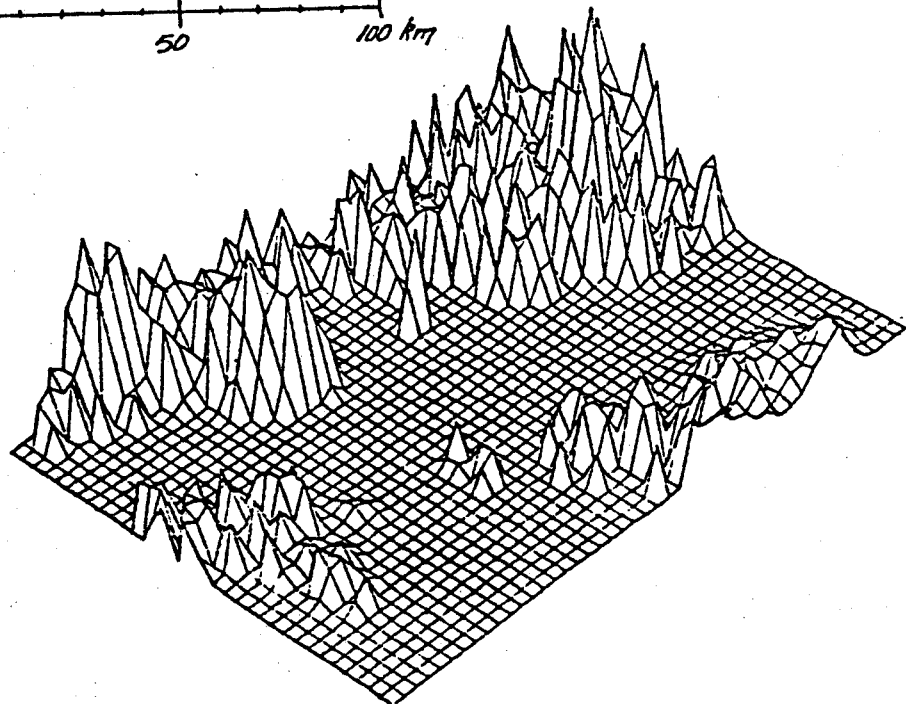
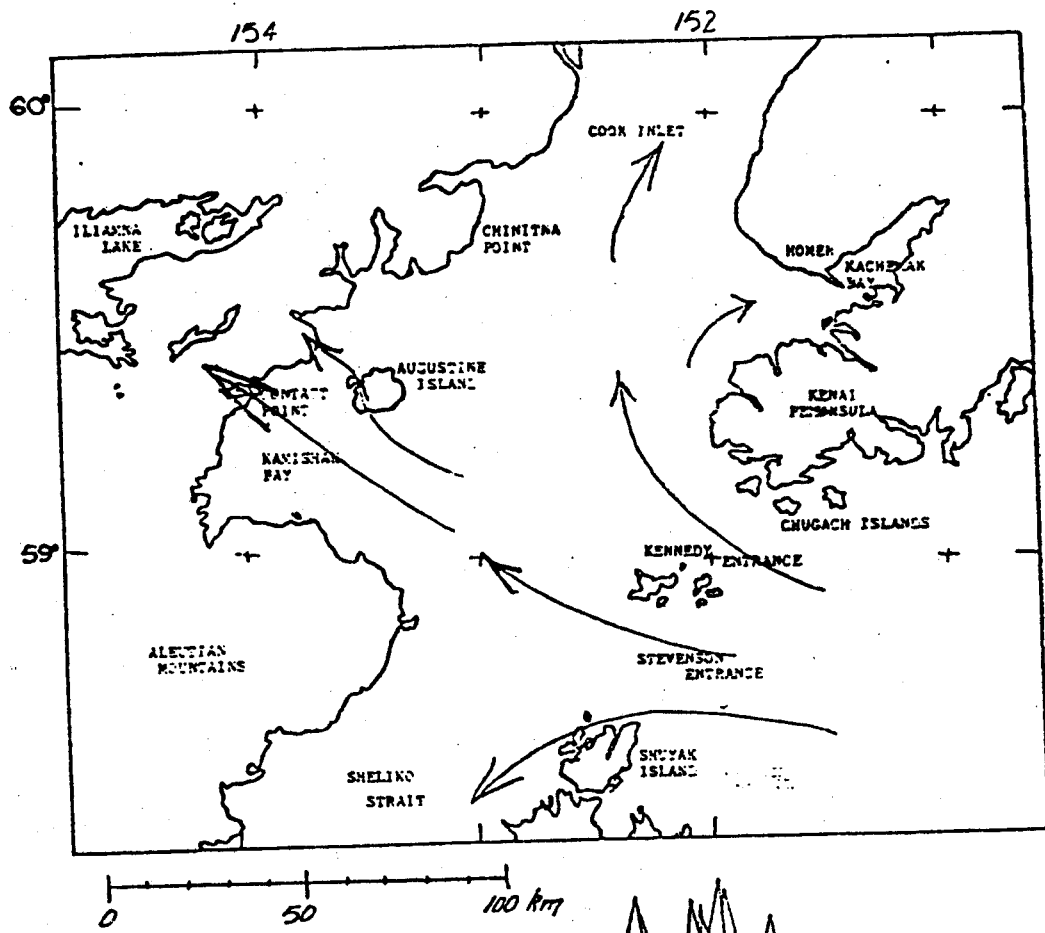


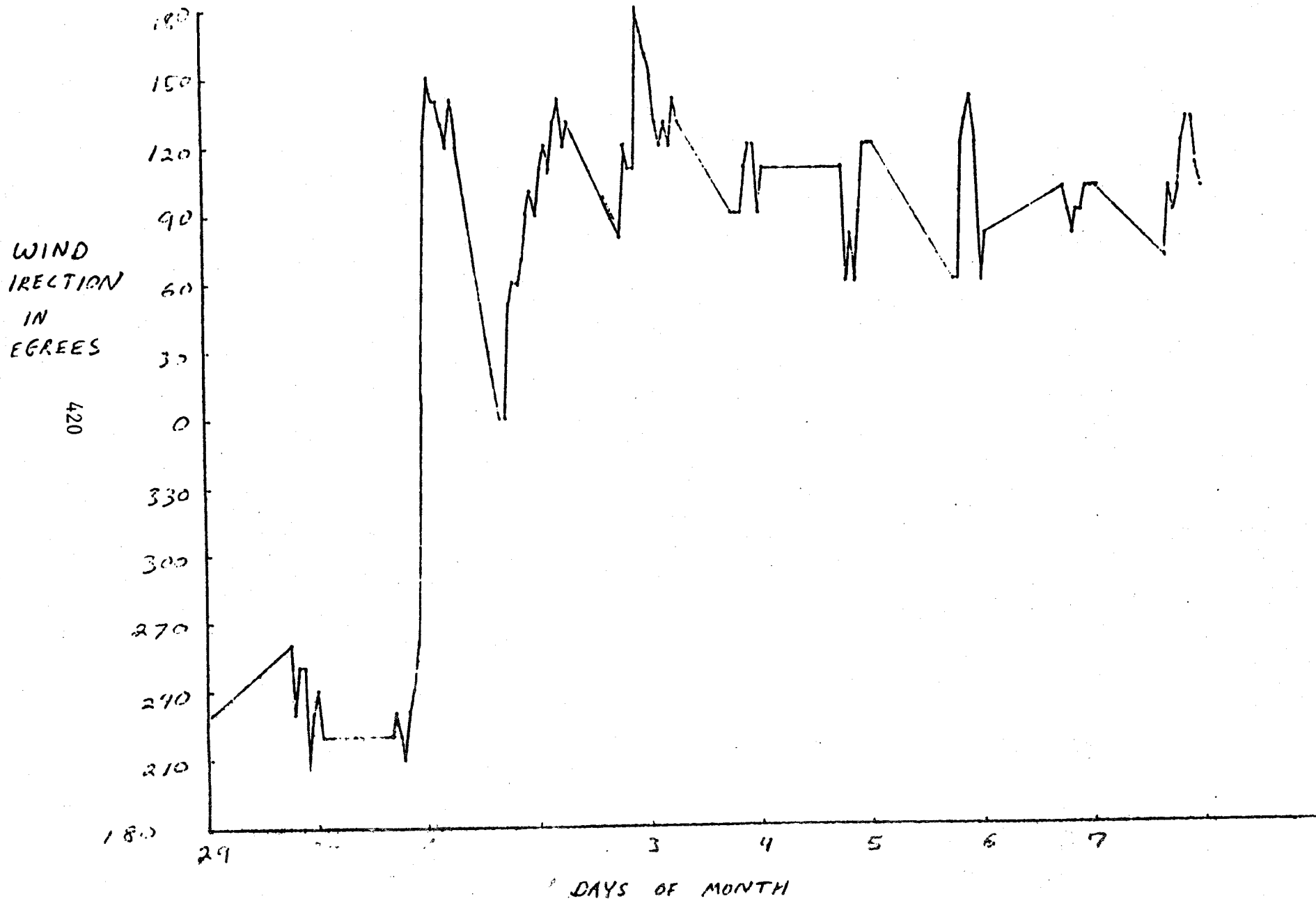
Suggest Wind Pattern

29 JUNE 1979



Suggest Wind Pattern 2 July 1979

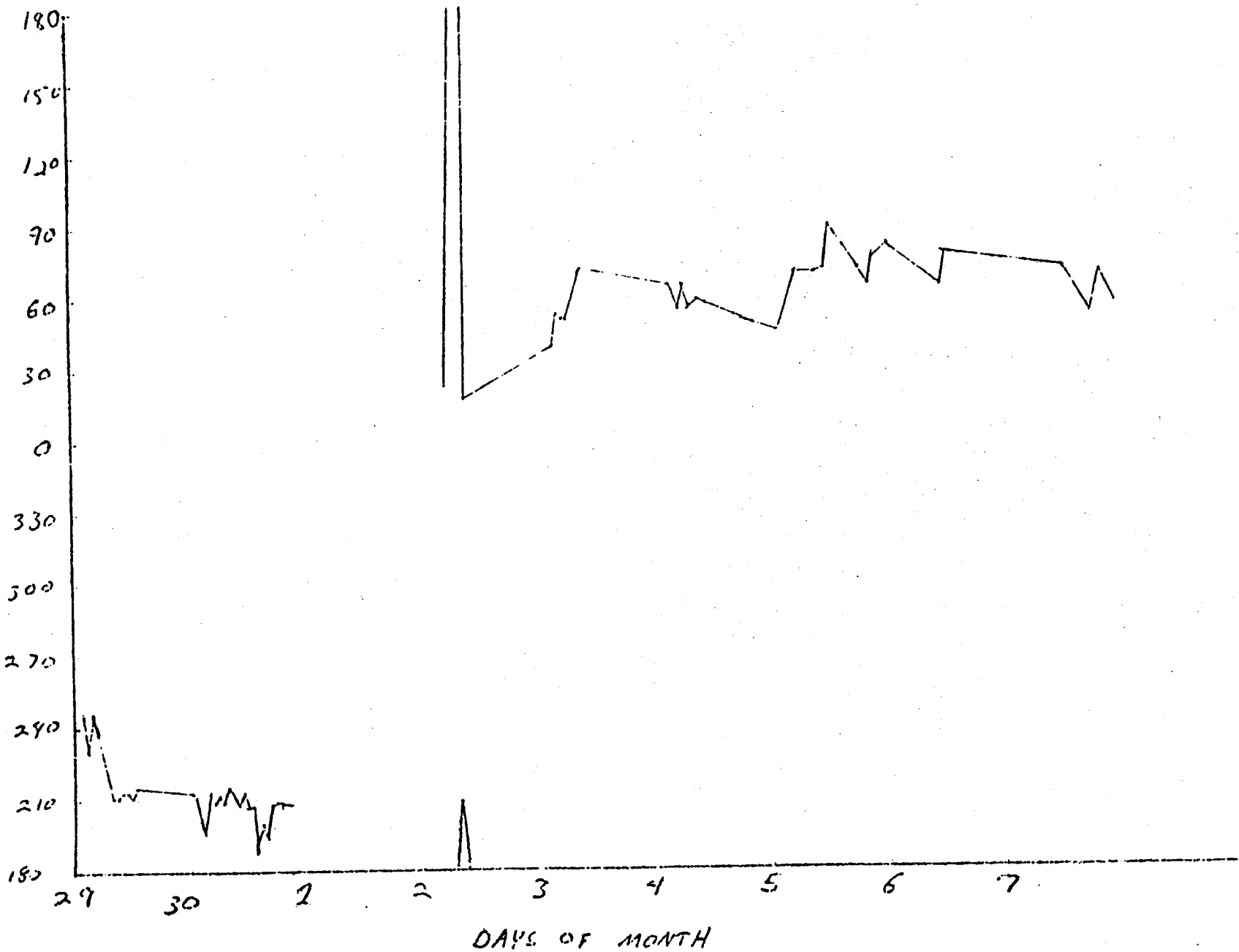




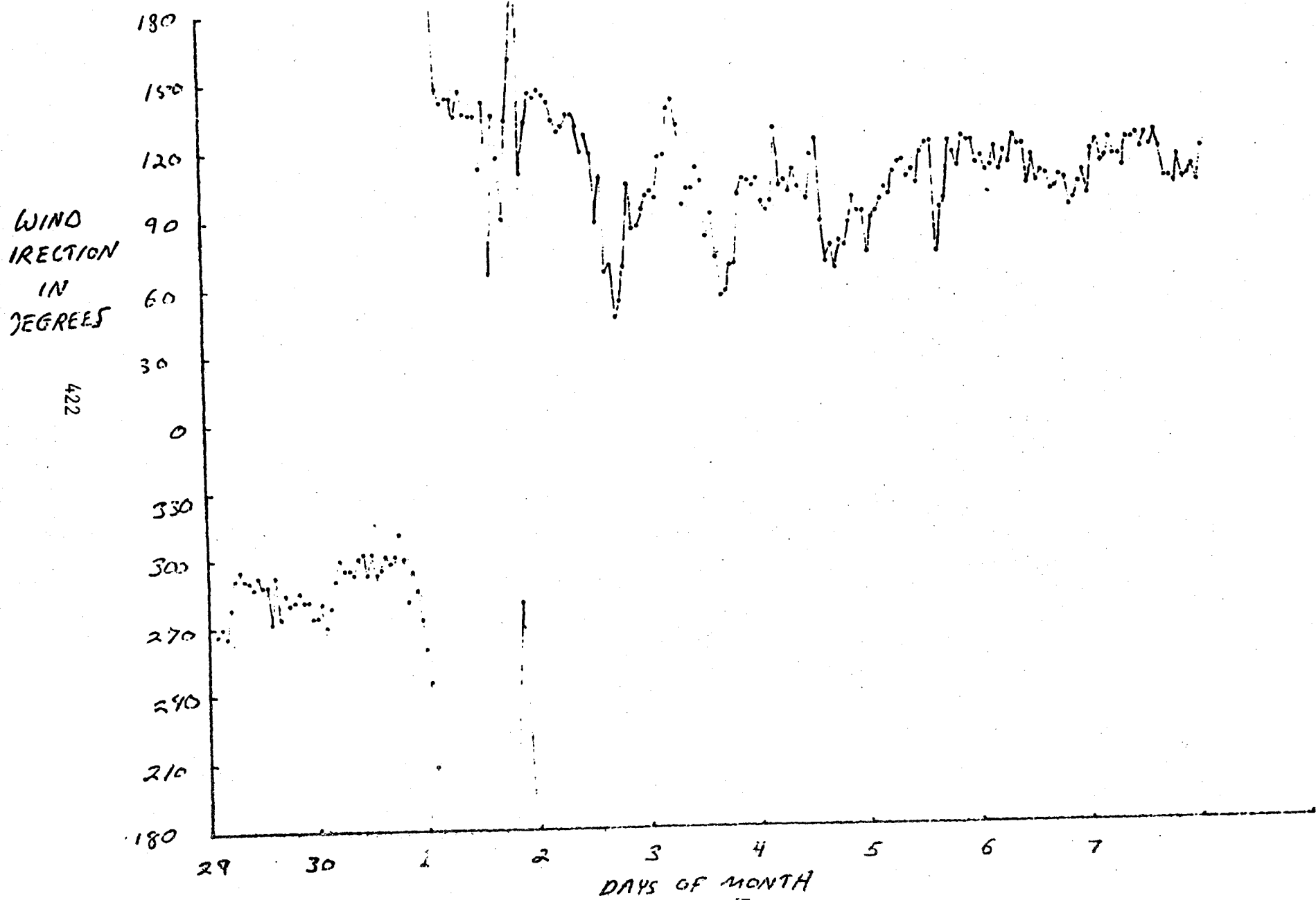
Ilhanna

WIND
DIRECTION
IN
DEGREES

421



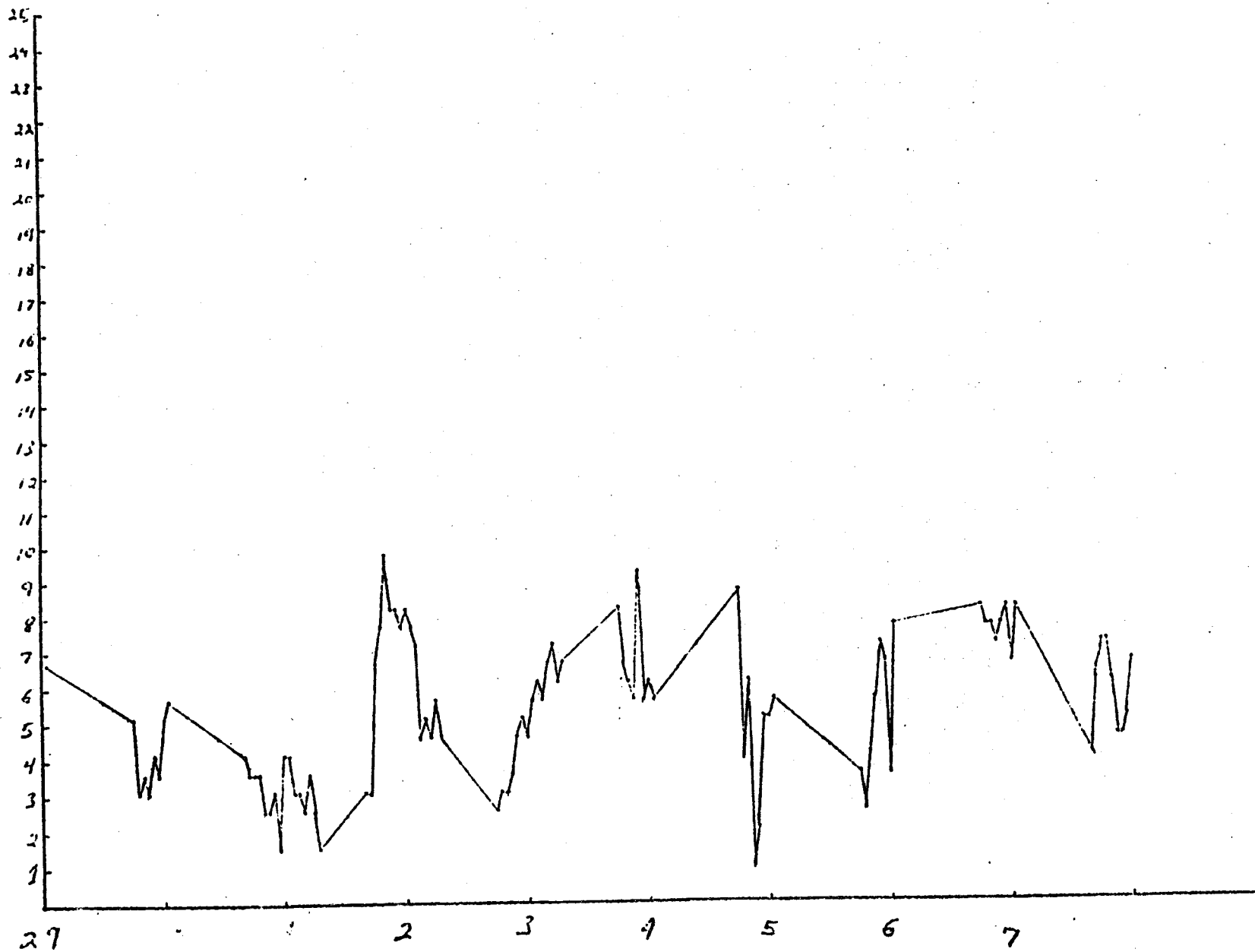
Shuyak



Augustine Island

WIND
SPEED
IN
m/sec

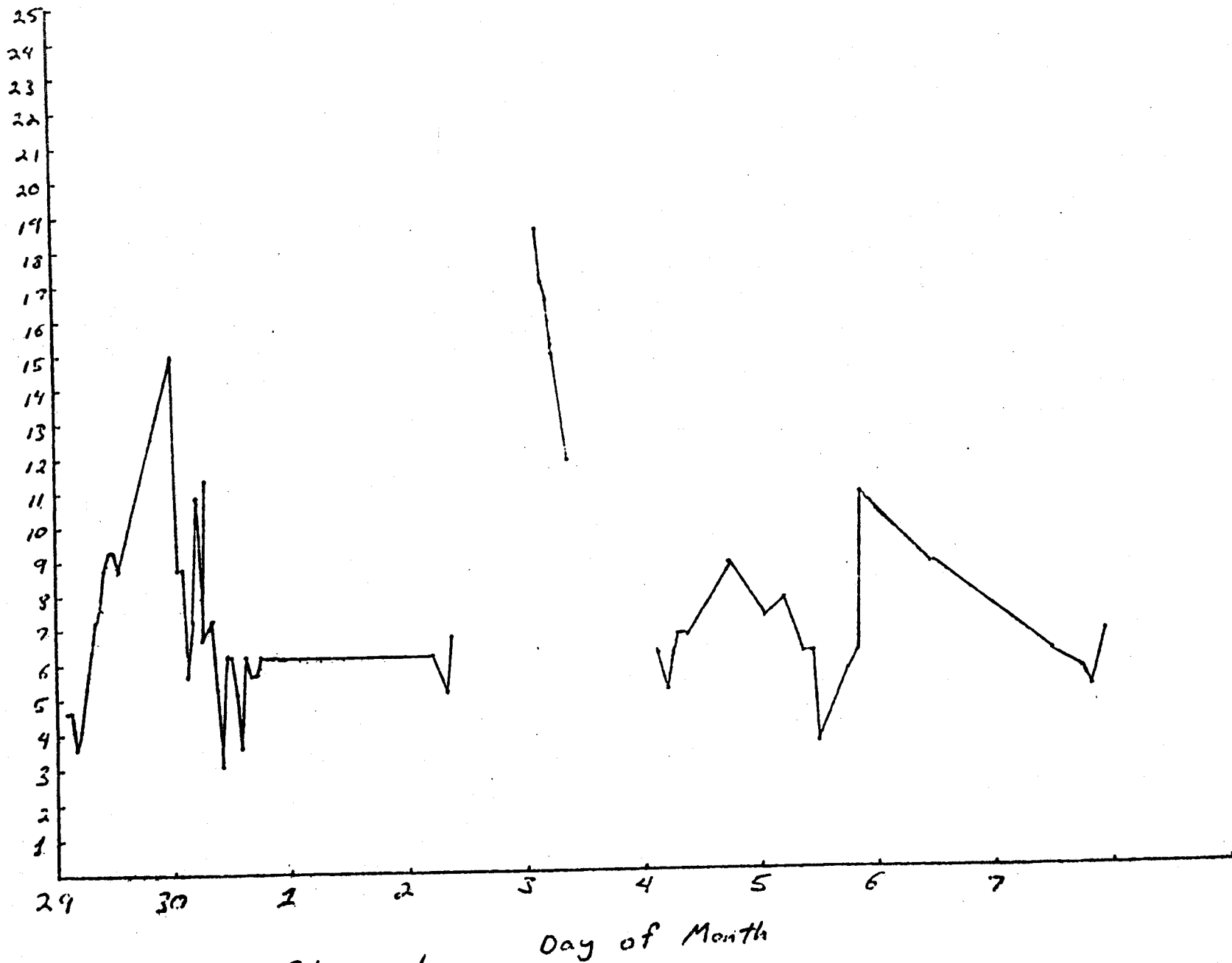
423



Day of Month

Iliamna

WIND
PEED
IN
m/sec



Shuyak

Day of Month

THE TRANSPORT AND BEHAVIOR OF OIL
SPILLED IN AND UNDER SEA ICE

Final Report
Research Unit 568
Contract 03-78-B01-62
Reporting Period: 1 May 1978-30 Sept. 1980

THE TRANSPORT AND BEHAVIOR OF OIL
SPILLED IN AND UNDER SEA ICE

J. C. Cox, L. A. Schultz, R. P. Johnson
and R. A. Shelsby

ARCTEC, Incorporated
9104 Red Branch Road
Columbia, Maryland 21045

30 September 1980

TABLE OF CONTENTS

	<u>Page</u>
PREFACE	429
LIST OF TABLES	430
LIST OF FIGURES	431
LIST OF VARIABLES	435
1. INTRODUCTION	440
2. SUMMARY	445
3. THEORETICAL FORMULATIONS	449
3.1 Horizontal Transport of Oil Under Ice	449
3.2 Vertical Migration of Oil Through Ice	457
4. SUMMARY OF EXPERIMENTAL PROGRAM AND PROCEDURES	460
4.1 Selection of Test Oils	460
4.2 Scaling Considerations	462
4.3 Static Equilibrium Thickness of Oil Under Ice	463
4.4 Oil Under Smooth Ice	463
4.5 Oil Interaction with Small Ice Roughness Elements	467
4.6 Oil Interaction with Large Ice Roughness Elements	468
4.7 Flow Pattern in the Wake of Large Ice Roughness Elements	470
4.8 Oil in the Wake of Large Ice Roughness Elements	471
4.9 Oil in Cavities	472
5. TEST RESULTS	475
5.1 General Observations	475
5.1.1 Static Equilibrium Thickness of Oil Under Ice	475
5.1.2 Oil Under Smooth Ice	475
5.1.3 Oil Interaction with Small Ice Roughness Elements	476
5.1.4 Oil Interaction with Large Ice Roughness Elements	476
5.1.5 Oil Interaction with Porous Ice Roughness	477
5.1.6 Behavior of Oil in Wakes	478
5.1.7 Behavior of Oil in Cavities	478
5.2 Summary of Quantitative Data	479

TABLE OF CONTENTS (Continued)

	<u>Page</u>
6. ANALYSIS OF TEST RESULTS	496
6.1 Static Equilibrium Thickness	496
6.2 Oil Under Smooth Ice	496
6.3 Oil Interaction with Small Ice Roughness	504
6.4 Oil Interaction with Large Ice Roughness	508
6.5 Wake Trapping of Oil	513
6.6 Cavity Trapping of Oil	514
6.7 Discussion of Small and Large Roughness Results	522
6.8 Vertical Entrapment of Oil by First-Year Ice	524
6.9 Vertical Entrapment of Oil by Multi-Year Ice	526
7. APPLICATION OF RESULTS	
7.1 Calculational Procedure	528
7.2 Sample Calculations	533
7.2.1 Small Roughness Ice	533
7.2.2 Individual Large Roughness Element with Flushing Failure	534
7.2.3 Individual Large Roughness Element with Frontal and Wake Containment	535
7.2.4 Cavity Containment with Vortex and Shear Control	537
7.2.5 Cavity Containment with Shear Control Only	538
8. RECOMMENDATIONS	540
9. REFERENCES	543
APPENDIX A - VERTICAL MIGRATION	545
APPENDIX B - STATIC EQUILIBRIUM SLICK THICKNESS	557
APPENDIX C - OIL INTERACTION WITH SMALL ROUGHNESS	560
APPENDIX D - OIL INTERACTION WITH LARGE ROUGHNESS	563
APPENDIX E - VELOCITY PROFILES	582
APPENDIX F - TEST EQUIPMENT	594

PREFACE

The assistance, cooperation, and support of Dr. Gunter Weller and Dr. William Stringer, the Technical Representatives for the Outer Continental Shelf Environmental Assessment Program, contributed substantially to the success of the program. In an experimental program such as this where new insight into governing physical phenomena is constantly being realized, it is often necessary to redirect portions of the program in order to keep the results in perspective. Their guidance and insight is gratefully acknowledged.

Significant contributions to the project were also made under sub-contract by Dr. Timothy Kao of Catholic University and Dr. Seelye Martin of the University of Washington. Dr. Kao contributed much to the analysis of the horizontal transport and containment of oil, while Dr. Martin provided information on field and laboratory studies of the vertical migration of oil through sea ice. The coordinating efforts of Dr. Max Coon, Program Manager of Tasks 2 and 3 of the project, of Flow Research Co. are also gratefully acknowledged. His efforts continually insured that the results of this laboratory study would properly interface with other portions of the three task research effort.

Finally, the authors wish to recognize the talented staff members of ARCTEC, Incorporated who participated in this program. Mr. William Grosskopf led portions of the early laboratory tests and assisted in formulating some of the basic oil containment theory. In addition to Mr. Grosskopf, the test team consisted of L. Schnebelen, W. Devane, D. Tinkle, T. Worrell, S. Burrows, P. Dobson, D. Martin, A. Radzius, and S. Wallace. The entire project team is to be complimented on the excellence of their performance, especially under very difficult working conditions.

LIST OF TABLES

<u>No.</u>	<u>Title</u>	<u>Page</u>
4.1	Target Oil Properties	461
5.1	Pre-Test Oil Properties	480
5.2	Static Equilibrium Oil Thicknesses	481
5.3	Oil Under Smooth and Small Roughness Ice Test Results	483
5.4	Oil Interaction with Large Roughness Ice Test Results	484
5.5	Results of Wake Measurement Tests	485
5.6	Results of Cavity Tests	486
6.1	Nondimensional Data for Oil Under Smooth and Small Roughness Ice	
6.2	Nondimensional Data for Oil Interaction with Large Roughness Ice	
6.3	Analysis of Cavity Test Results	516
7.1	Summary of Equations for Calculating the Transport or Containment of Oil Beneath Ice in the Presence of a Current . . .	
7.2	Definition of Terms for Equations for Calculating the Transport or Containment of Oil Beneath Ice in the Presence of a Current	
E.1	Flume Velocity Profile Data	584
E.2	Velocity Profiles Measured Downstream of a 10 cm Deep Ice Roughness Element for a Current Velocity of 20.5 cm/sec	591
E.3	Velocity Profiles Measured Downstream of a 10 cm Deep Ice Roughness Element for a Current Velocity of 31 cm/sec	592

LIST OF FIGURES

<u>No.</u>	<u>Title</u>	<u>Page</u>
3.1	Sketch of an Oil Drop Beneath an Ice Sheet	450
3.2	Sketch of the Shape Taken by a Slick Confined Behind a Large Roughness Element or Obstruction	453
3.3	Sketch of Oil Leakage From Upstream of a Large Roughness Element to the Wake Region Behind the Element	456
3.4	Generalized Description of Oil Contained in an Ice Roughness Cavity Under the Influence of a Current	458
4.1	Section View of the Piston Injector	464
4.2	Sketch of Oil Injection Cylinder	466
4.3 *	Photograph of Under-Ice Small Roughness Consisting of 1 cm Amplitude Recesses on 4 cm Spacing	
4.4	Schematic Representation of a Large Roughness Element	469
4.5 *	Photograph Showing the Insertion of a Large Roughness Element in the Level Ice Sheet	
4.6	Sketches of Protruding and Recessed Cavities	474
5.1 *	Photograph of Small Oil Droplets Moving Beneath an Ice Sheet with Small Roughness Elements by Bouncing from Element to Element	
5.2 *	Photograph Showing the Onset of Headwave Instability for a Slick Contained Upstream of a Large Roughness Element	
5.3 *	Photograph Showing Flushing Failure Initiating from the Headwave for a Slick Contained Upstream of a Triangular Large Roughness Element	
5.4 *	Photograph of the Oil-Water Interface Shape for Oil Contained in a Cavity Showing the Offset or Thinner Slick Thickness Behind the Upstream Tip in Comparison to the Thicker Slick Farther Downstream	
5.5	Typical Transformation of an Oil/Water Interface With Changes of Free Stream Current for a Number 4 Oil Trapped in a Half Meter Cavity of 14 cm Depth	488

* These photographs have been deleted from this report since copies provided were not reproducible.

LIST OF FIGURES (Continued)

<u>No.</u>	<u>Title</u>	<u>Page</u>
5.6	Typical Transformation of an Oil/Water Interface with Changes of Free Stream Current for a Number 4 Oil Trapped in a Half Meter Cavity of 19 cm Depth	489
5.7	Typical Transformation of an Oil/Water Interface with Changes of Free Stream Current for a Number 4 Oil Trapped in a 1 Meter Cavity of 9 cm Depth	490
5.8	Typical Transformation of an Oil/Water Interface with Changes of Free Stream Current for a Number 4 Oil Trapped in a 2 Meter Cavity of 9 cm Depth	491
5.9	Typical Transformation of an Oil/Water Interface with Changes of Free Stream Current for a Number 4 Oil Trapped in a 1 Meter Recessed Cavity of 9 cm Depth	492
5.10	Typical Transformation of an Oil/Water Interface with Changes in Free Stream Current for a Number 5 Heavy Oil Trapped in a Half Meter Cavity of 15 cm Depth	493
5.11	Typical Transformation of an Oil/Water Interface with Changes in Free Stream Current for a Number 5 Heavy Oil Trapped in a 1 Meter Cavity of 9 cm Depth	494
5.12	Typical Transformation of an Oil/Water Interface with Changes in Free Stream Current for a Number 5 Heavy Oil Trapped in a 2 Meter Cavity of 11 cm Depth	495
6.1	Empirical Relationship Between Slick Thickness and Density Difference	497
6.2	Slick Speed vs Current Speed for No. 2 Fuel Oil Under Smooth Ice	498
6.3	Slick Speed vs Current Speed for No. 4 Oil Under Smooth Ice	499
6.4	Slick Speed vs Current Speed for No. 5L Oil Under Smooth Ice	500
6.5	Slick Speed vs Current Speed for No. 5H Oil Under Smooth Ice	501
6.6	Plot of Oil Slick Threshold Velocity vs Oil Viscosity for Oil Beneath Smooth Ice	502
6.7	Plot of Oil Slick Velocity vs Current Velocity for the Horizontal Transport of Oil Beneath Smooth Ice Cover	503

LIST OF FIGURES (Continued)

<u>No.</u>	<u>Title</u>	<u>Page</u>
6.8	Plot of Nondimensionalized Data for the Transport of Oil Beneath Smooth and Small Roughness Ice	505
6.9	Variation of Under-Ice Slick Threshold Velocity with Ice Surface Roughness	506
6.10	Projection of Friction Coefficient Amplification Factor as a Function of the Roughness Amplitude to Spacing Ratio	509
6.11	Relationship Between Failure Velocity and Water-Oil Density Difference for Containment of Oil Upstream of an Obstruction . .	510
6.12	Vortex Zone Offset vs Local Current Speed for Oil Trapped in a Cavity	515
6.13	Densimetric Froude Number Based on Offset Size vs Local Current Speed for Oil Trapped in a Cavity	518
6.14	Vortex Zone Length Versus Local Current Speed for Oil Trapped in a Cavity	520
6.15	Schematic Representation of the Shift in Oil-Water Interface Position within a Cavity as a Function of Increasing Current . .	525
7.1	Flow Chart of the Procedure for Calculating the Transport or Containment of Oil Beneath Ice in the Presence of a Current .	529
A.1	Brine Channel Patterns in Young and Multi-Year Sea Ice	546
A.2	Static Oil Rise in an Open Brine Channel	548
A.3	Equilibrium Oil Level in a Brine Channel Only Partially Extending to Datum Level	551
A.4	Equilibrium Oil Level in a Brine Channel Extending Through the Datum Level But Not to the Ice Surface	552
B.1	Sessile Drop of Oil Beneath an Ice Cover	558
D.1	Sketch of Frontal Trapping of an Oil Slick by a Large Roughness Element	564
D.2	Slick Thickness Ratio vs Free Stream Densimetric Froude Number for Large Roughness	566

LIST OF FIGURES (Continued)

<u>No.</u>	<u>Title</u>	<u>Page</u>
D.3	Sketch of the Viscous Region of a Contained Slick	569
D.4	Sketch Showing the Method of Approximating the Volume Per Unit Width of a Frontally Trapped Slick	573
D.5	Sketch of Oil Leakage from Upstream of a Large Roughness Element to the Wake Region Behind the Element	574
D.6	Velocity Measurements in the Wake of a Fence Taken from Rouse [24].	576
D.7	Variation of Wake Length with Roughness Height	577
D.8	Generalized Description of Oil Contained in an Ice Roughness Cavity Under the Influence of a Current	579
D.9	Schematic Representation of the Shift in Oil-Water Interface Position Within a Cavity as a Function of Increasing Current . . .	581
E.1	Locations Where Velocity Profiles were Measured in the Flume . .	583
E.2	Velocity Profile at Position No. 1 with Flow Rate of 1100 gpm . .	585
E.3	Velocity Profile at Position No. 2 with Flow Rate of 1100 gpm . .	586
E.4	Velocity Profile at Position No. 3 with Flow Rate of 1100 gpm . .	587
E.5	Velocity Profile at Position No. 4 with Flow Rate of 1100 gpm . .	588
E.6	Velocity Profile at Posotion No. 5 with Flow Rate of 1100 gpm . .	589
E.7	Velocity Profile at Position No. 6 with Flow Rate of 1100 gpm . .	590
E.8	Plots of Velocity Profiles Measured Downstream of a 10 cm Deep Ice Roughness Element for a Current Velocity of 20.5 cm/sec . . .	593
E.9	Plots of Velocity Profiles Measured Downstream of a 10 cm Deep Ice Roughness Element for a Current Velocity of 31 cm/sec	593
F.1	Schematic Drawing of ARCTEC Ice Flume	595
F.2	ARCTEC Ice Flume Carriage Arrangement	597

LIST OF VARIABLES

a	characteristic drop thickness = $\sqrt{\frac{\sigma_o/w}{\Delta\rho_w g}}$	cm
A	empirical coefficient	--
A_{frontal}	frontal projected slick area	cm ²
A_{plan}	horizontal areal coverage of slick	cm ²
A_{total}	gross areal coverage	cm ²
A_{voids}	areal coverage of voids	cm ²
b	intercept of upper oil-smooth ice relation	cm/sec
B	empirical coefficient	--
C_D	roughness form drag coefficient	--
C_f	slick form drag coefficient	--
C_i	oil-smooth ice friction coefficient	--
C_s	interfacial shear coefficient	--
d	brine channel diameter	cm
d_{crit}	diameter where vertical oil migration ceases	cm
$d_{\text{inception}}$	diameter for initiating vertical oil migration	cm
D	water depth	cm
D_H	hydraulic diameter of flume = $\frac{4 \text{ (area)}}{\text{wetted perimeter}}$	cm
f_s	interfacial friction factor	--
F_D	freestream densimetric Froude Number $\frac{U_w}{\sqrt{\Delta g D}}$	--
F_f	form drag force	gm-cm/sec ²
F_i	oil ice sliding friction force	gm-cm/sec ²
F_s	interfacial shear force	gm-cm/sec ²

F_{δ}	slick densimetric Froude Number $\frac{U_w}{\sqrt{\Delta g \delta}}$	--
F_{ϵ_1}	offset densimetric Froude Number $\frac{U_w}{\sqrt{\Delta g \epsilon_1}}$	--
g	gravitational constant	gm/sec ²
h	pressure head	cm
k_{ice}	thermal conductivity of ice	gm-cal/°C sec-cm
K	friction amplification factor for rough ice	--
l_1	ice draft	cm
l_2	brine channel related dimension	cm
l_3	brine channel related dimension	cm
$L, L(t)$	ice thickness	cm
m	slope of lower oil-smooth ice curve	--
n	porosity	--
N	number of brine channels	--
N'	number of brine channels per unit area	--
P	pressure	gm/cm-sec ²
\bar{P}	pressure change	gm/cm-sec ²
P'	incremental pressure	gm/cm-sec ²
P_B	buoyant pressure	gm/cm-sec ²
P_c	capillary pressure	gm/cm-sec ²
P_{∞}	pressure far upstream of slick	gm/cm-sec ²
q_{ice}	heat flux through ice	gm-cal/sec-cm ²
q_{water}	heat flux from water	gm-cal/sec-cm ²
Q	flow rate	cm ³ /sec
r	sessile drop radius	cm
R	radius of curvature	cm
t	time	sec

T	time interval	sec
\bar{u}_2	vertical migration speed	cm/sec
$u_{1,2,3}$	velocity components	cm/sec
$u'_{1,2,3}$	turbulent velocity perturbations	cm/sec
U	under-ice velocity profile values	cm/sec
$U_\infty - u$	velocity defect in the wake	cm/sec
U_*	friction velocity = $\sqrt{\frac{\tau_0}{\rho_w}}$	cm/sec
U_{crit}	critical velocity for Kelvin-Helmholtz instability	cm/sec
U_{fail}	freestream velocity when containment failure occurs	cm/sec
U_s	slick speed	cm/sec
U_{th}	threshold current speed for slick movement	cm/sec
U_w	mean current speed	cm/sec
U_∞	freestream current outside the boundary layer	cm/sec
V	slick volume	cm ³
V'	slick volume per unit width	cm ³ /cm
V_{total}	gross volume of ice including voids	cm ³
V_{voids}	volume of voids in ice	cm ³
w	slick width	cm
x	horizontal dimension	cm
X	slick length	cm
X_{shear}	length of the shear zone	cm
y	vertical dimension	cm

α	interfacial tension contact angle	--
β	empirical wake growth parameter	--
δ	slick thickness	cm
δ_{eq}	static equilibrium slick thickness	cm
δ_{head}	thickness of contained slick headwave	cm
δ_{neck}	thickness of contained slick neck	cm
$\delta_{stagnation}$	thickness of contained slick at point of flow reattachment	cm
δ_{tail}	thickness of contained slick tail	cm
Δ	relative density difference = $\frac{\rho_w - \rho_o}{\rho_w}$	--
ϵ_1	offset of the oil-water interface in the vortex zone	cm
ϵ_2	offset of the oil-water interface at the stagnation point	cm
ξ	wake length	cm
η	ice roughness height	cm
θ_m	melting temperature	°C
θ_o	ice surface temperature	°C
θ	temperature difference = $\theta_m - \theta_o$	°C
θT	thawing degree time	°C-sec
l	vortex cell length	cm
κ	von Karman's constant = 0.35	--
λ	ice roughness spacing	cm
Λ	heat of fusion	gm-cal/gm
μ_o	viscosity of oil	gm/cm-sec
ν	kinematic viscosity of water	cm ² /sec
ν_o	kinematic viscosity of oil	cm ² /sec
ρ_f	ice density after time interval T	gm/cm ³

ρ_i	initial ice density	gm/cm ³
ρ_{ice}	ice density	gm/cm ³
ρ_o	oil density	gm/cm ³
ρ_w	water density	gm/cm ³
$\sigma_{o/w}$	interfacial tension	gm/sec ²
τ_B	boundary shear stress	gm/cm-sec ²
τ_s	interfacial shear stress	gm/cm-sec ²
ϕ	interfacial angle	--
ψ	nondimensional slick thickness = $\frac{\delta}{D}$	--

1. INTRODUCTION

The continuing dependence of our nation on foreign sources of oil and gas, and the continuing undependability of these sources of supply, indicate that the petroleum reserves already found, and expected to be found, in the Alaskan offshore region will be developed in a timely manner. While the development of these petroleum reserves will proceed with an unprecedented concern for protection of the environment, the simple fact is that any petroleum industry activity related to exploration, development, production, or transportation of Alaskan oil and gas in areas where such activity has not occurred previously must necessarily increase the potential for accidental spills of oil in the region.

The Outer Continental Shelf Environmental Assessment Program (OCSEAP) is a comprehensive environmental study program associated with the proposed development of oil and gas on the outer continental shelf. The program is managed by the National Oceanic and Atmospheric Administration (NOAA) for the Bureau of Land Management (BLM). The OCSEAP studies are designed to provide an environmental information base to support management decisions associated with the identification and selection of lease sale areas. The program is organized into topical areas of contaminant baselines, sources, hazards, transport, reconnaissance, and effects.

The primary objective of the Alaskan OCSEAP is to provide the technical information required to support management decisions associated with the protection of the OCS marine environment from damage due to oil and gas exploration, development, and production activities in Alaska. The program is geared towards the development of providing meaningful data in a readily usable form and in a timely manner so that any required corrective action can be taken before serious or irreversable environmental damage can occur. A major portion of this effort is allocated to a description and characterization of the fate of oil spilled in and under sea ice within the Alaskan OCS lease areas. As part of this effort, NOAA issued a Request for Proposal (RFP) in December 1977 for a study entitled "The Transport and Behavior of Oil Spilled In and Under Sea Ice." In broad terms, this study was to be concerned with the containment potential and transport of oil by ice moving over the continental shelf, and the determination of the likely long-range trajectories of ice and spilled oil contained in the ice. The work of this project was formulated in the RFP in terms of three tasks as follows:

TASK 1 - To determine by field and laboratory experiments the physical processes by which spilled oil gets incorporated in and transported under sea ice.

TASK 2 - To determine by numerical modeling the ice velocity field and the deformation of sea ice on the continental shelves of both the Beaufort and Chukchi Seas so that oil spill trajectories and percent oil incorporation can be deduced for different ice conditions

under mean climatological conditions and extreme events, including a major sea ice breakout from the Chukchi Sea to the Northern Bering Sea.

- TASK 3 - To determine by combining the relevant information obtained under Tasks 1 and 2 as well as any other relevant information the sequence of events, likely trajectories, and destination points for oil in a number of hypothetical oil spill scenarios.

Contracts for this work were awarded by NOAA in June 1978, with the contract for Task 1 awarded to ARCTEC, Incorporated of Columbia, Maryland, and the contract for Tasks 2 and 3 awarded to Flow Research Company of Kent, Washington. These contracts were designated within the OCSEAP project structure as Research Units 568 and 567 respectively, and administered through the OCSEAP Arctic Project Office in Fairbanks, Alaska by Dr. Gunter Weller and Dr. William Stringer. This report is the final report on the work performed by ARCTEC, Incorporated under Task 1 of the program. In keeping with the original program plan, the results of this work on oil-ice interaction have been combined with the work of Task 2 consisting of a numerical model of ice dynamics, and the work of Task 3 consisting of the projection of likely trajectories and destination points, for specific offshore Alaskan oil spill scenarios. The work completed under Tasks 2 and 3 of the program have been separately reported by Flow Research Company.

The work of Task 1 of the program was further divided in the RFP into three subtasks as follows:

- Subtask 1.1 - To determine how and at what rates oil moves upward through multi-year ice to the surface.
- Subtask 1.2 - To determine how and at what rates oil gets incorporated into pressure ridges formed from ice of various thicknesses.
- Subtask 1.3 - To determine how oil of different viscosities spreads and is moved by ocean currents under sea ice with different underside roughness characteristics.

The three subtasks were therefore basically concerned with the vertical migration of oil through ice, the interaction of oil with pressure ridges, and the horizontal transport of oil beneath ice cover. The RFP also raised a number of questions which hopefully would be answered by the work of this study as follows:

1. How does oil move through first-year and multi-year ice? Under what conditions will it reach the surface, and how long will it take to reach the surface?

2. How does oil get incorporated into pressure ridges, and how and when does it get released?
3. How much oil can be expected to be trapped within pressure ridges, in rafted ice, hummocks, leads, and surface relief in the bottom of the ice surface?
4. How does oil move horizontally under ice of different surface roughnesses through the action of ocean currents? How thick are the oil films likely to be under ice cover having a range of surface conditions?
5. What is the bulk transport of spilled oil by sea ice of different concentrations?
6. How does oil of different viscosities respond to these various vertical and horizontal dispersion processes?

The program was therefore initially formulated in terms of the interaction of spilled oil with various ice conditions and ice features including smooth ice, undulating ice, rough ice, broken ice fields, rafted ice, hummocks, unconsolidated pressure ridges, consolidated pressure ridges, leads, and ice edges. In performing the preliminary theoretical analysis of oil-ice interaction and in planning the laboratory test program in more detail, it quickly became apparent that the problems could be addressed in more generalized categories rather than in terms of specific ice conditions and ice features. The problems to be addressed in this study were then reorganized in terms of the interaction of spilled oil with smooth ice, with ice having small roughness characteristics, and with ice having large roughness characteristics. For the purposes of this study, small ice roughness was defined as roughness whose amplitude is less than the smooth ice equilibrium slick thickness of the oil. A large roughness element is therefore defined as an element of roughness whose amplitude is greater than the smooth ice equilibrium slick thickness of oil. The interaction of spilled oil with large roughness elements was then further categorized in terms of the interaction of spilled oil with a single element where the interest lies in the oil containment capability of the element in terms of its upstream barrier-type containment and its downstream wake region containment, and interaction with multiple large roughness elements which form a cavity having the potential to contain spilled oil. The smooth ice case, while unlikely to be a significant case in most field applications, was a necessary base case for this study. The analysis and interpretation of results for the small roughness and large roughness cases were built upon the analysis and interpretation of results obtained for the simpler smooth ice case.

One final introductory comment concerns the constraints imposed upon these studies of the interaction of spilled oil with ice in the presence of a current by the specific application to be addressed as specified in the RFP

and subsequent meetings with the project administrators. The source of the hypothetical spills for use in the development of spill scenarios was specified as the nearshore Beaufort Sea along the Prudhoe Bay meridian. The spill discharge area is therefore characterized in general terms as an area of relatively shallow water depths, typically less than 60 ft; relatively low currents, typically less than 30 cm/sec; and relatively continuous and well mannered ice conditions over the long term. In terms of the study of the interaction of spilled oil with ice, the shallow water release was interpreted to impose the requirement that the material being dealt with was indeed an oil, rather than an oil-water emulsion, or mousse, which could result from a deep water blowout. The limited currents meant that the upper limit of water current for testing in the laboratory was 30 cm/sec. The well behaved ice conditions and the relatively long time frame of the ice dynamics mathematical model meant that broken ice fields, leads, and ice edges were short-term phenomena, not capable of existing in the mathematical model, and therefore not studied in this program of oil-ice interaction. It was also assumed that any gas released with the oil would quickly, relative to the time frame of the mathematical model of ice dynamics, result in rupture of the ice cover, from which time the gas would be vented to the atmosphere as the oil continued to be released and spread beneath the ice surface. As a result, none of the oil-ice interaction situations investigated in this study included the presence of gas beneath the ice sheet.

As for the incorporation of oil-ice interaction into the mathematical model of ice dynamics to result in the projection of oil spill trajectories, the behavior of the spilled oil is analyzed in four distinct stages consisting of the initial spread of the oil, the incorporation of oil into the ice, the transport of oil with, or relative to, the ice, and the ultimate release of the oil from the ice. The oil-ice interaction problems can therefore be reduced in their simplest terms to a determination of whether oil spilled beneath ice in the presence of a current is contained by the ice and therefore transported with the ice, or whether it is transported by the current relative to the ice. The level of capability for quantitatively defining the behavior of spilled oil beneath ice in the presence of a current has been advanced substantially as a result of the work reported herein, however, this capability still remains far from complete. The emphasis throughout this program was placed on extending the results of the limited laboratory tests to the greatest extent possible through extrapolations based upon theoretical analysis. Approximations and estimates have been made where necessary to provide as complete an assembly of relationships describing the interaction of spilled oil with ice as is possible in a form readily allowing application of the results to both mathematical modeling and field spill situations. These assumptions and approximations were made by the authors with some degree of boldness, however the authors feel that such approximations and estimates would have to be made by someone in order to provide a complete statement of oil-ice interaction, and feel obliged to make the best assumptions and approximations possible based upon the insight into the behavior of spilled oil beneath ice gained during the course of this program. The alternative is to leave holes in the statement of oil-ice interaction which must be filled by each individual user to the best of his or her ability. All assumptions, approximations, and estimates made by the authors are, of course, identified as such.

The next section of this report consists of a summary of the results of this study in very broad terms. Following this, the report addresses the theoretical formulations of various oil-ice interaction situations, a summary of the experimental program and procedures, the test results presented both in terms of general observations and quantitative data, and the analysis of the test results. In keeping with the emphasis imposed throughout the project on making the results on the work useful and applicable, a section of the report is then devoted to the application of the results of this study. In this section, the recommended approach to be used in studying and analyzing the behavior of spilled oil beneath ice in the presence of a current is presented in flowchart form, with the necessary equations governing oil-ice interaction summarized and demonstrated through a series of sample calculations. The final section of the report consists of a series of recommendations for future work. This work would address the less well defined areas of oil-ice interaction which required the making of estimates, assumptions, and approximations as discussed above and, in addition, would address the oil-ice interaction problem in more general terms beyond the specific region of interest and specific oil spill scenarios which were of concern in the present study. The detailed theoretical analysis performed for each of the oil-ice interaction situations is then presented in the appendices.

2. SUMMARY

The objective of this program has been to study the behavior of oil spilled beneath ice cover in the presence of a current. While the problem of oil-ice interaction was originally stated in terms of ice characteristics and ice features such as smooth ice, undulating ice, rough ice, broken ice fields, rafted ice, hummocks, unconsolidated pressure ridges, consolidated pressure ridges, leads, and ice edges, it was found convenient to categorize ice conditions, and address the problem in terms of oil interaction with smooth ice, small ice roughness features and large ice roughness features. For the purposes of this program, a small roughness element was defined as an obstruction whose depth was less than the equilibrium slick thickness of the oil beneath smooth ice, while large roughness elements were defined as those having a depth greater than the equilibrium slick thickness of the oil beneath smooth ice. The study of the interaction of spilled oil with large roughness elements was further divided into the containment and transport characteristics of a single element, with the potential for containment both upstream of the element acting in the manner of a containment boom and downstream of the element in the wake region on the downstream side, and the behavior of oil in cavities formed by multiple large roughness elements. The project included both an analytical investigation of the mechanisms of oil-ice interaction and laboratory studies conducted in ARCTEC's glass-walled Ice Flume. Since the properties of the oil expected to be found in the offshore regions of the Alaskan Beaufort Sea are still unknown, tests were conducted with refined oils having known, repeatable physical properties, ranging from No. 2 fuel oil having the lowest value of viscosity and density to No. 5 heavy fuel oil having the highest value of viscosity and density. The quantitative relationships developed in this study to characterize the behavior of spilled oil beneath ice in the presence of a current were intended to be combined with an ice dynamics model to obtain predictions of the long-term trajectory and disposition of oil spilled in the ice infested waters of the Alaskan Beaufort Sea. The results are, of course, generally applicable to the interaction of spilled oil with ice cover in the presence of a current for any location covered by the parameter range investigated. In using these relationships to project the trajectory and disposition of spilled oil in ice infested waters, potential spill impact zones can be identified, and appropriate environmental safeguards can be implemented. In addition, the most promising oil spill cleanup procedures can be identified if a more precise knowledge of oil-ice interaction is available.

The major results obtained from this study of the behavior of oil spilled beneath ice in the presence of a current expressed in general terms are as follows:

1. Slick Thickness. While a force balance between the surface tension and buoyancy forces on an oil slick beneath smooth ice under static conditions leads one to expect a second order relationship between the slick thickness and the density difference between the water and the oil, for the four oil types tested in this study the equilibrium slick thickness of oil beneath smooth ice was empirically found to be a linear function of the density

difference between water and oil. The smooth ice equilibrium slick thickness was determined to range from 0.52 cm for No. 2 oil to 1.16 cm for No. 5 heavy oil.

2. Smooth Ice. While the smooth ice case is unlikely to be a case of significance in field applications, it serves as a base case for the following work concerned with ice having small and large roughness features. The threshold velocity for oil slicks beneath smooth ice, defined as the value of the water current at which the slick starts to move beneath the ice, ranged from 3 to 4 cm/sec for the lighter oils including No. 2, No. 4, and No. 5 light, to about 7 cm/sec for No. 5 heavy oil. A two-step linear curve relating the slick velocity to the current velocity was developed for each of the four oils studied. In addition, without a great loss in accuracy, a single two-step linear relationship between slick velocity and current velocity was developed for all oils covering the range of oils tested, assuming that the temperature of the oil is above its pour point. This relationship is useful for obtaining a first estimate of slick speed beneath ice when the properties of the oil are not known.

3. Small Roughness. When small roughness, defined as roughness having an amplitude less than the equilibrium slick thickness of the oil beneath smooth ice, of 1 mm amplitude on 4 cm spacing was added to the under ice surface, the threshold velocity for No. 4 oil increased substantially from about 4 cm/sec to 12 cm/sec. When the roughness amplitude was further increased to 1 cm, the threshold velocity increased to about 22 cm/sec. The threshold velocity for No. 5 heavy oil changed similarly. For a 1 mm amplitude roughness the threshold velocity increased from about 7 cm/sec to 16 cm/sec, while for a 1 cm amplitude roughness the threshold velocity increased further to about 25 cm/sec. These results revealed, therefore, that even a slight amount of under ice surface roughness causes a substantial increase in the threshold velocity of an under ice oil slick. In addition, once underway, the speed of the slick relative to the water current is similarly reduced. A generalized slick velocity relationship has been developed for smooth ice and small roughness ice in terms of the current velocity, a densimetric Froude Number, and an amplification factor for the oil-ice friction factor.

4. Large Roughness-Frontal Trapping. When the amplitude of an ice roughness element exceeds the equilibrium thickness of a slick beneath smooth ice, the roughness is defined as large roughness, and has the potential of totally restraining an advancing oil slick up to some critical value of current velocity. A frontally trapped oil slick is an oil slick contained upstream of a projection under the ice cover in the same manner as oil contained by a containment boom. Its behavior can be described by a theory similar to that used for containment booms with the addition of a lid imposed by the ice cover upstream of the obstruction or boom. A slick so confined develops into the now classic contained oil slick shape including three distinct regions, a head region, a neck region and a tail region. For a given oil, the dimensions of each of these regions is a function of the current speed. Two types of containment failure, or oil release, can occur. The first is the result of the slick growing in volume to a point where its length and thickness exceed an

equilibrium point prescribed by the flow. When this occurs, leakage from the tail region results until the equilibrium volume is restored. The second type of failure which occurs at higher current velocities, consists of the total flushing of the oil as the result of a Kelvin-Helmholtz instability in the slick. In this case, the head wave is continually being re-built as oil is being torn away, and the slick gradually decreases in length until it is entirely flushed out and all containment is lost from the upstream side of the roughness element. For the oil tested in this program, oil trapped upstream of a large roughness element can typically be flushed out at current velocities in the range of 15 to 25 cm/sec. Quantitative relationships have been developed for both the containment capacity of frontally trapped slicks, and the critical current velocity at which containment is lost.

5. Large Roughness-Wake Trapping. For oil lost from containment on the upstream side of a large roughness element below the frontal flushing velocity, some small containment capacity at the equilibrium slick thickness over about 70% of the wake length is available. Above the magnitude of the frontal flushing velocity, oil contained in a wake region downstream of a large roughness element clears in a time period of minutes to hours, resulting in a negligible long-term containment capacity.

6. Porous Large Roughness. No frontal trapping of an oil slick upstream of a porous large roughness element occurred. The oil migrated into the pores of the porous roughness element, and, depending upon oil type and test conditions, either moved vertically through the obstruction and poured out on the ice surface, or moved very slowly through the obstruction to the downstream side of the roughness element. Behavior in the wake region for the porous large roughness element case was qualitatively similar to that observed in the solid large roughness element case.

7. Large Roughness-Cavity Trapping. A region of under ice roughness bounded by two large roughness elements can be characterized either as a cavity or as two individual roughness elements depending upon oil properties, flow conditions, and cavity or roughness element geometry. Oil contained in a cavity is characterized by two zones, a vortex zone and a shear zone. Requirements for the existence of a cavity, as opposed to separate large roughness frontal and wake trapping, have been established quantitatively. The volume of oil contained in a cavity is a function of cavity geometry, oil properties, and flow conditions. The volume of contained oil is less as the oil density increases and as the current velocity increases.

8. Vertical Migration. While no laboratory work related to the vertical migration of oil through ice was included in this study, the results of the latest investigations are summarized here for the sake of completeness. In the case of first-year ice, limited field and laboratory work suggests that oil trapped beneath or within first-year sea ice will flow to the surface at a rate of 0.07 cm/sec when the minimum interior ice temperature increases to -4°C . In the case of multi-year ice, limited field and laboratory studies indicate that there is no vertical migration of oil through the ice sheet, rather the oil is only released from the ice sheet when enough bulk melting of the ice has occurred to melt the ice down to the oil.

Based upon the results of this study, the following broad generalizations regarding the containment and transport of oil spilled beneath ice cover having varying roughness characteristics in the presence of a current can be made:

1. In general terms, oil spilled beneath ice cover will not be transported by the current relative to the ice until the relative current velocities are in the range of 15 to 25 cm/sec.

2. At current velocities below 15 to 25 cm/sec a typical ice field has substantial oil spill containment capacity for even the largest conceivable spill volumes. Oil will be trapped within the under ice roughness cavities of the ice, and the areal coverage of the spill will be substantially less than that which would result from an open water spill.

3. Oil trapped upstream of a large obstruction can be flushed out at current velocities in the range of 15 to 25 cm/sec depending on the properties of the oil involved. Also, no significant containment potential exists in wake regions behind ice roughness features at these velocities in the long term.

4. Cavities in the ice have the potential to at least partially contain oil even for current velocities exceeding values which cause oil trapped upstream of a single large obstruction to be flushed downstream.

5. For the Alaskan Beaufort Sea, vertical migration of oil trapped beneath ice will only occur in first-year ice in the spring season. Multi-year ice is not porous enough to allow for the vertical migration of the oil. The release of oil trapped beneath multi-year ice requires that the ice melt down to the oil.

3. THEORETICAL FORMULATIONS

A complete theoretical development of the behavior of oil transport or containment under ice is presented in Appendices A through D at the end of this report. The following sections highlight the most significant characteristics and relationships, and serve to introduce the combined analytical and experimental work completed in the course of this program.

3.1 Horizontal Transport of Oil Under Ice

As oil is released beneath an ice sheet, it forms into droplets whose dimensions are based upon a balance between the interfacial tension forces and the buoyancy forces. The buoyancy of the oil will force the droplet to spread laterally as its volume increases. Since oil in contact with water and ice is a partially wetting fluid, it will spread with an obtuse contact angle within the oil. A schematic representation of the oil drop is shown in Figure 3.1. For large diameter oil slicks, the thickness, δ , of the slick can be predicted by a simple relationship based upon the interfacial tension between oil and water, $\sigma_{o/w}$, the contact angle of the oil with the ice, α , and the relative density of the oil, $\Delta \rho_w$:

$$\delta^2 = \frac{2 \sigma_{o/w}}{\Delta \rho_w g} (1 + \cos \alpha). \quad (3.1)$$

Estimates of the magnitude of the contact angle or the appropriate value for the interfacial surface tension are difficult to obtain, particularly since the determination of one is based upon knowledge of the other. Mackay and Medir [14] have measured the thickness, interfacial tension, density, and contact angle on Norman Wells and Prudhoe Bay crudes. Mean values for Norman Wells crude were 0.86 cm, 31 dn/cm, 0.847 gm/cc, and 42° respectively. Values for Prudhoe Bay crude were 1.2 cm, 33 dn/cm, 0.911 gm/cc, and 20° respectively. Based on this data, we should expect the static thickness of the oil to be most strongly influenced by density difference rather than interfacial tension.

To establish a thickness prediction for a moving oil slick, a dynamic pressure force should be included in the force balance used to derive Equation 3.1. However, for slicks of finite length the dynamic pressure will balance on the front and back faces of the slick. Therefore, the net effect of the dynamic pressure would be zero. It would appear, then, that the equilibrium thickness should be the same for both unaccelerated moving slicks and static slicks.

If the slick is being driven by an ocean current, the rate at which it can move under the ice can be predicted by a moving force balance between the oil, the ice, and the ocean current. The three primary forces involved are a form drag which is based upon the frontal area that the slick presents to the moving current, an interfacial shear stress force which is due to the shear applied to the underside of the oil slick by the moving current, and a retarding oil-ice friction force which is modeled as a mechanical sliding friction. In this force balance, the oil is treated basically as a solid rather than as a

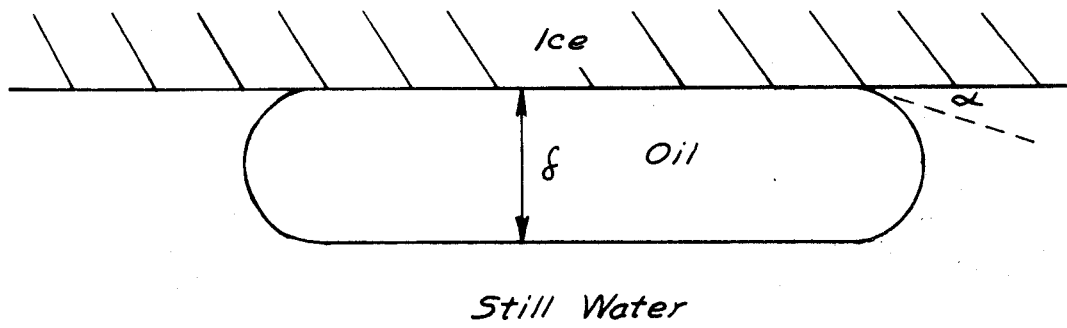


Figure 3.1. Sketch of an Oil Drop Beneath an Ice Sheet

fluid. This is for simplicity of analysis since oil exhibits certain rheological properties, and its buoyancy aids in applying a normal friction force to the ice sheet in addition to maintaining the slick integrity. The force balance between the friction, form drag, and interfacial shear is then given as:

$$F_i = F_f + F_s. \quad (3.2)$$

Both the form drag and the interfacial shear force are based upon the relative velocity of the slick to the water. By carrying out the balance as is done in Appendix C, a simple nondimensional relationship can be derived in terms of nondimensional velocity and slick densimetric Froude number for any oil in the form:

$$\left(1 - \frac{U_s}{U_w}\right)^2 = \left(\frac{2 C_i}{C_f \frac{\delta}{X} + C_s}\right) \frac{1}{F \delta^2}. \quad (3.3)$$

Notice that the coefficient on the right hand side of the equation contains three different drag coefficients. In addition, it contains a factor of the ratio of slick thickness to slick length. This factor seems to indicate that, as would be expected, the form drag is more significant when the slick length is small. This would be true for oils whose slicks would tend to orient themselves transversely with the mean current. Conversely, when the slick length is very long, the shear stress applied to the slick will dominate. Equation 3.3 can be transformed into a simple expression between slick speed and current speed. This is given as:

$$U_s = U_w - \left(\frac{2 C_i \Delta g \delta}{C_f \frac{\delta}{X} + C_s}\right)^{1/2}. \quad (3.4)$$

Picking some reasonable values for the drag coefficients such as $C_{i,smooth} = 0.1$, $C_f = 1.0$, and $C_s = 0.01$, unusually high estimates for typical threshold velocities are obtained. This is the result of assuming that the shear stress coefficient, is a constant, when it is actually a function of velocity, changing radically at lower current speeds. Therefore, Equation 3.3 is not really a linear relation between nondimensional velocity and inverse Froude Number. As suggested in Appendix C, it actually takes a hyperbolic form, given typically as:

$$\left(1 - \frac{U_s}{U_w}\right)^2 = \frac{1}{AF \delta^2 + B}. \quad (3.5)$$

This equation has asymptotes for both large Froude Numbers and small Froude Numbers. In the limits, this equation can be reduced to give two linear relationships between slick velocity and current velocity similar to Equation 3.4. For the low current speeds, the slick is dominated by a static friction, and the slick speed relation is simply of the form:

$$U_s = m U_w. \quad (3.6)$$

At high current speeds, the slick has overcome the static friction and now can be freely advected with the local mean flow and follows a relation of the form:

$$U_s = U_w - b. \quad (3.7)$$

In this expression, the slope of the line is unity, indicating that the slick is moving at a constant speed relative to the current, differing numerically only by a constant. This constant corresponds to the point where static friction has been overcome and a transition is made to dynamic friction. Based on this analysis, it appears that oil slicks moving beneath the ice should exhibit a two-step linear curve for slick speed. For low currents, the slope of the curve is very small. For higher currents, the slope of the curve should approach unity.

As the oil moves, it will encounter numerous forms of surface relief. Some of the ice roughness would be small enough to be wholly contained within the slick thickness. Typically this might be granular ice, finger ice, or slush ice. When this is the case, the prediction for slick speed just derived should still be valid. Only the oil-ice friction coefficient will change based upon the small scale roughness characteristics. The prediction of the actual magnitude of a rough ice friction factor is very difficult. However, a change in the friction factor for rough ice could be established experimentally, given a value for the smooth ice friction factor. Equation 3.5 can be adjusted to account for this amplification factor in the oil-ice friction coefficient. In general, then, oil moving over a rough ice sheet would be expected to follow a relation of the form:

$$\left(1 - \frac{U_s}{U_w}\right)^2 = \frac{K}{AF\delta^2 + B}, \quad (3.8)$$

where K , the amplification factor, will vary from a minimum value of 1.0 for smooth ice to some larger range of numbers which will be determined experimentally for rough ice.

When the relief on the under-ice surface exceeds the static equilibrium thickness of the oil, the spread of the oil will be halted or diverted, and blocking and pooling of the oil can occur. Depending upon the size of the relief and the speed of the freestream current, this trapped oil will grow upstream of the obstruction in both length and thickness until some critical volume is reached beyond which no further containment is possible. When this occurs, the slick becomes unstable and some leakage occurs.

A fully developed contained oil slick is characterized by two regimes; a head wave regime which is due to a momentum force applied to the slick, and a viscous regime which is due to shear stress applied to the slick. This is schematically shown in Figure 3.2. The two regimes are essentially independent, and the behavior of each regime can be analyzed individually. The solutions can be

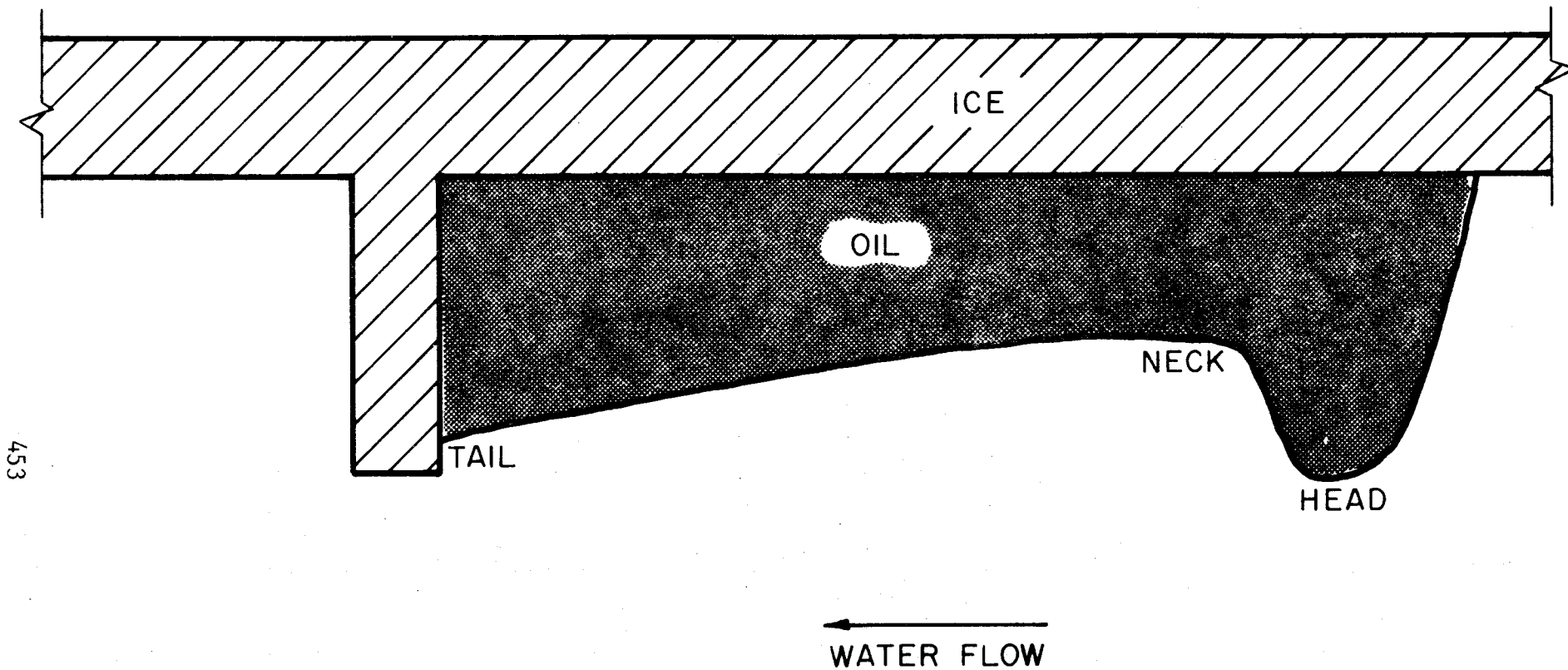


Figure 3.2. Sketch of the Shape Taken by a Slick Confined Behind a Large Roughness Element or Obstruction

matched at a neck in the slick which occurs just behind the head wave. The thickness of this neck is approximately one-half the thickness of the head wave.

By carrying out the force balance of hydrostatic and momentum forces both upstream of the slick and at a section taken through the head wave, a nondimensional relationship between slick thickness and densimetric Froude Number can be developed. This relationship is given as:

$$F_D^2 = \psi (2 - \psi) \frac{(1 - \psi)}{(1 + \psi)}, \quad (3.9)$$

or in terms of slick thickness as:

$$F_\delta^2 = (2 - \psi) \frac{(1 - \psi)}{(1 + \psi)}. \quad (3.10)$$

These expressions predict the equilibrium thickness for any slick given a particular flow condition. As the volume of the contained slick is increased, it may grow in length until its overall maximum volume is achieved. When this occurs, some leakage beneath the ice roughness will result until the equilibrium volume is reestablished. Equation 3.9 has a theoretical maximum value for freestream Froude Numbers. When Froude Numbers exceed this critical number, which is approximately 0.5, the slick is no longer capable of maintaining the required thickness and a failure occurs at the crest of the head wave. The result is that total flushing of the slick will take place since the head wave must be continually recharged by the remaining oil in the slick in an attempt to maintain the increased thickness. This failure is totally independent of the relief in the ice; therefore, it is possible for a failure to occur for high enough currents under any magnitude of ice relief.

In deep water, Equation 3.10 simplifies to give an expression for the deep water head thickness as:

$$\delta_{\text{head}} = \frac{U^2}{2 \Delta g}. \quad (3.11)$$

The maximum size of the head thickness is limited by the formation of a Kelvin-Helmholtz type instability. This occurs when:

$$U_w = 2.2 \left\{ 2 \left(\frac{\rho_o + \rho_w}{\rho_o \rho_w} \right) \left[\sigma_{o/w} g(\rho_w - \rho_o) \right]^{1/2} \right\}^{1/2}. \quad (3.12)$$

In the viscous region the oil grows from the neck which is approximately half of the head thickness, to some tail thickness. In deep water the shape of the curve is parabolic. In subcritical flow situations, the slick tail thickness can generally grow to equal the ice roughness height. At critical flow, when an instability develops, the tail thickness and the head thickness are forced to be equal. In general the slick length is given by:

$$X = \frac{4 \Delta g}{f_s U_w^2} (\delta_{\text{tail}}^2 - \delta_{\text{neck}}^2) . \quad (3.13)$$

Estimates for values of f_s range from 0.007 to 0.032 [8, 4]. The slick length decreases with increasing velocity.

Because the curvature of the shear region interface is very slight, the volume per unit width of the contained slick can be taken as the trapezoidal area bounded by the tail thickness and the neck thickness of the slick. The added volume of the head wave can generally be ignored since it is taken to be only 10 to 20 slick thicknesses in length in comparison to the length of the shear region which would typically be meters in length.

When the stability of a frontally trapped slick fails, some of the oil will be carried downstream with the current. The majority of the oil however will initially rise due to its buoyancy into a shadow, or wake, zone on the lee side of the roughness element formed by the current flow separating at the tip. Because there is no strong opposing flow as in frontal trapping, the captured oil will assume its equilibrium thickness, spreading toward the end of the shadow zone. This behavior is suggested in Figure 3.3. Experimental investigations have indicated that the length of the wake region in deep water can be described by [25]:

$$\xi = \frac{C_D}{0.11} \eta , \quad (3.14)$$

where C_D is the form drag coefficient of the roughness, and η is the roughness height. For a flat plate, C_D is 1.98, which gives a wake length to roughness height ratio of 18. Triangular shaped roughness elements are more streamlined, with C_D equal to 1.55. The wake length ratio is then reduced to 14 for triangular elements.

In depth dependent cases, the wake length varies according to [21]:

$$\frac{\xi}{\eta} = 18.13 - 31.67 \frac{\eta}{D} , \quad (3.15)$$

for blockage ratios, η/D , less than 25%. For blockage ratios greater than this value, the wake length roughness height ratio approaches a constant value equal to 8.

Oil which gathers in the wake will not be able to span any further than the wake length since the reattaching freestream flow will tend to tear any excess oil away at that point. The maximum volume of oil trapped in a wake would therefore be expected to be that required to fill the wake length to the smooth ice equilibrium thickness.

When oil encounters a field of rough ice, as would most often be the case, the oil will begin to pool in the cavities formed by the roughness. Depending on the size of the cavities, the pooling of the oil may be controlled by frontal

456

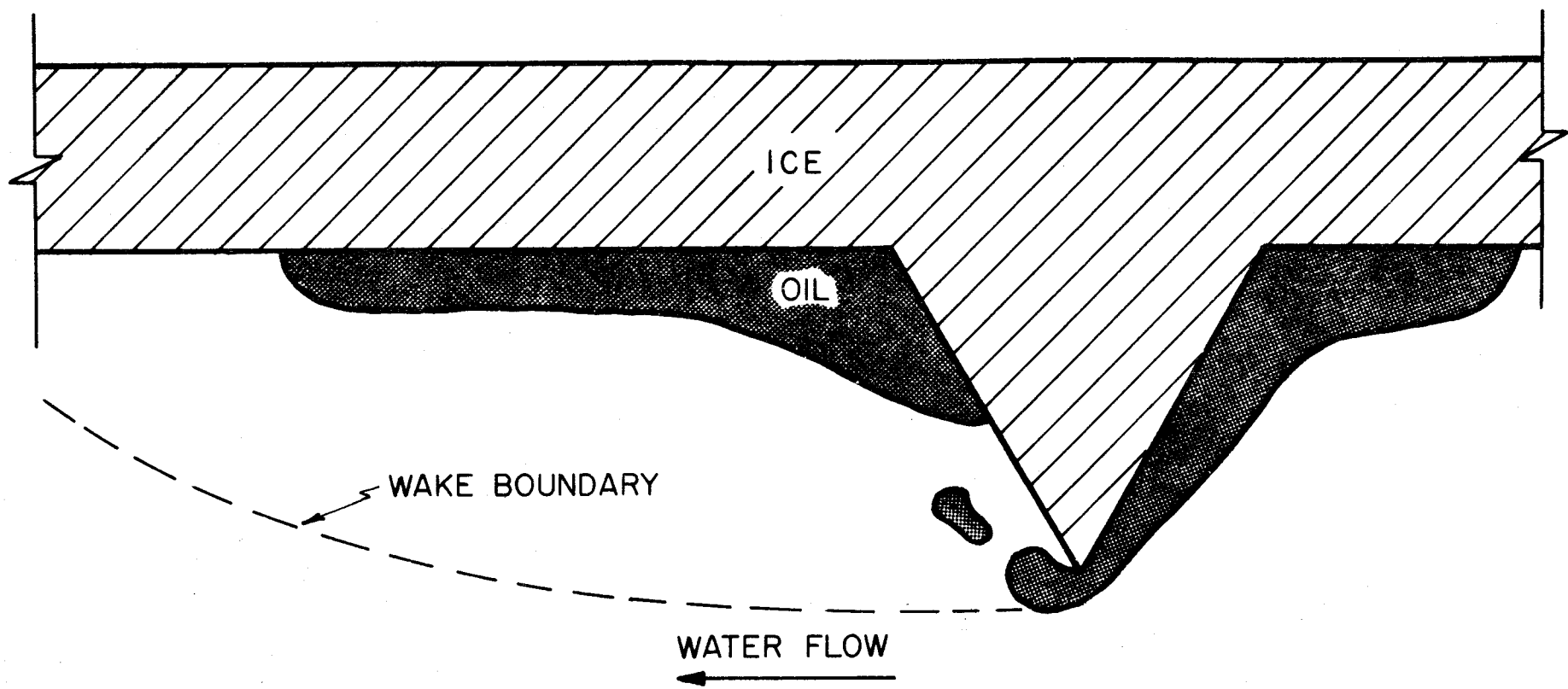


Figure 3.3. Sketch of Oil Leakage From Upstream of a Large Roughness Element to the Wake Region Behind the Element

trapping of oil, wake trapping of oil, or a combination of both. The two former cases have already been considered. In the latter case a portion of the trapped slick will be controlled by a separated vortex zone caused by the upstream presence of ice roughness. The rest of the slick will be controlled by shear stress acting on the oil-water interface, analogous to the viscous region which forms ahead of a single large ice roughness feature. This control is suggested by Figure 3.4. As current speeds increase, turbulent eddies grow in strength in the vortex cell, carving deeper into the trapped oil-water interface.

Beyond the vortex zone, the interface will grow parabolically toward the back wall according to the deep water viscous relation:

$$X = \frac{4 \Delta g}{f_s U_w^2} (\delta_{\text{tail}}^2 - \delta_{\text{stagnation}}^2), \quad (3.16)$$

where $\delta_{\text{stagnation}}$ is the thickness of the oil behind the vortex zone. If the vortex cell cuts deeply enough into the cavity, the shear zone interface can no longer remain parabolic, and drainage of oil will occur until the interface has retreated high enough into the cavity to form a new stable parabolic interface. The depth of penetration, ϵ , of the vortex cell will have to be found experimentally. Ultimately the cell will penetrate the entire depth of the cavity and divide the slick into separate frontal and wake contained slicks.

3.2 Vertical Migration of Oil Through Ice

Sea ice, particularly young sea ice, is very porous, possessing numerous vertical brine channels. If the oil slick advance has been halted, the oil is then free to begin to rise through those brine channels due to its buoyancy. If this takes place during a freezeup period, some oil may rise to some height in these channels, and the remainder of the oil will be surrounded by new growing ice and end up in the form of a lens of oil within the ice sheet. Once oil becomes impregnated into the ice cover, release will not occur until thaw begins and the brine channels begin to open up allowing the oil to rise to the ice surface.

The minimum diameter of a brine channel open to the ice surface which will allow vertical oil migration is defined from a balance between buoyancy forces and interfacial tension as follows:

$$d_{\text{inception}} = \frac{4 \sigma_{o/w}}{\delta} \frac{\cos \alpha}{(\rho_w - \rho_o) g}. \quad (3.17)$$

The diameter is strongly dependent on the interfacial tension between the oil and water, and upon the underlying oil slick thickness, δ . It is weakly dependent on contact angle, α , between the oil and ice. If a typical trapped slick thickness is taken to be 3 cm, then for $\sigma_{o/w} = 30 \text{ dn/cm}$, $\alpha \approx 30^\circ$, and $(\rho_w - \rho_o) = 0.1 \text{ gm/cc}$, a typical $d_{\text{inception}}$ would be 0.35 cm. Lake and Lewis [10] suggest that typical brine channel openings range in diameter from 1 cm for

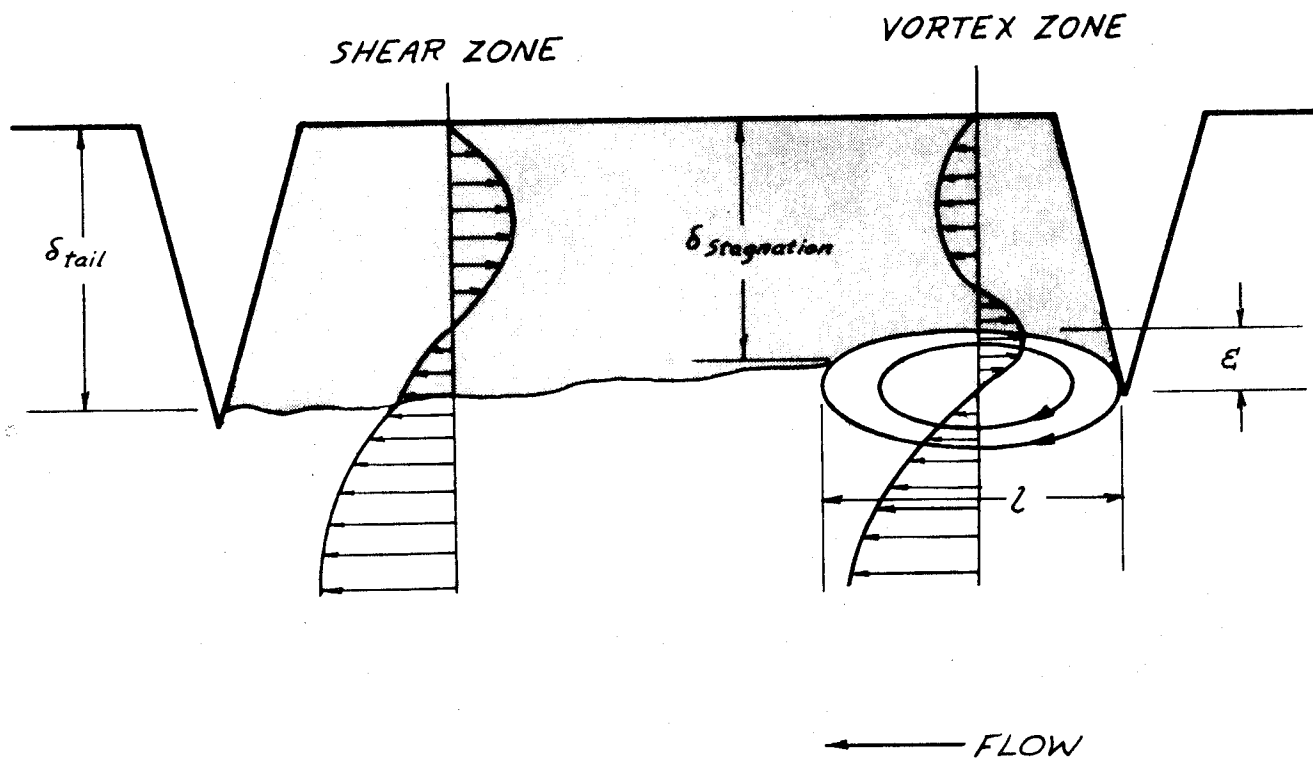


Figure 3.4. Generalized Description of Oil Contained in an Ice Roughness Cavity Under the Influence of a Current

multi-year ice to 2 to 3 mm "necks" in young ice. In this case, an oil thickness of 1.4 cm would be required for inception of migration in multi-year ice. In first year ice a 7.0 cm thick oil slick would be needed for migration to start.

The rate that oil can migrate up through the ice is determined from the pressure drop which takes place in the capillary. This rise velocity is given as:

$$\bar{u}_2 = \frac{(\rho_w - \rho_o) g \delta d^2}{32 L \mu_o} \quad (3.18)$$

By again assigning typical values of $(\rho_w - \rho_o) = 0.1$ gm/cc, $\mu_o = 50$ cp, picking $d = 1$ cm, and assuming that the ratio of the slick thickness to the ice thickness is approximately 0.01, a rise velocity can be predicted to be $\bar{u}_2 \approx 0.086$ cm/sec. Also, since oil and ice have approximately the same density, oil should generally rise completely to the ice surface, and pool on the ice.

It appears that for typical sea ice, as soon as thawing of the brine channels have allowed them to enlarge to diameters not greater than 1 cm, migration can occur and will occur very rapidly. Equation 3.19 determines when the diameter of a brine channel will thaw enough to allow migration to occur under quiescent conditions:

$$d = 3.05 \left(\frac{\theta T}{N' L^2} \right)^{1/2} \quad (3.19)$$

Here d , the diameter, and L , the ice thickness are in centimeters, θT is in thawing degree-seconds, and N' is the number of brine channels per square centimeter. For an ice thickness of 35 cm, an inception diameter of 0.75 cm, and a channel spacing of 1 channel per square centimeter, vertical migration of oil with a surface tension of 30 dn/cm should be possible after 74 thawing degree days.

4. SUMMARY OF EXPERIMENTAL PROGRAM AND PROCEDURES

To verify the theoretical development presented in Section 3, and to establish values for experimental coefficients, experiments were conducted in ARCTEC's glass walled Ice Flume. The experimental program was concerned with the horizontal transport of an oil slick under an ice cover.

4.1 Selection of Test Oils

The majority of the projects carried out in investigating oil spills under arctic conditions have understandably used typical crude oils obtained from land wells. However, the properties of these crude oils vary significantly between the different oil fields, and even the properties of oil obtained from a single well can vary drastically from sample to sample. Furthermore, the primary area of concern for this study is the nearshore and offshore Alaskan Beaufort Sea where exploratory drilling has not yet begun and the geological formations are thought to be different than the shoreside formations. Therefore, in order to make the oil-ice interaction relations as general as possible, it seemed prudent to use a variety of processed or refined oils of known repeatable physical properties having a wide range of viscosity. The oils selected for use were a No. 2 fuel oil, two No. 4 fuel oils obtained from different suppliers and designated as No. 4E and No. 4S, a No. 5 light oil, and a No. 5 heavy oil. The range of viscosity for these oils measured at 0°C varied from 7 centipoise to approximately 3,000 centipoise. This upper value of viscosity falls short of the viscosity of many typical crude oils, which generally have a viscosity approaching 30,000 centipoise. The pour point of refined oils having viscosities in the range of 30,000 centipoise was well above the freezing point, however, and therefore were unsuitable for test purposes. The target values of test oil properties are listed in Table 4.1.

Acquiring these different oils proved to be more difficult than anticipated, particularly since the volume of oil required to carry out the test program was relatively small, and most of these oils are only used in bulk and therefore not sold in small quantities. It was also discovered that a No. 5 heavy oil is no longer refined by the oil companies due to the effort to cut down on the potential pollutants that this heavy oil might produce. It was therefore necessary to mix a No. 5 heavy oil through a combination of a No. 5 light oil and a No. 6 oil so that the viscosity at 0°C would be near the target of 3,000 centipoise.

A viscosity blending chart was used to estimate the percentage of No. 5 light oil and No. 6 oil to be mixed. The oils would not mix thoroughly at low temperatures, so it was necessary to heat the oils to 50°C prior to combining them. The oil obtained from this mixture was then chilled to 0°C and viscosity measurements made. If the oil viscosity was not near the target of 3,000 centipoise, the mixing process was repeated, changing the component percentages. A solution of 60% No. 5 light oil and 40% No. 6 oil resulted in approximating No. 5 oil with the desired viscosity.

TABLE 4.1 TARGET OIL PROPERTIES

OIL	VISCOSITY @ 0°C (poise)	DENSITY @ 0°C (gm/cc)	POUR POINT (°C)
No. 2	0.15	0.87	-18
No. 4	1.50	0.91	-18
No. 5 Light	3.0	0.93	- 9
No. 5 Heavy	30.0	0.95	- 9

4.2 Scaling Considerations

Because the properties of the oils used in the experiment are full-scale by nature, it was necessary to perform the entire program as a full-scale test. In order to verify that the tests were actually run at full-scale, a comparison of laboratory and field conditions is required.

The primary driving force in the spreading of oil under ice is the shear stress applied to the oil by the water current. Therefore, to verify that the laboratory tests are, in fact, full-scale, a comparison of shear stresses existing in the test flume and in the field is necessary. This information requires that a determination be made of the velocity profiles under both field and laboratory ice sheets.

McPhee and Smith measured velocity profiles in a study of the planetary boundary layer beneath a multi-year ice sheet off the north coast of Alaska [18]. Current speeds were measured at 2 meter increments beneath the ice. In approximating the velocity profiles by a logarithmic curve and extending this curve up to the under-ice surface, the velocity at any point beneath the ice can be determined for a given mean current speed. Using this information, a friction velocity at the ice, U_* , can be calculated from the relationship:

$$U_* = \frac{\kappa(U_4 - U_2)}{\ln 2} , \quad (4.1)$$

where $\kappa = 0.35$, the terms U_4 and U_2 are the water velocities at 4 m and 2 m below the ice cover, and the 2 in the denominator is the spacing between the readings. This friction velocity is then substituted into an expression yielding shear stress at the water-ice interface:

$$\tau_b = \rho_w U_*^2 . \quad (4.2)$$

McPhee and Smith computed shear stresses by this method with a range from 0.273 to 1.38 dynes/cm².

Similarly, velocity profiles were measured in the laboratory flume as reported in Appendix E. The data points were approximated by a best fit power curve of water velocity as a function of distance from the bottom of the ice sheet. The average exponent for six profiles is 0.140 which corresponds to the exponent used in the one-seventh power law for the velocity distribution in the boundary layer of a flat plate. Therefore, flow beneath the ice sheet in the flume can be described by this power law. The shear stress along the ice for this type of profile is given by Schlichting as [25]:

$$\tau_b = 0.03955 \rho_w (U_w)^{7/4} (\nu)^{1/4} (D_H)^{-1/4} . \quad (4.3)$$

This relationship can be used to compute the shear stress for any mean water velocity. In this expression, ρ_w is the water density, U_w is the water velocity, ν is the kinematic viscosity of the water, and D_H is the hydraulic diameter of the flume.

A shear stress of 1.38 dynes/cm² occurs in the flume when the average velocity reaches 23.86 cm/sec. This is roughly the observed free stream current measured under ice in the field by McPhee and Smith. This suggests that the magnitude of shear stress in the field and in the flume are comparable over the same range of currents. The laboratory results can therefore be correlated by matching shear stresses, and in a qualitative sense by matching currents directly.

4.3 Static Equilibrium Thickness of Oil Under Ice

Preliminary tests were conducted to determine the equilibrium thickness of oil beneath smooth ice in a static condition. A smooth ice sheet 25 mm in thickness was grown in the flume, and the properties of the oil, ice and water were measured.

Four different oils were tested in this experiment, including No. 2, No. 4E, No. 5 Light, and No. 5 Heavy oil. The oils were injected in quiescent water through a hole in the ice sheet using the piston injector shown in Figure 4.1. They were allowed to spread and settle to their equilibrium thickness. After one hour, the thickness of each oil was measured by several different methods. One method of obtaining oil thickness was to align the oil interface visually through the glass walls of the flume with the jaws of a vernier caliper. A second approach was to cut a hole in the ice next to the slick and measure a combined oil and ice thickness directly with a vernier caliper. By subsequently measuring the ice thickness independently, the static oil thickness could be calculated.

A final approach was to insert a calibrated probe under the ice and up into the oil. The scale was raised vertically through the oil until contact was made with the ice and the thickness was read directly from the scale.

The oil recovery process was quite simple for this test. By turning on the pump and creating a flow, the oil moved downstream to the tail tank. Once in the open water of the tail tank, the oil was recovered using a weir-type skimmer and oil absorbent cloths.

4.4 Oil Under Smooth Ice

The experiments for this investigation were conducted in the insulated glass walled ARCTEC Ice Flume which is described in detail in Appendix F. The first step for each test was to freeze an ice sheet in the flume using ARCTEC's patented liquid nitrogen freezing system. The freeze was controlled remotely from a control room.

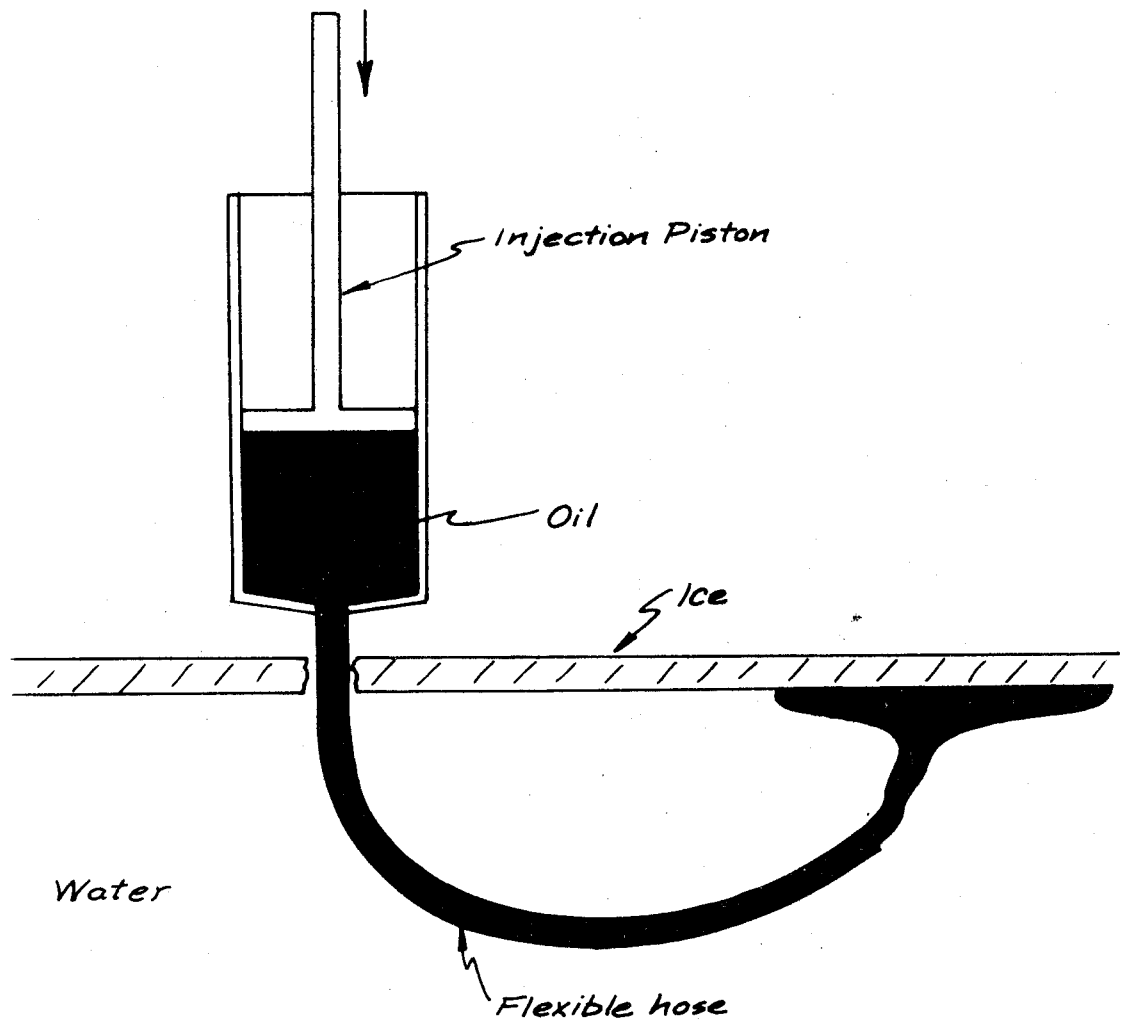


Figure 4.1. Section View of the Piston Injector

Once the ice sheet had formed and the flume insulation had been removed, the test team began to collect pre-test data. Oil properties were measured daily to ensure that no property variations occurred due to aging, temperature changes, or nonuniformity of oil samples. The oil properties measured were viscosity, density, and temperature. All of the measurements were taken inside the refrigerated area where the oil was maintained at 0°C. The oil viscosity was measured with a Brookfield synchroelectric viscometer, model LVF, as described in Appendix F. Oil density was measured with two specific gravity scale hydrometers, and oil temperature was measured with an ASTM approved -20°C to +10°C thermometer accurate to 0.1°C. Other pre-test data taken included air and water temperature, water depth, and ice thickness. Air and water temperatures were also measured with the ASTM approved thermometer. A hole was cut in the ice near the head tank of the flume for the measurement of water depth with a meter stick accurate to 0.5 mm, and ice thickness was measured with a vernier caliper.

Occurring simultaneously with the collection of pre-test data was the installation of test apparatus and instrumentation. The work carriage, described in Appendix F, was mounted on the rails of the flume. The work carriage served as a portable platform for various pieces of instrumentation. A pointer bar was attached to the carriage so the leading edge of a moving oil slick could be visually followed downstream. A magnetic read switch and a DC tach generator were mounted on the work carriage to measure both instantaneous and average oil slick velocity. The photographic equipment used for test documentation was also mounted on the work carriage. A Millikan high speed movie camera was installed on the top of the carriage to take overhead movies of the advancing oil slick. A 35 mm camera was hung from the side of the carriage to take still shots of the slick thickness and oil-water interfacial waves. A string of fluorescent lights was placed at the bottom of the glass walls down each side of the flume. The lights provided for good test visibility and illumination of the under-ice surface for the cameras.

An Annubar flow sensor, described in Appendix F, was inserted into the return pipe of the flume. The Annubar is an annular averaging velocity head sensor for the measurement of flow through a pipe. The Annubar was connected to its readout devices, two parallel Eagle Eye flow meters. These precalibrated meters give the flume flow directly in gallons per minute. A meter tape was laid down the center of the ice sheet as a reference for slick dimensions and slick velocity.

Once the flume apparatus was installed and the oil properties measured, the test began. An upstream hole was cut in the ice sheet at the first glass section of the flume. The oil injection cylinder, shown in Figure 4.2, was inserted in the hole. The cylinder was filled with 15 to 20 liters of oil. To maintain the same water level beneath the ice sheet, 15 to 20 liters of water were simultaneously removed. The flume pump was started and the flow rate was set to the desired level. All of the instrumentation was turned on and the carriage was rolled into position. The injection cylinder was removed from the hole, resulting in an instantaneous release of oil under the ice with no horizontal velocity component. If the flow rate was not sufficient to move the

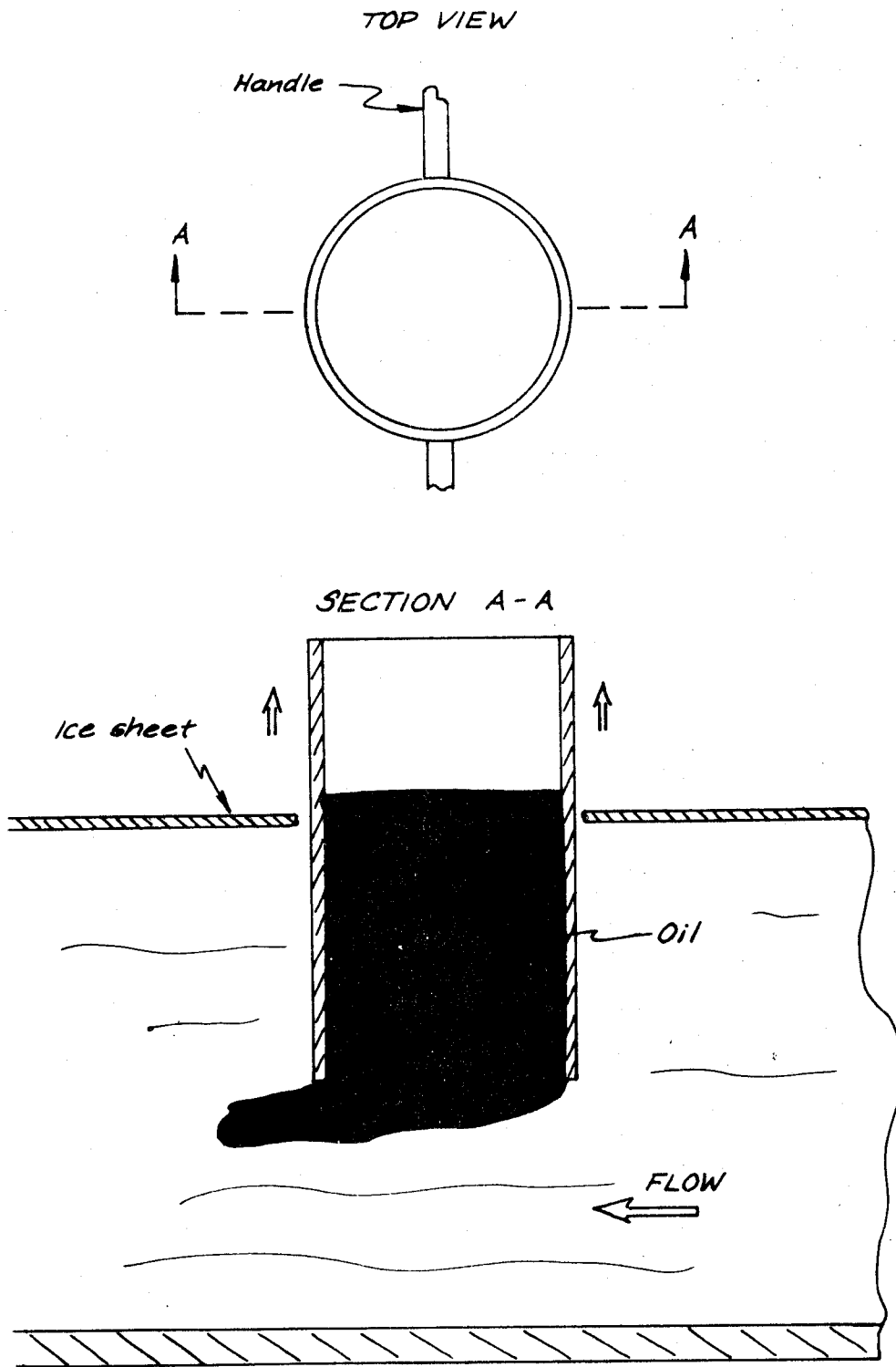


Figure 4.2. Sketch of Oil Injection Cylinder

oil slick, the flow rate was increased to the next level specified in the test plan. The water velocities used in this experiment were typically 5, 10, 20, and 30 cm/sec. At 30 cm/sec the flume pump was running at nearly full capacity for the water depth used.

As the slick moved downstream, the carriage pointer was kept aligned with the leading edge of the slick thereby following the oil downstream. The movie camera, mounted on the carriage, was turned on and operated throughout the test. The carriage mounted movie camera automatically took overhead shots of the changing slick configuration, while profile shots of the oil thicknesses and oil-water interfacial waves were manually taken from the side of the flume. The entire test was documented with the use of a tape recorder.

The test concluded when the oil slick reached the tail tank of the flume. After all of the instrumentation was turned off, oil recovery and cleanup began. The water in the tail tank was insulated during the freeze so that this area remained ice free. A weir type skimmer was used to remove 95% of the oil. The remaining oil was cleaned up with oil absorbent cloths.

4.5 Oil Interaction with Small Ice Roughness Elements

The next phase of the experimental program was concerned with the horizontal transport of oil under an ice sheet containing small roughness elements. Two different roughness patterns were created in the ice sheet. One roughness consisted of tiny undulations 1 to 2 millimeters in amplitude, spaced 4 centimeters apart. This roughness was created by fastening strips of high density styrofoam on the water surface before the freeze. As the freeze progressed, the styrofoam strips insulated the water, causing localized retardation of ice growth. The ice grew to a nominal thickness of 25 millimeters, and 1 to 2 millimeter roughness elements appeared underneath the ice sheet. The second roughness pattern had undulations 1 centimeter in amplitude, spaced 4 centimeters apart. The undulations were made by melting grooves in the ice with heated steel rods. These rods, each 1.27 centimeters in diameter, were mounted on a frame spaced four centimeters apart. The rods were heated with an oxy-acetylene torch and pressed into the surface of the ice sheet. Six meters of rough ice were created in this manner. The ice sheet was cut free from the sides of the glass walls and flipped over, positioning the undulations on the bottom of the ice as shown in Figure 4.3. All cracks and holes in the ice were sealed by refreezing using carbon dioxide gas.

The No. 4E and No. 5H oils were selected for this segment of the test program because of their wide viscosity range. No. 2 oil was not used because it caused the ice sheet to deteriorate more rapidly.

Once again, all of the pre-test data was gathered. In addition to the pre-test data collected in the smooth ice experiment, data on ice roughness was also obtained. The period and amplitude of the undulations were measured with a vernier caliper.

The only change in test apparatus occurred in photography. The high speed movie camera which was used in the smooth ice test for overhead photography was replaced by a hand-held 16 mm Canon movie camera. The camera was operated manually from the side of the flume. Profile movies of the oil slick were taken to visually document the slick waves propagating downstream from one undulation to the next.

The tests of oil transport with small roughness elements were conducted in the same manner as the oil under smooth ice experiments. Oil recovery was, however, more difficult with rough ice. The flow rate had to be increased significantly to flush out the oil which was trapped within the undulations. Once the oil was in the tail tank, the weir skimmer and oil absorbent cloths were again used for oil removal.

4.6 Oil Interaction with Large Ice Roughness Elements

This test segment involved the interaction of oil with large, two dimensional roughness elements. A large roughness element, shown in Figure 4.4, is defined as any protrusion from the ice whose amplitude is greater than the equilibrium slick thickness of the oil. To make this roughness, molds were fabricated from sheet metal, riveted together, and sealed with hypalon caulking. By freezing water in the molds, large roughness elements in either a 32° wedge shape, or having a 90° keel, were obtained. The keel depth varied from 8 cm to 12 cm.

Once the roughness element was removed from the mold it could be inserted into a smooth ice sheet as shown in Figure 4.5. A slot was cut in the ice sheet and the roughness element was placed in the void. Carbon dioxide gas was used to freeze the roughness element in place and seal any cracks between the roughness element and the level ice sheet. Once installed, a two-dimensional roughness element was formed across the flume.

Three different configurations were tested. One roughness type had a keel depth of 8 cm and a keel angle of 32°. The second roughness type had a 12 cm keel depth with the same 32° keel angle. The last roughness type used in the experiment had an 8 cm keel depth and a keel angle of 90°.

Following the same pre-test procedures as described for the previous tests, the flume was prepared for the test and the oil properties measured. Additional measurements were made on the dimensions of the installed roughness element.

Two changes were made in test apparatus. The work carriage was eliminated since the point of interest was now stationary. All photography was taken from a fixed location alongside the flume. The oil injection technique was also altered.

Once all the pre-test procedures had been completed, a hole approximately 10 cm in diameter was cut in the ice sheet. The hole was located 2 m upstream

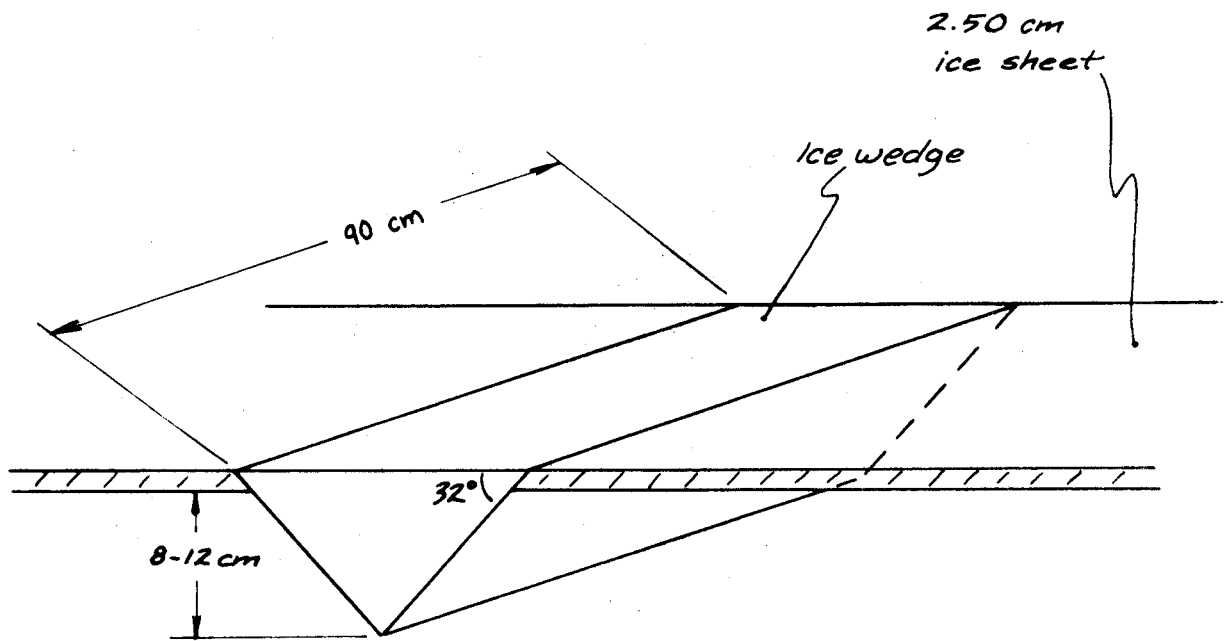


Figure 4.4. Schematic Representation of a Large Roughness Element

of the roughness element. The flow rate in the flume was fixed at 700 gpm. The oil was then simply poured from a graduated cylinder through the hole and underneath the ice. This oil injection procedure allowed an easy means for accounting for the amount of oil injected.

The oil moved slowly downstream and stopped at the barrier. Once the entire slick had migrated against the roughness element, the flow rate was increased slowly. When the flow rate reached a critical point, the slick became unstable. Small drops of oil were torn from the head wave of the slick and leaked under the roughness. When this droplet failure occurred, the flow rate and slick dimensions were documented. The flow rate was then increased further until the entire slick started flushing under the roughness element. When flushing failure occurred, the flow rate was recorded and the test concluded.

Oil recovery was a more difficult procedure in this experiment. Some of the oil that had flushed under the roughness element became trapped in the shadow zone downstream of the roughness element. Increasing the flow rate would not dislodge all the oil from the shadow zone. A hole was then cut in the ice downstream of the roughness element to gain access to the trapped oil. The majority of the oil was recovered from the hole by direct suction or the use of a weir-type skimmer. The remaining oil was cleaned up with oil absorbent cloths.

A portion of this test segment included oil interacting with porous roughness elements. Molds in the shape of an open ended triangular prism were constructed to make these roughness elements. The molds were lined with plastic bags to waterproof them, filled with nut ice approximately 2.5 cm square, and placed in an insulated container where they were subjected to a one-hour freeze with liquid nitrogen. Additional misting with water increased the strength of the element. When the freeze terminated, the molds and plastic bags were removed from the ice, resulting in porous wedge shapes. By weighing these and comparing their weight to the weight of solid ice, the porosity of each roughness element could be calculated. The porosity of the roughness elements obtained from this process varied from 20 to 40 percent. These porous forms were inserted into an ice sheet in the same manner as the solid forms, using carbon dioxide gas to freeze them in place.

4.7 Flow Pattern in the Wake of Large Ice Roughness Elements

As previously noted, the oil that was caught in the shadow or wake region downstream from the large roughness elements could not be quickly flushed out by simply increasing the flow rate through the flume. This test segment was directed towards establishing the size of the wake region and the flow pattern within the wake.

The large roughness elements were constructed, as described previously, by freezing water in a mold. The elements had a keel angle of 32° and varied in depth from 8 to 12 cm. In this test segment the elements were placed in the flume prior to the freeze and wedged into place. An ice sheet was then frozen over the flume, bonding the level ice directly to the roughness element.

The wake of the roughness element was mapped using a solution of potassium permanganate and water discharged into the flow field through a glass pitot tube. Holes were drilled in the level ice immediately upstream of the element and at intervals downstream from the element along the centerline of the flume. The glass pitot tube was inserted into the flow under the ice. The potassium permanganate dye was discharged through the pitot tube into the flow. The dye discharge was provided by gravity from a bottle suspended approximately 30 cm above the flume and regulated by a needle valve. The dye stream in the flow was observed visually through the glass walls of the flume. The depth of the probe beneath the ice was noted. The direction in which the dye was flowing, upstream or downstream, was also noted and recorded photographically on color slides and on 16 mm movie film using the hand-held movie camera. The edge of the region of counterflow, flow downstream of the roughness element moving in the upstream direction, was defined to be the location where the dye from the pitot tube appeared to move as much with the general flow as against it. The point where the free stream flow reattached to the level ice sheet downstream from the roughness element was defined to be the point where the dye, injected immediately beneath the level ice, moved as much downstream as upstream.

In addition to the dye injection procedure, the average flow field in the wake of a large roughness element was mapped using a Nixon velocity probe. The probe was inserted to various depths through the holes drilled in the level ice downstream from the element along the centerline of the flume. The water velocity was obtained by counting the number of revolutions of the small impeller over a fixed time interval and noting the direction of spin. The water velocity was obtained from a calibration curve relating the number of revolutions to the water velocity. Due to the highly turbulent nature of the flow, the vortices constantly being shed from the apex of the roughness element, and the counterflow set up by the eddy in the wake region, care and judgement were required in obtaining the velocity measurements. Mean velocity profiles measured at various locations in the wake are shown in Appendix E.

It should be noted that both the dye study and the study using the Nixon probe were conducted with water only. No oil of any kind was present in the wake during these tests. Fouling of the Nixon probe with oil prevented velocity measurements when oil was present. Therefore, the flow field observed in the wake may be slightly different from the actual flow field in the wake when oil is present.

4.8 Oil in the Wake of Large Ice Roughness Elements

This segment of the study was directed towards determining the volume of oil that would be trapped in the wake of a large roughness element subject to various current speeds. The elements had a keel angle of 32° and varied in depth from 8 to 14 cm. The roughness elements were wedged into place in the flume. An ice sheet was then frozen over the flume, bonding the level ice directly to the element.

Both No. 4 and No. 5 oils were tested to determine the volume contained at free stream velocities ranging from 15 to 30 cm/sec. Because of the blockage caused by the roughness element, the local current was higher. As in the previous test segments, the oil density and oil viscosity were measured taking samples from the oil used in the experiments. The No. 4 oil was injected using a Little Giant Tube Pump capable of discharging at a rate up to 4.8 gpm. The No. 5 oil was too viscous for the pump to handle so that it had to be poured from buckets through a funnel. The quantity of oil injected was determined by weighing the full oil containers before injection and the empty containers after injection.

The oil was injected through a hole drilled in the ice immediately downstream of the roughness element. The oil was injected while the free stream water velocity was held at 15 cm/sec. The length of the slick was measured from the downstream edge of the element where the level ice bonded to it. The dimensions were measured using a tape measure graduated in millimeters. The thickness of the slick was measured through the glass walls of the flume. The free stream water velocity was increased and, typically, some oil was lost from the wake region. The dimensions were measured again, after it appeared that the size of the oil slick had stabilized. The oil that was lost from the wake moved downstream into the flume tail tank, where it was recovered. The oil lost to the tail tank was weighed to determine the quantity lost.

In one test a hole was drilled in the level ice immediately upstream of the roughness element. The free stream water velocity was set at 30 cm/sec, which is greater than the head wave failure velocity found in the previous test segments. The oil was injected through this upstream hole to determine how much oil would become trapped in the wake region compared to how much would be transported downstream. After it appeared that the oil slick behind the element had stopped increasing in size the slick dimensions were measured with the tape measures. The quantity of oil that moved into the flume tail tank was determined.

As previously noted, some of the oil in the wake of the large roughness elements would not flush out quickly even at the highest possible flume discharge. It was then necessary to cut a hole in the level ice downstream from the element and dip the oil out by hand. The quantity of oil that could not be flushed was determined by weighing the recovered oil.

4.9 Oil in Cavities

This test segment was directed towards establishing the volume of oil that would be trapped between two roughness elements for varying free stream water velocities. The nominal element heights were 10 and 20 cm. The walls of the cavity were sloped at 32°. Nominal cavity lengths, the length of the level ice between the elements, were 0.5 m, 1.0 m, and 2.0 m. In some cases, when the cavity tests were conducted after the wake tests, the downstream element was positioned by cutting a slot in the level ice, inserting the element, and freezing it to the level ice with carbon dioxide. In other cases, the

roughness elements were wedged into place in the flume and the level ice was frozen around them.

Both No. 4 and No. 5 heavy oils were tested. The oil properties, density and viscosity, were measured for samples taken from the oil used in the experiments. The oil was injected through a hole drilled in the level ice between the two roughness elements. In the 0.5 m cavity the No. 4 oil was injected using the Little Giant Tube Pump. In the other cavity tests, the pump was too slow so the oil was injected by pouring it through a funnel. The No. 5 Heavy oil was too viscous for the pump to handle; therefore, it was poured through a funnel under the ice in all cases.

In the 0.5 m cavity the oil was injected while the free stream water velocity was maintained at 15 cm/sec. In the 1.0 and 2.0 m cavities, the oil was injected while there was no flow through the flume. In all of the tests the quantity of oil injected into the cavity was measured by weighing. The dimensions of the slick in the cavity were measured using a tape measure marked off in millimeters. The length of the slick was measured from the trailing edge of the upstream element. The thickness was measured from the bottom side of the level ice.

When the water velocity was increased, some of the oil would leak out of the cavity by spilling under the downstream roughness element. In the case of the more viscous No. 5 heavy oil, it typically required a time period of close to an hour for leaking to stop and a steady state condition to develop. The less viscous No. 4 oil did not take as long to reestablish an equilibrium volume, but still required as much as 15 minutes. After the oil had established a new equilibrium volume at the higher velocity, the dimensions of the slick were measured using the tape measure. Still and motion pictures were taken to record the appearance of the slick and its approximate dimensions. The presence and size of the oil slick in the wake of the downstream element were also noted.

Oil that had escaped from the cavity and the downstream wake was transported into the flume tail tank where it was collected and weighed. The oil that was not flushed out of the cavities was recovered by cutting out a section of the level ice between the roughness elements and dipping the oil out by hand. The quantity of oil that remained in the cavity was determined by weighing.

One final test series was run with a depression type cavity instead of the standard protruding cavity. This cavity was formed by placing a false floor flush with the tip of the ice roughness on the upstream side. The free stream flow then behaved as if the ice cover was smooth until it encountered the recessed cavity. The two cavity types are shown in Figure 4.6.

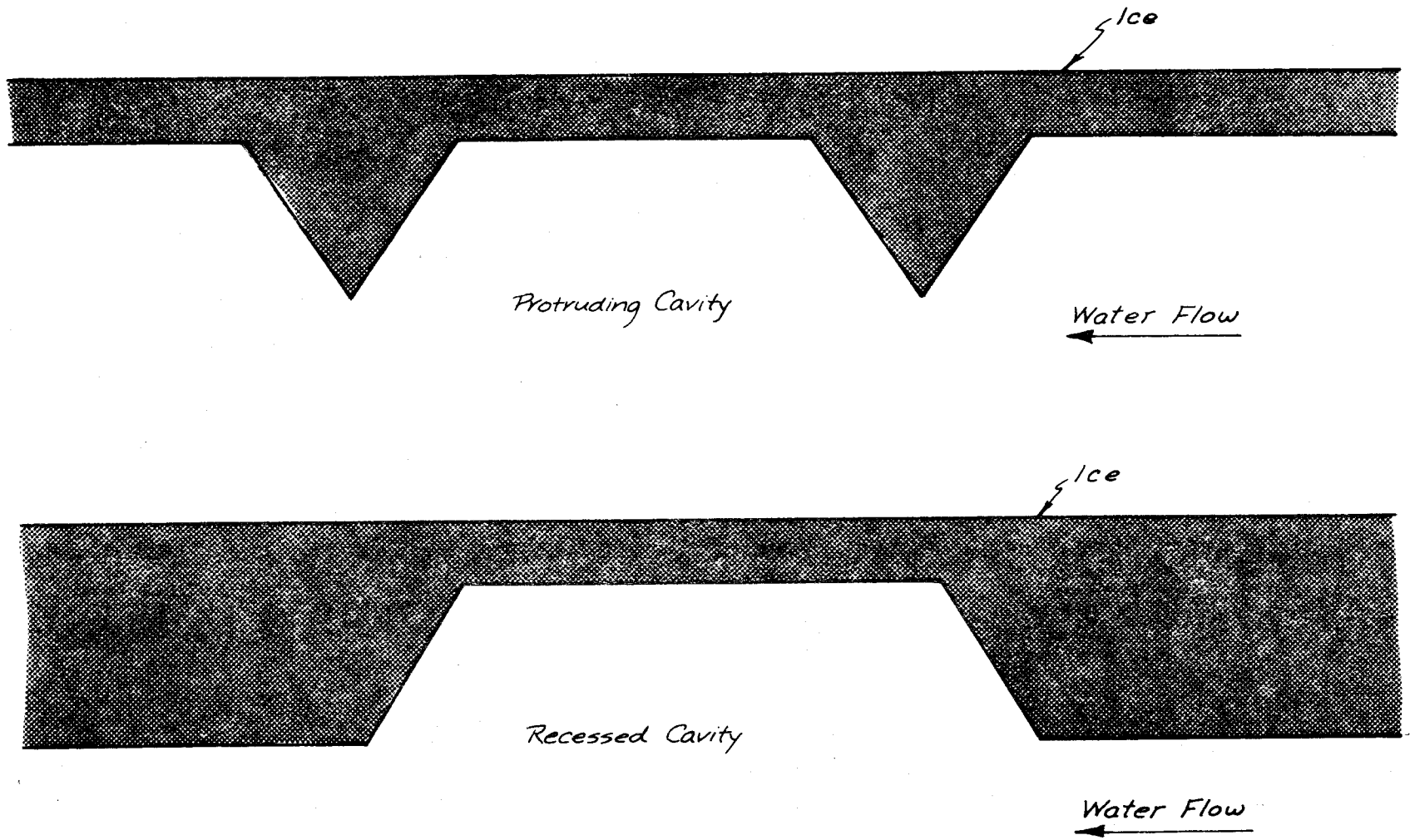


Figure 4.6. Sketches of Protruding and Recessed Cavities

5. TEST RESULTS

The test results obtained from this program, both qualitative and quantitative, are summarized in this section of the report. The test results are analyzed in the following section. The test results are separated into two sections with the first section consisting of a summary of general observations made throughout the test program, and the second section consisting of a summary of the quantitative data gathered during the program.

5.1 General Observations

5.1.1 Static Equilibrium Thickness of Oil Under Ice

Three of the four oils tested, the No. 4E, the No. 5 light, and the No. 5 heavy, showed smooth ice static equilibrium thicknesses of approximately the same magnitude, between 0.9 and 1.2 cm, appearing to depend basically upon the differences in their densities. Only the No. 2 fuel showed significant variation from this, with a very consistent thickness of 0.5 cm. It was difficult to measure the contact angles for any of the oils. However, all contact angles when measured outside the oil were acute, and were estimated to be about 45 degrees or less. The shape and thickness of the slick did seem to be related to the overall dimension of the slick. Small quantities of oil were able to form perfect spheres of oil with near zero wetting properties. As the slicks grew larger, they did wet the ice. There seemed to be a rim to each slick which was possibly one or two millimeters thicker than the center of the slick. As the slicks further increased in diameter, the thickness appeared to become more uniform throughout.

5.1.2 Oil Under Smooth Ice

The behavior of the four oils tested varied drastically, although the overall speed of advance of each oil slick was surprisingly close. No. 2 oil appeared to have the lowest threshold velocity, somewhere around 3 to 4 cm/sec estimated upon the relative ease of motion at a current speed of 5 cm/sec. The highest threshold velocity was about 7 cm/sec for the No. 5 Heavy oil, based upon the slick behavior at 5 and 10 cm/sec. It appears that the viscosity or rheologic properties of the very thick oil have some impact upon the threshold velocity. At low current speeds the slicks seem to maintain a basic circular configuration and move in a completely consolidated form downstream. As velocity was increased, the No. 2 oil slick would tend to stretch itself out longitudinally with the current. As velocities approached 30 cm/sec, the No. 2 oil was the easiest to break up into smaller slicks. The No. 4, the No. 5 light, and the No. 5 heavy oils tended to move in just the opposite manner, with the slicks tending to become elongated transversely to the flow. At high velocities the slick would deform further into a crescent shape. Small slicks would then tear from the ends of the crescent, and again both the parent and offspring slicks would orient themselves transversely to the flow.

At higher viscosities, significant interfacial phenomena were observed. With the No. 2 oil, rippling could be seen at the interface. The higher

viscosity oils also formed waves; for these oils, typically large waves would form at the tail of the slick and move forward until it reached the head of the slick where it collapsed, and then a new wave would form to repeat the process. No entrainment of any of the oils occurred for current speeds up to 30 cm/sec. In all cases, small diameter slicks were able to move with the current at significantly higher speeds than larger slicks. This would suggest that at least in some ways the oil does behave not as a solid but rather as a fluid, since the frictional drag between the oil and the ice would be increased for larger surface areas if the oil were treated as a fluid rather than a solid.

Occasionally discontinuities existed in the ice. These discontinuities were sufficient to drastically alter the speed of an advancing slick. When air bubbles were encountered by the moving slick, the presence of the air bubble was often sufficient to stop or slow down the advancing oil. The oil would tend to coat the bubble, probably because of the surface tension, until the entire bubble was surrounded by oil. Similarly, small depressions or protruding pieces of ice were often enough to stop the oil or force it to change its direction.

5.1.3 Oil Interaction with Small Ice Roughness Elements

Oil transported over small roughness elements demonstrated a dramatic reduction in the slick speed in comparison to the smooth ice case. For roughness of only 0.1 cm amplitude on 4 cm spacing, the threshold velocity of No. 4 oil was increased from about 4 to 12 cm/sec. The threshold velocity for No. 5 Heavy oil was increased from about 7 to 16 cm/sec. For a larger roughness of 1 cm amplitude and 4 cm spacing, neither oil moved downstream at a water current velocity of 10 cm/sec. By increasing the water velocity to 29 cm/sec, the No. 5 Heavy oil moved at a speed of 0.73 cm/sec, and the No. 4 oil moved at a speed of 2.13 cm/sec. For a somewhat larger roughness of 1 cm amplitude on the same 4 cm spacing the threshold velocities for No. 4 and No. 5 Heavy oils were 22 and 25 cm/sec respectively. The thickness of these slicks appeared to be approximately the same as the thickness of the slicks under smooth ice. Oil would fill into the roughness interstices, and a uniform layer of oil would build up over them. Larger slicks did not actually move in bulk over the rough surface, but rather advanced by dislodging from the ice at the tail of the slick and moving as a wave forward over the slick, and finally collapsing into a new roughness depression at the front of the slick. Small slicks on the other hand were able to maintain a spherical form and would bounce very quickly along the rough ice surface. This behavior can be detected in Figure 5.1.

5.1.4 Oil Interaction with Large Ice Roughness Elements

All four oils were tested for containment by large single roughness elements. Two different obstructions were used. One, a 90 degree barrier which presented a blunt surface to the oil, and the other an angular barrier with an angle of 32 degrees from the horizontal. A comparison of the containment between the two different roughness forms indicated that the slope angle of the roughness for the range covered has minimal impact on containment capability. As the

oil began to pool in front of the obstacle, a head wave began to form at the upstream end of the slick. This head wave was generally thicker than the slick further downstream. Due to test constraints, sufficient oil was usually not introduced to allow the slick to build totally to its equilibrium shape; therefore, failure would always occur in the head region. When oil would fail beneath the barrier, the failure occurred at generally the same Froude numbers for all the oils. This is because the failure is density dependent rather than viscosity dependent.

Two stages in the slick failure were observed. When the slick grew to its maximum thickness for a given flow speed, oil droplet loss was observed from the head wave. Since the loss rate was small, the measured dimensions of the slick were considered to be the equilibrium dimensions. This failure stage is shown in Figure 5.2. As the flow rate was increased further, the droplet loss developed into a total flushing loss. The oil completely flushed out upstream of the barrier so that after a short period of time there was absolutely no oil remaining upstream of the barrier. In this stage of failure, oil moved as a head wave under the barrier as shown in Figure 5.3. Some oil escaped with the free stream, and the rest was deposited immediately behind the barrier.

An upstream limiting slick length was measured in one test. For this case, both the head and the tail of the trapped slick achieved nearly the same dimensions prior to any failure. The tail seemed to grow in thickness faster than the head of the slick. However, the maximum tail thickness remained independent of the barrier depth and never grew in thickness to the tip of the barrier.

5.1.5 Oil Interaction with Porous Ice Roughness

Porous barriers could not permanently restrain oil upstream for any current condition. At lower free stream velocities, all the oils tested gradually migrated into the porous barrier and upward to their equilibrium height. The No. 2 oil, with a density less than that of the ice, totally surfaced and spilled out onto the surface of the ice. The volume of the pores in the ice barrier was sufficient to totally absorb the test oil slick.

Oil was never lost beneath a porous barrier. Even at current velocities well above those which would cause flushing for a solid barrier, the oil still worked into the barrier rather than under it.

When the current speed reached 30 cm/sec, some oil could be driven through the pores, however the leakage rate was very low. This is due to the tremendous pressure loss that occurs as the oil meanders through the ice pores. In the field where the breadth of a porous barrier would be much greater, leakage would probably not occur due to the friction losses in the crevices.

Any oil that managed to leak through the porous barrier became captured in the wake region, analogous to the consolidated case. A porous barrier apparently can trap oil downstream, even though it cannot do so upstream. Whether the dimensions of this wake differ substantially from the solid barrier could not be determined based upon the visual observations alone.

5.1.6 Behavior of Oil in Wakes

Two oils, No. 4S and No. 5 heavy, were tested for containment within the wake region behind a single large roughness element. The shape of the roughness element was triangular, with the slope of the element making an angle of 32° from the horizontal. The nominal height of the element was 10 centimeters. Dye studies and velocity profiles made in the wake region indicated that the end of the wake was roughly 80 cm behind the tip of the roughness, which was much less than expected. Observations of the behavior of the impeller blades on the Nixon velocity probe showed that the flow pattern in the wake was highly erratic, with the flow changing direction and velocity rapidly and continuously, rather than a clean, well behaved, reverse circulating cell.

When oil was injected into the wake, it was observed that the oil could spread roughly to the apparent end of the wake as long as the slick was continuously fed with oil. Once the oil feed was shut off, the length of the slick was reduced to not more than roughly 30 cm behind the back edge of the roughness, which was roughly 45 cm behind the tip of the roughness. Over a long period of time, on the order of an hour, even this oil gradually dissipated. In all cases the oil was observed not to exceed the equilibrium thickness except immediately behind the roughness where the reverse mean flow would pull the oil partially down the back face of the roughness element.

Two kinds of failure modes were observed for oil trapped in the wake. When the volume of the oil in the wake was too large, draining of the oil would occur at the downstream end, with the oil being torn away by the reattaching free stream. When currents were high, a strong reverse flow would push the oil down the back face of the roughness element and small drops of oil would be torn away at the tip of the roughness and carried into the free stream.

When oil was allowed to flush upstream of a roughness element, it was estimated that 60 to 75% of the oil settled into the wake region, and the rest was immediately carried away by the free stream.

Wakes observed when the mean current was on the order of 15 cm/sec or less appeared to be much more stable, allowing oil to stay constrained from moving for longer time periods.

5.1.7 Behavior of Oil in Cavities

Containment of No. 4S and No. 5 heavy oil was observed in cavities of 2 m, 1 m, and 1/2 m lengths, and 10 and 20 cm depths. The cavities were formed by positioning two triangular shaped ice blocks beneath a smooth ice cover. When the cavities were filled under static conditions it was never possible to take advantage of the meniscus effect and overflow the cavities. The oil was never observed to be thicker than the depth of the cavity. As the free stream velocity was increased, the shape of the interface deformed slightly. Depressions in the interface were observed behind the upstream tip and at the downstream end of the cavity. The oil always remained attached to the tip. Minimal

leakage of oil occurred for low velocities. Not until the local flow approached 10 cm/sec for the No. 5 heavy oil and 15 cm/sec for the No. 4 oil did a significant change in the interface occur. At these speeds the depression or offset behind the upstream tip became more pronounced. For No. 4 oil, the length of this offset in the interface was very distinct in terms of a reduced thickness as shown in Figure 5.4. This length correlated well with the location of the formation of waves on the No. 5 heavy oil interface. As the freestream velocity was increased further, the offset continued to grow and the position of the tail of the slick gradually retreated from the tip of the downstream wall up into the cavity, resulting in a major release of oil. A new stable oil-water interface position was observed for every flow speed until the offset was sufficient to pierce the slick, separating the oil into two individual slicks. The amount of offset that formed seemed to be relatively independent of the length of the cavity, and quasi-independent of the depth of the cavity.

Flow in the cavities whose lengths were comparable to the wake length seemed to develop a more stable behavior. Some oil remained trapped in these cavities even for very high current speeds, up to 40 cm/sec.

For each current speed there appeared to be some natural equilibrium volume of trapped oil. Once the oil had leaked to that equilibrium volume, surging or cycling of the free stream flow did not result in any further leakage. The oil slick simply adjusted its shape to accommodate the change in current, shifting some of the oil to one end of the cavity or the other.

In one series of tests a recessed cavity under the ice was modeled by masking the ice roughness with a false cover. The containment of oil for these tests was qualitatively the same as for the protruding cavities.

5.2 Summary of Quantitative Data

Table 5.1 summarizes the pre-test oil property data measured prior to the start of the test program. The table includes all of the oils associated with the test program. The oils directly employed in the testing included a No. 2 oil, two No. 4 oils designated as No. 4E and No. 4S, a No. 5 light oil, and a No. 5 heavy oil. Also listed is a No. 6 oil which was combined with the No. 5 Light oil to approximate the properties of a No. 5 heavy oil. The oil properties measured included viscosity, specific gravity, and temperature. Note that the properties listed in Table 5.1 were obtained while the oils were at temperatures of 22 to 50°C.

Table 5.2 lists the results of the static equilibrium oil slick thickness under smooth ice experiment. The four oils were injected under a smooth ice sheet and allowed to spread to their equilibrium thickness. The thickness of each oil was measured several ways. The preferred method involved boring a hole in the ice adjacent to the oil and directly measuring the ice and slick thickness with a vernier caliper.

Table 5.3 summarizes the results for the test segments defined as oil under smooth ice and small roughness ice. The table contains the test oil

TABLE 5.1 PRE-TEST OIL PROPERTIES

OIL TYPE	OIL VISCOSITY (poise)	OIL TEMPERATURE (°C)	OIL DENSITY (gm/cc)
2	0.051	25.0	0.847
2	0.051	25.0	0.847
4E	0.262	25.1	0.895
4E	0.261	25.1	0.895
4E	0.264	25.1	0.895
4S	0.354	25.0	0.913
4S	0.358	25.0	0.913
4S	0.359	25.0	0.913
5L	0.649	22.0	0.905
5L	0.647	22.0	0.906
5L	0.648	22.0	0.906
6	34.550	25.3	0.963
6	34.550	25.3	0.963
5H	0.668	50.0	---
5H	0.659	50.0	---
5H	0.670	50.0	---
5H	0.572	50.0	---
5H	0.583	50.0	---
5H	0.585	50.0	---

TABLE 5.2 STATIC EQUILIBRIUM OIL THICKNESSES

OIL TYPE	OIL DENSITY (gm/cc)	OIL TEMPERATURE (°C)	PROBE THICKNESS (cm)	CALIPER THICKNESS (cm)	VISUAL THICKNESS (cm)
2	0.864	-0.2	---	0.52	0.56
4E	0.913	0.1	0.9	0.94	0.91
5L	0.925	0.5	1.10	1.03	1.02
5H	0.937	0.5	1.25	1.16	0.70

TABLE 5.3 OIL UNDER SMOOTH AND SMALL ROUGHNESS ICE TEST RESULTS

TEST NO.	OIL TYPE	ROUGHNESS AMPLITUDE (cm)	ROUGHNESS SPACING (cm)	OIL VISCOSITY (poise)	OIL DENSITY (gm/cc)	DENSITY DIFFERENCE (gm/cc)	OIL THICKNESS (cm)	SLICK VELOCITY (cm/sec)	CURRENT VELOCITY (cm/sec)
1	2	---	---	0.075	0.870	0.130	0.52	0.230	5.00
2	2	---	---	0.076	0.870	0.130	0.52	0.961	9.60
3	2	---	---	0.076	0.870	0.130	0.52	3.522	18.43
4	2	---	---	0.076	0.870	0.130	0.52	8.680	27.85
5	4E	---	---	1.215	0.912	0.088	0.94	0.145	4.81
6	4E	---	---	1.195	0.912	0.088	0.94	0.492	9.62
7	4E	---	---	1.203	0.912	0.088	0.94	5.319	18.80
8	4E	---	---	1.203	0.912	0.088	0.94	12.270	26.24
9	5L	---	---	4.793	0.926	0.074	1.03	0.186	5.25
10	5L	---	---	4.793	0.926	0.074	1.03	0.746	9.62
11	5L	---	---	4.390	0.930	0.070	1.03	3.167	18.80
12	5L	---	---	4.343	0.927	0.073	1.03	9.499	26.24
13	5H	---	---	43.050	0.952	0.048	1.16	0.00	5.25
14	5H	---	---	52.100	0.950	0.050	1.16	1.110	9.79
15	5H	---	---	48.700	0.950	0.050	1.16	5.020	19.24
16	5H	---	---	46.200	0.952	0.048	1.16	9.234	27.99
17	4E	0.1	4	---	0.912	0.088	0.62	0.00	5.0
18	4E	0.1	4	---	0.912	0.088	0.62	0.00	10.0
19	4E	0.1	4	---	0.912	0.088	0.62	0.58	13.7
20	4E	1.0	4	---	0.912	0.088	0.62	0.00	18.9
21	4E	1.0	4	---	0.912	0.088	0.62	2.13	29.1
22	5H	0.1	4	---	0.948	0.052	1.00	0.00	5.0
23	5H	0.1	4	---	0.948	0.052	1.00	0.00	10.0
24	5H	0.1	4	---	0.948	0.052	1.00	0.00	13.7
25	5H	1.0	4	---	0.948	0.052	1.00	0.00	18.9
26	5H	1.0	4	---	0.948	0.052	1.00	0.73	29.1

properties, the water and oil viscosity as well as the oil thickness for each speed. Delta, Δ , is the relative density difference between water and oil. For tests with ice possessing small roughness elements, the table also gives information on roughness amplitude and spacing.

Table 5.4 summarizes the data obtained from tests with oil interacting with large roughness elements. A large roughness element, as stated earlier, is a protrusion in the ice with an amplitude greater than the equilibrium oil slick thickness. The table includes information on the large roughness characteristics, test oil data, oil slick length and width, head wave, neck and tail thickness, and the current speed when an oil slick containment failure occurred as indicated by droplet loss.

Table 5.5 presents data on visual estimates and velocity probe estimates of the wake formed behind large ice roughness as measured in the flume. The mean velocity profiles measured in the wake are presented in Appendix E. The table also presents the properties of the oils used in the tests and the observed slick dimensions. Because the ice roughness causes blockage of flow, the currents given are local accelerated currents averaged immediately below the tip of the roughness element.

Table 5.6 summarizes the dimensions of the cavities and the properties of the oils used in the cavity test series. The length of the cavities given are the inside dimensions measured between the bases of the triangular ice blocks and not tip-to-tip measures. The current speeds presented are adjusted local currents resulting from the blockage of flow caused by the presence of the ice roughness.

Figures 5.5 through 5.12 are representations of the position of the oil-water interface as a function of local current speed and cavity dimensions. Figure 5.8 describes the oil-water interfacial position for the case of a recessed cavity, a cavity formed not by roughness protruding into the free stream, but rather by a cavity recessed away from the free stream.

TABLE 5.4 OIL INTERACTION WITH LARGE ROUGHNESS TEST RESULTS

TEST NO.	OIL TYPE	WATER DEPTH (cm)	OIL DENSITY (gm/cc)	OIL VISCOSITY (poise)	KEEL ANGLE (°)	KEEL DEPTH (cm)	FAILURE VELOCITY (cm/sec)	HEAD THICKNESS (cm)	TAIL THICKNESS (cm)	NECK THICKNESS (cm)	SLICK LENGTH (cm)
1	2	35.5	0.864	0.08	90	7.0	22.41	2.50	1.00	---	15
2	2	35.6	0.865	0.076	32	7.0	20.61	2.30	0.40	---	22
3	2	35.2	0.865	0.075	32	11.7	22.99	2.00	1.00	---	26
4	4E	35.6	0.912	1.280	90	8.0	21.19	---	---	---	--
5	4E	35.6	0.911	1.160	32	8.0	21.17	3.60	1.00	---	12
6	4E	35.2	0.913	1.138	32	11.7	21.43	4.15	2.60	---	35
7	5H	35.6	0.944	26.050	90	7.0	13.46	2.00	3.50	---	9
8	5H	35.3	0.946	37.430	32	8.0	13.99	1.50	5.60	---	13
9	5H	35.2	0.946	33.170	32	11.7	15.58	2.78	2.34	---	--
10	4E	38.5	0.912	1.210	32	6.2	21.45	3.60	5.50	---	32
11	4E	38.5	0.911	1.241	32	9.9	23.37	3.00	5.00	---	16
12	5H	38.5	0.946	27.900	32	6.2	16.29	3.00	2.00	---	43
13	5H	38.5	0.949	30.800	32	9.9	15.77	3.00	1.00	---	30
14	4S	40.6	0.934	---	90	8.0	20.57	4.0	4.4	3.3	210
15	4S	40.6	0.934	---	90	8.0	20.57	5.5	5.5	2.9	200

TABLE 5.5 RESULTS OF WAKE MEASUREMENT TESTS

TEST NO.	OIL TYPE	DENSITY (gm/cc)	VISCOSITY (poise)	MEAN CURRENT (cm/sec)	LOCAL CURRENT (cm/sec)	WATER DEPTH (cm)	ROUGHNESS HEIGHT (cm)	VISUAL WAKE LENGTH (cm)	MEASURED WAKE LENGTH (cm)	TRAPPED SLICK TERMINUS (cm)
1	--	---	---	20.7	27.7	40	10	75	70	--
2	--	---	---	31.0	41.4	40	10	50	65	--
3	4E	0.914	0.636	20.7	27.7	40	10	--	--	45
4	4E	0.914	0.636	31.0	41.4	40	10	--	--	25
5	5H	0.949	13.540	12.0	14.5	40	7	--	--	45
6	5H	0.949	13.540	15.5	18.8	40	7	--	--	0
7	5H	0.949	13.540	20.7	25.0	40	7	--	--	0

TABLE 5.6* RESULTS OF CAVITY TESTS

TEST NO.	OIL TYPE	OIL VISCOSITY (poise)	OIL DENSITY (gm/cc)	MEAN CURRENT (cm/sec)	LOCAL CURRENT (cm/sec)	WATER DEPTH (cm)	CAVITY DEPTH (cm)	CAVITY LENGTH (cm)	WALL SLOPE (°)
1	4E	1.364	0.915	20.70	27.60	40	10.0	50	32
2	4E	1.364	0.915	31.00	41.40	40	10.0	50	32
3	4E	1.368	0.912	31.00	41.40	40	10.0	50	32
4	4E	1.900	0.910	15.50	23.90	40	14.0	50	32
5	4E	1.900	0.910	20.70	31.80	40	14.0	50	32
6	4E	1.900	0.910	25.90	39.80	40	14.0	50	32
7	4E	1.900	0.910	31.00	47.70	40	14.0	50	32
8	4S	6.900	0.930	0.00	0.00	50	17.9	50	32
9	4S	6.900	0.930	5.50	8.55	50	17.9	50	32
10	4S	6.900	0.930	9.60	14.95	50	17.9	50	32
11	4S	6.900	0.930	12.30	19.22	50	17.9	50	32
12	4S	6.900	0.930	12.30	19.22	50	17.9	50	32
13	4S	6.900	0.930	15.10	23.50	50	17.9	50	32
14	4S	6.900	0.930	20.57	32.04	50	17.9	50	32
15	4S	6.900	0.930	24.69	38.46	50	17.9	50	32
16	4S	6.900	0.930	28.80	44.86	50	17.9	50	32
17	4	6.000	0.949	0.00	0.00	48	9.0	90	32
18	4	6.000	0.949	5.80	7.10	48	9.0	90	32
19	4	6.000	0.949	10.10	12.40	48	9.0	90	32
20	4	6.000	0.949	12.90	15.90	48	9.0	90	32
21	4	6.000	0.949	15.80	19.40	48	9.0	90	32
22	4	6.000	0.949	21.60	26.60	48	9.0	90	32
23	4	6.000	0.949	25.90	31.90	48	9.0	90	32
24	4	8.400	0.939	0.00	0.00	48	9.0	190	32
25	4	8.400	0.939	5.80	7.10	48	9.0	190	32
26	4	8.400	0.939	10.10	12.40	48	9.0	190	32
27	4	8.400	0.939	12.90	15.90	48	9.0	190	32
28	4	8.400	0.939	15.80	19.40	48	9.0	190	32
29	4	8.400	0.939	18.70	23.00	48	9.0	190	32
30	4	8.400	0.939	21.60	26.00	48	9.0	190	32
31	4	8.400	0.939	25.90	31.90	48	9.0	190	32

(continued)

TABLE 5.6 (continued)

TEST NO.	OIL TYPE	OIL VISCOSITY (poise)	OIL DENSITY (gm/cc)	MEAN CURRENT (cm/sec)	LOCAL CURRENT (cm/sec)	WATER DEPTH (cm)	CAVITY DEPTH (cm)	CAVITY LENGTH (cm)	WALL SLOPE (°)
32*	4	6.000	0.949	0.00	0.00	48	9.0	90	32
33*	4	6.000	0.949	5.80	7.10	48	9.0	90	32
34*	4	6.000	0.949	10.10	12.40	48	9.0	90	32
35*	4	6.000	0.949	15.80	19.40	48	9.0	90	32
36*	4	6.000	0.949	21.60	26.60	48	9.0	90	32
37	5H	156.000	0.951	15.50	23.90	40	14.0	50	32
38	5H	156.000	0.951	20.70	31.80	40	14.0	50	32
39	5H	156.000	0.951	25.90	39.80	40	14.0	50	32
40	5H	156.000	0.951	31.00	47.70	40	14.0	50	32
41	5H	70.000	0.978	0.00	0.00	50	9.0	100	32
42	5H	70.000	0.978	5.49	8.35	50	9.0	100	32
43	5H	70.000	0.978	9.60	14.95	50	9.0	100	32
44	5H	70.000	0.978	12.34	19.22	50	9.0	100	32
45	5H	70.000	0.978	15.09	23.50	50	9.0	100	32
46	5H	44.000	0.955	0.00	0.00	50	10.5	202	32
47	5H	44.000	0.955	5.49	6.95	50	10.5	202	32
48	5H	44.000	0.955	9.60	12.15	50	10.5	202	32
49	5H	44.000	0.955	12.34	15.62	50	10.5	202	32

* Recessed Cavity.

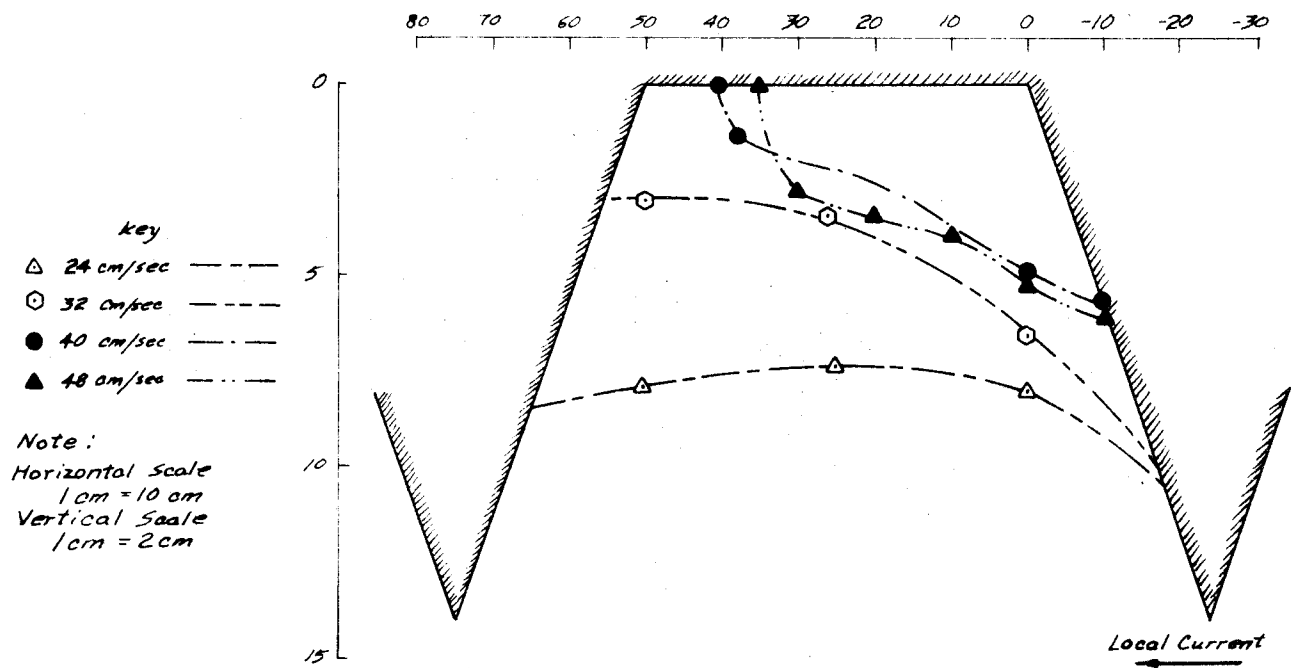


Figure 5.5. Typical Transformation of an Oil/Water Interface With Changes of Free Stream Current for a Number 4 Oil Trapped in a Half Meter Cavity of 14 cm Depth

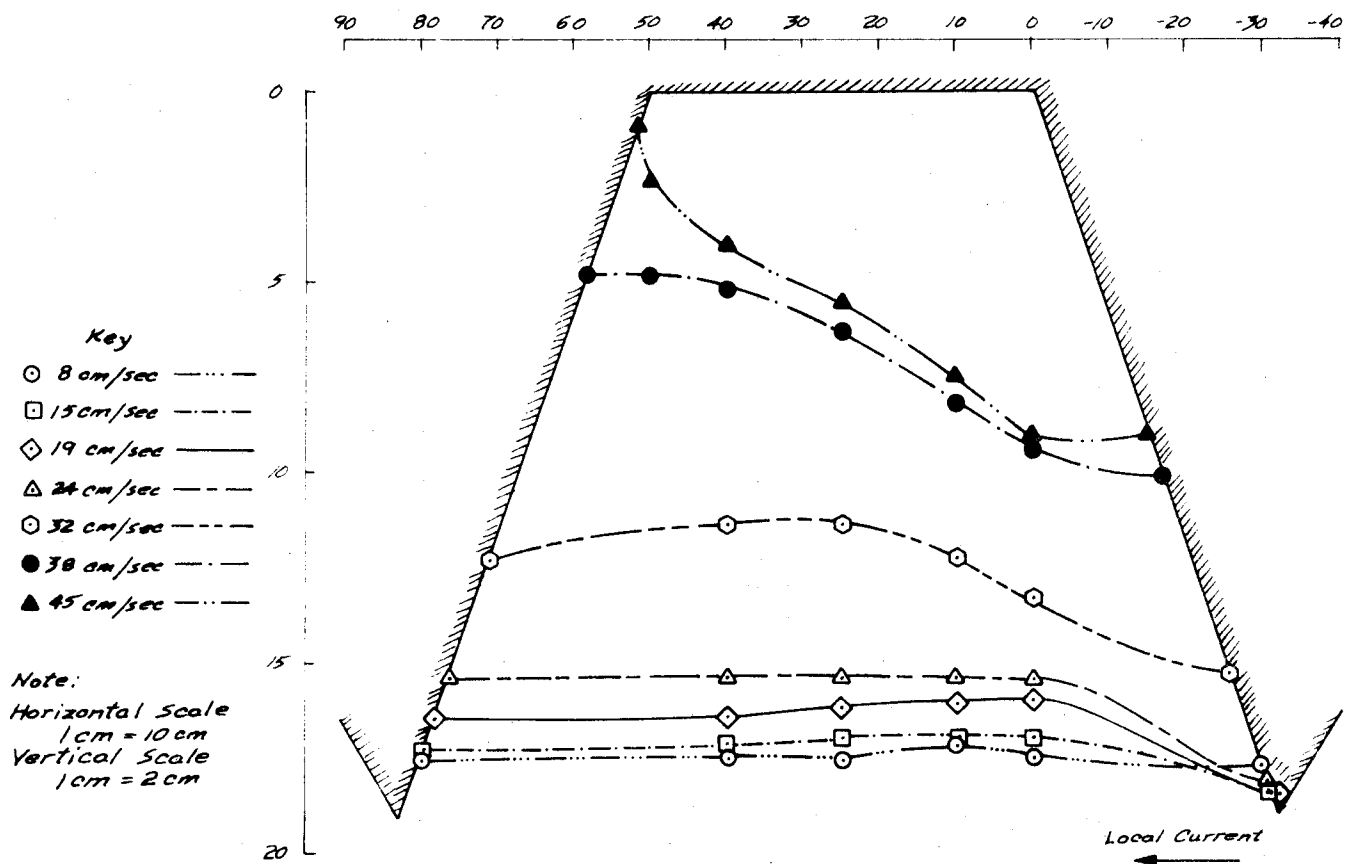
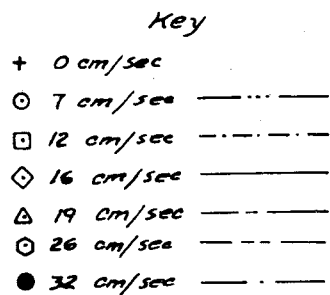


Figure 5.6. Typical Transformation of an Oil/Water Interface With Changes of Free Stream Current for a Number 4 Oil Trapped in a Half Meter Cavity of 19 cm Depth



Note:
 Horizontal Scale: 1 cm = 10 cm
 Vertical Scale: 1 cm = 2 cm

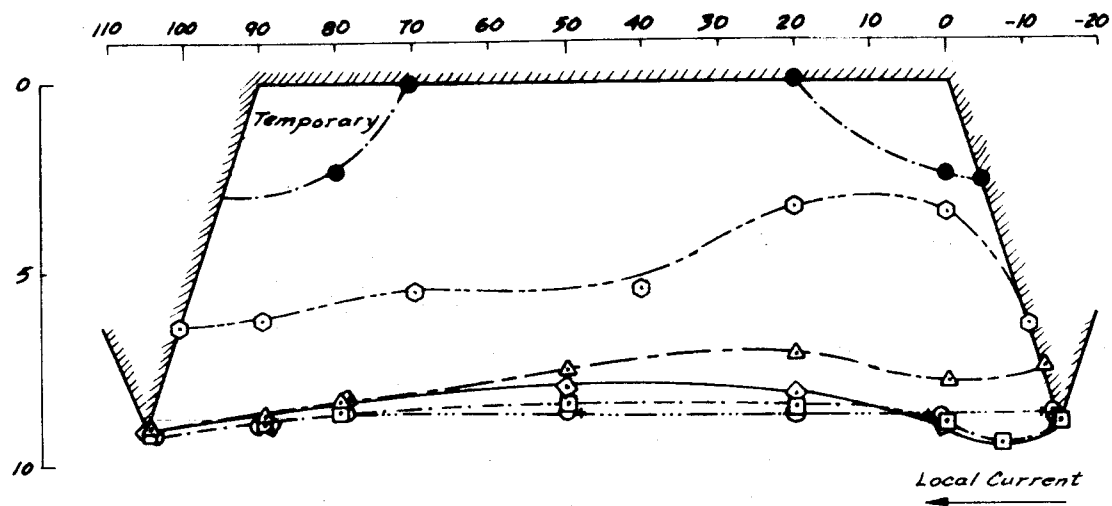


Figure 5.7. Typical Transformation of an Oil/Water Interface With Changes of Free Stream Current for a Number 4 Oil Trapped in a 1 Meter Cavity of 9 cm Depth

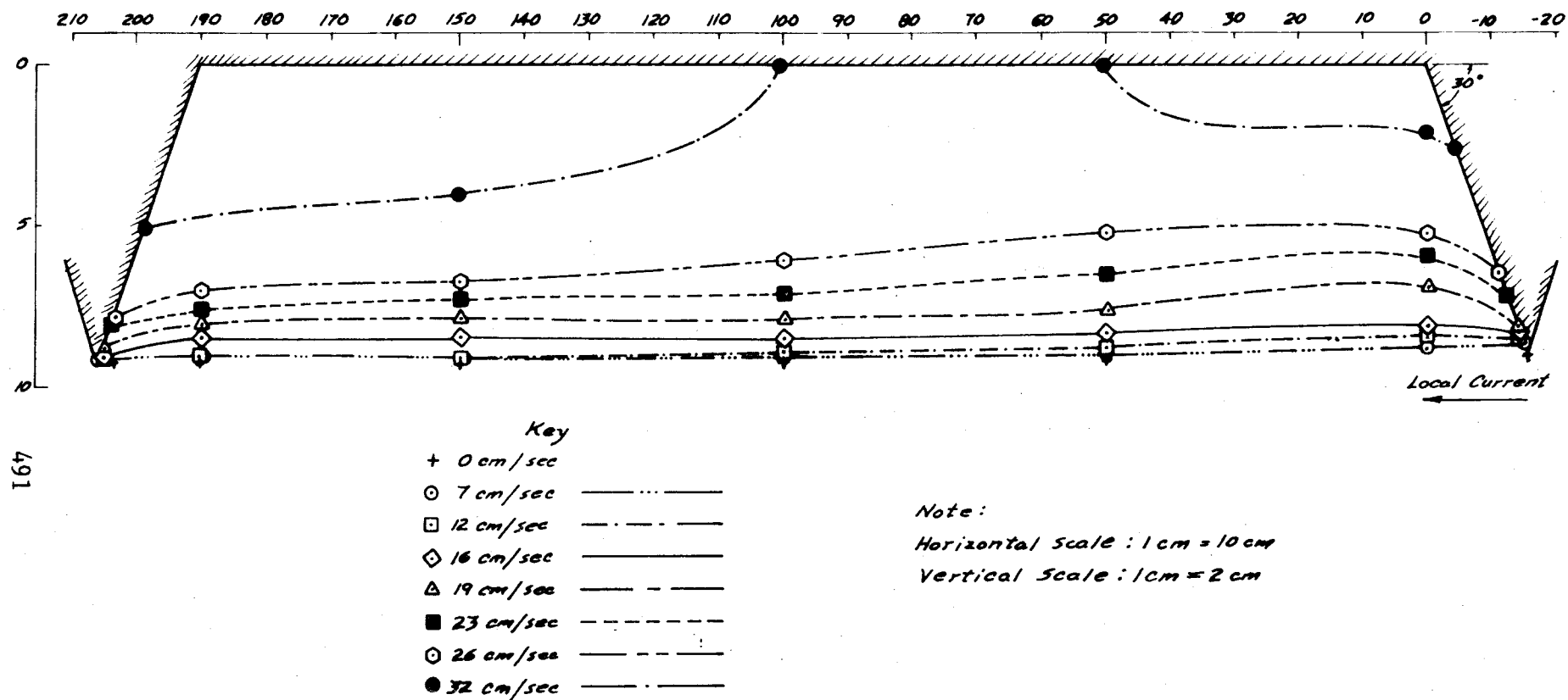
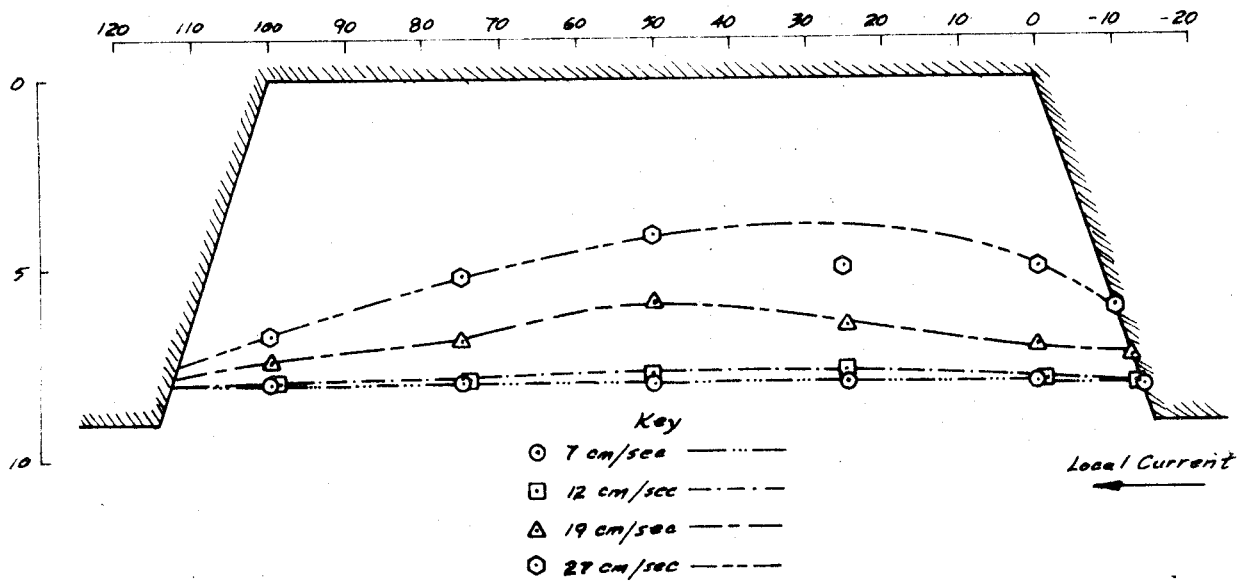


Figure 5.8. Typical Transformation of an Oil/Water Interface With Changes in Free Stream Current for a Number 4 Oil Trapped in a 2 Meter Cavity of 9cm Depth



Note:
 Horizontal Scale: 1cm = 10cm
 Vertical Scale: 1cm = 2cm

Figure 5.9. Typical Transformation of an Oil/Water Interface With Changes in Free Stream Current for a Number 4 Oil Trapped in a 1 Meter Recessed Cavity of 9cm Depth

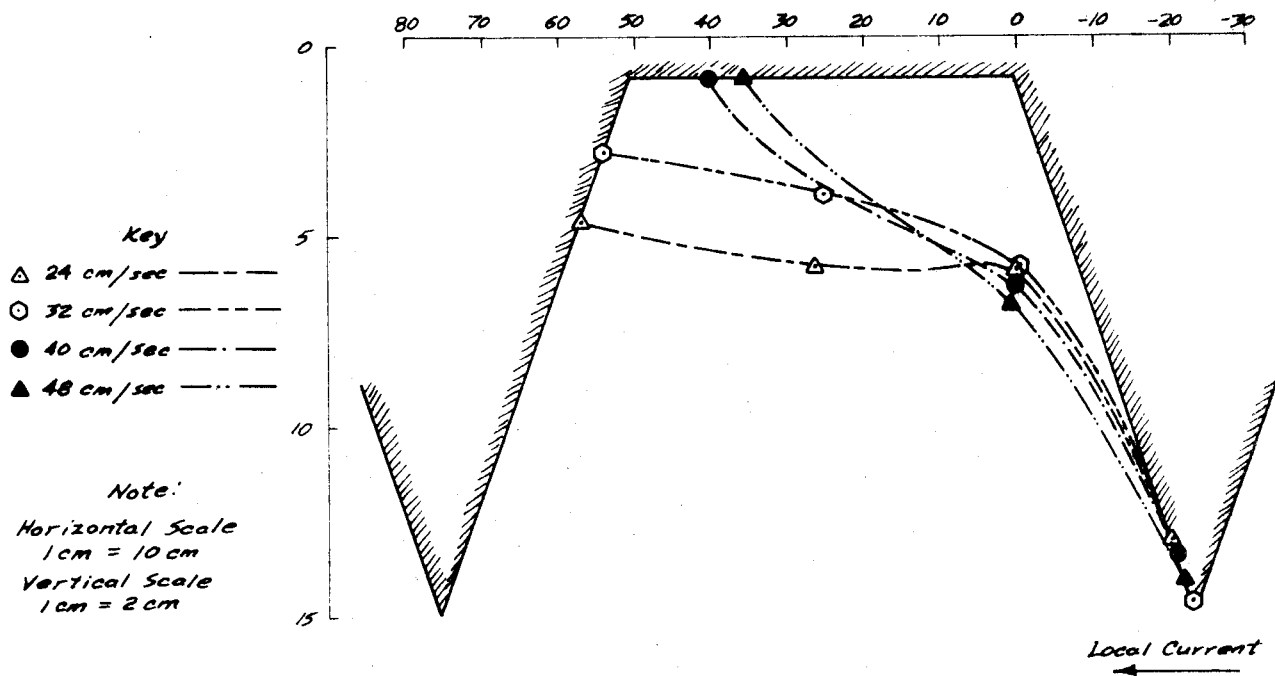


Figure 5.10. Typical Transformation of an Oil/Water Interface With Changes in Free Stream Current for a Number 5 Heavy Oil Trapped in a Half Meter Cavity of 15 cm Depth

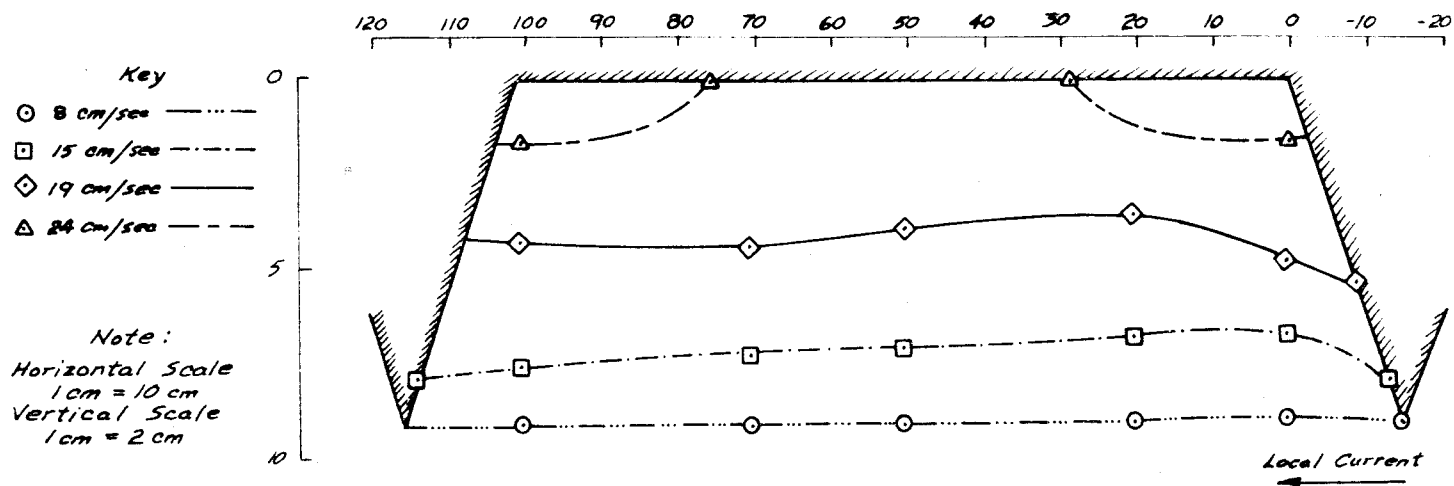


Figure 5.11. Typical Transformation of an Oil/Water Interface With Changes in Free Stream Current for a Number 5 Heavy Oil Trapped in a 1 Meter Cavity of 9 cm Depth

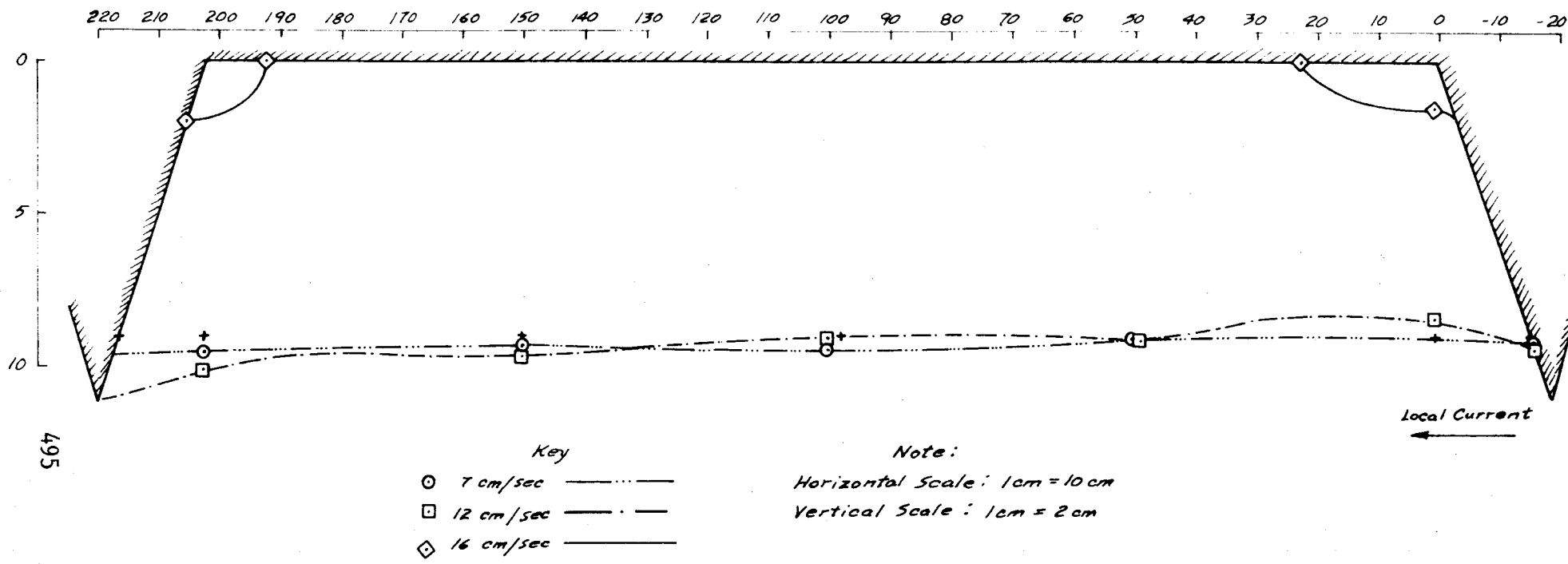


Figure 5.12. Typical Transformation of an Oil/Water Interface With Changes in Free Stream Current for a Number 5 Heavy Oil Trapped in a 2 Meter Cavity of 11cm Depth

6. ANALYSIS OF TEST RESULTS

6.1 Static Equilibrium Thickness

No measurements of interfacial tension or contact angle were possible during the tests, therefore the theoretical expression for static equilibrium thickness given previously by Equation 3.1 cannot be verified exactly. However, if the contact angle is assumed to equal 45° in all cases, then the interfacial tension can be computed to equal 10.5 dynes/cm for No. 2 fuel oil, 22.0 dynes/cm for No. 4E oil, 22.8 dynes/cm for No. 5 light oil, and 24.3 dynes/cm for No. 5 heavy oil. These values fall in the observed range for various crude oils [23]. As mentioned earlier, the effect of small changes in contact angle is much less than the effect of small changes in density. Therefore, the inaccuracies caused by misestimating contact angle are minimal, and the interfacial tension values computed can be considered realistic.

According to the theory, the square of the slick thickness, δ^2 , should vary inversely with the density difference, $\Delta \rho_w$. However, over the range in density of interest, the data plotted in Figure 6.1 shows that slick thickness and density difference can be related linearly. This approximate relationship is given by:

$$\delta_{eq} = 1.67 - 8.50 (\Delta \rho_w) . \quad (6.1)$$

For most oils, when little else is known about the oil properties, this relationship can be used to estimate the probable under ice static equilibrium slick thickness for smooth ice.

6.2 Oil Under Smooth Ice

Plotted in Figures 6.2 through 6.5 are the slick velocities versus current velocities for the No. 2, No. 4E, No. 5 light, and No. 5 heavy fuel oils. Also plotted on these curves are the two step linear relations suggested by the theory. The slope of the upper leg is unity, while the lower branch has been adjusted to fit the data. Extrapolation of the lower lines to the axis suggests that the threshold velocity for No. 2, No. 4E, and No. 5 light oil is around 4 cm/sec. The extrapolation for No. 5 heavy is somewhat more conjectural since the oil did not move at about 5 cm/sec, but did at about 10 cm/sec. Apparently for oils having a viscosity below about 10 poise, a smooth ice threshold velocity of 4 cm/sec is reasonable. Above this viscosity, a threshold velocity of around 7 cm/sec should be used. This is shown in Figure 6.6 with an empirical relation between threshold velocity, U_{th} , and oil viscosity, μ_0 , for smooth ice.

Plotted in Figure 6.7 is a composite relationship based on combining the data for all of the oils tested. The data falls on a relatively narrow band, and suggest that without a great loss of accuracy a single broken line might be used to describe the slick speed versus current speed relationship for all oils. This is especially of value if little is known about the oil properties.

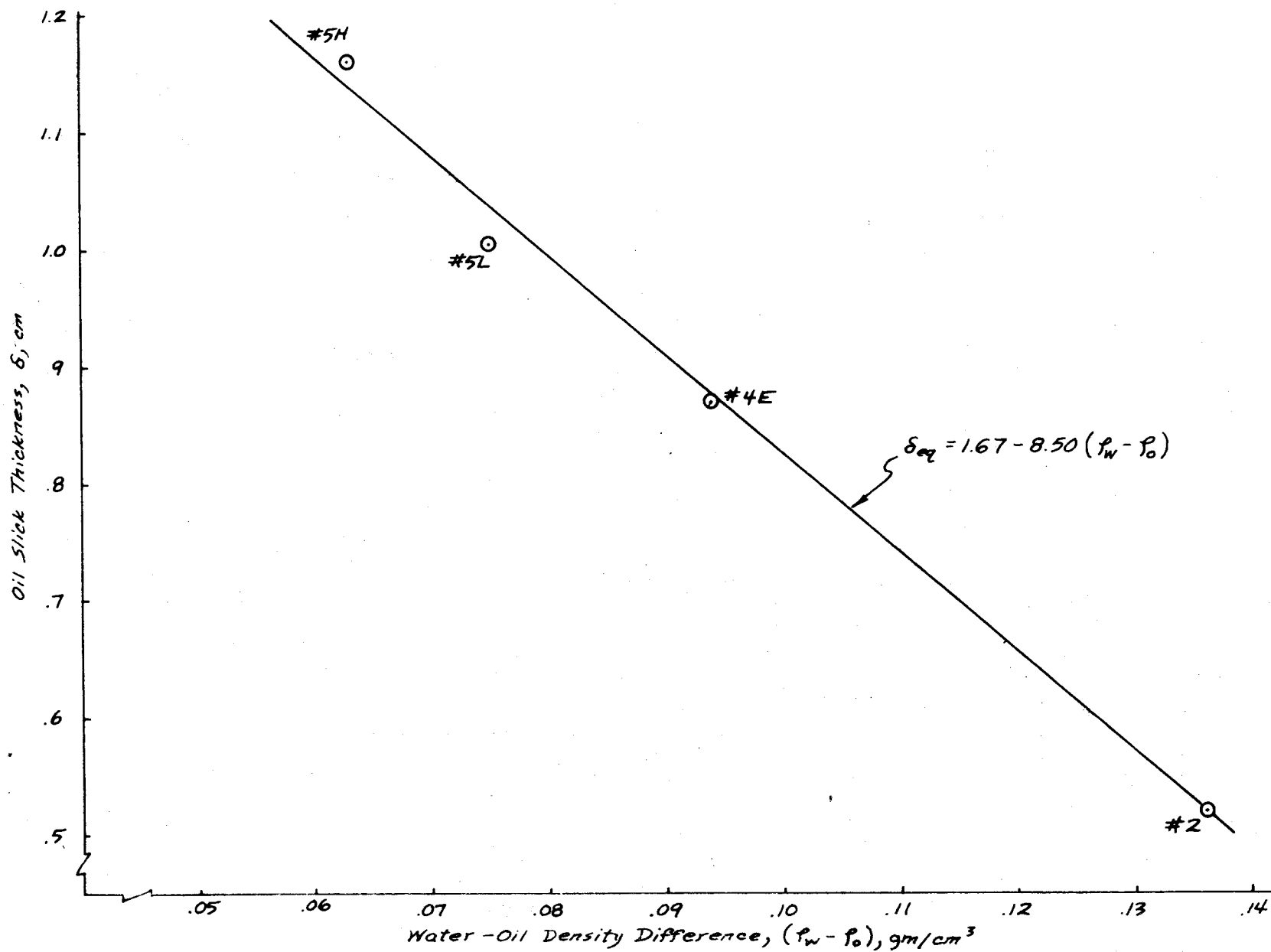


Figure 6.1. Empirical Relationship Between Slick Thickness and Density Difference

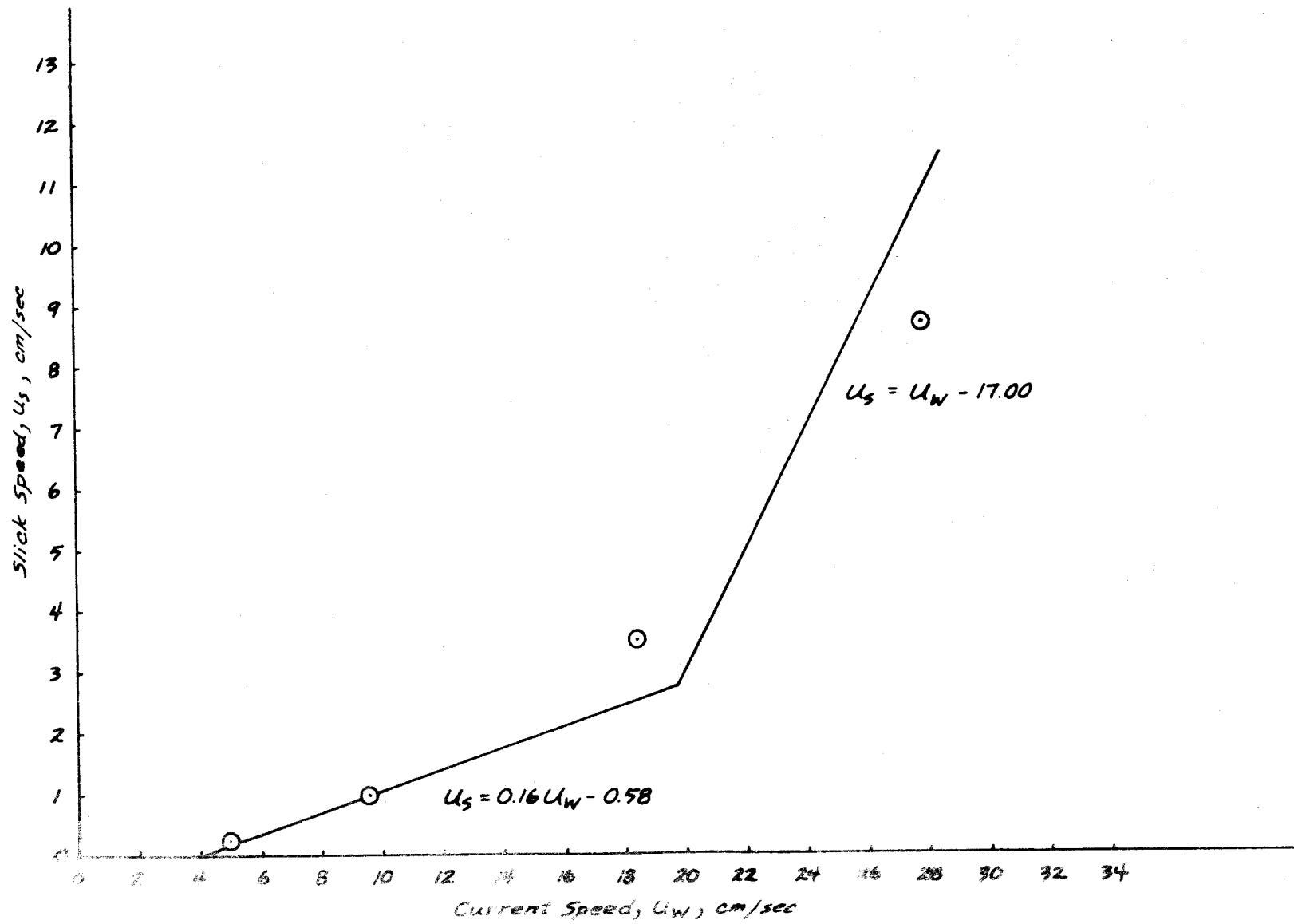


Figure 6.2. Slick Speed vs. Current Speed for No. 2 Fuel Oil Under Smooth Ice

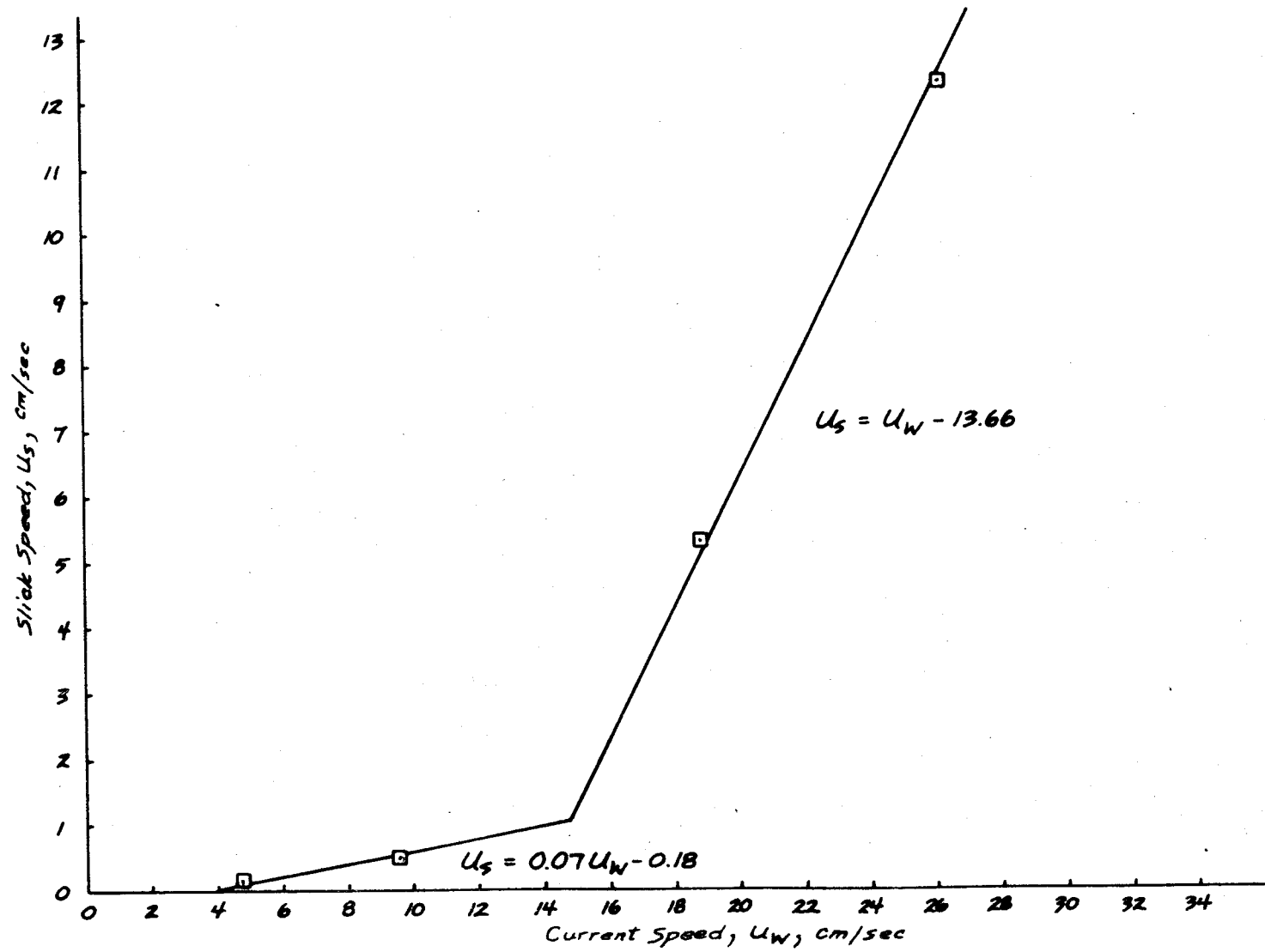


Figure 6.3. Slick Speed vs. Current Speed for No. 4 Oil Under Smooth Ice

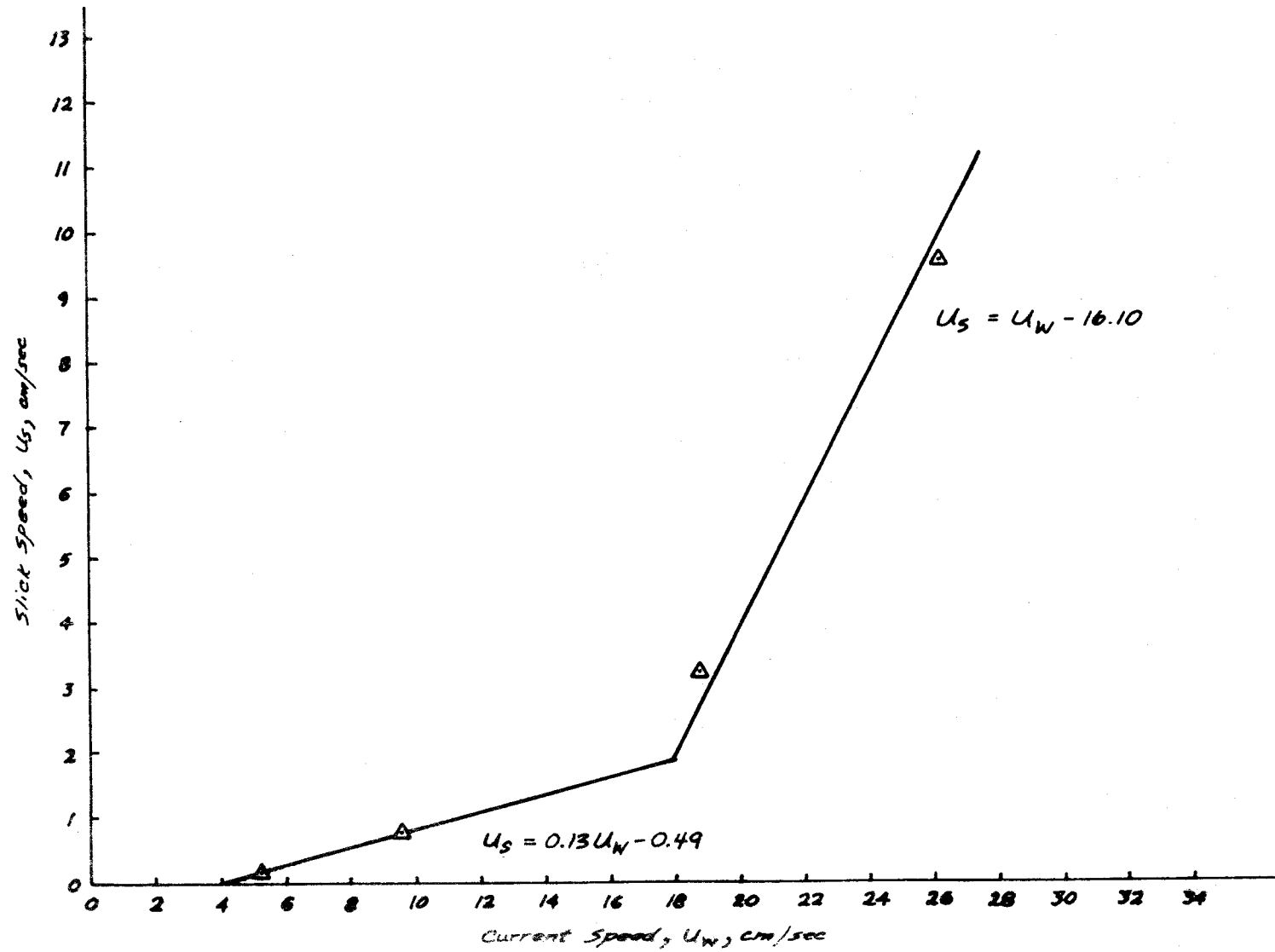


Figure 6.4. Slick Speed vs Current Speed for No. 5L Oil Under Smooth Ice

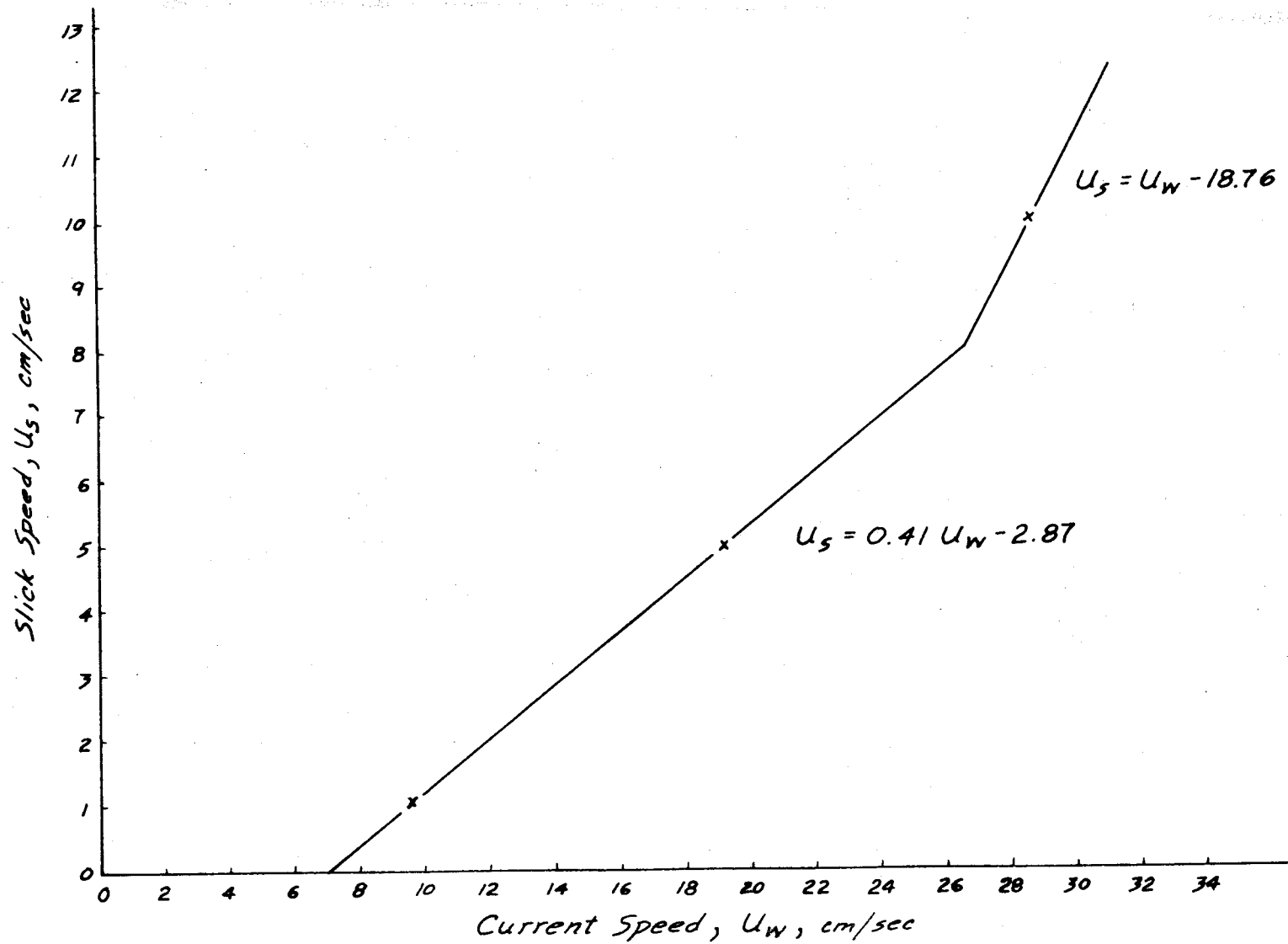


Figure 6.5. Slick Speed vs. Current Speed for No. 5H Oil Under Smooth Ice

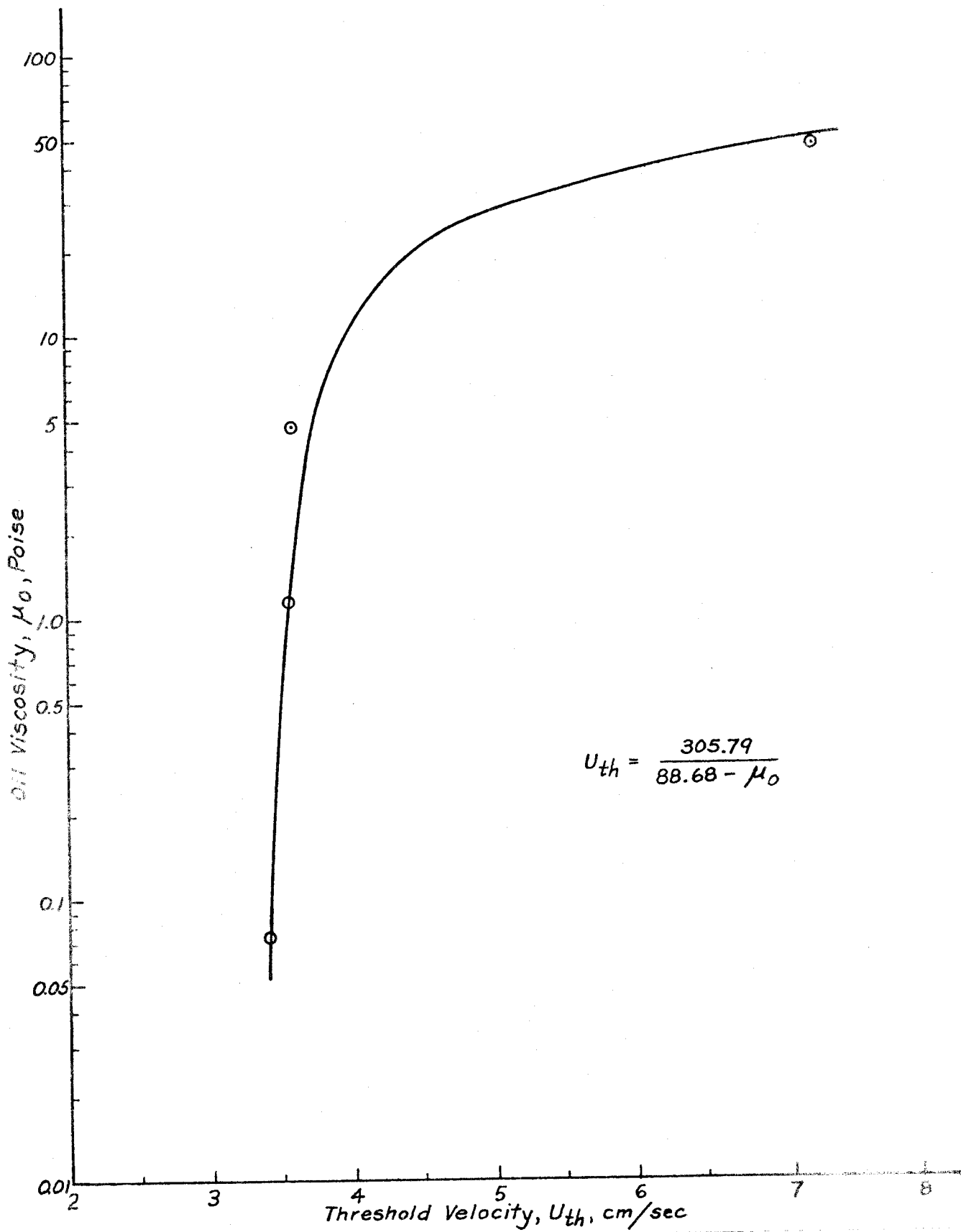


Figure 6.6. Plot of Oil Slick Threshold Velocity versus Oil Viscosity for Oil Beneath Smooth Ice

In order to generalize the results to all oils and all current conditions, the data has been non-dimensionalized according to Equation 3.5, summarized in Table 6.1, and plotted in Figure 6.8. The plot shows the general hyperbolic form of the relation. The curve has two asymptotes which intersect at an abscissa value of about 0.4. Near this value is also where the break occurs in the previous U_s versus U_w curves. Below 0.4, the slope of the U_s curve is unity. Above 0.4, the U_s curves are also linear but with a slope much less than unity. Also overlaid on Figure 6.8 are the crude oil and No. 2 oil transport data as presented in Uzuner, et al [26]. These points even further support this hyperbolic relationship, and in the case of the crude oil, it appears that the slope of the lower end of the U_s curve must be virtually zero. The least squares best fit curve for this generalized expression is given as:

$$\left(1 - \frac{U_s}{U_w}\right)^2 = \frac{1}{0.115 F_\delta^2 + 1.105} \quad (6.2)$$

As velocities get very large, the inverse Froude Number squared gets very small, and we would expect from the following the generalized curve, the slick speed would begin to approach the freestream current. At the other end of the curve, which represents slow currents and threshold velocities, the threshold values generally appear to decrease with decreasing viscosity. However, although the generalized equation predicts that for a large enough freestream velocity the slick approaches the freestream velocity, it is more likely that entrainment of the oil would occur at some lower current velocity and the slick would become broken up and turbulently distributed vertically throughout the water column.

6.3 Oil Interaction with Small Ice Roughness

As indicated in the theoretical development, the friction coefficient between the oil and the ice is not known. However, an increase in the friction coefficient can be determined for rough ice by comparing the smooth ice velocity relationships with the rough ice test results. Tests were conducted to determine the slick speed relation to current speed for oil spreading under two different rough ice forms; one roughness having a 0.1 cm amplitude and 4 cm spacing, the other having a roughness of 1 cm amplitude and 4 cm spacing. Both of these features were depression type roughness. As can be seen in Figure 6.9 the added friction due to small roughness has a drastic affect on threshold velocity. By rewriting Equation 6.2 as the equation for rough ice spreading in the form suggested in Section 3:

$$\left(1 - \frac{U_s}{U_w}\right)^2 = \frac{K}{0.115 F_\delta^2 + 1.105} \quad (6.3)$$

and substituting the nondimensional parameters from Table 6.1, we find that the increase in the friction coefficient for the 1:40 ratio of roughness is a factor of approximately 1.4. The increase in the friction coefficient for a roughness ratio of 1:4 is found to be a factor of 2.5 to 2.8. A basically

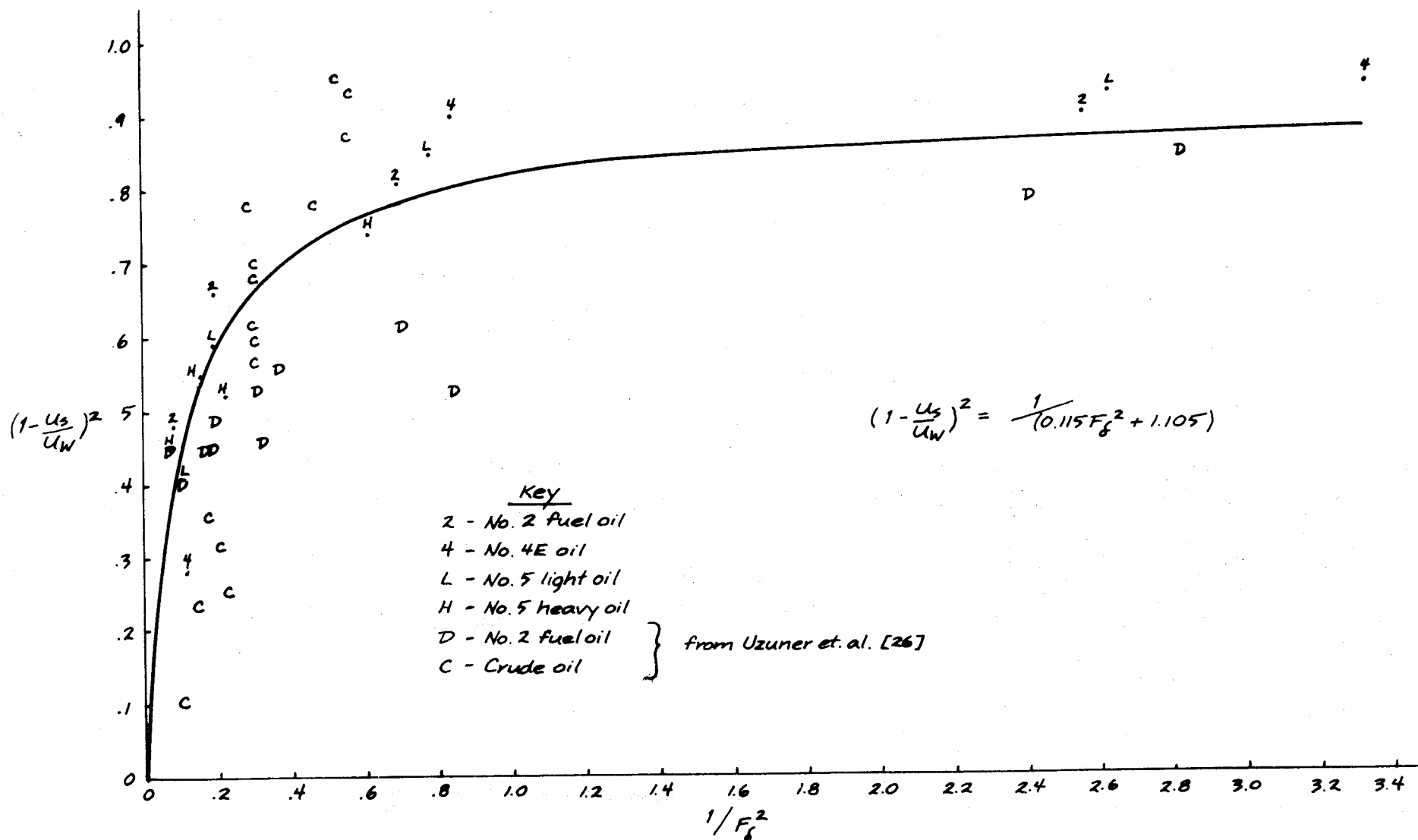


Figure 6.8. Plot of Nondimensionalized Data for the Transport of Oil Beneath Smooth and Small Roughness Ice

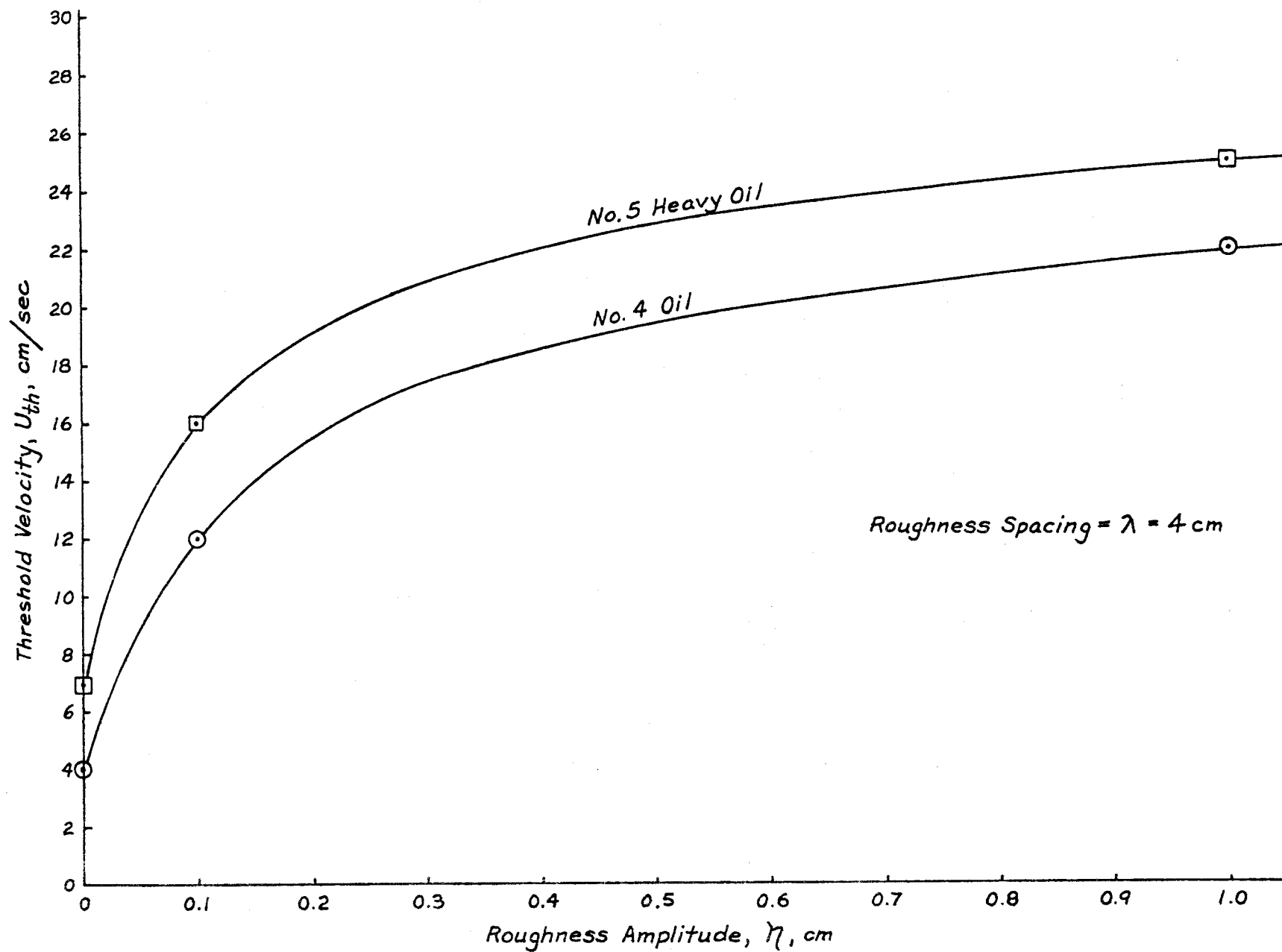


Figure 6.9. Variation of Under Ice Slick Threshold Velocity with Ice Surface Roughness

TABLE 6.1 NONDIMENSIONAL DATA FOR OIL UNDER SMOOTH AND SMALL ROUGHNESS ICE

TEST NO.	OIL TYPE	F_{δ}^2	$\frac{1}{F_{\delta}^2}$	$\frac{U_S}{U_W}$	$\left(1 - \frac{U_S}{U_W}\right)^2$	η/λ	DERIVED THRESHOLD VELOCITY (cm/sec)
1	2	0.39	2.56	0.05	0.903	0	4.0
2	2	1.45	0.69	0.10	0.810	0	4.0
3	2	5.33	0.19	0.19	0.656	0	4.0
4	2	12.17	0.08	0.31	0.476	0	4.0
5	4E	0.30	3.33	0.03	0.941	0	4.0
6	4E	1.19	0.84	0.05	0.903	0	4.0
7	4E	4.55	0.22	0.28	0.518	0	4.0
8	4E	8.86	0.11	0.47	0.281	0	4.0
9	5L	0.38	2.63	0.04	0.931	0	4.0
10	5L	1.28	0.78	0.08	0.846	0	4.0
11	5L	5.15	0.19	0.17	0.689	0	4.0
12	5L	9.62	0.10	0.36	0.410	0	4.0
13	5H	0.49	2.04	0.00	0.000	0	6.0-7.0
14	5H	1.63	0.61	0.11	0.787	0	6.0-7.0
15	5H	6.29	0.16	0.26	0.546	0	6.0-7.0
16	5H	13.87	0.07	0.33	0.449	0	6.0-7.0
17	4E	--	--	--	--	1/40	--
18	4E	--	--	--	--	1/40	--
19	4E	3.51	0.28	0.04	0.922	1/40	12.0-13.0
20	4E	6.68	0.15	--	--	1/4	--
21	4E	15.83	0.06	0.07	0.865	1/4	22.0-25.0
22	5H	--	--	--	--	1/40	--
23	5H	--	--	--	--	1/40	--
24	5H	3.68	0.27	--	--	1/40	15.0-16.0
25	5H	7.00	0.14	--	--	1/4	--
26	5H	16.60	0.06	0.03	0.941	1/4	22.0-25.0

conjectural curve describing the increase in friction with ice roughness is shown in Figure 6.10. There is very little data to support this curve, and caution should be exercised when trying to apply it to other roughness forms, however, the shape of the curve is reasonable in that while the drag coefficient is increasing with decreased spacing, the rate of increase is falling off. This seems reasonable since as the roughness peaks more closer together, they begin to form an apparent new smooth interface with lower drag characteristics.

6.4 Oil Interaction with Large Ice Roughness

Shown in Figure 6.11 is the range of current speeds where oil contained ahead of large roughness elements would begin to fail beneath the blockage. It shows that the containment is strongly a function of the oil density rather than of viscosity. In fact, the No. 5H oil, which was the most viscous, was also the easiest to flush out. Since the flume tests are strongly dependent on the water depth, i.e. not deep water, the application of the results of Figure 6.11 should be limited to values of the nondimensional slick thickness, ψ , ranging between 0.04 and 0.12. For values of ψ outside this range, a similarly shaped curve might be expected, but with different magnitude.

To compare the failure velocities to predicted Kelvin-Helmholtz instability velocities, assume values for interfacial tension as computed in Section 6.1 based on the static oil thickness. The critical velocities are 13 cm/sec for No. 2 fuel oil, 13.5 cm/sec for No. 4E oil, and 12.1 cm/sec for No. 5 heavy oil. According to Liebovich [11] $U_{fail} = 2.2 U_{crit}$ in deep water, which gives predictions for U_{fail} much larger than those observed in these tests. The test results suggest that if the containment failure observed is of the Kelvin-Helmholtz type, then

$$U_{fail} \approx 1.5 U_{crit} \quad (6.4)$$

The difference is probably due to the depth limited test conditions. However, the results are certainly realistic, considering the range for U_{fail} cited by Jones [9] who gives $1.04 U_{crit} \leq U_{fail} \leq 3.02 U_{crit}$. In terms of the oil properties, failure will then occur at:

$$U_{fail} = 1.5 \left\{ 2 \left(\frac{\rho_o + \rho_w}{\rho_o \rho_w} \right) \left[\sigma_{o/w} g (\rho_w - \rho_o) \right]^{1/2} \right\}^{1/2} \quad (6.5)$$

Shown in Table 6.2 is the nondimensional slick thickness data for oil trapped ahead of an ice roughness element. Also listed are the measured free-stream densimetric Froude Numbers, and a theoretical freestream densimetric Froude Number calculated for each nondimensional slick thickness from Equation 3.9. Since, in general, the slicks were not allowed to grow to their full equilibrium length, the theoretical Froude Numbers are calculated based upon the head thickness only. There is very close agreement between the theoretically predicted equilibrium Froude Numbers and those measured. The value of failure

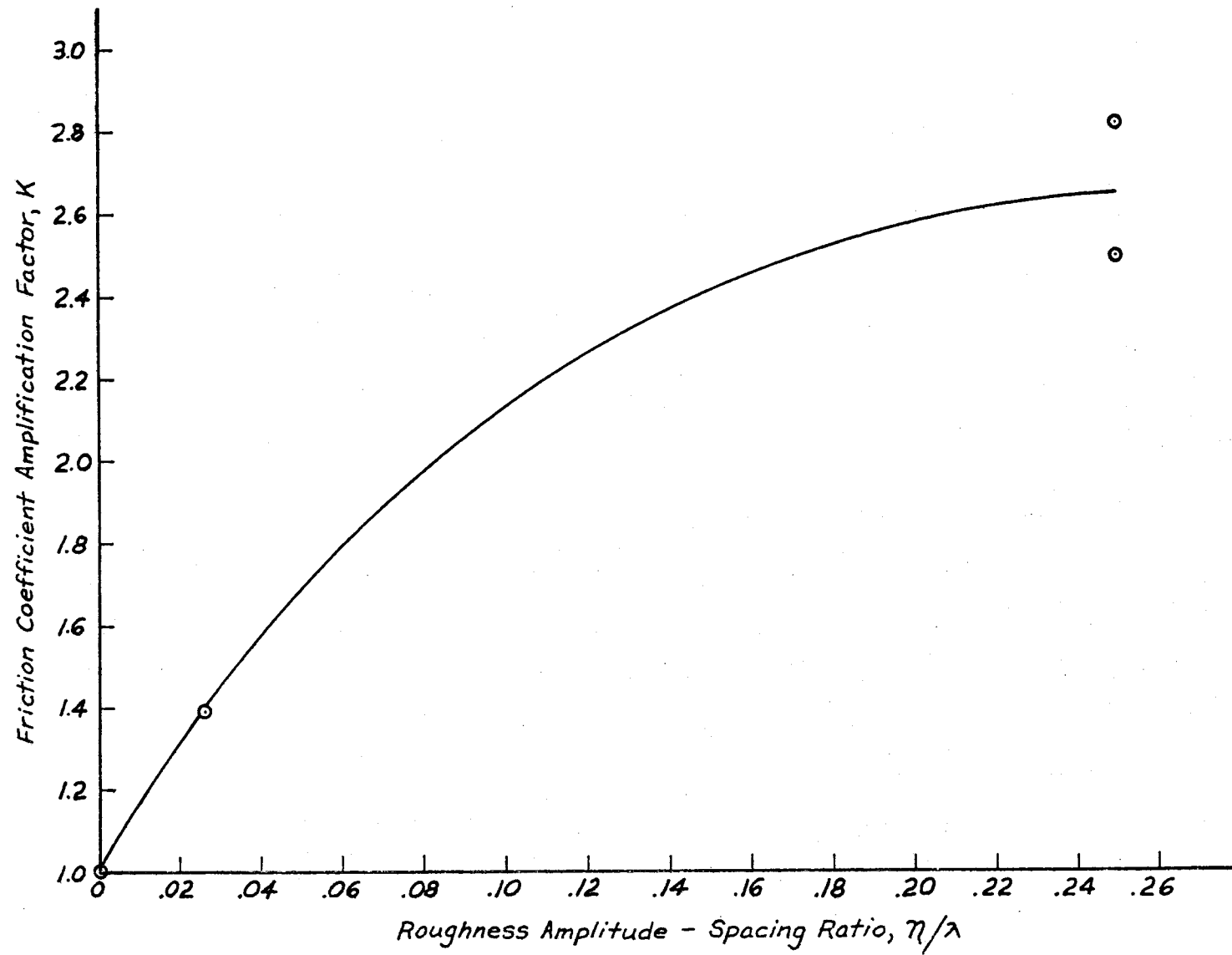


Figure 6.10. Projection of Friction Coefficient Amplification Factor as a Function of the Roughness Amplitude to Spacing Ratio

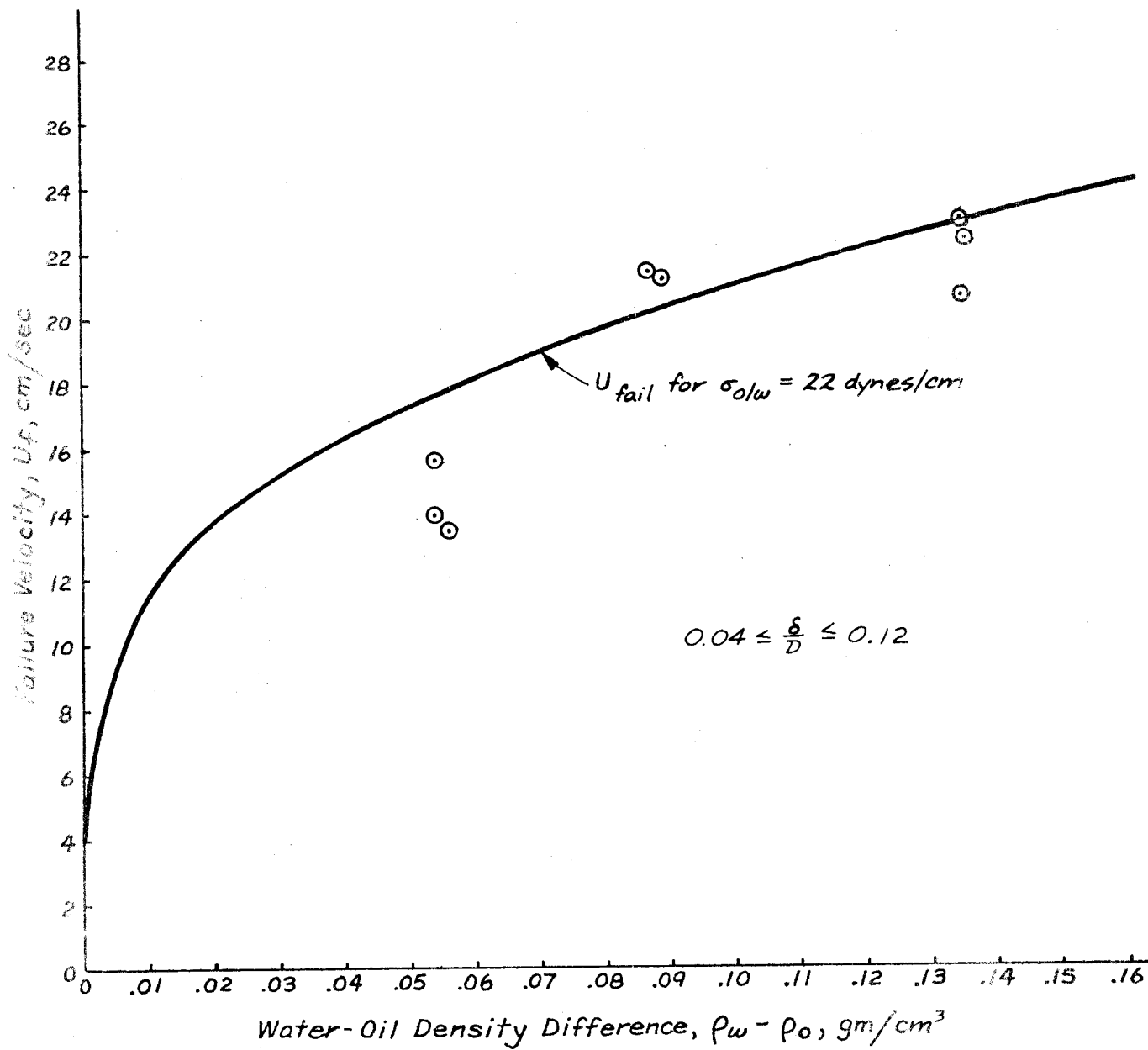


Figure 6.11 Relationship Between Failure Velocity and Water-Oil Density Difference for Containment of Oil Upstream of an Obstruction

TABLE 6.2 NONDIMENSIONAL DATA FOR OIL INTERACTION WITH LARGE ROUGHNESS

TEST NO.	OIL TYPE	RIDGE SIZE (cm)	$\psi = \frac{\delta}{D}$	Δ	U_{fail}	F_D^2	F_{theory}^2
1	2	8	0.070	0.136	22.41	0.11	0.12
2	2	8	0.065	0.135	20.61	0.09	0.11
3	2	12	0.056	0.135	22.99	0.11	0.10
4	4E	8	--	--	21.19	--	--
5	4E	8	0.101	0.089	21.17	0.14	0.16
6	4E	12	0.118	0.087	21.43	0.15	0.17
7	5H	8	0.056	0.056	13.46	0.09	0.10
8	5H	8	0.042	0.054	13.99	0.10	0.08
9	5H	12	0.078	0.054	15.58	0.13	0.13
10	4E	8	0.090	0.088	21.45	0.14	0.14
11	4E	12	0.080	0.089	23.37	0.16	0.13
12	5H	8	0.080	0.054	16.29	0.13	0.13
13	5H	12	0.080	0.051	15.77	0.13	0.13

Froude Number appears to be about 0.42 for light oils and 0.37 for heavy oils, as compared with the theoretical value of 0.5. These Froude Numbers are, however, consistent with the results of Wilkinson [27], who found 0.4 to be a practical upper limit on Froude Number.

Tests 1, 4, and 7 correspond to a vertical barrier. All other tests correspond to a barrier which has its faces at 32° to the horizontal. The experimental results indicate very strongly that there is minimal difference between a vertical or sloping barrier. This is consistent with the results of Moir and Lau [19] who observed that significant changes in the slope of the keel face resulted in only minor shifts in the maximum containment flow condition. Tests 10 through 13 represent measures of containment when the ice cover upstream of the barrier was artificially roughened. The measured failure Froude Numbers are slightly higher than those measured with a smooth upstream ice cover, and are actually closer to the theoretical predictions. Also, in comparing the failure thickness of a slick in front of an 8 cm barrier and in front of a 12 cm barrier, we do not observe any significant difference. This supports the theory that once a failure Froude Number is reached, the barrier, regardless of its size or depth, will be insufficient to confine the oil.

The dimensions of a slick allowed to grow to its natural critical dimensions were previously given in Table 5.4. The slick length relation given in Section 3 is strictly valid only in deep water cases. Since the flume tests are not deep water tests, the equilibrium length for most field applications should be numerically solved from the generalized slick length relation derived in Appendix D. This deep water slick length relation can be used to obtain an estimate of the interfacial friction factor in these tests:

$$X = \frac{4}{f_s} \frac{\Delta g}{U_w^2} (\delta_{\text{tail}}^2 - \delta_{\text{neck}}^2) \quad (6.6)$$

Substitution of slick dimensions into Equation 6.6 results in an interfacial friction factor, f_s , of 0.032. This is within the range of observed friction factors, consistent with the results of Cross and Houtt [4] but larger than those found by Jirka, et al [8] for stratified flows. However, our derivation has ignored secondary circulation within the slick, and the added boundary shear due to the ice cover and the flume walls. Ignoring these added frictional effects requires the calculated interfacial friction to absorb all the energy losses and appear larger. By accounting for these boundary effects, Wilkinson [28] suggests that the true interfacial friction factor for oil should be taken as approximately $f_s = 0.016$. The slick length prediction in deep water then becomes simply:

$$X = 250 \frac{\Delta g}{U_w^2} (\delta_{\text{tail}}^2 - \delta_{\text{neck}}^2) \quad (6.7)$$

6.5 Wake Trapping of Oil

Measurements of the wake length behind a triangular roughness element shown previously in Table 5.5 indicate that the wake length downstream of the ice roughness element is significantly less than 17 times the roughness height. However, due to the depth limitations of the flume, the blockage of the flow was as large as 25%. From the wake prediction made in Section 3, the depth dependent wake length for a flat plate should be 9 times the roughness height. Adjusting this for the triangular shape of the roughness further reduces the predicted wake length to 7 times the roughness height. The data and observations made seem to support this prediction. Velocity profiles measured in the wake of the triangular pattern roughness forms are shown in Appendix E, and define the mean reverse flow pattern in the wake behind the roughness element.

In general, the containment of oil in a wake was examined only in ranges of current speeds near levels that would result in frontal failure of the trapped slick. As such, little data on the trapping ability of the wake at very low currents is presented. Mean local currents taken immediately below the tip of the roughness element typically ran in the range of 20 to 40 cm/sec. At these current speeds, neither the No. 4E oil nor the No. 5 heavy oil exhibited any long term containment potential. During short time periods of the order of tens of minutes, the downstream end of the trapped slick was observed never to exceed 70% of the observed wake length, except during filling when it was able to totally span the wake length. In all cases the slick thickness equalled the equilibrium value except immediately behind the ice roughness element where reverse circulation thickened the oil layer somewhat. In a time frame of hours, however, any oil initially trapped dissipated, clearing the wake region of any trace of oil.

In one test which was run at a local current speed below 15 cm/sec, the containment of oil was more stable and little decrease or change in the size of the slick was observed in this case with time. This might be expected if the oil trapped within the wake was considered as another frontal wave forming from the opposite direction on the back face of the roughness, opposed by the mean reverse flow in the wake. Wake failure velocities might therefore occur in approximately the same range as frontal failure velocities. Additionally, 15 cm/sec is roughly the transition current speed for major movement of oil under smooth ice. Since it takes a current of this magnitude to cause a significant movement of the slick under smooth ice, it might be reasonable to expect this to be a minimum current which would result in a less stable containment in the wake.

Although the oil slick ended 45 cm behind the tip of the ice roughness element, the actual slick length was only 30 cm due to the sloping back face of the ice roughness filling part of the wake region. By analogy with frontal trapping, the end of the trapped slick should occur at this same relative position within the wake, independent of the shape of the roughness. Therefore, a slick trapped behind a square shape would also fill to not more than 70% of its total wake.

Based on presently available information, it appears reasonable to expect the length of a slick trapped in a wake can be approximately predicted by:

$$x = 6 C_D \eta . \quad (6.8)$$

The thickness of the trapped slick should be roughly the equilibrium thickness. When local currents are below the flushing velocities measured for frontal trapping, long term containment can be expected. When local currents exceed this value, only a quasi-short term stability of the wake is expected, and in the long term total flushing of the oil will occur.

6.6 Cavity Trapping of Oil

In the sketches of the change of the oil-water interface in a cavity with current speed, shown previously in Figures 5.5 through 5.12, a marked depression in the interface is always apparent in the first 50 to 100 cm of the cavity for all current speeds. The depth and length of the depression is tabulated in Table 6.3. The half meter long cavities totally absorb the depression in the interface. The 1 and 2 meter cavities are long enough to allow the shape of the interface to reform further downstream. This depression, or offset, which develops in the position of the interface is caused by vortex sheading from the tip of the upstream ice roughness element. The non-linear increase in the magnitude of the offset is most apparent in previously presented Figure 5.6, which shows the No. 4 oil in the 20 cm deep cavity. The magnitude of the offset increases as a power of the current speed until the thickness of the oil in the cavity approaches some apparent minimum thickness. This thickness is more stable and harder to remove with further increase in the freestream velocity. Plotted in Figure 6.12 is the magnitude of the offset zone versus local current speed. The curves suggest that the offset varies with the square of the velocity until the magnitude of the offset approaches the depth of the cavity. The curves also show that the less the density of the oil, the smaller is the offset for a given current speed. This implies that a greater volume of lighter density oil can be contained in cavities for much higher velocities than more dense oils.

In order to generalize the predictive relation for the magnitude of the offset as a function of oil properties and current speed, the test results have been non-dimensionalized into a densimetric Froude Number relationship based on offset size. The results are tabulated in Table 6.3. Plotted in Figure 6.13 is the local current speed versus this densimetric Froude Number, $U_w / \sqrt{\Delta g \epsilon_1}$. Allowing for variations in the measured magnitude of the offset due to errors in visually estimating the actual thickness of the slick, Figure 6.13 suggests that particularly as the current speed increases, the Froude Number is nearly constant, empirically taken to be 1.86. Lower current speeds seem to exhibit somewhat higher values for Froude Number, however since the Froude Number is based upon the size of the offset, when the offset is small the magnitude of the error in estimating its size has a greater impact on the

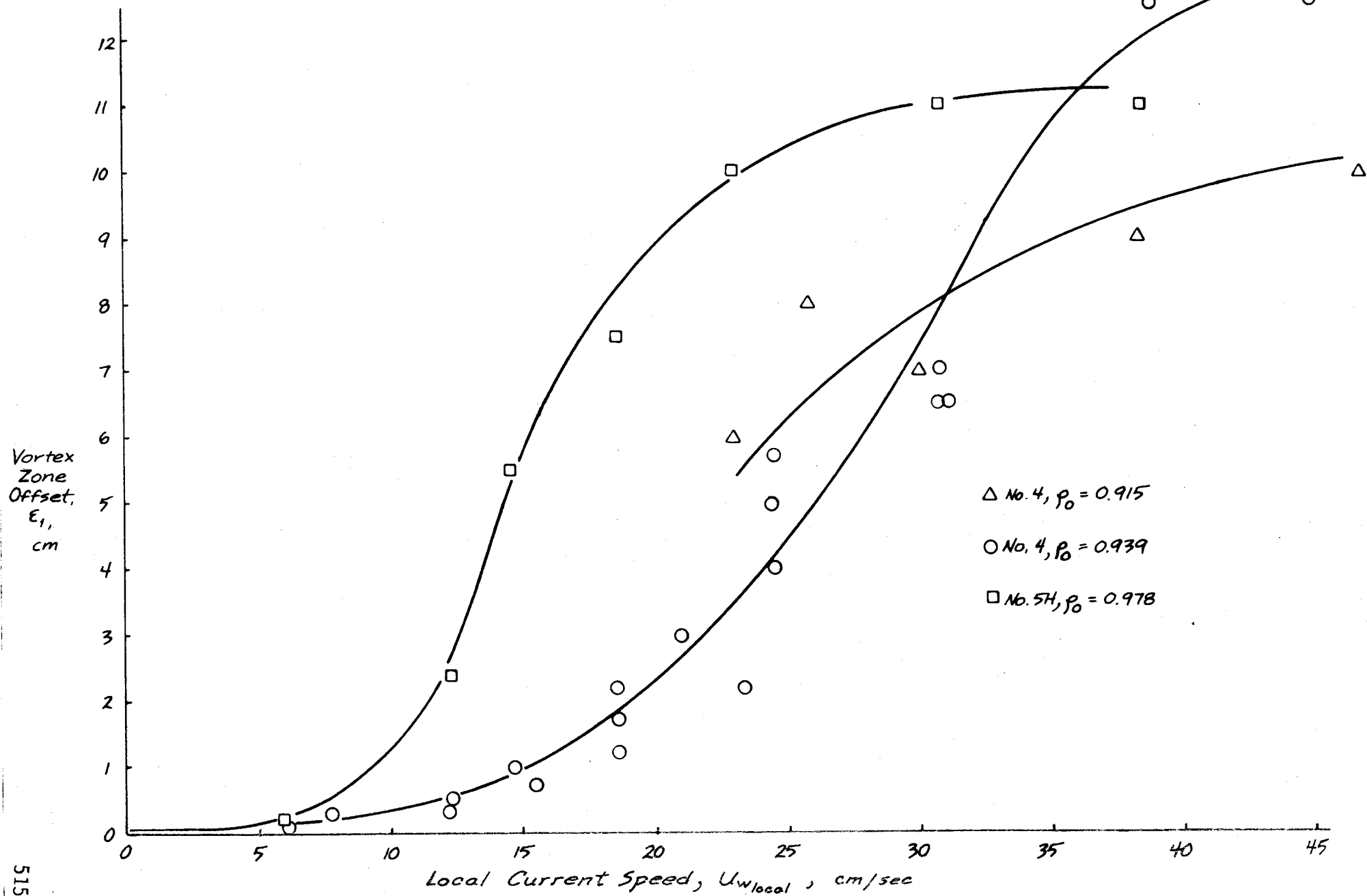


Figure 6.12 Vortex Zone Offset versus Local Current Speed for Oil Trapped in a Cavity

TABLE 6.3 ANALYSIS OF CAVITY TEST RESULTS

TEST NO.	OIL TYPE	DENSITY (gm/cc)	CAVITY DEPTH (cm)	CAVITY LENGTH (cm)	LOCAL CURRENT (cm/sec)	VORTEX ZONE OFFSET ϵ_1 (cm)	VORTEX LENGTH (cm)	FROUDE NUMBER F_{ϵ_1}	SHEAR ZONE OFFSET ϵ_2 (cm)	ϵ_2/ϵ_1
1	4E	0.915	10.0	50	27.60	8.0	50	1.07	0	--
2	4E	0.915	10.0	50	41.40	--	--	--	0	--
3	4E	0.912	10.0	50	41.40	--	--	--	0	--
4	4E	0.910	14.0	50	23.90	~6.0	--	1.04	0	--
5	4E	0.910	14.0	50	31.80	~7.0	--	1.28	0	--
6	4E	0.910	14.0	50	39.80	~9.0	--	1.41	0	--
7	4E	0.910	14.0	50	47.70	~10.0	--	1.61	0	--
8	4S	0.930	17.9	50	0.00	--	--	--	--	--
9	4S	0.930	17.9	50	8.55	0.3	~40	1.88	0	--
10	4S	0.930	17.9	50	14.95	0.7	50	2.16	0	--
11	4S	0.930	17.9	50	19.22	1.7	60	1.78	0	--
12	4S	0.930	17.9	50	19.22	1.2	60	2.12	0	--
13	4S	0.930	17.9	50	23.50	2.2	80	1.91	0	--
14	4S	0.930	17.9	50	32.04	6.5	>80	1.52	0	--
15	4S	0.930	17.9	50	38.46	12.5	>80	1.31	0	--
16	4S	0.930	17.9	50	44.86	12.4	>80	1.54	0	--
17	4	0.949	9.0	90	0.00	--	--	--	--	--
18	4	0.949	9.0	90	7.10	0.2	--	2.25	0	0
19	4	0.949	9.0	90	12.40	0.4	--	2.77	0.3	0.75
20	4	0.949	9.0	90	15.90	1.0	~70	2.25	0.5	0.50
21	4	0.949	9.0	90	19.40	1.8	~80	2.05	0.6	0.33
22	4	0.949	9.0	90	26.60	5.7	~85	1.58	3.7	0.65
23	4	0.949	9.0	90	31.90	6.5	--	1.77	~6.0	0.92
24	4	0.939	9.0	190	0.00	--	--	--	--	--
25	4	0.939	9.0	190	7.10	0.2	~20	2.05	0	0
26	4	0.939	9.0	190	12.40	0.5	~30	2.27	0.2	0.40
27	4	0.939	9.0	190	15.90	1.0	65	2.06	0.5	0.50
28	4	0.939	9.0	190	19.40	2.2	~100	1.69	1.1	0.50
29	4	0.939	9.0	190	23.00	~3.0	~100	1.72	1.8	0.60
30	4	0.939	9.0	190	26.60	~4.0	~100	1.72	2.5	0.63
31	4	0.939	9.0	190	31.90	7.0	--	1.56	4.2	0.60

TABLE 6.3 (continued).

TEST NO.	OIL TYPE	DENSITY (gm/cc)	CAVITY DEPTH (cm)	CAVITY LENGTH (cm)	LOCAL CURRENT (cm/sec)	VORTEX ZONE OFFSET ϵ_1 (cm)	VORTEX LENGTH (cm)	FROUDE NUMBER F_{ϵ_1}	SHEAR ZONE OFFSET ϵ_2 (cm)	ϵ_2/ϵ_1
32*	4	0.949	9.0	90	0.00	--	--	--	1.0	--
33*	4	0.949	9.0	90	7.10	0.4	~40	1.59	0.2	0.50
34*	4	0.949	9.0	90	12.40	0.5	80	2.48	0.3	0.60
35*	4	0.949	9.0	90	19.40	2.1	90	1.89	1.2	0.57
36*	4	0.949	9.0	90	26.60	3.8	100	1.93	2.8	0.74
37	5H	0.951	14.0	50	23.90	10.0	--	1.09	0	--
38	5H	0.951	14.0	50	31.80	11.0	--	1.38	0	--
39	5H	0.951	14.0	50	39.80	11.0	--	1.73	0	--
40	5H	0.951	14.0	50	47.70	10.0	--	2.18	0	--
41	5H	0.978	9.0	100	0.00	--	--	--	--	--
42	5H	0.978	9.0	100	8.35	0.3	~30	3.36	0.2	0.67
43	5H	0.978	9.0	100	14.95	2.4	~50	2.08	1.8	0.75
44	5H	0.978	9.0	100	19.22	5.5	~70	1.77	4.7	0.85
45	5H	0.978	9.0	100	23.50	7.5	--	1.85	7.5	1.00
46	5H	0.955	10.5	202	0.00	--	--	--	--	--
47	5H	0.955	10.5	202	6.95	0.1	80	3.31	0	0
48	5H	0.955	10.5	202	12.15	8.5	50	1.49	8.5	1.0
49	5H	0.955	10.5	202	15.62	9.0	--	--	8.5	0.89

* Recessed Cavity.

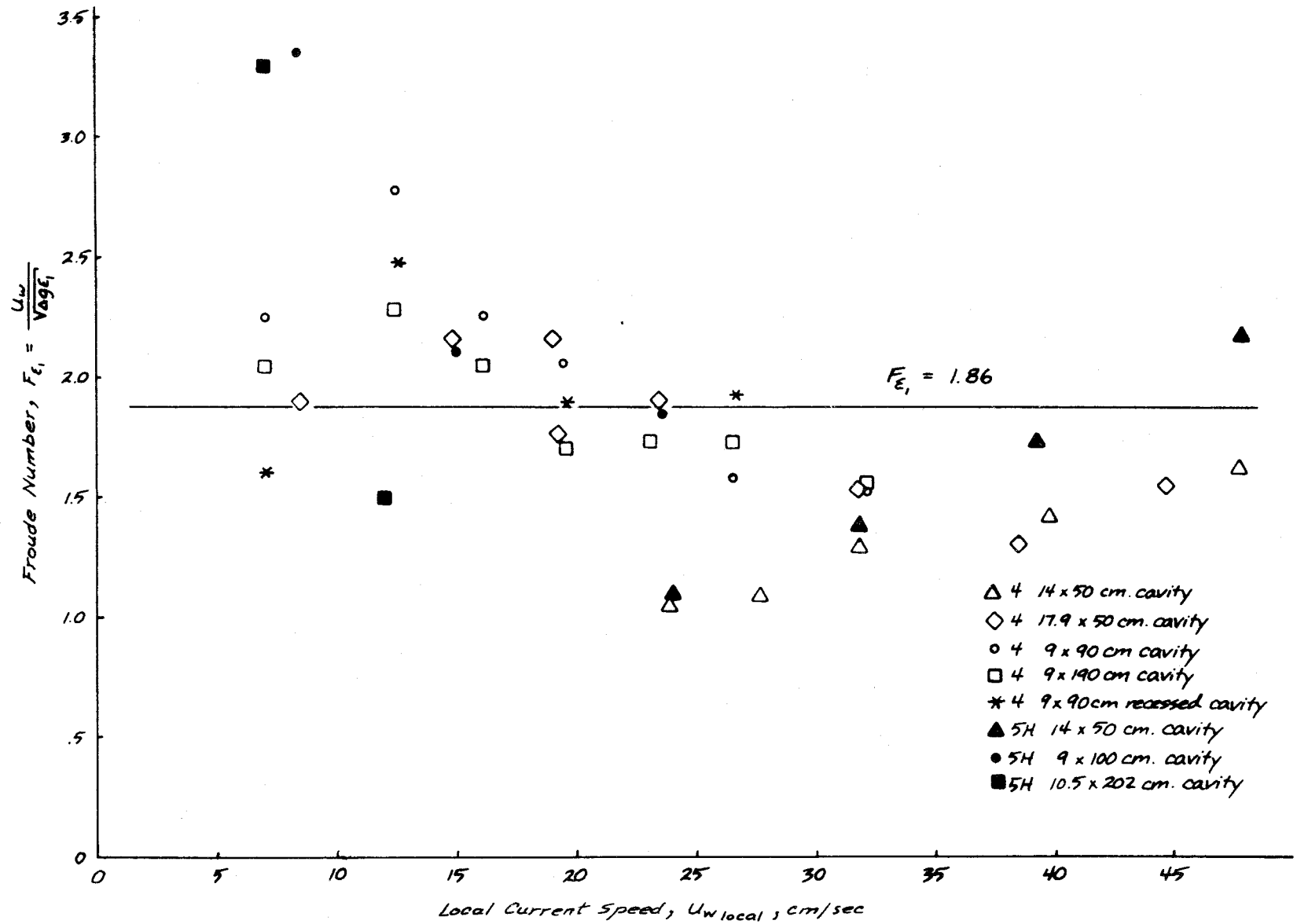


Figure 6.13. Densimetric Froude Number Based on Offset Size versus Local Current Speed for Oil Trapped in a Cavity

value of the Froude Number. Fortunately, at low currents the absolute value of the offset is so small that the adverse impact of small errors in estimating its size is insignificant. An empirical estimate of offset magnitude is then given as:

$$\epsilon_1 = 0.29 \frac{U_w^2}{\Delta g} . \quad (6.9)$$

The length of the offset vortex zone is plotted in Figure 6.14 versus local current speed. Initially, it was expected that the length of this vortex zone would approach some constant proportional to the offset magnitude. This would be consistent with the general observations of a relationship between wake length and roughness height. However, Figure 6.14 demonstrates a strong linear relationship between the cell length and current velocity, rather than the squared Froude Number relationship observed in the size of the offset versus velocity. This suggests that, within the range of accuracy of our estimates, the cell length grows linearly with current speed. A least squares analysis of the data gives a relation between cell length and current speed as:

$$l = 3.79 U_w + 1.65 . \quad (6.10)$$

Intuitively the relationship for cell length should go to zero as the current speed goes to zero. A visual curve fit of cell length versus current speed suggests that the cell length could be approximated by:

$$l = 4 U_w . \quad (6.11)$$

The largest cell observed was of the order of 100 cm in length. This value may be a natural limiting length of the cell, or it may be due to the cavity depth limiting the size of the offset that can develop. The scale of roughness used in these tests would then limit the cell to be not greater than 100 cm in length.

When cavities are short in comparison to the length of the vortex zone, a relatively stable vortex region develops at the mouth of the cavity. Some oil seems to be trapped within the cavity even when current speeds reach 40 cm/sec. However, the layer of oil that remains can no longer be predicted by the simple densimetric Froude Number relation proposed for offset magnitude. Once the oil layer becomes comparatively thin, the freestream current is able to "feel" the presence of the ice cover through the oil slick resulting in substantial adjustment in the flow profile. The remaining oil becomes more stable and harder to remove. This is in contrast to the behavior of a wake at the same current speed. The thickness of this minimum layer cannot be determined with presently available information.

The size of the offset seems to be insensitive to the overall length of the cavity. An offset of the same magnitude will develop for the same current speed in a cavity which just encompasses the vortex zone as in a cavity which includes a vortex zone and a shear zone. This suggests that the two zones act independently, and allows for computation of the captured oil volume for any size cavity.

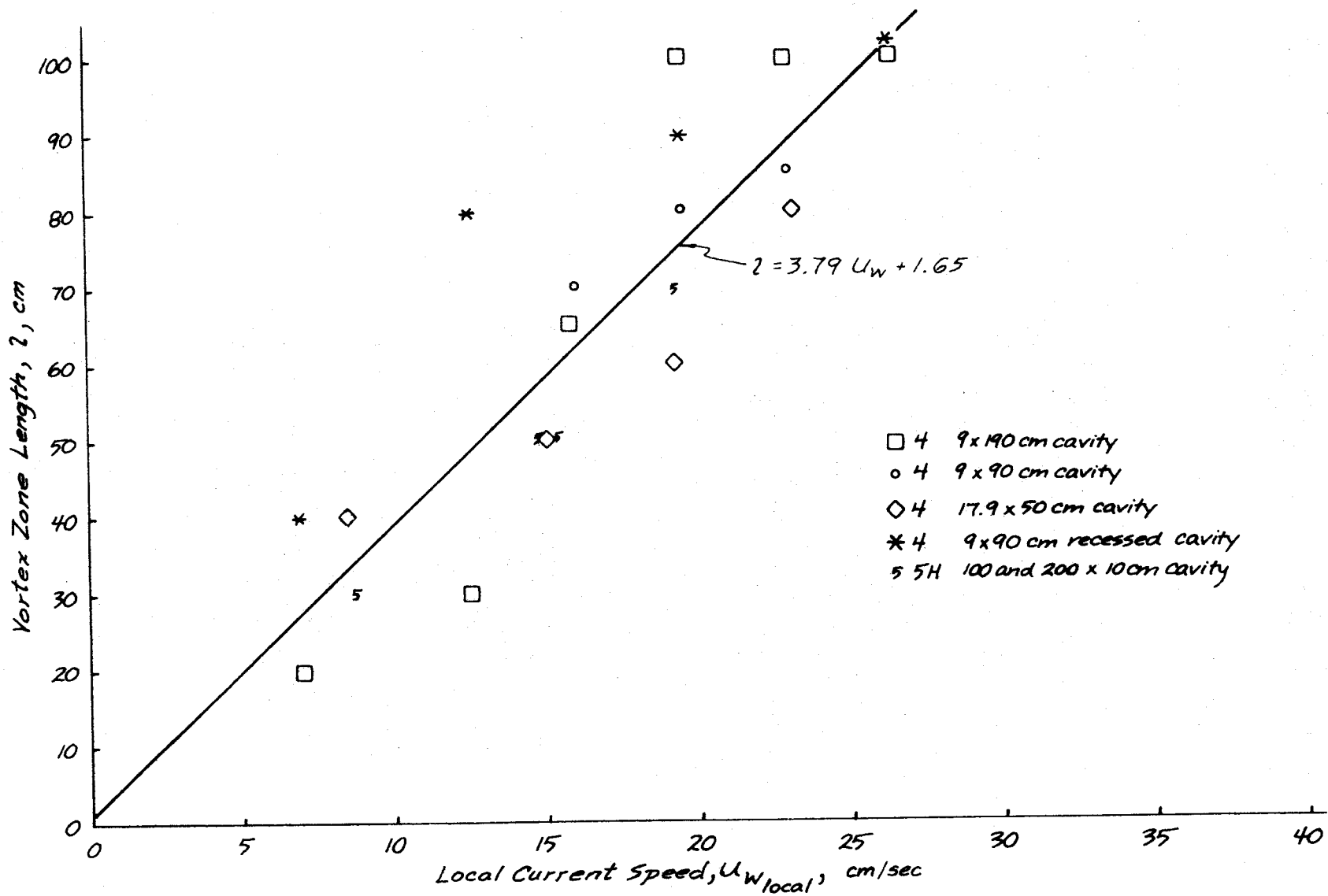


Figure 6.14. Vortex Zone Length versus Local Current Speed for Oil Trapped in a Cavity

Downstream of the vortex zone in a cavity, a shear region develops analogous to the frontal shear zone. With the No. 4 oil in both the 1 and 2 meter cavities, a very distinct shift in the position of the interface occurs when the freestream reattaches behind the vortex zone. Recognizing that the slope of the interface of the shear zone is relatively flat over long distances, the magnitude of the offset, ϵ_2 , which develops in this region can be estimated. A comparison of the offset in the vortex zone to the offset in the shear zone is shown in Table 6.3. For the No. 4 oil, the average ratio of the two offsets is 0.59. For the No. 5 heavy oil, the average is slightly higher at 0.86. However, the No. 5 heavy oil was less responsive, tending to peel off layers of oil rather than redevelop a new profile. Because of this nature, it was more difficult to define a stable offset thickness in the shear zone for No. 5 heavy oil.

The location of the shear interface is determined by the offset formed in the vortex zone; when the vortex offset grows, the initial shear offset also grows. As the current speed increases, the oil will initially remain attached at the downstream wall, while the interface tilts to accommodate the growth of the offset zone. If the offset grows too large, it becomes no longer possible to maintain the stable parabolic interfacial shape, and substantial amounts of oil drain until the interface can reestablish itself higher in the cavity. For increasing velocity, this procedure will continue until the offset finally penetrates the oil layer and divides the slick at the cavity roof, forming a separate frontal slick and a wake contained slick.

The location of an oil-water interface in a cavity based upon presently available data can therefore be defined in terms of two regions. In the vortex zone, the depth of the offset follows the empirical relation:

$$\epsilon_1 = \frac{0.29 U_w^2}{\Delta g}, \quad (6.12)$$

and the length of the offset follows an empirical relation:

$$l = 4 U_w. \quad (6.13)$$

The shear zone will develop with an initial offset of:

$$\epsilon_2 = 0.15 \frac{U_w^2}{\Delta g}, \quad (6.14)$$

and continue to grow parabolically to the back wall of the cavity according to:

$$x = 250 \frac{\Delta g}{U_w^2} (\delta_{\text{tail}}^2 - \delta_{\text{stagnation}}^2), \quad (6.15)$$

where $\delta_{\text{stagnation}}$ is the oil thickness at ϵ_2 . The tail thickness is controlled by either the depth of the cavity or the magnitude of the offset.

Figure 5.9 and the corresponding results given in Table 6.3 describe the behavior of the oil-water interface in a pure recess in the ice cover. The offset depth and the shear zone shape appear to be consistent with the test results observed for the protruding type of cavity. However, the vortex zone appears to extend somewhat farther downstream.

6.7 Discussion of Small and Large Roughness Results

Two sets of equations evolved from the theoretical development of descriptions of oil movement under ice. One set of equations applies to the case of oil spreading under ice of small roughness, and another set to the case of oil spreading under ice having large roughness features. The theoretical developments appear in Appendix C and D respectively. This section of the report outlines the criteria for which each theory applies.

The first theory yields the velocity of an oil slick moving under ice having roughness features smaller than the static thickness of the slick under smooth ice. This type of roughness does not contain the oil, but merely decreases the slick velocity. Examining the equation describing this situation:

$$\left(1 - \frac{U_s}{U_w}\right)^2 = \frac{K}{0.115 F_\delta^2 + 1.105}, \quad (6.16)$$

the factor K in the numerator is the term which is most sensitive to the roughness of the ice. This term varies from unity for smooth ice to about 2.8 for the 1 cm roughness tested in the laboratory. Such a dramatic effect on the slick velocity demonstrates that even minute roughness can substantially retard the advance of a slick. Therefore, in order to accurately predict oil slick transport velocities in the field, a detailed knowledge of under ice roughness is required. Field information of this type is difficult to obtain, since measurements made to date by sonar profiling do not have adequate resolution.

Large roughness features are more easily identified in the field. Large roughness elements, defined as under-ice elements with keel depths greater than the smooth ice equilibrium slick thickness, have the potential to contain oil under ice until certain limits are reached.

Equation 3.10 describes the containment of oil behind a large roughness element in deep water as follows:

$$F_\delta^2 = (2 - \psi) \frac{(1 - \psi)}{(1 + \psi)}. \quad (6.17)$$

This value of ψ represents the nondimensional critical thickness of the head region of a contained oil slick, and also the maximum thickness of the tail region as determined by Kelvin-Helmholtz instabilities. Note that the limiting head region thickness, ψ , is not dependent upon the scale of roughness. As long as the roughness is deep enough to support at least the neck thickness of the slick, a slick can form. On the other hand, if the velocity of the free-stream is large enough for instability to occur, containment of the slick will be lost regardless of roughness size. When ψ reaches a value less than approximately 0.01, Equation 6.17 approaches an asymptotic limit of 2, and the solution becomes independent of water depth. For a freestream velocity of 20 cm/sec,

Equation 3.9 suggests that slick thicknesses should typically be 2 cm. Therefore, the deep water condition does not occur for typical oils until the water depth exceeds 200 cm. This water depth increases by the square of the velocity as the current increases further. Tests in the 40 cm deep flume therefore cannot model deep water conditions.

Due to the depth limitation of the flume, complete development of the shear region into a parabolic interface was impossible. However, limiting conditions on the size of the shear region still satisfied depth dependent estimates. In deep water the shear region will be limited only by the size of the under-ice roughness for subcritical current speeds. In this case, the pooled oil can continue to build until the addition of excess oil causes the parabolically shaped interface to exceed the ice roughness depth. Leakage from the slick will then occur until its natural equilibrium condition is reestablished. When currents approach critical speed for Kelvin-Helmholtz instability, droplet initiation can occur at any location along the oil-water interface. Because of this instability, complete flushing of the frontally trapped oil slick will ultimately occur.

Wake regions behind ice roughness features are far less stable than originally assumed, particularly at higher current speeds. The length of the wake is affected by the shape of the ice roughness and the local water depth. Turbulent fluctuations within the separated regions are large enough to continuously tear off small drops of oil, releasing them to the freestream. Although a mean reverse circulation is apparent in the wake, the region is not a well behaved closed cell, and the fluid entrapped there is continuously being washed and replenished. Oil will therefore not remain contained within a wake for any extended period of time unless local currents are low enough so as not to overcome the natural inertia of the oil.

Ice cavities represent the most likely means for trapping oil in a rough ice field. The shape and location of the oil-water interface has been shown to be controlled both by a vortex region of separated flow causing a major offset in the oil-water interface, and a shear region analogous to the frontal trapped shear region. The depth of the offset seems very consistent for different types of oils and different cavity sizes, and is approximately described by a constant densimetric Froude Number relationship. However, when the penetration of the offset becomes comparable to the total depth of the cavity, this relation is no longer valid. When the oil is reduced to some minimum thickness, the free-stream flow begins to feel the presence of the ice cover through the oil. The interfacial shear stress becomes adjusted for this added shear, and the containment stability of the oil changes. Present knowledge of immiscible fluid behavior in cavities is not sufficient to allow a prediction of this minimum thickness, or the level of stability to be anticipated. A second major unknown is the length of the vortex cell. Presently available information strongly suggest that cell length increases linearly with current speed. However, this appears inconsistent with observations of separated regions behind ice roughness which

approach a constant length. Cell growth needs to be explored more fully for a wider range of oil densities and viscosities, and cavity geometries, before a conclusive statement can be made.

The behavior of the cavity viscous zone and the location of the interface seem to be fairly well understood. As current speed increases, the offset of the vortex zone retreats higher into the cavity. The viscous region which appears to develop at half the vortex offset, suves parabolically back to the trailing wall of the cavity. When the magnitude of the offset becomes too great, the parabolic shape of the viscous zone becomes too steep and can no longer be maintained. Draining of some oil occurs until the oil-water interface is able to redevelop a stable form deeper into the cavity. With increasing velocity, the shift in the oil-water interface will continue until the vortex zone finally is able to separate the oil in the cavity into two slicks, a frontal slick and a wake trapped slick. If local currents in the cavity are large enough, a Kelvin-Helmholtz instability will develop at the oil-water interface, and complete flushing of oil from the cavity will occur regardless of this depth. A depiction of the shift in the oil-water interface in the cavity with increasing current speed is shown in Figure 6.15.

One cavity case cannot be explained by Equation 6.12. If the cavity length exceeds the combined length of the shear zone and the vortex zone, draining will occur until the interface shifts enough to reattach to the tip of the trailing cavity wall. For very long cavities the interface will curve upward until it terminates at the roof of the cavity, dividing the slick into individual frontal and wake trapped slicks. However, a range of cavity geometries exist for which it is possible that the interface does not intersect with the cavity roof but is rather projected through the vortex zone. In this case the relative position of the interface is above the vortex offset so the slick in this area is less controlled by the vortex shedding. A prime example of this case is the asymmetrically shaped cavity in which the trailing wall does not extend as deep as the leading wall. Presently there are no physical or mathematical hypothesis for the interfacial shape or position for this case. However, a reasonable approximation, which is offered until more information is available, is that in this special case the entire cavity falls into the shear zone, and the interfacial shape and position can be defined by projecting the interface parabolically all the way from the tip of the trailing cavity wall to the front wall, ignoring the vortex zone completely. Through the use of this assumption, a trapped volume of oil can be estimated for any cavity geometry and flow condition.

6.8 Vertical Entrapment of Oil by First-Year Ice

Martin [15, 17] summarizes the results of much of the field and laboratory work devoted to the study of oil entrapment by first-year ice. The results show that if oil is released beneath winter ice, the oil will become entrapped as a lens within the ice. Because the oil can become significantly colder than the

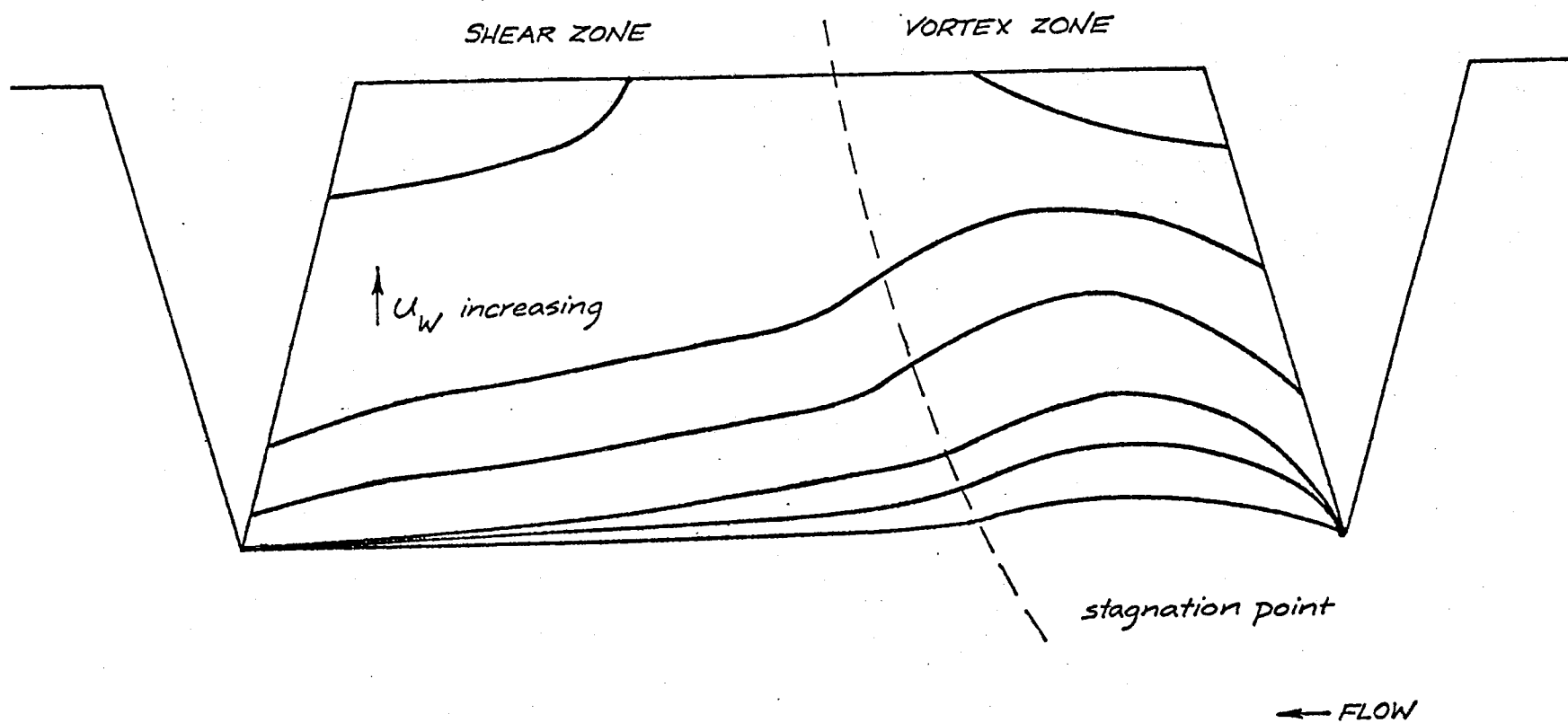


Figure 6.15. Schematic Representation of the Shift in Oil-Water Interface Position Within a Cavity as a Function of Increasing Current

surrounding sea water, ice lips first begin to grow around the slick. Because this growth is much faster than the surrounding vertical ice growth rate, the oil is constricted from further horizontal spreading by these ice lips very quickly. As ice grows beneath the oil, the oil lens becomes pressurized due to the added buoyancy of the ice below. This pressurization can force the oil upward.

In the spring, top-to-bottom brine channels with a horizontal spacing of 0.1 to 0.3 m on a grid open up within the ice. The observations cited by Martin and the laboratory work reported by Purves [22] suggest that the oil first flows to the surface when the minimum ice interior temperature reaches -4°C . The flow to the surface accelerates as the ice continues to warm.

Under controlled laboratory conditions, Purves observed that Norman Wells crude oil was able to migrate through a 35 cm thickness of first-year ice with a brine channel spacing of 1 channel per square cm after 1768 ± 20 melting degree-hours. This correlates very closely with the predicted 1777 melting degree-hours calculated from Equation 3.19.

In the field observations made at Balaena Bay a discharge of 0.42 m of Norman Wells crude was made beneath 1.95 meters of ice [17]. Oil first appeared on the ice surface 45 minutes later. This corresponds to a vertical migration rate of 0.07 cm/sec, and is very close to the theoretical prediction of 0.086 cm/sec. Additionally, the distance between centers of oiled areas varied from 0.1 to 0.5 m, which correlates well with the brine channel spacing. Once on the ice surface, the solar radiation absorbed by the oil through the snow causes the formation of oiled melt ponds. Once the melt ponds form, the continued energy absorption by the oil eventually causes the melt pond to melt through the ice, so that the oil is again released into the ocean.

In terms of the months of the year in the nearshore Beaufort Sea, the oil first reaches the surface in May, with oiled melt ponds forming in June. The re-entry of the oil into ocean probably will take place in July or August, and in some years it is possible that some oil will remain both on the surface and inside the ice for the September freeze-up [16].

6.9 Vertical Entrapment of Oil by Multi-Year Ice

There has been one laboratory study by Martin [16] and a continuing field study sponsored by Environment Canada [3] concerned with oil entrapment by multi-year ice. Both of these studies suggest that vertical oil migration through brine channels is not important for multi-year ice.

The difference between multi-year ice and first-year ice is that multi-year ice has gone through the summer thaw, which both desalinates and melts the upper part of the ice, so that when the autumn refreezing occurs, the upper meter or some of this ice is nearly fresh water ice. This process greatly reduces the porosity of the ice to oil.

In the laboratory, Martin [16] simulated multi-year ice by growing 8 cm of sea ice in a cold room tank, warming it to the point at which melt water formed on the surface, then adding an average of 2 mm of fresh water to simulate melted snow. The ice was next recooled to the point that new ice grew beneath the old. Then 500 cm³ of Prudhoe Bay crude oil was released beneath the ice, and freezing continued until the oil was entrained in the ice.

After the oil was entrained, the ice was warmed up in two different ways, first, in the dark to see if temperature effects alone would bring the oil to the surface; and second, with a simulated sun shining on the surface. When the ice was warmed up in the dark, although melting occurred on the ice surface, there was no evidence of oil rising through brine channels to the surface. The ice was then refrozen, then warmed up again with the addition of an overhead light with its power adjusted to model the incident arctic solar radiation. The energy of this source both caused surface melting, and was absorbed by the dark oil 8 cm beneath the ice surface, so that the oil melted slowly upward from below while the surface melted downward. This process continued until there was a large release of oil. The bulk melting of the ice therefore provided a pathway for the oil, with no signs of an upward flow through brine channels.

The field experiment was carried out in the Canadian Arctic by R. F. Brown of NORCOR [3] beginning with an oil discharge on 1 June 1978. The discharge consisted of three spills separated from one another by 30 m under 4 m thick multi-year ice. An overflight on 1 July showed oil on the surface from a large crack which ran through the middle of one of the under ice pools. An additional flight on 1 August showed that the oil from the crack site had spread on the surface of melt ponds. Cores taken at the site on 1 August, however, showed no evidence of oil entrained within the ice. A later examination of a time-lapse film photographed at one of the spill sites away from the crack suggested, on the basis of pictures of oil slowly bubbling up to a melt pond surface, that some oil came up through brine channels. However, observers at the site agree that most of the oil came up through the crack.

In summary, the field and laboratory evidence suggests that the low porosity of multi-year ice greatly restricts the upward movement of oil through brine channels, and that the release of entrapped oil occurs when the multi-year ice melts down to the entrapped oil.

7. APPLICATION OF RESULTS

7.1 Calculational Procedure

In order to make the results of this study immediately useful for projecting oil spill behavior in ice infested waters, a methodology has been developed for addressing any under-ice spill situation. As discussed elsewhere in this report, the confidence level varies for the different oil-ice interaction situations, but an effort was made to assemble the most complete, and best available, statement of the containment and transport of oil beneath ice in the presence of a current, making reasonable approximations and estimates where more concrete information was not available.

Figure 7.1 presents in flowchart form the procedure for quantitatively determining the transport or containment of oil beneath ice in deep water. Table 7.1 summarizes the equations referred to in the flowchart and Table 7.2 summarizes the nomenclature and units for the parameters used in the equations. For a given spill, the properties of the oil, the current speed, and the under-ice roughness characteristics are required as input data. The class of ice roughness is then established relative to the smooth ice equilibrium slick thickness given by Equation 7.1. If the roughness is classed as small roughness, the slick will advance at a speed given by Equation 7.2. If the roughness is classed as large roughness, the slick has the potential of being trapped or contained by the under-ice roughness. Equation 7.3 tests to determine whether the roughness elements can form a cavity, or simply act as individual barriers or obstructions. If the offset of the oil-water interface as calculated by Equation 7.3 is greater than or equal to the local roughness height, the slick will divide and the roughness elements act as individual barriers. The containment of oil by a barrier will be possible if the local current is below the critical value which causes an instability to develop at the oil-water interface. This criteria is given by Equation 7.4. If the current is below the critical value, the volume of oil trapped in front of, and behind, the barrier can be computed using Equations 7.9 and 7.10. If the current is above the critical value, complete flushing of the oil will occur beneath the barrier and no oil will be contained. In this case, envisioned as a small roughness ice field with occasional large roughness elements present, the advance of the slick will largely be controlled by its transport beneath the surrounding small roughness ice, and the speed of advance can be approximated by using Equation 7.2.

If the offset as determined by Equation 7.3 is less than the local roughness height, the volume of oil trapped in the cavity is dependent on the cavity length. If the cavity length is less than the combined length of the calculated slick shear length and vortex length as defined by Equations 7.5 and 7.6, the volume of contained oil can be calculated from Equation 7.7.

If the cavity length exceeds the sum of the calculated shear and vortex lengths, the slick may completely divide, or it may equilibrate to some intermediate position. If the curvature of the interface causes the shear zone to

TABLE 7.1 SUMMARY OF EQUATIONS FOR CALCULATING THE TRANSPORT OR CONTAINMENT OF OIL BENEATH ICE IN THE PRESENCE OF A CURRENT.

$$\delta_{eq} = 1.67 - 8.50 (\rho_w - \rho_o) \quad (7.1)$$

$$\left(1 - \frac{U_s}{U_w}\right)^2 = \frac{K}{(0.115F\delta^2 + 1.105)} \quad (7.2)$$

$$\epsilon = \frac{U_w^2}{3.46\Delta g} \quad (7.3)$$

$$U_{fail} = 1.5 \left[2 \left(\frac{\rho_w + \rho_o}{\rho_w \rho_o} \right) (\sigma_{o/w} g (\rho_w - \rho_o))^{1/2} \right]^{1/2} \quad (7.4)$$

$$\lambda = 4U_w \quad (7.5)$$

$$X_{shear} = \frac{4\Delta g}{f_s U_w^2} \left(\eta^2 - \left(\eta - \frac{\epsilon}{2} \right)^2 \right) \quad (7.6)$$

$$V' = \lambda (\eta - \epsilon) + \left[\frac{\delta_{tail} + \left(\eta - \frac{\epsilon}{2} \right)}{2} \right] (\lambda - 1) \quad (7.7)$$

$$\text{where } \delta_{tail} = \sqrt{\frac{(\lambda - 1) f_s U_w^2}{4\Delta g} + \left(\eta - \frac{\epsilon}{2} \right)^2}$$

$$\delta_{stagnation} = \sqrt{\eta^2 - \frac{(\lambda - 1) f_s U_w^2}{4\Delta g}} \quad (7.8)$$

$$V' = \frac{\left(\eta + \frac{U_w^2}{4\Delta g} \right) \left(\frac{4\Delta g}{f_s U_w^2} \right) \left[\eta^2 - \left(\frac{U_w^2}{4\Delta g} \right)^2 \right]}{2} \quad (7.9)$$

$$V' = 6 C_D \eta \delta_{eq} \quad (7.10)$$

$$V' = \frac{1}{2} \left(\eta + \sqrt{\eta^2 - \frac{\lambda f_s U_w^2}{4\Delta g}} \right) \lambda \quad (7.11)$$

TABLE 7.2 DEFINITION OF TERMS FOR EQUATIONS FOR CALCULATING THE TRANSPORT OR CONTAINMENT OF OIL BENEATH ICE IN THE PRESENCE OF A CURRENT.

<u>Symbol</u>	<u>Definition</u>	<u>Units</u>
C_D	roughness form drag coefficient $C_D = 1.98$ for flat plate $C_D = 1.55$ for triangular shape	--
F_δ	densimetric Froude number - $F_\delta = U_w / \sqrt{\Delta g \delta}$; for this case, $\delta = \delta_{eq}$.	--
f_s	oil-water interfacial friction factor empirically assumed in this report as 0.016	--
g	gravitational acceleration	cm/sec ²
K	ice friction amplification factor $K = 1.0$ for smooth ice K approximated from Figure 6.10 for small roughness ice	--
U_{fail}	current speed for containment failure	cm/sec
U_s	oil slick speed	cm/sec
U_w	water current speed	cm/sec
v'	approximate volume of trapped oil per unit width	cc/cm
x_{shear}	length of the shear dominated portion of the slick in a cavity	cm
Δ	relative density ratio = $(\rho_o - \rho_w) / \rho_w$	--
δ	local slick thickness	cm
$\delta_{stagnation}$	thickness of slick in a cavity at the end of the vortex zone	cm
δ_{eq}	equilibrium oil slick thickness beneath smooth ice	cm
δ_{tail}	thickness of contained slick at the downstream wall	cm
ϵ	vortex zone offset into a cavity	cm

TABLE 7.2 Continued.

<u>Symbol</u>	<u>Definition</u>	<u>Units</u>
η	ice roughness height or cavity depth	cm
l	length of vortex cell	cm
λ	cavity length	cm
ρ_o	density of oil	gm/cc
ρ_w	density of water	gm/cc
$\sigma_{o/w}$	interfacial tension between oil and water typically 30 to 35 dynes/cm for crude oils	dynes/cm

neck down to zero somewhere in the cavity, as determined by Equation 7.8, the slick will divide and the cavity transforms to simple individual barriers with the corresponding containment potential determined as previously described through the use of Equations 7.4, 7.9, and 7.10. If the shear zone thickness as determined by Equation 7.8 does not dissipate to zero, the entire cavity will fall under the influence of the shear zone and the trapped volume can be estimated by projecting the shear zone interface back through the vortex zone to the front wall of the cavity as given by Equation 7.11.

The theoretical and experimental relations for the transport or containment of oil beneath an ice cover have been developed and tested for two dimensional situations. Three dimensional trapping, although more complicated, can be reasonably predicted based on the two dimensional results. In applying these predictive relations, the user is advised to keep two major points in mind:

1. If spilled oil is blocked by under-ice roughness, the oil that becomes trapped will fill the void to its maximum allowable volume first before continuing to spread to the next roughness element.
2. The slick behavior must be analyzed for a particular type of roughness. Regions of transition between roughness forms which involve simultaneous slick interaction with different roughness types must be treated individually. Generally a particular roughness type will dominate slick behavior, and this roughness type should be used as the basis for the analysis.

7.2 Sample Calculations

The application of the preceding calculational procedure is demonstrated in the following series of sample calculations.

7.2.1 Small Roughness Ice

What is the speed of an oil slick moving beneath relatively smooth fresh water ice having a roughness amplitude of 0.2 cm on 2 cm spacing when the current speed is 30 cm/sec?

Input Data:

$$\begin{aligned}\rho_o &= 0.9 \text{ gm/cc} \\ \rho_w &= 1.0 \text{ gm/cc} \\ \sigma_{o/w} &= 30 \text{ dynes/cm}\end{aligned}$$

$$\begin{aligned}U_w &= 30 \text{ cm/sec} \\ \eta &= 0.2 \text{ cm} \\ \lambda &= 2.0 \text{ cm}\end{aligned}$$

Solution:

From Equation 7.1, the equilibrium thickness of the oil beneath smooth ice is:

$$\delta_{eq} = 1.67 - 8.50(1.0 - 0.9) = 0.82 \text{ cm} .$$

Since this value is greater than the roughness height of 0.2 cm, the roughness is classed as small roughness, and the slick speed can be determined from Equation 7.2. It is first necessary to determine that K is 2.12 from Figure 6.10, and to calculate the Froude Number:

$$F_{\delta} = \frac{30}{[(0.10)(980)(0.82)]^{1/2}} = 3.35 .$$

Then the slick speed is determined to be:

$$\begin{aligned} U_s &= U_w - U_w \left[\frac{K}{(0.115 F_{\delta}^2 + 1.105)} \right]^{1/2} \\ &= 30 - 30 \left[\frac{2.12}{(0.115)(3.35)^2 + 1.105} \right]^{1/2} \\ &= 1.78 \text{ cm/sec.} \end{aligned}$$

7.2.2 Individual Large Roughness Element with Flushing Failure

What is the oil containment capacity of an ice sheet with roughness characteristics of 5 cm amplitude on 200 cm spacing with a current speed of 30 cm/sec?

Input Data:

$$\begin{array}{ll} \rho_o = 0.95 \text{ gm/cc} & U_w = 30 \text{ cm/sec} \\ \rho_w = 1.0 \text{ gm/cc} & \eta = 5 \text{ cm} \\ \sigma_{o/w} = 30 \text{ dynes/cm} & \lambda = 200 \text{ cm} \end{array}$$

Solution:

From Equation 7.1, the equilibrium thickness of the oil beneath smooth ice is:

$$\delta_{eq} = 1.67 - 8.50(1.0 - 0.95) = 1.25 \text{ cm} .$$

Since this value is less than the roughness height of 5 cm, the roughness is classed as large roughness. From Equation 7.3, the possible vortex offset is:

$$\epsilon = \frac{30^2}{3.46(0.05)(980)} = 5.3 \text{ cm} .$$

Since this value is greater than the roughness height of 5 cm, the slick divides and the roughness elements are treated as individual roughness elements rather than a cavity. The individual roughness elements have the potential of frontal and wake containment if the current velocity is below the failure velocity defined by Equation 7.4:

$$u_{\text{fail}} = 1.5 \left\{ 2 \left(\frac{1.0 + 0.95}{1.0(0.95)} \right) \left[30(980)(1.0 - 0.95) \right]^{1/2} \right\}^{1/2}$$

$$= 18.8 \text{ cm/sec.}$$

Since the current speed of 30 cm/sec is well above the failure speed of 18.8 cm/sec, total flushing will occur. No oil will be contained and the transport of the oil will essentially be controlled by the small roughness characteristics of the surrounding level ice sheet.

7.2.3 Individual Large Roughness Element with Frontal and Wake Containment

What is the oil containment capacity of an ice sheet with triangular roughness elements of 10 cm amplitude on 8000 cm spacing with a current speed of 20 cm/sec?

Input Data:

$\rho_o = 0.9 \text{ gm/cc}$	$U_w = 20 \text{ cm/sec}$
$\rho_w = 1.0 \text{ gm/cc}$	$\eta = 10 \text{ cm}$
$\sigma_{o/w} = 30 \text{ dynes/cm}$	$\lambda = 8000 \text{ cm}$
	$C_D = 1.55$

Solution:

From Equation 7.1, the equilibrium thickness of the oil beneath smooth ice is:

$$\delta_{eq} = 1.67 - 8.50(1.0 - 0.9) = 0.82 \text{ cm} .$$

Since this value is less than the roughness height of 10 cm, the roughness is classed as large roughness. From Equation 7.3, the possible vortex offset is:

$$\epsilon = \frac{20^2}{3.46(0.1)(980)} = 1.18 \text{ cm} .$$

Since this value is less than the roughness height of 10 cm, the slick does not divide due to the formation of the vortex. The sum of the calculated lengths of

the vortex zone and shear zone must then be compared with the roughness spacing of 8000 cm using Equations 7.5 and 7.6, where f_s is taken at the recommended value of 0.016:

$$l = 4(20) = 80 \text{ cm} ,$$

and:

$$x_{\text{shear}} = \frac{4(0.1)(980)}{0.016(20)^2} \left[10^2 - \left(10 - \frac{1.18}{2} \right)^2 \right] = 701 \text{ cm} ,$$

then:

$$l + x_{\text{shear}} = 701 + 80 = 781 \text{ cm} .$$

Since this length is less than the roughness spacing of 8000 cm, it is next necessary to check the thickness of the slick at the forward end of the shear zone using Equation 7.8:

$$\begin{aligned} \delta_{\text{stagnation}} &= \left[10^2 - \frac{(8000 - 80)(0.016)(20)^2}{4(0.1)(980)} \right]^{1/2} \\ &= (-29)^{1/2} . \end{aligned}$$

The slick therefore divides, since $\delta_{\text{stagnation}}$ cannot be less than zero, and the roughness elements are treated as individual roughness elements rather than a cavity. The roughness elements have the potential for frontal and wake containment if the current velocity is below the failure velocity defined by Equation 7.4:

$$\begin{aligned} u_{\text{fail}} &= 1.5 \left\{ 2 \left(\frac{1.0 + 0.9}{1.0(0.9)} \right) \left[30(980)(1.0 - 0.9) \right]^{1/2} \right\}^{1/2} \\ &= 22.7 \text{ cm/sec} . \end{aligned}$$

Since the failure velocity is above the current speed of 20 cm/sec, containment is possible, and the volume of oil contained by frontal trapping and wake trapping per unit width is obtained from Equations 7.9 and 7.10:

$$\begin{aligned} v'_{\text{front}} &= \frac{\left(10 + \frac{20^2}{4(0.1)(980)} \right)}{2} \left(\frac{4(0.1)(980)}{0.016(20)^2} \right) \left[10^2 - \left(\frac{20^2}{4(0.1)(980)} \right)^2 \right] \\ &= 33,397 \text{ cc/cm}^2 , \end{aligned}$$

and:

$$v'_{\text{wake}} = 6(1.55)(10)(0.82) = 76 \text{ cc/cm} ,$$

then:

$$V'_{\text{total}} = 33,397 + 76 = 33,473 \text{ cc/cm} .$$

In comparing the contained unit volume to the maximum possible unit volume of a cavity of the same size, $8000(10) = 80,000 \text{ cc/cm}$, it is seen that the contained volume is only about 42% of the maximum possible containment which would be achieved if the volume bounded by two roughness elements were 100% filled with oil.

7.2.4 Cavity Containment with Vortex and Shear Control

What is the oil containment capacity of an ice sheet with roughness characteristics of 10 cm amplitude on 100 cm spacing with a current speed of 20 cm/sec?

Input Data:

$$\begin{array}{ll} \rho_o = 0.9 \text{ gm/cc} & U_w = 20 \text{ cm/sec} \\ \rho_w = 1.0 \text{ gm/cc} & \eta = 10 \text{ cm} \\ \sigma_{o/w} = 30 \text{ dynes/cm} & \lambda = 100 \text{ cm} \end{array}$$

Solution:

From Equation 7.1, the equilibrium thickness of the oil beneath smooth ice is:

$$\delta_{eq} = 1.67 - 8.50 (1.0 - 0.9) = 0.82 \text{ cm} .$$

Since this value is less than the roughness height of 10 cm, the roughness is classed as large roughness. From Equation 7.3, the possible vortex offset is:

$$\epsilon = \frac{20^2}{3.46(0.1)(980)} = 1.18 \text{ cm} .$$

Since this value is less than the roughness height of 10 cm, the slick does not divide due to the formation of the vortex. The sum of the calculated lengths of the vortex zone and shear zone must then be compared with the cavity length of 100 cm using Equations 7.5 and 7.6, where f_s is taken at the recommended value of 0.016:

$$l = 4(20) = 80 \text{ cm} ,$$

and:

$$x_{\text{shear}} = \frac{4(0.1)(980)}{0.016(20)^2} \left[10^2 - \left(10 - \frac{1.18}{2} \right)^2 \right] = 701 \text{ cm} ,$$

then:

$$l + X_{\text{shear}} = 80 + 701 = 781 \text{ cm} .$$

This length exceeds the cavity length of 100 cm, therefore the slick does not separate and cavity containment occurs. The volume of oil contained in the cavity per unit width is then obtained from Equation 7.7:

$$\delta_{\text{tail}} = \left[\frac{(100 - 80)(0.016)(20)^2}{4(0.1)(980)} + \left(10 - \frac{1.18}{2} \right)^2 \right]^{1/2} = 9.43 \text{ cm} ,$$

then:

$$v' = 80(10 - 1.18) + \left[\frac{9.43 + \left(10 - \frac{1.18}{2} \right)}{2} \right] (100 - 80)$$

$$= 894 \text{ cc/cm} .$$

In comparing this contained unit volume with the maximum possible unit volume of $100(10) = 1,000 \text{ cc/cm}$, it is seen that the cavity is filled to about 89% of its maximum capacity.

7.2.5 Cavity Containment with Shear Control Only

What is the oil containment capacity of an ice sheet with roughness characteristics of 10 cm amplitude on 4,000 cm spacing with a current speed of 20 cm/sec?

Input Data:

$$\begin{aligned} \rho_o &= 0.9 \text{ gm/cc} \\ \rho_w &= 1.0 \text{ gm/cc} \\ \sigma_{o/w} &= 30 \text{ dynes/cm} \end{aligned}$$

$$\begin{aligned} U_w &= 20 \text{ cm/sec} \\ \eta &= 10 \text{ cm} \\ \lambda &= 4,000 \text{ cm} \end{aligned}$$

Solution:

From Equation 7.1, the equilibrium thickness of the oil beneath smooth ice is:

$$\delta_{eq} = 1.67 - 8.50(1.0 - 0.9) = 0.82 \text{ cm} .$$

Since this value is less than the roughness height of 10 cm, the roughness is classed as large roughness. From Equation 7.3, the possible vortex offset is:

$$\epsilon = \frac{20^2}{3.46(0.1)(980)} = 1.18 \text{ cm} .$$

Since this value is less than the roughness height of 10 cm, the slick does not divide due to the formation of the vortex. The sum of the calculated lengths of the vortex zone and the shear zone must then be compared with the cavity length of 4,000 cm using Equations 7.5 and 7.6, where f_s is taken at the recommended value of 0.016:

$$l = 4(20) = 80 \text{ cm} ,$$

and:

$$x_{\text{shear}} = \frac{4(0.1)(980)}{0.016(20)^2} \left[10^2 - \left(10 - \frac{1.18}{2} \right)^2 \right] = 701 \text{ cm} ,$$

then:

$$l + x_{\text{shear}} = 80 + 701 = 781 \text{ cm} .$$

Since this length is less than the roughness spacing of 4000 cm, it is next necessary to check the slick thickness at the forward end of the shear zone using Equation 7.8:

$$\delta_{\text{stagnation}} = \left[10^2 - \frac{(4000 - 80)(0.016)(20)^2}{4(0.1)(980)} \right]^{1/2} = 6 \text{ cm} .$$

Since this thickness is greater than zero, the slick does not divide, and the shear controlled cavity containment volume per unit width is given by Equation 7.11 as:

$$v' = \frac{1}{2} (4000) \left[10 + \left(10^2 - \frac{4000(0.016)(20)^2}{4(0.1)(980)} \right)^{1/2} \right]$$

$$= 31,780 \text{ cc/cm} .$$

In comparing this contained unit volume with the maximum possible unit volume of $4000(10) = 40,000 \text{ cc/cm}$, it is seen that the cavity is only filled to about 79% of its maximum capacity.

8. RECOMMENDATIONS

The results of this study provide considerable insight into the interaction of spilled oil with an ice cover. The theoretical predictions correlate well with the results of the laboratory tests of oil transported under ice having a variety of roughness characteristics. There remain, however, areas where there still are limitations on our capability to predict the behavior of oil spilled in ice infested waters. These limitations are described in this section of the report in the judged order of decreasing importance to the solution to the problem.

1. When the length of a cavity exceeds the flow controlled length of the confined slick, causing drainage of some oil but not enough to divide the slick, present theory is inadequate to define the interface shape and location. Further laboratory and analytical work is required to define the containment capacity of a cavity in this situation.

2. Present theory is inadequate to describe the interface shape or location when the upstream wall of the cavity extends deeper into the current than the downstream wall. Additional laboratory and analytical work needs to be done to further investigate the containment capabilities of a cavity formed by consecutive large roughness elements of unequal depth.

3. The mathematical expressions for the size of the vortex cell are empirical and relatively crude. An effort should be made to refine these expressions through additional experimentation and analysis.

4. The effect of cavity shape on containment capacity is not clearly established. The magnitude of the offset that develops may be strongly influenced by the shape of the parent roughness, particularly for relatively sinusoidal, large frequency and small amplitude roughness. Further experimentation and analysis is required.

5. A better knowledge of actual under-ice roughness characteristics in the field is needed in order to more accurately predict oil spill behavior. Such features as finger ice, slush ice, cavities, and other under-ice roughness types need to be more accurately defined in order to evaluate their effect on the transport and containment of oil in field situations. The collection of field data on under-ice roughness characteristics should therefore continue.

6. The lack of long term oil containment in wake regions has only been observed for high local free stream currents. Potential long term containment at lower current speeds needs further verification through additional experimentation.

7. The size and orientation of an under-ice oil slick have been observed to affect its velocity. Appropriately, these characteristics are parameters in the equation for predicting slick velocity. Knowledge of how and

why oil slicks may either breakup as they move and orient themselves transverse to the flow, or elongate themselves parallel to the current direction is important in slick trajectory predictions. Further experimentation and analysis is required to establish the reasons for these differences in slick behavior.

8. Oils widely ranging in viscosity and density seem to fit the generalized transport relations developed in this study. These relations are, however, based on very limited data. It would be desirable to obtain more data at very high and very low current speeds in order to establish greater confidence in the relationships developed.

9. Oil containment in front of large pressure ridges found in the field may not be as sensitive to changes in water velocity as was found to be the case in the laboratory. The deflection of higher velocity water particles beneath the barrier may occur further upstream for larger roughness elements. Current flow near ridges should be studied in the field to evaluate the possibility of such effects on oil spill transport.

10. This study was directed towards defining the transport and containment of oil beneath ice in the Alaskan Beaufort Sea following a nearshore release by incorporating oil-ice interaction into a model of ice dynamics to result in predictions of spilled oil trajectories. The major constraints imposed on the study because of this application were that the maximum currents of interest were in the neighborhood of 30 cm/sec, and the situations of oil interaction with broken ice cover and oil behavior at an ice edge were judged to be short term phenomena relative to the time frame of the ice trajectory model. These constraints would have to be modified, for example, if the application was the Bering Sea, where broken ice fields are a long term situation, where spill behavior at ice edges could be very important, and where currents measured relative to the ice can reach 50 cm/sec. For Bering Sea applications, then, the work of this study should be extended to current values around 50 cm/sec, and the new oil-ice interaction situations of oil spilled in broken ice cover and the behavior of spilled oil at ice edges should be investigated.

11. Another implicit constraint imposed by the nearshore Alaskan Beaufort Sea release of oil is one of relatively shallow water depths in terms of offshore drilling standards. The eventuality of deeper water drilling farther offshore in the Beaufort or Chukchi Seas, or in even relatively nearshore areas of the Bering Sea, presents the possibility in the event of a seafloor blowout of an oil plume at sufficient depths to cause the formation of mousse. The resulting mousse would present a unique combination of physical properties, most significantly the density, viscosity, and interfacial tension, not previously covered in these studies of oil-ice interaction. A similar program of experimental and analytical work would be required for mousse covering a broad range of component oil properties and oil and water percentages.

12. Once oil is contained by, or trapped within, an ice sheet, it moves with the ice and an ice movement model becomes a spill trajectory model. The next critical point in projecting spill behavior is to determine when the

oil is released from the ice to become free to move as an open water spill. The present level of capability for making such projections is extremely crude and should be refined such that the inception and release rate of oil through vertical migration are stated in terms of oil properties, ice conditions, and environmental conditions for first year and multi-year ice.

13. Finally, it would be desirable to verify and refine the applicability of the laboratory-based spill behavior predictions through field studies, either through a dedicated field test program or through the study of spills of opportunity. In the latter case, advance preparations should be made so that a spill response scientific team has equipment, objectives, and target operations plans available for immediate implementation when a spill occurs in ice infested waters.

9. REFERENCES

1. Ashton, G., "Evaluation of Ice Management Problems Associated with Operation of a Mechanical Ice Cutter on the Mississippi River," CRREL Special Report No. 214, 1974.
2. Bear, J., "Dynamics of Fluids on Porous Media," *Elsevier*, 1972.
3. Brown, R., NORCOR, Personal Communication.
4. Cross, R. and D. Hault, "Collection of Oil Slicks," *Journal of the Waterways and Coastal Engineering Division, ASCE*, Vol. 97, WW2, 1971.
5. Eide, L. and S. Martin, "The Formation of Brine Drainage Features on Young Sea Ice," *Journal of Glaciology*, Vol. 14, No. 70, 1975.
6. Ferguson, A., "The Measurement of Contact Angles," *Proceedings of the Physical Society of London*, Vol. 53, 1941.
7. Grove, A.S., F. H. Shair, E. E. Petersen, and A. Crivos, "An Experimental Investigation of Steady Separated Flow Past a Circular Cylinder," *Journal of Fluid Mechanics*, Vol. 19, Part 1, pp 60-80, 194.
8. Jirka, G., G. Abraham, D. Harleman, "An Assessment of Techniques for Hydro Thermal Prediction," R. M. Parsons Laboratory for Water Resources and Hydrodynamics, MIT, Report No. 203, July 1975.
9. James, W. T., "Instability at an Interface Between Oil and Flowing Water," *Transactions of the ASME, Journal of Basic Engineering*, Dec. 1972, pp. 874-878.
10. Lake, R. and E. Lewis, "Salt Rejection by Sea Ice During Growth," *Journal of Geophysical Research*, Vol. 75, No. 3, 1970.
11. Leibovich, S., "Oil Slick Instability and the Entrainment Failure of Oil Containment Booms," *Transactions, ASME*, 1976.
12. Lewis, E., "Oil on Sea Ice," unpublished manuscript, Institute of Ocean Sciences, Sidney, B.C., 1976.
13. Lin, A. and L. Landweber, "Lavrentiev Wake Model and Its Cascade," *Journal of Fluid Mechanics*, Vol. 79, Part 4, 1977.
14. Mackay, D. and M. Medir, "The Interfacial Behavior of Oil Under Ice," *The Canadian Journal of Chemical Engineering*, Vol. 54, Feb-April 1976.
15. Martin, S., "A Field Study of Brine Drainage and Oil Entrainment in First Year Sea Ice," Submitted to *Journal of Glaciology*, Dec. 22, 1978.

9. REFERENCES (Continued)

16. Martin, S., University of Washington, Personal Communication.
17. Martin, S., "The Seasonal Variation of Oil Entrainment in First-Year Arctic Sea Ice: A Comparison of NORCOR/OCS Observations," Special Report No. 71, Department of Oceanography, University of Washington, March 1977.
18. McPhee, M. and J. Smith, "Measurements of the Turbulent Boundary Under Pack Ice," AIDJEX Bulletin No. 29, 1975.
19. Moir, J. and Y. Lau, "Some Observations of Oil Slick Containment by Simulated Ice Ridge Keels" for the Frozen Sea Research Group, Victoria, B.C., Hydraulics Division, C.C.I.W., March 1975.
20. Ono, N., "Specific Heat and Heat Fusion of Sea Ice," The Institute of Low Temperature Science, Hokkaido University.
21. Pande, P., R. Prakash, and M. Agarwal, "Flow Past Fence in Turbulent Boundary Layer," ASCE HY1, January 1980, pp. 191-207.
22. Purves, W., "The Interaction of Crude Oil and Natural Gas with Laboratory-Grown Saline Ice," Environmental Protection Service, Environment Canada, 1978.
23. Rosenegger, L., "Movement of Oil Under Sea Ice," Beaufort Sea Project Technical Report No. 28, Department of the Environment, Victoria, B.C., Dec. 1975.
24. Rouse, H., "Energy Transformation in Zones of Separation," 9th International Congress IAHR Dubrovnik, 1971, pp. 1291-1302.
25. Schlichting, H. *Boundary Layer Theory*, New York: McGraw-Hill, 1968.
26. Uzuner, S., F. Weiskopf, J. Cox and L. A. Schultz, "Transport of Oil Slicks Under a Uniform Smooth Ice Cover," Report No. EPA-600/3-79-041, Environmental Protection Agency, Corvallis, Oregon, April 1979.
27. Wilkinson, D., "Dynamics of Contained Oil Slicks," *Journal of the Hydraulics Division*, ASCE, No. HY6, 1972.
28. Wilkinson, D., "Limitations to Length of Contained Oil Slicks," *Journal of the Hydraulics Division*, ASCE, No. HY5, 1973.

APPENDIX A
VERTICAL MIGRATION

In order to examine the manner in which oil penetrates vertically into ice, we must consider the ice as a porous medium. Eide and Martin [5] show that vertical brine channels exist in both young sea ice and in multi-year ice. These channels are the result of differential thawing which allows the release of brine trapped in pockets during the initial freeze. Brine channels in young sea ice are defined as non-arborescent in that a neck exists in the channel just above the ice-water interface. This may imply the existence of an inter-connection of larger brine pockets with only a minute connection to open water. As the ice ages and reworks, the brine pockets become smaller; however, the main channels have enlarged, creating an arborescent pattern with channel radii increasing toward the exit as shown in Figure A.1.

A.1 Inception of Migration

Assume that brine channels communicate with the ice surface and are initially filled to the mean water level with seawater which is the wetting fluid. If a non-wetting fluid such as oil appears at the mouth of the capillary-sized channel opening, a certain pressure must be reached in the non-wetting fluid before it can begin to penetrate the brine channel, overcoming the interfacial tension and displacing the wetting fluid [2]. In other words, a certain capillary pressure must be built up at the interface between the two fluids before drainage of the wetting fluid can occur. This capillary pressure is given as:

$$P_c = \frac{4\sigma_{o/w}}{d} \cos\alpha \quad (A.1)$$

where $\sigma_{o/w}$ is the interfacial tension between oil and water, α is the contact angle with ice, and d is the diameter of the brine channel mouth.

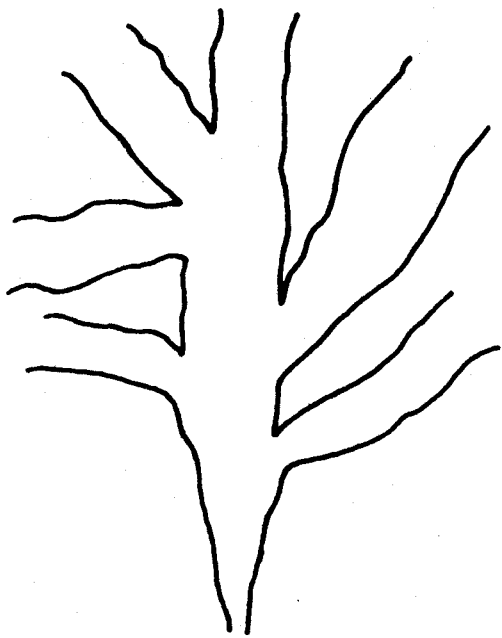
The driving buoyant static pressure due to the oil is defined as:

$$P_B = \rho_w g (\ell_1 + \delta) - \rho_o g \delta - \rho_w g \ell_1 = (\rho_w - \rho_o) g \delta \quad (A.2)$$

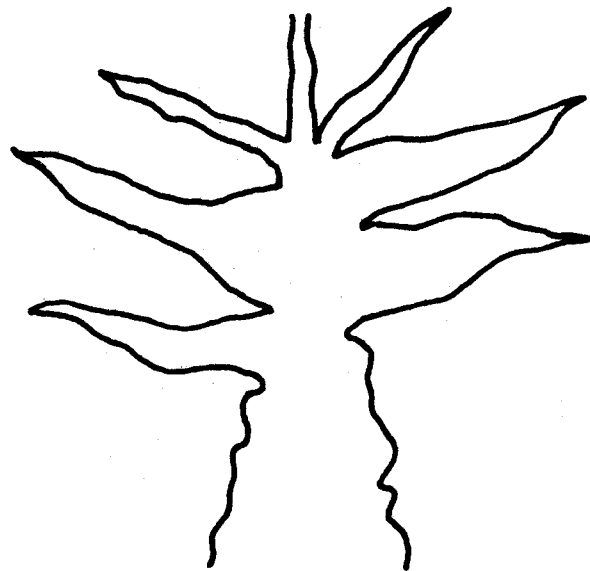
where δ is the thickness of the oil and ℓ_1 is the depth to the under-ice surface from mean water level.

Balancing Equations (A.1) and (A.2) and solving for the critical diameter where migration begins gives:

$$d_{\text{inception}} = \frac{4\sigma_{o/w}}{\delta} \frac{\cos\alpha}{(\rho_w - \rho_o)g} \quad (A.3)$$



Non-arborescent



Arborescent

*Figure A.1. Brine Channel Patterns in Young
and Multi-year Sea Ice*

which is a function of the oil-water interfacial tension $\sigma_{o/w}$, the thickness of the underlying slick δ , and the density difference $(\rho_w - \rho_o)$. The diameter is less sensitive to the contact angle α . Conversely, if a typical brine channel diameter can be specified, a minimum slick thickness causing migration can be defined:

$$\delta = \frac{4\sigma_{o/w}}{d} \frac{\cos\alpha}{(\rho_w - \rho_o)} g \quad . \quad (A.4)$$

This could predict whether vertical migration was possible for different aged ice.

A.2 Progression of Migration

The branching characteristics of a brine channel makes modeling difficult. In order to simplify the analytical model, the vertical brine channels can be treated as capillaries passing completely through the ice sheet. Horizontal dispersion through the channel branches can be considered negligible.

For laminar flow in a capillary, the pressure drop, \bar{P} , over a length, L , is given by the Hagen-Poiseuille Law as:

$$\bar{P} = 32\bar{u}_2 L \mu_o / d^2 \quad (A.5)$$

where \bar{u}_2 is the average flow velocity, L is the ice thickness, μ_o is the oil viscosity, and d is the capillary diameter. The flow rate through capillary tubes is given as:

$$Q = N \frac{\pi d^2}{4} \bar{u}_2 \quad . \quad (A.6)$$

Solving for \bar{u}_2 in Equation (A.5) and substituting in Equation (A.6) gives:

$$Q = N \left(\frac{\pi d^2}{4} \right) \left(\frac{P d^2}{32 L \mu} \right) \quad . \quad (A.7)$$

The pressure change \bar{P} must be overcome by the buoyant force of oil beneath the ice sheet so that:

$$\bar{P} = (\rho_w - \rho_o)gh \quad , \quad (A.8)$$

where h is head of the oil yet to be determined. To find h , consider the hypothetical case given in Figure A.2.

Assuming an equilibrium state has been reached, i.e., the oil cannot rise any further because the oil "head" has reached its critical level, then:

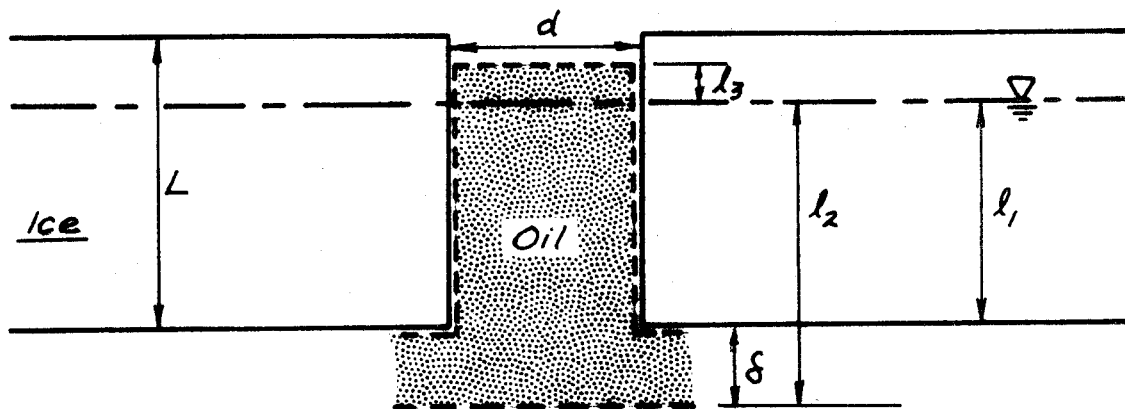


Figure A.2. Static Oil Rise in an Open Brine Channel

$$\rho_0 g(\ell_3 + \ell_2) = \rho_w g \ell_2 \quad , \quad (\text{A.9})$$

or

$$\ell_3 = \left(\frac{\rho_w}{\rho_0} - 1 \right) \ell_2 \quad . \quad (\text{A.10})$$

Noting also that:

$$\rho_{\text{ice}} L = \rho_w \ell_1 \quad , \quad (\text{A.11})$$

solving for L , and subtracting ℓ_1 from both sides gives:

$$L - \ell_1 = \left(\frac{\rho_w}{\rho_{\text{ice}}} - 1 \right) \ell_2 \quad . \quad (\text{A.12})$$

To determine what the minimum thickness, if any, must be to drive the oil to the surface, let $\ell_3 = L - \ell_1$ and equate Equations (A.10) and (A.12):

$$\left(\frac{\rho_w}{\rho_{\text{ice}}} - 1 \right) \ell_1 = \left(\frac{\rho_w}{\rho_{\text{oil}}} - 1 \right) \ell_2 \quad . \quad (\text{A.13})$$

Solving for ℓ_2 ,

$$\ell_2 = \frac{\left(\frac{\rho_w}{\rho_{\text{ice}}} - 1 \right)}{\left(\frac{\rho_w}{\rho_{\text{oil}}} - 1 \right)} \ell_1 \quad . \quad (\text{A.14})$$

Typical values for ρ_{ice} vary between 0.85 and 0.924. Typical values of ρ_{oil} are also in this range. Therefore:

$$\ell_2 \approx \ell_1 \quad , \quad (\text{A.15})$$

and oil can be expected to migrate upward until the oil-water interface coincides with the water-ice interface. For large differences in ρ_{oil} and ρ_{ice} , this will be only approximately true. Only for volumes of oil less than the volumes of the brine channels will the oil fail to reach the surface.

The analysis above indicates that the driving head h becomes simply δ , the under ice slick thickness. Substituting Equation (A.8) into Equation (A.7) gives:

$$Q = N \left(\frac{\pi d^4}{4} \right) \frac{(\rho_w - \rho_o) g \delta}{32 L \mu_o} , \quad (\text{A.16})$$

and the rise velocity in any brine channel becomes:

$$\bar{u}_2 = \frac{(\rho_w - \rho_o) g \delta d^2}{32 L \mu_o} . \quad (\text{A.17})$$

When brine channels do not naturally extend to the surface of the ice, some vertical migration can still occur. Two cases can occur. The first case is brine channels which do not extend to the mean water level as shown in Figure A.3. The second case is when the channels extend to or through the mean water level as shown in Figure A.4. Both cases can be solved by the same set of equations if the dimensions ℓ_2 and ℓ_3 of Figure A.3 are allowed to be both positive and negative.

In Figures A.3 (and A.4) assume that the channel is filled with oil and/or water totally. Let the pressure at A_1 be P_{A_1} , and the pressure on the other side of the oil-water interface at A_2 be P_{A_2} :

$$P_{A_1} = g \rho_w (\ell_2 - \ell_3) + P' , \quad (\text{A.18})$$

and:

$$P_{A_2} = g \rho_w (\ell_1 + \delta) - g \rho_o (\ell_1 - \ell_2 + \delta) . \quad (\text{A.19})$$

For equilibrium, these two pressures can only balance if surface tension is included and totally offsets the incremental pressure P' that the buoyancy of the oil is transmitting to the ice cover. Then:

$$g \rho_w (\ell_2 - \ell_3) + \frac{4\sigma_{o/w} \cos \alpha}{d} = g \rho_w (\ell_1 + \delta) - g \rho_o (\ell_1 - \ell_2 + \delta) , \quad (\text{A.20})$$

where P' is taken up in the surface tension term. This simplifies to:

$$\frac{4\sigma_{o/w} \cos \alpha}{d} = (\rho_w - \rho_o) g (\ell_1 - \ell_2 + \delta) + \rho_w g \ell_3 \quad (\text{A.21})$$

$$= (\rho_w - \rho_o) g \delta \left(1 + \frac{\ell_1}{\delta} - \frac{\ell_2}{\delta} + \frac{\rho_w}{(\rho_w - \rho_o)} \frac{\ell_3}{\delta} \right) . \quad (\text{A.22})$$

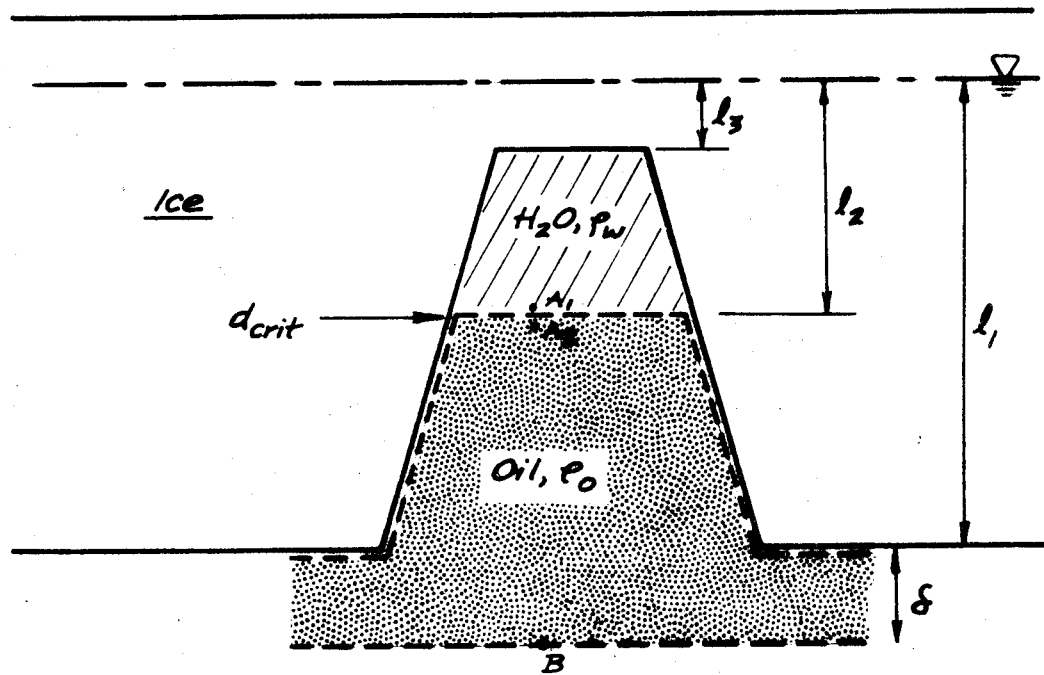


Figure A.3. Equilibrium Oil Level in a Brine Channel Only Partially Extending to Datum Level

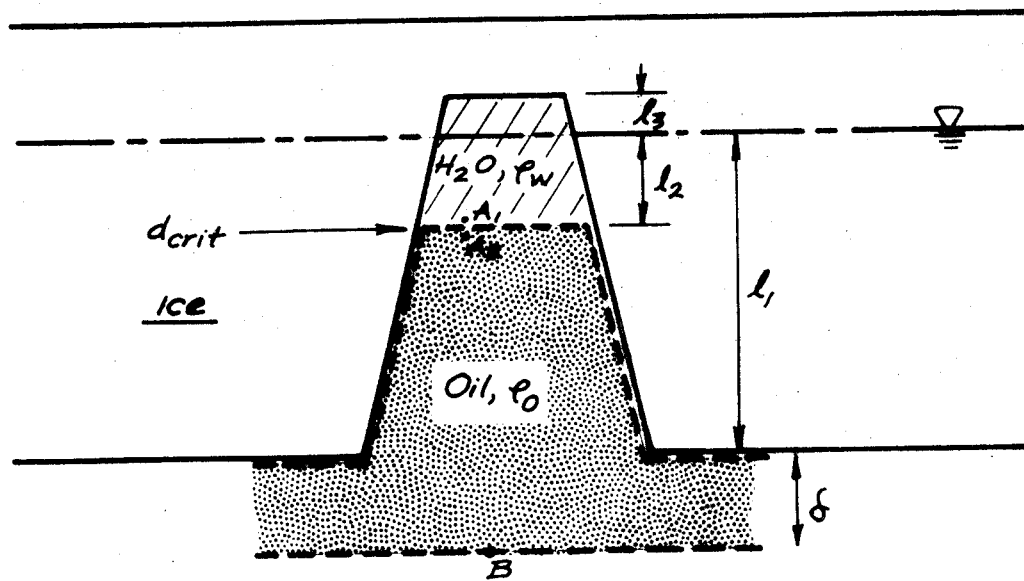


Figure A.4. Equilibrium Oil Level in a Brine Channel Extending through the Datum Level but not to the Ice Surface

Solving for the diameter where vertical migration ceases gives:

$$d_{\text{crit}} = \frac{4\sigma_{o/w} \cos\alpha}{\left(1 + \frac{l_1}{\delta} - \frac{l_2}{\delta} + \frac{\rho_w}{(\rho_w - \rho_o)} \frac{l_3}{\delta}\right) (\rho_w - \rho_o) g \delta} \quad (\text{A.23})$$

When the top of the brine channel coincides with the mean water level, i.e., $l_3 = 0$, and the channel is filled with water, i.e., $l_2 = l_1$, then $d_{\text{crit}} = d_{\text{inception}}$, as would be expected. If the brine channel does not extend to the mean water level, then $d_{\text{inception}}$ is adjusted by a factor $1/[1+(\rho_w/(\rho_w-\rho_o))l_3/\delta]$ from the free brine channel case examined earlier. When the partial channel stops below the mean water level, $d_{\text{inception}}$ is reduced. When the channel passes through the mean water level (l_3 negative), $d_{\text{inception}}$ is increased.

Setting $l_2 = l_3$ gives the minimum top diameter to totally fill the brine channel with oil. In general, a relation describing the channel geometry is needed to determine how far oil can migrate into a partial brine channel.

Having found the critical diameters of brine channels which allow vertical migration, it is now necessary to be able to predict when the channels open enough to permit migration. To do this consider the simple case of a slab of ice having initially a uniform thickness and always maintaining a linear temperature profile between the top surface of the ice and the bottom. The governing heat conduction equation for this case takes the form:

$$q_{\text{ice}}(t) = k_{\text{ice}} \frac{\theta_m - \theta_o}{L(t)}, \quad (\text{A.24})$$

where $q_{\text{ice}}(t)$ is the heat flux through the ice slab at time t , k_{ice} is the thermal conductivity of the ice, $L(t)$ is the thickness of the ice at time t , θ_m is the temperature at the upper air-ice interface, and θ_o is the constant surface temperature at the lower ice-water interface. For freezing, the energy boundary condition at the ice/water interface is given by:

$$q_{\text{ice}}(t) - q_{\text{water}}(t) = \rho_{\text{ice}} \Lambda \frac{dL}{dt}, \quad (\text{A.25})$$

where q_{water} is the heat flux from the underside of the ice to the water below, ρ_{ice} is the ice density, and Λ is heat of fusion. Assume a more general form of this boundary condition as:

$$\begin{aligned}
 q_{\text{ice}} - q_{\text{water}} &= \Lambda \frac{d}{dt} (\rho_{\text{ice}} L) \\
 &= \Lambda \rho_{\text{ice}} \frac{dL}{dt} + \Lambda L \frac{d\rho_{\text{ice}}}{dt} .
 \end{aligned}
 \tag{A.26}$$

If we say that in a freezing process ρ_{ice} remains constant, then Equation (A.26) degenerates to Equation (A.25). However, in melting L tends to remain constant. In particular, sea ice is known to "rot" and materially breaks up while the thickness does not substantially decrease. The appropriate melting boundary condition is then given as:

$$q_{\text{ice}} - q_{\text{water}} = \Lambda L \frac{d\rho_{\text{ice}}}{dt} .
 \tag{A.27}$$

If we assume that no heat is transferred through the ice to the water, meaning that all heat is expended in melting the ice [1], then $q_{\text{water}} = 0$ and substituting Equation (A.27) into Equation (A.24) gives:

$$k_{\text{ice}} \frac{\theta_m - \theta_0}{L} = \Lambda L \frac{d\rho_{\text{ice}}}{dt} ,
 \tag{A.28}$$

or

$$\frac{k_{\text{ice}}}{\Lambda} (\theta_m - \theta_0) \frac{dt}{L^2} = d\rho_{\text{ice}} ,
 \tag{A.29}$$

then integrating over a time interval (t_2, t_1) :

$$\rho_{\text{ice}}_{t_2} - \rho_{\text{ice}}_{t_1} = \frac{k_{\text{ice}}}{\Lambda} \frac{(\theta_m - \theta_0)}{L^2} (t_2 - t_1) .
 \tag{A.30}$$

This says that bulk density of the ice, ρ_{ice} , is changing linearly with time. Rewriting this equation with the initial density denoted as ρ_i and the density after time interval T as ρ_f :

$$\frac{\rho_i - \rho_f}{\rho_i} = - \frac{k_{\text{ice}}}{\Lambda} \frac{(\theta_m - \theta_0)}{L^2 \rho_i} T ,
 \tag{A.31}$$

or

$$n = \frac{k_{\text{ice}}}{\Lambda} \frac{(\theta T)}{L^2 \rho_i} ,
 \tag{A.32}$$

where n is porosity and (θT) is now thawing degree-time. But also

$$n = \frac{V_{\text{voids}}}{V_{\text{total}}}, \quad (\text{A.33})$$

and since the thickness of the slab is remaining constant:

$$n = \frac{A_{\text{voids}}}{A_{\text{total}}}. \quad (\text{A.34})$$

Also, $A_{\text{voids}} = N\pi(d^2/4)$ where d is the brine channel diameter and N is the number of channels. Solving for d and substituting Equation (A.34) for the porosity;

$$d = \sqrt{\frac{2}{N\pi} \left(\frac{2k_{\text{ice}}}{\Lambda\rho_i} \right) \frac{(\Theta T)}{L^2} A_{\text{total}}}, \quad (\text{A.35})$$

but N , the number of brine channels must equal $N'A_{\text{total}}$ where N' is the number of channels per unit surface area. Equation (A.35) becomes:

$$d = \sqrt{\frac{2}{\pi} \left(\frac{2k_{\text{ice}}}{\Lambda\rho_i} \right) \frac{(\Theta T)}{N'L^2}}. \quad (\text{A.36})$$

For typical sea ice [20]:

$$\begin{aligned} k_{\text{ice}} &= 53 \cdot 10^{-4} \text{ gm cal}/(\text{°C sec cm}), \\ \Lambda &= 70 \text{ gm cal/gm}, \\ \rho_i &= 0.90 \text{ gm/cm}^3, \end{aligned}$$

Then the factor $(2k_{\text{ice}}/\Lambda\rho_i)^{1/2}$ has a magnitude of $1.30 \text{ cm}/(\text{°C sec})^{1/2}$. Equation (A.36) for the growth in brine channel diameter simplifies to:

$$d = 3.05 \sqrt{\frac{\Theta T}{N'L^2}}, \quad (\text{A.37})$$

where d is measured in centimeters, ΘT in thawing degree-seconds, and L in centimeters. Ashton [1] suggests that, due to atmospheric variations, the theoretical factor computed above should be reduced by 30%. Then an empirical prediction for brine channel growth becomes:

$$d = 2.13 \sqrt{\frac{\Theta T}{N'L^2}}. \quad (\text{A.38})$$

The appearance of brine channel spacing in the prediction may initially be a little unsettling. However, in the field N' tends to be a constant. Equation (A.37) is arguing that all of the heat is expended in the melting of the brine channels. When a larger number of channels exist in the ice, a greater amount of heat must be applied to achieve channel enlargement to a specified size.

Finally, Lake and Lewis [10] suggest that a typical field brine channel density (N') is one channel per 100 square centimeters. Then:

$$d = 21.3 \sqrt{\frac{\theta T}{L^2}}, \quad (\text{A.39})$$

giving the diameter of the brine channel for any melting condition in real sea-ice. It should be stressed that this prediction for brine channel diameter growth is representative of a typical channel in a field of typically spaced channels, rather than being a specific solution for an individual channel.

APPENDIX B

STATIC EQUILIBRIUM SLICK THICKNESS

As oil begins to pool beneath an ice sheet, it forms in a sessile droplet whose dimensions are determined by a balance of surface tension forces and hydrostatic forces [6]. The surface tension force is a net result of surface energies between oil and ice, water and ice, and oil and water. The last has been found to be negative. The hydrostatic force is due to the density difference between oil and water. Referring to Figure B.1, if the oil spreads so that it forms a contact angle greater than 0° with the ice, the oil is said to "wet" the ice. A contact angle of 180° would be pure wetting and the oil could spread indefinitely. The measurement of contact angle understandably is difficult, yet, as will be seen later, the results of this force balance depends upon the cosine of the angle rather than the angle directly, and as such makes prediction of the bubble size much less cumbersome.

Consider the pressure excess at a point $M(x,y)$ in a large bubble flat at the vertex O (see Figure B.1). If R_1 and R_2 are the principal radii of curvature at M , the balance between hydrostatic pressure and interfacial tension becomes:

$$\Delta gpy = \sigma_{o/w} \left(\frac{1}{R_1} + \frac{1}{R_2} \right), \text{ or } \frac{y}{a^2} = \frac{1}{R_1} + \frac{1}{R_2}, \quad (\text{B.1})$$

where

$$a^2 = \frac{\sigma_{o/w}}{\Delta \rho g}, \text{ and } \sigma_{o/w} \text{ is interfacial tension.}$$

But $R_1 = \sec\phi / (d\phi/dx)$ and $R_2 = x/\sin\phi$, leading to:

$$a^2 x \cos\phi \cdot \frac{d\phi}{dx} + a^2 \sin\phi = xy. \quad (\text{B.2})$$

If we transfer the origin to O' , and divide through by x , we arrive at an equation in which the small terms occur with x in the denominator. Neglecting these terms, the solution to first order becomes:

$$y^2 = 2a^2(1 - \cos\phi), \quad (\text{B.3})$$

so that $\cos\phi = (2a^2 - y^2)/2a^2$ and $\sin\phi = y\sqrt{(4a^2 - y^2)}/2a^2$, the positive sign being the relevant one in our investigation.

If we insert these approximate values in the small terms of the original equation and integrate again, we obtain:

$$2a^2(1 - \cos\phi) = y^2 + \frac{(4a^2 - y^2)^{3/2}}{3r} - \frac{8a^3}{3r}. \quad (\text{B.4})$$

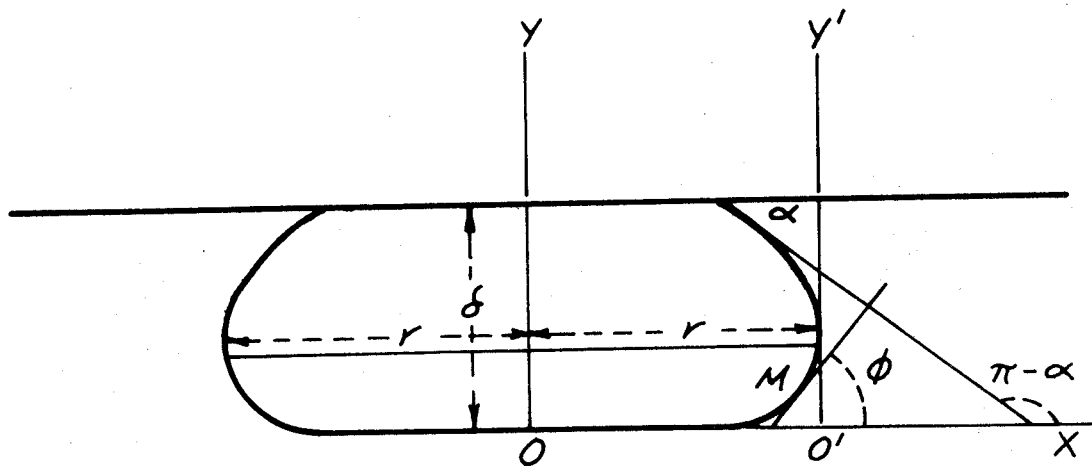


Figure B.1. Sessile Drop of Oil beneath an Ice Cover

When $y = \delta$, $\phi = \pi - \alpha$, where α is the contact angle and:

$$2a^2(1 + \cos\alpha) = \delta^2 + \frac{(4a^2 - \delta^2)^{3/2}}{3r} - \frac{8a^3}{3r} \quad , \quad (\text{B.5})$$

or

$$\delta^2 = 4a^2 \cos^2 \alpha / 2 + \frac{8a^3}{3r} (1 - \sin^3 \alpha / 2) \quad . \quad (\text{B.6})$$

When r becomes indefinitely large, this reduces to the well-known simple form:

$$\delta^2 = \frac{2\sigma_{o/w}}{\Delta\rho_w g} (1 + \cos\alpha) \quad . \quad (\text{B.7})$$

The thickness of the sessile drop can be seen to be directly proportional to the square root of the interfacial tension and inversely proportional to the square root of the density difference between the oil and water. Because of the appearance of $\cos\alpha$ on the right side of Equation (B.7), the thickness is only weakly a function of the contact angle.

APPENDIX C

OIL INTERACTION WITH SMALL ROUGHNESS

In this section we will examine the spread of oil under ice, driven by a current, when the entire body of oil is advancing at all times. The scale of any roughness encountered by the oil shall be small enough to be engulfed within the slick itself. A force balance can be written between the slick and the current in the form suggested by Uzuner, et al. for smooth ice [26]:

$$F_i = F_f + F_s \quad (C.1)$$

F_i is an ice-oil friction force similar to a solid friction force. This force is attributable to the normal force applied to the ice and is due to the buoyant nature of the oil:

$$F_i = C_i (\rho_w - \rho_o) g V, \quad (C.2)$$

C_i is an oil-smooth ice sliding friction coefficient, $(\rho_w - \rho_o)$ is the density difference between water and oil, and V is volume of oil.

F_f is the form drag of the oil slick, and is dependent upon the relative velocity of the slick:

$$F_f = \frac{1}{2} C_f \rho_w (U_w - U_s)^2 A_{\text{frontal}}, \quad (C.3)$$

C_f is a form drag coefficient, $(U_w - U_s)$ is the relative velocity between the current and the slick, and A_{frontal} is blockage area of the slick.

F_s is a shear force acting on the oil-water interface:

$$F_s = \frac{1}{2} C_s \rho_w (U_w - U_s)^2 A_{\text{plan}}, \quad (C.4)$$

C_s is an interfacial shear stress coefficient, and A_{plan} is the area on which the shear is applied.

Substituting Equations (C.2), (C.3), and (C.4) into (C.1) gives a non-dimensional expression for the spreading of oil due to a current as:

$$\left(1 - \frac{U_s}{U_w}\right)^2 = \left(\frac{2 C_i}{C_f \frac{\delta}{X} + C_s}\right) \frac{1}{F_\delta^2}, \quad (C.5)$$

where F_δ is a slick densimetric Froude number given by $F_\delta = U_w / \sqrt{\Delta g \delta}$.

The form of Equation (C.5) can be simplified to a linear relation between slick speed and current speed:

$$U_s = U_w - \left(\frac{2 C_f \Delta g \delta}{C_f \frac{\delta}{X} + C_s} \right)^{1/2}, \quad (C.6)$$

where δ is the slick thickness and X is the slick length. This expression indicates that the slick velocity differs from the current velocity only by a constant, and this constant gives an estimate of the threshold velocity. The constant also has a dependency on the slick length and would suggest that as the slick length increases, shear stress will dominate.

In Equation (C.5), the coefficients C_i and C_f are constants but the interfacial shear stress coefficient may vary to some extent with velocity. Based on the general definition of wall shear stress, $\tau_o = 1/2 C_s \rho_w U_w^2$, C_s might be argued to vary inversely with U_w^2 , particularly when U_w is small. Then an empirical form of Equation (C.5) would look like:

$$\left(1 - \frac{U_s}{U_w} \right)^2 = \frac{1}{A F_\delta^2 + B}, \quad (C.7)$$

where A and B have absorbed the constants in Equation (C.5) and will be evaluated experimentally.

Equation (C.7) has linear asymptotes for both large and small Froude numbers. When F_δ is large, Equation (C.7) degenerates to a form similar to Equation (C.6) since $A F_\delta^2$ dominates B . This simplification results in an expression:

$$U_s = U_w - b. \quad (C.8)$$

At small Froude numbers, Equation (C.7) degenerates to a different linear form:

$$U_s = m U_w. \quad (C.9)$$

Equations (C.8) and (C.9) show that the relation between slick velocity and current velocity should actually approach a two step linear curve. When currents are small, Equation (C.9) suggests that the slick can only move at a fraction of the current speed. This would correspond to the slick having to overcome static friction. At higher current speeds, the slick is freely advected with the mean current as indicated by a slope of unity in Equation (C.8). The constant may correspond to the point where static friction is overcome or be the result of the slick moving within the reduced flow of the free stream boundary layer.

The equations derived in this section can actually apply to ice of any roughness, so long as that roughness remains wholly contained within the oil slick. Shear stress and form drag applied to a slick by a moving current would be the same for smooth or rough ice. Only the value of the oil-ice friction

factor would change from smooth to rough ice. The change can be represented as an amplification factor acting on the smooth-ice friction coefficient. A generalized predictive relation for smooth or small roughness ice then becomes:

$$\left(1 - \frac{U_s}{U_w}\right)^2 = \frac{K}{AF\delta^2 + B}, \quad (C.10)$$

where $K = 1$ for smooth ice and $K > 1$ for rough ice. This amplification factor will need to be determined experimentally.

APPENDIX D

OIL INTERACTION WITH LARGE ROUGHNESS

D.1 Frontal Trapping

When the relief on the under-ice surface exceeds the equilibrium thickness of a spreading oil slick, blockage and trapping of the oil can occur. Oil will begin to pool upstream of the hindrance. Depending upon the size of the relief and the speed of the free stream current, the trapped slick will grow in length and thickness until some critical volume is reached. When this occurs, the slick becomes unstable and leakage occurs. This is analogous to slick behavior when confined by a boom in open water. Wilkinson [27, 28] has done an excellent analysis of the slick formation in open water. Following the form of this work, a similar analysis can be developed for containment under a solid ice cover.

A fully developed contained oil slick is characterized by a head wave, a neck, and a thickening viscous region as shown in Figure D.1. The formation of the head wave is due to a normal, momentum force applied to the slick. The neck, immediately downstream of the head wave, is approximately half the thickness of the head wave and is the result of flow separating behind the head. The slick again increases downstream due to the shear stress applied to the slick by the current. Solutions are developed for the slick behavior in two regions; a head wave region and a viscous region. The solutions are then matched at the neck.

D.1.1 Head Wave Region

Consider a region near the upstream end of the trapped oil about 10 to 20 slick thicknesses in length, shown as the Head Region in Figure D.1. Assuming that the acceleration of the slick is negligible (steady state), a balance of the change in momentum and pressure forces upstream with that at a section through the slick leads to:

$$\rho_w U_w^2 D + \frac{\rho_w g D^2}{2} = \frac{\rho_w U_w^2 D^2}{D - \delta} + (1 - \Delta) \left(\frac{\rho_w g}{2} \right) D^2 + \frac{\Delta \rho_w g}{2} (D - \delta)^2 + P' D, \quad (D.1)$$

where

δ = slick thickness

D = water depth

P' = incremental pressure due to the buoyant force of oil on the ice cover

Δ = relative density difference between water and oil = $\frac{\rho_w - \rho_o}{\rho_w}$

U_w = free stream current.

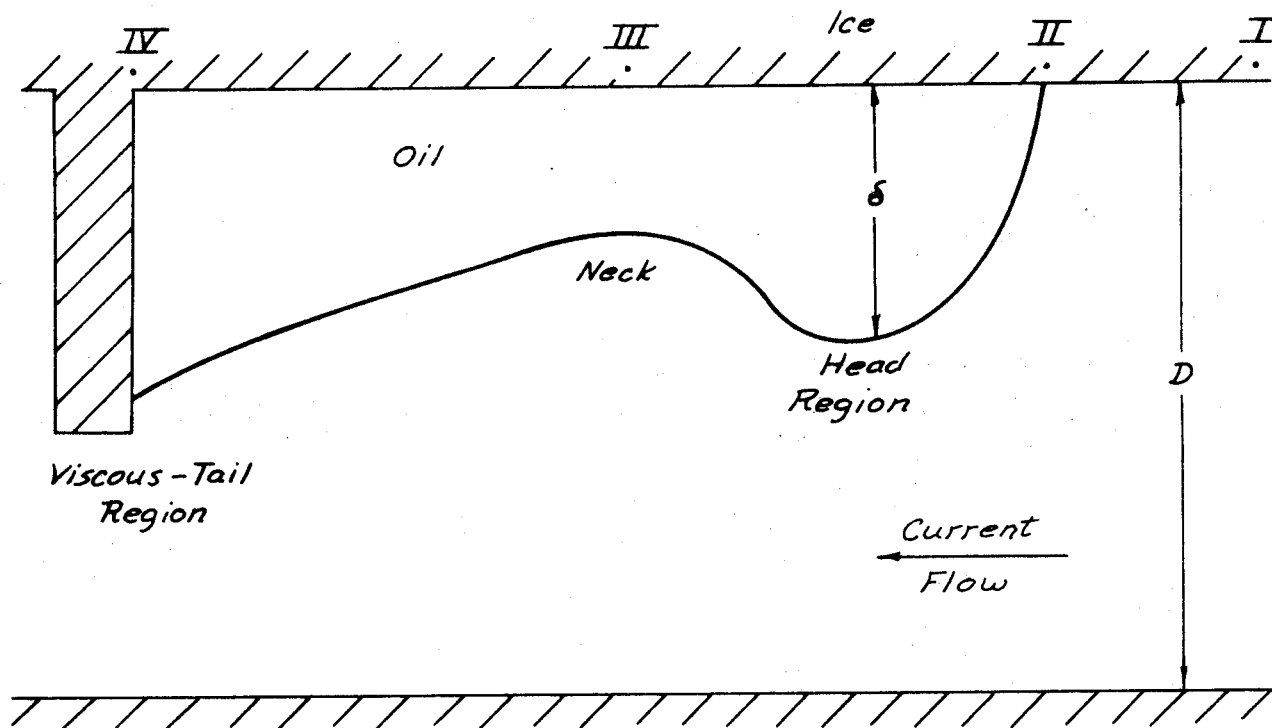


Figure D.1 Sketch of Frontal Trapping of an Oil Slick by a Large Roughness Element

We can expand and simplify this to give:

$$\rho_w \frac{U^2 D}{w} = \frac{\rho_w U^2 D^2}{D - \delta} - \Delta \rho g D \delta + \frac{\Delta \rho g \delta^2}{2} + P' D \quad (D.2)$$

To evaluate P' , apply the Bernoulli equation along a streamline between Point I far upstream and Point II, the stagnation point. For steady state:

$$\frac{\rho_w U^2}{2} + P_\infty = P_{II} = P' + P_\infty \quad (D.3)$$

or

$$P' = \frac{\rho_w U^2}{2} \quad (D.4)$$

Then:

$$\rho_w \frac{U^2 D}{w} = \frac{\rho_w U^2 D^2}{D - \delta} - \Delta \rho_w g D \delta + \frac{\Delta \rho_w g \delta^2}{2} + \frac{\rho_w U^2 D}{2} \quad (D.5)$$

Dividing by $\Delta \rho_w g D^2$ gives:

$$\frac{1}{2} \frac{U^2}{\Delta g D} = \frac{U^2}{\Delta g D (1 - \frac{\delta}{D})} - \frac{\delta}{D} + \frac{1}{2} \left(\frac{\delta}{D}\right)^2 \quad (D.6)$$

Defining $F_D^2 = \frac{U^2}{\Delta g D}$ and $\psi = \frac{\delta}{D}$ gives:

$$\frac{F_D^2}{2} = \frac{F_D^2}{1 - \psi} - \psi + \frac{1}{2} \psi^2 \quad (D.7)$$

which simplifies to:

$$F_D^2 = \psi (2 - \psi) \frac{(1 - \psi)}{(1 + \psi)} \quad (D.8)$$

Equation (D.8) represents the equilibrium slick thickness for a given free stream Froude number. Once the slick has grown to its full equilibrium thickness, the addition of any additional oil will cause an instability which will result in leakage until equilibrium is restored. Equation (D.8) is plotted for $\Delta \rightarrow 0$ in Figure D.2. It can be seen that ψ is double valued for $F_D < 0.527$, and no

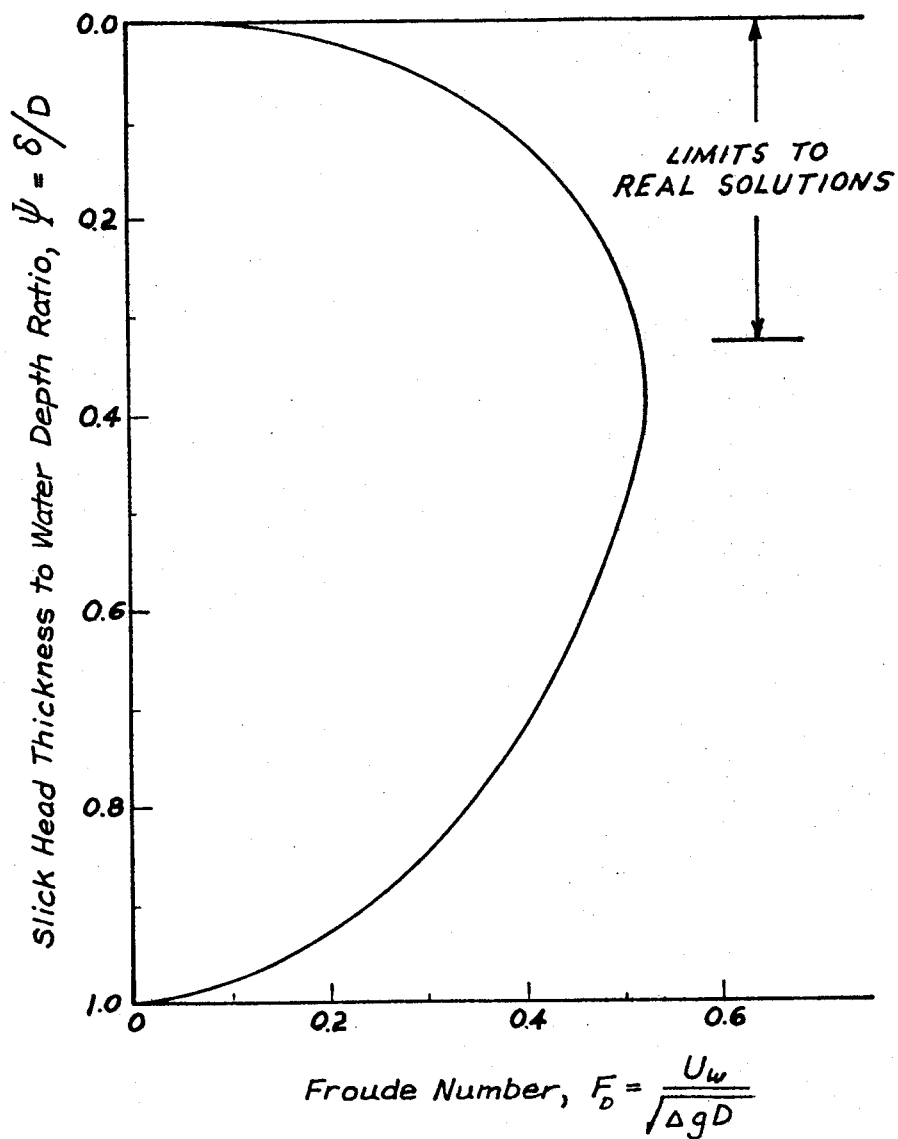


Figure D.2. Slick Thickness Ratio versus Freestream Densimetric Froude Number for Large Roughness

solution exists for $F_D > 0.527$. A critical Froude number exists when $F_D = 0.527$. At this flow condition, the head wave has been forced to grow to a point where the buoyancy can no longer balance the induced forces. Total flushing occurs since, in maintaining the head thickness dictated by the free stream, the loss of the oil from the head wave must be replenished by the downstream portion of the slick until all of the oil has been dissipated. Note that this is totally independent of the scale of roughness. Both a 1 meter relief and a 10 meter ridge would be subject to the same failure criteria.

A difficulty arises when Equation (D.8) is applied in very deep water, $\psi \rightarrow 0$. Wilkinson extended his theory to account for deep water cases by defining a slick Froude number:

$$F_\delta^2 = \frac{U^2}{\Delta g \delta} \quad (D.9)$$

This can be related to the free stream Froude number through ψ as:

$$F_\delta = \frac{F_D}{\psi^{1/2}} \quad (D.10)$$

so that in our case, Equation (D.8) becomes for deep water:

$$F_\delta^2 = (2 - \psi) \frac{(1 - \psi)}{(1 + \psi)} \quad (D.11)$$

Then as $D \rightarrow \infty$, $\psi \rightarrow 0$, and the limiting slick Froude number becomes in deep water $F_\delta = \sqrt{2}$. By inserting different small values for ψ into Equation (D.11), it appears that ψ must be less than 0.01 before the water can be considered deep water. The deep water slick thickness can then be found from the definition of slick Froude number to be:

$$\delta = \frac{U^2}{2\Delta g} \quad (D.12)$$

This relation has no limiting value in deep water. However, a limiting condition must certainly exist. The thickness is limited by the formation of a Kelvin-Helmholtz type instability which occurs because the local shear on the slick exceeds the interfacial tension. The instability begins to develop when:

$$U_{\text{crit}} = \left[2 \left(\frac{\rho_o + \rho_w}{\rho_o \rho_w} \right) (\sigma_{o/w} g (\rho_w - \rho_o))^{1/2} \right]^{1/2} \quad (D.13)$$

where $\sigma_{o/w}$ is the interfacial tension between the oil and water.

Droplet tearing and ultimate failure in the integrity of the slick occurs when [11]:

$$U_w \geq 2.2 U_{\text{crit}} \quad (\text{D.14})$$

The limiting slick thickness of the head wave in deep water would then become:

$$\delta_{\text{max}} = \frac{1.1}{\Delta g} U_{\text{crit}}^2 \quad (\text{D.15})$$

D.1.2 Viscous Region

Consider now the downstream region of trapped oil controlled by viscous shear at the oil-water interface shown in Figure D.3. Balancing the streamwise gradient of pressure and inertial forces with boundary shear forces gives:

$$\frac{\partial}{\partial x} \left[\frac{\Delta \rho_w g (D - \delta)^2}{2} + P' D + \frac{\rho_w U^2 D^2}{D - \delta} \right] = -\tau_B \quad (\text{D.16})$$

where P' is an incremental (small) pressure acting on the upper surface due to the buoyant effect of the oil, and can be shown to be equal to a hydrostatic set up term in open channel flow. Note that the interfacial shear stress is internal to the system and therefore can exert no net force on the system. Equation (D.16) can be expanded and nondimensionalized by dividing by $\Delta \rho g D$ to give:

$$\frac{1}{\Delta \rho_w g} \frac{\partial (P')}{\partial x} + \frac{\partial \delta}{\partial x} \left(\psi + \frac{F_D^2}{(1 - \psi)^2} - 1 \right) = \frac{-\tau_B}{\Delta \rho_w g D} \quad (\text{D.17})$$

To determine the excess pressure P' a second expression describing the equilibrium of slick interface must take the form:

$$\frac{\partial}{\partial x} \left[\left(P' + \frac{\rho(1-\Delta)g\delta}{2} \right) \delta \right] = \tau_s + \rho_w(1-\Delta)g\delta \frac{\partial \delta}{\partial x} \quad (\text{D.18})$$

where the last term represents the x-component of hydrostatic pressure at the sloping oil-water interface. Equation (D.18) reduces to:

$$\frac{\partial}{\partial x} (P' \delta) = \tau_s \quad (\text{D.19})$$

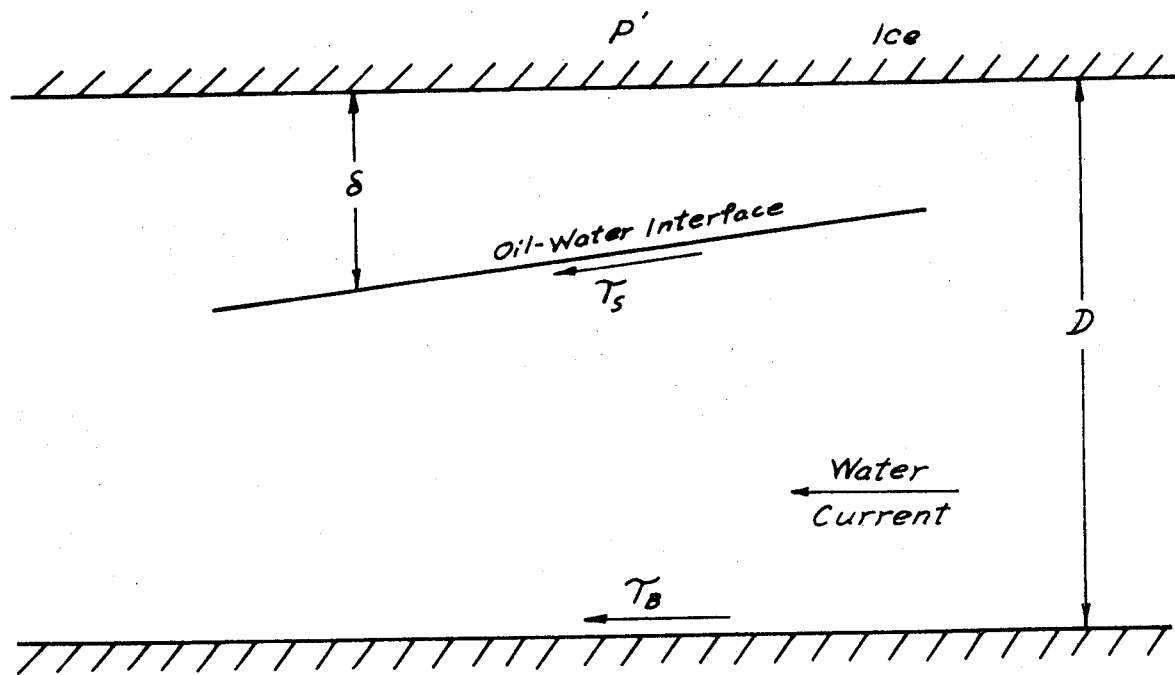


Figure D.3. Sketch of the Viscous Region of a Contained Slick

or:
$$P' \frac{\partial \delta}{\partial x} + \delta \frac{\partial P'}{\partial x} = \tau_s \quad (D.20)$$

Now the first term on the left is the product of two small terms while the second is the product of a large and a small. The first term is second order and may thus be ignored. Therefore:

$$\frac{\partial P'}{\partial x} = \frac{\tau_s}{\delta} \quad (D.21)$$

Substituting this into Equation (D.17) gives:

$$\frac{\partial \delta}{\partial x} \left(1 - \frac{F^2 D^2}{(1-\psi)^2} - \psi \right) = \frac{\tau_B}{\Delta \rho_w g D} + \frac{\tau_s}{\Delta \rho_w g \delta} \quad (D.22)$$

Equation (D.22) can be expanded and rearranged to give:

$$\frac{\partial \delta}{\partial x} \left(1 - \frac{F^2 D^2}{(D-\delta)^2} - \frac{\delta}{D} \right) - \frac{\tau_B}{\Delta \rho_w g D} = \frac{\tau_s}{\Delta \rho_w g \delta} \quad (D.23)$$

Making this equation dimensional by multiplying by δ gives:

$$\delta \frac{\partial \delta}{\partial x} \left(1 - \frac{F^2 D^2}{(D-\delta)^2} - \frac{\delta}{D} \right) - \frac{\tau_B}{\Delta \rho_w g} \frac{\delta}{D} = \frac{\tau_s}{\Delta \rho_w g} \quad (D.24)$$

and generalizing it to any water depth:

$$\delta \frac{\partial \delta}{\partial x} \left(1 - \frac{F^2 \delta^2 \psi}{(1-\psi)^2} - \psi \right) - \frac{\tau_B}{\Delta \rho_w g} \psi = \frac{\tau_s}{\Delta \rho_w g} \quad (D.25)$$

This equation must be solved numerically. However, for the deep water case when $D \gg \delta$, $\psi \rightarrow 0$ so that an approximate solution can be found. Equation (D.25) then degenerates to the simple form:

$$\delta \frac{\partial \delta}{\partial x} = \frac{\tau_s}{\Delta \rho_w g} \quad (D.26)$$

Separating variables and integrating gives an indication of the length and shape of the interface in the viscous region for deep water:

$$\frac{1}{2} \delta^2 \left[\begin{array}{l} \delta_{IV} \\ \delta_{III} \end{array} \right] = \frac{\tau_s}{\Delta \rho_w g} X \quad , \quad (D.27)$$

or:

$$X = \frac{1}{2} \frac{\Delta \rho_w g}{\tau_s} (\delta_{IV}^2 - \delta_{III}^2) \quad . \quad (D.28)$$

The shape of the interface is parabolic, and the length varies with the square of the thickness and inversely with the interfacial shear stress.

The limits of integration remain to be defined. In a depth dependent case, the maximum thickness occurs when the slope of the interface changes sign. From Equation (D.24), this occurs when:

$$\frac{F_D^2 D^2}{(D-\delta)^2} + \frac{\delta}{D} = 1 \quad . \quad (D.29)$$

Since head wave failure occurs if $F_D \geq 0.527$, Equation (D.29) is physically limited to densimetric Froude numbers less than this critical value. In this range a slick can build to a substantial portion of the available depth, limited only by the roughness height. When the value of the Froude number is critical Equation (D.29) gives the same slick thickness prediction as Equation (D.8). Physically this means that at critical flow an instability forms on both the head and tail at the same oil slick thickness, limiting further growth and forcing the two thicknesses to be equal. This occurs independent of roughness height.

In deep water the shear region can grow parabolically to the tip of the barrier for subcritical flow conditions. At critical flow when a Kelvin-Helmholtz type failure is occurring at the head wave, the maximum tail thickness is again limited to the same thickness as the head wave because further growth in tail thickness would lead to a local instability.

The other limit of the shear region is controlled by the neck which forms in the slick behind the head wave. Since this neck is approximately half of the head wave thickness, the parabolically shaped shear region grows from half the head wave thickness to the maximum possible tail thickness. The tail thickness will be limited only to the volume of oil available, the ice roughness, or critical current speed. Equation (D.28) then becomes:

$$X = \frac{\Delta \rho_w g}{2\tau_s} (\delta_{tail}^2 - \delta_{neck}^2) \quad . \quad (D.30)$$

In terms of an interfacial friction factor the slick length becomes:

$$X = \frac{4\Delta q}{f_s U^2 w} (\delta_{\text{tail}}^2 - \delta_{\text{neck}}^2) \quad (D.31)$$

The slick length decreases with increasing velocity, while the slope of the interface flattens as the head and tail thicknesses approach each other.

Since the curvature in the interface is very mild the volume per unit width of oil trapped in the viscous region can be approximated by the trapezoid region shown in Figure D.4. Generally, the length of the head wave is considered small (10 to 20 slick thicknesses) compared to the length of the viscous region. The decrease in accuracy of predicting contained oil volume by ignoring the volume of oil in the head wave is insignificant.

D.2 Wake Trapping

A region exists in the shadow of ice roughness which also has potential for trapping of oil. Oil which has slipped under the tip of ice roughness can rise because of buoyancy back into this separated flow region as suggested in Figure D.5. This region persists, in the mean, at very high flow rates and therefore may contain oil when containment is not possible elsewhere.

An analytical description for flow in the wake remains largely unsolved. Several models have been attempted to define the wake but most have problems in dealing with the reattachment process and the general instability of the wake itself. By a method of conformal mapping of closed free streamlines surrounding a region of vorticity, Lin and Landweber [13] have been able to model quasi-steady wakes of flat plates and wedges. However a generalized theory does not exist.

In contrast, considerable experimental data is available on wakes behind flat plates and blunt objects. The wake length has been observed to grow linearly with the body Reynolds number up to a Reynolds number of 280 [7]. At higher Reynolds numbers, the wake length appears to approach a constant proportional to the barrier height. In deep water the ratio of wake length to barrier height of a flat plate has been observed to be seventeen. The wake of a roughness peak might therefore be expected to be 17 times its height, independent of velocity:

$$\xi = 17 \eta \quad (D.32)$$

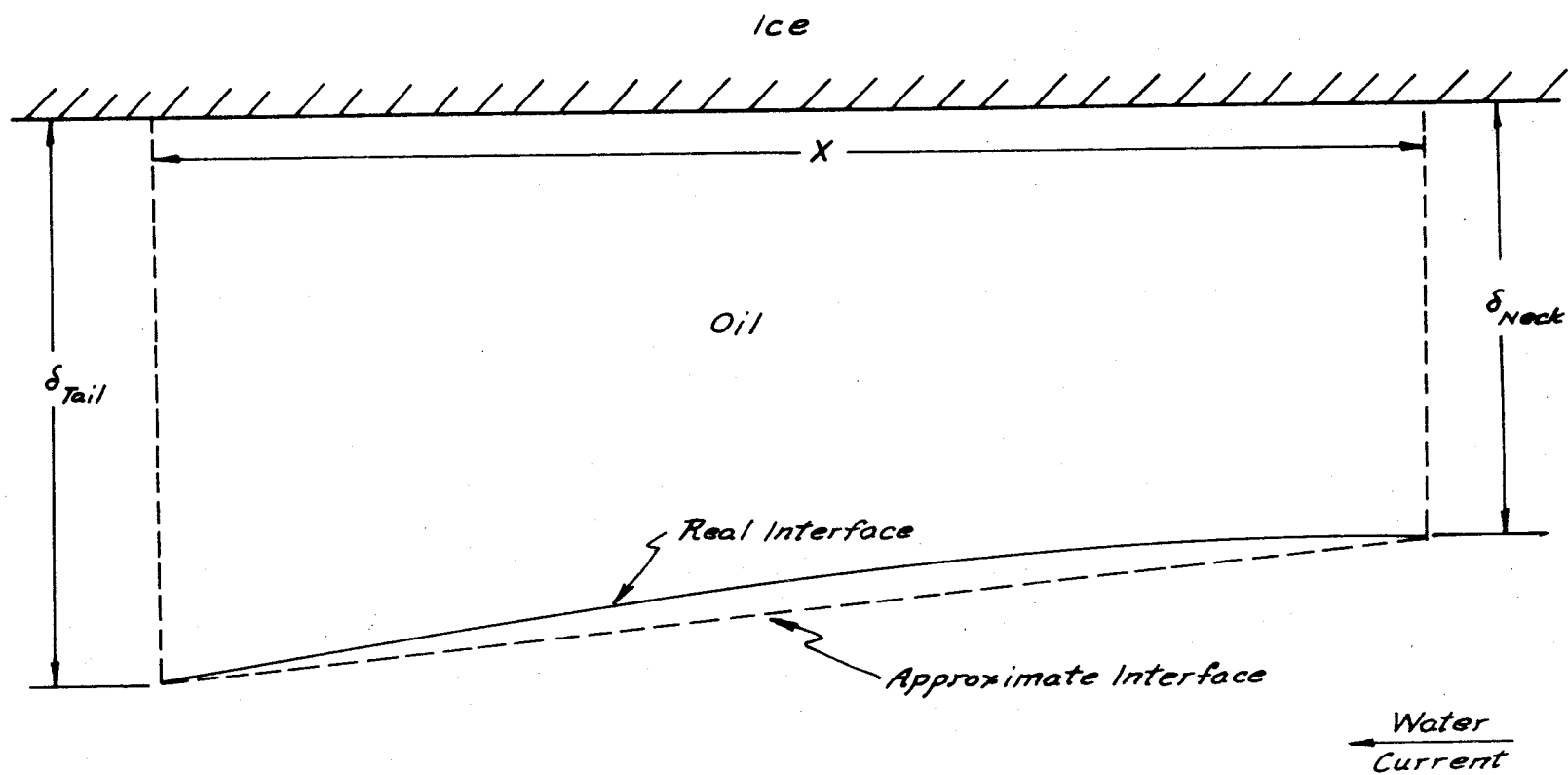
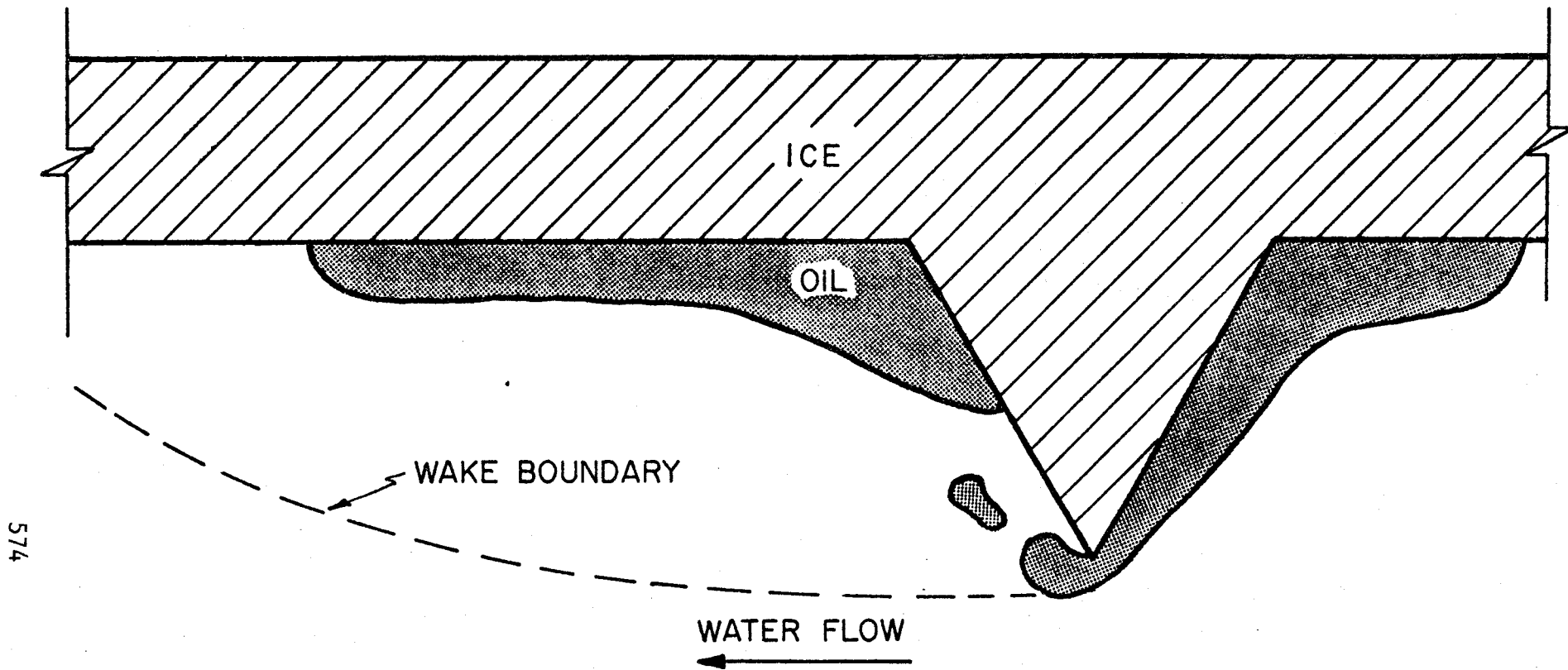


Figure D.4. Sketch Showing the Method of Approximating the Volume per Unit Width of a Frontally Trapped Slick



574

Figure D.5. Sketch of Oil Leakage From Upstream of a Large Roughness Element to the Wake Region Behind the Element

Shown in Figure D.6, taken from Rouse [24], are velocity profiles, mean streamlines and turbulent fluctuations observed in the wake. Mean turbulent perturbations approach 25% of the free stream velocity suggesting that the wake is not a smooth reverse circulating region, but rather a highly agitated vortex shedding zone.

Nearness of the bottom to the wake has the effect of suppressing the wake length. Pande et al. [21] have gathered the results of several wake experiments and have observed that the wake length falls off linearly from seventeen as the ratio of barrier height to water depth approaches 20%. In this range the wake length is predicted by the empirical relation:

$$\frac{\xi}{\eta} = 18.13 - 31.67 \frac{\eta}{D} . \quad (D.33)$$

For larger blockage in the flow the wake length becomes more nearly constant, approximately eight times the barrier height. The change in wake length with blockage is shown in Figure D.7.

Shape of the roughness also affects the length of the wake, with certain shapes allowing more streamlining than others. At some distance behind a barrier a defect has formed in the velocity profile which can be given by $U_{\infty} - u_1$. Balancing the momentum loss in the wake with the form drag of the barrier results in an expression for the rate at which the velocity profile redevelops in the wake given by:

$$\frac{U_{\infty} - u_1}{U_{\infty}} = \left(\frac{C_D \eta}{\beta \xi} \right)^{1/2} , \quad (D.34)$$

where C_D is the drag coefficient for the shape of the roughness and β is an experimental constant related to the growth in the thickness of the wake [25]. For two dimensional wakes $\beta = 0.11$. At the end of the wake the velocity defect disappears so that $u_1 = 0$. The length of the wake would then be predicted by:

$$\xi = \frac{C_D}{0.11} \eta . \quad (D.35)$$

For a two dimensional flat plate $C_D = 1.98$, which gives a ratio of wake length to barrier height of eighteen. This is consistent with experimental observations, therefore Equation(D.35) can be used to predict wake length for any roughness shape in deep water.

Equations (D.33) and (D.35) provide a means of predicting the wake length as a function of any water depth or barrier shape. The length of a slick contained by the wake could not exceed this length since reattachment of the free stream

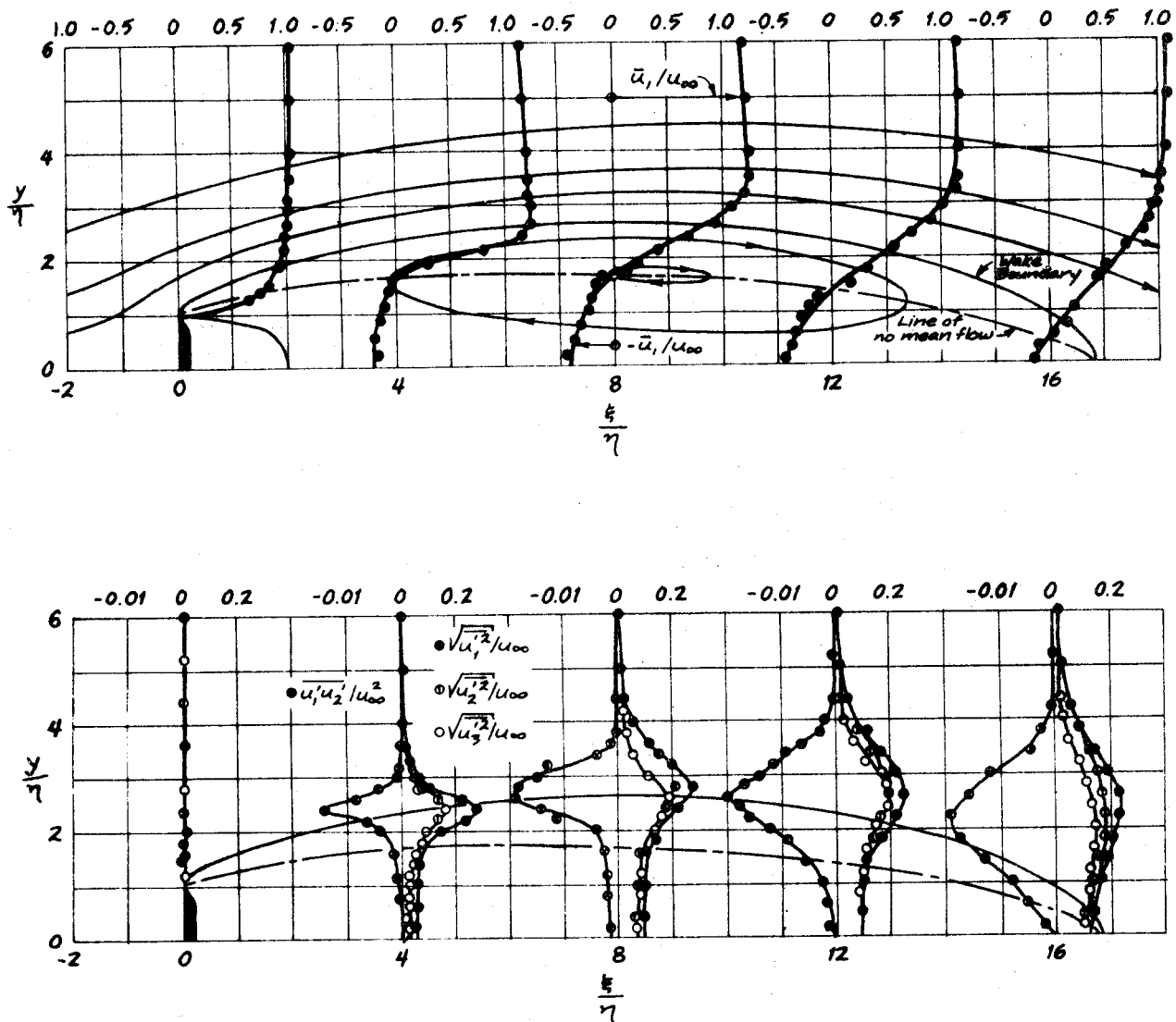


Figure D.6. Velocity Measurements in the Wake of a Fence Taken from Rouse [24]. The Upper Picture Shows, Nondimensionally, the Change in the Mean Horizontal Velocity Component Along the Length of the Wake. The Lower Picture Shows the Variation in Turbulent Perturbations Throughout the Wake. Note that Turbulence Perturbations are Strongest in all Directions Near the Wake Boundary.

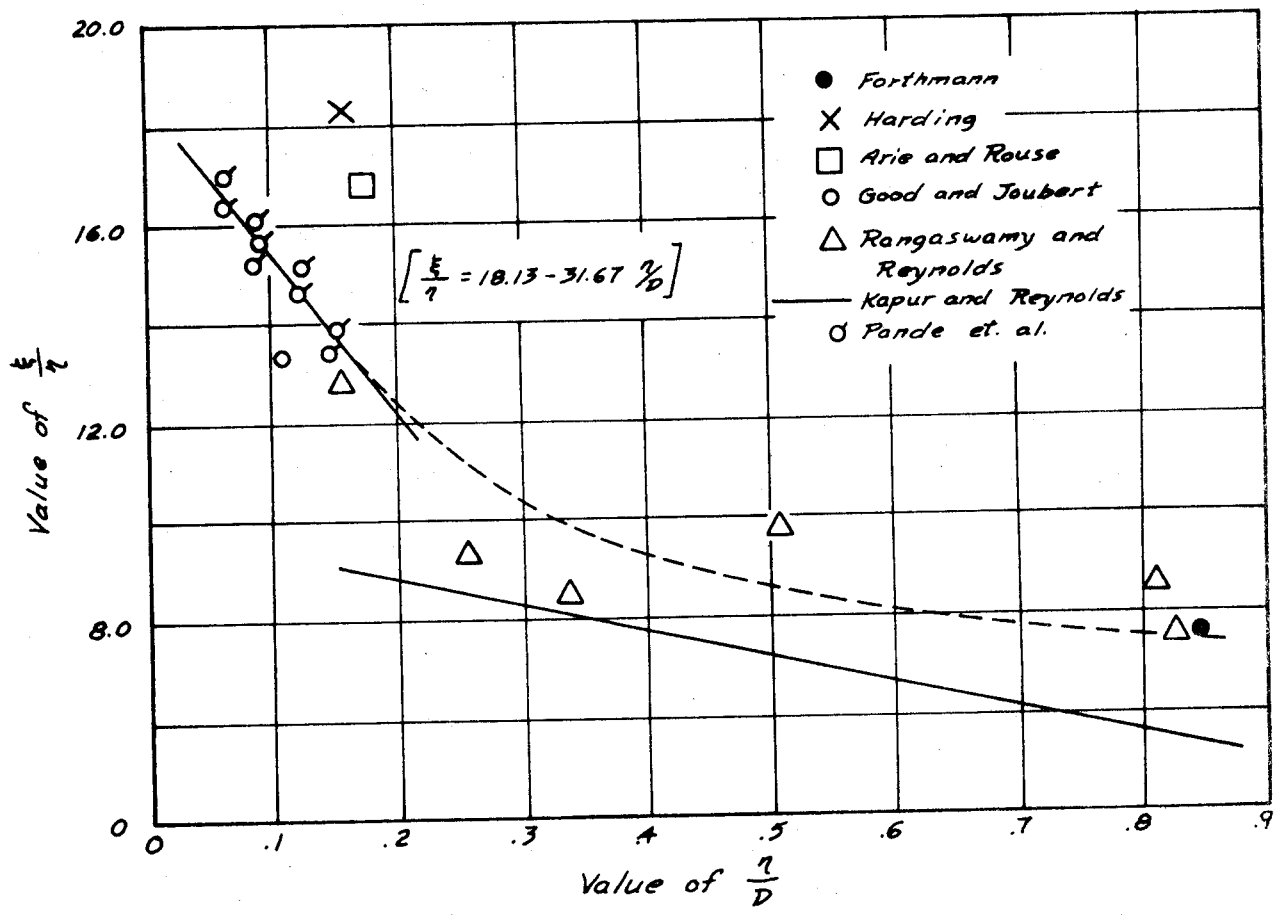


Figure D.7. Variation of Wake Length with Roughness Height [21]

current would result in tearing any excess oil away. The thickness of the oil slick trapped in the wake should be equal to the static equilibrium thickness (ignoring any local pressure drops in the wake). Upstream of a barrier the slick is able to grow thicker because buoyancy is opposing the shear stress; in the wake no equivalent balance exists. Therefore, the buoyancy of the oil will tend to spread the contained slick to its equilibrium thickness. Any excess oil will be pushed by buoyancy back into the free stream, beyond the end of the wake.

D.3 Cavity Trapping

In general, a cavity could be defined as a space between roughness peaks short enough that for a given current speed an oil slick can span the entire opening. Intuitively, from the previous discussions, the largest cavity possible would be one of length equal to the sum of the maximum frontally contained slick plus a wake contained slick. A portion of the slick would then be controlled by the separation of flow occurring at the upstream wall of the cavity, and the rest controlled by shear being applied at the oil-water interface. No head wave would be expected since there is no defined beginning to the slick. A general description of the contained oil slick is given in Figure D.8.

D.3.1 Vortex Region

Similar to the wake, a zone of flow separation will exist at the upstream end of the cavity caused by vortex shedding at the tip. The thickness of the oil in this region, unlike in the wake, may exceed equilibrium. This is possible because a wall exists further downstream which would inhibit the hydrostatic spreading of the oil. The length of the zone may also be different than a free wake since a thickened oil-water interface would create a new "wall" to the flow. The actual separation cell is a region of reverse circulation but with high turbulence and erratic shedding of vortices into the freestream. The penetration of the cell into the cavity ϵ , and the length of the cell l , will likely depend on the oil properties and the flow conditions. As flow increases, the strength and dimensions of the vortex zone may increase until it is able to penetrate all the way to the ice, dividing the slick.

D.3.2 Shear Region

At the end of the vortex region where the freestream current has re-attached to the slick, a mathematical stagnation point exists. From this point the slick becomes shear controlled, exactly analogous to the shear region developed for frontal trapping. The only difference is that the starting thickness is now established by the vortex zone rather than a neck behind a head wave. In deep water the interface will assume a shallow parabolic shape given by:

$$\delta_{\text{tail}}^2 - \delta_{\text{stagnation}}^2 = \frac{f_s U^2}{4\Delta g} x \quad . \quad (D.36)$$

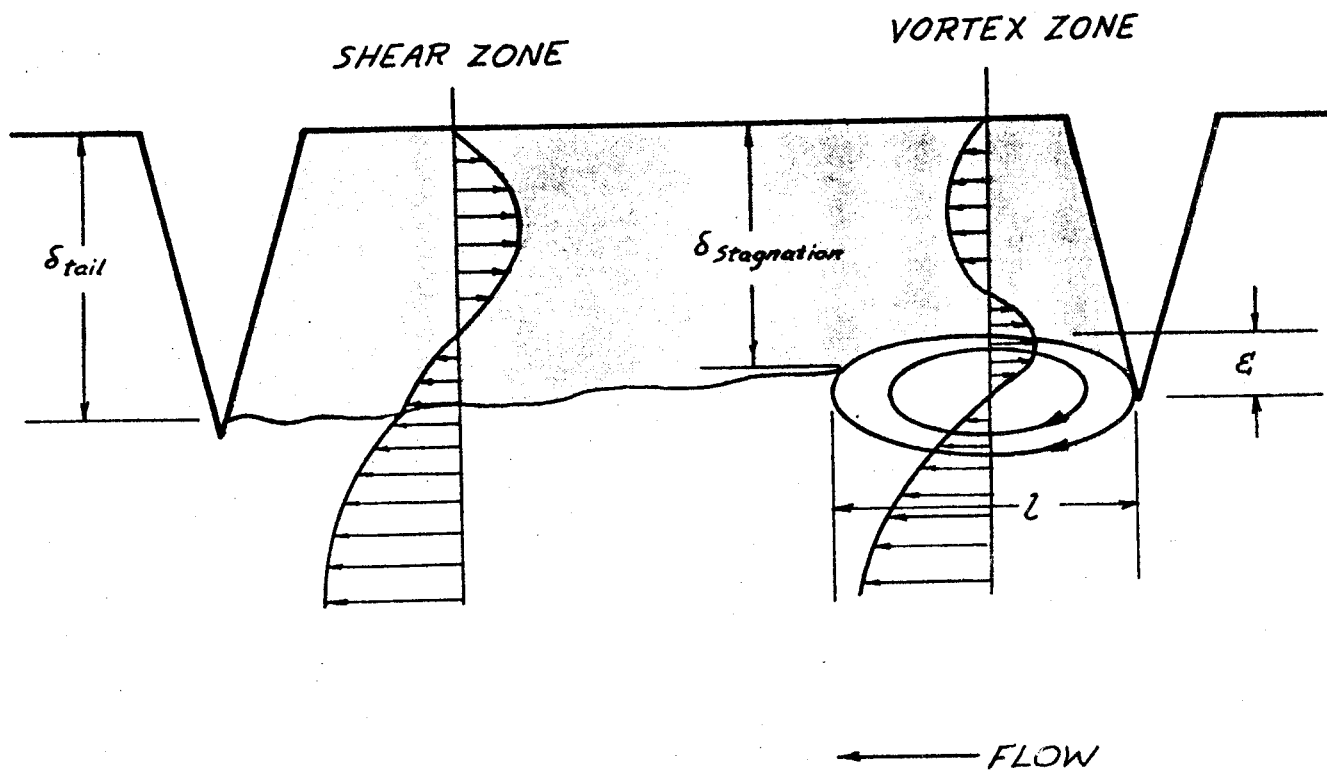


Figure D.8. Generalized Description of Oil Contained in an Ice Roughness Cavity Under the Influence of a Current

The thickness at the tail can never exceed the roughness height of the tail. If the vortex zone has penetrated the cavity so deep that the interfacial shape can no longer remain parabolic, and if the slick stays attached to the tip of the roughness, draining of oil from the cavity will occur until the oil-water interface has retreated to a parabolic shape higher up in the cavity. If local flow conditions are high enough, a Kelvin-Helmholtz type instability will develop and drain the oil from the cavity regardless of its depth. A representation of the total slick behavior as a function of increasing current speed is shown in Figure D.9.

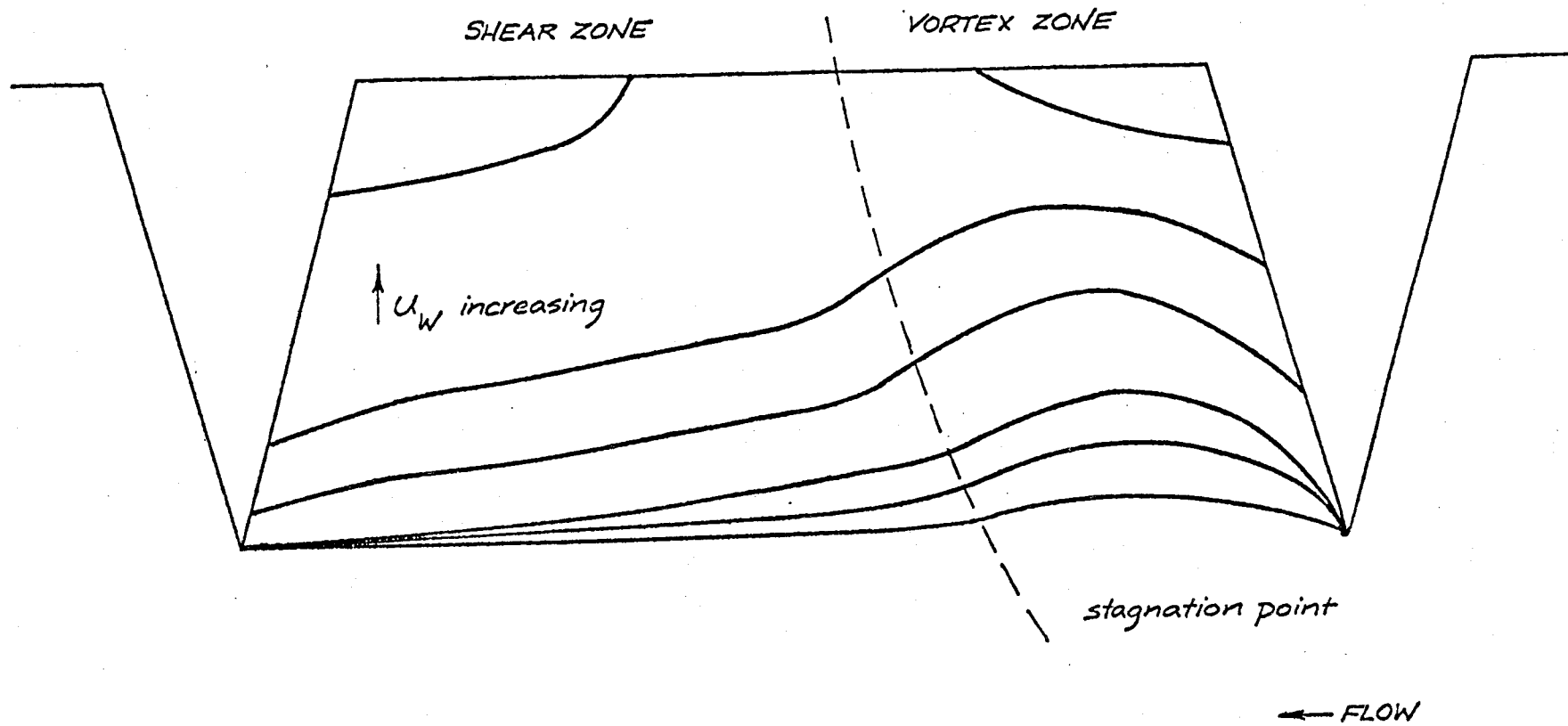


Figure D.9. Schematic Representation of the Shift in Oil-Water Interface Position Within a Cavity as a Function of Increasing Current

APPENDIX E
VELOCITY PROFILES

In order to calculate under ice shear stresses and establish the flow patterns in the wakes of ice roughness elements, it was necessary to obtain velocity profiles in the flume. To determine under ice shear stress, velocities were profiled in six different locations along the flume as shown in Figure E.1. The flowrate was set for a mean current of 16 cm/sec, and velocity profiles were measured with a Nixon probe. The measured velocities at various depths beneath the ice are given in Table E.1. The velocity profiles are plotted in Figures E.2 through E.7.

Using a similar procedure, velocity profiles were measured at various stations in the wake of a 10 cm ice roughness element for mean currents of 20.5 and 31 cm/sec. Because of the blockage caused by the ice roughness, local mean velocities were increased by 25%. The measured currents are tabulated in Tables E.2 and E.3. The profiles are plotted in Figures E.8 and E.9.

The Nixon probe is a miniature current flowmeter designed for measuring very low rates of flow in a conductive fluid, usually water. The miniature measuring head, with a cage approximately 1.5 cm in diameter, enables readings to be taken in small ducts and provides the means for accurate measurement of flow in hydraulic models of rivers. The system is highly sensitive, responding to flow velocities as low as 2 cm/sec. The measuring head consists of a five bladed impeller mounted on a hard stainless steel spindle. As a blade of the impeller passes the sensor, a change in resistance is sensed, and the frequency is counted and displayed on a variable time base counter. Using the calibration curve supplied with the probe, velocities can be obtained from the reading.

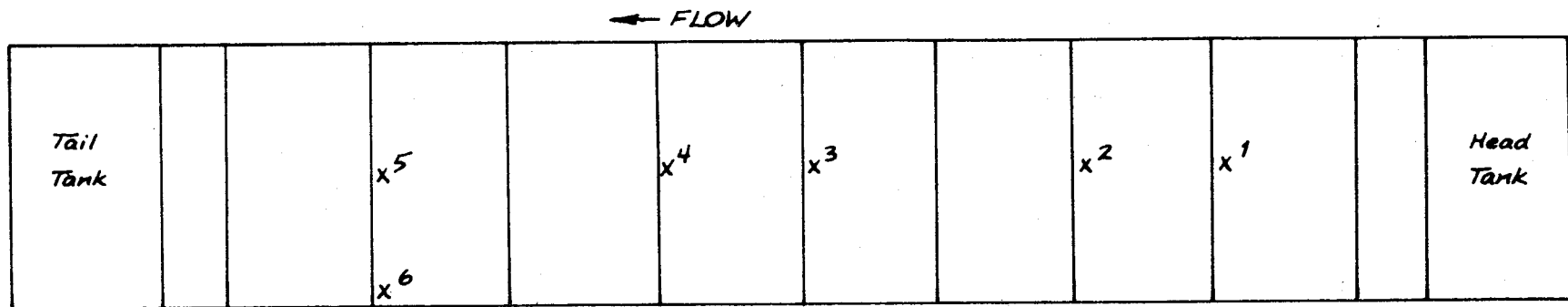


Figure E.1. Locations where Velocity Profiles were Measured in the Flume

TABLE E.1 FLUME VELOCITY PROFILE DATA

DEPTH FROM ICE BOTTOM (cm)	VELOCITY AT STATION 1 (cm/sec)	VELOCITY AT STATION 2 (cm/sec)	VELOCITY AT STATION 3 (cm/sec)	VELOCITY AT STATION 4 (cm/sec)	VELOCITY AT STATION 5 (cm/sec)	VELOCITY AT STATION 6 (cm/sec)
0.25	13.17	11.90	12.30	12.44	10.72	10.84
0.50	11.68	13.80	12.62	12.16	11.26	14.20
0.75	14.20	12.72	14.04	12.80	13.20	12.32
1.00	16.48	14.40	13.94	13.44	12.00	14.76
1.25	14.22	14.68	14.78	13.64	13.02	14.58
1.50	15.66	16.64	13.50	13.64	13.66	13.50
1.75	15.54	16.46	15.56	16.00	14.38	14.42
2.00	13.18	15.60	15.88	13.94	13.56	15.50
2.50	16.60	15.72	15.56	17.20	14.42	15.50
3.00	15.86	15.28	16.54	16.44	15.56	15.70
3.50	17.48	17.52	17.80	16.76	16.50	15.14
4.00	15.66	16.72	18.28	18.52	15.08	16.74
4.50	18.84	17.86	18.00	18.22	17.06	16.00
5.00	18.42	15.26	19.88	18.96	17.38	16.62
6.00	18.38	17.92	18.20	18.34	16.92	17.80
7.00	16.32	18.88	19.94	19.56	18.94	17.34
8.00	17.68	16.54	21.48	17.80	17.90	16.56
9.00	17.64	19.80	20.46	19.74	17.68	17.06
10.00	19.54	17.36	20.20	21.20	20.64	17.16

Water Depth = 46.5 cm

Nominal Current = 16 cm/sec

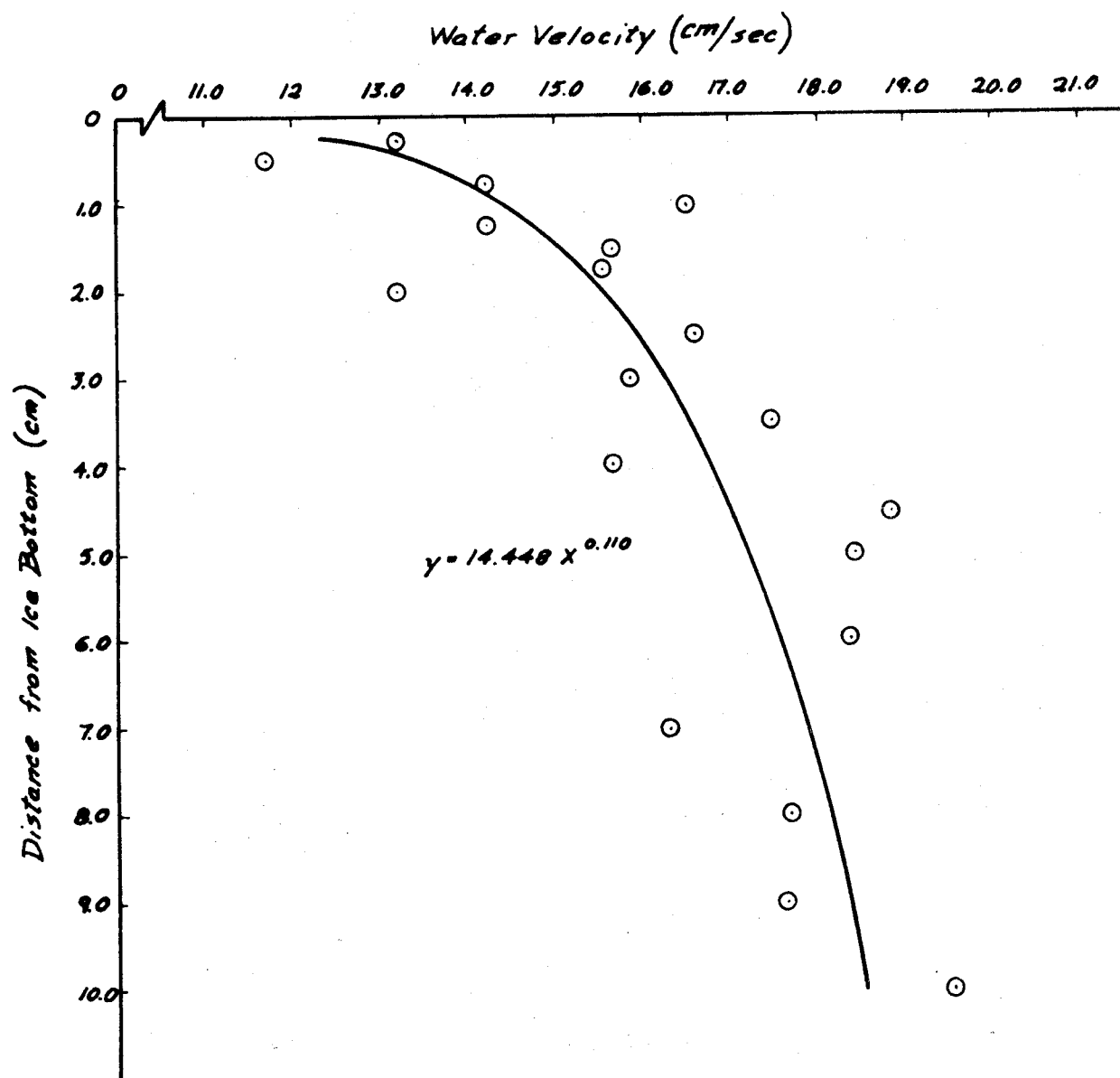


Figure E.2. Velocity Profile at Position No 1. With Flow Rate of 1100 gpm

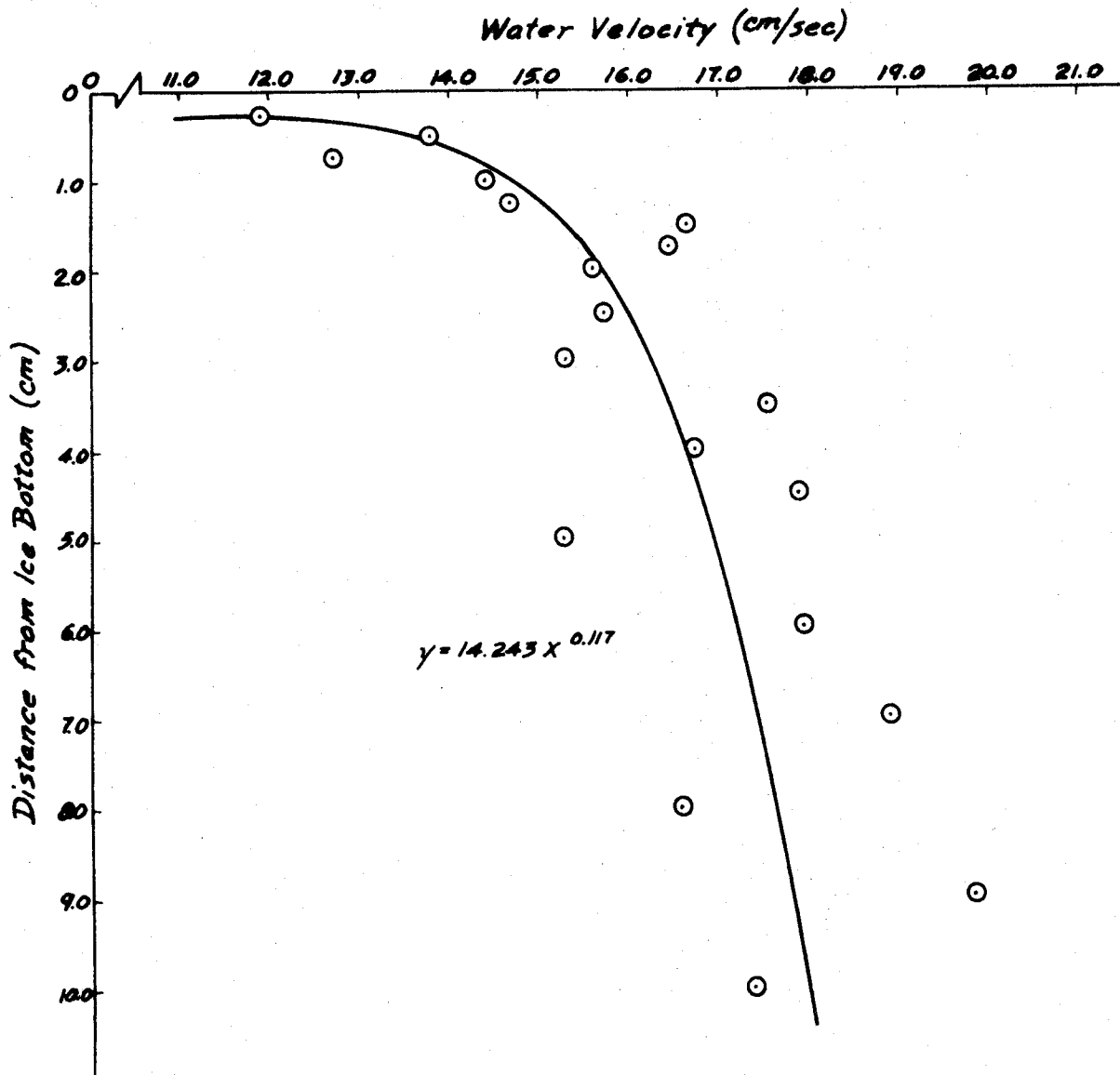


Figure E.3. Velocity Profile at Position No. 2 with Flow Rate of 1100 gpm

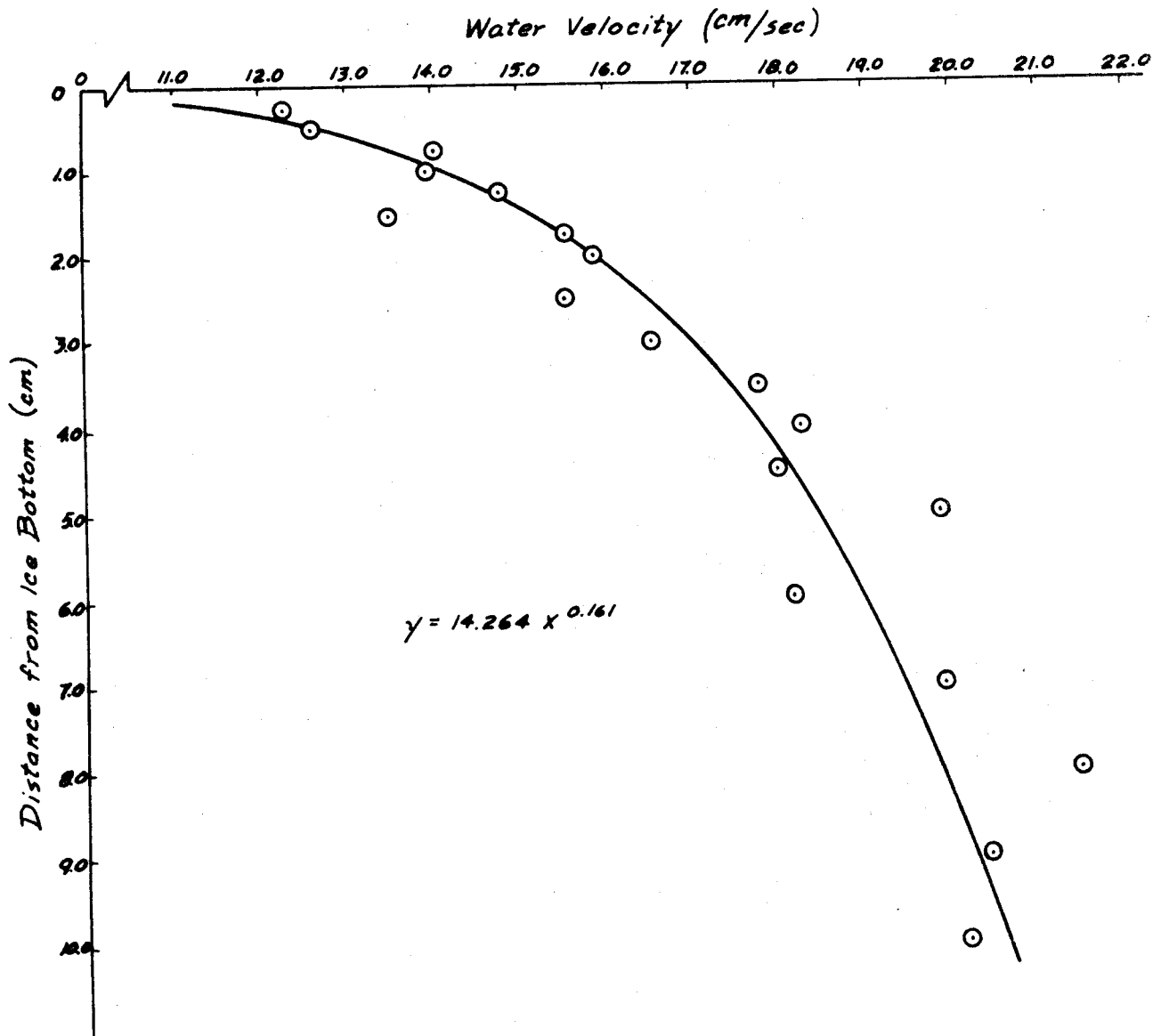


Figure E.4. Velocity Profile at Position No. 3 with Flow Rate of 1100 gpm

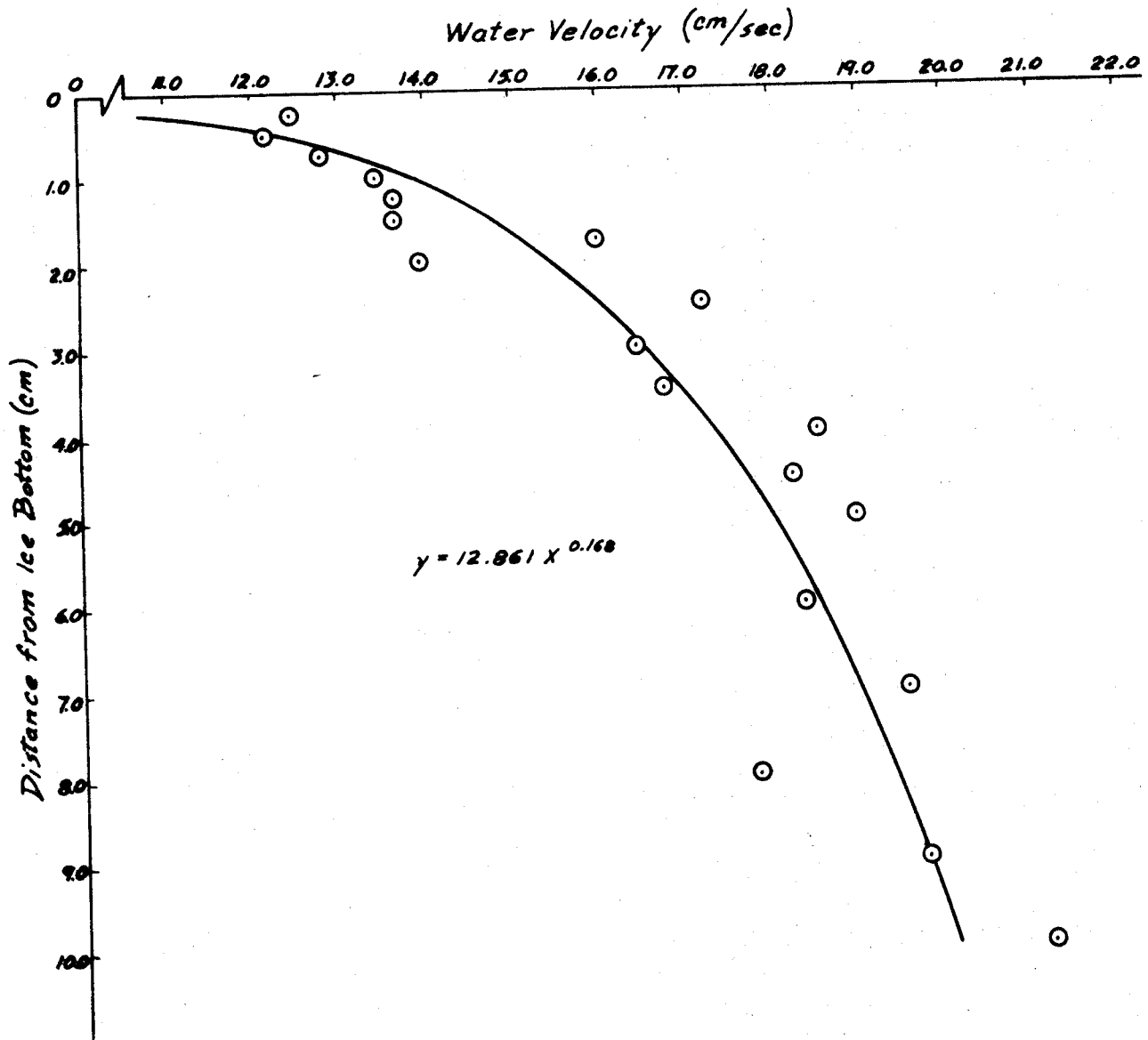


Figure E.5. Velocity Profile at Position No.4 with Flow Rate of 1100 gpm

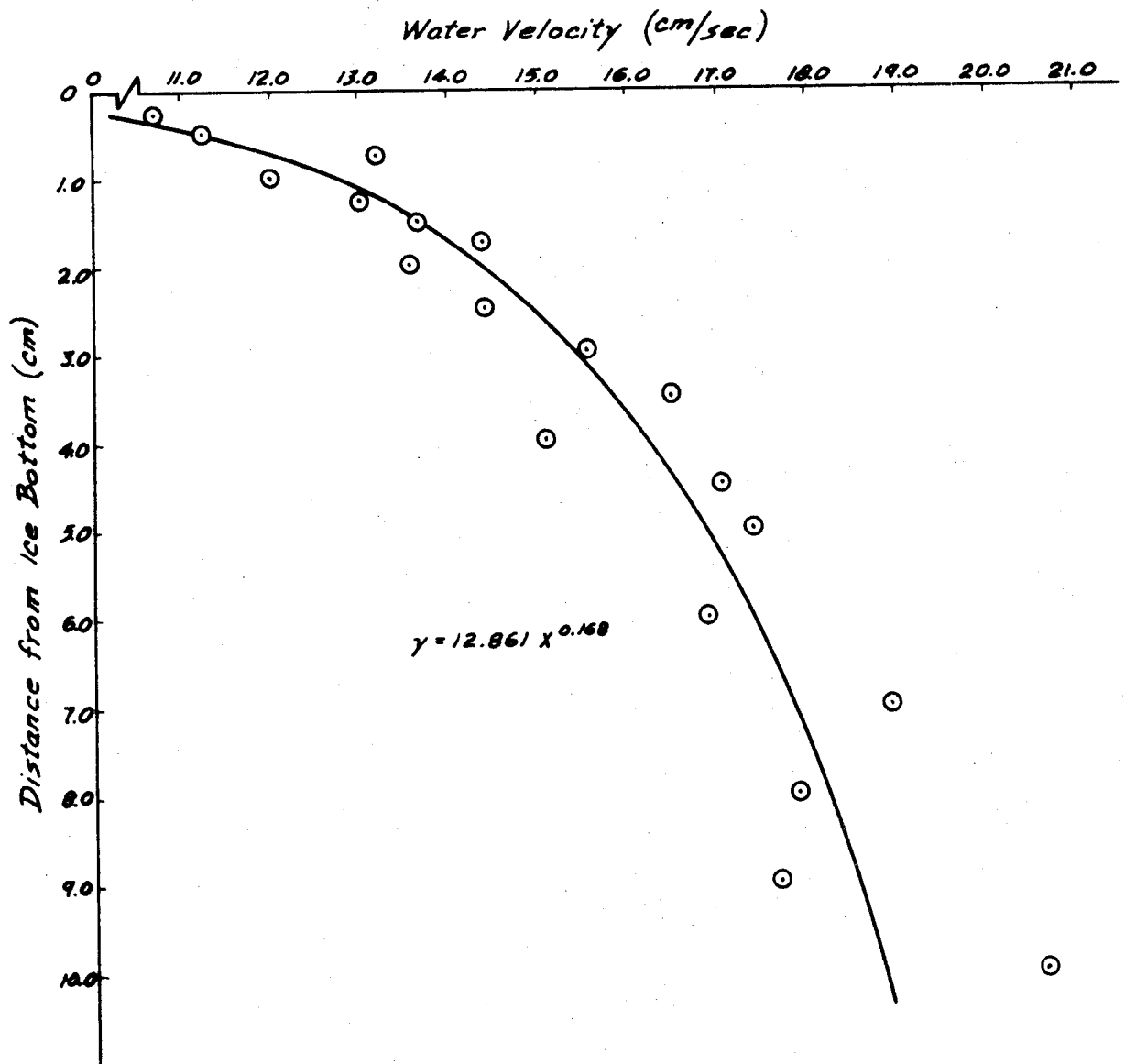


Figure E. 6. Velocity Profile at Position No. 5 with Flow Rate of 1100 gpm

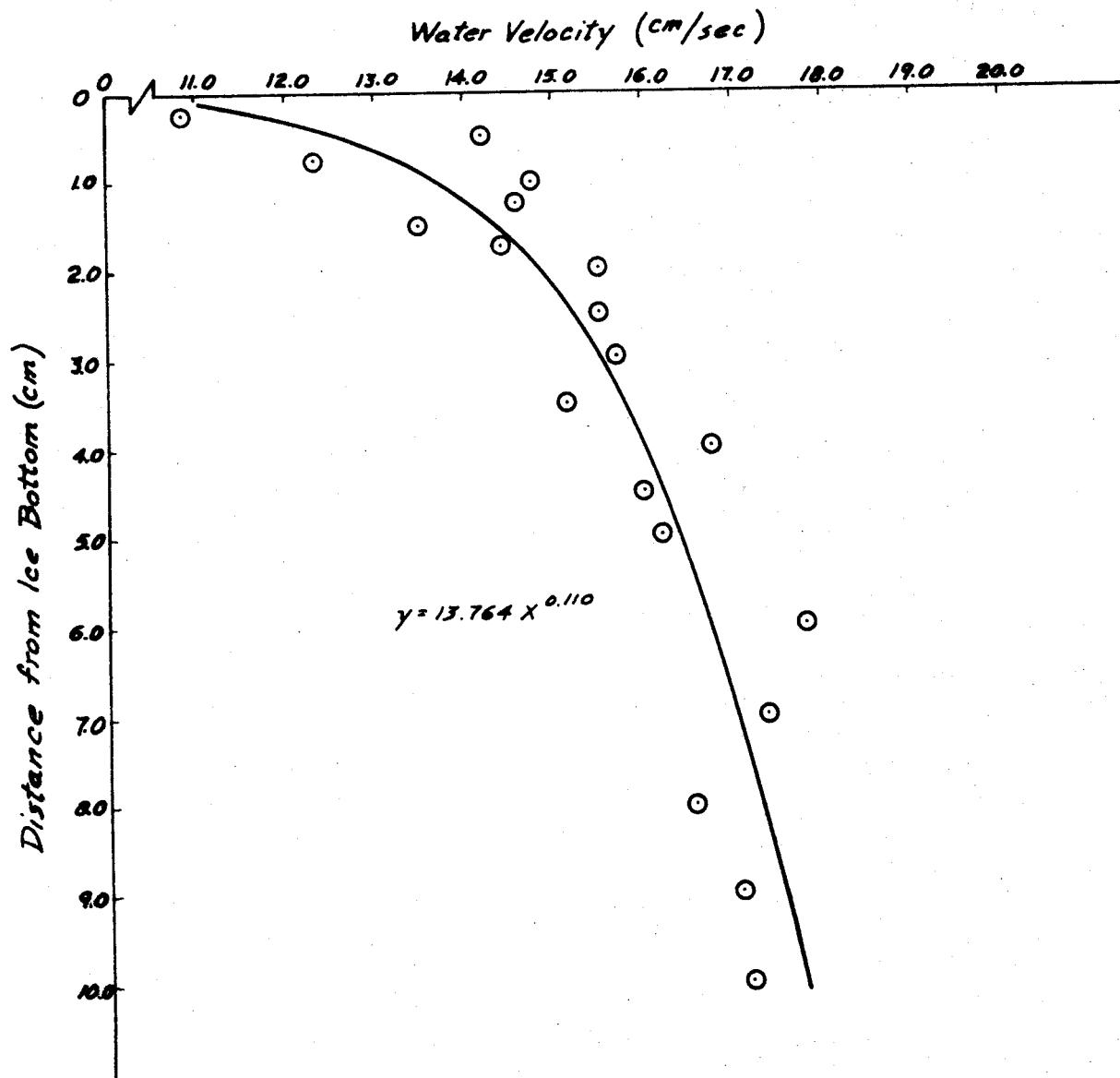


Figure E.7. Velocity Profile at Position No. 6 with Flow Rate of 1100 gpm

TABLE E.2 VELOCITY PROFILES MEASURED DOWNSTREAM OF A 10 CM DEEP ICE
ROUGHNESS ELEMENT FOR A CURRENT VELOCITY OF 20.5 CM/SEC

DEPTH BELOW LEVEL ICE (cm)	0 CM AFT		20 CM AFT		40 CM AFT		60 CM AFT	
	AVERAGE VELOCITY (cm/sec)	DIRECTION	AVERAGE VELOCITY (cm/sec)	DIRECTION	AVERAGE VELOCITY (cm/sec)	DIRECTION	AVERAGE VELOCITY (cm/sec)	DIRECTION
1	4.2	R	8.5	R	7.8	R	4.8	F/R
3	5.8	R	16.0	R	7.1	R	8.6	F
5	5.4	R	9.1	R	5.8	R		
7	4.7	R	7.7	R	6.1	F/R		
9	4.8	R	5.4	R	-	F/R		
11	8.5	F/R	6.8	F/R	9.6	F		
13	12.7	F	10.8	F/R	10.7	F		
15	-	-	16.2	F				

Notes: F indicates direction of mean flow
R indicates reverse flow

TABLE E.3 VELOCITY PROFILES MEASURED DOWNSTREAM OF A 10 CM DEEP ICE
ROUGHNESS ELEMENT FOR A CURRENT VELOCITY OF 31 CM/SEC

DEPTH BELOW LEVEL ICE (cm)	0 CM AFT		20 CM AFT		40 CM AFT		60 CM AFT	
	AVERAGE VELOCITY (cm/sec)	DIRECTION	AVERAGE VELOCITY (cm/sec)	DIRECTION	AVERAGE VELOCITY (cm/sec)	DIRECTION	AVERAGE VELOCITY (cm/sec)	DIRECTION
1	8.4	R	14.4	R	6.3	R	8.9	R
3	6.5	R	12.7	R	7.4	R		
5	7.0	R	12.0	R	7.4	R		
7	6.8	R	9.3	R	-	F/R		
9	7.5	R	-	F/R	10.1	F		
11	6.5	F/R	-	F/R	12.7	F		
13	18.0	F	18.4	F	16.8	F		
15	42.8	F	22.8	F				

Notes: F indicates direction of mean flow
R indicates reverse flow

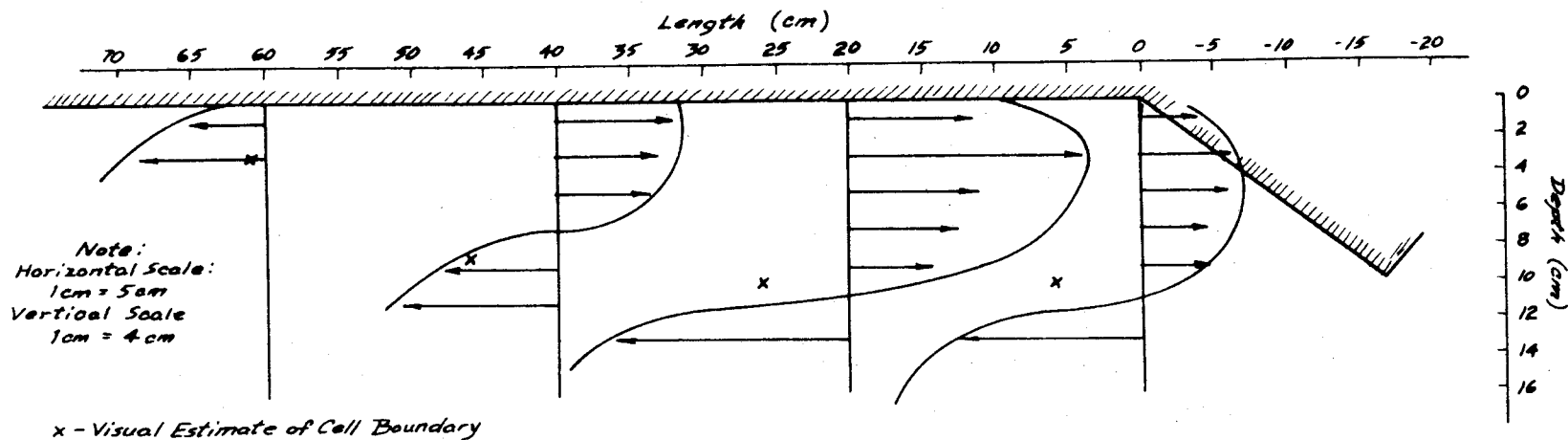


Figure E.8 Plots of Velocity Profiles Measured Downstream of a 10 cm Deep Ice Roughness Element for a Current Velocity of 20.5 cm/sec.

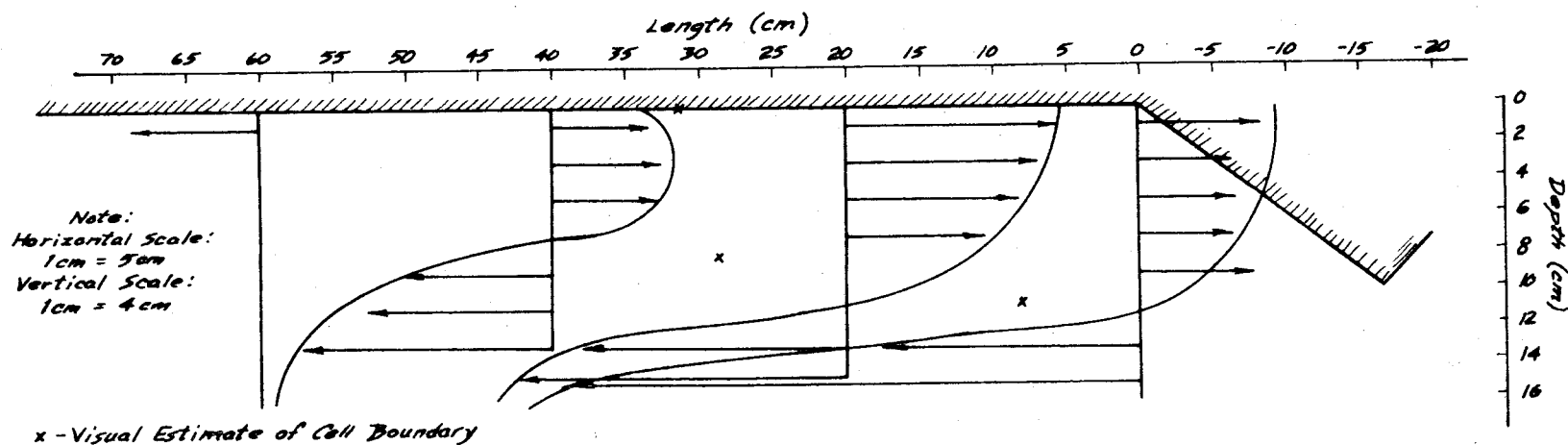


Figure E.9 Plots of Velocity Profiles Measured Downstream of a 10 cm Deep Ice Roughness Element for a Current Velocity of 31 cm/sec.

APPENDIX F

TEST EQUIPMENT

F.1 ARCTEC Ice Flume

The experiments of this study were conducted in the insulated glass walled ARCTEC Ice Flume. A sketch of the flume is presented as Figure F.1. The test section of the flume is 13.7 m long, 0.94 m wide, and 0.61 m deep. The flume is located in ARCTEC's insulated low temperature test facility. Ice is made in the flow section by using a patented liquid nitrogen system. The glass walls, channel bottom, return pipe, and the drive unit of the flume are insulated during the freezing process to prevent ice formation inside the system. The discharge capacity of the flume is about 140 liters per second with 40 centimeters of water, achieved by a 10 horsepower variable speed motor and a 25 centimeter axial flow pump. The maximum allowable water depth in the flume is 46 centimeters with 18 centimeters of freeboard. The discharge of the flume is measured by an annubar flow sensor connected in parallel with two eagle eye flow meters. This system measures the flow rate directly in gallons per minute.

F.2 Viscometer

A Brookfield Synchroelectric Viscometer, Model LVT, was used to measure apparent viscosity. The viscometer operates by rotating a cylinder or disc in the fluid and measuring the torque necessary to overcome the viscous resistance to movement. This is accomplished by driving the immersed element, which is called a spindle, through a beryllium copper spring. The degree to which the spring is wound, indicated by the position of a pointer on the viscometer's dial, is proportional to the viscosity of the fluid for any given speed and spindle. For a material of given viscosity, the drag will be greater as the spindle size and/or rotational speed increase. The minimum range of the viscometer is obtained by using the largest spindle at the highest speed, and the maximum range by using the smallest spindle at the slowest speed. The viscosity measurement procedures used are in accordance with ASTM specifications D 2983-72.

F.3 Annubar and Eagle Eye Meters

The annubar flow sensor is an annular averaging velocity head sensor designed for the measurement of flow through a pipe. It produces an extremely accurate and repeatable differential pressure proportional to the square of the fluid velocity with little permanent pressure loss. This sensor is accurate to 1.0% of actual value, and is repeatable to 0.1% of actual value.

The annubar may be installed in any plane of the pipe, vertical, horizontal, 45°, or any angle in between. Consideration must be given, however, to the type of flowing fluid and the secondary instrumentation. For a liquid flowing through a horizontal pipe, such as the flume situation, it is best to install the annubar in the bottom or side of the pipe so the instrument connections are below the pipe centerline. This will ensure that the instrument lines are full of liquid and not air or gas.

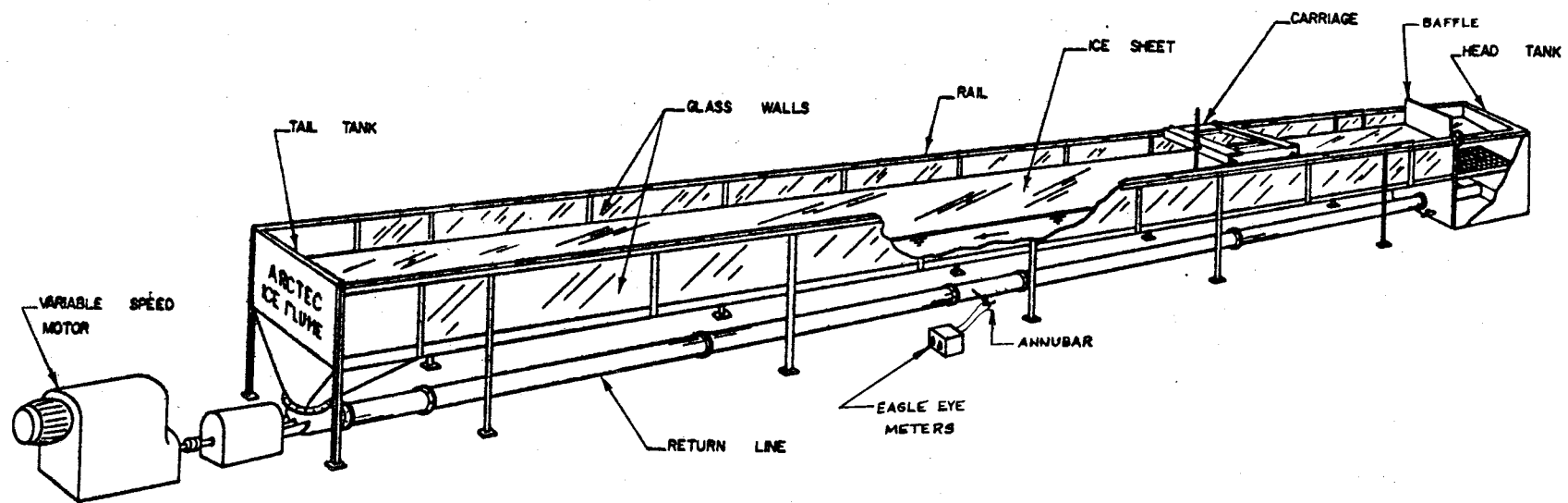


Figure F.1 - Schematic Drawing of ARCTEC Ice Flume

To complete the flow sensing package, the annubar was connected in parallel with two eagle eye flow meters. These precalibrated meters are accurate and repeatable to 1.5% of full-scale. Model 6000B had a scale of 0 to 1200 gpm in 20 gpm increments, and model 6004B ranged from 0 to 4000 gpm in 50 gpm increments. The meters were mounted below the annubar instrument lines as prescribed to ensure that no air or gas was introduced into the meters.

F.4 Flume Work Carriage

The work carriage, shown in Figure F.2, served as a portable platform for some of the test apparatus. The Milliken camera was mounted on the carriage to obtain overhead movies of the advancing oil slick. An additional function of the work carriage was to measure oil slick velocities. A pointer bar was attached to the work carriage for that purpose. By keeping the pointer bar aligned with the leading edge of a moving oil slick, the slick position was followed. Slick velocities were then determined with two instruments, a DC tach generator and a magnetic reed switch. Both instruments were fastened to the wheel assembly of the carriage. The tach generator shaft was installed in contact with the carriage wheel and rotated as the carriage wheel turned, thus producing a signal related to velocity. The magnetic reed switch was mounted on the carriage wheel assembly with its sensor pointed at the wheel. For every wheel revolution, the magnetic trip inserted in the wheel passed by the read switch sensor producing a contact within the switch. Both velocity probes were connected to a light pen oscillograph recorder.

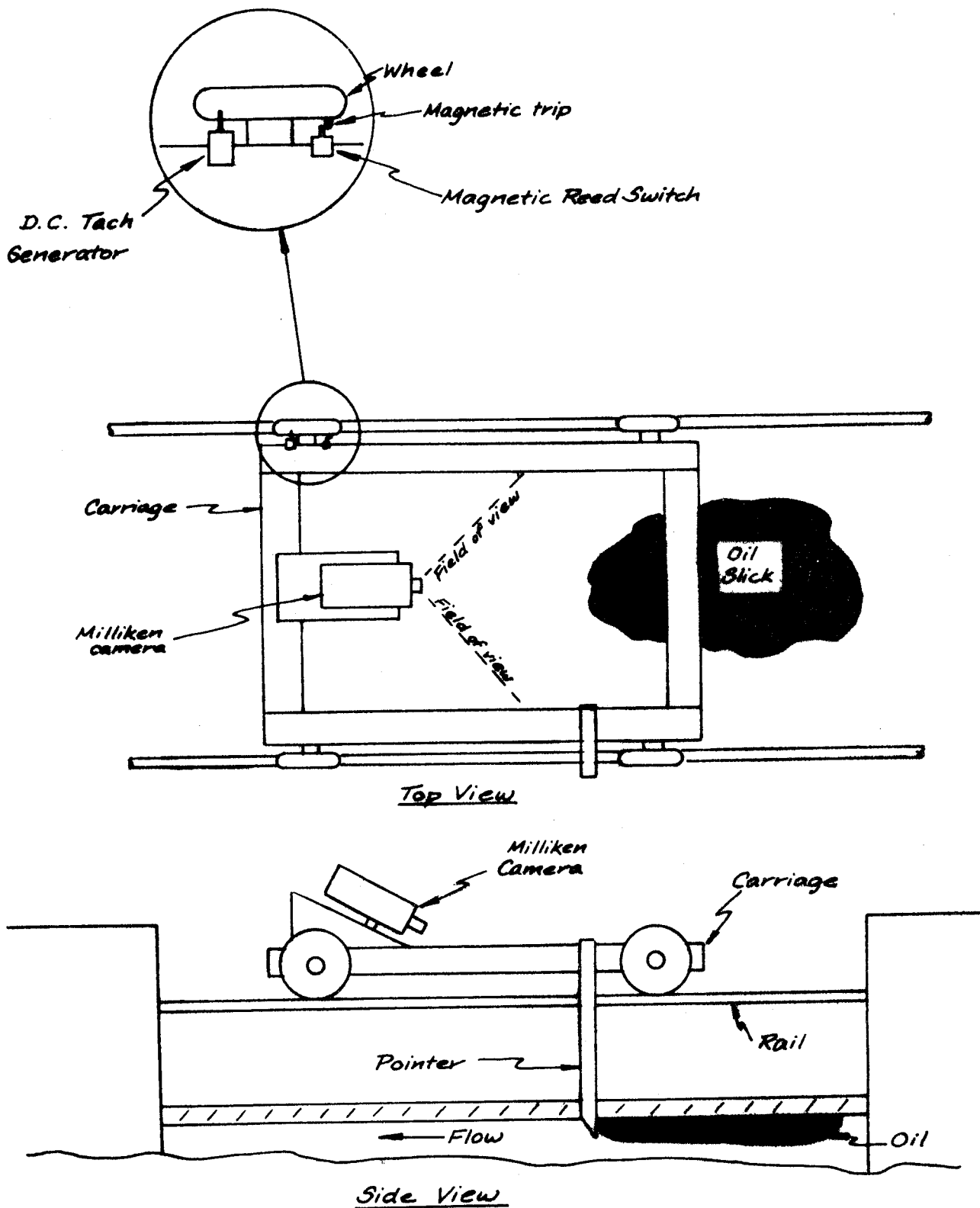


Figure F.2. ARCTEC Ice Flume Carriage Arrangement